Spin Dynamics of Correlated Radical Pairs in Quantum Biology and Quantum Information Science

Gediminas Jurgis Pažėra

Corpus Christi College
University of Oxford

A thesis submitted in partial fulfilment
of the requirements for the degree of

Doctor of Philosophy
in
Physical and Theoretical Chemistry

Physical and Theoretical Chemistry Laboratory

Trinity Term 2023

Spin Dynamics of Correlated Radical Pairs in Quantum Biology and Quantum Information Science

Gediminas Jurgis Pažėra

Abstract

of a thesis submitted for the degree of
Doctor of Philosophy

Coherently oscillating radical pairs are an important chemical system that can surprisingly appear in different domains, such as avian magnetoreception or as the basis of a qubit for quantum computation. This thesis is concerned with studying this system in different areas, focusing on simulations and the development of new computational tools.

First, we present two studies on avian magnetorecception. One is about how isotopic substitutions can affect the hypothesised compass mechanism of birds. The results of this study are planned to be used in future spectroscopic studies as well as behavioural experiments aimed at elucidating the origin of magnetic sensing in avian species. The other study involves examining the effect of stochastic, time-dependent magnetic fields on the compass mechanism. This study compares theoretical findings with behavioural experiments and provides evidence that the action-spectrum histogram, an approximate theoretical tool for quantifying the effect of radiofrequency noise, remains accurate in most circumstances.

In addition, we present a study on the design of EPR pulse sequences for organic molecular electron spin qubits. The study builds on existing work on this topic and demonstrates that previous studies had distinct flaws. As a result, a number of enhancements are proposed for producing improved pulse sequences, and an example of successful experimental use of pulse sequences is presented in one of the appendices. In addition, the study quantifies the effects of relaxation and nuclear spins on the performance of quantum logic gates.

The final chapter focuses on new additions to the software programme *MolSpin*, which is an advanced platform for calculations involving spin dynamics. These new additions are centred on the implementation of the stochastic Schrödinger equation and recent advances in the estimation of quantum mechanical traces. When you combine these methods with careful engineering, the use of modern linear algebra algorithms, and new ways to reduce the time it takes to integrate certain systems, you get a full toolkit that can simulate systems that weren't possible before. For instance, the singlet yield profile of a simulation of a system with 14 nuclear spins that follows the trajectory of a molecular dynamics simulation of a protein is shown in this chapter.

Publications

This thesis adopts the integrated thesis approach, which replaces the traditional thesis chapters with either published or unpublished articles that meet the standards of peer-reviewed publication. The articles listed below were included in this thesis:

1. **G. J. Pažėra**, P. Benjamin, H. Mouritsen, and P. J. Hore. Isotope Substitution Effects on the Magnetic Compass Properties of Cryptochrome-Based Radical Pairs: A Computational Study. *The Journal of Physical Chemistry B*, 127, 838–845, 2023.
2. **G. J. Pažėra**, and P. J. Hore. Simulation of Radiofrequency Magnetic Field Effects on a Radical Pair Cryptochrome-Based Magnetoreceptor. *Unpublished* 2024.
3. **G. J. Pažėra**, M. D. Krzyaniak, and M. R. Wasielewski. Pulse Sequences for Manipulating the Spin States of Molecular Radical-Pair-Based Electron Spin Qubit Systems for Quantum Information Applications. *The Journal of Chemical Physics*, 158(20), 204118 2023.
4. **G. J. Pažėra**, I. A. Solov'yov, P. J. Hore and L. Gerhards. Exploring the Radical Pair Mechanism in Large Spin Systems - Introducting the Stochastic Schrödinger Equation into *MolSpin*. *Unpublished* 2023.
5. H. Mao, **G. J. Pažėra**, R. M. Young, M. D. Krzyaniak, and M. R. Wasielewski. Quantum Gate Operations on a Spectrally Addressable Photogenerated Molecular Electron Spin-Qubit Pair. *Journal of the American Chemical Society*, 145, 6585–6593, 2023.

The vast majority of the thesis is my own work, but some work has been done by my collaborators. In particular, I would like to attribute the Redfield calculations in Article 4 on MolSpin to Dr Luca Gerhards, who is a co-author of that publication.

❧

Acknowledgements

Many people have been directly or indirectly responsible for the writing of this thesis, and I would like to express my sincere appreciation to each of them.

I thank Peter J. Hore and David E. Manolopoulos, my supervisors. Particularly Peter, who has maintained a high level of rigour in my research work, pushing my understanding and "carefulness" of conducting theoretical research while providing a lot of assistance while tackling spin dynamics, always answering any queries I had and guiding me throughout the entire process. Additionally, I appreciate David's expert advice on spin dynamics and numerical algorithms, which made my research studies much better. In addition to learning how to approach and solve simulation problems creatively.

I would like to thank the members of the Hore group, the other members of the Spin Chemistry group at Oxford, and our German collaborators at Oldenburg University. Luca Gerhards, with whom I thoroughly enjoyed working on *MolSpin* because he was always positive, patient, and willing to listen to my ideas on spin dynamics, deserves special recognition. In addition, I would like to thank Thomas Player from the Hore group for helping me get started with spin dynamics at the beginning of my thesis and Thomas Fay for his expert advice on spin dynamics throughout my thesis.

I want to thank the Oldenburg's Mouritsen and Solov'yov groups for their hospitality during my short visit to the University of Oldenburg in 2022. It was very insightful to see the set ups of behavioural experiments as well as how proteins are synthesized in the lab. It just makes me more grateful that I can be useful and participate in research in my front of my computer. No computational or theoretical study in any area of science would be possible without the work of numerous experimentalists over the years.

A huge thanks goes to the Hertford College, Oxford community, which has been my "home" during my almost 3 years of being a lecturer there, which was cut short due to my health issues. It has been a pleasure teaching first-year chemistry students, carrying out undergraduate admissions, and enjoying other perks of being a college lecturer. I want to thank everyone on the Chemistry team, Patrick, Thomas, Mike, Claire, and Fernanda, for making it a very enjoyable place to work. Also, I want to thank my fellow tutors and fellows of the college for great conversations during lunch and formal dinners: Alexandra, Andrew, Juuba, Oliver, Siddharth, Pat, Vladyslav, Clive, Benjamin, Thomas, Bohao, Tom, and many others.

Many thanks to Michael R. Wasielewski for permitting me to work in his Northwestern University lab during the summer of 2022. It has been the most enjoyable period of my degree in terms of science, during which I have learned so much about a variety of topics and experienced the research culture in the United States, which I wholeheartedly relished. Matthew Krzyaniak, who answered all of my "stupid" and "basic" EPR questions and has been an invaluable part of my trip, and Haochan Mao, who was a great person to work with and who was able to implement my ideas on pulse sequences to produce a great publication on quantum gate applications to molecular radical pair systems, deserve special recognition. Also deserving of special mention is Rytis Paulauskas, whom I visited in New York during my research stay at Northwestern. First, I want to thank him and his wife Rūta for their hospitality during my visit. Other than that, despite the brief time I've known him, Rytis has been a "deep well" of knowledge and inspiration for me, and I regard him as a model for an excellent leader. His dedication and devotion to my native country through his diplomatic work as a Lithuania's permanent representative in United Nations continues to inspire me to contribute to the development of our small nation in the best ways I can.

I would not likely be here today without the dance and martial arts communities, as well as movement in general. These areas have always pushed me to be better, helped me to better comprehend myself, provided me with energy during low points, and instilled in me the discipline that has carried over into other areas of my life. There are simply too many people in this field to name, so I would like to recognise a few of my teachers who, in addition to teaching me the mastery of their arts, imparted profound life lessons and perspectives through their lessons and conversations: Marcelo Alcazar, Donatas Mankevičius, James Halfhide, and Max Campos. In addition, I'd like to thank my peers from Dancesport and Latin dances at Oxford, as well as Latin dances in Lithuania, for all the memorable events and practises.

There have been other special people and friends that I want to mention: Elvinas J., Inga B., Miriam G., Adomas P., Vytautas V., Vytautas M., Christiana S., Kamilė S., Nik G., Matty M., Annie W. Y., Elvinas P., Liudas K., Michael W.,

Gedvydė C., Algirdas T., all of the old friends from the University of Warwick and their friends, and many other people that I have not named here.

Thanks to my parents and family members for their love and support throughout all of the years.

Gediminas Jurgis Pažėra
Oxford, September 2023

Contents

1 Introduction

The spin-correlated radical pair represents a noteworthy chemical system that serves as the fundamental foundation for the scientific discipline commonly known as "*Spin Chemistry*".[1–5] This phenomenon involves the interaction between two entangled unpaired electrons, along with the interplay of a surrounding "bath" consisting of nuclear spins and external magnetic fields that affects the outcome of the recombination reactions of electrons.[3,5] This kinetic scheme, called the radical pair mechanism (RPM), is able to capture magnetic field effects that show up as a change in the yields of recombination reactions.[1,3] Very weak magnetic fields that are insignificant compared to the thermal motion of molecules can have a significant impact on RPM.[1–5] This can be explained as an outcome of quantum mechanical coherence, which is observed even at room temperature for these systems.[3,6] The use of this system is ubiquitous, from forming the hypothesis of avian magnetoreception[5,7–9] to serving as a qubit for a quantum computer.[10–14] Radical pair reactions in different domains and their simulations on modern computers that aid experimental and theoretical research will be the central topic of this thesis.

This chapter begins with an overview of the quantum mechanical property of spin and then explores the fundamental ideas that underlie the RPM. Additionally, we will delve into the application of quantum dynamics to modelling these systems. Furthermore, we shall elucidate the significant interactions between electron and nuclear spins, which together form the spin Hamiltonian. Subsequently, we will examine the significant application of the radical pair mechanism in the fields of quantum biology, quantum information science, and related subjects. In the end, we will present the primary ideas of this thesis, which will provide a context for further discussion of RPM.

Spin 1.1

Spin is a quantum mechanical property of electrons and nuclei that manifests in relativistic quantum mechanics.[15] This is the central property under investigation in spin dynamics simulations and experiments. In this section, we will examine the fundamental characteristics and quantum mechanical attributes of spin. These features will be elaborated upon in subsequent sections as we delve into the quantum dynamics associated with these spin states.

Spin is a purely quantum property that is at times referred to as the "intrinsic" angular momentum (as opposed to the orbital angular momentum that describes the spatial part of the particles).[16] Spin for a particle is described by the total spin angular momentum quantum number, S, and the spin magnetic number m_S. S can take either non-negative integer or half-integer values and m_S can have values $m_S \in \{-S, -S+1, \dots, S-1, S\}$. For instance, for $S = 1/2$ the possible m_S values are $+1/2$ and $-1/2$. In general, a particle with S will have a total of $2S+1$ possible spin states.

The spin angular momentum $\hat{\mathbf{S}}$ is a vector property, with $\hat{\mathbf{S}} = \left(\hat{S}_x, \hat{S}_y, \hat{S}_z\right)^T$, where $\hat{S}_x$, $\hat{S}_y$, $\hat{S}_z$ are its three Cartesian components. These operators obey these commutations relations:[17]

$$\left[\hat{S}_j, \hat{S}_k\right] = i\hbar\epsilon_{jkl}\hat{S}_l \tag{1.1}$$

Here, j, k, l can be one of x, y, z, $[A, B] = AB - BA$, i.e. a commutator, and ϵ_{jkl} is the Levi-Civita symbol, in 3 dimensions defined as:[17]

$$\epsilon_{ijk} = \begin{cases} +1, & \text{if } (i, j, k) \text{ is } (1,2,3),\ (2,3,1) \text{ or } (3,1,2), \\ -1, & \text{if } (i, j, k) \text{ is } (3,2,1),\ (2,1,3) \text{ or } (1,3,2), \\ 0, & \text{if } i = j, \text{ or } j = k \text{ or } k = i \end{cases} \tag{1.2}$$

The square of the total spin angular momentum, $\hat{S}^2 = \hat{\mathbf{S}} \cdot \hat{\mathbf{S}}$, can be shown through the use of commutation relations to commute with each Cartesian spin operator:[17]

$$\left[\hat{S}^2, \hat{S}_i\right] = 0 \tag{1.3}$$

It follows that the eigenstates of spin, defined by m_S and S, for $\hat{S}^2$ and $\hat{S}_z$ operators are:[17]

$$\begin{aligned} \hat{S}^2 \left|S, m_S\right\rangle &= \hbar^2 S(S+1) \left|S, m_S\right\rangle \\ \hat{S}_z \left|S, m_S\right\rangle &= \hbar m_S \left|S, m_S\right\rangle \end{aligned} \tag{1.4}$$

In this thesis, the most common spin number S will be $1/2$ (such as for an electron spin or a ^{1}H nuclei) and 1 (such as for a ^{14}N nuclei). Also, the eigenstates of an electron spin (that has $S = 1/2$) are very frequent in simulations and experiments, thus, they have specific labels, $|\alpha\rangle$ for the "spin up" state and $|\beta\rangle$ for the "spin down" state:[17]

$$|\alpha\rangle = \left|\frac{1}{2}, \frac{1}{2}\right\rangle \text{ and } |\beta\rangle = \left|\frac{1}{2}, -\frac{1}{2}\right\rangle \tag{1.5}$$

Spin operators are defined as Hilbert space matrices and this formalism will be used throughout the thesis. Each Cartesian spin operator is defined through a

Pauli matrix σ_i, which for $S = 1/2$ are:[17]

$$\begin{aligned}\sigma_x &= \begin{pmatrix} 0 & 1 \\ 1 & 0 \end{pmatrix},\\ \sigma_y &= \begin{pmatrix} 0 & -i \\ i & 0 \end{pmatrix},\\ \sigma_z &= \begin{pmatrix} 1 & 0 \\ 0 & -1 \end{pmatrix}.\end{aligned} \tag{1.6}$$

Each spin operator will be $\hat{S}_i = \hbar\sigma_i/2$. Also, note that the dimensions of the Pauli matrices match the number of possible spin states–this remains true for any total spin angular momentum quantum number S. Pauli matrices are also examples of hermitian operators, since $\sigma_i = \sigma_i^\dagger$ († denotes conjugate transpose). This is an important property for quantum mechanical operators and is a fundamental property of the Hamiltonian, $\hat{H}$, constructed from Cartesian spin operators. Note, there are analogous Pauli matrices for other S values yet they will not be demonstrated here.

While modelling radical reactions, we will be interested in spin systems that interact with one another. Such as a pair of electron spins, which is central to the thesis and serves as the foundation for the radical pair model. The electron spins can couple in a similar way as angular momentum does. Two electron spins, $\hat{\mathbf{S}}_1$ and $\hat{\mathbf{S}}_2$, will have total angular momentum $S = 1, 0$ (the total spin angular momentum can be added parallel or anti-parallel). When the spins are coupled, we find that the total number of states is a multiple between possible states of each individual system, in this case 4. The first of these possible states comes from the situation $S = 0$, in which case the coupled systems spin magnetic number can only be equal to $M_S = 0$. This is referred to as a singlet state, $|S\rangle$:[17]

$$|S\rangle = |0,0\rangle = \frac{1}{\sqrt{2}}\left(|\alpha_1\rangle \otimes \left|\beta_2\right\rangle - \left|\beta_1\right\rangle \otimes |\alpha_2\rangle\right) \tag{1.7}$$

Here $\otimes$ is a tensor product that is used for coupled spin systems. When $S = 1$, the spin magnetic number has 3 different values $M_S = -1, 0, 1$, which correspond to these 3 states, labelled as $|T_-\rangle$, $|T_0\rangle$ and $|T_+\rangle$, respectively:[17]

$$\begin{aligned} |T_-\rangle &= |1,-1\rangle = \left|\beta_1\right\rangle \otimes \left|\beta_2\right\rangle \\ |T_0\rangle &= |1,0\rangle = \frac{1}{\sqrt{2}}\left(|\alpha_1\rangle \otimes \left|\beta_2\right\rangle + \left|\beta_1\right\rangle \otimes |\alpha_2\rangle\right) \\ |T_+\rangle &= |1,1\rangle = |\alpha_1\rangle \otimes |\alpha_2\rangle \end{aligned} \tag{1.8}$$

These are referred to as the Triplet states. When electrons are in orbitals, they follow the Pauli principle, which states that an electron in the orbitals of a single molecule has to have at least one unique quantum number.[17] Hence, the coupled electron states can only be in a singlet state where the electrons counteract each other and are paired. It is also called singlet because the multiplicity of this state is one. Also, the magnetic field does not influence this state because the total spin momentum is zero (splitting of spectral lines is governed by the Zeeman effect, extensively studied in this Sec. 1.4). When the electron spins, however, are unpaired and in different orbitals, they no longer have the symmetry constraint of the Pauli principle and can interconvert to other states, i.e., the three triplet states, which are magnetically active. This is illustrated in Fig. 1.1. This dynamic leads to the radical pair mechanism detailed more in Sec. 1.2.

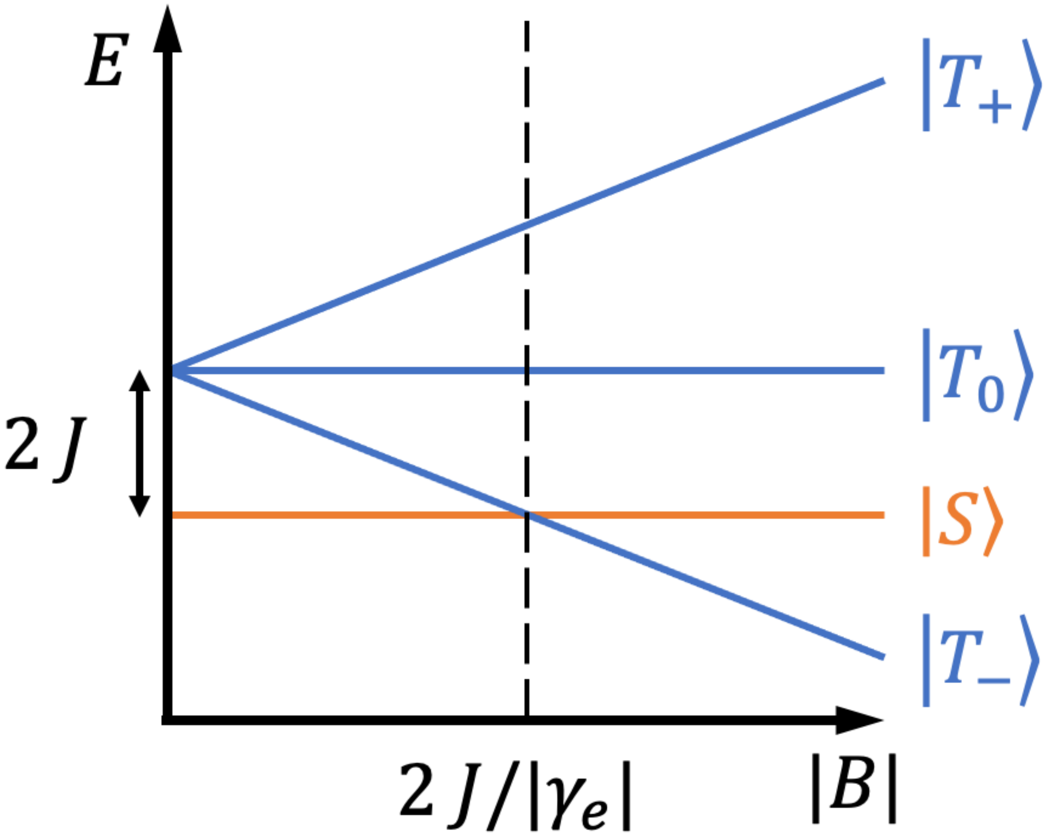

Figure 1.1 The relative energies of singlet, $|S\rangle$ and triplet states, $|T_{+,-,0}\rangle$, with increasing magnetic field strength $|\mathbf{B}|$. When $|\mathbf{B}| = 0$, then the singlet and triplet states are split by the exchange interaction J. We have assumed that $J > 0$, otherwise the singlet state would have higher energy than $|T_0\rangle$. γ_e is the gyromagnetic ratio of an electron.

In general, we will deal with systems that have more than two spins. The size of the system will grow exponentially with the number of spins (explained further in Sec. 2.1), so it will become harder to model these systems with increasing numbers of spins. There are different ways to circumvent this issue, and the discussion of this will be the basis of Chapter 2 which will go into the details of simulating complex spin systems.

Radical Pair Mechanism 1.2

In this section, we will examine the radical pair mechanism (RPM), the central point of study in much of spin chemistry and all of this thesis. The RPM reaction scheme, first proposed independently by Closs,[18] Kaptein, and Oosterhoff,[19] is detailed in Figure 1.2.[8,20]

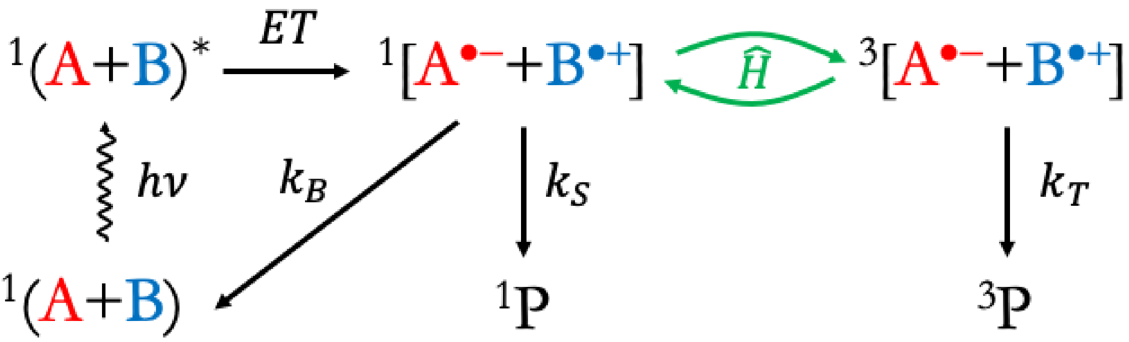

Figure 1.2 The general scheme of the radical pair mechanism. A spin correlated radical pair $^1[A^{\bullet-} + B^{\bullet+}]$ is formed after an initial excitation (usually by light, denoted by a label hv) followed by a series of electron transfers (denoted by a single arrow and label **ET**). This radical pair, initially in a singlet electronic state, coherently interconverts to the triplet state $^3[A^{\bullet-} + B^{\bullet+}]$, controlled by the system's Hamiltonian $\hat{H}$. During the reaction, the radicals can react to form either singlet ^1P or triplet ^3P products, as well as recombine to the ground state at a rate described by the backward recombination rate constant k_B.

The general mechanism of the RPM follows these steps:

1. Transition to an excited state by, usually, photoexcitation. Denoted as hv in the diagram.

2. Electron transfer step(s) (**ET**) to a spin correlated radical pair (SCRP) in an initial singlet state–$^1[A^{\bullet-} + B^{\bullet+}]$. The initial state is singlet due to the assumption that the spin is conserved during the electronic excitation and electron transfer step(s), due to small spin-orbit coupling.[7]

3. Singlet state coherently interconverts to the triplet state (defined as intersystem crossing, ISC) $^3[A^{\bullet-} + B^{\bullet+}]$ due to spin interaction described in Hamiltonian $\hat{H}$, which will be reviewed in detail in Sec. 1.4. This coherent inter-

conversion is illustrated for a model system without spin recombination in Fig. 1.3. The direction of applied field influences the S–T interconversion due to anisotropic hyperfine interactions in the system, hence, forming a basis of RPM systems being able to capture anisotropic effects, which could be the basis of radical pair based magnetoreception of birds.[7]

4. SCRPs can react from singlet state to form singlet products, ^1P, or from triplet state to form triplet products, ^3P. Both of these processes are described by first order rate constants, k_S for singlet pathway and k_T for triplet pathway. Also, SCRPs can recombine to ground state, described by rate constant k_B. The identities of reaction products and possible pathways depend on the system.

The identity of A and B depends on the model system. For instance, one of the models for animal magnetoreception involves a radical pair of $\left[\mathrm{FAD}^{\bullet-}\ \mathrm{TrpH}^{\bullet+}\right]$ found in cryptochrome proteins, where FAD is flavin adenine dinucleotide and Trp is tryptophan.[7] In this example, both radical pair precursors are separate molecules, and following a series of electron transfers from the tryptophan triad or tetrad, an electron is transferred to FAD and a radical pair is formed.[7] In other cases, both A and B can be a part of the same molecule such as PTZ-Ph$_n$-PDI molecular wires, shown in Fig. 1.4.[21,22] This system is a (Donor–Bridge–Acceptor) D–B–A system. Nonetheless, the physical basis of the mechanism stays the same in both cases.

Some of the physical systems studied in the literature may have a slightly more complex kinetic model that explains the observed experimental results and spin dynamics, despite the simplicity of the RPM scheme depicted here. An example is Fay *et al.*'s finding of magnetic-field-independent background contributions that are required to replicate the experimental results for charge recombination of molecular wires.[21] Due to the difficulty of simulating all possible processes,

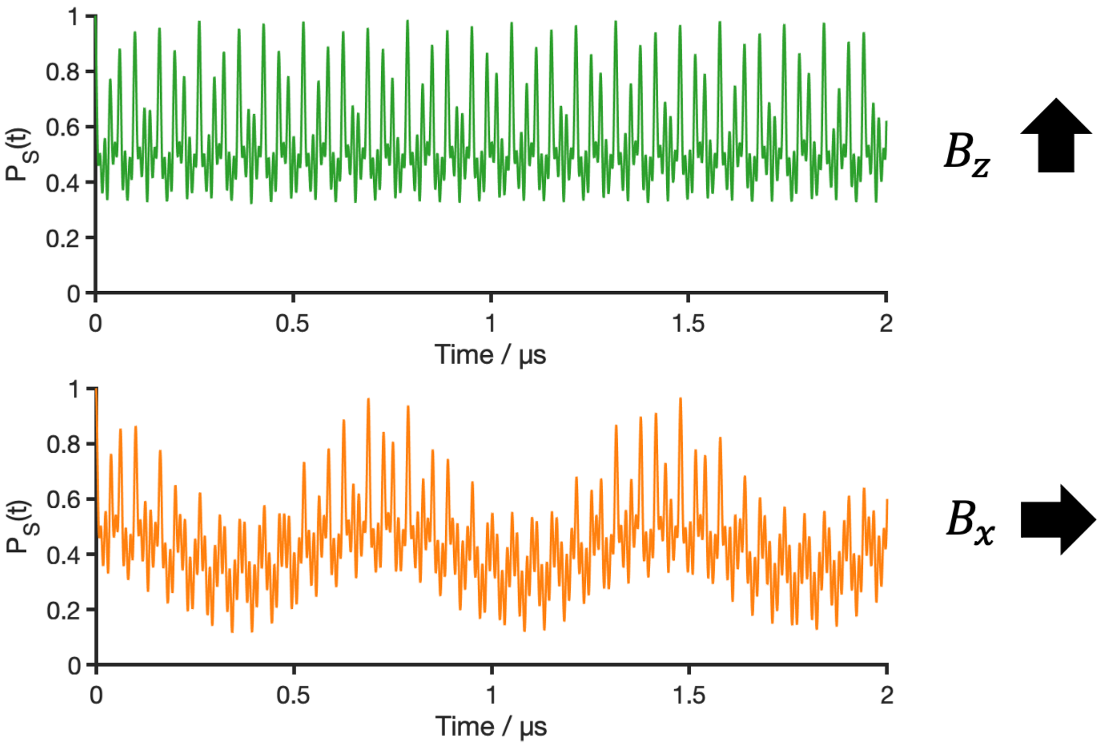

Figure 1.3 Coherent interconversion of singlet probability $P_S(t)$ with time ($0 \leq t \leq 2\ \mu s$) for a toy model radical pair that contains two nitrogen atoms (^{14}N). The direction of the magnetic field influences the profile of this process, which is determined by the strength of anisotropic hyperfine interactions and can be captured by the quantum yield measurements for different field values and/or directions. The top graph denotes a system where the magnetic field points along the z-axis, and the bottom graph showcases a system where the magnetic field points along the x-axis. The first nuclear spin that was coupled to the first electron had these elements in the hyperfine tensor: $A_{xx} = A_{yy} = -0.0989\ mT$ and $A_{zz} = 1.7569\ mT$. The second nuclear spin coupled to the second electron had these elements in the hyperfine tensor: $A_{xx} = A_{yy} = -0.0636\ mT$ and $A_{zz} = 1.0812\ mT$. No electron-electron interactions were present. Magnetic field strength was $|\mathbf{B}| = 50\ \mu T$. Note that recombination effects were omitted for these graphs.

however, simulations of these systems are restricted to RPM schemes similar to the one described above.

CISS Effect

1.2.1

In recent years, there has been a lot of research into chirally induced spin selectivity (CISS) that stems from observations that electron transfers through a chiral medium can result in different efficacy depending on the spin states of the electron.[23–25] Also, there is currently interest in molecular chiral donor-bridge-

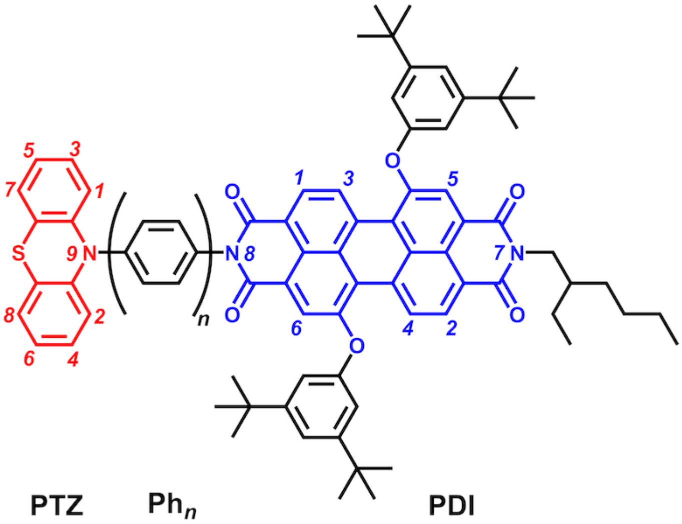

Figure 1.4 The chemical structure of $PTZ^{\bullet +} - Ph_n - PDI^{\bullet -}$ molecular wire with donor (PTZ) coloured in red and acceptor (PDI) coloured in blue.

acceptor systems as a platform for exploring the molecular origins of the CISS effect and researching the importance of it in natural phenomena.[26–33] In addition, the CISS effect can be applied in quantum computing applications utilising molecular qubits to aid in the initialization, processing, and readout of the qubits.[12,28,34]

If the CISS effect is present in the radical pair mechanism, then the formation of the spin correlated radical pair will be affected, through polarisation effects in the initial state and/or additional coherence effects, as well as affecting the recombination processes of the radicals.[35] This thesis will be limited to RPM dynamics without the CISS effect either due to no chilarity present in molecules during the electron transfer steps and/or negligible spin-orbit coupling. It is important to note that the magnetoreception hypothesis based on the $\left[FAD^{\bullet -}\ TrpH^{\bullet +}\right]$ radical pair has chirality in the system, and that there have been studies exploring the effects of a chiral medium on this mechanism, finding that the CISS effect could increase the sensitivity of the compass.[33,35,36] There are various hypotheses and theoretical models for this effect, but the phenomenon is not fully understood at this time. Future research should shed a light on whether or not CISS is involved in magnetoreception. In this thesis, we have examined different aspects of the compass mechanism without incorporating CISS effects.

Quantum Dynamics 1.3

The main equation that is used to model time-dependent behaviour of these systems is the Liouville-von-Neumann equation which is extended with an operator, $\hat{K}$, that is used to model radical recombination ($\hbar = 1$):[3,37–39]

$$\frac{d\hat{\rho}(t)}{dt} = -i\left[\hat{H}, \hat{\rho}(t)\right] - \left\{\hat{K}, \hat{\rho}(t)\right\} \tag{1.9}$$

$[\cdot,\cdot]$ is the commutator and $\{\cdot,\cdot\}$ is the anti-commutator. Here, $\hat{\rho}(t)$ is the density matrix that describes the quantum state of the system. To understand what is a density matrix and how it is useful for modelling quantum mechanical systems, we look at the expectation value of an observable $\langle O\rangle$ for a quantum system described by an ensemble of N identical copies:[40,41]

$$\langle O\rangle = \frac{1}{N}\sum_{n=1}^{N}\left\langle\phi_n\right|\hat{O}\left|\phi_n\right\rangle \tag{1.10}$$

These are the quantities that map quantum mechanical theory and simulations to real world and experiments. This will one of the main tools in simulation.

We can find a more concise definition of $\langle O\rangle$ by defining quantum mechanical trace for an operator $\hat{A}$ on a Hilbert space $\mathcal{H}$ with basis a $|k\rangle$:

$$\mathrm{Tr}\left[\hat{A}\right] = \sum_{k}\langle k|\,\hat{A}\,|k\rangle \tag{1.11}$$

Hence, the expectation value of an observable $\hat{O}$:

$$\begin{aligned}\langle O\rangle &= \frac{1}{N}\sum_{n=1}^{N}\langle\phi_n|\,\hat{O}\hat{\mathbb{I}}\,|\phi_n\rangle \\ &= \frac{1}{N}\sum_{n=1}^{N}\langle\phi_n|\,\hat{O}\sum_k|k\rangle\langle k|\,\phi_n\rangle \\ &= \sum_k\langle k|\,\frac{1}{N}\sum_{n=1}^{N}|\phi_n\rangle\langle\phi_n|\,\hat{O}\,|k\rangle \\ &= \mathrm{Tr}\left[\frac{1}{N}\sum_{n=1}^{N}|\phi_n\rangle\langle\phi_n|\,\hat{O}\right]\end{aligned} \tag{1.12}$$

A resolution of the identity, $\hat{\mathbb{I}} = \sum_k |k\rangle\langle k|$, was used in the 2nd line. Naturally, a quantity ρ emerges that we define as the density operator and this will be the main way systems will be described in RPM calculations:[41]

$$\hat{\rho} = \frac{1}{N}\sum_{n=1}^{N}|\phi_n\rangle\langle\phi_n| \tag{1.13}$$

Hence, the expectation value for an observable $\hat{A}$ and time-dependent density operator of the system (note that the common $\langle\cdot\rangle$ is not used for expectation values, and this formalism will be used throughout the thesis):[41]

$$A(t) = \mathrm{Tr}\left[\hat{A}\hat{\rho}(t)\right] \tag{1.14}$$

$\hat{K}$ is called the phenomenological Haberkorn operator:[37]

$$\hat{K} = \frac{k_S}{2}\hat{P}_S + \frac{k_T}{2}\hat{P}_T \tag{1.15}$$

Here k_S is the rate constant for spin-selective singlet state recombination, and k_T is the rate constant for spin-selective triplet state recombination. This form of $\hat{K}$ accounts only for the pathways leading to ^{1}P and ^{3}P in Figure 1.2, and it is the most common form of the recombination operator used in modelling. If the pathway leading back to the ground state is necessary, $k_B\hat{P}_S/2$ must be added to $\hat{K}$, where k_B is the constant of backward recombination. $\hat{P}_S$ and $\hat{P}_T$ are projection operators for singlet and triplet states, that can be defined as:[17]

$$\begin{aligned} \hat{P}_S &= \frac{1}{4}\hat{\mathbb{I}} - \hat{\mathbf{S}}_1 \cdot \hat{\mathbf{S}}_2 \\ \hat{P}_T &= \frac{3}{4}\hat{\mathbb{I}} + \hat{\mathbf{S}}_1 \cdot \hat{\mathbf{S}}_2 \end{aligned} \qquad 1.16$$

These projectors have these important mathematical properties:

$$\hat{P}_S + \hat{P}_T = \hat{\mathbb{I}} \text{ and } \hat{P}_i^2 = \hat{P}_i \qquad 1.17$$

Here $\hat{P}_i$ is a generic projection operator. The first property is a simple extension from $\hat{P}_S$ and $\hat{P}_T$ definitions in Eq. 1.16. The second property comes from the algebraic definition of a projection operator, which is called idempotence.[42] Also, we refer to $\hat{P}_S$ as a complementary projection operator to $\hat{P}_T$, and *vice versa*.[42] Both of these properties are utilized in derivations of algorithms.

The initial proposition of the Haberkorn operator was a way to explain experimental observations and was not derived from theory. This form has been well accepted in the community[38,43,44] and has been successfully used for many years in explaining spin phenomena. However, recently, there have been questions about the validity of this approach and a number of alternative suggestions based on a quantum measurement approach: 1) the quantum Zeno approach by Kominis;[45] and 2) the Jones-Hore approach.[46] Quantum measurement approaches include a description of recombination processes through probabilistic "measurement" processes that collapse the wave function, which is a more fundamental description than phenomenological rate equation-based approaches. The main addition to the recombination dynamics that Jones and Hore have found from the quantum measurement approach is an additional singlet-triplet dephasing term:[46,47]

$$\frac{d\hat{\rho}(t)}{dt} = \cdots - k_{ST}\left(\hat{P}_S\hat{\rho}(t)\hat{P}_T + \hat{P}_T\hat{\rho}(t)\hat{P}_S\right) \tag{1.18}$$

$k_{ST} = (k_S + k_T)/2$. This additional term will definitely affect the dynamics and there are computational approaches to add these affects to spin dynamics.[47] Yet, the authors of Jones-Hore approach noted themselves that this addition will most likely be hardly distinguished in experiments and could also come from other decohorence sources in spin dynamics., such as modulation of hyperfine interactions or translational modulation of electron-electron interactions (both of these types of interactions will be reviewed in Sec. 1.4).[46] Moreover, the Haberkorn operator has been rigorously shown to appear from non-adiabatic rate theory by the use of the Nakajima-Zwanzig projector approach.[39] The authors concluded that the Haberkorn operator should account for most of the recombination processes, although there are higher order contributions which in principle are not in the operator (like the dephasing terms) yet they could appear in the other forms in the dynamics from $\hat{H}$. Hence, taking into account all the recent progress in understanding the microscopic nature of these recombination processes and the evidence of Haberkorn operator reappearing in rigorous analysis from non-adiabatic rate theory and quantum master equation approaches, we will exclusively use the Haberkorn form for radical pair recombination throughout the thesis.

The solution to Eq. 1.9 for time-independent $\hat{H}$ and $\hat{K}$ (time-dependent case will be explored in Sec. 2.3):[41]

$$\hat{\rho}(t) = e^{-i\hat{H}t-\hat{K}t}\hat{\rho}(0)e^{+i\hat{H}t-\hat{K}t} \tag{1.19}$$

The initial state will always be considered as a singlet state, due to spin conservation of electron transfer reactions, as discussed before.[7] Nuclear spin states will be assumed to be in a maximally mixed state[48] (essentially identity operators for nuclear spin density operators) which remains true unless the system operates at very low temperatures, which will not be true for any of the systems described in the thesis. Thus, the initial state for a radical pair system, $\hat{\rho}(0)$:[48]

$$\hat{\rho}(0) = \frac{1}{Z}\hat{P}_S \otimes \hat{\mathbb{I}}_Z \tag{1.20}$$

Here Z is the size of the nuclear spin subspace, $\hat{P}_S$ is a singlet projection operator in the electron subspace (a 4×4 matrix) and $\hat{\mathbb{I}}_Z$ is an identity operator of size $Z \times Z$. Hence, the resultant dimensions of $\hat{\rho}(0)$ will be $4Z \times 4Z$, as required.

Some of the main observables of interest for RPM are the the time-dependent populations of the singlet, $P_S(t)$, the triplet $P_T(t)$ electronic states and the total radical population $P_{\mathbb{I}}$:

$$\begin{aligned} P_S(t) &= \mathrm{Tr}\left[\hat{P}_S\hat{\rho}(t)\right] \\ P_T(t) &= \mathrm{Tr}\left[\hat{P}_T\hat{\rho}(t)\right] \\ P_{\mathbb{I}}(t) &= \mathrm{Tr}\left[\hat{\mathbb{I}}_N\hat{\rho}(t)\right] \end{aligned} \tag{1.21}$$

N is the size of the full spin space of the radical pair. Using properties in Eq. 1.17 we can show that:

$$P_S(t)+P_T(t) = \mathrm{Tr}\left[\hat{P}_S\hat{\rho}(t)\right]+\mathrm{Tr}\left[\hat{P}_T\hat{\rho}(t)\right] = \mathrm{Tr}\left[\left(\hat{P}_S + \hat{P}_T\right)\hat{\rho}(t)\right] = \mathrm{Tr}\left[\hat{\mathbb{I}}_N\hat{\rho}(t)\right] = P_{\mathbb{I}}(t) \tag{1.22}$$

These are the main variables of interest that will be used as comparison to experiment and for formulation of the model of magnetoreception. Specifically, we will be interested in the total yields of singlet and triplet projection operators when the radical pair will be fully recombined:

$$\begin{aligned} \Phi_S(\infty) &= k_S\int_0^{\infty} P_S(t)dt \\ \Phi_T(\infty) &= k_T\int_0^{\infty} P_T(t)dt \end{aligned} \tag{1.23}$$

Where Φ_S is the singlet yield, and Φ_T is the triplet yield. All simulations of these systems are concerned with evaluating these yield values, and different strategies, which are the central points of this thesis, will be reviewed in Chapter 2, and as a part of studies in Chapters 3, 4, and 6. Moreover, in some cases, such as in molecular wires, or other experiments, the yield may be evaluated at an earlier time T. Hence, definitions in Eq. 1.23 are adapted to (only shown for the singlet yield):

$$\Phi_S(T) = k_S \int_0^T P_S(t)dt \tag{1.24}$$

There is an alternative definition of the quantum mechanical trace in Eq. 1.14 where the observable is time-dependent. By considering the expectation value of a generic observable $\hat{A}$ and plugging in Eq. 1.19, we find:[49]

$$\begin{aligned} A(t) &= \mathrm{Tr}\left[\hat{\rho}(t)\hat{A}\right] = \mathrm{Tr}\left[e^{-i\hat{H}t-\hat{K}(t)}\hat{\rho}(0)e^{+i\hat{H}t-\hat{K}t}\hat{A}\right] \\ &= \mathrm{Tr}\left[\hat{\rho}(0)e^{+i\hat{H}t-\hat{K}t}\hat{A}e^{-i\hat{H}t-\hat{K}t}\right] = \mathrm{Tr}\left[\hat{\rho}(0)\hat{A}(t)\right] \end{aligned} \tag{1.25}$$

This definition where the observable is time-dependent is named as the *Heisenberg picture* (in contrast to the *Schrödinger picture* where the density operator is time-dependent). Here, the general time-dependent operator is defined as:

$$\hat{A}(t) = e^{+i\hat{H}t-\hat{K}t}\hat{A}e^{-i\hat{H}t-\hat{K}t} \tag{1.26}$$

This property is derived by applying the cyclic property of a trace:[50]

$$\mathrm{Tr}\left[ABC\right] = \mathrm{Tr}\left[BCA\right] = \mathrm{Tr}\left[CAB\right] \tag{1.27}$$

It should be clear that $\Phi_S(\infty)+\Phi_T(\infty)=1$, and this can be shown rigorously:[51]

$$\begin{aligned}
\Phi_S(\infty)+\Phi_T(\infty) &= \mathrm{Tr}\left\{\hat{\rho}(0)\int_0^\infty \left(k_S\hat{P}_S(t)+k_T\hat{P}_T(t)\right)dt\right\}\\
&= \mathrm{Tr}\left\{\hat{\rho}(0)\int_0^\infty 2\hat{K}(t)dt\right\}\\
&= \mathrm{Tr}\left\{\hat{\rho}(0)\int_0^\infty e^{+i\hat{H}t-\hat{K}t}2\hat{K}e^{-i\hat{H}t-\hat{K}t}dt\right\}\\
&= \mathrm{Tr}\left\{\hat{\rho}(0)\int_0^\infty \frac{d}{dt}\left(-e^{+i\hat{H}t-\hat{K}t}e^{-i\hat{H}t-\hat{K}t}\right)dt\right\}\\
&= \mathrm{Tr}\left\{\hat{\rho}(0)\left[-e^{+i\hat{H}t-\hat{K}t}e^{-i\hat{H}t-\hat{K}t}\right]_0^\infty\right\}\\
&= \mathrm{Tr}\left\{\hat{\rho}(0)\hat{\mathbb{I}}_N\right\}=\mathrm{Tr}\left\{\hat{\rho}(0)\right\}=1
\end{aligned} \tag{1.28}$$

This derivation utilizes the definition of the trace in Eq. 1.25.

Spin Interactions 1.4

The RPM is primarily governed by the coherent interconversion of the singlet and triplet states. This interconversion process can be fully explained by the interactions of spin within the spin Hamiltonian of the system, $\hat{H}$:[1,3]

$$\hat{H} = \hat{H}_1 + \hat{H}_2 + \hat{H}_J + \hat{H}_D \tag{1.29}$$

Here, $\hat{H}_J$ denotes the exchange interaction and $\hat{H}_D$ denotes the electron-electron dipolar (EED) interaction, which are interradical interactions, i.e. between the electron spins. $\hat{H}_i$, where i is either radical 1 or 2, denotes the intraradical interactions, which are split to hyperfine, $\hat{H}_{hyp}$, and Zeeman, $\hat{H}_Z$ interactions:

$$\hat{H}_i = \hat{H}_{hyp,i} + \hat{H}_{Z,i} \tag{1.30}$$

This section will explain the origins and characteristics of the Zeeman, exchange, EED, and hyperfine spin interactions. Additionally, we will examine the spin Hamiltonian employed in Electron Paramagnetic Resonance (EPR) experiments, particularly in the context of high magnetic field strengths.

All the spin interactions, quantum master equations and density operators will assume units for which $\hbar = 1$.

Zeeman Interaction 1.4.1

Zeeman interaction is the splitting of electron spin energy levels due to the interaction between external magnetic field and the magnetic moment created by the spin:[52]

$$\hat{H}_Z = \boldsymbol{\omega} \cdot \hat{\mathbf{S}} = -\gamma_e \mathbf{B} \cdot \hat{\mathbf{S}} \tag{1.31}$$

Here $\boldsymbol{\omega} = -\gamma_e \mathbf{B}$ where γ_e is the gyromagnetic ratio of the electron spin and $\mathbf{B}$ is the magnetic field vector. γ_e can also be defined as $\gamma_e = -g_e \mu_B / \hbar$ ($\hbar = 1$), relating it to the electron g-factor, g_e, and Bohr magneton, μ_B. g_e can be thought of as a dimensionless proportionality constant between the observed magnetic moment and the angular momentum of the spin, where as μ_B is a unit for magnetic moments. $\hat{\mathbf{S}}$ is a vector for Cartesian electron spin angular momentum operators $\hat{\mathbf{S}} = \left(\hat{S}_x, \hat{S}_y, \hat{S}_z\right)^T$.

In the simulation of molecular systems containing radicals, it is commonly assumed that the interaction between the magnetic field produced by the electron's orbital motion (known as the orbital angular momentum) and its spin angular momentum, commonly referred to as the spin-orbit coupling, is typically considered to be negligible.[7,17] The prerequisite for this condition is the absence of heavy atoms and the absence of high symmetry in the radical, such as linearity.[7] Negligible spin-orbit coupling has two important consequences for the Zeeman effect. First, the g-factor is regarded as isotropic (generally speaking, the g factor is a tensor property that can have asymmetric terms). This is due to the requirement of significant spin orbit coupling to introduce anisotropic terms in the g factor.[53] Moreover, it is worth noting that in numerous instances, radical pairs exhibit rapid tumbling behaviour in solution. This characteristic further leads to the insignificance of any anisotropic contributions, as the anisotropic components of the tensor effectively average out to zero if the radical is rapidly tumbling.[52] Second, it is commonly assumed that the value of g_e is equivalent to the free electron g-factor in situations where there are no measured g-factors. This is also an outcome of small spin-orbit coupling, which can be illustrated by considering the value of isotropic g-factor determined by second order perturbation theory:[52,54]

$$g = g_e - \frac{2\lambda}{3} \sum_{n>0} \frac{\langle 0 | \hat{\mathbf{L}} | n \rangle \cdot \langle n | \hat{\mathbf{L}} | 0 \rangle}{E_n - E_0} \tag{1.32}$$

Where λ is the spin-orbit coupling, $\hat{\mathbf{L}}$ is the electron orbital angular momentum vector operator, $|n\rangle$ is an eigenstate of the spatial Hamiltonian with energy E_n.

Unless, λ is much larger then the energy difference $E_n - E_0$, $g \approx g_e$, revealing the basis of the assumption that g_e is equal to the free electron value. The experimental determination of the g-factor can also serve as a reliable means to assess the degree of spin-orbit coupling.

B is the magnetic field vector, defined as:

$$\mathbf{B} = |\mathbf{B}| \left(\sin(\theta)\cos(\phi),\ \sin(\theta)\sin(\phi),\ \cos(\theta)\right)^T \tag{1.33}$$

The direction of the magnetic field vector is defined by two angles, inclination angle θ and azimuthal angle ϕ. Inclination angle is the angle between the magnetic field vector and the z-axis. Azimuthal angle is the angle of the magnetic field vector's projection onto the xy plane and the x-axis. The strength of the magnetic field is defined as $|\mathbf{B}|$.

Another important property of the electron's Zeeman effect is its Larmor frequency. A system for a single electron, with states $|\alpha\rangle$ and $|\beta\rangle$, can be solved analytically for the Zeeman Hamiltonian in Eq. 1.31, to yield energy of the states as $-\gamma_e m_S |B|$. The energy difference between these two states, defined as the Larmor frequency, ν_L, is:[55]

$$\nu_L = \frac{\gamma_e |\mathbf{B}|}{2\pi} \tag{1.34}$$

Larmor Frequency is an important value for radical-pair based magnetoreception. It is used as a rough estimate of the required lifetime for a radical pair to significantly interact with an external magnetic field.[7] For instance, for Earth's magnetic field strength $|\mathbf{B}| = 50\ \mu T$, the period of Larmor frequency is $T_L = 1/\nu_L \approx 0.71\ \mu s$. This means radical-pair lifetimes of $1\ \mu s$ are required for this effect. There are currently no found biological radical systems that have such a long lifetime, this fact being one of the arguments against this mechanism as a basis for animal magnetoreception.[7]

Nuclear spins can also interact with the magnetic field through nuclear spin Zeeman effect:[52]

$$\hat{H}_{Z,nuc} = \sum_i \gamma_i \mathbf{B} \cdot \hat{\mathbf{I}}_i \tag{1.35}$$

Here $\hat{\mathbf{I}}_i$ are nuclear spin quantum operators for nuclei i and γ_i is the gyromagnetic ratio of nuclei i. In all simulations for this thesis, the effect will be neglected. Primarily because the gyromagnetic ratios of nuclear spins are much smaller than those of electron spins, and because the magnetic fields considered in this thesis are also too small for this interaction to be significant.For illustration, the ratios between electron spin gyromagnetic ratio and two common nuclei considered in spin dynamics, ^{1}H and ^{13}N (g-factor values for these nuclear spins are shown in Appendix A):

$$\frac{\gamma_e}{\gamma_N(^1H)} \approx 658; \ \frac{\gamma_e}{\gamma_N(^{14}N)} \approx 9105 \tag{1.36}$$

Moreover, the same argument can be applied to explain why nuclear spin-nuclear spin interactions are usually neglected in radical pair spin dynamics. The interaction scales with the gyromagnetic ratios of nuclear spins, hence, those interactions will be tiny compared to the terms that involve electron spins.[3,56]

Note, $\gamma_e = 176.086\ \mu s^{-1}\ mT^{-1}$.[57]

Dipolar Interaction 1.4.2

One of the interactions between electron spins is the electron-electron dipolar (EED) interaction. It is a coupling that arises from the interaction of magnetic dipole moments created by the electron spins.[17] The usual form for this interaction in a spin Hamiltonian is:[56]

$$\hat{H}_D = \hat{\mathbf{S}}_1 \cdot \mathbf{D} \cdot \hat{\mathbf{S}}_2 \tag{1.37}$$

Where $\mathbf{D}$ is the dipolar interaction tensor. It can be derived by considering how the magnetic field created by one of the electrons interacts with the magnetic dipole moment of the second electron. The magnetic dipole moment created by an electron with spin operators $\hat{\mathbf{S}}_i$, g-factor, g_e and gyromagnetic ratio, γ_e:[17]

$$\mathbf{m}_i = g_e \gamma_e \hat{\mathbf{S}}_i \tag{1.38}$$

The electron i creates magnetic field $\mathbf{B}_i$ at a point in space described by $\mathbf{r}$. Point dipole approximation is employed here:[17,54]

$$\mathbf{B}_i = -\frac{\mu_0}{4\pi r^3}\left(\mathbf{m}_i - \frac{3\mathbf{r}(\mathbf{r}\cdot\mathbf{m}_i)}{r^2}\right) = -\frac{\mu_0 g_e \gamma_e}{4\pi r^3}\left(\hat{\mathbf{S}}_i - \frac{3\mathbf{r}(\mathbf{r}\cdot\hat{\mathbf{S}}_i)}{r^2}\right) \tag{1.39}$$

$r = |\mathbf{r}|$ is the distance between two radicals, and μ_0 is the magnetic constant. The EED interaction between the two electrons is given as:

$$\hat{H}_D = -\mathbf{B}_1 \cdot \mathbf{m}_2 = \frac{\mu_0 g_e^2 \gamma_e^2}{4\pi r^3}\left(\hat{\mathbf{S}}_1 \cdot \hat{\mathbf{S}}_2 - \frac{3(\hat{\mathbf{S}}_1 \cdot \mathbf{r})(\mathbf{r}\cdot\hat{\mathbf{S}}_2)}{r^2}\right) \tag{1.40}$$

This expression can be rewritten in the form of Eq. 1.37, by setting $\mathbf{D}$ as:[54]

$$\mathbf{D} = \frac{\mu_0 g_e^2 \gamma_e^2}{4\pi r^3}\left(\mathbf{I} - 3\frac{\mathbf{r}\otimes\mathbf{r}}{r^2}\right) = D\left(\mathbf{I} - 3\frac{\mathbf{r}\otimes\mathbf{r}}{r^2}\right) \tag{1.41}$$

D is the dipolar constant, $\mathbb{I}$ is the unit matrix and $\otimes$ is the outer product. From this form, we can observe that the strength of this interaction scales with r^{-3}.

The EED interaction can be ignored when the radical pair is rapidly tumbling in a solution because the traceless tensor $\mathbf{D}$ vanishes.[17,54] In addition, EED is sometimes referred to as zero field splitting because it eliminates triplet state degeneracy even in the absence of a magnetic field.[54] However, it is important to note that EED is not the only possible source of zero field splitting, which can also be caused by spin-orbit coupling.[52]

Exchange Interaction 1.4.3

The exchange interaction is an isotropic electron-electron interaction that manifests from the orbital overlap between two electron spins. It is a spin coupling, despite being a consequence of the spatial parts of the wavefunction, and is incorporated into the Hamiltonian as:[3]

$$\hat{H}_J = -2J\hat{\mathbf{S}}_1 \cdot \hat{\mathbf{S}}_2 \tag{1.42}$$

Where J is exchange constant. This interaction is a combination of direct exchange interaction between the radicals and long range superexchange interaction.[3,56]

The exchange interaction is assumed to have an exponential relationship with the radical-pair distance r, which is the distance between the centres of the two radicals, and has no relationship with radical-pair orientation:[1]

$$J(r) \approx J_0 e^{-r/r_J} \tag{1.43}$$

Here J_0 and r_J are empirical parameters.

Hyperfine Interaction 1.4.4

Hyperfine interaction is the interaction between an electron spin and a nuclear spin of a radical. The hyperfine interaction between an electron i and nucleus j is defined as:

$$\hat{H}_{hyp.,i} = \hat{\mathbf{S}}_i \cdot \mathbf{A}_{ij} \cdot \hat{\mathbf{I}}_{ij} \tag{1.44}$$

$\mathbf{A}_{ij}$ is the hyperfine tensor that describes the interactions' strength and directionality. This tensor decomposes to two terms, an isotropic part with constant a_{iso} and an anisotropic tensor $\mathbf{A}_{aniso}$:

$$\mathbf{A} = \mathbf{A}_{aniso} + a_{iso}\mathbb{I} \tag{1.45}$$

The anisotropic terms come from the dipolar coupling between the nuclear spin and electron spin magnetic moments, analogous to EED coupling between electron spins.[56] The other term comes from the Fermi contact interaction and it's generally isotropic. It can be described as a correction to the point dipole approximation made in the derivation of the dipole interaction and considers the coupling of the electron spin when electron is inside the nucleus.[3,56] In general, both of these quantities are computed by utilizing the wavefunction of the electron in the radical[17] that is generally calculated by Density Functional Theory (DFT).[58] Also, Electron Paramagnetic Resonance (EPR) techniques such as Electron-Nuclear Double Resonance Spectroscopy (ENDOR) can be utilized to measure these properties.[59–62] Yet, usually there is an issue of finding the sign of the hyperfine interactions, for which DFT method can be utilized, as seen in different studies.[11,21]

At times, it is useful to quantify the magnetic field generated by the isotropic hyperfine coupling interactions and we will use the effective hyperfine field for radical i for this comparison:[63]

$$B_{hyp,i} = \sqrt{\sum_{k=1}^{N_i} a_{ik}^2 I_{ik}(I_{ik}+1)} \tag{1.46}$$

Here, a_{ik} are isotropic hyperfine constants for nuclei k coupled to electron i.

Hyperfine interaction constants used in Chapter 3 were computed in Gaussian-03[64] at the UB3LYP/EPR-III level[56] and we would like to acknowledge Dr. Ilya Kuprov, Department of Chemistry, University of Southampton for calculating those constants.

High Field Hamiltonian 1.4.5

When the magnetic field strength $|\mathbf{B}|$ is much higher in strength than other interactions in the system we can employ a secular approximation that significantly simplifies the spin Hamiltonian to:[57,65–67]

$$\begin{aligned}\hat{H} &= \hat{H}_Z + \hat{H}_{hyp,1} + \hat{H}_{hyp,2} + \hat{H}_J + \hat{H}_D \\ \hat{H}_Z &= -\gamma_1 |\mathbf{B}| \hat{S}_{1z} - \gamma_2 |\mathbf{B}| \hat{S}_{2z} \\ \hat{H}_J &= 2J\hat{\mathbf{S}}_1 \cdot \hat{\mathbf{S}}_2 \\ \hat{H}_D &= \frac{1}{2}\mathcal{D}\left(3\hat{S}_{1z}\hat{S}_{2z} - \hat{\mathbf{S}}_1 \cdot \hat{\mathbf{S}}_2\right) \\ \hat{H}_{hyp,i} &= \hat{S}_{iz} \otimes \left(\sum_{k=1}^{N_i}\left(A_{ik}\hat{I}_{ik,z} + B_{ik}\hat{I}_{ik,x}\right)\right)\end{aligned} \tag{1.47}$$

Here $\mathcal{D} = D(\cos^2(\theta) - 1/3)$ with D as the strength of dipolar interaction, θ as the angle between the applied magnetic field and the dipolar axis, J is the exchange interaction, γ_i is the gyromagnetic ratio of electron i, N_i is the number of nuclear spins on radical i and $A,\ B$ are hyperfine coupling coefficients. $\hat{H}_{hyp,i}$ is an anisotropic hyperfine interaction despite, on a first look, omitting some "pseudo-secular" terms, as demonstrated in Ref. 66.

This form of the spin Hamiltonian has a lot of simplifications which arise with high magnetic fields and is used to explain EPR experiments. This form will be used in Chapter 5 and Appendix D for studies that aimed to carry out a CNOT gate operation on organic molecular spin qubits based on the RPM.

Applications 1.5

The RPM model can be utilised in a variety of contexts, either to explain natural phenomena or to design practical systems for scientific and other applications. We will examine in depth two application-related topics: 1) avian magnetoreception and 2) organic molecular spin qubits. Also, at the conclusion, we will discuss additional systems that have significant RPM applications.

Avian Magnetoreception 1.5.1

It is established that birds have the remarkable ability to sense the direction of Earth's magnetic field.[68–71] Birds use this sense, combined with the ability to use visual cues (stars,[72–74] landmarks[75,76] or the sun),[77–80] to fly extraordinarily large distances while migrating.[81–84] Other species are also capable of sensing the magnetic field, but the majority of recent biological research and evidence regarding this sense has focused on migratory birds. In this section, we will focus on the mechanism of avian magnetoreception.

Despite the fact that the physical origins of this sense in birds are still being debated, there are a variety of current hints regarding it. The sense depends on the inclination of the magnetic field rather than its polarity.[70,71] Moreover, behavioural experiments have revealed that it is a light-mediated sense.[85–88] Also, behavioural experiments have demonstrated that weak, time-dependent magnetic fields can disrupt the compass sense.[89? –94] Radical pair-based magnetic sensing is the only current hypothesis which may fully or partially explain all of these observations of avian magnetic sense.[5,7]

The current hypothesis, first suggested in 2000[8] (although cryptochrome independent mechanism was first suggested in 1978[95]), is that a radical pair can be formed in photoreceptor proteins called Cryptochrome (CRY),[96,97] that are found in the eyes of birds (amongst many other places in the body) and it is the only known vertebrate photoreceptor molecule that can form radical pairs under light illumination[98–100] (Chlorophyll can as well,[101] yet it is not found in birds). Hence, after light illumination, there is a series of electron transfers that produces a radical pair which can capture the inclination of Earth's magnetic field which the bird can sense. The current thought identities of these radicals is that one of them is a non-covalently bound redox-active flavin adenine dinucleotide cofactor (FAD), which is known to absorb blue light when in its fully oxidized state.[7] Next, after photoactivation of FAD, four consecutive electron transfers along a tetrad of tryptophan (Trp) residues[102,102–106] form a radical pair composed of a flavosemiquinone radical ($\mathrm{FAD}^{\bullet-}$) and a radical $\mathrm{TrpH}^{\bullet+}$ that is the terminal Trp residue in the triad.[7,106] This process is illustrated in Fig. 1.5.

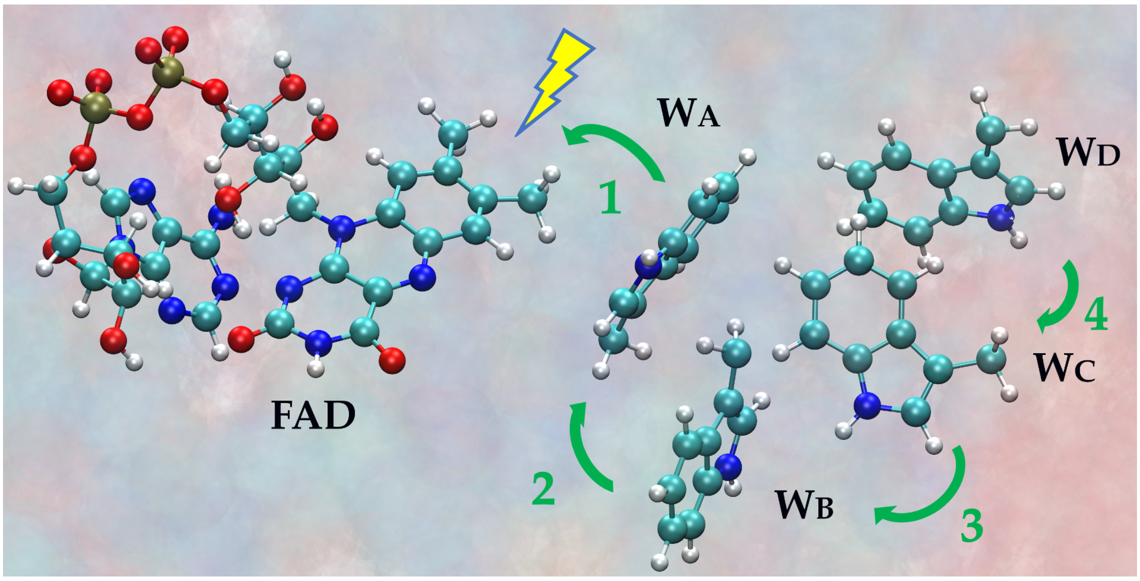

Figure 1.5 Arrangement of FAD cofactor and 4 tryptophan residues (W_A, W_B,, W_C, W_D) in European Robin Cry4a during formation of a $\left[\mathrm{FAD}^{\bullet-}\ \mathrm{Trp}_C\mathrm{H}^{\bullet+}\right]$ radical pair. Initially light activates the FAD cofactor (denoted by the lighting bolt), which initiates a four electron transfer cascade until the fourth tryptophan (W_D, also denoted as TRP_D) forms a cation $\mathrm{Trp}_D\mathrm{H}^{\bullet+}$. The arrangements of molecules are from homology protein model of European Robin Cry4a taken from Ref. 107.

Hence, the current hypothesis is that $\left[\mathrm{FAD}^{\bullet-}\ \mathrm{Trp}_C\mathrm{H}^{\bullet+}\right]$ radical pair is central to the avian magnetoreception. The RPM mechanism of avian magnetoreception for this radical pair is detailed in Fig 1.6. The possibility of this mechanism is supported through a number of experimental[85–88,106,108–110] and theoretical[107,111–121] investigations. Also, an artificial radical pair system composed of carotenoid–porphyrin–fullerene has been able to detect magnetic field effects with $|\mathbf{B}|$ as low as Earth's magnetic field and was able to detect directional magnetic field effects in stronger fields (3.1 mT).[9] This gives the radical pair-based avian magnetoreception hypothesis a strong foundation, because a chemical radical pair system that can pick up on very weak magnetic fields can be built.

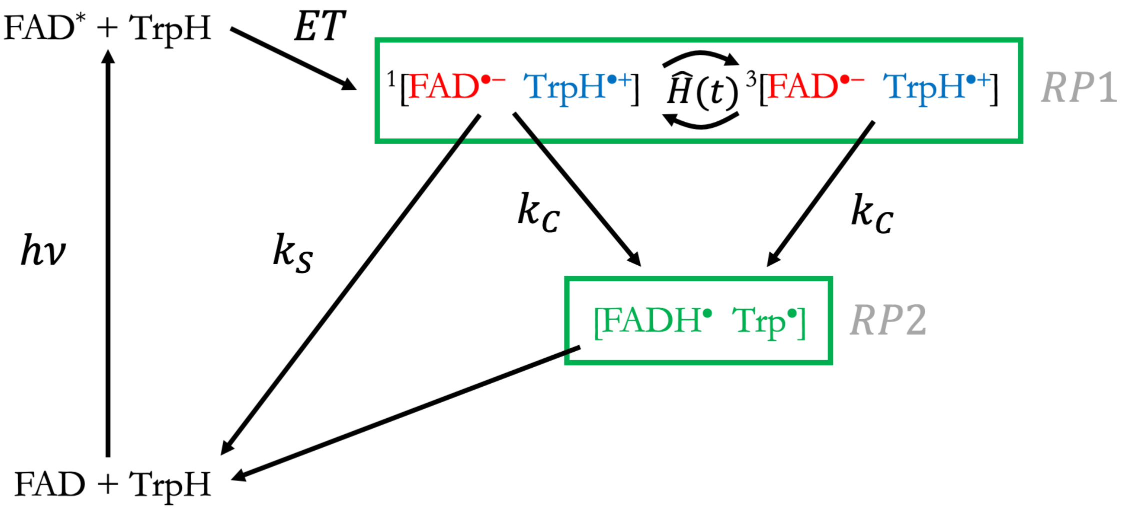

Figure 1.6 Photochemical reaction scheme for radical pair based magnetoreception. Initial photoexcitation of FAD and sequential electron transfer reactions produce a radical pair $\left[\mathrm{FAD}^{\bullet-}\ \mathrm{TrpH}^{\bullet+}\right]$, denoted as $RP1$. $RP1$ can coherently interconvert between singlet and triplet states, which is controlled by the direction of the magnetic field and interactions of electron and nuclear spins of radicals. $RP1$ can either recombine to the ground state with a rate constant k_S or convert to $\left[\mathrm{FADH}^{\bullet}\ \mathrm{Trp}^{\bullet}\right]$ (denoted as $RP2$) by deprotonation with a rate constant k_C. $RP2$ is thought not to be sensitive to magnetic fields and believed to be involved in the signalling mechanism for the magnetic field effect's sensing. This scheme is adapted from Ref. 7

Yet, there are currently a few theoretical and biological issues regarding this model. When full interactions and large spin spaces are taken into account, the spin dynamics of $\left[\mathrm{FAD}^{\bullet-}\ \mathrm{TrpH}^{\bullet+}\right]$ exhibit a relatively small anisotropy (the measure of compass sensitivity), which may be insufficient for sensing.[7,20] There have been hints in the literature that a quantum mechanical needle effect[114] could provide this required sensitivity, but a realistic theoretical model with full quantum effects that would have this effect has not been proposed, and it has also been demonstrated that this effect does not appear in a more realistic $\left[\mathrm{FAD}^{\bullet-}\ \mathrm{TrpH}^{\bullet+}\right]$ system.[122] In addition, the radical pair lifetime must be long enough for the magnetic field to alter the spin coherence sufficiently for the Earth's magnetic field to be detected, ideally on the order of 1 μs.[7,123] As a result, a significant amount of current research is focused on either potential alternative mechanisms of this sense or theoretical modifications to the current model that would increase either the anisotropy or the lifetime of these radical pairs.

One of the possible alternative mechanisms is that FAD is paired with a hypothetical radical Z, which would have no hyperfine coupling values.[115] This radical pair has demonstrated increased sensitivity in simulations and was initially proposed to address the behavioural experiments demonstrating that radiofrequency noise at the Larmor frequency disrupted the compass sense.[55] However, a more recent and meticulously conducted behavioural experiment was unable to replicate this result, casting serious doubt on this hypothesis.[94] Additionally, Z's plausible or probable identity is currently unknown. There have been several proposed identities for Z, including superoxide radical $\mathrm{O}_2^{\bullet-}$[7] and ascorbic acid radical $\mathrm{Asc}^{\bullet}$.[124] Ascorbic acid is only bound to cryptochrome for a few nanoseconds, whereas the radical pair lifetime required for magnetic sensing would be between 1 and 10 μs, according to molecular dynamics studies,[7,91] and theoretical studies of superoxide involvement in spin dynamics with $\mathrm{FAD}^{\bullet-}$ have shown that it may be too speculative due to, among other things, the rapid relaxation of the superoxide radical.[125] Consequently, there are no currently accepted identities for Z, nor is there consensus that it is involved in the mechanism of the magnetic compass.

In addition, it has been proposed that the compass sensor consists of two radical pairs between FAD and W_C and W_D tryptophans, with the electron hopping between these two residues during spin dynamics.[106,111] This alternative mechanism is shown in Fig. 1.7. Simulations show that this dynamical equilibrium between RP_C and RP_D sites could be an ideal combination of necessary properties of magnetic field sensing and signalling.[106,111]

Furthermore, another proposed alternative is that the compass sensor is composed of two radical pairs between FAD and W_C and W_D tryptophans, with the electron hopping between these two residues during spin dynamics.This alternative mechanism is shown in Fig. 1.7. Simulations show that this dynamical equilibrium between RP_C and RP_D sites could be an ideal combination of necessary properties of magnetic field sensing and signalling.[106,111] Also, a study determined[111] that a weighted average of both site spin couplings is sufficient to incorporate the effects into spin dynamics; essentially, a radical pair that is intermediate between the two sites will have similar spin effects as the composite radical pair. Therefore, it is not necessary to simulate the composite radical pair for modelling purposes in order to examine the effects of interests, such as time-dependent field effects, on this mechanism. In addition, additional experimental observation is necessary for this model to be accepted.

Also, a number of hypotheses exists which propose special conditions in the spin dynamics that would amplify $\left[\mathrm{FAD}^{\bullet-}\ \mathrm{TrpH}^{\bullet+}\right]$ radical pair's anisotropy, such as a special form of electron-electron interactions,[113,126] scavenging radicals,[127–129] nuclear polarization effects[111] or extra motions in the dynamics that increase anisotropy.[20] Although, these considerations are promising corrections to the current mechanism, none of these claims have yet been rigorously proven with experimental studies.

In recent years, there has been a growing consensus that the mechanism of avian magnetoreception may not be explicable using classical physics models.[130–132,132,133] Seen as requiring a quantum mechanical explanation are the sensing of such low magnetic fields and radiofrequency disruptions to the compass sense. Consequently, this field of study belongs to the emerging field of Quantum Biology, which also investigates diverse topics such as enzyme reac-

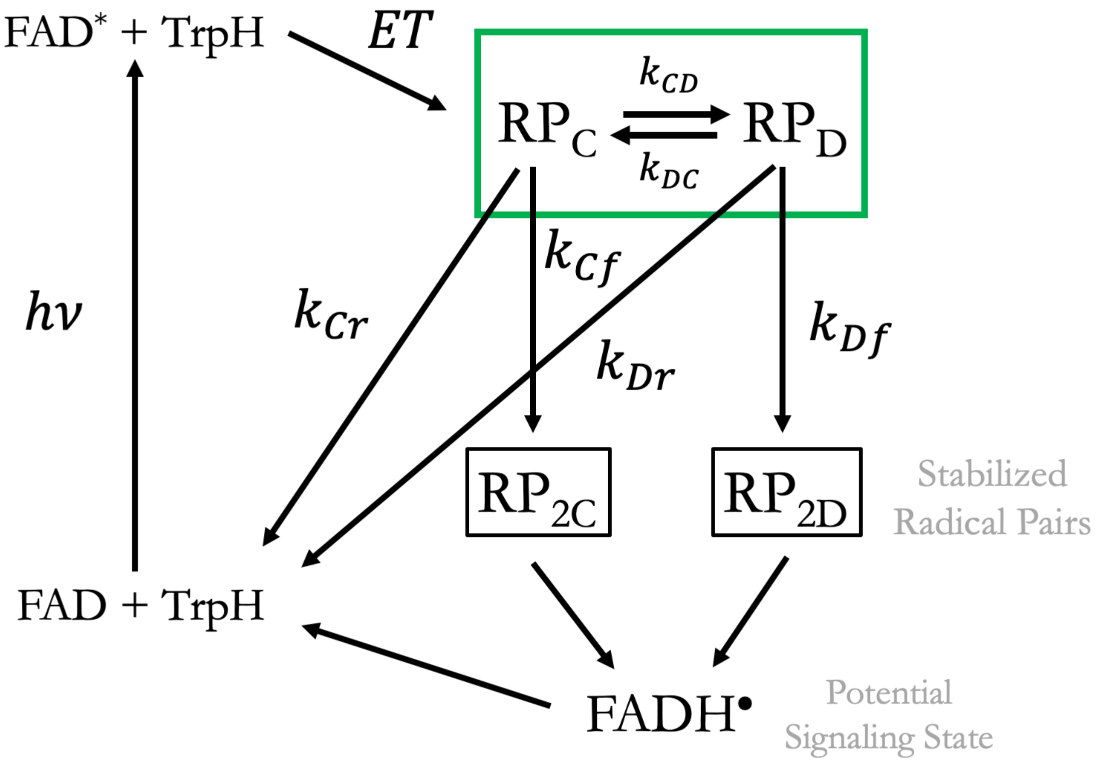

Figure 1.7 An alternative mechanism of magnetoreception. After initial photoexcitation and electron transfer reactions, a composite radical pair is formed that includes RP_C and RP_D that interchange between each other with rate constants k_{CD} and k_{DC}. Hence, the mechanism would an average of properties of the two distinct reaction centres. Both of these sites can recombine to the ground state with rate constants k_{CR} and k_{Cf}. As well as form stabilized radical pairs with rate constants k_{Cf} and k_{Df}. Analogous to the mechanism with just one radical pair centre. The stabilized radical pairs can form a potential signalling state that would transfer the magnetic field information. Adapted from Ref. 106

tions,[134–149] photosynthesis,[150–153] and DNA proton tunnelling.[154,154–156] These biological phenomena could be explained by *non-trivial* quantum effects, which are central to this field's characteristics. Due to the requirement of spin coherence for singlet-triplet interconversion, the current hypothetical RPM model for avian magnetoreception aligns well with the field of Quantum Biology.

Our simulations in this thesis will model currently the most probable mechanism to explain avian magnetoreception shown in Fig. 1.6. We will look at new theoretical insights to this mechanism via investigations of isotope substitutions effects and the effects of time-dependent white noise on the compass mechanism. This will be the basis of Chapters 3 and 4.

Molecular Qubits 1.5.2

Quantum computing is now one of the largest fields in physics, computer science, and engineering, and many research groups and private companies are attempting to exploit quantum mechanical phenomena in order to perform computer simulations that would otherwise be incredibly challenging with classical computers. This is precisely the concept Feynman outlined in his groundbreaking 1982 paper[157] describing quantum computers. He proposed that a classical simulation of quantum mechanical systems is too difficult for a classical computer, and that these systems should instead be simulated by computers that adhere to quantum mechanical laws. Consequently, the fundamental principle of quantum computing is that certain computational tasks can be simulated on a quantum computer with a quantum algorithm with much better scaling of time and space complexity than on a classical computer. After the initial proposal of Feynman, a number of quantum algorithms surfaced that have a quantum speedup, such as the Deutsch-Jozsa algorithm for solving oracle problems in 1985,[158] Shor's algorithms for breaking widely used RSA and Diffie-Hellman encryption protocols in 1994,[159] and Grover's algorithm for unstructured search problems in 1996.[160] In 1996, Lloyd also demonstrated that a quantum computer could simulate quantum mechanical systems with local interactions without the exponential overhead of classical algorithms.[161] As a result, it is accepted in principle that a working computer that employs the laws of quantum mechanics can be a very powerful device for various computational tasks; however, there are still known current obstacles to achieving this objective.

A quantum computer is a physical quantum mechanical system composed of different particles, such as spins, atoms, or photons, with specific interactions and unitary time evolution that can be altered with different control techniques (such as time-dependent magnetic fields) and tailored to perform other computations or mimic other quantum systems.[161,162] Any two-level quantum mechanical system is, in theory, capable of functioning as a quantum computer. Nonetheless, DiVincenzo's criteria for a quantum computer impose stricter requirements. Here is a list of the five prerequisites for a system to act as a quantum computer:[163]

1. A scalable physical system with well-characterized qubits
2. The ability to initialize the state of the qubits to a simple fiducial state
3. Long relevant decoherence times
4. A "universal" set of quantum gates
5. A qubit-specific measurement capability

Therefore, there are straightforward and well-defined "rules" for creating new quantum systems for quantum computing. In some respects, none of the current platforms meet all of the requirements, as methods of scaling systems to 10,000 or more qubits, which would be required for a future quantum computer, remains unknown. However, decoherence is one of the most important properties that must be reduced. Quantum mechanical coherence is lost when a quantum computer, which is ultimately an open quantum system, interacts with the environment and someone "controls" the machine, resulting in significant errors in results.[162] Therefore, systems with a low decoherence rate are preferred.

In fact, there are calculations that utilise the quantum mechanical computer's inherent noise to simulate open quantum systems, such as RPM systems,[164,165] as first proposed by Lloyd.[161] This will be discussed briefly in Sec. 2.7. In addition, there are numerous quantum error correction techniques that seek to mitigate quantum mechanical errors caused by decoherence using larger quantum circuits.[166–168] This is a very important and expanding field of study, but we are not concerned with such advanced quantum computing concepts in this thesis. Therefore, neither topic will be discussed further.

The fundamental units of information in a quantum computer are qubits, which are two-level systems (the higher-dimensional alternatives are known as qudits,[169] but we will focus on qubits). Qubits are a system that can exist in either the $|0\rangle$ or $|1\rangle$ state, or in a superposition of the two (when the state is pure):[162]

$$|\Psi\rangle = \alpha\,|0\rangle + \beta\,|1\rangle \tag{1.48}$$

$|\Psi\rangle$ can be anything in between $|0\rangle$ and $|1\rangle$ with the only requirement that $|\alpha|^2 + |\beta|^2 = 1$. These states are then programmed with various quantum logic gates—quantum alternatives to the classical logic gates, that can be either single qubit or multi-qubit.

The most plausible candidates for qubits include semiconducting materials,[170–172] neutral atoms,[173–175] trapped ions,[176–178] and nitrogen-vacancy centres.[179–181] All of these systems have extended coherence times, low decoherence and examples of high fidelity single and two qubit gates. Nevertheless, almost all of these systems are currently affected by the "scaling problem". For practical applications, quantum computing will require a very large number of qubits that interact with one another and can be individually controlled, and the scale is not tens of qubits but at least 100-1000, if not much more. Currently, each of these systems has a qubit maximum in the hundreds.[182] Trapped ions and semiconductors (the platform on which Google recently conducted a quantum supremacy[170] experiment) are among the leaders in terms of all variables necessary for engineering quantum computers.

Intriguingly, we will focus in this thesis on molecular qubits, a platform that is unlikely to be used for universal quantum computations. At the present time, none of these molecular systems could claim to be a dominant quantum computing platform in the future. However, they possess a number of fascinating properties and characteristics that make research on them worthwhile. Molecular systems and organic synthesis have a number of advantages over other platforms that rely primarily on solid state materials: 1) Extensive control over the nature of the qubits through synthesis, 2) Ease of spatially positioning individual molecular qubits via covalent or non-covalent assemblies, and 3) Reproducibility of qubits, i.e. the same molecule synthesised in different laboratories will always have the same atomic distances (unlike other technologies that deal with materials).[13,183] Numerous examples of molecular qubit systems exist, including spin systems in heterodimetallic lanthanide complexes,[184] hybrid rotaxanes,[185] vanadium complexes,[186,187] photogenerated radical pairs in triradical Pt complexes,[188] and photoisomerization-induced spin-charge Co complexes.[189] Moreover, there are numerous solid state systems based on nuclear and electron spins, such as nitrogen-vacancy (NV),[190–193] silicon-vacancy centres (SV),[194,195] phosphorus donor qubits in silicon,[196,197] and silicon quantum dots.[198–200]

In this thesis, we will focus on a system that is devoid of transition metals: a molecular spin qubit that is based on electron spins in an organic RPM system. The main task of Chapter 5 and Appendix D chapters will be to map the RPM to a quantum circuit that can do computations, such as the two-qubit operation CNOT. This is pictorially illustrated in Fig. 1.8. The opposite of this, modelling RPM on a quantum circuit, will be briefly mentioned in 2.7.

Other Systems 1.5.3

Radical pair phenomena can be observed in systems other than the two primary examples studied and described in this thesis. Molecular conductors that mimic the long-distance transport of electrons found in photosynthetic reaction centres have been designed using radical pairs.[22,201–204] These systems are desirable for use in photosynthetic light-harvesting complexes,[201,205] in addition to molecular

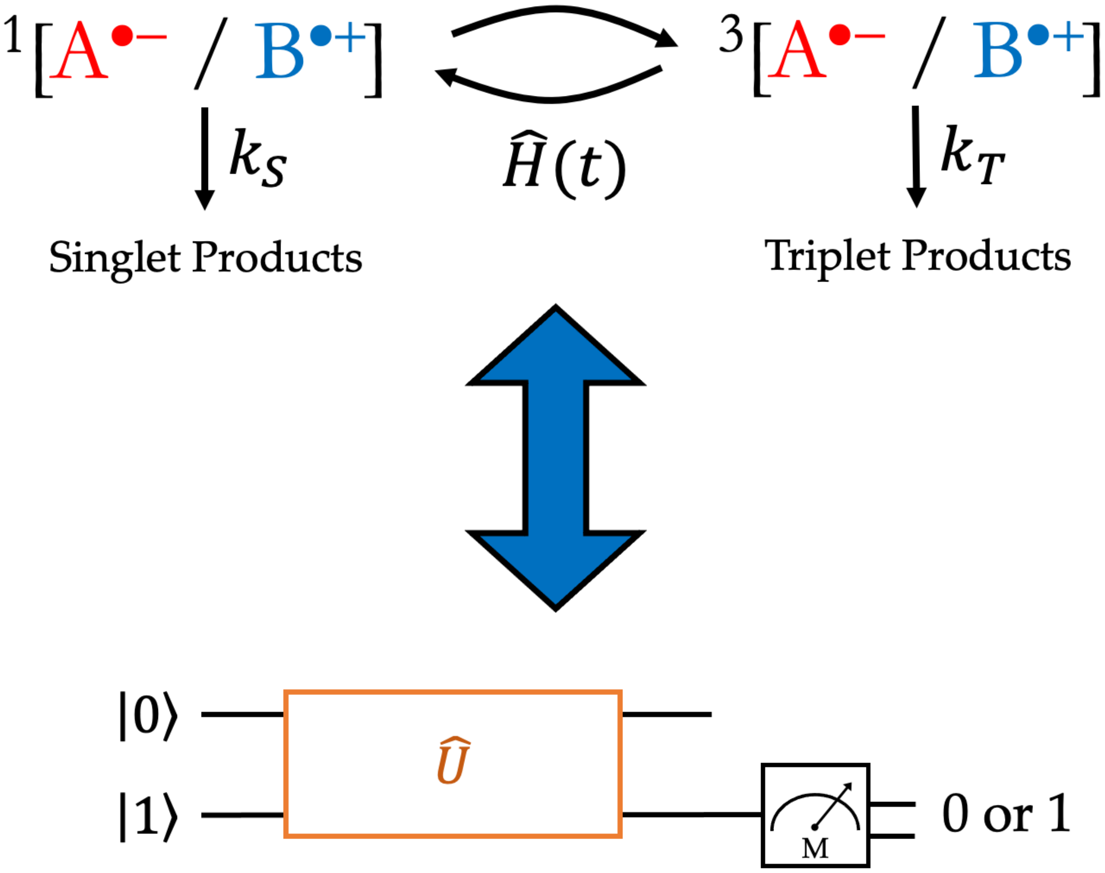

Figure 1.8 An illustration of the central aims of Chapter 5 and Appendix D): mapping a quantum circuit (shown below) from a RPM model. The circuit pictured at the bottom of the picture, is a circuit of two qubits (like the 2 electrons in a radical pair) that is controlled by some unitary action $\hat{U}$ which can be modelled with spin interactions and time-dependent magnetic fields. At the end, either one qubit (shown in this graph) or two qubits are measured to get classical information about the state of the qubit. Although real schemes of measurements are more complicated, this sort of approach with certain algorithms can do computational tasks that would have an exponential speed-up compared to classical approaches. Chapter 5 will elaborate on quantum logic gates and other aspects of mapping RPM to a quantum circuit.

electronics and nanotechnology.[206,207] Furthermore, it is believed that polaron pairs are involved in organic light-emitting diodes (OLEDs) that exhibit magnetic field effects.[208–210] Radical pair theory has provided a recent theoretical analysis of this topic.[211] Also, it has been mentioned that an artificial system based on RPM can detect extremely weak magnetic fields.[9] Recently, a similar detection use for sensing electric fields was proposed;[212] this is an intriguing new avenue for RPM that is still in its early stages and must be investigated further through experiments and theory. Lastly, there have been some suggestions that RPM can be the basis of other biological processes besides magnetoreception, such as the effects of hypomagnetic fields and radical pair formation in proteins that may contribute to harmful byproducts.[213–215] Many of these interesting systems can be modelled with *MolSpin*, a sophisticated software package for efficient modelling of spin systems;[216,217] the new additions to this software will serve as the foundation for Chapters 2 and 6.

Outline of the thesis 1.6

This thesis, following the integrated thesis structure, will start with Chapter 2 detailing all the technical details of the simulation methods used in the whole thesis.

Then, two articles examining novel concepts for investigating the radical pair-based magnetoreception hypothesis will be presented. Chapter 3 will investigate the effects of isotopic substitution on the $\left[\mathrm{FAD}^{\bullet-}\ \mathrm{TrpH}^{\bullet+}\right]$ radical pair-based compass mechanism. Specifically, simulations involving isotopic substitutions of nitrogen, carbon, and hydrogen in FAD were conducted. The purpose of this study was to determine which substitution patterns have the greatest impact on the compass mechanism, either by eradicating the information the magnetic sensor provides or altering its directional response. Using this knowledge of isotopic substitution effects, we intend to design a "killer" experiment that will provide concrete evidence of radical pair involvement in magnetoreception. The birds (most likely European robins) would be administered isotopically enriched riboflavin, an essential nutrient that can only be obtained through their diet. After a period of time during which all flavins would be replaced with isotopically enriched versions, behavioural tests would be conducted to determine the directional response of these "modified birds". A great deal of preliminary work is presently being conducted in preparation for these experiments. Furthermore, we aim to clarify a technical detail that was not fully explained in Chapter 3 which is crucial for understanding the simulations of these systems. The methods available at the time of publishing Chapter 3 had a maximum threshold of 12 or 13 nuclear spins included in simulations.Therefore, simulations of these systems involved a reduced number of nuclear spins, which is smaller than the real number in the full system. The selection of which nuclear spins to include is based on the size of the hyperfine coupling and its anisotropy. Therefore, the spins that are anisotropic and have the highest coupling constants are given priority, while isotropic spin (almost always hydrogens) with small hyperfine constants are typically excluded. This is a widely used simplification used in important studies such as Ref. 114 and 115. It is believed that omitting the isotropic hydrogen spins would not significantly affect the spin dynamics. However, large-scale studies are needed to confirm this claim, which is now possible due to the algorithmic advances made in Chapter 6.

The second study in Chapter 4 examined the effects of time-dependent magnetic fields, specifically radiofrequency noise, on the RPM of avian magnetoreception. We utilised a novel method capable of incorporating stochastic radiofrequency noise, and contrasted the results to behavioural experiments. In addition, we examined whether the action-spectrum histogram, an approximative tool for evaluating radiofrequency effects, is an accurate tool by comparing its predictions with calculations of spin dynamics.

Chapter 5 is a study on the EPR pulse sequence design for radical pair-based organic molecular spin qubits. This work expands on previous research on pulse sequences[65] that was utilised in the experimental realisation of CNOT gate action on molecular spin qubits in Ref. 14, which claimed that this operation was accomplished with a fidelity of 0.97. This is an exceptionally high number for an organic system at the relatively high experimental temperature of 85 K. Our research demonstrates that this is not feasible. For these systems, an upper bound for the fidelity of this quantum gate operation was derived, and it is evident that 0.97 fidelity is an impossible value for these experiments. In addition, flaws were discovered in the initial pulse sequence protocols described in Ref. 65 , meaning that the study described in Ref. 14 did not accomplish a CNOT gate operation but rather a similar quantum gate operation. Instead, we have proposed the correct sequences for these experiments, which are also significantly more concise and straightforward to implement. For instance, for a more complex high-field Hamiltonian, Ref. 65 proposed a pulse sequence consisting of 16 selective pulses and 3 non-selective pulses, whereas the same result can be obtained with as few as 5 selective pulses (for a radical pair initialised in a singlet state). Consequently, there is no definitive instance of a CNOT quantum gate experiment for an RPM-based organic molecular spin qubit. In the experimental investigation presented in Appendix D, we will demonstrate a successful application of a CNOT quantum logic gate to a radical-pair based molecular spin qubit.

Lastly, Chapter 6 was dedicated to novel implementations to software package *MolSpin*, which is an advanced platform for simulating radical pair systems. We incorporated new research into the Stochastic Schrödinger Equation (SSE)[218] and the approximations of quantum mechanical traces[49] to generate a comprehensive framework of methods capable of modelling a wide variety of interesting and previously inaccessible RPM systems. This is the result of rigorous engineering, the incorporation of modern linear algebra algorithms, and the introduction of new simulation ideas. For instance, we developed a heuristic that in some instances can reduce by a factor of 5 the required integration time of quantum mechanical yields. This new framework will be presented with different replicated results from the literature and with new simulations that demonstrate the power of these new software additions.

* * *

2 Simulation of Radical Pairs

In this section, we will first review some theory important to understanding simulations of RPM. Then, we will review some of the common methods of simulating radical pairs that were used in Chapters 3 and 4. The discussion will then be extended to a complete framework of spin dynamics that is the foundation of Chapter 6 and has been implemented into the *MolSpin* software package. Two state vector propagation methods, *stochastic* and *direct*, will be overviewed which constitute a complete toolkit for simulating any radical pair reaction of interest. We will continue with a quick review of methods that are not part of this thesis yet are important parts of simulating radical pair processes: semi-classical approximations and quantum computer algorithms. Finally, we will conclude with a short review of the molecular dynamics methods that were used in Chapter 6

Hamiltonian Matrix 2.1

The Hamiltonian $\hat{H}$ is the fundamental object of modelling any quantum mechanical system. When we are modelling RPM, this object is a matrix of $N \times N$ dimensions, where N is the size of the full spin space, calculated as:

$$N = 4 \prod_{n} (2I_n + 1) \tag{2.1}$$

Here 4 accounts for 2 electron spins of multiplicity 2, and I_n is the spin quantum number of nuclear spin n. The growth of N is exponential in relation to the total number of nuclear spins that are involved in the dynamics. This poses a challenge when attempting to translate mathematical concepts related to spin dynamics into computer code.

If the Hamiltonian $\hat{H}$ is stored in *dense* format, it will consist of a total of N^2 elements. The term "*dense*" is used to describe a scenario in which all elements of a matrix are stored in random access memory (RAM), regardless of whether the element has a value of zero. Every element necessitates a storage capacity of 16 bytes. The reason for this is mostly attributed to the utilisation of double precision, which necessitates the allocation of 8 bytes for each numerical value.[219] In the context of complex numbers, a single complex number requires two numerical values, resulting in a total requirement of 16 bytes. Hence, the memory requirement for allocating $\hat{H}$ in *dense* format:

$$M_{Dense}(N) = 16 \times N^2 \text{ bytes} = \frac{16 \times N^2}{1024} \text{ kB} = \frac{16 \times N^2}{1024^2} \text{ MB} = \frac{16 \times N^2}{1024^3} \text{ GB} \qquad 2.2$$

As demonstrated in Table 2.1, storage requirement M_{Dense} quickly increases as N increases.

No. of Nuc. Spins	N	$M_{Dense}(N)$	$M_{Sparse}(N)$	$\mathcal{S}$
2	16	4 kB	3 kB	50%
4	64	64 kB	18 kB	18.75%
6	256	1 MB	96 kB	6.25%
8	1024	16 MB	480 kB	1.95%
10	4096	256 MB	2.25 MB	0.59%
12	16384	4 GB	10.5 MB	0.17%
14	65536	64 GB	48 MB	0.05%
16	262144	1 TB	216 MB	0.014%
18	1048576	16 TB	960 MB	0.004%
20	4194304	256 TB	4.13 GB	0.001%

Table 2.1 A table that illustrates how N, size of the full spin space, $M_{Dense}(N)$, memory requirement to store a *dense* matrix of dimensions $N \times N$, $M_{Sparse}(N)$, memory requirement to store a *sparse* matrix (for a typical spin Hamiltonian) of dimensions $N \times N$, and, $\mathcal{S}$, sparsity, scales with the number of nuclear spins. We exclusively use nuclear spins with spin quantum number $I = 1/2$ to allow the use of Equations 2.7 and 2.6.

Spin Hamiltonians typically exhibit a high degree of *sparsity*. A matrix is classified as *sparse* if the majority of its elements are equal to zero. Therefore, a reduced quantity of data would be required to store during a simulation. Specifically, it would be enough to store the coordinates of each element together with their corresponding values. Every coordinate can be stored as a single precision number, which only use 4 bytes per value.[219] Therefore, the memory required to store a *sparse* matrix with nnz non-zero elements:

$$\begin{aligned} M_{Sparse}(nnz) &= 16\times nnz + 4\times 2\times nnz \text{ bytes} = 24\times nnz \text{ bytes} \\ &= \frac{24\times nnz}{1024}\text{ kB} = \frac{24\times nnz}{1024^2}\text{ MB} = \frac{24\times nnz}{1024^3}\text{ GB} \end{aligned} \tag{2.3}$$

This is one of the simpler sparse matrix formats, but there are numerous sparse storage techniques.[219]

Spin Hamiltonian, in the uncoupled spin basis, will have this estimated number of non-zero elements:[54]

$$nnz = 16Z + 16Z\left(\sum_{i=1}^{2}\sum_{k=1}^{N_i}\frac{2I_{ik}}{2I_{ik}+1}\right) \tag{2.4}$$

nnz will depend on spin interactions of the system and Eq. 2.4 is taken as a general guideline useful for illustration purposes. Here, Z is total number of nuclear spin states, i.e. $N = 4Z$. If $I_{ik} = 1/2$, then nnz reduces to:[54]

$$nnz = 16Z + 8Z\log_2 Z = 2N\log_2 N \tag{2.5}$$

Examples below will assume that $I_{ik} = 1/2$ for all nuclear spins. If we plug in Eq. 2.5 into Eq. 2.3, we get:

$$M_{Sparse}(N) = 48N\log_2 N \text{ bytes} = \frac{48N\log_2 N}{1024}\text{ kB} = \frac{48N\log_2 N}{1024^2}\text{ MB} = \frac{48N\log_2 N}{1024^3}\text{ GB} \tag{2.6}$$

We can also define sparsity of spin, $\mathcal{S}$, which is the ratio between the number of nnz elements and the total number of elements:

$$\mathcal{S} = \frac{2\log_2 N}{N} \times 100\% \tag{2.7}$$

All of these trends are illustrated in Table 2.1.

The computer clusters utilised for computational purposes in this thesis were typically equipped with a maximum of 96 GB of Random Access Memory (RAM). In the context of conducting simulations and employing numerical linear algebra algorithms, it is customary to store all variables and matrices in RAM, a dedicated storage medium intended specifically for temporary data storage purposes. If the method mandates the utilisation of a *dense* format for matrix storage, it becomes evident that a matrix with the dimensions of a 14 nuclear spin matrix, as presented in Table 2.1, will approach the upper threshold of possible storage, particularly when considering the presence of additional objects involved in calculations. In contrast, the utilisation of a *sparse* format for storing the spin Hamiltonian matrix enables the routine storage and utilisation of matrices of considerable size, such as those encompassing 20 nuclear spins. Additionally, it is worth noting that the level of sparsity, $\mathcal{S}$, exhibits a decreasing trend as the magnitude of the complete spin space increases. Hence, algorithms that can leverage sparse matrix storage are preferred to algorithms that require dense matrix storage.

The choice of a matrix storage type also has an impact on the computational performance scaling of algorithms. In this thesis, the "big O" notation will be employed to represent the performance evaluation of algorithms, denoted by the symbol $\mathcal{O}$. This demonstrates the relationship between the time or space complexity of an algorithm and the scale of the system.[50,219] For instance, $\mathcal{O}(N^2)$ exhibits that the algorithm scales quadratically with the size of the system N. Hence, the storage of a *dense* matrix scales with $\mathcal{O}(N^2)$ as shown in Eq. 2.2 and seen in Table

2.1. Whereas, the storage of a *sparse* matrix scales with $\mathcal{O}(N \log_2 N)$ as shown in Eq. 2.6 and seen in Table 2.1. In practical scenarios, the scaling of time may deviate from the predetermined scaling due to several external factors that influence the efficiency of a computer programme. These factors include compilers, system architecture, computer code, and other relevant elements. However, it is often advisable to use this as a guiding principle when determining the most appropriate algorithm for a certain situation.

We can use this logic and notation to investigate two main operations that are fundamental to spin dynamics simulations, *matrix* × *matrix* multiplication and *matrix* × *vector* multiplication. First, for *matrix* × *vector* multiplication, with matrix $N \times N$ and vector $N \times 1$, *dense* matrix format for both objects requires N multiplications and additions to generate the first component of the vector. This will be repeated N times for N components, so the scaling of the whole operation becomes $\mathcal{O}(N^2)$. However, in *sparse* matrix format we will only have $N \log_2 N$ components in the matrix, reducing the scaling of the operation to $\mathcal{O}(N \log_2 N)$. Exactly the same applies to *matrix* × *matrix* multiplication, for *dense* storage it is $\mathcal{O}(N^3)$ whereas for *sparse* storage (one of matrix is sparse and the other dense) it is $\mathcal{O}(N^2 \log_2 N)$. These ideas will be important when considering the speed and computational power of algorithms.

Liouville Space 2.2

The Liouville-von-Neumann equation in Eq. 1.9 can be written in alternative form, through the Liouville space representation:[56]

$$\frac{d\left|\hat{\rho}(t)\right\rangle}{dt} = -\hat{\hat{\mathcal{L}}}\left|\hat{\rho}(t)\right\rangle \tag{2.8}$$

Here, this equation is linear in $\hat{\rho}$ and this can be achieved by defining the Liouvillian *superoperator*:

$$\hat{\hat{\mathcal{L}}} = i\left[\hat{H},\cdot\right] + \left\{\hat{K},\cdot\right\} \tag{2.9}$$

The matrix form of $\hat{\hat{\mathcal{L}}}$:

$$\hat{\hat{\mathcal{L}}} = i\left(\hat{H}\otimes\mathbb{I}_N - \mathbb{I}_N\otimes\hat{H}^T\right) + \left(\hat{K}\otimes\mathbb{I} + \mathbb{I}\otimes\hat{K}^T\right) \tag{2.10}$$

This simplifies to this form for *symmetric* recombination (reviewed in Sec.2.5.1):[114]

$$\hat{\hat{\mathcal{L}}} = i\left(\hat{H}\otimes\mathbb{I}_N - \mathbb{I}_N\otimes\hat{H}^T\right) + k_S\mathbb{I}_{N^2} \tag{2.11}$$

Note that the density operator in Eq. 2.8 is in a different form–we refer to this as "flatten" form of a density matrix, for instance for a 2 × 2 density matrix $\hat{\rho}$:

$$\hat{\rho} = \begin{pmatrix} \rho_{11} & \rho_{12} \\ \rho_{21} & \rho_{22} \end{pmatrix} \Longleftrightarrow \left|\hat{\rho}\right\rangle = \begin{pmatrix} \rho_{11} \\ \rho_{12} \\ \rho_{21} \\ \rho_{22} \end{pmatrix} \tag{2.12}$$

The solution to the Eq. 2.8 is:

$$\left|\hat{\rho}(t)\right\rangle = e^{-\hat{\hat{\mathcal{L}}}t}\left|\hat{\rho}(t)\right\rangle \tag{2.13}$$

We can use this solution to calculate Φ_S:

$$\Phi_S = k_S \int_0^\infty P_S(t)dt \tag{2.14}$$

Here,

$$P_S(t) = \mathrm{Tr}\left[\left\langle \hat{P}_S \middle| e^{-\hat{\hat{\mathcal{L}}}t} \middle| \hat{\rho}(0) \right\rangle\right] = \left\langle \hat{P}_S \middle| e^{-\hat{\hat{\mathcal{L}}}t} \middle| \hat{\rho}(0) \right\rangle \tag{2.15}$$

Hence,

$$\begin{aligned}
\Phi_S &= k_S \int_0^\infty \left\langle \hat{P}_S \middle| e^{-\hat{\hat{\mathcal{L}}}t} \middle| \hat{\rho}(0) \right\rangle dt \\
&= k_S \left\langle \hat{P}_S \middle| \int_0^\infty e^{-\hat{\hat{\mathcal{L}}}t} dt \middle| \hat{\rho}(0) \right\rangle \\
&= -k_S \left\langle \hat{P}_S \middle| \left[\hat{\hat{\mathcal{L}}}^{-1} e^{-\hat{\hat{\mathcal{L}}}t} \right]_{t=0}^{t=\infty} \middle| \hat{\rho}(0) \right\rangle \\
&= k_S \left\langle \hat{P}_S \middle| \hat{\hat{\mathcal{L}}}^{-1} \middle| \hat{\rho}(0) \right\rangle
\end{aligned} \tag{2.16}$$

Only the basics of this approach are outlined here. This is a very expansive topic and one of the main tools for analysing open quantum systems.[220] It has extensively been used in RPM research for calculating quantities, deriving new master equations, and proving mathematical properties.[32,35,39,40,47,114,221–223]

The scope of this thesis will be constrained to a narrow examination of this subject matter, as Louiville space algorithms are not well-suited for modelling large spin systems. The solution of Eq. 2.16 corresponds to the solution of a linear system of equations, for which there are several efficient iterative methods available that exhibit good scalability, depending on the particular features of the system under consideration.[219] However, the primary concern arises from the system's complexity, as it requires the utilisation of superoperators with dimensions of $N^2 \times N^2$. Therefore, despite the computational complexity of solving this system (at the best case) being $\mathcal{O}(D^2)$, with D representing the system size, the effective complexity would be $\mathcal{O}(N^4)$,where N denotes the size of the entire spin Hilbert space. The scalability of this approach is suboptimal, and it is anticipated that storage limitations would arise expeditiously, even in the case when all matrices are sparse. As a consequence, the focus of our research in this thesis was to use Hilbert space methods for addressing spin dynamics problems.

Time Dependence in Spin Dynamics 2.3

The central equation for modelling dynamics of RPM is the modified Liouville-von-Neumann equation, that includes Haberkorn recombination operator, in Eq. 1.9, reviewed in Chapter 1.3. Eq. 1.9 assumes that there are no time-dependent change in $\hat{H}$ or $\hat{K}$–only $\hat{\rho}(t)$ changes in times. This case will be refereed to as the *Static* case.

The Liouville-von-Neumann equation can be expanded to incorporate time variation in the interaction terms:[47,218]

$$\frac{d\hat{\rho}(t)}{dt} = -i\left[\hat{H}(t), \hat{\rho}(t)\right] - \left\{\hat{K}(t), \hat{\rho}(t)\right\} \tag{2.17}$$

This case will be refereed to as the *Dynamic* case. The time-dependence in the Hamiltonian is incorporated by separating it to a static, $\hat{H}_0$, and time-dependent part, $\hat{V}(t)$:

$$\hat{H} = \hat{H}_0 + \hat{V}(t) = \hat{H}_0 + \sum_j f_j(t)\hat{A}_j \tag{2.18}$$

Here $f_j(t)$ are scalar stochastic fluctuation functions for a spin operator $\hat{A}_j$. To illustrate this notation with an example, imagine a system that has a magnetic field that points to the z-direction with strength $|\mathbf{B}|$ which oscillates as a sinusoid with frequency ν_D:

$$\hat{H} = (1 - cos(\nu_D t))(\mathbf{B} \cdot \hat{\mathbf{S}}_1 + \mathbf{B} \cdot \hat{\mathbf{S}}_2) = (1 - cos(\nu_D t))|\mathbf{B}|\hat{S}_{1z} + (1 - cos(\nu_D t))|\mathbf{B}|\hat{S}_{2z} \tag{2.19}$$

There will two time-dependent components: $f_1(t) = f_2(t) = (1 - cos(\nu_D t))|\mathbf{B}|$ and $\hat{A}_1 = \hat{S}_{1z}$ and $\hat{A}_2 = \hat{S}_{2z}$. All time-dependent spin interactions can be described in this way.

The time-dependent reaction recombination operator, $\hat{K}(t)$, has the following form:

$$\hat{K}(t) = \sum_{\Theta} \frac{k_{\Theta}(t)}{2} \hat{P}_{\Theta} \tag{2.20}$$

Where k_{Θ} is the reaction rate coefficient for state Θ, $\Theta \in \{S, T_+, T_-, T_0\}$ and P_{Θ} is the projection operator of state Θ.

The solution to Eq. 2.17 is:

$$\hat{\rho}(t) = \hat{U}(t,0)\hat{\rho}(0)\hat{U}(t,0)^{\dagger} \tag{2.21}$$

Time propagator $\hat{U}(t,0)$, which evolves the state from t_0 to t_1 is defined as:

$$\hat{U}(t_1, t_0) = \hat{T} \exp\left[\int_{t_0}^{t_1} \left(-i\hat{H}(\tau) - \hat{K}(\tau)\right) d\tau\right] \tag{2.22}$$

$\hat{T}$ is time-ordering operator (or path-ordering in general).[224] It is an operator that orders the multiplication of operators in terms of time, earlier operators appearing on the right. The use of $\hat{T}$ can be exemplified by an example of its application to two operators at different times:

$$\hat{T}\left(\hat{A}(t_1)\hat{B}(t_2)\right) = \theta(t_1 - t_2)\hat{A}(t_1)\hat{B}(t_2) + \theta(t_2 - t_1)\hat{B}(t_2)\hat{A}(t_1) \tag{2.23}$$

Here, $\theta(t)$ is "heaviside step function":

$$\theta(t) = \begin{cases} +1, & t > 0 \\ 0, & t < 0 \end{cases} \tag{2.24}$$

The need for time-ordering is more apparent when we think about the Taylor series form of the matrix exponential, $\exp(\hat{A}) = \sum_{k=0}^{\infty} 1/k!\ (\hat{A})^k$. The Eq. 2.22 can be approximated by the first order Magnus expansion, removing the need to consider time-ordering:[225]

$$\begin{aligned} \hat{U}(t_0+\delta t, t_0) &\approx \exp\left[\int_{t_0}^{t_0+\delta t} \left(-i\hat{H}(\tau) - \hat{K}(\tau)\right) d\tau\right] \\ &= \exp\left[-i\Omega(t_0+\delta t, t_0)\delta t\right] \end{aligned} \tag{2.25}$$

This approximation is valid only for small time differences $t_1 - t_0 = \delta t$. Ω is called the generator, which is used to evolve the spin state, and is given by:[218]

$$\Omega(t_0+\delta t, t_0) = \hat{H}_0 - \frac{i}{2\delta t}\sum_{\Theta} \hat{P}_{\Theta} \int_{t_0}^{t_0+\delta t} k_{\Theta}(\tau)d\tau + \frac{1}{\delta t}\sum_{j} \hat{A}_j \int_{t_0}^{t_0+\delta t} f_j(\tau)d\tau \tag{2.26}$$

The use of this will be extended in Secs. 2.6 and 2.5.2.

Time Step Choice 2.4

Prior to discussing the algorithms, it is important to examine an essential yet sometimes overlooked question, which is the choice of the time step size.

A common calculated value for RPM is the singlet yield (yet the described ideas will be analogous and important to any other yield calculation):

$$\Phi_S = k_S \int_0^\infty P_S(t)dt \tag{2.27}$$

Some of the common simulation algorithms evaluate $P_S(t)$ for a fixed number of time points N_t from 0 to T (defined as total integration time which is not necessarily $T = \infty$, discussed thoroughly in Sec. 2.6 and Chapter 6) and then numerically integrate $P_S(t)$ to find the singlet yield. Hence, we need to choose a time step δt, defined as:

$$\delta t = \frac{T}{N_t} \tag{2.28}$$

The selection of δt is non-trivial and it must be sufficiently small to effectively capture the quantum dynamics of the spin system. In order to adhere to the Nyquist sampling condition, it is necessary to ensure that the system is evolved using a time step equivalent to a minimum of two data points per period of the most rapid oscillation:[226]

$$\delta t = \frac{T_{fast}}{2} \tag{2.29}$$

Here T_{fast} is the period of the fastest motion. T_{fast} can be approximated by examining the coupling strengths within the Hamiltonian and the rates of recombination processes. Alternatively, in can be calculated with the eigenvalue decomposition of $\hat{H}$: $\hat{H} = \hat{V}\hat{E}\hat{V}^{-1}$, with eigenvalues λ_i. The dominant frequency within the system will correspond to the transition occurring between the highest and lowest energy levels present:

$$\nu_{fast} = \frac{\max_i(\lambda_i) - \min(\lambda_i)}{h} \tag{2.30}$$

Here h is Planck's constant, $\max(\cdot)$ and $\min(\cdot)$ are the maximum and minimum functions. The time step will be evaluated as:

$$\delta t = \frac{1}{2\left(\nu_{fast}\right)} \tag{2.31}$$

Note that this approach only works for *static* systems and *dynamic* system that have low amplitude changes. Also, computing eigenvalues might not be possible for a large spin systems. In this case, δt can be estimated from smaller spin systems, or determined empirically.

A common choice of δt in this thesis was $\delta t = 4\,ns$ for $\left[\mathrm{FAD}^{\bullet-}\ \mathrm{TrpH}^{\bullet+}\right]$ radical pair systems, yet, this is not a rule of thumb and depends on the system to be simulated.

Simulation Methods 2.5

In this section we will review the simulation methods used the throughout thesis which are not state vector propagation based, i.e. ones reviewed in Sec. 2.6.

Full Quantum Dynamics via Matrix Diagonalization 2.5.1

This is a fully accurate method that is used for *static* simulations and *symmetric* recombination. *Symmetric* recombination refers to a case when the recombination rate constants for spin-selective singlet and triplet pathways are equal, $k_S = k_T$. This is a very common simplification to the dynamics that reduces computational cost and mathematical complexity of $\hat{K}$:

$$\hat{K} = \frac{k_S}{2}\hat{P}_S + \frac{k_T}{2}\hat{P}_T = \frac{k_S}{2}\left(\hat{P}_S + \hat{P}_T\right) = \frac{k_S}{2}\mathbb{I}_N \tag{2.32}$$

Hence, reducing the recombination processes to a scalar value ($\mathbb{I}_N$ is commutative with any matrix and hence the exponentials from Eq. 1.19 can be simplified; this will be demonstrated below in the derivation of the method).

This method utilizes eigenvalue decomposition of $\hat{H}$:[219]

$$\hat{H} = \hat{V}\ \hat{E}\ \hat{V}^{-1} \tag{2.33}$$

Here $\hat{V}$ are the eigenvectors and $\hat{E}$ are the eigenvalues of $\hat{H}$. The method described below requires the full spectrum of $\hat{H}$ (i.e. all eigenvalues) and all eigenvectors that are generally *dense*. The main algorithm that is used to compute the eigenvalue decomposition, QR algorithm, requires that the $\hat{H}$ is stored in *dense* format.[219] The intricacies of this will be not explored here, yet the outcome of storing the Hamiltonian as a *dense* matrix has a far reaching consequence of this method having a clear limit of the size of the system, around 12 – 14 nuclear spins. This is explored further in Chapter 6. Overall, this is a great method for intermediate-size problems, as well as benchmarking new methods.

The formula to compute the Singlet Yield is given as:[227]

$$\Phi_S = \frac{1}{Z}\sum_{m=1}^{4Z}\sum_{n=1}^{4Z}\left|\left(\hat{P}_S\right)_{nm}\right|^2 \frac{k_S^2}{k_S^2+\omega_{nm}^2} \qquad 2.34$$

Where Z is the size of nuclear spin subspace of the radical pair, k_S is the symmetric recombination constant, $\left(\hat{P}_S\right)_{nm} = \langle n|\,\hat{P}_S\,|m\rangle$, $|n\rangle$ is eigenstate n and $\omega_{nm} = E_n - E_m$, where E_n is the energy of eigenstate n.

Derivation of the method[227]

Singlet yield is defined as:

$$\Phi_S = k_S \int_0^{\infty} P_S(t)dt \qquad 2.35$$

Here,

$$P_S(t) = \mathrm{Tr}\left[\hat{P}_S\hat{\rho}(t)\right] = \mathrm{Tr}\left[\hat{P}_S e^{-i\hat{H}t-\hat{K}t}\hat{\rho}(0)e^{+i\hat{H}t-\hat{K}t}\right] \qquad 2.36$$

The definition of $\hat{\rho}(t)$ in Eq. 1.19 was used here. It was shown in Eq. 2.32 that $\hat{K} = k_S\,\mathbb{I}_N\,/2$, hence, the exponential propagator can be simplified as:

$$e^{-i\hat{H}t-\hat{K}t} = e^{-i\hat{H}t-\frac{k_S}{2}t\mathbb{I}_N} = e^{-i\hat{H}t}e^{-\frac{k_S}{2}t\mathbb{I}_N} = e^{-\frac{k_S}{2}t}e^{-i\hat{H}t} \qquad 2.37$$

The simplification can be made since $\left[\hat{H}, \mathbb{I}_N\right] = 0$, that can be shown through the Lie formula for an exponential matrix:[50]

$$e^{\hat{A}+\hat{B}} = \lim_{k\to\infty}\left(e^{\frac{1}{k}\hat{A}}e^{\frac{1}{k}\hat{B}}\right)^k \qquad 2.38$$

Plugging in the Taylor form of the exponential matrix, we find:

$$\begin{aligned}
e^{\frac{1}{k}\hat{A}}e^{\frac{1}{k}\hat{B}} &= \left(\sum_{n=0}^{\infty}\frac{1}{n!k^n}\hat{A}^n\right)\left(\sum_{m=0}^{\infty}\frac{1}{m!k^m}\hat{B}^m\right)\\
&= \left(\mathbb{I}+\frac{1}{k}\hat{A}+\frac{1}{2k^2}\hat{A}^2+\frac{1}{6k^3}\hat{A}^3+\ldots\right)\left(\mathbb{I}+\frac{1}{k}\hat{B}+\frac{1}{2k^2}\hat{B}^2+\frac{1}{6k^3}\hat{B}^3+\ldots\right)\\
&= \mathbb{I}+\frac{1}{k}\left(\hat{A}+\hat{B}\right)+\frac{1}{2k^2}\left(\hat{A}^2+2\hat{A}\hat{B}+\hat{B}^2\right)+\ldots\\
&= \mathbb{I}+\frac{1}{k}\left(\hat{A}+\hat{B}\right)+\frac{1}{2k^2}\left(\hat{A}+\hat{B}\right)^2+\ldots = e^{\frac{1}{k}(\hat{A}+\hat{B})}
\end{aligned} \tag{2.39}$$

The change from 3rd line to the last line required $\left[\hat{A},\hat{B}\right]=0$.

Hence, the trace in Eq. 2.36 is simplified to:

$$P_S(t) = e^{-k_S t}\mathrm{Tr}\left[\hat{P}_S e^{-i\hat{H}t}\hat{\rho}(0)e^{+i\hat{H}t}\right] = e^{-k_S t}P_S'(t) \tag{2.40}$$

$P_S(t)'$ is the expectation value of the singlet projection operator acting on the spin system when only $\hat{H}$ interactions influence spin dynamics. Thus, the singlet yield when recombination rates are *symmetric* is given as:

$$\Phi_S = k_S\int_0^{\infty} e^{-k_s t}P_S'(t)\,dt \tag{2.41}$$

Inserting eigenvalue decomposition of $\hat{H}$ to $P_S'(t)$ gives:

$$\begin{aligned}
P_S'(t) &= \mathrm{Tr}\left[\hat{P}_S e^{-i\hat{H}t}\hat{\rho}(0)e^{+i\hat{H}}\right] = \frac{1}{Z}\mathrm{Tr}\left[e^{-i\hat{H}t}\hat{P}_S e^{+i\hat{H}t}\hat{P}_S\right]\\
&= \frac{1}{Z}\mathrm{Tr}\left[\hat{V}e^{-i\hat{E}t}\hat{V}^{-1}\hat{P}_S\hat{V}e^{+i\hat{E}t}\hat{V}^{-1}\hat{P}_S\right] = \frac{1}{Z}\mathrm{Tr}\left[e^{-i\hat{E}t}\hat{P}_S''e^{+i\hat{E}t}\hat{P}_S''\right]
\end{aligned} \tag{2.42}$$

$\hat{E}$ is diagonal with eigenvalues as elements. Derivations were made with the cyclic property of the trace and we defined $\hat{P}_S'' = \hat{V}^{-1}\hat{P}_S\hat{V}$.

$\hat{P}''_S$ can be further redefined by inserting resolutions of identity of the Hamiltonian eigenstates, $\mathbb{I}_N = \sum_{n=1}^{4Z} |n\rangle\langle n|$, to $P'_S(t)$:

$$\begin{aligned}
P'_S(t) &= \frac{1}{Z}\mathrm{Tr}\left[e^{-i\hat{E}t}\left(\sum_{m=1}^{4Z}|m\rangle\langle m|\right)\hat{P}''_S\left(\sum_{n=1}^{4Z}|n\rangle\langle n|\right)e^{+i\hat{E}t}\left(\sum_{k=1}^{4Z}|k\rangle\langle k|\right)\hat{P}''_S\left(\sum_{n=1}^{4Z}|l\rangle\langle l|\right)\right] = \\
&= \frac{1}{Z}\sum_{m,n,k,l=1}^{4Z}\langle l|e^{-i\hat{E}t}|m\rangle\langle m|\hat{P}''_S|n\rangle\langle n|e^{+i\hat{E}t}|k\rangle\langle k|\hat{P}''_S|l\rangle = \\
&= \frac{1}{Z}\sum_{m,n,k,l=1}^{4Z}\langle l|e^{-i\hat{E}t}|m\rangle\langle n|e^{+i\hat{E}t}|k\rangle\langle m|\hat{P}''_S|n\rangle\langle l|\hat{P}''_S|k\rangle^* = \\
&= \frac{1}{Z}\sum_{m,n=1}^{4Z}e^{-iE_mt}e^{+iE_nt}\left|\langle m|\hat{P}''_S|n\rangle\right|^2 = \frac{1}{Z}\sum_{m=1}^{4Z}\sum_{n=1}^{4Z}\left|\left(\hat{P}''_S\right)_{mn}\right|^2 e^{-i\omega_{mn}t}
\end{aligned}$$

2.43

The trace operation in the third line can be removed since we have a scalar number as the argument. Also, in the third line the hermiticity property of the hermitian operator $\hat{P}''_S$, $\langle k|\hat{P}''_S|l\rangle = \langle l|\hat{P}''_S|k\rangle^*$, was used. Going from the third line to the fourth, it was assumed that $l = m$ and $n = k$. In fourth line, the full notation for the double sum is used for clarity. $\left(\hat{P}''_S\right)_{mn} = \langle m|\hat{P}''_S|n\rangle$ and $\omega_{mn} = E_m - E_n$.

Inserting Eq. 2.43 to Eq. 2.41 yields:

$$\Phi_S = \frac{k_S}{Z}\sum_{m=1}^{4Z}\sum_{n=1}^{4Z}\left|\left(\hat{P}''_S\right)_{mn}\right|^2\int_0^\infty e^{-(k_S+\omega_{mn}i)t}\,dt = \frac{k_S}{Z}\sum_{m=1}^{4Z}\sum_{n=1}^{4Z}\left|\left(\hat{P}''_S\right)_{mn}\right|^2\frac{1}{k_S+\omega_{mn}i}$$

2.44

Since,

$$\int_0^\infty e^{-(k_S+\omega_{mn}i)t}\,dt = \left[-\frac{1}{k_S+\omega_{mn}i}e^{-(k_S+\omega_{mn}i)t}\right]_0^\infty = \frac{1}{k_S+\omega_{mn}i}$$

2.45

Lastly, rationalizing complex denominator:

$$\Phi_S = \frac{k_S}{Z}\sum_{m=1}^{4Z}\sum_{n=1}^{4Z}\left|\left(\hat{P}_S''\right)_{mn}\right|^2 \frac{1}{k_S+\omega_{mn}i}\times\frac{k_S-\omega_{mn}i}{k_S-\omega_{mn}i} = \frac{k_S}{Z}\sum_{m=1}^{4Z}\sum_{n=1}^{4Z}\left|\left(\hat{P}_S''\right)_{mn}\right|^2 \frac{k_S-\omega_{mn}i}{k_S^2+\omega_{mn}^2}$$
$$= \frac{1}{Z}\sum_{m=1}^{4Z}\sum_{n=1}^{4Z}\left|\left(\hat{P}_S''\right)_{mn}\right|^2 \frac{k_S^2}{k_S^2+\omega_{mn}^2} - i\left(\frac{k_S}{Z}\sum_{m=1}^{4Z}\sum_{n=1}^{4Z}\left|\left(\hat{P}_S''\right)_{mn}\right|^2 \frac{\omega_{mn}}{k_S^2+\omega_{mn}^2}\right) \tag{2.46}$$

By noticing that $\omega_{mn} = -\omega_{nm}$, we can deduce that the imaginary part in the second line of Eq. 2.46 disappears, and we find a closed form solution of the singlet yield:

$$\Phi_S = \frac{1}{Z}\sum_{m=1}^{4Z}\sum_{n=1}^{4Z}\left|\left(\hat{P}_S''\right)_{mn}\right|^2 \frac{k_S^2}{k_S^2+\omega_{mn}^2} \tag{2.47}$$

Time-Dependent Effects for Symmetric Recombination System 2.5.2

This is a method for a *dynamic* system with *symmetric* recombination rates. Also, it is a method for *non-coupled* radicals, a term that refers to a situation when there are no interactions between electron spins and each radical has its own Hamiltonian, $\hat{H}_i$, i.e. $\left[\hat{H}_1, \hat{H}_2\right] = 0$. Hence, the Hamiltonian for the whole system will be:[63]

$$\hat{H} = \hat{H}_1 \oplus \hat{H}_2 = \hat{H}_1 \otimes \mathbb{I}_{2Z_2} + \mathbb{I}_{2Z_1} \otimes \hat{H}_2 \tag{2.48}$$

$\oplus$ denotes the Kronecker sum.[50] Z_i is the size of nuclear spin subspace of radical i. An important property of the Kronecker sum is that it can simplify exponential matrices:[50]

$$e^{\hat{A}\oplus\hat{B}} = e^{\hat{A}} \otimes e^{\hat{B}} \tag{2.49}$$

More generally, the dynamics of the individual *non-coupled* radicals can be separated–this greatly reduces the computational cost and the storage requirements for the algorithm. It is shown in the derivation below how that works in practise.

The singlet yield is calculated by:

$$\Phi_S = k_S \int_0^{\infty} e^{-k_S t} P_S^{'}(t) dt \tag{2.50}$$

Where,[48,63,228]

$$P_S^{'}(t) = \frac{1}{4} + \sum_{\alpha\beta}^{x,y,z} R_{\alpha\beta}^{(1)}(t) \otimes R_{\alpha\beta}^{(2)}(t) \tag{2.51}$$

$R_{\alpha\beta}^{(i)}(t)$ is the electron spin correlation tensors for radical i. More details and definitions are shown below in the derivation of the method.

This is a great method overall yet it has five major disadvantages: 1) it uses *dense* matrices, 2) it only describes *symmetric* recombination processes, 3) the time scaling is some form of $O(N_i^3)$, hence, it gets too expensive for large systems, 4) it does not include electron spin - electron spin effects which are necessary for modelling real systems, 5) the split operator form is used in the algorithm which has an intrinsic error–hence, either the time step or the time-dependent interactions have to be small (shown below and derived in Appendix B). The described approach proves to be highly effective in addressing particular systems, particularly those with approximately seven nuclear spins within each radical. However, subsequent sections will delve into more sophisticated methods for studying time-dependent dynamics. This was the main computational approach used in Chapter 4.

Derivation of the method[63]

The singlet yield for a *symmetric* system (from Eq. 2.41):

$$\Phi_S = k_S \int_0^{\infty} e^{-k_S t} P_S^{'}(t) dt \tag{2.52}$$

With,

$$P'_S(t) = \mathrm{Tr}[\hat{\rho}(t)\hat{P}_S] = \frac{1}{Z}\mathrm{Tr}[\hat{P}_S e^{+i\hat{H}t}\hat{P}_S e^{-i\hat{H}t}] \tag{2.53}$$

Substituting the definition of $\hat{P}_S$ from Eq. 1.16 to $P'_S(t)$:

$$\begin{aligned} P'_S(t) =& \frac{1}{Z}\mathrm{Tr}\left[\left(\frac{1}{4}\mathbb{I}_N - \hat{\mathbf{S}}_1 \cdot \hat{\mathbf{S}}_2\right) e^{+i\hat{H}t} \left(\frac{1}{4}\mathbb{I}_N - \hat{\mathbf{S}}_1 \cdot \hat{\mathbf{S}}_2\right) e^{-i\hat{H}t}\right] \\ =& \frac{1}{Z}\mathrm{Tr}\left[\frac{1}{16}\mathbb{I}_N - \frac{1}{2}\hat{\mathbf{S}}_1 \cdot \hat{\mathbf{S}}_2 + \hat{\mathbf{S}}_1 \cdot \hat{\mathbf{S}}_2 e^{+i\hat{H}t}\hat{\mathbf{S}}_1 \cdot \hat{\mathbf{S}}_2 e^{-i\hat{H}t}\right] \\ =& \frac{1}{Z}\left(\mathrm{Tr}\left[\frac{1}{2}\hat{P}_S - \frac{1}{16}\mathbb{I}\right] + \mathrm{Tr}\left[\hat{\mathbf{S}}_1 \cdot \hat{\mathbf{S}}_2 e^{+i\hat{H}t}\hat{\mathbf{S}}_1 \cdot \hat{\mathbf{S}}_2 e^{-i\hat{H}t}\right]\right) \end{aligned} \tag{2.54}$$

The first term:

$$\frac{1}{Z}\mathrm{T}r\left[\frac{1}{2}\hat{P}_S - \frac{1}{16}\mathbb{I}\right] = \frac{1}{2Z}\mathrm{Tr}[\hat{P}_S] - \frac{1}{16Z}Tr[\mathbb{I}] = \frac{1}{2Z}Z - \frac{1}{16Z}4Z = \frac{1}{4} \tag{2.55}$$

The second term (using the facts that $\hat{H} = \hat{H}_1 \oplus \hat{H}_2$ and that $[\hat{H}_1, \hat{H}_2] = 0$):

$$\begin{aligned} &\frac{1}{Z}\mathrm{Tr}\left[\hat{\mathbf{S}}_1 \cdot \hat{\mathbf{S}}_2 e^{+i\hat{H}t}\hat{\mathbf{S}}_1 \cdot \hat{\mathbf{S}}_2 e^{-i\hat{H}t}\right] = \\ &= \frac{1}{Z}\sum_{\alpha\beta}^{x,y,z}\mathrm{Tr}\left[\left(\hat{S}_{1\alpha} \otimes \hat{S}_{2\alpha}\right) e^{+i\hat{H}t} \left(\hat{S}_{1\beta} \otimes \hat{S}_{2\beta}\right) e^{-i\hat{H}t}\right] \\ &= \frac{1}{Z}\sum_{\alpha\beta}^{x,y,z}\mathrm{Tr}\left[\left(\hat{S}_{1\alpha} \otimes \hat{S}_{2\alpha}\right) e^{+i(\hat{H}_1 \oplus + \hat{H}_2)t} \left(\hat{S}_{1\beta} \otimes \hat{S}_{2\beta}\right) e^{-i(\hat{H}_1 \oplus \hat{H}_2)t}\right] \\ &= \frac{1}{Z}\sum_{\alpha\beta}^{x,y,z}\mathrm{Tr}\left[\left(\hat{S}_{1\alpha} \otimes \hat{S}_{2\alpha}\right)\left(e^{+i\hat{H}_1 t} \otimes e^{+i\hat{H}_2 t}\right)\left(\hat{S}_{1\beta} \otimes \hat{S}_{2\beta}\right)\left(e^{-i\hat{H}_1 t} \otimes e^{-i\hat{H}_2 t}\right)\right] \\ &= \frac{1}{Z_1 Z_2}\sum_{\alpha\beta}^{x,y,z}\mathrm{Tr}\left[\left(\hat{S}_{1\alpha}e^{+i\hat{H}_1 t}\hat{S}_{1\beta}e^{-i\hat{H}_1 t}\right) \otimes \left(\hat{S}_{2\alpha}e^{+i\hat{H}_2 t}\hat{S}_{2\beta}e^{-i\hat{H}_2 t}\right)\right] \\ &= \sum_{\alpha\beta}^{x,y,z} R^{(1)}_{\alpha\beta}(t) \otimes R^{(2)}_{\alpha\beta}(t) \end{aligned} \tag{2.56}$$

The sum $\sum_{\alpha\beta}$ is a double sum over α, β which are simply Cartesian directions x, y and z. $R^{(i)}_{\alpha\beta}$ are electron spin correlation tensors for the spin in radical i:[63]

$$R^{(i)}_{\alpha\beta}(t) = \frac{1}{Z_i}\mathrm{Tr}_{2Z_i}\left[\hat{S}_{i\alpha}e^{+i\hat{H}_i t}\hat{S}_{i\beta}e^{-i\hat{H}_i t}\right] = \frac{1}{Z_i}\mathrm{Tr}_{2Z_i}\left[\hat{S}_{i\alpha}(0)\hat{S}_{i\beta}(t)\right] \tag{2.57}$$

$\mathrm{Tr}_{2Z_i}[\cdot]$ is the trace over $2Z_i$ elements of the spin subspace of radical i. With, $\hat{S}_{i\beta}(t) = e^{+i\hat{H}_i t}\hat{S}_{i\beta}e^{-i\hat{H}_i t}$. Hence, $P'_S(t)$ will simplify to:[48,63,228]

$$\hat{P}'_S(t) = \frac{1}{4} + \sum_{\alpha\beta}^{x,y,z} R^{(1)}_{\alpha\beta}(t) \otimes R^{(2)}_{\alpha\beta}(t) \tag{2.58}$$

Hence, to compute $P'_S(t)$ we need to find the 9 terms in the double sum and collect them for each time point t. From this point there are different approaches to solve Eq. 2.52. We will choose to time-evolve each spin correlation tensor, done by equation:

$$R^{(i)}_{\alpha\beta}(t+\delta t) = \frac{1}{Z_i}\mathrm{Tr}_{2Z_i}\left[\hat{S}_{i\alpha}(0)\hat{S}_{i\beta}(t+\delta t)\right] \text{ and } \hat{S}_{i\beta}(t+\delta t) = e^{+i\hat{H}_i \delta t}\hat{S}_{i\beta}(t)e^{-i\hat{H}_i \delta t} \tag{2.59}$$

By evolving the correlation tensors for N_t with some time step dt, and evolving long enough so that the radical pair is mostly recombined, we can numerically integrate Eq. 2.52 with trapezium rule to find the singlet yield. Also, one reduction in computational cost comes from realizing that only $\hat{S}_{ix}(t)$ and $\hat{S}_{iy}(t)$ are needed to describe the dynamics for each radical i at some time t, because:

$$\hat{S}_{iz} = -2i\hat{S}_{ix}(t)\hat{S}_{iy}(t) \tag{2.60}$$

This comes from the properties of electron spin operators.

The Hamiltonian $\hat{H}$ can be extended from this point to a time-dependent case, following the dynamics described in Eq. 2.17. This is done by replacing the exponentials of a *static* Hamiltonian with the exponentials of a *dynamic* Hamiltonian, discussed in Sec. 2.3 and showed in Eqs. 2.25 and 2.26:

$$e^{-i\hat{H}\delta t} \Rightarrow \hat{T}e^{\int_t^{t+\delta t}\left(-i\hat{H}(\tau)\right)d\tau} \approx e^{-i\Omega(t+\delta t,t)\delta t} \tag{2.61}$$

The generator Ω has a time-dependent part, $\hat{H}_{TD}$ and a *static* part, $\hat{H}_S$:

$$\begin{aligned} \Omega(t+\delta t,t) &= \hat{H}_S + \hat{H}_{TD}(t+\delta t,t) \\ \hat{H}_S &= \hat{H}_0 \\ \hat{H}_{TD}(t+\delta t,t) &= \frac{1}{\delta t}\sum_j \hat{A}_j \int_t^{t+\delta t} f_j(\tau)d\tau \end{aligned} \tag{2.62}$$

The split operator form (second order Trotter expansion) is used to decompose this as:[229]

$$e^{-i\left(\hat{H}_S+\hat{H}_{TD}(t+\delta t,t)\right)\delta t} = e^{-\frac{i}{2}\hat{H}_{TD}(t+\delta t,t)\delta t}e^{-i\hat{H}_S\delta t}e^{-\frac{i}{2}\hat{H}_{TD}(t+\delta t,t)\delta t} + \mathcal{O}(\delta t^3) \tag{2.63}$$

The error of this decomposition is derived in in Appendix B. The reason for using the split operator format is that we can evaluate the *static* and *dynamic* contributions separately. The exponential of $\hat{H}_S$ can be evaluated once, and re-used multiple times. It is evaluated by calculating the eigenvalue decomposition of $\hat{H}_S$:

$$\hat{H}_S = \hat{V}\hat{E}\hat{V}^{-1} \text{ and } e^{-i\hat{H}_S\delta t} = \hat{V}e^{-i\hat{E}\delta t}\hat{V}^{-1} \tag{2.64}$$

The exponential propagator of $\hat{H}_{TD}$ will have to be recalculated for each time propagation step. Usually, the structure of the time-dependent interactions can be exploited to simplify the calculations of this exponential operator. For instance, in the study in Chapter 4, $\hat{H}_{TD}$ only included time-dependent magnetic fields:

$$\hat{H}_{TD,i}(t+\delta t,t) = \frac{1}{\delta t}\left(\int_t^{t+\delta t} f_B(\tau)d\tau\right)\mathbf{B}_i(t)\cdot\hat{\mathbf{S}}_i = \tilde{\mathbf{B}}_i(t)\cdot\hat{\mathbf{S}}_i \tag{2.65}$$

$\hat{H}_{TD,i}$ is time-dependent Hamiltonian for radical i. $\mathbf{B}_i(t)$ is unit vector that denotes the magnetic field direction at time t, $f_B(t)$ is a scalar function that denotes the magnetic field's strength which can fluctuate during the reaction. Since $\mathbf{B}_i(t) = \left(B_{ix}(t),\ B_{iy}(t),\ B_{iz}(t)\right)^T$, then we can define:

$$\begin{aligned}\tilde{\mathbf{B}}_i(t) &= \frac{1}{\delta t}\left(\left(\int_t^{t+\delta t} f_B(\tau)d\tau\right)B_{ix}(t),\ \left(\int_t^{t+\delta t} f_B(\tau)d\tau\right)B_{iy}(t),\ \left(\int_t^{t+\delta t} f_B(\tau)d\tau\right)B_{iz}(t)\right)^T \\ &= \left(\tilde{B}_{ix}(t),\ \tilde{B}_{iy}(t),\ \tilde{B}_{iz}(t)\right)^T\end{aligned} \qquad 2.66$$

$\hat{H}_{TD,i}$ can be evaluated in the single electron subspace and multiplied by the identity matrix for the larger nuclear spin subspace of radical i to get the needed matrix in the full subspace of radical i:

$$\hat{H}_{TD}(t+\delta t, t) = \left(\tilde{\mathbf{B}}_i(t)\cdot\hat{\mathbf{S}}_i\right)\otimes\mathbb{I}_{Z_i} = \mathcal{B}_i(t)\otimes\mathbb{I}_{Z_i} \qquad 2.67$$

By the properties of electron spin operators and their matrix form for spin 1/2 particles:

$$\mathcal{B}_i(t) = \frac{1}{2}\begin{pmatrix}\tilde{B}_{iz}(t) & \tilde{B}_{ix}(t) - i\tilde{B}_{iy}(t) \\ \tilde{B}_{ix}(t) + i\tilde{B}_{iy}(t) & -\tilde{B}_{iz}(t)\end{pmatrix} \qquad 2.68$$

Hence the exponential propagator for $\hat{H}_{TD,i}$ is:

$$e^{-\frac{i}{2}\hat{H}_{TD}(t+\delta t,t)\delta t} = e^{-\frac{i}{4}\left(\mathcal{B}_i(t)\otimes\mathcal{I}_{Z_i}\right)\delta t} = e^{-\frac{i}{4}\mathcal{B}_i(t)\delta t}\otimes\mathbb{I}_{Z_i} \qquad 2.69$$

Note, that the exponential property $e^{A\otimes\mathbb{I}} = e^A\otimes\mathbb{I}$ was used. By leveraging the inherent structure of the Hamiltonian, the computational resources required for calculating the exponential matrix pertaining to time-dependent terms can be significantly reduced. Also, an analytical expression for the exponential of $\mathcal{B}_i(t)$

can be found via the eigenvalue decomposition, $\mathcal{B}_i = \hat{W}\hat{D}\hat{W}^{-1}$:

$$e^{c\mathcal{B}_i} = \hat{W}e^{cD}\hat{W}^{-1} \tag{2.70}$$

Here, $c = -i\delta t/4$. Expressions for $\hat{D}$ and $\hat{W}$ are found through solving a simple characteristic equation:

$$\hat{D} = \begin{pmatrix} -L & 0 \\ 0 & L \end{pmatrix} \tag{2.71}$$

$$\hat{W} = \begin{pmatrix} \frac{z-L}{x+iy} & \frac{z+L}{x+iy} \\ 1 & 1 \end{pmatrix} \tag{2.72}$$

$$\hat{W}^{-1} = \frac{1}{2L}\begin{pmatrix} -x-iy & Z+L \\ x+iy & 2L-z \end{pmatrix} \tag{2.73}$$

With,

$$\begin{aligned} x &= \tilde{B}_{ix}(t), y = \tilde{B}_{iy}(t), z = \tilde{B}_{iz}(t) \\ L &= \sqrt{x^2+y^2+z^2} \end{aligned} \tag{2.74}$$

The time complexity of the algorithm will depend on each individual case but generally, since calculating matrix exponentials will become the major bottleneck, the general scaling should be $O(N_i^3)$. Here N_i is the larger spin subspace out of N_1 and N_2.

Two Site Relaxation 2.5.3

Two site relaxation model refers to a very simple site hopping model between two radical pair sites $\hat{H}_A$ and $\hat{H}_B$, were jumps occur at rate k_m:

$$\hat{H}_A \underset{k_m}{\overset{k_m}{\rightleftarrows}} \hat{H}_B \tag{2.75}$$

It is a simple model that has been used in different studies to quantify the magnitude of relaxation effects caused by tumbling of radicals[114,218] and it was used in Chapter 3 to evaluate the relaxation caused by different nuclear isotopes of $\mathrm{FAD}^{\bullet -}$ radical. It is a method that uses *symmetric* recombination and assumes that both sites are *static*. Although in principle the algorithm is a *dynamic* method, the calculations use *static* Hamiltonians for both sites.

The singlet yield is given by:[230]

$$\Phi_S = k_S \left(\left\langle \hat{P}_S \middle| \hat{W}_1 \right\rangle + \left\langle \hat{P}_S \middle| \hat{W}_2 \right\rangle \right) \tag{2.76}$$

Here $\left\langle \hat{P}_S \right| = \left| \hat{P}_S \right\rangle^{\dagger}$ are the Liouville space representations of the singlet projection operator and $\left| \hat{W}_i \right\rangle$ are the Liouville space state vectors that will be described below in the derivation of the method.

Derivation of the method[230]

The dynamics of the scheme in Eq. 2.75 can be mapped to a simple kinetics scheme:[230]

$$\begin{pmatrix} \frac{d\left|\hat{\rho}_A(t)\right\rangle}{dt} \\ \frac{d\left|\hat{\rho}_B(t)\right\rangle}{dt} \end{pmatrix} = \begin{pmatrix} -\hat{\hat{\mathcal{L}}}_A - k_m & k_m \\ k_m & -\hat{\hat{\mathcal{L}}}_B - k_m \end{pmatrix} \begin{pmatrix} \left|\hat{\rho}_A(t)\right\rangle \\ \left|\hat{\rho}_B(t)\right\rangle \end{pmatrix} \tag{2.77}$$

$\left|\hat{\rho}_i(t)\right\rangle$ is the Liouville space representation of the density matrix for site i and $\hat{\hat{\mathcal{L}}}_i$ is the Liuoville space superoperator for site i. This equation can be written as:

$$\frac{d\left|\hat{\rho}_{TS}(t)\right\rangle}{dt} = -\hat{\hat{\mathcal{L}}}_{TS} \left|\hat{\rho}_{TS}(t)\right\rangle \tag{2.78}$$

With,

$$\hat{\hat{\mathcal{L}}}_{TS} = \begin{pmatrix} \hat{\hat{\mathcal{L}}}_A + k_m & -k_m \\ -k_m & \hat{\hat{\mathcal{L}}}_B + k_m \end{pmatrix} \tag{2.79}$$

Where TS denotes the density matrix and the superoperator for both sites. The solution to this equation is:

$$\left|\hat{\rho}_{TS}(t)\right\rangle = e^{-\hat{\hat{\mathcal{L}}}_{TS}t}\left|\hat{\rho}_{TS}(0)\right\rangle \tag{2.80}$$

The singlet yield, according to Eq. 2.16:

$$\Phi_S = k_S\left\langle \hat{P}_S\middle|\hat{\hat{\mathcal{L}}}^{-1}_{TS}\middle|\,\hat{\rho}_{TS}(0)\right\rangle \tag{2.81}$$

If we set:

$$\begin{aligned}\hat{\hat{\mathcal{L}}}^{-1}_{TS}\left|\hat{\rho}_{TS}(0)\right\rangle &= |W\rangle\\ \left|\hat{\rho}_{TS}(0)\right\rangle &= \hat{\hat{\mathcal{L}}}_{TS}\,|W\rangle\end{aligned} \tag{2.82}$$

and denote $\left|\hat{W}\right\rangle = \left(\left|\hat{W}_1\right\rangle, \left|\hat{W}_2\right\rangle\right)^T$, then the singlet yield is given as:

$$\Phi_S = k_S\left(\left\langle\hat{P}_S\middle|\,\hat{W}_1\right\rangle + \left\langle\hat{P}_S\middle|\,\hat{W}_2\right\rangle\right) \tag{2.83}$$

Expanding the second line of Eq. 2.82 in matrix form:

$$\begin{pmatrix}\left|\hat{\rho}_A(0)\right\rangle\\ \left|\hat{\rho}_B(0)\right\rangle\end{pmatrix} = \begin{pmatrix}\hat{\hat{\mathcal{L}}}_A + k_m & -k_m\\ -k_m & \hat{\hat{\mathcal{L}}}_B + k_m\end{pmatrix}\begin{pmatrix}\left|\hat{W}_1\right\rangle\\ \left|\hat{W}_2\right\rangle\end{pmatrix} \tag{2.84}$$

By a simple Gaussian elimination step we reduce this to:[50,230]

$$\begin{pmatrix}\left|\hat{\rho}_A(0)\right\rangle\\ \left|\hat{\rho}_B(0)\right\rangle + k_m\left(\hat{\hat{\mathcal{L}}}_A + k_m\right)^{-1}\end{pmatrix} = \begin{pmatrix}\hat{\hat{\mathcal{L}}}_A + k_m & -k_m\\ 0 & \left(\hat{\hat{\mathcal{L}}}_B + k_m\right) - k_m^2\left(\hat{\hat{\mathcal{L}}}_A + k_m\right)^{-1}\end{pmatrix}\begin{pmatrix}\left|\hat{W}_1\right\rangle\\ \left|\hat{W}_2\right\rangle\end{pmatrix} \tag{2.85}$$

Hence, we get these two simultaneous equations to solve:

$$\begin{cases} \left|\hat{\rho}_A(0)\right\rangle & = \left(\hat{\hat{\mathcal{L}}}_A + k_m\right)\left|\hat{W}_1\right\rangle - k_m\left|\hat{W}_2\right\rangle \\ \left|\hat{\rho}_B(0)\right\rangle + k_m\left(\hat{\hat{\mathcal{L}}}_A + k_m\right)^{-1} & = \left(\left(\hat{\hat{\mathcal{L}}}_B + k_m\right) - k_m^2\left(\hat{\hat{\mathcal{L}}}_A + k_m\right)^{-1}\right)\left|\hat{W}_2\right\rangle \end{cases} \tag{2.86}$$

This linear system of equations is solved by finding $\left|\hat{W}_2\right\rangle$ and then using it to find $\left|\hat{W}_1\right\rangle$:

$$\begin{aligned} \left|\hat{W}_2\right\rangle &= \left(\left(\hat{\hat{\mathcal{L}}}_B + k_m\right) - k_m^2\left(\hat{\hat{\mathcal{L}}}_A + k_m\right)^{-1}\right)^{-1}\left(\left|\hat{\rho}_B(0)\right\rangle + k_m\left(\hat{\hat{\mathcal{L}}}_A + k_m\right)^{-1}\right) \\ \left|\hat{W}_1\right\rangle &= \left(\hat{\hat{\mathcal{L}}}_A + k_m\right)^{-1}\left(\left|\hat{\rho}_A(0)\right\rangle + k_m\left|\hat{W}_2\right\rangle\right) \end{aligned} \tag{2.87}$$

This calculation can be accomplished by performing two evaluations of matrix inverses using any linear system of equations algorithm, which can be easily implemented in computer code.

Complete Simulation Toolkit in MolSpin 2.6

In Chapter 6 an extensive study is presented on the new implementations to *MolSpin*–an advanced spin dynamics computing software written in C++ that offers high flexibility in defining reactions, spin interactions, user-friendly extensibility, an intuitive input interface and high computational speed through CPU parallelization.[216,217] *MolSpin* already had an extensive library of algorithms for spin dynamics, such as the ability to model complex spin relaxation models with Bloch-Redfield-Wangsness (BRW) theory.[217] Nonetheless, the unique contribution to this computer suite presented in Chapter 6 is the implementation of recent discoveries of computational approaches based on the stochastic sampling of the trace and the *Stochastic Schrödinger Equation* formalism.[49,218] These approaches are groundbreaking as they enable the simulation of large and intricate time-dependent spin systems that were previously unattainable. An example of such a system is the spin dynamics of a 14-nuclear spin system, where the spin interactions are derived from the trajectory obtained from protein molecular dynamics simulations. Furthermore, the new additions to *MolSpin* include a new heuristic for reducing integration time of estimating quantum yields and an automated algorithm for time-propagation with exponential algorithms which handles parameter choice–allowing non-experts of numerical simulations start using *MolSpin* more easily for their research questions. The main theory behind the new implementations will be reviewed in this section with a mention of how it can be integrated in *MolSpin* at the end.

Direct Method 2.6.1

We will first review a method named *Direct*. It is solves the quantum master equation in Eq. 2.17, as explained in Sec. 2.3.

We can evaluate the trace of some observable $\hat{A}$ in Eq. 1.14 in the basis of:[49]

$$\{\mathcal{B}\} = \{|\Theta\rangle \otimes |\mathbf{M}_1\rangle \otimes |\mathbf{M}_2\rangle\} \tag{2.88}$$

Where $|\Theta\rangle$ are the electron spin states and $|\mathbf{M}_i\rangle$ is the nuclear spin state of radical i, given by:

$$|\mathbf{M}_i\rangle = |M_{i1}\rangle \otimes |M_{i2}\rangle \otimes \cdots \otimes |M_{iN_i}\rangle \tag{2.89}$$

The initial state is defined as:

$$\hat{\rho}(0) = \frac{1}{Z} |\Theta_{init}\rangle \langle\Theta_{init}| \otimes \mathbb{I}_Z \tag{2.90}$$

Here Θ_{init} is either S, T_0, T_+ and T_-. In most RPM reactions, the initial state is always singlet, but there could be pathways that would lead to an initial triplet state.[3] Hence, the new implementations in *MolSpin* include a choice of the initial state, allowing flexibility for modelling.

M_{ik} is the projection of k-th nuclear spin in the radical i onto the z-axis, i.e. the magnetic quantum number. The expectation value of $\hat{A}$ then is:

$$\begin{aligned} A(t) &= \sum_{\Theta} \sum_{\mathbf{M}_1} \sum_{\mathbf{M}_2} \langle \Theta, \mathbf{M}_1, \mathbf{M}_2 | \hat{A}\hat{\rho}(t) | \Theta, \mathbf{M}_1, \mathbf{M}_2 \rangle \\ &= \frac{1}{Z} \sum_{\Theta} \sum_{\mathbf{M}_1} \sum_{\mathbf{M}_2} \langle \Theta, \mathbf{M}_1, \mathbf{M}_2 | \hat{U}(t,0)^{\dagger} \hat{A} \hat{U}(t,0) \hat{\rho}(0) | \Theta, \mathbf{M}_1, \mathbf{M}_2 \rangle \\ &= \frac{1}{Z} \sum_{\mathbf{M}_1} \sum_{\mathbf{M}_2} \langle \Theta_{\text{init}}, \mathbf{M}_1, \mathbf{M}_2;\ t | \hat{A} | \Theta_{\text{init}}, \mathbf{M}_1, \mathbf{M}_2;\ t \rangle \, . \end{aligned} \tag{2.91}$$

Since $\hat{\rho}(0) = |\Theta_{init}\rangle \langle\Theta_{init}| \otimes \mathbb{I}_Z/Z$, the sum over Θ vanishes with only Θ_{init} state remaining, because all terms for $\Theta \neq \Theta_{\text{init}}$ are zero. Also, we used this definition, $|\Theta_{\text{init}}, \mathbf{M}_1, \mathbf{M}_2;\ t\rangle = \hat{U}(t,0)\,|\Theta_{\text{init}}, \mathbf{M}_1, \mathbf{M}_2\rangle$, where $\hat{U}$ is defined in Eq. 2.25. Thus, the trace is computed by expanding it over all nuclear spin states and propagating each state until time t. Each nuclear spin state follows the *Stochastic Schrödinger Equation* (SSE):[218]

$$\frac{d}{dt}\,|\Theta_{\text{init}}, \mathbf{M}_1, \mathbf{M}_2;\ t\rangle = \left(-i\hat{H}(t) - \hat{K}(t)\right)|\Theta_{\text{init}}, \mathbf{M}_1, \mathbf{M}_2;\ t\rangle\,, \qquad 2.92$$

Hence, the expensive part of this algorithm is the time propagation of nuclear spin states, with $\hat{U}$ taken from Eq. 2.25 (more information is in Sec. 2.3):

$$|\Theta_{\text{init}}, \mathbf{M}_1, \mathbf{M}_2;\ t+\delta t\rangle = e^{-i\Omega(t+\delta t, t)\delta t}\,|\Theta_{\text{init}}, \mathbf{M}_1, \mathbf{M}_2;\ t\rangle \qquad 2.93$$

Although this equation seems complicated, this equation is just $\vec{v} = f(\hat{A})\vec{b}$, where $\vec{v}$ and $\vec{b}$ are vectors and $f(\hat{A})$ is a function of matrix $\hat{A}$. Also, $f(\hat{A})\vec{b}$ is defined as the action of $f(\hat{A})$ on $\vec{b}$.[231] There are a number of algorithms that allows us to calculate $f(\hat{A})\vec{b}$ directly without calculating $f(\hat{A})$. Hence, $\hat{A}$ can just be stored in *sparse* format and used later when needed, whereas $f(\hat{A})$ (in our case the function is an exponential of a matrix) will most likely be *dense* for a *sparse* matrix input.

The most common algorithms that compute the action of an exponential matrix are based on the Krylov subspace approaches.[232,233] They will not be explored here in detail because we have utilized a different method that is based on scaling and squaring of matrix exponential (among many other things) and it will be reviewed extensively in the SI of Chapter 6. Furthermore, the limiting step of the algorithm for calculating the action of the matrix exponential is *sparse matrix* × *vector* calculation, which is shown to scale as $O(N \log N)$ in Sec. 2.1. The overall scaling of the method will be $O(N^2 \log N)$ since we are propagating Z nuclear spin states (although technically Z is not equal N, we will choose to use it in the notation, because this will not change the overall scaling).

Direct method is a very versatile tool for simulating small spin systems since it is fast and can include time-dependency in any interaction. Despite being a less commonly employed and relatively simple approach, we consider this method to possess significant computational capabilities for simulating spin dynamics on modern computer systems. This method should be the algorithm of choice for most spin systems that have $< 8 - 10$ nuclear spins. In the subsequent section, we will examine a methodology that is going to be the preferred computational approach for larger spin systems.

Stochastic Method 2.6.2

The starting point in deriving the *Stochastic* method will be the same as in Sec. 2.6.1–evaluation of the quantum mechanical trace. Yet, in this case a resolution of identity of the following form will be utilized:[218]

$$\mathbb{I}_Z = Z \int p(\xi) \left|\psi(\xi)\right\rangle \left\langle\psi(\xi)\right| \, d\xi \tag{2.94}$$

$\left|\psi(\xi)\right\rangle$ are normalized nuclear spin states, parametrized by a set of real variables ξ, which has a normalized probability density $p(\xi)$.

Plugging it into Eq. 1.14 with $\hat{\rho}(0)$ definition in Eq. 2.90:

$$
\begin{aligned}
A(t) &= \mathrm{Tr}\left[\hat{A}\hat{\rho}(t)\right] \\
&= \mathrm{Tr}\left[\hat{U}(t,0)^{\dagger}\hat{A}\hat{U}(t,0)\hat{\rho}(0)\left(\hat{I}_4 \otimes \hat{I}_Z\right)\right] \\
&= \mathrm{Tr}\left[\hat{U}(t,0)^{\dagger}\hat{A}\hat{U}(t,0)\left(\left|\Theta_{init}\right\rangle\left\langle\Theta_{init}\right| \otimes \mathbb{I}_Z\right)\left(\mathbb{I}_4 \otimes \int \left(p(\xi)\left|\psi(\xi)\right\rangle\left\langle\psi(\xi)\right|\right) d\xi\right)\right] \\
&= \mathrm{Tr}\left[\hat{U}(t,0)^{\dagger}\hat{A}\hat{U}(t,0)\int \left(p(\xi)\left|\Theta_{Init},\psi(\xi)\right\rangle\left\langle\Theta_{init},\psi(\xi)\right|\right) d\xi\right] \\
&= \mathrm{Tr}\left[\int p(\xi)\left(\left\langle\Theta_{init},\psi(\xi)\right|\hat{U}(t,0)^{\dagger}\hat{A}\hat{U}(t,0)\left|\Theta_{Init},\psi(\xi)\right\rangle\right) d\xi\right] \\
&= \int p(\xi)\mathrm{Tr}\left[\left\langle\Theta_{init},\psi(\xi)\right|\hat{U}(t,0)^{\dagger}\hat{A}\hat{U}(t,0)\left|\Theta_{Init},\psi(\xi)\right\rangle\right] d\xi \\
&= \int p(\xi)\left\langle\Theta_{init},\psi(\xi);t\right|\hat{A}\left|\Theta_{Init},\psi(\xi);t\right\rangle d\xi
\end{aligned}
\tag{2.95}
$$

Here we defined:

$$
\left|\Theta_{Init},\psi(\xi);t\right\rangle = \hat{U}(t,0)\left|\Theta_{Init},\psi(\xi)\right\rangle \tag{2.96}
$$

This time-propagation is done analogously to Sec. 2.6.1 and Eq. 2.96 follows SSE. Also, the trace in Eq. 2.95 is analogous to Eq. 2.91 yet it is an integral instead of a summation. This integral can be approximated with Monte Carlo sampling and we will have to choose M normalized states $\left|\psi(\xi)\right\rangle$ to time-propagate. The choice of these states are crucial and determines the performance of the method. We want in general $M << Z$ for this method to be a viable alternative to the direct method.

The two main choices for the normalized states $\left|\psi(\xi)\right\rangle$ have been the coherent spin states and the SU(Z) spin states.[49,218] Coherent spin states has been the choice of states when this efficient state sampling was initially proposed. However, it is now evident that this method is suboptimal, as the error of the approximation scales only as $\mathcal{O}(1/\sqrt{M})$.[49] Hence, the mention and implementation of coherent spin states in *MolSpin* can be considered as a legacy of its development; for an extensive reviews on coherent spin states we point to other sources.[49,54,218,234] The main choice of states for Monte Carlo sampling will be the SU(Z) coherent states, with an error of approximation scaling as $\mathcal{O}(1/\sqrt{MZ})$.[218] SU(Z) states will be defined in Sec. 2.6.2 and the derivation of the error scaling will be reviewed in Appendix C.

It can be observed that the *stochastic* method is analogous almost in every way to *direct* method, besides the difference in trace sampling approach. The time propagation will scale as $\mathcal{O}(N \log N)$, identical to *direct* method. However, the overall scaling of the method reduces to $\mathcal{O}(MN \log N)$ since we are propagating M states that are required for approximating the integral. We will show in Chapter 6 that $M = 1$ can be enough for very large spin systems to produce an error that is sufficient for "graphical accuracy"–the scaling of this approach can be as low as $\mathcal{O}(N \log N)$ which is almost linear. Lastly, the time scaling of *direct* and *stochastic* methods also depend on the number of time propagation steps N_t. Thus, the scaling for *direct* method–$\mathcal{O}(N_t N^2 \log N)$, and for *stochastic* method-$\mathcal{O}(N_t MN \log N)$.

SU(Z) Spin States

SU(Z) coherent state is denoted as $|\mathbf{Z}\rangle$. $\mathbf{Z}$ is a vector of complex numbers $Z_n = X_n + iY_n$ where X_n and Y_n are randomly sampled independent random deviates. $|\mathbf{Z}\rangle$ state in a chosen basis $\{|n\rangle\}$:[235]

$$|\mathbf{Z}\rangle = \sum_{n=1}^{Z} Z_n |n\rangle \qquad 2.97$$

The original labelling of these states is SU(N) states where N is just dimensionality, i.e. N=Z. $|\mathbf{Z}\rangle$ states are normalized, i.e. $\langle \mathbf{Z}|\mathbf{Z}\rangle = 1$. Hence, the general resolution of identity operator for nuclear spins in Eq. 2.94 can be resolved as:[218,235]

$$\mathbf{I}_Z = Z \int_{\mathcal{R}_Z} \int_{\mathcal{R}_Z} \left(\frac{\delta(|\mathbf{Z}| - 1)}{\mathcal{S}_{2Z}} |\mathbf{Z}\rangle \langle \mathbf{Z}| \right) d\mathbf{X} d\mathbf{Y} \tag{2.98}$$

$\mathcal{S}_{2Z}$ is the surface area of a $2Z$ dimensional hypersphere of unit radius:

$$\mathcal{S}_{2Z} = \frac{2\Gamma(\frac{1}{2})^{2Z}}{\Gamma(Z)} \tag{2.99}$$

The distribution from which the states are sampled is $p(\mathbf{Z}) = \delta(|\mathbf{Z}| - 1)/\mathcal{S}_{2Z}$. An important property of this distribution is that it is invariant under unitary transformations of the vector $\mathbf{Z}$, $\mathbf{Z} \to \mathbf{UZ}$. Hence, this method is independent of the choice of basis $|n\rangle$.

In practise, $\mathbf{Z}$ is sampled by sampling $2Z$ independent normal deviates X_n and Y_n–very straightforward to implement computationally.

Observables in State Vector Propagation Approaches 2.6.3

In both methods, the quantum mechanical yields are calculated by:

$$\Phi_\Theta = \frac{k_\Theta}{1 - e^{-k_\Theta T}} \int_0^T P_\Theta(t) dt \tag{2.100}$$

Here $\Theta = S, T_0, T_-, T_+$. k_Θ is the recombination rate constant for state Θ. The term $1 - e^{-k_\Theta} T$ is a novel heuristic explained extensively in Chapter 6. It approximates the quantum yield of $T = \infty$ with a reduced T, that can lessen the required integration time by 2 to 5 times, depending on the system in question. Yet, this currently works only for *symmetric* recombination rates and time-independent recombination terms k_Θ.

Table 2.2 Available tasks and properties in *MolSpin* to use the SSE method. The tasks are divided into two Hilbert Space (**HS**) regimes: **StaticHS** (time-independent Hamiltonian) and **DynamicHS** (time-dependent Hamiltonian). Furthermore, direct (**Direct**) and stochastic (**Stoch**) methods are available for quantum yields (**Yields**) and pure time-evolution of spin states (**TimeEvo**). **Type:** Describes what can be calculated, which is either the time-evolution (TE) or quantum yields (QY). **TD** (**Time-Dependency**): describes if the method can be used with time-dependent interactions. All of the methods utilize Haberkorn reaction operators for describing radical reactions.**Memory and speed:** the memory and calculation scaling of a task class, which for most task types scales exponentially with system size. M is the number of Monte Carlo samples, N is the size of the full spin spin subspace and Z is the size of the nuclear spin subspace. **Error**: describes the error in the final results of the simulations. *Exact* means that there are no errors in the calculations and the scaling was given only for SU(Z) spin states. In the case of coherent spin states, the scaling would be $\mathcal{O}(1/\sqrt{M})$.)

Task class	Type	TD	Memory	Speed	Error
StaticHS-StochYields	QY	No	$\mathcal{O}(N\log(N))$	$\mathcal{O}(N_t MN\log(N))$	$\mathcal{O}(1/\sqrt{MZ})$
StaticHS-StochTimeEvo	TE	No	$\mathcal{O}(N\log(N))$	$\mathcal{O}(N_t MN\log(N))$	$\mathcal{O}(1/\sqrt{MZ})$
StaticHS-DirectYields	QY	No	$\mathcal{O}(N\log(N))$	$\mathcal{O}(N_t N^2\log(N))$	Exact Method
StaticHS-DirectTimeEvo	TE	No	$\mathcal{O}(N\log(N))$	$\mathcal{O}(N_t N^2\log(N))$	Exact Method
DynamicHS-StochYields	QY	Yes	$\mathcal{O}(N\log(N))$	$\mathcal{O}(N_t MN\log(N))$	$\mathcal{O}(1/\sqrt{MZ})$
DynamicHS-StochTimeEvo	TE	Yes	$\mathcal{O}(N\log(N))$	$\mathcal{O}(N_t MN\log(N))$	$\mathcal{O}(1/\sqrt{MZ})$
DynamicHS-DirectYields	QY	Yes	$\mathcal{O}(N\log(N))$	$\mathcal{O}(N_t N^2\log(N))$	Exact Method
DynamicHS-DirectTimeEvo	TE	Yes	$\mathcal{O}(N\log(N))$	$\mathcal{O}(N_t N^2\log(N))$	Exact Method

MolSpin Implementations 2.6.4

All of the above mentioned algorithms described in this section have been added to the newest release of *MolSpin*, and are summarised in Table 2.2.

Time-dependent interactions, i.e. integrals of $f_j(\tau)$ terms in Eq. 2.26 definition of the generator, can be easily implemented by .mst files as a *MolSpin* trajectory that can integrate complex time-dependencies into a spin dynamics calculation.

The following example shows a .mst file for an N5 nucleus in its eigenframe, when only the A_{zz} component of the hyperfine coupling tensor is modulating:

```
time  mat.xx mat.xy mat.xz mat.yx mat.yy mat.yz mat.zx mat.zy mat.zz
0.00 -0.00009359 0.00 0.00 0.00 -0.00009359 0.00 0.00 0.00 0.00185977
0.05 -0.00009359 0.00 0.00 0.00 -0.00009359 0.00 0.00 0.00 0.00188710
0.10 -0.00009359 0.00 0.00 0.00 -0.00009359 0.00 0.00 0.00 0.00188667
0.15 -0.00009359 0.00 0.00 0.00 -0.00009359 0.00 0.00 0.00 0.00188617
0.20 -0.00009359 0.00 0.00 0.00 -0.00009359 0.00 0.00 0.00 0.00188876
0.25 -0.00009359 0.00 0.00 0.00 -0.00009359 0.00 0.00 0.00 0.00188732
.
.
.
```

Each .mst file can be attributed to a specific object in the input via the *trajectory* keyword:

```
// -------------------------
// Hyperfine interactions
// -------------------------
Interaction FADHYP1
{
    IgnoreTensors = true;
    CommonPrefactor = false;
    type = hyperfine;
    group1 = E1;
    group2 = FADN5;
    tensor = trajectory("motions_azz005ns.mst");
    trajectory = "motions_azz_005ns.mst";
}
```

Further descriptions of the input files and the documention for new implementations of the study in Chapter 6 can be found in the *MolSpin* manual.[236]

Other Methods 2.7

There is a large number of studies and methods in the spin dynamics community which have not been used in this thesis. The two main areas of these methods are *semi-classical* methods[48,51,63,223,237] and *quantum algorithms*.[164,165] This thesis was fully concerned with classical algorithms that compute spin dynamics without approximations to the equation of motion in Eq. 2.17 or interaction terms, yet the other two classes of methods can be useful depending on the simulation case. *Semi-classical* methodologies possess the capability of capturing the dynamics of systems that are beyond the reach of non-approximate methods, and their accuracy improves with the increase of the number of nuclear spins.[48] Yet, these methods are not effective in studying the intricate time-dependent spin interaction effects in mid-sized spin systems. *Quantum algorithms* designed for quantum circuits represent a highly promising trajectory for the future of computation, particularly once quantum computers achieve fault tolerance. Nevertheless, even with the current state of Noisy Intermediate Scale Quantum (NISQ) computers, the algorithms for simulating RPM have the capability to compute precise quantum dynamics data. The primary strategy employed involves leveraging the inherent noise present in quantum computers as the primary factor contributing to the system's decoherence. Additionally, the researchers consider recombination and other related phenomena within this framework.[164] Moreover, it is currently postulated that these systems possess the capability to replicate dynamics that are beyond the reach of any conventional classical algorithm.[164] The intended meaning of the authors' studies remains uncertain, and it is our belief that our framework in *MolSpin* has the capability to simulate any system of interest, including quantum circuits with noisy qubits. In principle, these circuits can be mapped to the dynamics of the RPM system, which allows for fluctuations and time-dependent variations in the Hamiltonian and recombination terms that can correspond to any desired system. However, it is not currently possible to assert this claim with confidence without replicating the aforementioned results.

Molecular Dynamics 2.8

Molecular Dynamics (MD) is not a central theme of this thesis, however, this technique has been utilized in Chapter 6, hence, we shortly review the methods in this section. The methodology was adapted from Ref. 107.

In Chapter 6 we aimed to explore the SSE method and explore the possible scope of applications it could be applied to. Hence, we presented a spin dynamics simulation of a radical pair system with dynamics determined by a MD simulation of ErCry4a. There is no available crystal structure for this system, hence, we employed a homology model created in prior investigation.[106,238,239] This model was constructed by aligning the amino acid sequence of ErCry4a[240] with the known crystal structure of ClCry4a (PDB ID: 6PU0).[241] We conducted all-atom molecular dynamics (MD) simulations for the RPC (Radical Pair C) states of ErCry4a using the NAMD software[242,243] and set up the calculations using the VIKING online platform.[244]

The simulations involved solvating ErCry4a in an aqueous solution containing 50 mM NaCl, resulting in a system with 100,518 atoms, and were run for a total of 953 nanoseconds (ns). The simulations featured the oxidized $\mathrm{TrpC}^{\bullet+}$ residue (W318) and reduce $\mathrm{FAD}^{\bullet-}$. These simulations initially utilized radical charges and structures obtained from a previous 200+ ns study of ErCry4a, which were considered well-equilibrated.[106] The CHARMM36 force field with CMAP corrections was used to model standard residues in the protein,[245–247] the TIP3P model was used for the water,[245,248] and the temperature was maintained at 310 K with a Langevin thermostat. In the studies of the librational motions of the radicals, the protein structures in each simulation were aligned using VMD[249] by minimizing the difference in the positions of all backbone Cα atoms in each MD frame from the corresponding Cα positions in the first frame of the production simulation.

Conclusions 2.9

In this chapter we have made an extensive review of the computational methods that form the theoretical and computational basis of Chapters 3, 4 and 6. Also, we introduced a novel computational framework for complex spin dynamics calculations implemented in the software package *MolSpin*. We believe this toolkit of methods to be a state-of-the-art way to simulate spin dynamics of RPM. Although, other software packages for spin dynamics exists, like *Spinach*[250] or *EasySpin*,[251] they are geared towards simulating NMR and EPR data. In fact, *Spinach* has a spin dynamics module for RPM simulations,[250] yet, it cannot include complex time-dependent trajectories for spin interactions and it uses approximate relaxation theories (such as BRW theory) instead of the full description of the motion. Hence, there are currently no alternative simulation packages that are as similar or as powerful to the methodology we illustrated in this section and in Chapter 6. It is hoped that this software package will be beneficial for future investigations in various domains, such as the study of radical pair based magnetoreception or the development of spin qubits utilising molecular spin systems.

* * *

3 Article 1: Isotope Substitution Effects on the Magnetic Compass Properties of Cryptochrome-Based Radical Pairs: A Computational Study

Statement of Authorship for joint/multi-authored papers for PGR thesis

To appear at the end of each thesis chapter submitted as an article/paper

The statement shall describe the candidate's and co-authors' independent research contributions in the thesis publications. For each publication there should exist a complete statement that is to be filled out and signed by the candidate and supervisor **(only required where there isn't already a statement of contribution within the paper itself).**

Title of Paper	Isotope Substitution Effects on the Magnetic Compass Properties of Cryptochrome-Based Radical Pairs: A Computational Study
Publication Status	☑Published ☐ Accepted for Publication ☐Submitted for Publication ☐Unpublished and unsubmitted work written in a manuscript style
Publication Details	Pažėra G. J., Benjamin P., Mouritsen H., & Hore P. J. (2023) Isotope Substitution Effects on the Magnetic Compass Properties of Cryptochrome-Based Radical Pairs: A Computational Study. The Journal of Physical Chemistry B, *127* (4), 838-845, DOI: 10.1021/acs.jpcb.2c05335

Student Confirmation

Student Name:	Gediminas Jurgis Pažėra		
Contribution to the Paper	Contributed to the theoretical formalism, wrote all computer code for simulations, performed vast majority of the calculations, produced and analyzed all data, aided in interpretating data and commented on the manuscript.		
Signature		Date	2023.09.07

Supervisor Confirmation

By signing the Statement of Authorship, you are certifying that the candidate made a substantial contribution to the publication, and that the description described above is accurate.

Supervisor name and title: Professor Peter J. Hore			
Supervisor comments			
Signature		Date	7 September 2023

This completed form should be included in the thesis, at the end of the relevant chapter.

THE JOURNAL OF PHYSICAL CHEMISTRY B
A JOURNAL OF THE AMERICAN CHEMICAL SOCIETY

pubs.acs.org/JPCB Article

Isotope Substitution Effects on the Magnetic Compass Properties of Cryptochrome-Based Radical Pairs: A Computational Study

Published as part of The Journal of Physical Chemistry B virtual special issue "Honoring Michael R. Berman".

Gediminas Jurgis Pažėra, Philip Benjamin, Henrik Mouritsen, and P. J. Hore*

Cite This: *J. Phys. Chem. B* 2023, 127, 838−845

Read Online

ACCESS | Metrics & More | Article Recommendations | Supporting Information

ABSTRACT: The biophysical mechanism of the magnetic compass sense of migratory songbirds is thought to rely on the photochemical reactions of flavin-containing radical pairs in cryptochrome proteins located in the birds' eyes. A consequence of this hypothesis is that the effect of the Earth's magnetic field on the quantum yields of reaction products should be sensitive to isotopic substitutions that modify the hyperfine interactions in the radicals. In this report, we use spin dynamics simulations to explore the effects of $^1H \rightarrow {}^2H$, $^{12}C \rightarrow {}^{13}C$, and $^{14}N \rightarrow {}^{15}N$ isotopic substitutions on the functioning of cryptochrome 4a as a magnetic direction sensor. Two main conclusions emerge. (1) Uniform deuteration of the flavin chromophore appears to be the best way to boost the anisotropy of the magnetic field effect and to change its symmetry. (2) ^{13}C substitution of three of the 12 flavin carbons, in particular C4, C4a, and C8*α*, seems to be the best recipe for attenuating the anisotropy. These predictions should give insight into the factors that control the magnetic sensitivity once spectroscopic techniques are available for measuring magnetic field effects on oriented protein samples.

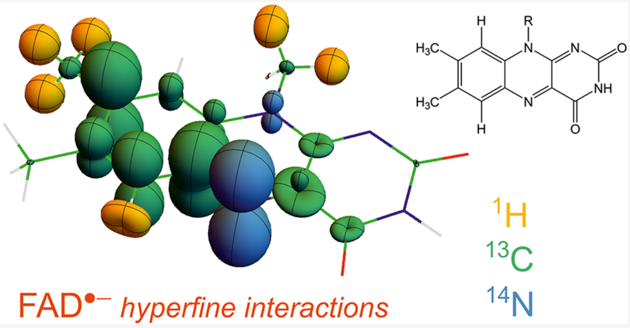

INTRODUCTION

Migratory songbirds have a remarkable ability to use the direction of the Earth's magnetic field to help them navigate between their breeding and wintering grounds.[1,2] The biophysical mechanism of this light-dependent magnetic compass is uncertain but seems to involve magnetically sensitive photochemical reactions within photoreceptor cells in the retina.[3−7] The most likely magnetoreceptor is Cry4a, one of the six known avian cryptochrome (Cry) proteins, in which short-lived radical pairs can be formed by the passage of an electron along a chain of four tryptophan (TrpH) residues to the photoexcited flavin adenine dinucleotide (FAD) chromophore in the center of the protein.[3,8−13] In support of this proposal, flavin-tryptophan radical pairs, $[FAD^{\bullet-}TrpH^{\bullet+}]$, in purified Cry4a from the migratory European robin (*Erithacus rubecula*, *Er*) have recently been shown to be sensitive to weak applied magnetic fields.[14,15] However, it has yet to be demonstrated that Cry4a has the same photochemistry *in vivo* or that it satisfies other requirements for a viable magnetic direction sensor. Another possibility, for which there is currently less evidence, is that the magnetic sensitivity *in vivo* originates in a different radical pair, formed during the dark recovery of a photochemically reduced state of the protein.[16−18] There has also been some discussion of Cry1a as an alternative to Cry4a, even though it does not bind FAD strongly *in vitro*.[19−21]

It is well established that radical pair reactions can be influenced by weak magnetic fields when certain chemical and physical conditions are satisfied.[3,22−25] One of the most important in the context of magnetoreception is that, in at least one of the radicals, the unpaired electron must have magnetic hyperfine interactions with one or more atomic nuclei such as ^1H and ^{14}N.[3] These interactions, which drive coherent interconversion of the singlet and triplet electronic states of the radical pair, determine to a large degree the effect of a weak applied magnetic field on the yields of the reaction products. If, as is usually the case for organic radicals, the hyperfine interactions are anisotropic, the radical pair can form the basis of a magnetic direction sensor. Both $FAD^{\bullet-}$ and $TrpH^{\bullet+}$ radicals satisfy these conditions, and indeed, the ^1H and ^{14}N hyperfine interactions in $FAD^{\bullet-}$ seem to be near optimum for magnetic compass sensing.[26]

A consequence of the fundamental role of hyperfine interactions in the spin dynamics of radical pairs is that

Received: July 28, 2022
Revised: December 29, 2022
Published: January 20, 2023

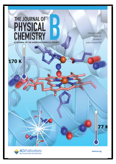

https://doi.org/10.1021/acs.jpcb.2c05335

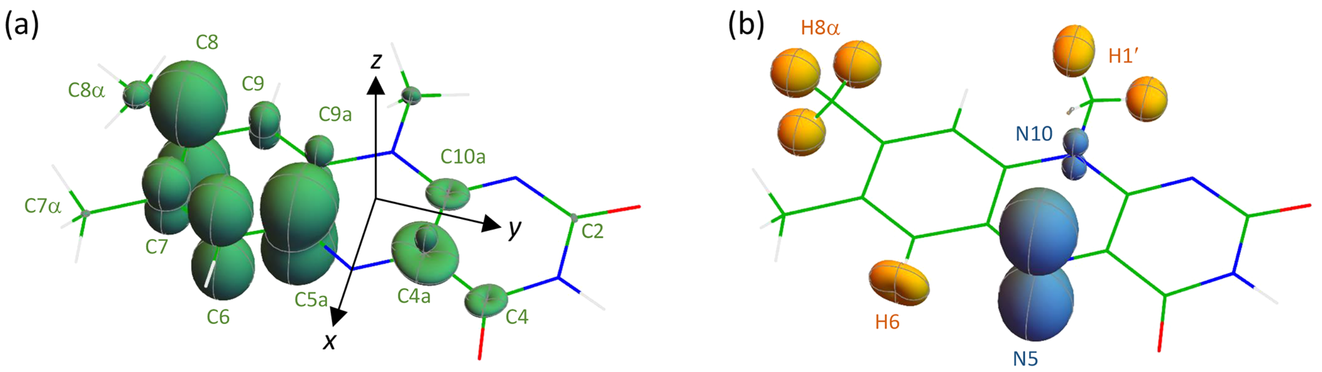

Figure 1. Representations of the hyperfine tensors of (a) ^{13}C (green) and (b) ^{1}H (yellow) and ^{14}N (blue) in $FAD^{\bullet-}$. Nuclei with strongly anisotropic hyperfine interactions have large, nonspherical surfaces, e.g., N5 and C8. Atom labels follow IUPAC nomenclature. The molecular axis system is shown in (a).

isotopic substitution can in principle be used to provide insight into the factors that control the magnetic sensitivity.[27,28] Replacing one isotope of an element by another either changes the nuclear magnetic moment and therefore the hyperfine interaction (e.g., $^{1}H \rightarrow {}^{2}H$, $^{14}N \rightarrow {}^{15}N$) or introduces a hyperfine interaction where none existed before (e.g., $^{12}C \rightarrow {}^{13}C$). In this report, we use spin dynamics simulations to explore the effects of H, C, and N isotopic substitution on the operation of Cry4a as a compass magnetosensor. Results for both $[FAD^{\bullet-}TrpH^{\bullet+}]$ and $[FAD^{\bullet-}Z^{\bullet}]$ radical pairs, hereinafter abbreviated to FAD-Trp and FAD-Z, are presented ($Z^{\bullet}$ is a hypothetical radical with no hyperfine interactions). The aim is to determine patterns of isotopic substitution that could be interesting for future *in vitro* measurements of anisotropic magnetic field effects on oriented proteins using optical spectroscopic methods.[14,29−32]

■ METHODS

The spin dynamics of FAD-Trp and FAD-Z radical pairs were simulated as described in ref 33, using a density matrix master equation to account for the relevant magnetic interactions and recombination kinetics. Singlet and triplet radical pairs were assumed to react spin-selectively with equal rate constants, $k = 10^5\ s^{-1}$, to give distinct products.[34] Reaction product fields were calculated as a function of the direction of an external Earth-strength (49 μT) magnetic yield. The dipolar (D) and exchange (J) interactions in FAD-Trp were taken from a preliminary analysis of electron paramagnetic resonance data obtained from an *Er*Cry4 mutant in which the fourth (terminal) tryptophan of the Trp-tetrad had been replaced by phenylalanine to block the final electron transfer step: $D = -11.2$ MHz, $J = -0.65$ MHz. Within the point−dipole approximation, this value of D corresponds to a center-to-center separation of 1.91 nm. A subsequent, more refined analysis[14] of the same data gave slightly different values of the two parameters; however we do not expect these differences to affect the conclusions of the present study. The orientation of $TrpH^{\bullet+}$ relative to $FAD^{\bullet-}$ is that of Trp318 (the third component of the Trp-tetrad) relative to FAD in the crystal structure of pigeon (*Columba livia*) Cry4a,[35] which has been predicted to closely resemble the structures of other bird Cry4s including Cry4a from the European robin.[36] The third tryptophan was chosen, rather than the fourth (Trp369), because it seems to make a much larger contribution to the magnetic field effects on wild-type Cry4a.[14,15] The same values of D and J were used for the FAD-Z radical pair. The g-values of both radicals were taken to be equal to the free-electron value, g_e.

$^{1}H \rightarrow {}^{2}H$, $^{12}C \rightarrow {}^{13}C$, and $^{14}N \rightarrow {}^{15}N$ isotopic substitutions were considered. The natural abundance of ^{1}H, ^{12}C, and ^{14}N in the unsubstituted radicals was taken to be 100% for all three isotopes. The hyperfine tensors for ^{1}H, ^{13}C, and ^{14}N nuclei in $FAD^{\bullet-}$ were calculated using density functional theory (Supporting Information Tables S1−S3).[26] The corresponding tensors for ^{2}H and ^{15}N were obtained using the proportionality between the strength of the coupling and the nuclear magnetogyric ratio (γ): $\gamma(^{15}N)/\gamma(^{14}N) = -1.402$ and $\gamma(^{2}H)/\gamma(^{1}H) = 0.154$. The flavin component of $FAD^{\bullet-}$ has 11 hydrogens and 4 nitrogens, and $TrpH^{\bullet+}$ has 10 hydrogens and 2 nitrogens. Exact simulations of the spin dynamics of multiple isotopologues of such a large spin system would be prohibitive. Therefore, unless otherwise stated, we chose the seven nuclei in $FAD^{\bullet-}$ with the largest hyperfine interactions: N5, N10, H6, 3 × H8α, and one of the H1′ protons.[26] The spin system of the $TrpH^{\bullet+}$ radical comprised the electron spin coupled to the indole nitrogen via its strongly anisotropic hyperfine interaction.[26] See Figure 1 for atom labeling and representations of the $FAD^{\bullet-}$ ^{1}H, ^{13}C, and ^{14}N hyperfine tensors.

To assess the directional information available from each radical pair, we calculated $\Phi_S(\theta, \phi)$, the fractional yield of the singlet recombination reaction. θ (colatitude) and ϕ (azimuth) define the direction of the magnetic field vector, $\mathbf{B} = |\mathbf{B}|(\sin\theta\cos\phi,\ \sin\theta\sin\phi,\ \cos\theta)$, relative to the flavin axis system (shown in Figure 1a). $\mathbf{B}$ is parallel to the z-axis when $\theta = 0$ and the x-axis when $\theta = 90°$, $\phi = 0$. The hyperfine tensor representations in Figure 1 were calculated as follows. The distance from the nucleus in question to the plotted three-dimensional surface in the direction (θ, ϕ) is proportional to $\mathbf{b}^{T}\cdot\mathbf{A}\cdot\mathbf{b}$ where $\mathbf{A}$ is the hyperfine tensor and $\mathbf{b}^{T} = (\sin\theta\cos\phi,\ \sin\theta\sin\phi,\ \cos\theta)$.

In some calculations, a two-site hopping model was used to assess the impact of electron spin relaxation induced by small-amplitude librational motions of the $FAD^{\bullet-}$ within its binding site in the protein. The $FAD^{\bullet-}$ radical was allowed to jump back and forth (with rate constant k_m) between two equally probable orientations, rotated by ±5° around the flavin x-axis. The reaction yield was calculated by solving two coupled stochastic Liouville equations, one for each site. Reference 37 gives full details of this calculation.

RESULTS

Hydrogen and Nitrogen Isotopologues: Coherent Spin Dynamics. We start by investigating the effects of hydrogen and nitrogen isotopic substitution in the FAD$^{\bullet-}$ component of the FAD-Trp and FAD-Z radical pairs. The results are summarized in Figures 2 and 3. Figure 2a,b shows the anisotropy of the singlet reaction yield, defined as

$$\Delta\Phi_S = \max[\Phi_S(\theta, 0)] - \min[\Phi_S(\theta, 0)] \tag{1}$$

for several isotopologues. $\Delta\Phi_S$ is regarded as the "signal" that provides the information a bird would need to orient itself in the geomagnetic field: we assume that the bigger the signal, the better the compass sensor. For the same radical pairs, Figure 3a–d plots the dependence of $\Phi_S(\theta,0)$ on θ, the direction of the magnetic field vector in the xz-plane of FAD$^{\bullet-}$.

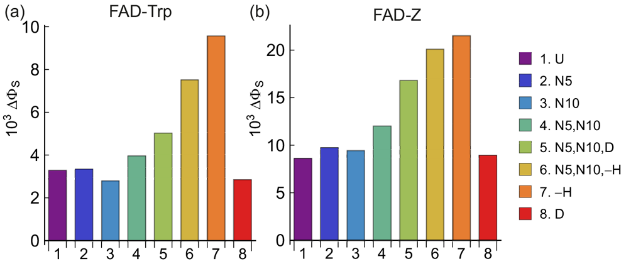

Figure 2. Values of $\Delta\Phi_S$ for nitrogen and hydrogen isotopologues of FAD$^{\bullet-}$ in (a) FAD-Trp and (b) FAD-Z radical pairs. U denotes the unsubstituted radical pair. N5 and N10 denote ^{15}N substitution. −H and D indicate that all five hydrogens in FAD$^{\bullet-}$ were omitted or replaced by deuterium, respectively. See Supporting Information Tables S4 and S5 for a summary of the nuclei included in these calculations and a key to the notation.

The signals for the FAD-Z isotopologues (Figures 2b and 3b,d) are about twice the size of those of FAD-Trp (Figures 2a and 3a,c). Otherwise, FAD-Trp and FAD-Z show broadly similar magnetic isotope effects; we concentrate here on FAD-Trp (Figures 2a and 3a,c). All the $\Delta\Phi_S$ values shown in Figures 2 and 3 are small ($\sim 10^{-3}$) because of the inclusion of a realistic dipolar interaction ($-400\ \mu$T) which inhibits the singlet–triplet interconversion caused by the somewhat smaller Zeeman interaction ($49\ \mu$T).

The first bar in Figure 2a, labeled U, is the FAD-Trp pair without isotopic substitution, i.e., two ^{14}N nuclei and five ^{1}H in FAD$^{\bullet-}$ and a single ^{14}N in TrpH$^{\bullet+}$. The next three bars in Figure 2a show the effects of $^{14}\text{N} \rightarrow {}^{15}\text{N}$ substitution of either N5 alone, N10 alone or N5 and N10 together. The change in $\Delta\Phi_S$ is small. One might have expected a modest increase in $\Delta\Phi_S$ on the basis that the ^{14}N hyperfine interactions of the nitrogens at positions 5 and 10 in FAD$^{\bullet-}$ are strongly anisotropic (Figure 1) and increase by 40% on ^{15}N substitution. Presumably, any such increase is offset by the smaller spin quantum number of ^{15}N ($I = 1/2$) compared to ^{14}N ($I = 1$): the magnetic moments ($\propto \gamma\sqrt{I(I+1)}$) of ^{15}N and ^{14}N are in the ratio 0.86 to 1 which would be consistent with the small magnetic isotope effects in Figure 2.

The fifth bar in Figure 2a, labeled N5, N10, D, is for a radical pair in which N5 and N10 are ^{15}N, and all five hydrogens have been replaced by deuterium. The result is a modest increase in $\Delta\Phi_S$, compared to the unsubstituted case (U). This can be understood in terms of the ~6.5-fold reduction in the hyperfine interactions on deuteration. Most of the ^{1}H interactions in FAD$^{\bullet-}$ are either nearly isotropic (e.g., H8α), small (e.g., H7α), or both (see Figure 1). Deuteration reduces

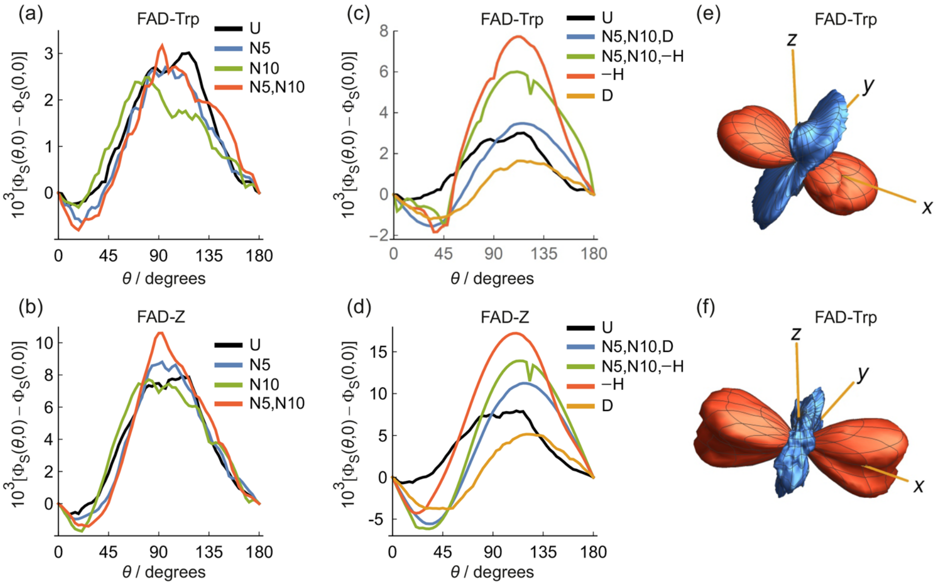

Figure 3. (a–d) Plots of $\Phi_S(\theta,0) - \Phi_S(0,0)$ as a function of magnetic field direction, θ, for nitrogen and hydrogen isotopologues of (a, c) FAD-Trp and (b, d) FAD-Z radical pairs. (e, f) Anisotropy of $\Phi_S(\theta, \phi)$, i.e., $\bar{\Phi}_S(\theta, \phi) = \Phi_S(\theta, \phi) - \langle\Phi_S\rangle$ where $\langle\Phi_S\rangle$ is the isotropic component of $\Phi_S(\theta, \phi)$. In (e) and (f), red and blue indicate reaction yields that are, respectively, larger and smaller than the isotropic (i.e., average) reaction yield. (e) FAD-Trp radical pair with two ^{14}N and no ^{1}H in FAD$^{\bullet-}$ and one ^{14}N in TrpH$^{\bullet+}$. Axis lengths = 0.008. (f) FAD-Trp radical pair with two ^{14}N and five ^{1}H in FAD$^{\bullet-}$ and one ^{14}N in TrpH$^{\bullet+}$. Axis lengths = 0.003. The plot labels are the same as in Figure 2. The small dips at $\theta \approx 120°$ in the N5, N10, −H traces in (c) and (d) arise from avoided level crossings. See Supporting Information Tables S4 and S5 for a summary of the nuclei included in these calculations and a key to the notation.

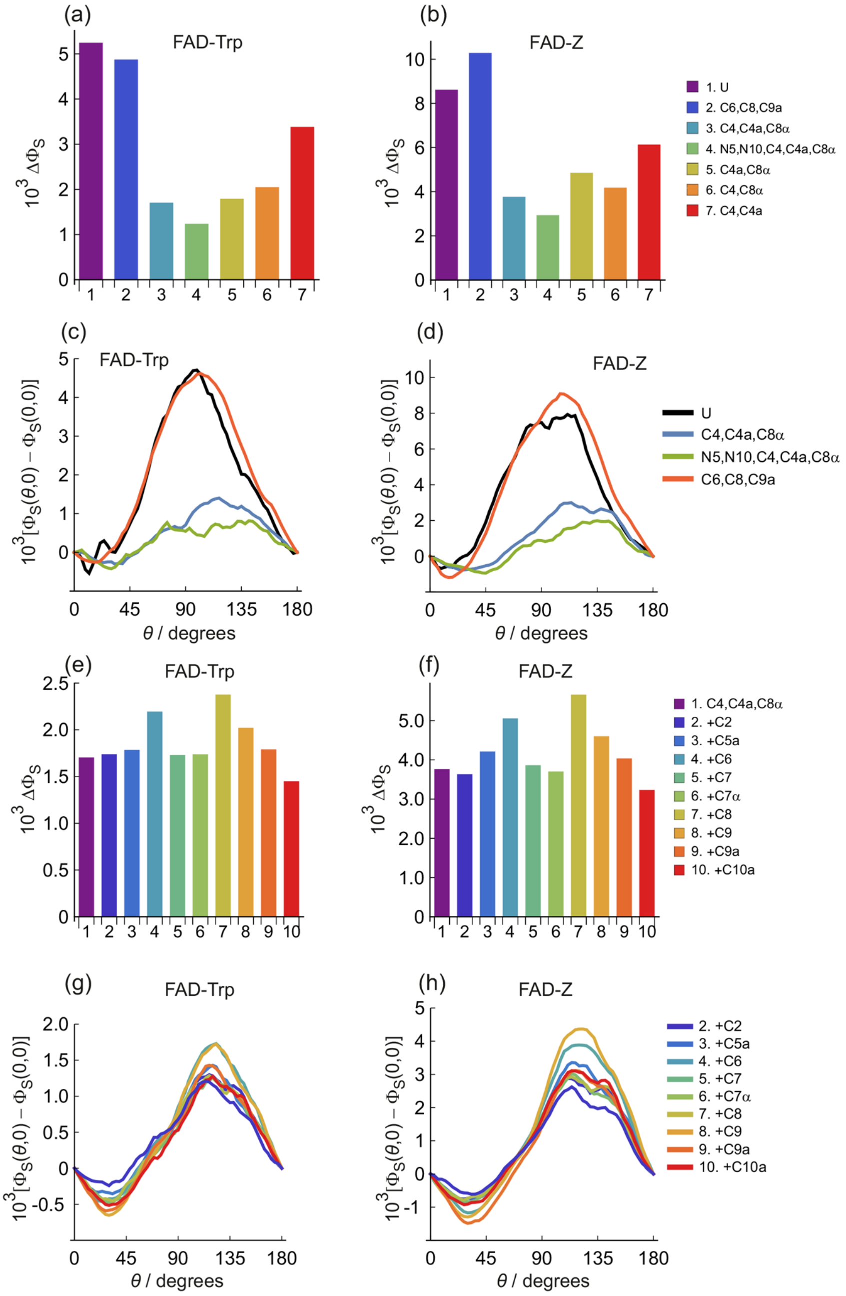

Figure 4. (a, b) Values of $\Delta\Phi_S$ for carbon isotopologues of FAD-Trp and FAD-Z radical pairs, respectively. (c, d) Plots of $\Phi_S(\theta, 0) - \Phi_S(0, 0)$ as a function of magnetic field direction, θ, for carbon isotopologues of FAD-Trp and FAD-Z radical pairs, respectively. (e, f) Values of $\Delta\Phi_S$ for carbon isotopologues of FAD-Trp and FAD-Z radical pairs, respectively. (g, h) Plots of $\Phi_S(\theta, 0) - \Phi_S(0, 0)$ as a function of magnetic field direction, θ, for carbon isotopologues of FAD-Trp and FAD-Z radical pairs, respectively. The plot and bar chart labels are explained in the text. See Supporting Information Table S4 for a summary of the nuclei included in these calculations.

these couplings so that, overall, the flavin radical is magnetically more anisotropic; i.e., the effect of the two anisotropic nitrogens is less diluted by the approximately isotropic hydrogens. This is confirmed by the sixth and seventh bars in Figure 2a: complete removal of the five hydrogens, whether the nitrogens are substituted (N5, N10, −H) or not (−H), results in a further increase in $\Delta\Phi_S$. Deuteration of all five hydrogens in $FAD^{\bullet-}$, without substituting the nitrogens (eighth bar in Figure 2) gave $\Delta\Phi_S$ values comparable to the unsubstituted case.

As well as increasing $\Delta\Phi_S$, deuteration also changes the form of $\Phi_S(\theta, 0)$ in a way that ^{15}N substitution does not. The four traces in Figure 3a (which show the effects of $^{14}N \rightarrow {}^{15}N$ replacement and correspond to the first four bars of Figure 2a) have essentially the same shape, with maxima near $\theta = 90°$ and minima around $\theta = 0°, 180°$. The four colored traces in Figure 3c (corresponding to bars 5−8 in Figure 2a), however, have maxima and minima around $\theta = 110°{-}125°$ and $\theta = 30°{-}45°$, respectively, suggesting that deuterated radical pairs could signal a different compass bearing. This effect is confirmed by Figure 3e,f which shows the anisotropic part of $\Phi_S(\theta, \phi)$ for

(e) −H (where both nitrogens are ^{14}N and all five hydrogens were omitted) and (f) U (where both nitrogens are ^{14}N and all 5 ^{1}H are present). Removal of the ^{1}H hyperfine interactions rotates the anisotropy by about 30° around the *y*-axis. We anticipate that deuteration would have a similar effect.

Carbon Isotopologues: Coherent Spin Dynamics. We now turn to carbon isotopologues with the expectation that replacement of a nonmagnetic nucleus (^{12}C) with one that has a magnetic moment (^{13}C) might lead to larger changes in $\Delta\Phi_S$ than found for ^{1}H → ^{2}H or ^{14}N → ^{15}N substitutions. The 10 ring carbons (C2, C4, C4a, C5a, C6, C7, C8, C9, C9a, C10a) and the two methyl carbons (C7α, C8α) in the isoalloxazine portion of FAD$^{\bullet-}$(Figure 1) were considered. All 220 combinations of three ^{12}C → ^{13}C substitutions were simulated for both FAD-Trp and FAD-Z. Some of the results are summarized in bar-chart form in Figure 4a,b and as a function of θ in Figure 4c,d. In both cases, the hyperfine interaction of the H1′ proton in FAD$^{\bullet-}$ in FAD-Trp was omitted to reduce the size of the calculation.

Once again, the results for FAD-Z (Figure 4b,d,f,h) were larger by a factor of ~2 but otherwise similar to those for FAD-Trp (Figure 4a,c,e,g). Focusing now on the bar chart for FAD-Trp (Figure 4a), none of the 220 carbon isotopologues gave a value of $\Delta\Phi_S$ larger than the unsubstituted case (U, the first bar in Figure 4a). The combination that came closest to the unsubstituted radical pair was C6, C8, C9a (second bar). Even though these carbons have strongly anisotropic hyperfine tensors, with the same symmetry as N5 and N10 (large *z*-component, small *x*- and *y*-components, Figure 1), they do not enhance the anisotropy of the magnetic field effect, which appears to be largely "saturated" by the effects of N5 and to a lesser extent N10.

The combination of three carbons that produced the smallest $\Delta\Phi_S$ (3.1 times smaller than the unsubstituted case, U) was C4, C4a, C8α (third bar in Figure 4a). $\Delta\Phi_S$ is smaller still (4.2 times smaller than U) if, in addition, N5 and N10 are replaced by ^{15}N (fourth bar). C4, C4a, and C8α are among the carbons with the largest hyperfine components in the *xy*-plane of the flavin (Figure 1). The large *xy*-components of these nuclei could reduce $\Delta\Phi_S$ by offsetting the effect of the large *z*-components of N5 and N10, i.e., by making FAD$^{\bullet-}$ less anisotropic overall.

A smaller reduction in $\Delta\Phi_S$ (compared to the unsubstituted case) is seen when any two of C4, C4a, and C8α are substituted (bars 5−7 in Figure 4a). Replacing a fourth ^{12}C by ^{13}C, in addition to C4, C4a, and C8α, gave neither a further reduction in $\Delta\Phi_S$ (Figure 4e) nor much of a change in the θ-dependence (Figure 4g).

Smaller reductions in $\Delta\Phi_S$ were found for other combinations of three carbons. Table 1 shows the ten "best" sets (best at reducing $\Delta\Phi_S$), starting with C4, C4a, C8α and working down. All but one of the ten sets contain two of C4, C4a, and C8α. C8α was present in all ten, C4a in six, and C4 in four. The reductions in $\Delta\Phi_S$, relative to the unsubstituted case, varied between 2.9-fold (set 2) and 2.6-fold (set 10) compared to 3.1 for C4, C4a, C8α (set 1).

Table 1. Ten Sets of Three ^{12}C → ^{13}C Substitutions That Give the Biggest Reductions in $\Delta\Phi_S$[a]

	C2	C4	C4a	C7	C7α	C8α	C9a	C10a	$10^3\,\Delta\Phi_S$
1		•	•			•			1.70
2	•		•			•			1.81
3		•				•		•	1.85
4			•			•	•		1.91
5			•			•		•	1.94
6			•	•		•			1.96
7			•		•	•			1.97
8		•				•	•		1.98
9						•	•	•	1.99
10		•		•		•			2.00

[a] The largest reduction was found for C4, C4a, C8α. The final column gives values of the reaction yield anisotropy.

Nitrogen Isotopologues: Spin Relaxation. None of the calculations reported above included spin relaxation, a process that is unlikely to be negligible *in vivo* and is expected to attenuate the magnetic field effects that arise from the coherent spin dynamics.[38−41] To explore the magnetic isotope effect on the loss of spin coherence, we modeled the librational motion of the FAD radical in its binding site in a protein by allowing it to wobble back and forth between two equally probable orientations, rotated by ±5° around the flavin *x*-axis.[37] Very similar results were found when this rocking motion was around the *y*-axis. Little relaxation is expected either in the motional narrowing limit, when the rate constant k_m for the wobbling motion is much larger than the hyperfine interactions, or in the static limit in which k_m is much smaller than the hyperfine interactions. It is when k_m is comparable to the hyperfine interactions, i.e., 10^7 s^{-1} < k_m < 10^8 s^{-1}, that the spin relaxation should be most effective at destroying the coherence on which the magnetic sensitivity relies.

Figure 5a shows the dependence of $\Delta\Phi_S$ on k_m for unsubstituted (black) and ^{14}N → ^{15}N substituted (color) FAD-Z radical pairs. Similar results are expected for FAD-Trp. $\Delta\Phi_S$ for the unsubstituted radical pair (U) is reduced 11-fold from 0.0160 when $k_m = 10^4$ s^{-1} to 0.0015 when $k_m = 10^8$ s^{-1}. Replacing either N5 or N10 or both by ^{15}N reduced $\Delta\Phi_S$ for all but the k_m values (10^7−10^8 s^{-1}) that induce the fastest relaxation. Given that the difference between the unsubstituted radical pair and the ^{15}N isotopologues in Figure 5a is only present for very slow and very fast motions, where spin relaxation is ineffective, it seems that the majority of the ^{14}N → ^{15}N effect arises from the coherent spin dynamics (shown in Figure 2) rather than this form of spin relaxation.

Carbon Isotopologues: Spin Relaxation. We anticipate that replacement of nonmagnetic ^{12}C nuclei by ^{13}C nuclei that have strongly anisotropic hyperfine interactions (Figure 1) could enhance spin relaxation effects and lead to bigger differences between substituted and unsubstituted radical pairs. To keep the computational demands within reasonable bounds, FAD-Z was modeled for a single value of k_m (= 10^8 s^{-1}, chosen to give a large change in $\Delta\Phi_S$) with just four hyperfine interactions in FAD$^{\bullet-}$ (N5, N10, H6 and one of the H8α protons). As above, all 220 three-carbon substitutions were considered.

Data for the five sets of three carbons that produce the largest reductions in $\Delta\Phi_S$ compared to the unsubstituted case (bar 1) are shown as bars 2−7 in Figure 5b. All six attenuate the signal by ~75%. Similar reductions were found when spin relaxation was not included (Figure 5c). The similarity of Figure 5b,c suggests that the spin relaxation induced by the librational motion of FAD$^{\bullet-}$ is dominated by the modulation of the ^{14}N hyperfine tensors.

Magnitude of $\Delta\Phi_S$. Finally in this section, we comment briefly on the strength of the signal ($\Delta\Phi_S$) assumed to allow a bird to orient in the geomagnetic field. In all of the simulations

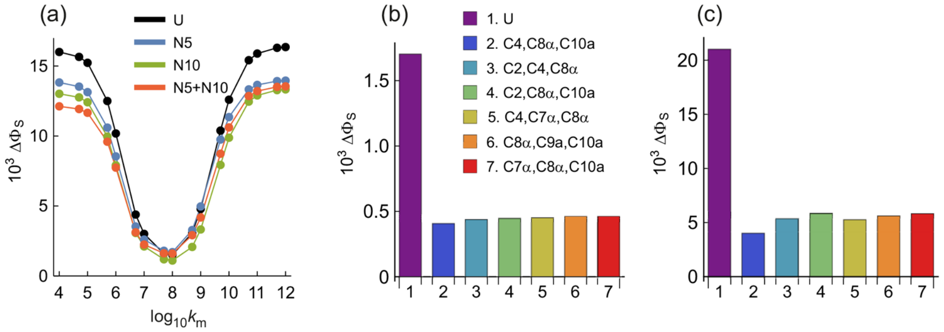

Figure 5. (a) Plots of $\Delta\Phi_S$ for nitrogen isotopologues as a function of the rate constant for the wobbling motion of FAD$^{\bullet-}$ in a FAD-Z radical pair. (b, c) Values of $\Delta\Phi_S$ for carbon isotopologues of FAD-Z radical pairs with and without spin relaxation, respectively. The plot and bar chart labels are explained in the text. See Supporting Information Table S4 for a summary of the nuclei included in these calculations.

presented here, $\Delta\Phi_S$ is of the order of 10^{-3}, corresponding to a ~0.1% change in the reaction yield for a ~90° change in orientation with respect to the ~50 μT magnetic field. One might reasonably ask whether such a small magnetic field effect is sufficient to form the basis of a viable compass magnetoreceptor. An answer to this important question will have to wait until more is known about the structure, binding partners, and signaling of cryptochromes *in vivo*. We have so little knowledge of factors such as spin relaxation, amplification mechanisms, spatial and temporal integration of information from receptors distributed around the retina, and so on that it is impossible to say how big $\Delta\Phi_S$ would need to be. Magnetic field effects at the level of 0.1% are undeniably small but if cryptochromes really are the magnetoreceptors, Nature must have found a way to cope with weak signals.

DISCUSSION AND CONCLUSIONS

The dominant effect of isotopic substitution on the spin dynamics of radical pairs is to scale the strength of the hyperfine interactions and thereby alter the sensitivity to external magnetic fields. In the context of magnetoreception, the relevant quantities are the variation of the reaction yield, $\Phi_S(\theta, \phi)$, with the direction of a ~50 μT magnetic field and the magnitude of this anisotropy, $\Delta\Phi_S$ (eq 1). In the calculations reported here, we explored the effects of replacing ^{1}H by ^{2}H, ^{12}C by ^{13}C, and ^{14}N by ^{15}N, for both of the candidate radical pairs in cryptochrome: FAD-Trp and FAD-Z.

Broadly similar magnetic isotope effects were found for FAD-Trp and FAD-Z, with FAD-Z having $\Delta\Phi_S$ values about twice those of FAD-Trp, other things being equal (Figures 2−4). The difference between the two radical pairs is less pronounced than reported by Lee et al.[26] because of the inclusion of a realistic dipolar coupling.[42]

Nitrogen substitution does not produce large changes in either $\Phi_S(\theta, \phi)$ or $\Delta\Phi_S$ whether spin relaxation arising from librational modulation of the hyperfine interactions is included or not (Figures 2 and 5a). This is consistent with the similarity of the magnetic moments of the two isotopes (^{15}N:^{14}N = 0.86:1.00).

Replacement of hydrogen by deuterium, which scales hyperfine couplings by a factor of 0.154 and the nuclear magnetic moment by 0.251, has the effect of increasing $\Delta\Phi_S$ and changing the shape of $\Phi_S(\theta, \phi)$ (Figure 3). This seems to occur because the approximately isotropic ^{1}H hypefine interactions dilute the contributions of N5 and N10 to $\Delta\Phi_S$, an effect that is diminished by deuteration.[26] Spin relaxation of the deuterated FAD$^{\bullet-}$ radical was not investigated. Recalling the quadratic dependence on the hyperfine coupling strength,[43] spin relaxation arising from modulation of ^{2}H hyperfine couplings should be $[\gamma(^2\mathrm{H})/\gamma(^1\mathrm{H})]^2$ = 42 times slower than that from the corresponding ^{1}H hyperfine couplings.

The set of three ^{12}C → ^{13}C substitutions that produces the largest reduction in $\Delta\Phi_S$ is C4, C4a, and C8α (Figure 4). This reduction is smaller when only two of C4, C4a, and C8α are replaced or when another carbon is added to this set of three. These three carbons feature strongly in the 10 best sets (Table 1).

It is not clear why C4, C4a, C8α have the largest effect on $\Delta\Phi_S$; a clue comes from the scatter plot in Figure 6 in which the principal components (A_{xx}, A_{yy}, A_{zz}) of the ^{13}C hyperfine interactions are shown in red for C4, C4a, and C8α, in green for the carbons that feature in the top 10 sets in Table 1, and in orange for the rest. Broadly speaking, it is the carbons with small $|A_{zz}|$ and large $|A_{xx} + A_{yy}|/2$ that have the greatest effect on $\Delta\Phi_S$. Inclusion of these ^{13}C atoms seems to offset the

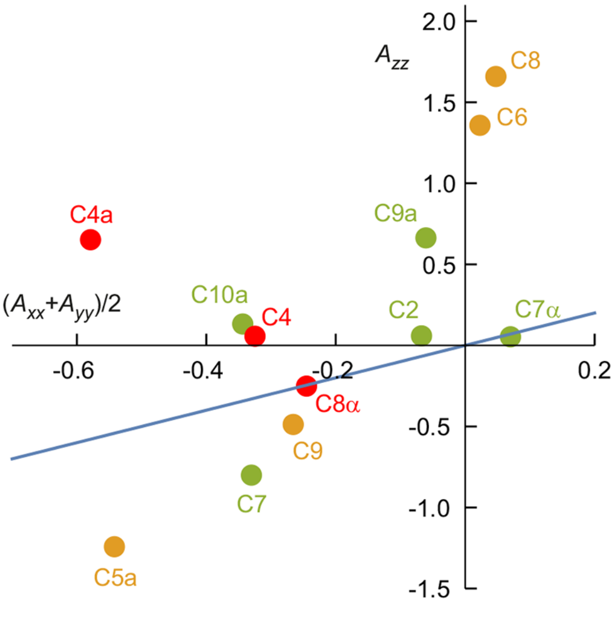

Figure 6. Principal hyperfine tensor components for the 12 carbons in the flavin portion of FAD$^{\bullet-}$. The color code is explained in the text. The blue line is $A_{zz} = (A_{xx} + A_{yy})/2$.

anisotropic effects of N5 and N10, which both have large $|A_{zz}| \gg |A_{xx} + A_{yy}|/2$, and so reduce the overall magnetic anisotropy.

Two main conclusions emerge from this work. (1) Perdeuteration of FAD appears to be the best way to boost the reaction yield anisotropy and to change its symmetry. (2) ^{13}C substitution of C4, C4a, and C8α, or one of the other nine combinations in Table 1 seems to be the best way of reducing the reaction yield anisotropy. Both predictions will be tested by measuring magnetic field effects on cryptochromes with the appropriate FAD isotopologues incorporated.

■ ASSOCIATED CONTENT

Supporting Information

The Supporting Information is available free of charge at https://pubs.acs.org/doi/10.1021/acs.jpcb.2c05335.

> Hyperfine coupling tensors, lists of nuclei included in calculations shown in Figures 2−5, and notation used in Figures 2 and 3 (PDF)

■ AUTHOR INFORMATION

Corresponding Author

P. J. Hore − *Department of Chemistry, University of Oxford, Oxford OX1 3QZ, U.K.*; orcid.org/0000-0002-8863-570X; Email: peter.hore@chem.ox.ac.uk

Authors

Gediminas Jurgis Pažėra − *Department of Chemistry, University of Oxford, Oxford OX1 3QZ, U.K.*

Philip Benjamin − *Department of Chemistry, University of Oxford, Oxford OX1 3QZ, U.K.*

Henrik Mouritsen − *Institut für Biologie und Umweltwissenschaften, Carl-von-Ossietzky Universität Oldenburg, Oldenburg 26111, Germany; Research Centre for Neurosensory Science, University of Oldenburg, Oldenburg 26111, Germany*

Complete contact information is available at: https://pubs.acs.org/10.1021/acs.jpcb.2c05335

Notes

The authors declare no competing financial interest.

■ ACKNOWLEDGMENTS

We thank Adelbert Bacher and Stefan Weber for helpful discussions. We are grateful to the following for generous financial support: the European Research Council (under the European Union's Horizon 2020 research and innovation program, Grant Agreement 810002, Synergy Grant QuantumBirds, awarded to P.J.H. and H.M.), the Office of Naval Research Global, Award N62909-19-1-2045, awarded to P.J.H., and the Deutsche Forschungsgemeinschaft (Projektnummer 395940726-SFB 1372 Magnetoreception and Navigation in Vertebrates awarded to H.M. and P.J.H.), and GRK 1885 Molecular Basis of Sensory Biology, awarded to H.M.

■ REFERENCES

(1) Wiltschko, R.; Wiltschko, W. *Magnetic Orientation in Animals*; Springer Verlag, 1995.

(2) Mouritsen, H. Long-Distance Navigation and Magnetoreception in Migratory Animals. *Nature* **2018**, *558*, 50−59.

(3) Hore, P. J.; Mouritsen, H. The Radical Pair Mechanism of Magnetoreception. *Annu. Rev. Biophys.* **2016**, *45*, 299−344.

(4) Karki, N.; Vergish, S.; Zoltowski, B. D. Cryptochromes: Photochemical and Structural Insight into Magnetoreception. *Protein Sci.* **2021**, *30*, 1521−1534.

(5) Kavet, R.; Brain, J. Cryptochromes in Mammals and Birds: Clock or Magnetic Compass? *Physiology* **2021**, *36*, 183−194.

(6) Wiltschko, R.; Niessner, C.; Wiltschko, W. The Magnetic Compass of Birds: The Role of Cryptochrome. *Front. Physiol.* **2021**, *12*, 667000.

(7) Wong, S. Y.; Frederiksen, A.; Hanic, M.; Schuhmann, F.; Grüning, G.; Hore, P. J.; Solov'yov, I. A. Navigation of Migratory Songbirds: A Quantum Magnetic Compass Sensor. *Neuroforum* **2021**, *27*, 141−150.

(8) Liedvogel, M.; Mouritsen, H. Cryptochromes—A Potential Magnetoreceptor: What Do We Know and What Do We Want to Know? *J. R. Soc. Interface* **2010**, *7*, S147−S162.

(9) Günther, A.; Einwich, A.; Sjulstok, E.; Feederle, R.; Bolte, P.; Koch, K. W.; Solov'yov, I. A.; Mouritsen, H. Double-Cone Localization and Seasonal Expression Pattern Suggest a Role in Magnetoreception for European Robin Cryptochrome 4. *Curr. Biol.* **2018**, *28*, 211−223.

(10) Wu, H.; Scholten, A.; Einwich, A.; Mouritsen, H.; Koch, K. W. Protein-Protein Interaction of the Putative Magnetoreceptor Cryptochrome 4 Expressed in the Avian Retina. *Sci. Rep.* **2020**, *10*, 7364.

(11) Hochstoeger, T.; Al Said, T.; Maestre, D.; Walter, F.; Vilceanu, A.; Pedron, M.; Cushion, T. D.; Snider, W.; Nimpf, S.; Nordmann, G. C.; et al. The Biophysical, Molecular, and Anatomical Landscape of Pigeon Cry4: A Candidate Light-Based Quantal Magnetosensor. *Sci. Adv.* **2020**, *6*, eabb9110.

(12) Chetverikova, R.; Dautaj, G.; Schwigon, L.; Dedek, K.; Mouritsen, H. Double Cones in the Avian Retina Form an Oriented Mosaic Which Might Facilitate Magnetoreception and/or Polarized Light Sensing. *J. R. Soc. Interface* **2022**, *19*, 20210877.

(13) Görtemaker, K.; Yee, C.; Bartölke, R.; Behrmann, H.; Voss, J. O.; Schmidt, J.; Xu, J. J.; Solovyeva, V.; Leberecht, B.; Behrmann, E.; et al. Direct Interaction of Avian Cryptochrome 4 with a Cone Specific G-Protein. *Cells* **2022**, *11*, 2043.

(14) Xu, J.; Jarocha, L. E.; Zollitsch, T.; Konowalczyk, M.; Henbest, K. B.; Richert, S.; Golesworthy, M. J.; Schmidt, J.; Déjean, V.; Sowood, D. J. C.; et al. Magnetic Sensitivity of Cryptochrome 4 from a Migratory Songbird. *Nature* **2021**, *594*, 535−540.

(15) Wong, S. Y.; Wei, Y.; Mouritsen, H.; Solov'yov, I. A.; Hore, P. J. Cryptochrome Magnetoreception: Four Tryptophans Could Be Better Than Three. *J. R. Soc. Interface* **2021**, *18*, 20210601.

(16) Pooam, M.; Arthaut, L. D.; Burdick, D.; Link, J.; Martino, C. F.; Ahmad, M. Magnetic Sensitivity Mediated by the *Arabidopsis* Blue-Light Receptor Cryptochrome Occurs During Flavin Reoxidation in the Dark. *Planta* **2019**, *249*, 319−332.

(17) Wiltschko, R.; Ahmad, M.; Niessner, C.; Gehring, D.; Wiltschko, W. Light-Dependent Magnetoreception in Birds: The Crucial Step Occurs in the Dark. *J. R. Soc. Interface* **2016**, *13*, 20151010.

(18) Player, T. C.; Hore, P. J. Viability of Superoxide-Containing Radical Pairs as Magnetoreceptors. *J. Chem. Phys.* **2019**, *151*, 225101.

(19) Niessner, C.; Denzau, S.; Peichl, L.; Wiltschko, W.; Wiltschko, R. Magnetoreception in Birds: I. Immunohistochemical Studies Concerning the Cryptochrome Cycle. *J. Exp. Biol.* **2014**, *217*, 4221−4224.

(20) Niessner, C.; Denzau, S.; Peichl, L.; Wiltschko, W.; Wiltschko, R. Magnetoreception: Activation of Avian Cryptochrome 1a in Various Light Conditions. *J. Comp. Physiol. A* **2018**, *204*, 977−984.

(21) Bolte, P.; Einwich, A.; Seth, P. K.; Chetverikova, R.; Heyers, D.; Wojahn, I.; Janssen-Bienhold, U.; Feederle, R.; Hore, P. J.; Dedek, K.; et al. Cryptochrome 1a Localisation in Light- and Dark-Adapted Retinae of Several Migratory and Non-Migratory Bird Species: No Signs of Light-Dependent Activation. *Ethol. Ecol. Evol.* **2021**, *33*, 248−272.

(22) Steiner, U. E.; Ulrich, T. Magnetic Field Effects in Chemical Kinetics and Related Phenomena. *Chem. Rev.* **1989**, *89*, 51−147.

(23) Rodgers, C. T. Magnetic Field Effects in Chemical Systems. D.Phil. Thesis, University of Oxford, 2007.

(24) Jones, A. R. Magnetic Field Effects in Proteins. *Mol. Phys.* **2016**, *114*, 1691−1702.

(25) Miura, T. Studies on Coherent and Incoherent Spin Dynamics That Control the Magnetic Field Effect on Photogenerated Radical Pairs. *Mol. Phys.* **2020**, *118*, e1643510.

(26) Lee, A. A.; Lau, J. C. S.; Hogben, H. J.; Biskup, T.; Kattnig, D. R.; Hore, P. J. Alternative Radical Pairs for Cryptochrome-Based Magnetoreception. *J. R. Soc. Interface* **2014**, *11*, 20131063.

(27) Woodward, J. R.; Timmel, C. R.; McLauchlan, K. A.; Hore, P. J. Radio Frequency Magnetic Field Effects on Electron-Hole Recombination. *Phys. Rev. Lett.* **2001**, *87*, 077602.

(28) Rodgers, C. T.; Norman, S. A.; Henbest, K. B.; Timmel, C. R.; Hore, P. J. Determination of Radical Re-Encounter Probability Distributions from Magnetic Field Effects on Reaction Yields. *J. Am. Chem. Soc.* **2007**, *129*, 6746−6755.

(29) Maeda, K.; Neil, S. R. T.; Henbest, K. B.; Weber, S.; Schleicher, E.; Hore, P. J.; Mackenzie, S. R.; Timmel, C. R. Following Radical Pair Reactions in Solution: A Step Change in Sensitivity Using Cavity Ring-Down Detection. *J. Am. Chem. Soc.* **2011**, *133*, 17807−17815.

(30) Neil, S. R. T.; Li, J.; Sheppard, D. M. W.; Storey, J.; Maeda, K.; Henbest, K. B.; Hore, P. J.; Timmel, C. R.; Mackenzie, S. R. Broadband Cavity-Enhanced Detection of Magnetic Field Effects in Chemical Models of a Cryptochrome Magnetoreceptor. *J. Phys. Chem. B* **2014**, *118*, 4177−4184.

(31) Maeda, K.; Robinson, A. J.; Henbest, K. B.; Hogben, H. J.; Biskup, T.; Ahmad, M.; Schleicher, E.; Weber, S.; Timmel, C. R.; Hore, P. J. Magnetically Sensitive Light-Induced Reactions in Cryptochrome Are Consistent with Its Proposed Role as a Magnetoreceptor. *Proc. Natl. Acad. Sci. U.S.A.* **2012**, *109*, 4774−4779.

(32) Sheppard, D. M. W.; Li, J.; Henbest, K. B.; Neil, S. R. T.; Maeda, K.; Storey, J.; Schleicher, E.; Biskup, T.; Rodriguez, R.; Weber, S.; et al. Millitesla Magnetic Field Effects on the Photocycle of *Drosophila Melanogaster* Cryptochrome. *Sci. Rep.* **2017**, *7*, 42228.

(33) Efimova, O.; Hore, P. J. Role of Exchange and Dipolar Interactions in the Radical Pair Model of the Avian Magnetic Compass. *Biophys. J.* **2008**, *94*, 1565−1574.

(34) Timmel, C. R.; Till, U.; Brocklehurst, B.; McLauchlan, K. A.; Hore, P. J. Effects of Weak Magnetic Fields on Free Radical Recombination Reactions. *Mol. Phys.* **1998**, *95*, 71−89.

(35) Zoltowski, B. D.; Chelliah, Y.; Wickramaratne, A.; Jarocha, L.; Karki, N.; Xu, W.; Mouritsen, H.; Hore, P. J.; Hibbs, R. E.; Green, C. B.; et al. Chemical and Structural Analysis of a Photoactive Vertebrate Cryptochrome from Pigeon. *Proc. Natl. Acad. Sci. U.S.A.* **2019**, *116*, 19449−19457.

(36) Hanic, M.; Schuhmann, F.; Frederiksen, A.; Langebrake, C.; Manthey, G.; Liedvogel, M.; Xu, J. J.; Mouritsen, H.; Solov'yov, I. A. Computational Reconstruction and Analysis of Structural Models of Avian Cryptochrome 4. *J. Phys. Chem. B* **2022**, *126*, 4623−4635.

(37) Hiscock, H. G.; Worster, S.; Kattnig, D. R.; Steers, C.; Jin, Y.; Manolopoulos, D. E.; Mouritsen, H.; Hore, P. J. The Quantum Needle of the Avian Magnetic Compass. *Proc. Natl. Acad. Sci. U.S.A.* **2016**, *113*, 4634−4639.

(38) Lau, J. C. S.; Wagner-Rundell, N.; Rodgers, C. T.; Green, N. J. B.; Hore, P. J. Effects of Disorder and Motion in a Radical Pair Magnetoreceptor. *J. R. Soc. Interface* **2010**, *7*, S257−S264.

(39) Kattnig, D. R.; Solov'yov, I. A.; Hore, P. J. Electron Spin Relaxation in Cryptochrome-Based Magnetoreception. *Phys. Chem. Chem. Phys.* **2016**, *18*, 12443−12456.

(40) Kattnig, D. R.; Sowa, J. K.; Solov'yov, I. A.; Hore, P. J. Electron Spin Relaxation Can Enhance the Performance of a Cryptochrome-Based Magnetic Compass Sensor. *New J. Phys.* **2016**, *18*, 063007.

(41) Worster, S.; Kattnig, D. R.; Hore, P. J. Spin Relaxation of Radicals in Cryptochrome and Its Role in Avian Magnetoreception. *J. Chem. Phys.* **2016**, *145*, 035104.

(42) Babcock, N. S.; Kattnig, D. R. Electron-Electron Dipolar Interaction Poses a Challenge to the Radical Pair Mechanism of Magnetoreception. *J. Phys. Chem. Lett.* **2020**, *11*, 2414−2421.

(43) Atherton, N. M. *Principles of Electron Spin Resonance*; Ellis Horwood, 1993.

https://doi.org/10.1021/acs.jpcb.2c05335
J. Phys. Chem. B 2023, 127, 838−845

Isotope Substitution Effects on the Magnetic Compass Properties of Cryptochrome-Based Radical Pairs: a Computational Study

[1]Gediminas Jurgis Pažėra, [1]Philip Benjamin, [2,3]Henrik Mouritsen and [1]P. J. Hore*

[1]Department of Chemistry, University of Oxford, Oxford OX1 3QZ, UK

[2]Institut für Biologie und Umweltwissenschaften, Carl-von-Ossietzky Universität Oldenburg, Oldenburg 26111, Germany

[3]Research Centre for Neurosensory Science, University of Oldenburg, Oldenburg 26111, Germany

* Author for correspondence: peter.hore@chem.ox.ac.uk

nucleus	hyperfine tensor / mT
^{14}N5	$\begin{pmatrix} -0.0995 & 0.0029 & 0 \\ 0.0029 & -0.0875 & 0 \\ 0 & 0 & 1.7569 \end{pmatrix}$
^{14}N10	$\begin{pmatrix} -0.0149 & 0.0021 & 0 \\ 0.0021 & -0.0237 & 0 \\ 0 & 0 & 0.6046 \end{pmatrix}$
^{1}H6	$\begin{pmatrix} -0.2009 & -0.0328 & 0 \\ -0.0328 & -0.5271 & 0 \\ 0 & 0 & -0.4336 \end{pmatrix}$
^{1}H8	$\begin{pmatrix} 0.4313 & 0.0369 & 0 \\ 0.0369 & 0.4786 & 0 \\ 0 & 0 & 0.4100 \end{pmatrix}$
^{1}H1′	$\begin{pmatrix} 0.3492 & -0.0015 & 0 \\ -0.0015 & 0.2459 & 0 \\ 0 & 0 & 0.2289 \end{pmatrix}$

Table S1. ^{1}H and ^{14}N hyperfine tensors for $\mathrm{FAD}^{\bullet-}$. Calculated by Dr Ilya Kuprov (University of Southampton) using density functional theory in Gaussian-03 at the UB3LYP/EPR-III level. The calculation was done for the radical anion of 7,8,10-trimethyl isoalloxazine (lumiflavin) *in vacuo*. The atom numbering scheme is as shown in Fig. 1.

nucleus	hyperfine tensor / mT
^{13}C2	$\begin{pmatrix} -0.0816 & -0.0186 & 0 \\ -0.0186 & -0.0534 & 0 \\ 0 & 0 & 0.0589 \end{pmatrix}$
^{13}C4	$\begin{pmatrix} -0.3217 & 0.0302 & 0 \\ 0.0302 & -0.3279 & 0 \\ 0 & 0 & 0.0564 \end{pmatrix}$
^{13}C4a	$\begin{pmatrix} -0.5995 & -0.0463 & 0 \\ -0.0463 & -0.5583 & 0 \\ 0 & 0 & 0.6520 \end{pmatrix}$
^{13}C5a	$\begin{pmatrix} -0.5851 & 0.0614 & 0 \\ 0.0614 & -0.4989 & 0 \\ 0 & 0 & -1.2420 \end{pmatrix}$
^{13}C6	$\begin{pmatrix} 0.0204 & -0.0004 & 0 \\ -0.0004 & 0.0251 & 0 \\ 0 & 0 & 1.3577 \end{pmatrix}$
^{13}C7	$\begin{pmatrix} -0.3265 & 0.0165 & 0 \\ 0.0165 & -0.3341 & 0 \\ 0 & 0 & -0.8004 \end{pmatrix}$
^{13}C7α	$\begin{pmatrix} 0.0667 & -0.0061 & 0 \\ -0.0061 & 0.0733 & 0 \\ 0 & 0 & 0.0531 \end{pmatrix}$
^{13}C8	$\begin{pmatrix} 0.0393 & 0.0122 & 0 \\ 0.0122 & 0.0555 & 0 \\ 0 & 0 & 1.6589 \end{pmatrix}$
^{13}C8α	$\begin{pmatrix} -0.2520 & 0.0134 & 0 \\ 0.0134 & -0.2383 & 0 \\ 0 & 0 & -0.2511 \end{pmatrix}$
^{13}C9	$\begin{pmatrix} -0.2846 & 0.0015 & 0 \\ 0.0015 & -0.2468 & 0 \\ 0 & 0 & -0.4877 \end{pmatrix}$
^{13}C9a	$\begin{pmatrix} -0.0711 & 0.0074 & 0 \\ 0.0074 & -0.0503 & 0 \\ 0 & 0 & 0.6632 \end{pmatrix}$
^{13}C10a	$\begin{pmatrix} -0.3215 & 0.0079 & 0 \\ 0.0079 & -0.3660 & 0 \\ 0 & 0 & 0.1320 \end{pmatrix}$

Table S2. ^{13}C hyperfine tensors for $\mathrm{FAD}^{\bullet-}$. For other details, see Table S1.

nucleus	hyperfine tensor / mT
^{14}N1	$\begin{pmatrix} 0.3176 & 0.4962 & -0.2092 \\ 0.4962 & 0.5919 & -0.2662 \\ -0.2092 & -0.2662 & 0.0551 \end{pmatrix}$

Table S3. ^{14}N hyperfine tensor for $\mathrm{TrpH}^{\bullet +}$. The calculation was done for the radical cation of tryptophan *in vacuo*. N1 is the indole nitrogen. For other details, see Table S1.

	FAD radical
Fig. 2, Fig. 3a-d	N5, N10, H6, 3×H8α, 1× H1′ except for –H and N5,N10, –H which were N5, N10
Fig. 3e	N5, N10
Fig. 3f	N5, N10, H6, 3×H8α
Fig. 4	N5, N10, H6, 3×H8α + 2, 3, or 4 carbons
Fig. 5a	N5, N10, H6, 3×H8α
Figs 5b,c	N5, N10, H6, 1×H8α + 3 carbons

Table S4. Nuclei included in the model $\mathrm{FAD}^{\bullet -}$ radical for the calculations shown in Figs 2-5.

	label	N5 isotope	N10 isotope	hydrogen isotopes
1	U	14	14	H
2	N5	15	14	H
3	N10	14	15	H
4	N5,N10	15	15	H
5	N5,N10,D	15	15	D
6	N5,N10,–H	15	15	none
7	–H	14	14	none
8	D	14	14	D

Table S5. Notation used in Figs 2 and 3.

4

Article 2: Simulation of Radiofrequency Magnetic Field Effects on a Radical Pair Cryptochrome-Based Magnetoreceptor

Statement of Authorship for joint/multi-authored papers for PGR thesis

To appear at the end of each thesis chapter submitted as an article/paper

The statement shall describe the candidate's and co-authors' independent research contributions in the thesis publications. For each publication there should exist a complete statement that is to be filled out and signed by the candidate and supervisor **(only required where there isn't already a statement of contribution within the paper itself).**

Title of Paper	Simulation of radiofrequency magnetic field effects on a radical pair cryptochrome-based magnetoreceptor
Publication Status	☐Published ☐ Accepted for Publication ☐Submitted for Publication ☑Unpublished and unsubmitted work written in a manuscript style
Publication Details	Pažėra G.J. & Hore P. J. (unpublished). Simulation of radiofrequency magnetic field effects on a radical pair cryptochrome-based magnetoreceptor.

Student Confirmation

Student Name:	Gediminas Jurgis Pažėra		
Contribution to the Paper	Contributed to the theoretical formalism, wrote all computer code for simulations, performed all calculations, produced and analyzed all data, aided in interpreting data and commented on the manuscript.		
Signature		Date	2023.09.07

Supervisor Confirmation

By signing the Statement of Authorship, you are certifying that the candidate made a substantial contribution to the publication, and that the description described above is accurate.

Supervisor name and title: Professor Peter J. Hore			
Supervisor comments			
Signature	PJHore	Date	7 September 2023

This completed form should be included in the thesis, at the end of the relevant chapter.

Simulation of radiofrequency magnetic field effects on a radical pair cryptochrome-based magnetoreceptor

Gediminas Jurgis Pažėra, and P. J. Hore*

Department of Chemistry, University of Oxford, Physical & Theoretical Chemistry Laboratory, Oxford, UK.

*Corresponding author: peter.hore@chem.ox.ac.uk

Abstract

Arguably the most convincing evidence that migratory songbirds detect the direction of the Earth's magnetic field by means of photochemical radical-pair reactions in their eyes comes from the finding that their magnetic compass sense can be disabled by weak time-dependent magnetic fields with frequencies between ~100 kHz and ~80 MHz. The choice of frequencies in the most recent behavioural tests (of Eurasian blackcaps) was guided by an approximate theoretical approach which uses "action-spectrum histograms" to predict the relative extents to which different frequencies could disrupt the operation of a cryptochrome-based magnetoreceptor. In this report, we compare the histogram calculated for a simplified flavin-tryptophan radical pair of the type found in cryptochrome with quantum spin dynamics simulations. We find that the histogram offers a useful qualitative experimental guide for frequencies above ~10 MHz, predicting a fairly uniform response at frequencies from ~10 MHz up to about 20 MHz below the maximum resonance frequency which falls at 100 MHz for the pared down spin system modelled here and at 116 MHz for the complete flavin-tryptophan spin system with 27 nuclear spins. Below 10 MHz, the histogram approach forecasts an increased disruptive effect which was not consistently seen in the spin dynamics simulations. We conclude that the action-spectrum histogram concept remains reliable for frequencies above ~10 MHz but should be used with caution at lower frequencies.

Introduction

It has been known since the 1960s that migratory songbirds possess a magnetic compass to help them navigate between their breeding and wintering grounds [1,2]. However, the biophysical mechanism of this extraordinary sense is still unclear [3,4]. The hypothesis for which there is currently the most evidence is that the sensor involves magnetically responsive photochemical reactions in the birds' retinas [5-7]. More specifically, electron transfer reactions in cryptochrome flavoproteins, triggered by the absorption of blue/green light, are thought to form transient chemical intermediates known as radical pairs [5-10]. Subsequent reactions produce a form of the protein – the signalling state – with a quantum yield that encodes information on the local direction of the geomagnetic field. *In vitro* measurements on purified cryptochrome 4a (Cry4a) from the migratory European robin (*Erithacus rubecula*) have shown that the coherent interconversion of the singlet and triplet electron-spin states of photo-induced flavin-tryptophan radical pairs is indeed sensitive to weak static magnetic fields and that the protein has properties consistent with a magnetosensory function [11,12].

The radical pair mechanism is a real phenomenon supported by a large number of laboratory studies of organic radical reactions [13-15]. It is clear not only that weak static magnetic fields can alter the yields of reaction products – even fields as weak as the Earth's (~50 μT) [16,17] – but also that such effects can be modified by time-dependent magnetic fields that oscillate at frequencies in resonance with the singlet-triplet interconversion, a technique known as reaction yield detected magnetic resonance, RYDMR [18-21]. This effect provides the basis for arguably the most convincing evidence that migratory birds have a radical pair compass, namely the finding that migratory birds can be prevented from orienting in the Earth's magnetic field by exposure to weak radiofrequency (RF) electromagnetic fields with frequencies from a few hundred kHz up to ~80 MHz [22-31]. Broadband noise-modulated RF fields have a stronger disorienting effect than single-frequency fields of comparable strength [28].

Recently, in a study of Eurasian blackcaps (*Sylvia atricapilla*), Leberecht *et al.* found that the birds' ability to orient in the Earth's field could be disrupted by 75-85 MHz RF noise but not by magnetic fields of similar intensity in the frequency bands 140-150 MHz and 235-245 MHz implying an upper limit or "cut-off" frequency between ~80 MHz and ~145 MHz [30,31]. Based on the eigenvalue spectrum of the spin Hamiltonian of the radical pairs formed in cryptochrome, the authors argued that the disruptive effects of RF fields should be approximately independent of frequency up to ~116 MHz and that the birds' sensitivity to disorientation by RF fields should be about two orders of magnitude smaller at frequencies above ~116 MHz. This study, taken together with earlier observations of RF disorientation at frequencies below ~10 MHz, [26-28] provides compelling evidence that the magnetic compass of migratory birds operates by a radical pair mechanism, in which one of the radicals is a flavosemiquinone such as that formed photochemically in Cry4a [31]. It also argues strongly against: (a) a detection mechanism based on magnetic nanoparticles [32]; (b) the disorientation being a bizarre effect on the birds' motivation to orient [33]; and (c) interference with some other aspect of magnetoreception, e.g., signal transduction [31].

The behavioural assays used to study RF disorientation are labour-intensive and time-consuming. To obtain statistically significant data, many birds need to be tested many times under meticulously controlled, double-blind conditions during at least two migratory seasons [27-31]. The magnetic exposure conditions for each new test must therefore be chosen carefully in order to make most efficient use of the available resources. Fortunately, the theoretical basis of the radical pair mechanism is well established and can be used to guide the choice of experimental conditions via computer simulations of the responses to different frequency bands of RF noise [33,34]. However, exact quantum mechanical calculations of this sort, which should ideally include all of the internal magnetic interactions in both radicals, are computationally challenging [34].

It was with this in mind that Hiscock *et al.* proposed an approximate and less computationally problematic approach – dubbed "action-spectrum histograms" – to assess the extent to which weak magnetic fields of different frequencies would compromise the ability of a radical pair to act as a compass magnetoreceptor [33]. Predictions derived from histograms calculated for flavin-tryptophan radical pairs were used to select the RF frequencies (75-85, 140-150, and 235-245 MHz) in the study by Leberecht *et al.* [30,31]. The histogram method was proposed, without detailed theoretical justification, by analogy with slow passage, low-power magnetic resonance spectroscopy [35,36]. To gain a better understanding of the conditions under which it provides a reliable picture of RF effects on magnetoreception, we here compare the histogram for a simplified flavin-tryptophan radical pair with the results of quantum spin dynamics simulations.

Methods

Spin dynamics simulations

We consider a model of the flavin-tryptophan radical pair in cryptochrome, with the two radicals labelled here A and B. Assuming negligible exchange and dipolar interactions, the time-dependent spin Hamiltonian can be written as a sum of single-radical terms: $\hat{H}(t) = \hat{H}_\mathrm{A}(t) + \hat{H}_\mathrm{B}(t)$. In the absence of recombination reactions, the time-dependence of the probability, $p_\mathrm{S}(t)$, that the pair is in a singlet state, having been created as a singlet at $t = 0$, is given by [37-39]:

$$p_\mathrm{S}(t+\delta t) \;=\; \frac{1}{4} + \sum_{\alpha \in x,y,z} \; \sum_{\beta \in x,y,z} R_{\mathrm{A}\alpha\beta}(t,\delta t)\, R_{\mathrm{B}\alpha\beta}(t,\delta t), \tag{1}$$

$$R_{\mathrm{Q}\alpha\beta}(t,\delta t) \;=\; \frac{1}{Z_\mathrm{Q}} \mathrm{Tr}\left[\hat{S}_{\mathrm{Q}\alpha}\left(t+\delta t\right) \hat{S}_{\mathrm{Q}\beta}\right], \tag{2}$$

$$\hat{S}_{\mathrm{Q}\alpha}\left(t+\delta t\right) \;=\; \mathrm{e}^{-i\hat{\Omega}_\mathrm{Q}(t+\delta t;t)\delta t}\, \hat{S}_{\mathrm{Q}\alpha}\left(t\right) \mathrm{e}^{+i\hat{\Omega}_\mathrm{Q}(t+\delta t;t)\delta t}\,. \tag{3}$$

Here, $p_\mathrm{S}(0) = 1$, $\hat{S}_{\mathrm{Q}\alpha}\left(0\right) = \hat{S}_{\mathrm{Q}\alpha}$, the $\alpha = x$-, y-, or z-component of the electron spin angular momentum operator for radical Q ($\in$ A, B), and Z_Q is the dimension of the nuclear spin space of radical Q. The generator, $\hat{\Omega}_\mathrm{Q}(t+\delta t, t)$, is defined below. The time step, δt, was 3 ns.

Assuming that the singlet and triplet states of the radical pair recombine spin-selectively by first-order kinetics with identical rate constants, k, the fraction of pairs that react to form the singlet product is obtained by evaluating the integral [40]:

$$\Phi_\mathrm{S} = k\int_0^\infty p_\mathrm{S}(t)\,\mathrm{e}^{-kt}\mathrm{d}t\,. \tag{4}$$

Neglecting spin-relaxation, the spin Hamiltonian of each radical can be divided into time-independent and time-dependent terms:

$$\hat{H}_\mathrm{Q}(t) = \hat{H}_\mathrm{Q0} + \hat{H}_\mathrm{Q1}(t)\,, \tag{5}$$

where

$$\hat{H}_\mathrm{Q0} = -\gamma_\mathrm{e}\mathbf{B}_0\cdot\hat{\mathbf{S}}_\mathrm{Q} + \sum_j \hat{\mathbf{S}}_\mathrm{Q}\cdot\mathbf{A}_{\mathrm{Q}j}\cdot\hat{\mathbf{I}}_{\mathrm{Q}j}\,, \tag{6}$$

$$\hat{H}_\mathrm{Q1}(t) = -\gamma_\mathrm{e}\mathbf{B}_1(t)\cdot\hat{\mathbf{S}}_\mathrm{Q}\,. \tag{7}$$

$\hat{H}_\mathrm{Q0}$ contains terms for the electron Zeeman interaction with the static magnetic field, $\mathbf{B}_0$, and the electron-nuclear hyperfine interactions, while $\hat{H}_\mathrm{Q1}(t)$ describes the electron Zeeman interaction with the radiofrequency field, $\mathbf{B}_1(t)$. $\hat{\mathbf{I}}_{\mathrm{Q}j}$ and $\mathbf{A}_{\mathrm{Q}j}$ are, respectively, the spin angular momentum operator and the hyperfine interaction tensor of nucleus j in radical Q. The elements of the vector $\hat{\mathbf{S}}_\mathrm{Q}$ are $\hat{S}_{\mathrm{Q}x}$, $\hat{S}_{\mathrm{Q}y}$, and $\hat{S}_{\mathrm{Q}z}$, and similarly for $\hat{\mathbf{I}}_{\mathrm{Q}j}$.

Treating $\hat{H}_\mathrm{Q1}(t)$ as a weak perturbation, the propagators in Eq. (3) were evaluated using a split operator approximation [41]:

$$\mathrm{e}^{\pm i\hat{\Omega}_\mathrm{Q}(t+\delta t;t)\delta t} \approx \exp\left[\pm i\hat{\Omega}_\mathrm{Q1}(t+\delta t;t)\delta t/2\right]\exp\left[\pm i\hat{H}_\mathrm{Q0}\delta t\right]\exp\left[\pm i\hat{\Omega}_\mathrm{Q1}(t+\delta t;t)\delta t/2\right], \tag{8}$$

where [42,43]:

$$\hat{\Omega}_\mathrm{Q}(t+\delta t;t) = \hat{H}_\mathrm{Q0} + \hat{\Omega}_\mathrm{Q1}(t+\delta t;t)\,, \tag{9}$$

$$\hat{\Omega}_\mathrm{Q1}(t+\delta t;t) = \frac{1}{\delta t}\int_t^{t+\delta t}\hat{H}_\mathrm{Q1}(\tau)\,\mathrm{d}\tau\,. \tag{10}$$

For a fixed time-step, δt, $\exp\left[\pm i\hat{H}_\mathrm{Q0}\delta t\right]$ need only be calculated once for each direction of $\mathbf{B}_0$, and $\exp\left[\pm i\hat{\Omega}_\mathrm{Q1}(t+\delta t;t)\delta t/2\right]$ is cheap to evaluate because $\hat{H}_\mathrm{Q1}(t)$ depends only on the electron spin degrees of freedom.

For each direction of the static field, the noise-modulated radiofrequency field was modelled as a sum of $M = 2000$ oscillating components:

$$\mathbf{B}_1(t) = \frac{1}{\sqrt{M}}\sum_{m=1}^{M} b_{1m}\,\mathbf{n}_{1m}\cos\left(\omega_m t + \gamma_m\right). \tag{11}$$

The frequencies ω_m and phases γ_m were sampled from uniform distributions $\mathcal{U}(\omega_{\min}, \omega_{\max})$ and $\mathcal{U}(0, 2\pi)$, respectively. The maximum and minimum radiofrequencies are related to the quantities ν_0 (centre frequency) and $\Delta\nu$ (bandwidth) by $\omega_{\min} = 2\pi\left(\nu_0 - \tfrac{1}{2}\Delta\nu\right)$ and $\omega_{\max} = 2\pi\left(\nu_0 + \tfrac{1}{2}\Delta\nu\right)$. The amplitudes were taken from a normal distribution with mean zero and standard deviation B_{rms} (rms = root-mean-square), and the directions $\mathbf{n}_{1m}$,

$$\mathbf{n}_{1m} = \left(\sin\theta_m \cos\phi_m, \sin\theta_m \sin\phi_m, \cos\theta_m\right)^{\mathrm{T}}, \qquad (12)$$

were uniformly spherically distributed with $\cos\theta_m = \mathcal{U}(-1,1)$ and $\phi_m = \mathcal{U}(0, 2\pi)$.

Results

Action-spectrum histograms

The concept of an action-spectrum histogram was introduced by Hiscock *et al.* to give a qualitative impression of the likely effects of weak time-dependent magnetic fields on the ability of a radical pair to act as a compass magnetoreceptor [33]. The "resonance effect" of a radiofrequency magnetic field in resonance with a transition between two energy levels of the radical pair, $|j\rangle$ and $|k\rangle$, was defined as the product of the transition probability and the difference in initial populations of the two levels. The height of the histogram bar covering the frequency interval $[\nu, \nu+\delta\nu]$ is then the sum of the resonance effects for all transitions with frequencies within that range:

$$\sum_{\nu_{jk} \in [\nu,\, \nu+\delta\nu]} N \left|\langle j|\hat{H}_{\perp}|k\rangle\right|^2 \left|\langle j|\hat{P}^{\mathrm{S}}|j\rangle - \langle k|\hat{P}^{\mathrm{S}}|k\rangle\right|. \qquad (13)$$

In Eq. (13), $|j\rangle$ and $|k\rangle$ are eigenstates of the time-independent spin Hamiltonian of the radical pair (see Methods section), $h\nu_{jk}$ is the energy gap between the two levels, $\hat{P}^{\mathrm{S}}$ is the singlet projection operator, and $\hat{H}_{\perp}$ is the Zeeman spin Hamiltonian for a weak static magnetic field perpendicular to the geomagnetic field. In Eq. (13), the first term, *N*, is a normalization constant that ensures the heights of the histogram bars sum to unity, the second is the transition probability and the third is the difference in the populations of the two energy levels at the instant the radical pair is formed in a singlet state. Normalization has the consequence that the strength of the Zeeman interaction in $\hat{H}_{\perp}$ is irrelevant [33].

Our aim here is to test the applicability of Eq. (13) by comparing it with spin dynamics simulations. We start by calculating action-spectrum histograms for a model of the flavin adenine dinucleotide (FAD)-tryptophan radical pair, $[\mathrm{FAD}^{\bullet-}\ \mathrm{TrpH}^{\bullet+}]$, containing the 14 nuclear spins, out of a total of 27 [44], that have the largest anisotropic hyperfine interactions: 7 in $\mathrm{FAD}^{\bullet-}$ and 7 in $\mathrm{TrpH}^{\bullet+}$ (the tensors are listed in the Supplementary Information). The orientation of $\mathrm{TrpH}^{\bullet+}$ relative to $\mathrm{FAD}^{\bullet-}$ was chosen to match that of the third tryptophan residue of the Trp-tetrad in the X-ray structure of pigeon Cry4a [45]. The resulting histograms were averaged over 100 randomly chosen directions of an Earth-strength (50 μT) magnetic field. The restriction to 14 anisotropic hyperfine interactions is a compromise between computational feasibility and the desire to model a fairly realistic spin system.

Figure 1(a) shows the complete histogram for this model of the $[\mathrm{FAD}^{\bullet-}\ \mathrm{TrpH}^{\bullet+}]$ radical pair together with an expanded view of the low-frequency region, Fig. 1(b). The widths of the histogram bins, $\delta\nu$, were 1 MHz and 50 kHz, respectively, and both plots were normalised over the frequency range 0-110 MHz. Following a ~3-fold drop in amplitude between 0 and 2 MHz, the resonance effect is approximately flat up to about 80 MHz. The histogram would undoubtedly have been smoother if a larger number of hyperfine interactions and/or the dipolar coupling had been included [30,31,33]. The resonance effect drops off above 80 MHz and is zero for frequencies above ~100 MHz. This upper limit on the resonance frequency corresponds to the separation of the highest- and lowest-energy eigenvalues of the time-independent spin Hamiltonian. It would have been 116 MHz had all 27 nuclear spins been included [31].

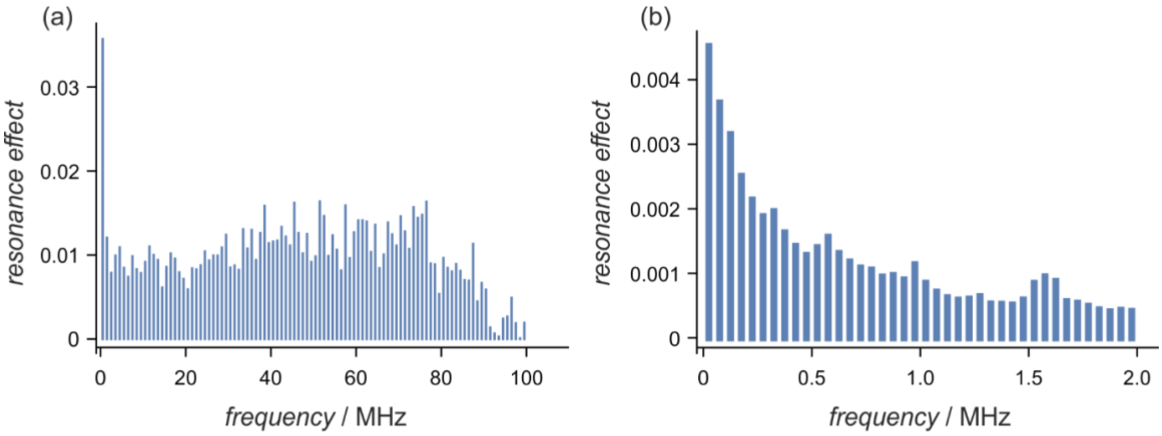

Fig. 1. Action-spectrum histograms of a model $[\mathrm{FAD}^{\bullet-}\ \mathrm{TrpH}^{\bullet+}]$ radical pair with 14 hyperfine anisotropic interactions. The widths of the histogram bins are (a) 1 MHz and (b) 0.05 MHz.

Note that there is no "Zeeman resonance" at 1.4 MHz (the Larmor frequency of a free electron in a 50 μT magnetic field) because both radicals have hyperfine interactions, many of which are larger than 50 μT. A strong resonance at this frequency is only expected if (a) one of the radicals has all hyperfine interactions much smaller than 50 μT, and (b) the exchange and dipolar interactions of the two radicals are also much smaller than 50 μT [33,46].

To summarize, Fig. 1 suggests that our model radical pair, with 14 nuclear spins, should be affected to approximately the same extent by RF magnetic fields with frequencies between ~2 MHz and ~80 MHz, with the effects being somewhat stronger below ~2 MHz and weaker in the range ~80-100 MHz. No effects are expected for radiofrequencies above 100 MHz. Similar predictions can be anticipated for a $[\mathrm{FAD}^{\bullet-}\ \mathrm{TrpH}^{\bullet+}]$ radical pair with 27 nuclear spins except that the cut-off frequency would be at ~116 MHz [31].

Spin dynamics simulations

To test the reliability of Fig. 1 as a guide to the frequency-dependence of RF magnetic field effects, we performed spin-dynamics simulations using the same model of $[\mathrm{FAD}^{\bullet-}\ \mathrm{TrpH}^{\bullet+}]$. Broadband, noise-modulated RF fields (root-mean-square magnetic flux density B_{rms} and frequency $\nu_0 - \frac{1}{2}\Delta\nu \le \nu \le \nu_0 + \frac{1}{2}\Delta\nu$) were included as described in the Methods section. For each RF field condition, the fraction of radical pairs that react spin-selectively from the singlet state, $\Phi_{\mathrm{S}}(\theta, B_{\mathrm{rms}})$, was calculated as a function of the direction, θ, of the static magnetic field, $B_0 = 50$ μT. As in previous work [47,48], the amplitude of the anisotropy of Φ_{S} was taken as a proxy for the output of the sensor from which the bird could derive a magnetic compass bearing [47]. The change in Φ_{S} produced by a broadband RF field was assessed using χ, the root-mean-square difference between the singlet yields for B_{rms} = 1 μT and B_{rms} = 1 nT, with the latter regarded as weak enough that it has no significant effect on the spin dynamics for the radical-pair lifetimes studied here:

$$\chi^2 = \frac{1}{N_\theta}\sum_{i=1}^{N_\theta}\left[\Phi_{\mathrm{S}}(\theta_i, 1\,\mu\mathrm{T}) - \Phi_{\mathrm{S}}(\theta_i, 1\,\mathrm{nT})\right]^2 . \qquad (14)$$

In Eq. (14), θ is the angle between the magnetic field vector and the *z*-axis of the flavin ring system (the normal to the isoalloxazine plane); when $\theta = \pi / 2$, the field is parallel to the vector connecting the two nitrogens (N5 and N10) in the central ring of the tricyclic flavin group. χ was evaluated by summing over N_θ = 101 equally spaced values of θ in the range [0, π].

Figure 2 shows the dependence of χ on ν_0 for radical pairs with lifetimes of 2 μs (green) and 100 μs (red), superimposed on the heights of the action-spectrum histogram bars (blue, 100 kHz bins). The full spectrum is presented in Fig. 2(a), with an expansion of the low-frequency region in Fig. 2(b). The three quantities plotted in both panels were scaled to have the same mean in the range ν_0 = 10-90 MHz.

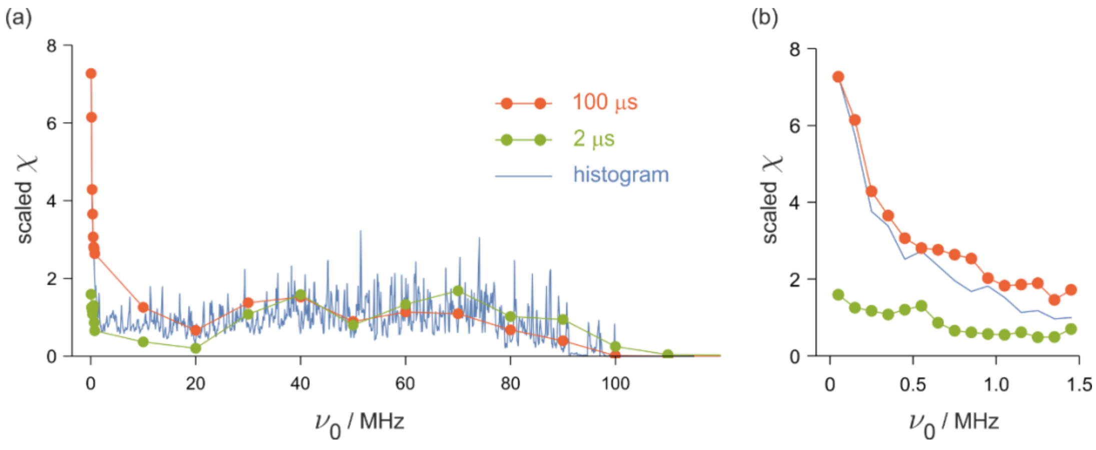

Fig. 2. Radiofrequency magnetic field effects, χ, for a model $[\mathrm{FAD}^{\bullet-}\ \mathrm{TrpH}^{\bullet+}]$ radical pair with 14 anisotropic hyperfine interactions and a lifetime of 2 μs (green) or 100 μs (red) superimposed on the heights of the action-spectrum histogram bars (blue, 100 kHz bins). The three traces have been scaled to have a mean of 1.0 in the range 10 to 90 MHz. The spin dynamics calculations were performed for $\Delta\nu$ = 100 kHz bands of RF noise centred at the frequencies of the green and red dots.

Both simulations agree reasonably well with the histogram at frequencies, ν_0, above ~10 MHz, confirming that the RF effect is approximately independent of frequency between ~10 MHz and ~80 MHz and that it then drops down to zero at $\nu_0 \approx$ 100 MHz and beyond. However, only the calculation for the 100-μs lifetime reproduces the rise in the resonance effect at frequencies below 2 MHz (Fig. 2(b)). For the radical pair with the shorter (2 μs) lifetime, the histogram seriously overestimates the effect of low-frequency RF fields.

The comparison of the quantum simulations and the histogram method in Fig. 2 is somewhat complicated by the use of an RF bandwidth ($\Delta\nu$ = 100 kHz) comparable to the frequencies (< 10 MHz) at which the two approaches disagree. A clearer picture should emerge by choosing a much narrower bandwidth. Figure 3 shows RF effects calculated for 2 μs (green) and 100 μs (red) lifetimes using $\Delta\nu$ = 1 kHz bands of RF noise, centred at frequencies, ν_0, between 1 kHz and 12.8 MHz, plotted with a logarithmic frequency axis. Once again, the heights of the histogram bars (100 kHz bins) are shown in blue. What we see now is that at frequencies below ~1 MHz, the histogram overestimates the true resonance effect for both choices of lifetime. In both cases, χ goes through a maximum at $\nu_0 \approx$ 100 kHz and then levels off when ν_0 < ~10 kHz. We discuss this behaviour in the next section.

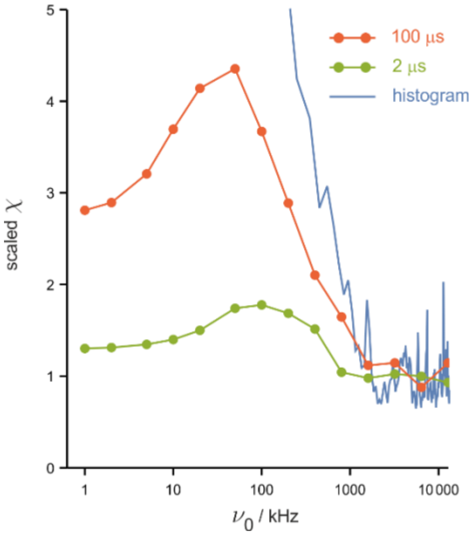

Fig. 3. Radiofrequency magnetic field effects, χ, for a model $[\mathrm{FAD}^{\bullet-}\ \mathrm{TrpH}^{\bullet+}]$ radical pair with 14 hyperfine interactions and a lifetime of 2 μs (green) or 100 μs (red) superimposed on the heights of the action-spectrum histogram bars (blue, 100 kHz). The three traces have been scaled to have a mean of 1.0 at frequencies above 1 MHz. The spin dynamics calculations were performed for $\Delta\nu$ = 1 kHz bands of RF noise centred at the frequencies of the green and red dots.

Discussion

We have tested the action-spectrum histogram concept [33] against spin dynamics simulations of flavin-tryptophan radical pairs in cryptochrome. Our results suggest that the histograms offer a useful qualitative guide for frequencies between ~10 MHz and the cut-off frequency which falls at 100 MHz for the pared down spin system modelled here and at 116 MHz for the complete spin system with 27 nuclear spins [31]. At frequencies below 10 MHz, the histogram predicts an increase in the resonance effect which was not seen in the spin dynamics simulations of radical pairs with 2 μs lifetimes subject to 100 kHz bands of RF noise (Fig. 2(b)), or for 2 μs or 100 μs lifetimes when the bandwidth was reduced to 1 kHz.

That the action-spectrum histogram fails at low frequencies, especially for short-lived radical pairs, is not unexpected: one of the approximations implicit in Eq. (13) is that the radical pairs are indefinitely stable. To have a significant *resonant* effect on the coherent spin dynamics of a radical pair, an RF field would need to undergo at least one period of oscillation before the radicals recombined (or before the spin-coherence relaxed, whichever happened first). An RF field at any lower frequency would be equivalent to an effectively static (and randomly oriented) magnetic field. Following this line of reasoning, the transition from time-dependent field to effectively static field, should occur at $\nu_0 \approx$ 500 kHz for a 2-μs lifetime and at $\nu_0 \approx$ 10 kHz for a 100-μs lifetime. Qualitatively, but not quantitatively, this seems to be consistent with the left-hand side of Fig. 3: the drop in χ occurs at a lower frequency for the longer of the two lifetimes, but not lower by a factor of 50 as the above argument would suggest.

This mismatch between this prediction and the results of the simulations has consequences for the interpretation of the behavioural tests. Kobylkov *et al.* found that 0.1–100 kHz noise-modulated RF fields did not disrupt the orientation of Eurasian blackcaps [29], while Engels *et al.* found that European robins were disoriented by 20-450 kHz noise of similar amplitude [27]. Taking these observations together, Kobylkov *et al.*[29] concluded that the spin-coherence lifetime must be in the range 2-10 μs (using the argument in the previous paragraph and $(450\ \text{kHz})^{-1} \approx 2\ \mu\text{s}$ and $(100\ \text{kHz})^{-1} = 10\ \mu\text{s}$). An assumption behind this argument was that a sufficiently low-frequency RF field would be much less effective at causing disorientation than one in resonance with spin transitions in the radical pair. This does not appear to be borne out by Figs 2 and 3 which suggest that RF fields below ~2 MHz should have a similar or larger effect than those in the range 2-80 MHz. Shortcomings of our simulation method include: (a) the use of RF fields ($B_{\text{rms}} = 1$ mT) much stronger than those in the behavioural tests ($B_{\text{rms}} \approx 10$ nT, [29]); (b) the omission of a dipolar interaction between the radicals; and possibly (c) the use of an inappropriate measure (χ) to quantify the effect of the RF fields on the singlet yield. Further work will be needed to shed light on this discrepancy.

Acknowledgements

We are grateful for the financial support provided by the European Research Council under the European Union’s Horizon 2020 research and innovation program, Grant Agreement No. 810002, Synergy Grant: QuantumBirds. GJP and PJH thank Prof. David E. Manolopoulos for his advice on how best to do the calculations, Dr. Thomas P. Fay for suggesting Fourier decomposition in Eq. 11, and Dr. Luca Gerhards for helpful discussions.

Simulation of radiofrequency magnetic field effects on a radical pair cryptochrome-based magnetoreceptor

Gediminas Jurgis Pažėra, and P. J. Hore*

Department of Chemistry, University of Oxford, Physical & Theoretical Chemistry Laboratory, Oxford, UK.

*Corresponding author: peter.hore@chem.ox.ac.uk

Supporting Information

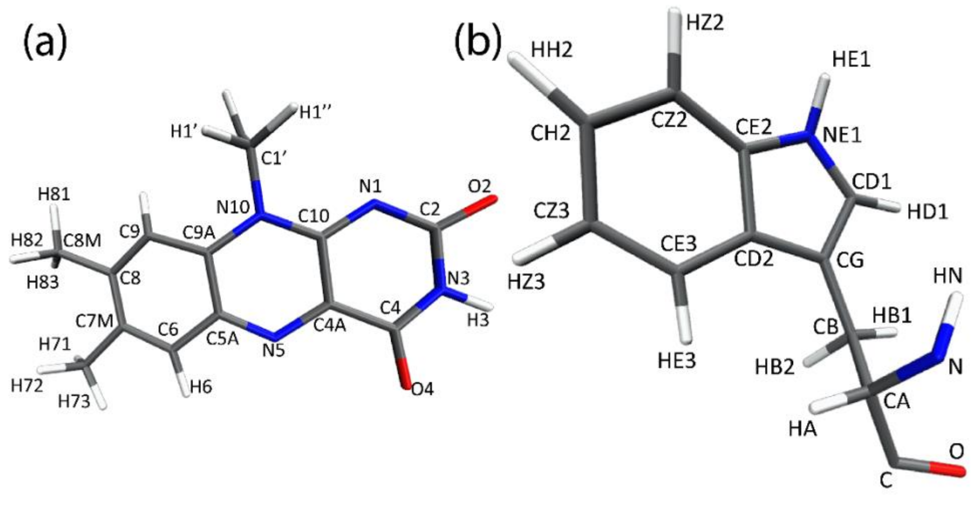

Fig. S1. Atom labelling in (a) FAD$^{\bullet-}$ and (b) TrpH$^{\bullet+}$ radicals

N5	$\begin{pmatrix} -0.09950 & -0.00287 & 0 \\ -0.00287 & -0.08749 & 0 \\ 0 & 0 & 1.75688 \end{pmatrix}$
N10	$\begin{pmatrix} -0.01485 & -0.00207 & 0 \\ -0.00207 & -0.02371 & 0 \\ 0 & 0 & 0.60459 \end{pmatrix}$
H6	$\begin{pmatrix} -0.20085 & 0.03280 & 0 \\ 0.03280 & -0.52717 & 0 \\ 0 & 0 & -0.43359 \end{pmatrix}$
H81, H82, H83	$\begin{pmatrix} 0.43990 & 0 & 0 \\ 0 & 0.43990 & 0 \\ 0 & 0 & 0.43990 \end{pmatrix}$
H1′	$\begin{pmatrix} 0.40701 & -0.00001 & -0.00002 \\ -0.00001 & 0.40704 & -0.00002 \\ -0.00002 & -0.00002 & 0.40700 \end{pmatrix}$

Table S1. Hyperfine coupling tensors for FAD$^{\bullet-}$ (in mT). Standard PDB/IUPAC nomenclature is used (Fig. S1(a)). Calculations were performed by Dr Ilya Kuprov, Department of Chemistry, University of Southampton using density functional theory in Gaussian-03 at the UB3LYP/EPR-III level, for the radical anion of 7,8,10-trimethyl isoalloxazine (lumiflavin). The hyperfine tensors for the three H8 protons were averaged to reflect the rapid rotation of this methyl group.

HE1	$\begin{pmatrix} -1.00093 & 0.20617 & 0.19326 \\ 0.20617 & -0.44157 & 0.30726 \\ 0.19326 & 0.30726 & -0.35248 \end{pmatrix}$
HE3	$\begin{pmatrix} -0.57128 & 0.16088 & 0.19595 \\ 0.16088 & -0.48444 & 0.08363 \\ 0.19595 & 0.08363 & -0.40819 \end{pmatrix}$
HZ2	$\begin{pmatrix} -0.44261 & 0.12694 & 0.14890 \\ 0.12694 & -0.35420 & 0.09527 \\ 0.14890 & 0.09527 & -0.29426 \end{pmatrix}$
HB1	$\begin{pmatrix} 1.57245 & 0.01567 & 0.04747 \\ 0.01567 & 1.51560 & 0.06305 \\ 0.04747 & 0.06305 & 1.72559 \end{pmatrix}$
NE1	$\begin{pmatrix} -0.05296 & 0.05866 & -0.04603 \\ 0.05866 & 0.56445 & -0.56480 \\ -0.04603 & -0.56480 & 0.45313 \end{pmatrix}$
HD1	$\begin{pmatrix} -0.27540 & -0.15716 & -0.17450 \\ -0.15716 & -0.27318 & 0.09233 \\ -0.17450 & 0.09233 & -0.28547 \end{pmatrix}$
HH2	$\begin{pmatrix} -0.04310 & -0.07438 & -0.06807 \\ -0.07438 & -0.27873 & -0.03238 \\ -0.06807 & -0.03238 & -0.30304 \end{pmatrix}$

Table S2. Hyperfine coupling tensors for TrpH$^{\bullet+}$ (in mT). Standard PDB/IUPAC nomenclature is used (Fig. S1(b)). Calculations were performed by Dr Ilya Kuprov, Department of Chemistry, University of Southampton using density functional theory in Gaussian-03 at the UB3LYP/EPR-III level.

References

[1]W. Wiltschko, "Über den einfluß statischer magnetfelder auf die zugorientierung der rotkehlchen (*erithacus rubecula*)," Z. Tierpsychol. **25**, 537 (1968).

[2]R. Wiltschko and W. Wiltschko, *Magnetic orientation in animals* (Springer Verlag, Berlin, 1995).

[3]H. Mouritsen, "Long-distance navigation and magnetoreception in migratory animals," Nature **558**, 50 (2018).

[4]G. C. Nordmann, T. Hochstoeger and D. A. Keays, "Magnetoreception - a sense without a receptor," PLoS Biol. **15**, e2003234 (2017).

[5]P. J. Hore and H. Mouritsen, "The radical pair mechanism of magnetoreception," Annu. Rev. Biophys. **45**, 299 (2016).

[6]K. Schulten, C. E. Swenberg and A. Weller, "A biomagnetic sensory mechanism based on magnetic field modulated coherent electron spin motion," Z. Phys. Chem. NF **111**, 1 (1978).

[7]T. Ritz, S. Adem and K. Schulten, "A model for photoreceptor-based magnetoreception in birds," Biophys. J. **78**, 707 (2000).

[8]N. Karki, S. Vergish and B. D. Zoltowski, "Cryptochromes: Photochemical and structural insight into magnetoreception," Protein Sci. **30**, 1521 (2021).

[9]R. Kavet and J. Brain, "Cryptochromes in mammals and birds: Clock or magnetic compass?," Physiology **36**, 183 (2021).

[10]R. Wiltschko, C. Niessner and W. Wiltschko, "The magnetic compass of birds: The role of cryptochrome," Front. Physiol. **12**, 667000 (2021).

[11]J. Xu, L. E. Jarocha, T. Zollitsch, M. Konowalczyk, K. B. Henbest, S. Richert, M. J. Golesworthy, J. Schmidt, V. Déjean, D. J. C. Sowood, M. Bassetto, J. Luo, J. R. Walton, J. Fleming, Y. Wei, T. L. Pitcher, G. Moise, M. Herrmann, H. Yin, H. Wu, R. Bartölke, S. J. Käsehagen, S. Horst, G. Dautaj, P. D. F. Murton, A. S. Gehrckens, Y. Chelliah, J. S. Takahashi, K.-W. Koch, S. Weber, I. A. Solov'yov, C. Xie, S. R. Mackenzie, C. R. Timmel, H. Mouritsen and P. J. Hore, "Magnetic sensitivity of cryptochrome 4 from a migratory songbird," Nature **594**, 535 (2021).

[12]S. Y. Wong, Y. Wei, H. Mouritsen, I. A. Solov'yov and P. J. Hore, "Cryptochrome magnetoreception: Four tryptophans could be better than three," J. R. Soc. Interface **18**, 20210601 (2021).

[13]U. E. Steiner and T. Ulrich, "Magnetic field effects in chemical kinetics and related phenomena," Chem. Rev. **89**, 51 (1989).

[14]A. R. Jones, "Magnetic field effects in proteins," Molec. Phys. **114**, 1691 (2016).

[15]E. W. Evans, C. A. Dodson, K. Maeda, T. Biskup, C. J. Wedge and C. R. Timmel, "Magnetic field effects in flavoproteins and related systems," Interface Focus **3**, 20130037 (2013).

[16]K. Maeda, K. B. Henbest, F. Cintolesi, I. Kuprov, C. T. Rodgers, P. A. Liddell, D. Gust, C. R. Timmel and P. J. Hore, "Chemical compass model of avian magnetoreception," Nature **453**, 387 (2008).

[17] C. Kerpal, S. Richert, J. G. Storey, S. Pillai, P. A. Liddell, D. Gust, S. R. Mackenzie, P. J. Hore and C. R. Timmel, "Chemical compass behaviour at microtesla magnetic fields strengthens the radical pair hypothesis of avian magnetoreception," Nat. Comm. **10**, 3707 (2019).

[18] K. B. Henbest, P. Kukura, C. T. Rodgers, P. J. Hore and C. R. Timmel, "Radio frequency magnetic field effects on a radical recombination reaction: A diagnostic test for the radical pair mechanism," J. Amer. Chem. Soc. **126**, 8102 (2004).

[19] C. T. Rodgers, K. B. Henbest, P. Kukura, C. R. Timmel and P. J. Hore, "Low-field optically detected EPR spectroscopy of transient photoinduced radical pairs," J. Phys. Chem. A **109**, 5035 (2005).

[20] M. K. Bowman, D. E. Budil, G. L. Closs, A. G. Kostka, C. A. Wraight and J. R. Norris, "Magnetic-resonance spectroscopy of the primary state, p^f, of bacterial photosynthesis," Proc. Natl. Acad. Sci. USA **78**, 3305 (1981).

[21] W. Lersch and M. E. Michel-Beyerle, in *Advanced EPR. Applications in biology and biochemistry*, edited by A. J. Hoff (Elsevier, Amsterdam, 1989), p. 685.

[22] P. Thalau, T. Ritz, K. Stapput, R. Wiltschko and W. Wiltschko, "Magnetic compass orientation of migratory birds in the presence of a 1.315 mhz oscillating field," Naturwissenschaften **92**, 86 (2005).

[23] T. Ritz, R. Wiltschko, P. J. Hore, C. T. Rodgers, K. Stapput, P. Thalau, C. R. Timmel and W. Wiltschko, "Magnetic compass of birds is based on a molecule with optimal directional sensitivity," Biophys. J. **96**, 3451 (2009).

[24] K. Kavokin, N. Chernetsov, A. Pakhomov, J. Bojarinova, D. Kobylkov and B. Namozov, "Magnetic orientation of garden warblers (*sylvia borin*) under 1.4 mhz radiofrequency magnetic field," J. R. Soc. Interface **11**, 20140451 (2014).

[25] A. Pakhomov, J. Bojarinova, R. Cherbunin, R. Chetverikova, P. S. Grigoryev, K. Kavokin, D. Kobylkov, R. Lubkovskaja and N. Chernetsov, "Very weak oscillating magnetic field disrupts the magnetic compass of songbird migrants," J. R. Soc. Interface **14**, (2017).

[26] T. Ritz, P. Thalau, J. B. Phillips, R. Wiltschko and W. Wiltschko, "Resonance effects indicate a radical-pair mechanism for avian magnetic compass," Nature **429**, 177 (2004).

[27] S. Engels, N. L. Schneider, N. Lefeldt, C. M. Hein, M. Zapka, A. Michalik, D. Elbers, A. Kittel, P. J. Hore and H. Mouritsen, "Anthropogenic electromagnetic noise disrupts magnetic compass orientation in a migratory bird," Nature **509**, 353 (2014).

[28] S. Schwarze, N.-L. Schneider, T. Reichl, D. Dreyer, N. Lefeldt, S. Engels, N. Baker, P. J. Hore and H. Mouritsen, "Weak broadband electromagnetic fields are more disruptive to magnetic compass orientation in a night-migratory songbird (*erithacus rubecula*) than strong narrow-band fields," Front. Behav. Neurosci. **10**, 55 (2016).

[29] D. Kobylkov, J. Wynn, M. Winklhofer, R. Chetverikova, J. J. Xu, H. Hiscock, P. J. Hore and H. Mouritsen, "Electromagnetic 0.1-100 khz noise does not disrupt orientation in a night-migrating

songbird implying a spin coherence lifetime of less than 10 microseconds," J. R. Soc. Interface **16**, 20190716 (2019).

[30]B. Leberecht, D. Kobylkov, T. Karwinkel, S. Doge, L. Burnus, S. Y. Wong, S. Apte, K. Haase, I. Musielak, R. Chetverikova, G. Dautaj, M. Bassetto, M. Winklhofer, P. J. Hore and H. Mouritsen, "Broadband 75-85 mhz radiofrequency fields disrupt magnetic compass orientation in night-migratory songbirds consistent with a flavin-based radical pair magnetoreceptor," J. Comp. Physiol. A **208**, 97 (2022).

[31]B. Leberecht, S. Y. Wong, B. Satish, S. Döge, J. Hindman, L. Venkatraman, S. Apte, K. Haase, I. Musielak, G. Dautaj, I. A. Solov'yov, M. Winklhofer, H. Mouritsen and P. J. Hore, "Upper bound for broadband radiofrequency field disruption of magnetic compass orientation in night-migratory songbirds," Proc. Natl. Acad. Sci. USA **120**, 2301153120 (2023).

[32]J. Shaw, A. Boyd, M. House, R. Woodward, F. Mathes, G. Cowin, M. Saunders and B. Baer, "Magnetic particle-mediated magnetoreception," J. R. Soc. Interface **12**, 20150499 (2015).

[33]H. G. Hiscock, H. Mouritsen, D. E. Manolopoulos and P. J. Hore, "Disruption of magnetic compass orientation in migratory birds by radiofrequency electromagnetic fields," Biophys. J. **113**, 1475 (2017).

[34]H. G. Hiscock, D. R. Kattnig, D. E. Manolopoulos and P. J. Hore, "Floquet theory of radical pairs in radiofrequency magnetic fields," J. Chem. Phys. **145**, 124117 (2016).

[35]A. Abragam, *The principles of nuclear magnetism* (Oxford University Press, Oxford, 1961).

[36]S. Schäublin, A. Höhener and R. R. Ernst, "Fourier spectroscopy of nonequilibrium states, application to CIDNP, Overhauser experiments and relaxation-time measurements," J. Magn. Reson. **13**, 196 (1974).

[37]K. Schulten and P. G. Wolynes, "Semi-classical description of electron-spin motion in radicals including effect of electron hopping," J. Chem. Phys. **68**, 3292 (1978).

[38]D. E. Manolopoulos and P. J. Hore, "An improved semiclassical theory of radical pair recombination reactions," J. Chem. Phys. **139**, 124106 (2013).

[39]U. Till, C. R. Timmel, B. Brocklehurst and P. J. Hore, "The influence of very small magnetic fields on radical recombination reactions in the limit of slow recombination," Chem. Phys. Lett. **298**, 7 (1998).

[40]C. R. Timmel, U. Till, B. Brocklehurst, K. A. McLauchlan and P. J. Hore, "Effects of weak magnetic fields on free radical recombination reactions," Molec. Phys. **95**, 71 (1998).

[41]M. D. Feit, J. A. Fleck and A. Steiger, "Solution of the schrödinger equation by a spectral method," J. Comput. Phys. **47**, 412 (1982).

[42]T. P. Fay, L. P. Lindoy and D. E. Manolopoulos, "Spin relaxation in radical pairs from the stochastic schrödinger equation," J. Chem. Phys. **154**, 084121 (2021).

[43]W. Magnus, "On the exponential solution of differential equations for a linear operator," Commun Pur Appl Math **7**, 649 (1954).

[44]S. Y. Wong, P. Benjamin and P. J. Hore, "Magnetic field effects on radical pair reactions: Estimation of $B_{1/2}$ for flavin-tryptophan radical pairs in cryptochromes," Phys. Chem. Chem. Phys. **25**, 975 (2023).

[45]B. D. Zoltowski, Y. Chelliah, A. Wickramaratne, L. Jarocha, N. Karki, W. Xu, H. Mouritsen, P. J. Hore, R. E. Hibbs, C. B. Green and J. S. Takahashi, "Chemical and structural analysis of a photoactive vertebrate cryptochrome from pigeon," Proc. Natl. Acad. Sci. USA **116**, 19449 (2019).

[46]H. J. Hogben, O. Efimova, N. Wagner-Rundell, C. R. Timmel and P. J. Hore, "Possible involvement of superoxide and dioxygen with cryptochrome in avian magnetoreception: Origin of zeeman resonances observed by *in vivo* EPR spectroscopy," Chem. Phys. Lett. **480**, 118 (2009).

[47]H. G. Hiscock, S. Worster, D. R. Kattnig, C. Steers, Y. Jin, D. E. Manolopoulos, H. Mouritsen and P. J. Hore, "The quantum needle of the avian magnetic compass," Proc. Natl. Acad. Sci. USA **113**, 4634 (2016).

[48]D. R. Kattnig, J. K. Sowa, I. A. Solov'yov and P. J. Hore, "Electron spin relaxation can enhance the performance of a cryptochrome-based magnetic compass sensor," New J. Phys. **18**, 063007 (2016).

5 Article 3: Pulse Sequences for Manipulating the Spin States of Molecular Radical-Pair-Based Electron Spin Qubit Systems for Quantum Information Applications

The Journal of Chemical Physics ARTICLE scitation.org/journal/jcp

Pulse sequences for manipulating the spin states of molecular radical-pair-based electron spin qubit systems for quantum information applications

Cite as: J. Chem. Phys. 158, 204118 (2023); doi: 10.1063/5.0145278
Submitted: 4 February 2023 • Accepted: 30 April 2023 •
Published Online: 31 May 2023

Gediminas J. Pazera,[1] Matthew D. Krzyaniak,[2] and Michael R. Wasielewski[2,a)]

AFFILIATIONS

[1] Department of Chemistry, University of Oxford, Physical and Theoretical Chemistry Laboratory, Oxford OX1 3QZ, United Kingdom

[2] Department of Chemistry and Center for Molecular Quantum Transduction, and Institute for Sustainability and Energy at Northwestern, Northwestern University, Evanston, Illinois 60208-3113, USA

[a)] Author to whom correspondence should be addressed: m-wasielewski@northwestern.edu

ABSTRACT

Molecular qubits are an emerging platform in quantum information science due to the unmatched structural control that chemical design and synthesis provide compared to other leading qubit technologies. This theoretical study investigates pulse sequence protocols for spin-correlated radical pairs, which are important molecular spin qubit pair (SQP) candidates. Here, we introduce improved microwave pulse protocols for enhancing the execution times of quantum logic gates based on SQPs. Significantly, this study demonstrates that the proposed pulse sequences effectively remove certain contributions from nuclear spin effects on spin dynamics, which are a common source of decoherence. Additionally, we have analyzed the factors that control the fidelity of the SQP spin state, following the application of the controlled-NOT gate. It was found that higher magnetic fields introduce a high frequency oscillation in the fidelity. Thereupon, it is suggested that further research should be geared toward executing quantum gates at lower magnetic field values. In addition, an absolute bound of the fidelity outcome due to decoherence is determined, which clearly identifies the important factors that control gate execution. Finally, examples of the application of these pulse sequences to SQPs are described.

I. INTRODUCTION

There is a growing interest in molecular qubit systems comprising electron and nuclear spins for quantum information science (QIS) and quantum computing (QC). It stems from the extensive control over the qubit nature that chemical synthesis allows, providing the ability to fine-tune qubit properties and spatially position individual molecular qubits via covalent and non-covalent assemblies that may be used for quantum sensing (QS) or for preparing multi-qubit arrays.[1] Additionally, there are already a number of candidates for molecular qubits, such as photogenerated radical-pairs in donor–bridge–acceptor (D–B–A) systems,[2,3] photogenerated radical pairs in triradical Pt complexes,[4] photoisomerization-induced spin-charge Co complexes,[5] and a recent example of a successful quantum teleportation experiment that utilized Electron Paramagnetic Resonance (EPR) for detection.[3] Besides the universal issue of coherence times and detection, alongside the experimental execution of quantum logic gates, further challenges need to be addressed. These challenges include a full description of the dynamical properties of spin systems via computational or experimental techniques, coupling to external fields, electron–nuclear hyperfine interactions, spin–orbit coupling, magnetic spin exchange, and their effect on controlling the spin states. Furthermore, there is the matter of understanding environmental contributions to decoherence and how these effects impact molecular qubits. Addressing all of these issues would greatly accelerate the utilization of molecular systems in QIS and QS and provide a toolbox for designing new experiments and applications, which are only at the beginning stages of this emerging second quantum revolution.[6]

In quantum information processing, there are several spin-based platforms outside molecular spin systems, such as impurities in semiconductors and quantum dots. Examples of impurities in semiconductors include colored centers in diamond, such as nitrogen-vacancy (NV)[7–10] and silicon-vacancy (SV) centers,[11,12] and phosphorus donor qubits in silicon.[13,14] Much research has been conducted on these systems, which have several desirable characteristics, such as extended coherence times and optical addressability, and have been applied to sensing applications. However, they have encountered engineering and production obstacles. These materials have impurities that are difficult to manage, and spatial placement of defects, scalability to multiple qubits, and coupling of a large number of qubits are all difficult. In addition, silicon[15–17] and germanium[18–20] quantum dots have been prominent QIS platforms. These are potential platforms with high fidelity rates, but similar to semiconductor impurities, they present fabrication and control issues, in addition to a high sensitivity to ambient and charge noise, which can reduce coherence times. This article is limited to molecular spin systems, which have been on the rise due to the ability of chemical synthesis to precisely control atomic placements.

Photogenerated spin-correlated radical pairs (SCRPs) in donor–bridge–acceptor (D–B–A) molecules are one class of molecular qubit candidates that shows great promise. Their advantages can be readily demonstrated by considering the widely researched preparation, photophysics, and spin dynamics of SCRPs, which are illustrated in Fig. 1.[21–25] In these systems, selective photoexcitation of D, B, or A produces an excited singlet state that undergoes rapid charge separation to produce a SCRP in an initial singlet spin state. This SCRP can be considered a spin qubit pair (SQP) and has been shown to satisfy a number of the DiVincenzo criteria.[26] The SCRPs are generated in a well-defined initial state, and the systems are well-characterized, potentially scalable, and have been shown to have long coherence times, around 2 μs at relatively high temperatures of 80 K.[2] SCRP coherence times can also be increased by reducing the electron–nuclear hyperfine interactions in each radical using deuteration and working in a nuclear spin free solvent, in addition to removing rapidly moving nuclear spins, such as the hydrogen atoms in methyl groups. Finally, a universal "set" of quantum logic gates exists, with initial attempts at implementation having been shown,[2,27] and there is evidence of a qubit-specific measurement capability based on quantum state tomography;[2] however, further research needs to be done (Fig. 2).

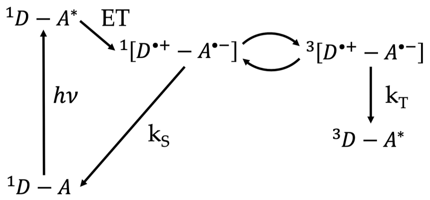

FIG. 1. Scheme of a typical spin selective charge recombination reaction in donor–acceptor (D–A) molecules. After initial light excitation and electron transfer reactions, a SCRP in a singlet state is produced, $^1[D^{\bullet+} - A^{\bullet-}]$. The singlet state can interconvert to the triplet state $^3[D^{\bullet+} - A^{\bullet-}]$ via hyperfine interactions of each of the spins. Both of these states relax to the ground state via different pathways. The singlet state relaxes to the ground state via the singlet pathway with recombination constant k_S, and the triplet state recombines to a triplet product via the triplet pathway with recombination constant k_T.

With respect to QIS, there are a few general criteria for a good SCRP system: First, the SCRP should have intermediate electron spin–spin coupling because this value will ultimately determine the speed at which a gate can be executed. Second, the SCRP should have long coherence times, T_2, to ensure that a sufficient number of gate operations can be made to be useful; Third, the SCRP should be capable of being oriented in a well-defined, controllable position to avoid overlapping transitions and to enable proper readout and control of the spin system. For example, oriented single crystals would be ideal in this regard.

In this article, we will explore how quantum logic gates can be implemented in a SCRP system. We will propose improved pulse sequences for most common two-qubit quantum logic gates in SCRPs and introduce ways to correct for different noise sources in the experimental application of these quantum logic gates. Furthermore, we will give a full dynamical description of how the fidelity of the SQP spin system following Controlled-NOT (CNOT) gate application will vary with different parameters in the experiment and give evidence for the advantages of performing these experiments at lower magnetic fields. Finally, a universal bound on the fidelity value of a CNOT gate operation will be given when T_2 relaxation effects are incorporated, providing an understanding of how decoherence affects SQPs.

II. THEORY

A. Spin Hamiltonian

The spin dynamics of an arbitrary SCRP in a fixed orientation are governed by its spin Hamiltonian, which includes the anisotropic electron Zeeman interaction, electron–nuclear hyperfine interaction, electron–electron dipolar interaction, and electron exchange interaction.[28–30] If the applied magnetic field is larger than other interactions in the system, then a secular approximation can be employed, which simplifies the Hamiltonian to[27,30–32]

$$\hat{H} = \hat{H}_{12} + \hat{H}_{hyp}, \tag{1}$$

where

$$\begin{aligned} \hat{H}_{12} &= g_1\mu_B|\mathbf{B}|\hat{S}_{1z} + g_2\mu_B|\mathbf{B}|\hat{S}_{2z} + J\hat{\mathbf{S}}_1^T\hat{\mathbf{S}}_2 + \frac{1}{2}\mathcal{D}\Big(3\hat{S}_{1z}\hat{S}_{2z} - \hat{\mathbf{S}}_1^T\hat{\mathbf{S}}_2\Big) \\ &= \omega_1\hat{S}_{1z} + \omega_2\hat{S}_{2z} + \mathcal{D}_1\hat{S}_{1z}\hat{S}_{2z} + \mathcal{D}_2\Big(\hat{S}_{1x}\hat{S}_{2x} + \hat{S}_{1y}\hat{S}_{2y}\Big), \end{aligned} \tag{2}$$

$$\begin{aligned} \hat{H}_{Hyp} = \hat{S}_{1z}&\left(\sum_{k=1}^{N_1}\Big(A_{1k}\hat{I}_{1k,z} + B_{1k}\hat{I}_{1k,x}\Big)\right) \\ &+ \hat{S}_{2z}\left(\sum_{p=1}^{N_2}\Big(A_{2p}\hat{I}_{2p,z} + B_{2p}\hat{I}_{2p,x}\Big)\right), \end{aligned} \tag{3}$$

and

$$\begin{aligned} \mathcal{D} &= D\left(\cos^2(\theta) - \frac{1}{3}\right), \\ \mathcal{D}_1 &= \mathcal{D} + J, \\ \mathcal{D}_2 &= -\frac{\mathcal{D}}{2} + J. \end{aligned} \tag{4}$$

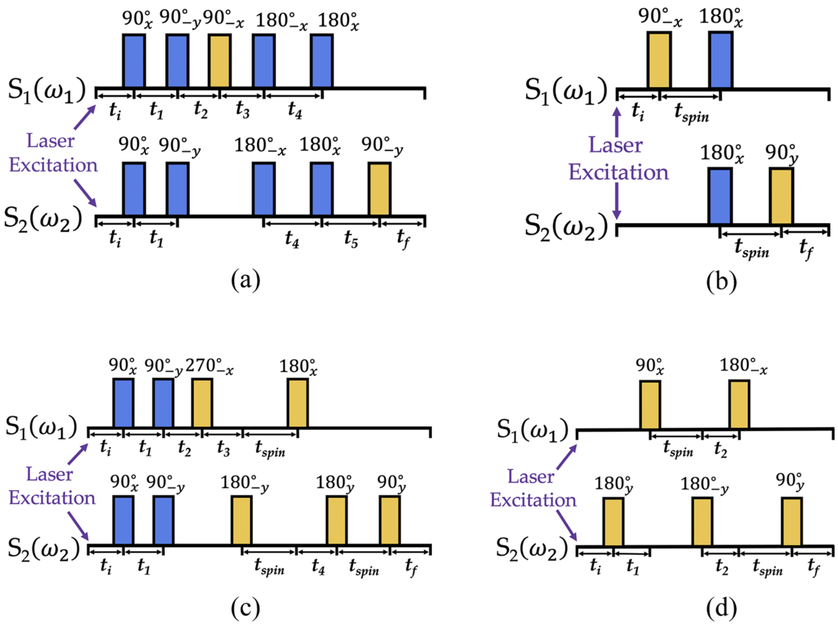

FIG. 2. Depiction of pulse EPR experiments for implementation of the CNOT gate. (a) and (b) show pulse sequences for $\hat{H}_2$ in Eq. (11), and (b) and (d) show pulse sequences for $\hat{H}_3$ in Eq. (12). (a) The pulse sequence in Eq. (32) with added correction in Eq. (36), (b) is the sequence in Eq. (59), (c) is the sequence in Eq. (32) with correction in Eq. (38), and (d) is the sequence in Eq. (58). (a) and (c) show universal quantum logic gates, and (b) and (d) show quantum logic gates when the initial state is $|S\rangle$. Each line corresponds to an electron with a Zeeman coupling strength of ω_i, frequency at which selective pulses are centered around. t_i is initial time needed after laser excitation for the formation of the radical pair, t_f is the final time needed between the end of the CNOT gate and read out, t_{spin} are spin evolution times, and the remaining times are intervals between pulses. The blue pulses are non-selective rotations for S_1 and S_2 electrons, and yellow pulses are selective rotations.

Here, $\mathbf{B}$ is the applied magnetic field, $\hat{\mathbf{S}}_i$ and $\hat{\mathbf{I}}_{ik}$ are electron and nuclear spin operators, respectively, N_i is the number of nuclear spins coupled to radical i, θ is the angle between the applied magnetic field and the dipolar axis, J is the electron exchange interaction constant, D is the strength of the dipolar interaction, μ_B is Bohr magneton, and g_i is the g tensor. With the additional simplification, ω_i is the Zeeman frequency of radical i under the applied magnetic field of strength $|\mathbf{B}|$.

Eigenvectors and eigenvalues for $\hat{H}_{12}$ are[33,34]

$$\begin{gathered}|1\rangle = |T_+\rangle,\ |2\rangle = \cos\xi|S\rangle + \sin\xi|T_0\rangle,\\ |3\rangle = -\sin\xi|S\rangle + \cos\xi|T_0\rangle,\ |4\rangle = |T_-\rangle,\end{gathered} \tag{5}$$

$$\begin{gathered}\lambda_1 = \frac{\Omega}{2} + \frac{\mathcal{D}_1}{4},\ \lambda_2 = -\frac{1}{2}\Theta - \frac{\mathcal{D}_1}{4},\\ \lambda_3 = \frac{1}{2}\Theta - \frac{\mathcal{D}_1}{4},\ \lambda_4 = -\frac{\Omega}{2} + \frac{\mathcal{D}_1}{4},\end{gathered} \tag{6}$$

where

$$\tan(2\xi) = \frac{-\Delta\omega}{\frac{2}{3}\mathcal{D}_1 + \frac{1}{3}\mathcal{D}_2}, \tag{7}$$

$$\Delta\omega = \omega_2 - \omega_1,\ \ \Omega = \omega_1 + \omega_2, \Theta = \sqrt{\Delta\omega^2 + \mathcal{D}_2^2}. \tag{8}$$

The electron spin–electron spin Hamiltonian, $\hat{H}_{12}$, can be further reduced at very high magnetic fields if the difference between Zeeman energies is much larger than spin interactions, i.e., $|\omega_2 - \omega_1| \gg \mathcal{D}_1$,

$$\hat{H}_{12} = \omega_1\hat{S}_{1z} + \omega_2\hat{S}_{2z} + \mathcal{D}_1\hat{S}_{1z}\hat{S}_{2z}. \tag{9}$$

In this study, only the $\hat{H}_{12}$ term of the full $\hat{H}$ will be used for the design of the pulse sequences, and the influence of $\hat{H}_{hyp}$ on dynamics will be discussed separately. Furthermore, the following three main cases of high field $\hat{H}$ will be discussed during the design of pulse sequences:

1. $\hat{H}$ with only $\hat{S}_{1z}\hat{S}_{2z}$ interaction:
$$\hat{H}_1 = \mathcal{D}_1\hat{S}_{1z}\hat{S}_{2z}. \tag{10}$$
2. High field $\hat{H}$ with $|\omega_2 - \omega_1| \gg \mathcal{D}_1$:
$$\hat{H}_2 = \omega_1\hat{S}_{1z} + \omega_2\hat{S}_{2z} + \mathcal{D}_1\hat{S}_{1z}\hat{S}_{2z}. \tag{11}$$
3. High field $\hat{H}$:
$$\hat{H}_3 = \omega_1\hat{S}_{1z} + \omega_2\hat{S}_{2z} + \mathcal{D}_1\hat{S}_{1z}\hat{S}_{2z} + \mathcal{D}_2\big(\hat{S}_{1x}\hat{S}_{2x} + \hat{S}_{1y}\hat{S}_{2y}\big). \tag{12}$$

B. Idempotent operators

A neat and simple tool to derive an analytical form of any two spin pulse sequence, first introduced by Price *et al.*,[35] involves the use of primitive idempotent operators, $E_\pm$, that satisfy the following properties:

$$E_+ + E_- = 1,\ \ E_\pm^2 = E_\pm,\ \ E_+E_- = 0. \tag{13}$$

Important idempotent operators for electron spins are

$$E_{\pm}^{i} = \frac{1}{2}\mathbb{I} \pm \hat{S}_{iz}, \quad E_{\pm}^{i,j} = \frac{1}{2}\mathbb{I} \pm 2\hat{S}_{iz}\hat{S}_{jz}. \tag{14}$$

Thus, an arbitrary density matrix

$$\hat{U} = \begin{pmatrix} u_{11} & u_{12} & u_{13} & u_{14} \\ u_{21} & u_{22} & u_{23} & u_{24} \\ u_{31} & u_{32} & u_{33} & u_{34} \\ u_{41} & u_{42} & u_{43} & u_{44} \end{pmatrix} \tag{15}$$

can be decomposed using idempotent operators,[27]

$$\begin{aligned} \hat{U} = {} & u_{11}E_{+}^{1}E_{+}^{2} + 2u_{12}\hat{S}_{2x}E_{+}^{1}E_{-}^{2} + 2u_{13}\hat{S}_{1x}E_{-}^{1}E_{+}^{2} + 4u_{14}\hat{S}_{1x}\hat{S}_{2x}E_{-}^{1}E_{-}^{2} \\ & + 2u_{21}\hat{S}_{2x}E_{+}^{1}E_{+}^{2} + u_{22}E_{+}^{1}E_{-}^{2} + 4u_{23}\hat{S}_{1x}\hat{S}_{2x}E_{-}^{1}E_{+}^{2} + 2u_{24}\hat{S}_{1x}E_{-}^{1}E_{-}^{2} \\ & + 2u_{31}\hat{S}_{1x}E_{+}^{1}E_{+}^{2} + 4u_{32}\hat{S}_{1x}\hat{S}_{2x}E_{+}^{1}E_{-}^{2} + u_{33}E_{-}^{1}E_{+}^{2} + 2u_{34}\hat{S}_{2x}E_{-}^{1}E_{-}^{2} \\ & + 4u_{41}\hat{S}_{1x}\hat{S}_{2x}E_{+}^{1}E_{+}^{2} + 2u_{42}\hat{S}_{1x}E_{+}^{1}E_{-}^{2} + 2u_{43}\hat{S}_{2x}E_{-}^{1}E_{+}^{2} + u_{44}E_{-}^{1}E_{-}^{2}. \end{aligned} \tag{16}$$

This provides a straightforward way to find a decomposition for any two-spin quantum gate. An important property for idempotent operators used throughout this work is

$$e^{AE_{\pm}} = e^{A}E_{\pm} + E_{\mp}, \quad \text{given that } [A, E_{\pm}] = 0 \tag{17}$$

Finally, an important property for the exponential of an arbitrary Pauli spin matrix $\hat{S}_k$ is

$$e^{i\theta\hat{S}_k} = \cos\left(\frac{\theta}{2}\right)\mathbb{I} + i2\hat{S}_k \sin\left(\frac{\theta}{2}\right). \tag{18}$$

C. Fidelity

The general measure of closeness between two quantum states is called the fidelity, and it can be computed with knowledge of their density matrices $\hat{\rho}$ and $\hat{\sigma}$ using the following equation:[36]

$$\mathcal{F}(\hat{\rho}, \hat{\sigma}) = \left(\mathrm{Tr}\sqrt{\hat{\rho}^{1/2}\hat{\sigma}\hat{\rho}^{1/2}}\right)^{2}. \tag{19}$$

Here, $\hat{\rho}$ is taken to be the ideal density matrix state, and $\hat{\sigma}$ is the experimentally measured density matrix, for instance, determined by quantum state tomography.[2]

In the case of an initial pure state $\hat{\rho}(0) = |\Psi\rangle\langle\Psi|$ and $\hat{\rho} = \hat{U}_{ideal}\hat{\rho}(0)\hat{U}_{ideal}^{\dagger}$, where $\hat{U}_{ideal}$ is trace preserving, the fidelity measure simplifies to

$$\mathcal{F} = \langle\Psi|\hat{U}_{ideal}^{\dagger}\hat{\sigma}\hat{U}_{ideal}|\Psi\rangle. \tag{20}$$

Given that $\hat{\rho}^{2} = \hat{\rho}$. Here, $\hat{U}_{ideal}$ is the ideal case propagation matrix. If we can easily decompose $\hat{\sigma} = \hat{U}_{spin}|\Psi\rangle\langle\Psi|\hat{U}_{spin}^{\dagger}$, then the fidelity measure will be

$$\mathcal{F} = \left|\langle\Psi|\hat{U}_{ideal}^{\dagger}\hat{U}_{spin}|\Psi\rangle\right|^{2}, \tag{21}$$

where $\hat{U}_{spin}$ is resultant propagator under arbitrary spin evolution and rotation pulses.

For instance, if the system has two electron spins that are initialized in a singlet state and the ideal gate is a CNOT gate, then the fidelity will be

$$\mathcal{F} = \left|\langle S|\hat{U}_{CNOT}^{\dagger}\hat{U}_{spin}|S\rangle\right|^{2}. \tag{22}$$

III. PULSE SEQUENCES FOR TWO QUBIT GATES

The general algorithm for deriving a pulse sequence is as follows: First, expand the target propagator using idempotent operators. Second, derive a pulse sequence for a Hamiltonian that only includes the electron spin–electron spin interaction. Third, apply correction terms to the pulse sequence to account for other Hamiltonian terms.[27,35]

In this section, the procedure for generating a pulse sequence will be demonstrated by finding the CNOT gate pulse sequence for a SCRP system. Considering that the pulse sequence is derived for a Hamiltonian without Zeeman and hyperfine interactions, a correction term will be proposed, which will also alleviate the influence of hyperfine interactions on the fidelity measure. In addition to the CNOT gate, the pulse sequence for other generally used two qubit gates will be introduced. Finally, a simplification for a CNOT gate for a SCRP starting in a singlet state will be demonstrated that will significantly reduce the number of pulses needed to execute the gate.

A. Pulse sequence for a CNOT gate

The CNOT gate is one of the fundamental two qubit quantum logic gates that when combined with several single qubit gates forms a complete set of quantum logic gates from which any arbitrary unitary transformation can be derived.[26] The propagator matrix takes the form

$$\hat{U}_{CNOT} = \begin{pmatrix} 1 & 0 & 0 & 0 \\ 0 & 1 & 0 & 0 \\ 0 & 0 & 0 & 1 \\ 0 & 0 & 1 & 0 \end{pmatrix}. \tag{23}$$

Its main action is the inversion of $|\beta\alpha\rangle$ and $|\beta\beta\rangle$ populations in a two-qubit system that manifests from the state of the first (called the control) qubit. If the first qubit is in $|\beta\rangle$ state, then the state of the second (called the target) qubit is flipped. The unitary matrix formed with the expansion in Eq. (16) for this gate is

$$\hat{U}_{CNOT} = E_{+}^{1} + 2\hat{S}_{2x}E_{-}^{1}. \tag{24}$$

Given that a pulse sequence is essentially a set of multiplied exponential matrices, it becomes possible to find a binomial multiplication for the expansion that will transform it into an experimentally feasible pulse sequence,

$$
\begin{aligned}
\hat{U}_{CNOT} &= E_+^1 + 2\hat{S}_{2x}E_-^1\\
&= E_+^1 + i(-i)2\hat{S}_{2x}E_-^1\\
&= \left(-i2\hat{S}_{2x}E_-^1 + E_+^1\right)\left(iE_-^1 + E_+^1\right).
\end{aligned}
\tag{25}
$$

By applying Eq. (17) and noting that $e^{i\pi/2} = i$ and $e^{-i\pi\hat{S}_{2x}} = -2i\hat{S}_{2x}$ according to Eq. (18), we find

$$
\hat{U}_{CNOT} = e^{-i\pi\hat{S}_{2x}E_-^1}e^{i\frac{\pi}{2}E_-^1}.
\tag{26}
$$

Using the definitions in Eq. (14), this is expanded as

$$
\hat{U}_{CNOT} = e^{i\frac{\pi}{4}}e^{-i\frac{\pi}{2}\hat{S}_{2x}}e^{-i\frac{\pi}{2}\hat{S}_{1z}}e^{i\pi\hat{S}_{1z}\hat{S}_{2x}}.
\tag{27}
$$

Due to the nature of the experimental setup and the spin Hamiltonian, the $\hat{S}_{1z}$ and $\hat{S}_{1z}\hat{S}_{2z}$ terms cannot be directly generated in the experiment. These exponential terms have to be decomposed into a form more suited for experimental implementation. There are a large number of ways to decompose these terms; in addition, the terms in Eq. (27) commute with each other, resulting in many different pulse sequences that can achieve the same unitary transformation. One possible solution, with a particularly clean structure, is as follows:

$$
e^{-i\frac{\pi}{2}\hat{S}_{1z}} = e^{i\frac{\pi}{2}\hat{S}_{1x}}e^{i\frac{\pi}{2}\hat{S}_{1y}}e^{-i\frac{\pi}{2}\hat{S}_{1x}},
\tag{28}
$$

$$
e^{i\pi\hat{S}_{1z}\hat{S}_{2x}} = e^{-i\frac{\pi}{2}\hat{S}_{2y}}e^{i\pi\hat{S}_{1z}\hat{S}_{2z}}e^{i\frac{\pi}{2}\hat{S}_{2y}}.
\tag{29}
$$

Substituting Eqs. (28) and (29) into Eq. (27) yields

$$
\hat{U}_{CNOT} = e^{i\frac{\pi}{4}}e^{-i\frac{\pi}{2}\hat{S}_{2y}}e^{i\pi\hat{S}_{1z}\hat{S}_{2z}}e^{i\frac{\pi}{2}\hat{S}_{1x}}e^{i\frac{\pi}{2}\left(\hat{S}_{1y}+\hat{S}_{2y}\right)}e^{-i\frac{\pi}{2}\left(\hat{S}_{1x}+\hat{S}_{2x}\right)}.
\tag{30}
$$

For the reduced high field Hamiltonian in Eq. (10), the rotation term, $\hat{S}_{1z}\hat{S}_{2z}$, can be treated as a time propagation under the spin Hamiltonian,

$$
\begin{aligned}
e^{-i\hat{H}_1\tau} &= e^{i\pi\hat{S}_{1z}\hat{S}_{2z}},\\
-i\hat{H}_1\tau &= i\pi\hat{S}_{1z}\hat{S}_{2z},\\
-i\mathcal{D}_1\tau\hat{S}_{1z}\hat{S}_{2z} &= i\pi\hat{S}_{1z}\hat{S}_{2z},\\
\tau &= -\frac{\pi}{\mathcal{D}_1} = \frac{\pi}{|\mathcal{D}_1|}.
\end{aligned}
\tag{31}
$$

Note that $\mathcal{D}_1 < 0$. The pulse sequence for the CNOT gate (read from left to right, this notation will be used throughout this paper) is

$$
90^\circ_{1x+2x},\quad 90^\circ_{-(1y+2y)},\quad 90^\circ_{-1x},\quad \frac{\pi}{|\mathcal{D}_1|},\quad 90^\circ_{2y}.
\tag{32}
$$

Here, the degrees show the magnitude of spin selective or non-selective rotations, and the subscripted index identifies each electron spin and its phase. The non-degree term represents the propagation time required for the system.

1. The sign of $\mathcal{D}_1$

The reported sequences in Ref. 27 have this form for the spin evolution time,

$$
\tau = \frac{\pi}{\mathcal{D}_1}.
\tag{33}
$$

Since, as defined in Eq. (2), $\mathcal{D}_1$ is a negative quantity for radical pairs, the reported SWAP and CNOT gate sequences for electron spins are not appropriate since $\pi/\mathcal{D}_1 \neq \pi/|\mathcal{D}_1|$. If $\tau = \pi/\mathcal{D}_1$, the actual CNOT pulse sequence suggested by Ref. 27, which was recently employed in Ref. 2, takes the form (with adjusted phase)

$$
\hat{U}_{CNOT} = \begin{pmatrix} 0 & -1 & 0 & 0\\ -1 & 0 & 0 & 0\\ 0 & 0 & 1 & 0\\ 0 & 0 & 0 & 1 \end{pmatrix}.
\tag{34}
$$

Care must be taken when using pulse sequences to be sure the right sequence is used for the appropriate case.

B. Corrections for Zeeman interactions

The derived pulse sequence in Eq. (32), namely, the $\hat{S}_{1z}\hat{S}_{2z}$ evolution, breaks down when including the electron Zeeman terms, such as in Eqs. (11) and (12). The general way to correct this is to split the spin evolution term into two equal parts and apply an additional pulse sequence, which will selectively rotate only the $\hat{S}_{iz}$ terms and cancel the other Zeeman terms.[27] Under the influence of Eq. (11), this method yields

$$
\begin{aligned}
e^{i\pi\hat{S}_{1z}\hat{S}_{2z}} &= e^{-i\hat{H}_2\frac{\tau}{2}}e^{-i\pi\left(\hat{S}_{1x}+\hat{S}_{2x}\right)}e^{-i\hat{H}_2\frac{\tau}{2}}e^{i\pi\left(\hat{S}_{1x}+\hat{S}_{2x}\right)}\\
&= e^{-i\left(\omega_1\hat{S}_{1z}+\omega_2\hat{S}_{2z}+\mathcal{D}_1\hat{S}_{1z}\hat{S}_{2z}\right)\frac{\tau}{2}}e^{-i\pi\left(\hat{S}_{1x}+\hat{S}_{2x}\right)}\\
&\quad\times e^{-i\left(\omega_1\hat{S}_{1z}+\omega_2\hat{S}_{2z}+\mathcal{D}_1\hat{S}_{1z}\hat{S}_{2z}\right)\frac{\tau}{2}}e^{i\pi\left(\hat{S}_{1x}+\hat{S}_{2x}\right)}\\
&= e^{-i\left(\omega_1\hat{S}_{1z}+\omega_2\hat{S}_{2z}+\mathcal{D}_1\hat{S}_{1z}\hat{S}_{2z}\right)\frac{\tau}{2}}\\
&\quad\times e^{-i\left(-\omega_1\hat{S}_{1z}-\omega_2\hat{S}_{2z}+\mathcal{D}_1\hat{S}_{1z}\hat{S}_{2z}\right)\frac{\tau}{2}}\\
&= e^{-i\mathcal{D}_1\hat{S}_{1z}\hat{S}_{2z}\tau}.
\end{aligned}
\tag{35}
$$

Hence, for each pulse sequence evolving under Eq. (11), the propagation time τ is replaced by

$$
\tau \;\rightarrow\; 180^\circ_{-(1x+2x)},\quad \frac{\tau}{2},\quad 180^\circ_{1x+2x},\quad \frac{\tau}{2}.
\tag{36}
$$

For the time evolution under Eq. (12), a correction sequence that divides the spin evolution time into four parts was suggested in Ref. 27. We note that the same result can be achieved with fewer dissections and pulse sequences,

$$
\begin{aligned}
e^{i\pi\hat{S}_{1z}\hat{S}_{2z}} &= e^{-i\hat{H}_3\frac{\tau}{2}}e^{-i\pi\hat{S}_{1x}}e^{-i\pi\hat{S}_{2y}}e^{-i\hat{H}_3\frac{\tau}{2}}e^{i\pi\hat{S}_{1x}}e^{i\pi\hat{S}_{2y}}\\
&= e^{-i\hat{H}_3\frac{\tau}{2}}e^{-i\left(-\omega_1\hat{S}_{1z}-\omega_2\hat{S}_{2z}+\mathcal{D}_1\hat{S}_{1z}\hat{S}_{2z}-\mathcal{D}_2\left(\hat{S}_{1x}\hat{S}_{2x}+\hat{S}_{1y}\hat{S}_{2y}\right)\right)\frac{\tau}{2}}\\
&= e^{-i\hat{D}_1\hat{S}_{1z}\hat{S}_{2z}\tau}.
\end{aligned}
\tag{37}
$$

The two exponential terms can be added because the expressions commute. For every pulse sequence that evolves under Eq. (12), the propagation time τ is replaced by

$$\tau \rightarrow 180^\circ_{-1x}, 180^\circ_{-2y}, \quad \frac{\tau}{2}, \quad 180^\circ_{1x}, \quad 180^\circ_{2y}, \quad \frac{\tau}{2}. \tag{38}$$

C. Hyperfine interaction effects

The hyperfine interaction, which arises from nuclear spins, is typically non-negligible in SCRP systems and is often of a similar order of magnitude to the D coupling. Nuclear spins significantly influence the experimental setting by altering the initial pulse response, affecting readout through modulation effects, and introducing additional sources of noise. Whenever possible, these effects should be mitigated through chemical synthesis or isotopic labeling, as well as by creating an environment that minimizes spin decoherence, such as employing specific solvents and maintaining low temperatures. Notably, the correction factors introduced earlier can also eliminate some contributions from hyperfine interaction terms, potentially enhancing the fidelity of the two qubit gate in situations where nuclear spin effects cannot be mitigated.

When we add static hyperfine coupling effects to the correction sequence in Eq. (36). We find

$$\begin{aligned} e^{i\pi\hat{S}_{1z}\hat{S}_{2z}} &= e^{-i\hat{H}_{hyp,2}\frac{\tau}{2}} e^{-i\pi\left(\hat{S}_{1x}+\hat{S}_{2x}\right)} e^{-i\hat{H}_{hyp,2}\frac{\tau}{2}} e^{i\pi\left(\hat{S}_{1x}+\hat{S}_{2x}\right)} \\ &= e^{-i\hat{H}_{hyp,2}\frac{\tau}{2}} e^{-i\hat{H}'_{hyp,2}\frac{\tau}{2}}, \end{aligned} \tag{39}$$

where

$$\hat{H}_{hyp,2} = \hat{H}_2 + \hat{H}_{hyp}, \tag{40}$$

$$\begin{aligned} \hat{H}_{hyp} = \hat{S}_{1z}\left(\sum_{k=1}^{N_1}\left(A_{1k}\hat{I}_{1k,z} + B_{1k}\hat{I}_{1k,x}\right)\right) \\ + \hat{S}_{2z}\left(\sum_{p=1}^{N_2}\left(A_{2p}\hat{I}_{2p,z} + B_{2p}\hat{I}_{2p,x}\right)\right), \end{aligned} \tag{41}$$

$$\hat{H}'_{hyp,2} = \hat{H}'_2 - \hat{H}_{hyp}, \tag{42}$$

$$\hat{H}'_2 = -\omega_1\hat{S}_{1z} - \omega_2\hat{S}_{2z} + \mathcal{D}_1\hat{S}_{1z}\hat{S}_{2z}. \tag{43}$$

Since $\left[\hat{H}_{hyp,2}, \hat{H}'_{hyp,2}\right] = 0$ (proof of which is shown in Appendix A),

$$\begin{aligned} e^{-i\hat{H}_{hyp,2}\frac{\tau}{2}} e^{-i\hat{H}'_{hyp,2}\frac{\tau}{2}} &= e^{-i\left(\hat{H}_{hyp,2}+\hat{H}'_{hyp,2}\right)\frac{\tau}{2}} \\ &= e^{-i\mathcal{D}_1\hat{S}_{1z}\hat{S}_{2z}\tau} = e^{i\pi\hat{S}_{1z}\hat{S}_{2z}}. \end{aligned} \tag{44}$$

This shows that the overall performance in terms of fidelity of a pulse sequence for $\hat{H}_2$ will be unaffected by the static hyperfine interactions of the system.

An equivalent result can be seen for the correction sequence in Eq. (38) since $\left[\hat{H}_{hyp,3}, \hat{H}'_{hyp,3}\right] = 0$ (proof in Appendix A), where

$$\hat{H}_{hyp,3} = \hat{H}_3 + \hat{H}_{hyp}, \tag{45}$$

$$\hat{H}'_{hyp,3} = \hat{H}'_3 - \hat{H}_{hyp}, \tag{46}$$

$$\hat{H}'_3 = -\omega_1\hat{S}_{1z} - \omega_2\hat{S}_{2z} + \mathcal{D}_1\hat{S}_{1z}\hat{S}_{2z} - \mathcal{D}_2\left(\hat{S}_{1x}\hat{S}_{2x} + \hat{S}_{1y}\hat{S}_{2y}\right). \tag{47}$$

TABLE I. Pulse sequences for CNOT, SWAP, Controlled-Z (CZ), and Controlled-Phase (CP) quantum logic gates for coupled electron spin systems. All of the pulse sequences were derived assuming $\hat{H}_1$ in Eq. (10), yet the pulse sequences can be extended with the proposed correction terms for other Hamiltonians. Pulse sequences are read from left to right.

Operation	Propagator	Pulse sequence
$\hat{U}_{CNOT}$	$\begin{pmatrix} 1 & 0 & 0 & 0 \\ 0 & 1 & 0 & 0 \\ 0 & 0 & 0 & 1 \\ 0 & 0 & 1 & 0 \end{pmatrix}$	$90^\circ{}_{1x+2x}, 90^\circ{}_{-(1x+2x)}, 90^\circ{}_{-1x}, \frac{\pi}{\lvert\mathcal{D}_1\rvert}, 90^\circ{}_{2y}$
$\hat{U}_{SWAP}$	$\begin{pmatrix} 1 & 0 & 0 & 0 \\ 0 & 0 & 1 & 0 \\ 0 & 1 & 0 & 0 \\ 0 & 0 & 0 & 1 \end{pmatrix}$	$90^\circ{}_{1x+2x}, \frac{\pi}{\lvert\mathcal{D}_1\rvert}, 90^\circ{}_{-(1x+2x)}, 90^\circ{}_{1y+2y}, \frac{\pi}{\lvert\mathcal{D}_1\rvert}\ 90^\circ{}_{-(1y+2y)}, \frac{\pi}{\lvert\mathcal{D}_1\rvert}$
$\hat{U}_{CZ}$	$\begin{pmatrix} 1 & 0 & 0 & 0 \\ 0 & 1 & 0 & 0 \\ 0 & 0 & 1 & 0 \\ 0 & 0 & 0 & -1 \end{pmatrix}$	$90^\circ{}_{-1x}, 90^\circ{}_{1y+2y}, 90^\circ{}_{1x+2x}, 90^\circ{}_{-2y}, \frac{\pi}{\lvert\mathcal{D}_1\rvert}$
$\hat{U}_{CP}(\phi)$	$\begin{pmatrix} 1 & 0 & 0 & 0 \\ 0 & 1 & 0 & 0 \\ 0 & 0 & 1 & 0 \\ 0 & 0 & 0 & e^{i\phi} \end{pmatrix}$	$90^\circ{}_{2x}, \left(\frac{\phi}{2}\right)^\circ{}_{-2y}, 90^\circ{}_{-2x}, 90^\circ{}_{-1y}, \left(\frac{\phi}{2}\right)^\circ{}_{-1x}, 90^\circ{}_{1y}, \frac{\phi}{\lvert\mathcal{D}_1\rvert}$

The result presented above assumes that nuclear Zeeman effects are negligible in the dynamics due to their small magnitude compared to the electron spin Zeeman effect. If these effects are included in the dynamics, the time-propagation sequence becomes

$$e^{-i\pi\hat{S}_{1z}\hat{S}_{2z}} = e^{-i\mathcal{D}_1\hat{S}_{1z}\hat{S}_{2z}\tau} e^{-i\sum_{k=1}^{N_1}\omega_{1k}\hat{I}_{1k,z}\tau} e^{-i\sum_{p=1}^{N_2}\omega_{2p}\hat{I}_{2p,z}\tau}, \tag{48}$$

where ω_{ij} is gyromagnetic ratio of nuclei j coupled to electron spin i.

Although this effect will undoubtedly influence the spin dynamics for high magnetic fields, if the nuclear spin space—which is commonly assumed to be in a fully mixed state—and the electron spin space are not coupled for the initial nuclear spin space, then the nuclear Zeeman effect will not affect the fidelity measure because it does not evolve the electron spin states. However, it is likely to affect the experimental readout, which is not addressed in this article.

D. Proposed pulse sequences

The most common two qubit quantum logical gates are the CNOT, SWAP, CZ, and CP gates.[36] Their propagators and pulses sequences are depicted in Table I. The pulse sequences were derived with evolution under Eq. (10) but can easily be expanded to account for Eqs. (11) and (12) as we have already demonstrated. All derivations are shown in Appendix B.

E. Simplification of the CNOT gate pulse sequence for an initial singlet state

The propagator for a CNOT gate according to Eq. (10) is

$$\hat{U}_{CNOT} = e^{i\frac{\pi}{4}} e^{-i\frac{\pi}{2}\hat{S}_{2y}} e^{-i\hat{H}_1\tau} e^{i\frac{\pi}{2}\hat{S}_{1x}} e^{i\frac{\pi}{2}\left(\hat{S}_{1y}+\hat{S}_{2y}\right)} e^{-i\frac{\pi}{2}\left(\hat{S}_{1x}+\hat{S}_{2x}\right)}. \tag{49}$$

Here, $\tau = \pi/\mathcal{D}_1$. If the starting state is a pure singlet state, which is true in most cases for radical pair systems, and owing to the fact that applying $\hat{U}_{CNOT}$ to an initial density matrix $\hat{\rho}(0)$ results in $\hat{\rho} = \hat{U}_{CNOT}\rho(0)\hat{U}^{\dagger}_{CNOT}$, we note that the two non-selective pulses will cancel,

$$e^{i\frac{\pi}{2}\left(\hat{S}_{1y}+\hat{S}_{2y}\right)} e^{-i\frac{\pi}{2}\left(\hat{S}_{1x}+\hat{S}_{2x}\right)} \hat{\rho}(0) e^{i\frac{\pi}{2}\left(\hat{S}_{1x}+\hat{S}_{2x}\right)} e^{-i\frac{\pi}{2}\left(\hat{S}_{1y}+\hat{S}_{2y}\right)} = \hat{\rho}(0), \tag{50}$$

reducing the propagator for pure singlet initial state to

$$\hat{U}_{CNOT} = e^{i\frac{\pi}{4}} e^{-i\frac{\pi}{2}\hat{S}_{2y}} e^{-i\hat{H}_1\tau} e^{i\frac{\pi}{2}\hat{S}_{1x}} \tag{51}$$

or to this pulse sequence

$$90^{\circ}_{-1x},\ \tau,\ 90^{\circ}_{2y}. \tag{52}$$

If the spin evolution is done according to Eq. (11) and correction in Eq. (36) is employed, the propagator is

$$\begin{aligned}\hat{U}_{CNOT} &= e^{i\frac{\pi}{4}} e^{-i\frac{\pi}{2}\hat{S}_{2y}} e^{-i\hat{H}_2\frac{\tau}{2}} e^{-i\pi\left(\hat{S}_{1x}+\hat{S}_{2x}\right)} e^{-i\hat{H}_2\frac{\tau}{2}} \\ &\quad\times e^{i\pi\left(\hat{S}_{1x}+\hat{S}_{2x}\right)} e^{i\frac{\pi}{2}\hat{S}_{1x}} \\ &= e^{i\frac{\pi}{4}} e^{-i\frac{\pi}{2}\hat{S}_{2y}} e^{-i\hat{H}_2\frac{\tau}{2}} e^{-i\pi\left(\hat{S}_{1x}+\hat{S}_{2x}\right)} \\ &\quad\times e^{-i\hat{H}_2\frac{\tau}{2}} e^{i\frac{\pi}{2}\hat{S}_{1x}} e^{i\pi\left(\hat{S}_{1x}+\hat{S}_{2x}\right)}.\end{aligned} \tag{53}$$

We can do another simplification since

$$e^{i\pi\left(\hat{S}_{1x}+\hat{S}_{2x}\right)} \hat{\rho}(0) e^{-i\pi\left(\hat{S}_{1x}+\hat{S}_{2x}\right)} = \hat{\rho}(0), \tag{54}$$

reducing the operator

$$\hat{U}_{CNOT} = e^{i\frac{\pi}{4}} e^{-i\frac{\pi}{2}\hat{S}_{2y}} e^{-i\hat{H}_2\frac{\tau}{2}} e^{-i\pi\left(\hat{S}_{1x}+\hat{S}_{2x}\right)} e^{-i\hat{H}_2\frac{\tau}{2}} e^{i\frac{\pi}{2}\hat{S}_{1x}}, \tag{55}$$

yielding a simple three pulse sequence

$$90^{\circ}_{-1x},\ \tau_1,\ 180^{\circ}_{1x+2x},\ \tau_2,\ 90^{\circ}_{2y}. \tag{56}$$

Here, τ_1 and τ_2 are arbitrary spin evolution times and should be multiples of $\pi/(2\mathcal{D}_1)$.

Finally, evolution according to Eq. (12) provides the corrected sequence in Eq. (38),

$$\begin{aligned}\hat{U}_{CNOT} &= e^{i\frac{\pi}{4}} e^{-i\frac{\pi}{2}\hat{S}_{2y}} e^{-i\hat{H}_3\frac{\tau}{2}} e^{-i\pi\hat{S}_{1x}} e^{-i\pi\hat{S}_{2y}} e^{-i\hat{H}_3\frac{\tau}{2}} e^{i\pi\hat{S}_{1x}} e^{i\pi\hat{S}_{2y}} e^{i\frac{\pi}{2}\hat{S}_{1x}} \\ &= e^{i\frac{\pi}{4}} e^{-i\frac{\pi}{2}\hat{S}_{2y}} e^{-i\hat{H}_3\frac{\tau}{2}} e^{i\pi\hat{S}_{1x}} e^{i\pi\hat{S}_{2y}} e^{-i\hat{H}_3\frac{\tau}{2}} e^{-i\pi\hat{S}_{1x}} e^{-i\pi\hat{S}_{2y}} e^{i\frac{\pi}{2}\hat{S}_{1x}} \\ &= e^{i\frac{\pi}{4}} e^{-i\frac{\pi}{2}\hat{S}_{2y}} e^{-i\hat{H}_3\frac{\tau}{2}} e^{i\pi\hat{S}_{1x}} e^{i\pi\hat{S}_{2y}} e^{-i\hat{H}_3\frac{\tau}{2}} e^{-i\frac{\pi}{2}\hat{S}_{1x}} e^{-i\pi\hat{S}_{2y}},\end{aligned} \tag{57}$$

yielding the following five pulse sequence

$$180^{\circ}_{2y},\ 90^{\circ}_{1x},\ \tau_1,\ 180^{\circ}_{-2y},\ 180^{\circ}_{-1x}, \tau_2,\ 90^{\circ}_{2y}. \tag{58}$$

IV. ANALYTICAL DERIVATIONS OF FIDELITY VALUES

Considering ideal pulses, we have derived in this section a number of functions that detail how the fidelity value would vary with time propagation and T_2 relaxation time. They provide a useful way to quantify the dynamics involved in application of a CNOT gate and what results when the pulses in an experiment are non-ideal. Two cases were investigated: pulse sequences in Eq. (56) with $\hat{H}_2$ for spin evolution and 58 with $\hat{H}_3$ for spin evolution. Finally, an upper bound will be given to the fidelity value for these systems that predicts the theoretical maximum possible for a gate, given a T_2 relaxation time. Derivations are shown in Appendix C (without T_2) and Appendix D (with T_2 and the upper bound).

A. Fidelity for CNOT gate pulse sequences

First, fidelity $\mathcal{F}_{3P}$ for the three pulse sequence with arbitrary spin evolution times τ_1, τ_2 is

$$\begin{aligned}\mathcal{F}_{3P} = \frac{1}{4}\bigg(&\cos^2\left(\frac{\Delta\omega}{2}(\tau_1-\tau_2)\right) + \cos^2\left(\frac{\Omega}{2}(\tau_1-\tau_2)\right) \\ &- 2\sin\left(\frac{\mathcal{D}_1}{2}(\tau_1+\tau_2)\right)\cos\left(\frac{\Delta\omega}{2}(\tau_1-\tau_2)\right) \\ &\times\cos\left(\frac{\Omega}{2}(\tau_1-\tau_2)\right)\bigg).\end{aligned} \tag{59}$$

When $\tau_1 = \tau_2$, $\mathcal{F}_{3P}$ simplifies to

$$\mathcal{F}_{3P} = \frac{1}{2}\left(1-\sin\left(\frac{\mathcal{D}_1}{2}\tau\right)\right). \tag{60}$$

As predicted by the derivations, $\mathcal{F}_{3P} = 1$ when $\tau = \pi/\mathcal{D}_1$. Additionally, this equation would predict the dynamics for the case when $\hat{H}_1$ would be used for time propagation.

Fidelity $\mathcal{F}_{5P}$ for the five pulse sequence is

$$\begin{aligned}\mathcal{F}_{5P} = \frac{1}{8}\Bigg(&1 + \sin^2\left(\frac{\Theta}{2}(\tau_1 - \tau_2)\right)\cos(4\xi) + 2\cos^2\left(\frac{\Omega}{2}(\tau_1 - \tau_2)\right)\\ &+ \cos^2\left(\frac{\Theta}{2}(\tau_1 - \tau_2)\right) + 4\cos\left(\frac{\Omega}{2}(\tau_1 - \tau_2)\right)\\ &\times\left(\cos\left(\frac{\mathcal{D}_1}{2}(\tau_1 + \tau_2)\right)\cos(2\xi)\sin\left(\frac{\Theta}{2}(\tau_1 - \tau_2)\right)\right.\\ &\left.- \sin\left(\frac{\mathcal{D}_1}{2}(\tau_1 + \tau_2)\right)\cos\left(\frac{\Theta}{2}(\tau_1 - \tau_2)\right)\right)\Bigg). \qquad (61)\end{aligned}$$

$\mathcal{F}_{5P}$ has a very similar form to $\mathcal{F}_{3P}$ and also reduces to Eq. (60) when $\tau_1 = \tau_2$. As predicted by the derivation, when $\tau_1 = \tau_2 = \pi/(2\mathcal{D}_1)$, $\mathcal{F}_{5P} = 1$.

The fidelity equations with T_2 are almost identical to Eqs. (59) and (61), the only difference being that some terms are multiplied by $e^{-\tau/T_2}$. They can be seen in Appendix D.

To recapitulate, these equations predict the fidelity value for a system with any number of nuclear spins whose influence on the dynamics will be canceled out due to the applied pulse sequence.

B. Upper bound to fidelity

It is shown in Appendix D that both $\mathcal{F}_{3P}$ and $\mathcal{F}_{5P}$ will be bounded by

$$\frac{1}{2} + \frac{1}{2}e^{-\frac{\tau}{T2}} \geq \mathcal{F}(\mathcal{D}_1, \mathcal{D}_2, \tau_1, \tau_2, \Delta\omega, \Omega, T_2). \qquad (62)$$

Here, τ is the total gate time, i.e., $\tau = \tau_1 + \tau_2$.

This provides a clear understanding of what would be the best values for certain experiments. For instance, maximum $\mathcal{F}$ values for varying T_2 for the model system are shown in Table II. For the model system, $\pi/|\mathcal{D}_1| = 142.9$ ns. Table II illustrates that for high T_2, $\mathcal{F}$ values around 0.9 or even higher can be achieved.

Two parameters ultimately determine the fidelity of the CNOT gate application, and both larger values of $\mathcal{D}_1$ and longer T_2 relaxation times produce higher fidelity values. Consequently, future engineering of these systems should be aimed at maximizing both of these parameters because theoretically such systems could access fidelity values >0.9.

TABLE II. Maximum $\mathcal{F}$ values (in the middle) for various T_2 and τ for a model SCRP system, for which $\pi/|\mathcal{D}_1| = 142.9$ ns.

	$T_2 = 1\ \mu s$	$T_2 = 2\ \mu s$	$T_2 = 4\ \mu s$	$T_2 = 8\ \mu s$
$\tau = \frac{\pi}{2\lvert\mathcal{D}_1\rvert}$	0.9310	0.9649	0.9823	0.9911
$\tau = \frac{\pi}{\lvert\mathcal{D}_1\rvert}$	0.8668	0.9310	0.9649	0.9823
$\tau = \frac{2\pi}{\lvert\mathcal{D}_1\rvert}$	0.7514	0.8668	0.9310	0.9649
$\tau = \frac{4\pi}{\lvert\mathcal{D}_1\rvert}$	0.5646	0.7514	0.8668	0.9310

V. SIMULATIONS OF THE EXPERIMENTS

A. Model system

We will introduce a model SCRP system **TTF–ANI–PI**, which consists of a tetrathiafulvalene (**TTF**) electron donor, a 4-amino-1,8-naphthalimide (**ANI**) chromophoric acceptor, and a pyromellitimide (**PI**) secondary acceptor that will be the basis for a computational analysis and has the necessary parameters for calculations already reported in the literature.[2,37–40] The structure of **TTF-ANI-PI** molecule can be seen in Fig. 3.

Following laser excitation of **TTF–ANI–PI**, a rapid two-step electron transfer produces a SCRP in an initial $|S\rangle$ state. The radical cation is localized on the **TTF,** while the radical anion is on the **PI**. The lifetime of the SCRP is sufficiently long (charge recombination lifetime $\tau_{CR} = 35.6\ \mu s^2$), as well as spin–spin relaxation lifetime ($T_2 = 1.8\ \mu s^2$, but for simplicity, $T_2 = 2\ \mu s$ will be used throughout this work), to be able to perform quantum gate operations. The g-tensor ($[g_{xx}g_{yy}g_{zz}]$) for TTF$^{\bullet+}$ is $[2.0159\ 2.0076\ 2.0031]^2$ and for PI$^{\bullet-}$ is $[2.0069\ 2.0069\ 2.0021]^2$. The g value in calculations will be the x-component of the full tensor since the molecule is in a single orientation that aligns the dipolar axis, magnetic field vector, and the x-axis of the g-tensor. This molecular design was chosen in order to exploit the g-value difference to perform qubit selective rotations. Moreover, the literature spin–spin coupling values are $\mathcal{D}_1 = -3.50$ MHz, and J is taken to be much smaller than $\mathcal{D}_1$.[40] The dipolar interaction axis lies approximately parallel to the applied magnetic field direction, i.e., $\theta = 0$. Finally, the radical around PI moiety will be defined as the target qubit, whereas TTF will be the control qubit. This choice is arbitrary and can be tailored to each experiment.

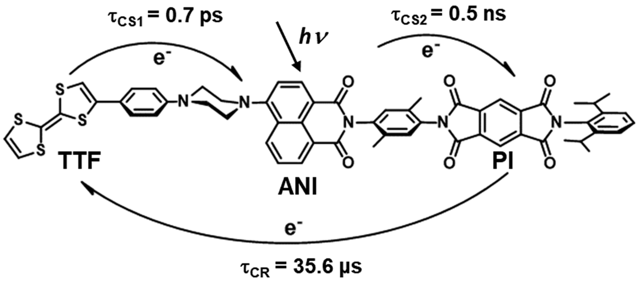

FIG. 3. Molecular structure of **TTF–ANI–PI** with outlined forward electron transfers (1), after initial photoexcitation, and backward electron transfer (2), during charge recombination. Adapted from Ref. 2.

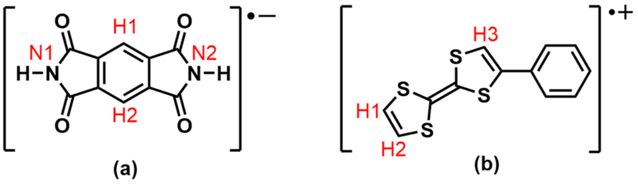

FIG. 4. Structures of (a) PI$^{\bullet-}$ and (b) TTF$^{\bullet+}$ that were used to calculate the isotropic hyperfine coupling constants given in Table III. Atom labels highlight magnetically important nuclei that have non-zero spin.

TABLE III. Isotropic hyperfine interaction parameters in MHz for $TTF^{\bullet+}$ and $PI^{\bullet-}$ radicals, which structures and atom labels are shown in Fig. 4.

Molecule	Nuclei	a_{iso}/MHz
$TTF^{\bullet+}$	H1	−3.32
	H2	−3.19
	H3	−5.26
$PI^{\bullet-}$	H1	1.46
	H2	1.46
	N1	−2.59
	N2	−2.59

There are a number of magnetically active nuclei in this system that will give rise to hyperfine couplings to the electron spins. Thus, it is important to quantify their effect on the dynamics. Isotropic hyperfine couplings for $TTF^{\bullet+}$ and $PI^{\bullet-}$ radicals (structure and atom labels are shown in Fig. 4) calculated by Density Functional Theory (DFT) are shown in Table III. The B3LYP functional,[41,42] def2-TZVP basis set,[43,44] and D3BJ dispersion correction[45–47] were used for geometry optimization, while the BP86 functional,[48] EPR-III basis set for $PI^{\bullet-}$,[49] and cc-PV5Z basis set[50,51] for $TTF^{\bullet+}$ were used to calculate the hyperfine parameters. These calculations were done with ORCA.[52,53] These values are not expected to be accurate compared to the experimentally determined values (especially for $TTF^{\bullet+}$ that contains sulfur for which hyperfine optimized EPR-III cannot be used and we had to use hyperfine-unoptimized cc-PV5Z)[25] and only provide qualitative comparison to the spin–spin coupling. We will compare spin–spin coupling with the effective hyperfine field for radical *i*,[54]

$$B_{hyp,i} = \sqrt{\sum_{k=1}^{N_i} a_{ik}^2 I_{ik}(I_{ik}+1)}. \qquad (63)$$

Here, a_{ik} are isotropic hyperfine constants for nuclei k coupled to electron i.

For $TTF^{\bullet+}$, $B_{hyp,1} = 6.0539$ MHz, and for $PI^{\bullet-}$, $B_{hyp,2} = 5.4799$ MHz. Since the magnitude of the effective hyperfine fields is in the order of magnitude of $\mathcal{D}_1$, it is vital to understand the influence of hyperfine interactions on the spin dynamics of applying quantum logic gates.

B. Simulations

Using the parameters obtained for **TTF–ANI–PI**, the fidelity following application of a CNOT gate under varying magnetic field conditions was simulated. Typically, EPR experiments are performed at X-band (9.5 GHz) or higher. We will first simulate the three pulse sequence at 9.5 GHz, which is high enough to invoke the weak coupling approximation and for the use of Eq. (36) for spin evolution. The simulation of Eq. (59) without T_2 relaxation at 9.5 GHz is shown in Fig. 5(a). The value of τ_1 is held constant at $\tau_1 = \pi/(2\mathcal{D}_1) = 71.43$ ns (optimal value according to theory), and τ_2 is varied from 0 to $\pi/|\mathcal{D}_1|$. There is a very fast oscillation in the fidelity, for which the principal driving factor is the sum of the electron Zeeman splitting, Ω, introducing a period of $T = 0.0523$ ns. The period of all of the important motions at this microwave frequency is summarized in Table IV. In a real experiment, pulses will not be ideal, and spectral inhomogeneities will make it impossible to replicate $\tau_1 = \tau_2 = \pi/(2\mathcal{D}_1)$, where the maximum is theorized to occur. One solution is working at a lower magnetic field strength. For instance, if the field is lowered by 20 times from the X-band value, then the resonance frequency is about 0.475 GHz and the period for Ω would be $T = 1.05$ ns, which is a more realistic timing

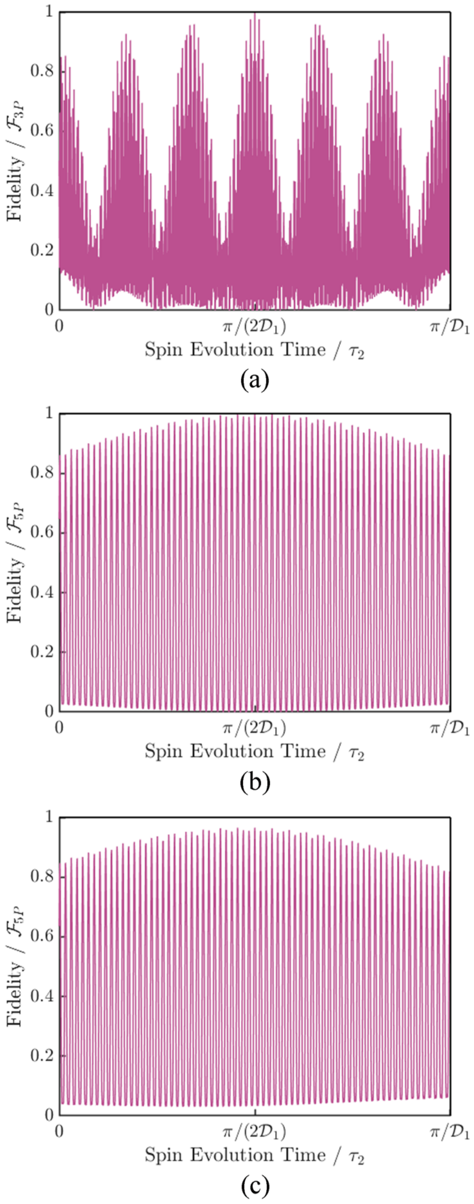

FIG. 5. Graphs of fidelity vs spin evolution time for model system introduced in Sec. V A. (a) uses Eq. (59) for fidelity and $\hat{H}_2$ in Eq. (11) for spin evolution. (b) and (c) uses Eq. (59) for fidelity and $\hat{H}_3$ in Eq. (12) for spin evolution. Case (c) has T_2 relaxation included. The resonance frequency is 9.5 GHz for (a) and 0.475 GHz for (b) and (c). In all cases, $\tau_1 = \pi/(2|\mathcal{D}_1|) = 71.43$ ns and τ_2 is varied from 0 to $\pi/|\mathcal{D}_1| = 142.9$ ns.

TABLE IV. Frequencies and periods of oscillatory motions in $\mathcal{F}_{3P}$ functions in Eq. (59) at a 9.5 GHz resonance frequency.

Term	Frequency	Period (ns)
$\lvert\Omega\rvert$	19.11 GHz	0.0523
$\left\lvert\frac{\Omega}{2}\right\rvert$	9.56 GHz	0.105
$\lvert\Delta\omega\rvert$	42.7 MHz	23.4
$\left\lvert\frac{\Delta\omega}{2}\right\rvert$	21.4 MHz	46.7
$\left\lvert\frac{\mathcal{D}_1}{2}\right\rvert$	1.75 MHz	571.4

parameter for digital electronics. The graph of $\mathcal{F}_{5P}$ for this magnetic field strength, with $\hat{H}_3$ for spin evolution, is shown in Fig. 5(b).

In addition, it can be seen that the fidelity values are relatively high for this case before $\tau_2 = \pi/\mathcal{D}_2$, and since T_2 will decrease $\mathcal{F}_{5P}$ values with total time τ, we note that it is possible to achieve a maximum earlier when decoherence effects are taken into account. Figure 5(c) shows the same graph as Fig. 5(b) but with T_2 relaxation included and the maximum for this graph occurs at $\tau_2 = 65.14$ ns, and it is $\mathcal{F}_{3P} = 0.9658$, which brings down the total time to $\tau = 136.57$ ns. This result exemplifies the fact that a better understanding of the spin dynamics results in ways to reduce the total gate times.

Even though the majority of issues of implementing quantum logic gates for these systems are alleviated at lower magnetic field values, engineering pulses for these magnetic field values propose another challenge. The spectral separation of the EPR lines of the two radicals will be reduced at lower magnetic fields so that their linewidths will be larger than their separation, prohibiting the selective rotations that are necessary for the quantum logic gate operations. Hence, designing new SCRPs in which hyperfine interactions are minimized or eliminated and that can also be ordered in crystalline environments may provide the required linewidth reductions. In addition, alternative experimental protocols, such as those done with the Gradient Ascent Pulse Engineering (GRAPE) approach,[55–57] may prove beneficial. Nonetheless, our results indicate that a lower magnetic field may be a prerequisite for controlling the spin states in these systems for QIS applications or that there is a need for methods to alleviate the fast oscillations from the dynamics.

VI. CONCLUSIONS

In this article, we introduced a variety of advances in pulse protocols for executing two qubit quantum logic gates on SCRP systems and provided the theoretical framework for understanding the dynamics of applying them to experiments. Specifically, we introduced pulse sequences for CNOT, SWAP, CZ, and CP gates that have the correct signs for the spin propagation term. In addition, we have introduced corrections for the Hamiltonians in Eqs. (11) and (12) in terms of extra pulse sequences, illustrating how these corrections cancel out static hyperfine interactions from the dynamics and how with a simplification for a singlet initial state, we can execute the CNOT gate in either three or five pulses. This is an improvement from the previous state of the art and will enable new experiments to be executed that will utilize these quantum logic gates. Finally, a theoretical treatment was given for fidelity values for varying spin evolution times, and a set of analytical equations were derived for both three and five pulse experiments. These equations highlight the upper bound for fidelity values that is imposed by T_2 relaxation and what are the important factors in the dynamics that control the fidelity value. As a main conclusion, we have shown that high fidelity values are possible for these systems, yet the resonance frequency has to be lower than the 9.5 GHz value typical of X-band to ensure that the fast oscillations have a long enough period for control.

There are many possible future directions of research that this study did not address, e.g., simulations with realistic pulses, executing selective rotations at lower magnetic fields, theoretical treatments of echo detection, proposals of new ways to do quantum state tomography for this system, using GRAPE for executing quantum logic gates, understanding how radical recombination affects the performance of the gate action, dynamic decoupling or other schemes to make the gate execution easier, and so on. In addition, experimentally testing these pulse sequences for different systems, magnetic field values and different pulse shapes will shed light on future research directions. Finally, we are currently planning to use these new pulse sequences in experimental studies on several newly designed SCRP systems suitable for QIS applications.

ACKNOWLEDGMENTS

G.J.P. is grateful to the European Research Council (under the European Union's Horizon 2020 research and innovation program, Grant Agreement No. 810002, Synergy Grant: "QuantumBirds"). This research was supported by the U.S. National Science Foundation under Award No. CHE-2154627 (M.R.W.).

AUTHOR DECLARATIONS

Conflict of Interest

The authors have no conflicts to disclose.

Author Contributions

Gediminas J. Pazera: Conceptualization (equal); Data curation (equal); Formal analysis (equal); Investigation (equal); Methodology (equal); Visualization (equal); Writing – original draft (equal). **Matthew D. Krzyaniak**: Conceptualization (equal); Formal analysis (equal); Methodology (equal); Validation (equal); Visualization (equal); Writing – review & editing (equal). **Michael R. Wasielewski**: Conceptualization (equal); Data curation (equal); Formal analysis (equal); Funding acquisition (equal); Investigation (equal); Methodology (equal); Resources (equal); Supervision (equal); Validation (equal); Visualization (equal); Writing – review & editing (equal).

DATA AVAILABILITY

The data that support the findings of this study are available within the article.

APPENDIX A: COMMUTATION OF HAMILTONIANS WITH HYPERFINE INTERACTION TERMS

First, we will derive $\left[\hat{H}_{hyp,2}, \hat{H}'_{hyp,2}\right]$, where

$$\hat{H}_{hyp,2} = \hat{H}_2 + \hat{H}_{hyp}, \tag{A1}$$

$$\hat{H}'_{hyp,2} = \hat{H}'_2 - \hat{H}_{hyp}. \tag{A2}$$

Hence, by using properties of commutators, we find that

$$\begin{aligned}\left[\hat{H}_{hyp,2}, \hat{H}'_{hyp,2}\right] &= \left[\hat{H}_2 + \hat{H}_{hyp}, \hat{H}'_2 - \hat{H}_{hyp}\right]\\ &= \left[\hat{H}_2, \hat{H}'_2\right] - \left[\hat{H}_2, \hat{H}_{hyp}\right] + \left[\hat{H}_{hyp}, \hat{H}'_2\right] - \left[\hat{H}_{hyp}, \hat{H}_{hyp}\right]\\ &= \left[\hat{H}_{hyp}, \hat{H}_2\right] + \left[\hat{H}_{hyp}, \hat{H}'_2\right].\end{aligned} \tag{A3}$$

By plugging in definitions of $\hat{H}_2$, $\hat{H}'_2$, and $\hat{H}_{hyp}$,

$$\begin{aligned}\left[\hat{H}_{hyp,2}, \hat{H}'_{hyp,2}\right] &= \left[\hat{H}_{hyp}, \omega_1\hat{S}_{1z} + \omega_2\hat{S}_{2z} + \mathcal{D}_1\hat{S}_{1z}\hat{S}_{2z}\right] + \left[\hat{H}_{hyp}, -\omega_1\hat{S}_{1z} - \omega_2\hat{S}_{2z} + \mathcal{D}_1\hat{S}_{1z}\hat{S}_{2z}\right]\\ &= \left[\hat{H}_{hyp}, \omega_1\hat{S}_{1z}\right] + \left[\hat{H}_{hyp}, \omega_2\hat{S}_{2z}\right] + \left[\hat{H}_{hyp}, \mathcal{D}_1\hat{S}_{1z}\hat{S}_{2z}\right] - \left[\hat{H}_{hyp}, \omega_1\hat{S}_{1z}\right] - \left[\hat{H}_{hyp}, \omega_2\hat{S}_{2z}\right] + \left[\hat{H}_{hyp}, \mathcal{D}_1\hat{S}_{1z}\hat{S}_{2z}\right]\\ &= 2\left[\hat{H}_{hyp}, \mathcal{D}_1\hat{S}_{1z}\hat{S}_{2z}\right]\\ &= 2\left[\hat{S}_{1z}\left(\sum_{k=1}^{N_1}\left(A_{1k}\hat{I}_{1k,z} + B_{1k}\hat{I}_{1k,x}\right)\right) + \hat{S}_{2z}\left(\sum_{p=1}^{N_2}\left(A_{2p}\hat{I}_{2p,z} + B_{2p}\hat{I}_{2p,x}\right)\right), \mathcal{D}_1\hat{S}_{1z}\hat{S}_{2z}\right]\\ &= 0.\end{aligned} \tag{A4}$$

The final result is zero because nuclear spin operators commute freely with electron spin operators; hence, the final line is identical to the $\left[\hat{S}_{1z} + \hat{S}_{2z}, \mathcal{D}_1\hat{S}_{1z}\hat{S}_{2z}\right]$ result, i.e., 0.

Evaluating $\left[\hat{H}_{hyp,3}, \hat{H}'_{hyp,3}\right]$ has equivalent initial steps, and we find that

$$\begin{aligned}\left[\hat{H}_{hyp,3}, \hat{H}'_{hyp,3}\right] &= \left[\hat{H}_{hyp}, \omega_1\hat{S}_{1z} + \omega_2\hat{S}_{2z} + \mathcal{D}_1\hat{S}_{1z}\hat{S}_{2z} + \mathcal{D}_2\left(\hat{S}_{1x}\hat{S}_{2x} + \hat{S}_{1y}\hat{S}_{2y}\right)\right] + \left[\hat{H}_{hyp}, -\omega_1\hat{S}_{1z} - \omega_2\hat{S}_{2z} + \mathcal{D}_1\hat{S}_{1z}\hat{S}_{2z} - \mathcal{D}_2\left(\hat{S}_{1x}\hat{S}_{2x} + \hat{S}_{1y}\hat{S}_{2y}\right)\right]\\ &= \left[\hat{H}_{hyp}, \omega_1\hat{S}_{1z}\right] + \left[\hat{H}_{hyp}, \omega_2\hat{S}_{2z}\right] + \left[\hat{H}_{hyp}, \mathcal{D}_1\hat{S}_{1z}\hat{S}_{2z}\right] + \left[\hat{H}_{hyp}, \mathcal{D}_2\left(\hat{S}_{1x}\hat{S}_{2x} + \hat{S}_{1y}\hat{S}_{2y}\right)\right]\\ &\quad - \left[\hat{H}_{hyp}, \omega_1\hat{S}_{1z}\right] - \left[\hat{H}_{hyp}, \omega_2\hat{S}_{2z}\right] + \left[\hat{H}_{hyp}, \mathcal{D}_1\hat{S}_{1z}\hat{S}_{2z}\right] - \left[\hat{H}_{hyp}, \mathcal{D}_2\left(\hat{S}_{1x}\hat{S}_{2x} + \hat{S}_{1y}\hat{S}_{2y}\right)\right]\\ &= 2\left[\hat{H}_{hyp}, \mathcal{D}_1\hat{S}_{1z}\hat{S}_{2z}\right] = 0.\end{aligned} \tag{A5}$$

APPENDIX B: DERIVATIONS OF PULSE SEQUENCES

1. SWAP gate

The expression for the SWAP gate found by the expansion in Eq. (16),

$$\hat{U}_{SWAP} = E_+^{1,2} + 4\hat{S}_{1x}\hat{S}_{2x}E_-^{1,2}. \tag{B1}$$

This can further be decomposed to

$$\begin{aligned}\hat{U}_{SWAP} &= E_+^{1,2} + 4\hat{S}_{1x}\hat{S}_{2x}E_-^{1,2}\\ &= \left(iE_-^{1,2} + E_+^{1,2}\right)\left(-4i\hat{S}_{1x}\hat{S}_{2x}E_-^{1,2} + E_+^{1,2}\right)\\ &= e^{i\frac{\pi}{2}E_-^{1,2}}e^{-i2\pi\hat{S}_{1x}\hat{S}_{2x}E_-^{1,2}}.\end{aligned} \tag{B2}$$

We note that

$$\begin{aligned}\hat{S}_{1x}\hat{S}_{2x}E_-^{1,2} &= \hat{S}_{1x}\hat{S}_{2x}\left(\frac{1}{2}\mathbb{I} - 2\hat{S}_{1z}\hat{S}_{2z}\right)\\ &= \frac{1}{2}\hat{S}_{1x}\hat{S}_{2x} - 2\hat{S}_{1x}\hat{S}_{2x}\hat{S}_{1z}\hat{S}_{2z}\\ &= \frac{1}{2}\hat{S}_{1x}\hat{S}_{2x} + \frac{1}{2}\hat{S}_{1y}\hat{S}_{2y}.\end{aligned} \tag{B3}$$

Hence, the unitary for the SWAP gate is

$$\hat{U}_{SWAP} = e^{i\frac{\pi}{4}}e^{-i\pi\hat{S}_{1z}\hat{S}_{2z}}e^{-i\pi\hat{S}_{1x}\hat{S}_{2x}}e^{-i\pi\hat{S}_{1y}\hat{S}_{2y}}. \tag{B4}$$

We do not have the right sign for the $\hat{S}_{1z}\hat{S}_{2z}$ operator; hence, we can take a Hermitian conjugate to get the right sign,

$$\hat{U}^{\dagger}_{SWAP} = \hat{U}_{SWAP} = e^{-i\frac{\pi}{4}}e^{i\pi\hat{S}_{1y}\hat{S}_{2y}}e^{i\pi\hat{S}_{1x}\hat{S}_{2x}}e^{i\pi\hat{S}_{1z}\hat{S}_{2z}}. \tag{B5}$$

We can decompose the x and y terms as

$$e^{i\pi\hat{S}_{1x}\hat{S}_{2x}} = e^{i\frac{\pi}{2}\left(\hat{S}_{1y}+\hat{S}_{2y}\right)}e^{i\pi\hat{S}_{1z}\hat{S}_{2z}}e^{-i\frac{\pi}{2}\left(\hat{S}_{1y}+\hat{S}_{2y}\right)}, \tag{B6}$$

$$e^{i\pi\hat{S}_{1y}\hat{S}_{2y}} = e^{i\frac{\pi}{2}\left(\hat{S}_{1x}+\hat{S}_{2x}\right)}e^{i\pi\hat{S}_{1z}\hat{S}_{2z}}e^{-i\frac{\pi}{2}\left(\hat{S}_{1x}+\hat{S}_{2x}\right)}. \tag{B7}$$

Hence, the final unitary is

$$\begin{aligned}\hat{U}_{SWAP} &= e^{-i\frac{\pi}{4}}e^{i\pi\hat{S}_{1z}\hat{S}_{2z}}e^{i\frac{\pi}{2}\left(\hat{S}_{1y}+\hat{S}_{2y}\right)}e^{i\pi\hat{S}_{1z}\hat{S}_{2z}}e^{-i\frac{\pi}{2}\left(\hat{S}_{1y}+\hat{S}_{2y}\right)}\\ &\quad\times e^{i\frac{\pi}{2}\left(\hat{S}_{1x}+\hat{S}_{2x}\right)}e^{i\pi\hat{S}_{1z}\hat{S}_{2z}}e^{-i\frac{\pi}{2}\left(\hat{S}_{1x}+\hat{S}_{2x}\right)}.\end{aligned} \tag{B8}$$

The pulse sequence is

$$90^{\circ}_{1x+2x},\ \frac{\pi}{|\mathcal{D}_1|},\ 90^{\circ}_{-(1x+2x)},\ 90^{\circ}_{1y+2y},\ \frac{\pi}{|\mathcal{D}_1|},\ 90^{\circ}_{-(1y+2y)},\ \frac{\pi}{|\mathcal{D}_1|}. \tag{B9}$$

2. CZ gate

The expression for the CZ gate is found by the expansion in Eq. (16),

$$\hat{U}_{CZ} = 2\hat{S}_{2z}E^1_- + E^1_+. \tag{B10}$$

Note that

$$2\hat{S}_{2z} = e^{i\pi\left(\frac{1}{2}\mathbb{I}-\hat{S}_{2z}\right)} = e^{-i\pi E^2_-}. \tag{B11}$$

Hence,

$$\hat{U}_{CZ} = e^{-i\pi E^2_-}E^1_- + E^1_+ = e^{-i\pi E^2_- E^1_-} = e^{-i\pi E^1_- E^2_-}. \tag{B12}$$

$E^1_- E^2_-$ is equal to

$$\begin{aligned} E^1_- E^2_- &= \left(\frac{1}{2}\mathbb{I} - \hat{S}_{1z}\right)\left(\frac{1}{2}\mathbb{I} - \hat{S}_{2z}\right) \\ &= \frac{1}{4}\mathbb{I} - \frac{1}{2}\hat{S}_{1z} - \frac{1}{2}\hat{S}_{2z} + \hat{S}_{1z}\hat{S}_{2z}. \end{aligned} \tag{B13}$$

Plugging it into the exponent,

$$\hat{U}_{CZ} = e^{-i\frac{\pi}{4}} e^{i\frac{\pi}{2}\hat{S}_{1z}} e^{i\frac{\pi}{2}\hat{S}_{2z}} e^{-i\pi\hat{S}_{1z}\hat{S}_{2z}}. \tag{B14}$$

The minus sign on the $\hat{S}_{1z}\hat{S}_{2z}$ is a problem; hence, we will take the Hermitian conjugate of this operator (which will leave it unchanged),

$$\hat{U}^{\dagger}_{CZ} = \hat{U}_{CZ} = e^{i\frac{\pi}{4}} e^{i\pi\hat{S}_{1z}\hat{S}_{2z}} e^{-i\frac{\pi}{2}\hat{S}_{2z}} e^{-i\frac{\pi}{2}\hat{S}_{1z}}. \tag{B15}$$

There are different ways to expand the $\hat{S}_{1z}$ and $\hat{S}_{2z}$, yet one of the ways is

$$e^{-i\frac{\pi}{2}\hat{S}_{1z}} = e^{-i\frac{\pi}{2}\hat{S}_{1x}} e^{-i\frac{\pi}{2}\hat{S}_{1y}} e^{i\frac{\pi}{2}\hat{S}_{1x}}, \tag{B16}$$

$$e^{-i\frac{\pi}{2}\hat{S}_{2z}} = e^{i\frac{\pi}{2}\hat{S}_{2y}} e^{-i\frac{\pi}{2}\hat{S}_{2x}} e^{-i\frac{\pi}{2}\hat{S}_{2y}}. \tag{B17}$$

The final unitary for the CZ gate is

$$\begin{aligned} \hat{U}_{CZ} &= e^{i\frac{\pi}{4}} e^{i\pi\hat{S}_{1z}\hat{S}_{2z}} e^{-i\frac{\pi}{2}\hat{S}_{2z}} e^{-i\frac{\pi}{2}\hat{S}_{1z}} \\ &= e^{i\frac{\pi}{4}} e^{i\pi\hat{S}_{1z}\hat{S}_{2z}} e^{i\frac{\pi}{2}\hat{S}_{2y}} e^{-i\frac{\pi}{2}\hat{S}_{2x}} e^{-i\frac{\pi}{2}\hat{S}_{2y}} e^{-i\frac{\pi}{2}\hat{S}_{1x}} e^{-i\frac{\pi}{2}\hat{S}_{1y}} e^{i\frac{\pi}{2}\hat{S}_{1x}} \\ &= e^{i\frac{\pi}{4}} e^{i\pi\hat{S}_{1z}\hat{S}_{2z}} e^{i\frac{\pi}{2}\hat{S}_{2y}} e^{-i\frac{\pi}{2}\left(\hat{S}_{1x}+\hat{S}_{2x}\right)} e^{-i\frac{\pi}{2}\left(\hat{S}_{1y}+\hat{S}_{2y}\right)} e^{i\frac{\pi}{2}\hat{S}_{1x}}. \end{aligned} \tag{B18}$$

This reproduces the correct gate action, and the pulse sequence is

$$90^{\circ}_{-1x},\ 90^{\circ}_{1y+2y},\ 90^{\circ}_{1x+2x},\ 90^{\circ}_{-2y},\ \frac{\pi}{|\mathcal{D}_1|}. \tag{B19}$$

3. CP gate

A general CP gate for the controlling phase of the $|\beta\beta\rangle$ state is

$$\hat{U}_{CP}(\phi) = \begin{pmatrix} 1 & 0 & 0 & 0 \\ 0 & 1 & 0 & 0 \\ 0 & 0 & 1 & 0 \\ 0 & 0 & 0 & e^{i\phi} \end{pmatrix}. \tag{B20}$$

A decomposition of the propagation matrix into rotation matrices is[58]

$$\begin{aligned} \hat{U}_{CP}(\phi) &= e^{i\frac{\phi}{4}\mathbb{I}} e^{-i\frac{\phi}{2}\hat{S}_{1z}} e^{-i\frac{\phi}{2}\hat{S}_{2z}} e^{i\phi\hat{S}_{1z}\hat{S}_{2z}} \\ &= e^{i\frac{\phi}{4}} e^{i\phi\hat{S}_{1z}\hat{S}_{2z}} e^{-i\frac{\phi}{2}\hat{S}_{1z}} e^{-i\frac{\phi}{2}\hat{S}_{2z}}. \end{aligned} \tag{B21}$$

The $\hat{S}_{1z}$ and $\hat{S}_{2z}$ exponents can be written as

$$e^{-i\frac{\phi}{2}\hat{S}_{1z}} = e^{-i\frac{\pi}{2}\hat{S}_{1y}} e^{i\frac{\phi}{2}\hat{S}_{1x}} e^{i\frac{\pi}{2}\hat{S}_{1y}}, \tag{B22}$$

$$e^{-i\frac{\phi}{2}\hat{S}_{2z}} = e^{i\frac{\pi}{2}\hat{S}_{2x}} e^{i\frac{\phi}{2}\hat{S}_{2y}} e^{-i\frac{\pi}{2}\hat{S}_{2x}}. \tag{B23}$$

The final CP gate is

$$\begin{aligned} \hat{U}_{CP}(\phi) &= e^{i\phi\hat{S}_{1z}\hat{S}_{2z}} e^{-i\frac{\phi}{2}\hat{S}_{1z}} e^{-i\frac{\phi}{2}\hat{S}_{2z}} \\ &= e^{i\phi\hat{S}_{1z}\hat{S}_{2z}} e^{-i\frac{\pi}{2}\hat{S}_{1y}} e^{i\frac{\phi}{2}\hat{S}_{1x}} e^{i\frac{\pi}{2}\hat{S}_{1y}} e^{i\frac{\pi}{2}\hat{S}_{2x}} e^{i\frac{\phi}{2}\hat{S}_{2y}} e^{-i\frac{\pi}{2}\hat{S}_{2x}}. \end{aligned} \tag{B24}$$

Hence, the general pulse sequence is

$$90^{\circ}_{2x},\ \left(\frac{\phi}{2}\right)^{\circ}_{-2y},\ 90^{\circ}_{-2x},\ 90^{\circ}_{-1y},\ \left(\frac{\phi}{2}\right)^{\circ}_{-1x},\ 90^{\circ}_{1y},\ \frac{\phi}{|\mathcal{D}_1|}. \tag{B25}$$

APPENDIX C: DERIVATIONS OF FIDELITY EQUATIONS

Two cases will be derived in this section—the fidelity equation for the three pulse sequence in Eq. (56) with $\hat{H}_2$ in Eq. (11) for spin evolution and the equation for the five pulse sequence in Eq. (58) with $\hat{H}_3$ for spin evolution. In each case, the fidelity definition in Eq. (22) will be used. Both pulse sequences have two spin evolution times; these will be set as arbitrary propagation times τ_1 and τ_2.

1. Three pulse sequence

$\hat{H}_2$ in the matrix form (in $|\alpha\alpha\rangle$, $|\alpha\beta\rangle$, $|\beta\alpha\rangle$, and $|\beta\beta\rangle$ basis) is

$$\hat{H}_2 = \begin{pmatrix} \langle\alpha\alpha|\hat{H}_2|\alpha\alpha\rangle & 0 & 0 & 0 \\ 0 & \langle\alpha\beta|\hat{H}_2|\alpha\beta\rangle & 0 & 0 \\ 0 & 0 & \langle\beta\alpha|\hat{H}_2|\beta\alpha\rangle & 0 \\ 0 & 0 & 0 & \langle\beta\beta|\hat{H}_2|\beta\beta\rangle \end{pmatrix}, \tag{C1}$$

where

$$\begin{aligned}\langle\alpha\alpha|\hat{H}_2|\alpha\alpha\rangle &= H_1 = \frac{1}{2}(\omega_1+\omega_2)+\frac{\mathcal{D}_1}{4} = \frac{\Omega}{2}+\frac{\mathcal{D}_1}{4},\\ \langle\alpha\beta|\hat{H}_2|\alpha\beta\rangle &= H_2 = \frac{1}{2}(\omega_1-\omega_2)-\frac{\mathcal{D}_1}{4} = -\frac{\Delta\omega}{2}-\frac{\mathcal{D}_1}{4},\\ \langle\beta\alpha|\hat{H}_2|\beta\alpha\rangle &= H_3 = \frac{1}{2}(\omega_2-\omega_1)-\frac{\mathcal{D}_1}{4} = \frac{\Delta\omega}{2}-\frac{\mathcal{D}_1}{4},\\ \langle\beta\beta|\hat{H}_2|\beta\beta\rangle &= H_4 = -\frac{1}{2}(\omega_1+\omega_2)+\frac{\mathcal{D}_1}{4} = -\frac{\Omega}{2}+\frac{\mathcal{D}_1}{4}.\end{aligned} \tag{C2}$$

The time-propagation operator in matrix form is

$$e^{-i\hat{H}_2\tau} = \begin{pmatrix} e^{-iH_1\tau} & 0 & 0 & 0\\ 0 & e^{-iH_2\tau} & 0 & 0\\ 0 & 0 & e^{-iH_3\tau} & 0\\ 0 & 0 & 0 & e^{-iH_4\tau}\end{pmatrix} = \begin{pmatrix} e^{-i\frac{\Omega}{2}\tau}e^{-i\frac{\mathcal{D}_1}{4}\tau} & 0 & 0 & 0\\ 0 & e^{i\frac{\Delta\omega}{2}\tau}e^{i\frac{\mathcal{D}_1}{4}\tau} & 0 & 0\\ 0 & 0 & e^{-i\frac{\Delta\omega}{2}\tau}e^{i\frac{\mathcal{D}_1}{4}\tau} & 0\\ 0 & 0 & 0 & e^{i\frac{\Omega}{2}\tau}e^{-i\frac{\mathcal{D}_1}{4}\tau}\end{pmatrix}. \tag{C3}$$

Hence, $\mathcal{F}_{3P}$ for the three pulse sequence is

$$\begin{aligned}\mathcal{F}_{3P} &= \left|\langle S|\hat{U}^{\dagger}_{spin}\hat{U}_{CNOT}|S\rangle\right|^2 = \left|\langle S|\left(e^{i\frac{\pi}{4}}e^{-i\frac{\pi}{2}\hat{S}_{2y}}e^{-\hat{H}\frac{\tau_1}{2}}e^{-i\pi(\hat{S}_{1x}+\hat{S}_{2x})}e^{-i\hat{H}\frac{\tau_2}{2}}e^{i\frac{\pi}{2}\hat{S}_{1x}}\right)^{\dagger}\hat{U}_{CNOT}|S\rangle\right|^2\\ &= \frac{1}{16}\left|e^{-i\frac{\Delta\omega}{2}(\tau_1-\tau_2)}e^{i\frac{\mathcal{D}_1}{4}(\tau_1+\tau_2)}+e^{i\frac{\Delta\omega}{2}(\tau_1-\tau_2)}e^{i\frac{\mathcal{D}_1}{4}(\tau_1+\tau_2)}-i\left(e^{i\frac{\Omega}{2}(\tau_1-\tau_2)}e^{-i\frac{\mathcal{D}_1}{4}(\tau_1+\tau_2)}+e^{-i\frac{\Omega}{2}(\tau_1-\tau_2)}e^{-i\frac{\mathcal{D}_1}{4}(\tau_1+\tau_2)}\right)\right|^2\\ &= \frac{1}{4}\left(\cos^2\left(\frac{\Delta\omega}{2}(\tau_1-\tau_2)\right)+\cos^2\left(\frac{\Omega}{2}(\tau_1-\tau_2)\right)-2\sin\left(\frac{\mathcal{D}_1}{2}(\tau_1+\tau_2)\right)\cos\left(\frac{\Delta\omega}{2}(\tau_1-\tau_2)\right)\cos\left(\frac{\Omega}{2}(\tau_1-\tau_2)\right)\right)\\ &= \frac{1}{4}\left(1+\frac{1}{2}\cos(\Delta\omega(\tau_1-\tau_2))+\frac{1}{2}\cos(\Omega(\tau_1-\tau_2))-2\sin\left(\frac{\mathcal{D}_1}{2}(\tau_1+\tau_2)\right)\cos\left(\frac{\Delta\omega}{2}(\tau_1-\tau_2)\right)\cos\left(\frac{\Omega}{2}(\tau_1-\tau_2)\right)\right).\end{aligned} \tag{C4}$$

This equation is maximum, i.e., $\mathcal{F} = 1$, when this set of simultaneous equations is solved,

$$\begin{cases}\cos\left(\frac{\Delta\omega}{2}(\tau_1-\tau_2)\right) = \pm 1,\\ \cos\left(\frac{\Omega}{2}(\tau_1-\tau_2)\right) = \pm 1,\\ \sin\left(\frac{\mathcal{D}_1}{2}(\tau_1+\tau_2)\right) = 1.\end{cases} \tag{C5}$$

The solutions are

$$\begin{cases}\tau_1-\tau_2 = \pm\frac{2\pi k_1}{\Delta\omega},\\ \tau_1-\tau_2 = \pm\frac{2\pi k_2}{\Omega},\\ \tau_1+\tau_2 = \frac{\pi}{\mathcal{D}_1}+\frac{2\pi k_3}{\mathcal{D}_1}.\end{cases} \tag{C6}$$

$k_1, k_2, k_3 \in \mathbb{Z}$. If $\tau_1+\tau_2 = \pi/\mathcal{D}_1$, then solutions for τ_1 and τ_2 are

$$\begin{aligned}\tau_1 &= \frac{\pi}{2\mathcal{D}_1}\pm\frac{\pi k_1}{\Delta\omega} = \frac{\pi}{2\mathcal{D}_1}\pm\frac{\pi k_2}{\Omega},\\ \tau_2 &= \frac{\pi}{2\mathcal{D}_1}\mp\frac{\pi k_1}{\Delta\omega} = \frac{\pi}{2\mathcal{D}_1}\mp\frac{\pi k_2}{\Omega}.\end{aligned} \tag{C7}$$

If $\tau_1 = \tau_2$ and $\tau_1+\tau_2 = \tau$, then

$$\mathcal{F} = \frac{1}{2}\left(1-\sin\left(\frac{\mathcal{D}_1}{2}\tau\right)\right). \tag{C8}$$

This is maximum when $\tau = \pi/\mathcal{D}_1 + 2\pi k/\mathcal{D}_1$ for $k \in \mathbb{Z}$, as expected from derivations.

2. Five pulse sequence

$\hat{H}_3$ can be decomposed into

$$\hat{H}_3 = \mathbf{RAR}^{-1}. \tag{C9}$$

Here,

$$\mathbf{A} = \begin{pmatrix} \lambda_1 & 0 & 0 & 0 \\ 0 & \lambda_2 & 0 & 0 \\ 0 & 0 & \lambda_3 & 0 \\ 0 & 0 & 0 & \lambda_4 \end{pmatrix}, \tag{C10}$$

$$\mathbf{R} = \begin{pmatrix} 1 & 0 & 0 & 0 \\ 0 & \frac{1}{\sqrt{2}}(\cos\xi + \sin\xi) & \frac{1}{\sqrt{2}}(\cos\xi - \sin\xi) & 0 \\ 0 & \frac{1}{\sqrt{2}}(\sin\xi - \cos\xi) & \frac{1}{\sqrt{2}}(\cos\xi + \sin\xi) & 0 \\ 0 & 0 & 0 & 1 \end{pmatrix}, \tag{C11}$$

$$\mathbf{R}^{-1} = \begin{pmatrix} 1 & 0 & 0 & 0 \\ 0 & \frac{1}{\sqrt{2}}(\cos\xi + \sin\xi) & \frac{1}{\sqrt{2}}(\sin\xi - \cos\xi) & 0 \\ 0 & \frac{1}{\sqrt{2}}(\cos\xi - \sin\xi) & \frac{1}{\sqrt{2}}(\cos\xi + \sin\xi) & 0 \\ 0 & 0 & 0 & 1 \end{pmatrix}. \tag{C12}$$

The matrix exponential of $\hat{H}_3$ can be expressed as

$$e^{-i\hat{H}_3\tau} = \mathbf{R}e^{-i\mathbf{A}\tau}\mathbf{R}^{-1} = \begin{pmatrix} H_{11} & 0 & 0 & 0 \\ 0 & H_{22} & H_{23} & 0 \\ 0 & H_{32} & H_{33} & 0 \\ 0 & 0 & 0 & H_{44} \end{pmatrix}, \tag{C13}$$

where

$$\begin{aligned} H_{11} &= e^{-i\frac{\Omega}{2}\tau}e^{-i\frac{\mathcal{D}_1}{4}\tau}, \quad H_{44} = e^{i\frac{\Omega}{2}\tau}e^{-i\frac{\mathcal{D}_1}{4}\tau}, \\ H_{22} &= \left(\cos\left(\frac{\Theta}{2}\tau\right) + i\sin(2\xi)\sin\left(\frac{\Theta}{2}\tau\right)\right)e^{i\frac{\mathcal{D}_1}{4}\tau}, \\ H_{33} &= \left(\cos\left(\frac{\Theta}{2}\tau\right) - i\sin(2\xi)\sin\left(\frac{\Theta}{2}\tau\right)\right)e^{i\frac{\mathcal{D}_1}{4}\tau}, \\ H_{23} &= H_{32} = -i\cos(2\xi)\sin\left(\frac{\Theta}{2}\tau\right)e^{i\frac{\mathcal{D}_1}{4}\tau}. \end{aligned} \tag{C14}$$

Finally, $\mathcal{F}_{5P}$ for the five pulse sequence is

$$\begin{aligned} \mathcal{F}_{5P} &= \left|\langle S|\hat{U}^{\dagger}_{spin}\hat{U}_{CNOT}|S\rangle\right|^2 \\ &= \frac{1}{4}|z|^2 \\ &= \frac{1}{4}\left(\mathrm{Re}(z)^2 + \mathrm{Im}(z)^2\right), \end{aligned} \tag{C15}$$

where

$$\begin{aligned} \mathrm{Re}(z) = &-\cos\left(\frac{\Omega}{2}(\tau_1 - \tau_2)\right)\sin\left(\frac{\mathcal{D}_1}{4}(\tau_1 + \tau_2)\right) \\ &+ \cos\left(\frac{\Theta}{2}(\tau_1 - \tau_2)\right)\cos\left(\frac{\mathcal{D}_1}{4}(\tau_1 + \tau_2)\right) \\ &+ \sin\left(\frac{\Theta}{2}(\tau_1 - \tau_2)\right)\cos(2\xi)\sin\left(\frac{\mathcal{D}_1}{4}(\tau_1 + \tau_2)\right), \end{aligned} \tag{C16}$$

$$\begin{aligned} \mathrm{Im}(z) = &-\cos\left(\frac{\Omega}{2}(\tau_1 - \tau_2)\right)\cos\left(\frac{\mathcal{D}_1}{4}(\tau_1 + \tau_2)\right) \\ &+ \cos\left(\frac{\Theta}{2}(\tau_1 - \tau_2)\right)\sin\left(\frac{\mathcal{D}_1}{4}(\tau_1 + \tau_2)\right) \\ &- \sin\left(\frac{\Theta}{2}(\tau_1 - \tau_2)\right)\cos(2\xi)\cos\left(\frac{\mathcal{D}_1}{4}(\tau_1 + \tau_2)\right). \end{aligned} \tag{C17}$$

The equation after expansion is

$$\begin{aligned} \mathcal{F}_{5P} = &\frac{1}{16}\Bigg(5 - \frac{1}{2}\cos(\Theta(\tau_1 - \tau_2) - 4\xi) - \frac{1}{2}\cos(\Theta(\tau_1 - \tau_2) + 4\xi) + \cos(4\xi) + 2\cos(\Omega(\tau_1 - \tau_2)) + \cos(\Theta(\tau_1 - \tau_2)) \\ &+ 8\cos\left(\frac{\Omega}{2}(\tau_1 - \tau_2)\right)\left(\cos\left(\frac{\mathcal{D}_1}{2}(\tau_1 + \tau_2)\right)\cos(2\xi)\sin\left(\frac{\Theta}{2}(\tau_1 - \tau_2)\right) - \sin\left(\frac{\mathcal{D}_1}{2}(\tau_1 + \tau_2)\right)\cos\left(\frac{\Theta}{2}(\tau_1 - \tau_2)\right)\right)\Bigg) \\ = &\frac{1}{8}\Bigg(1 + \sin^2\left(\frac{\Theta}{2}(\tau_1 - \tau_2)\right)\cos(4\xi) + 2\cos^2\left(\frac{\Omega}{2}(\tau_1 - \tau_2)\right) + \cos^2\left(\frac{\Theta}{2}(\tau_1 - \tau_2)\right) \\ &+ 4\cos\left(\frac{\Omega}{2}(\tau_1 - \tau_2)\right)\left(\cos\left(\frac{\mathcal{D}_1}{2}(\tau_1 + \tau_2)\right)\cos(2\xi)\sin\left(\frac{\Theta}{2}(\tau_1 - \tau_2)\right) - \sin\left(\frac{\mathcal{D}_1}{2}(\tau_1 + \tau_2)\right)\cos\left(\frac{\Theta}{2}(\tau_1 - \tau_2)\right)\right)\Bigg). \end{aligned} \tag{C18}$$

When $\mathcal{D}_2 = 0$, the fidelity reduces to the form in $\mathcal{F}_{3P}$. When $\tau_1 = \tau_2 = \tau/2$,

$$\mathcal{F}_{5P} = \frac{1}{2} - \frac{1}{2}\sin\left(\frac{\mathcal{D}_1}{2}\tau\right). \tag{C19}$$

In this form, $\mathcal{F}_{5P} = 1$ when $\tau = \pi/\mathcal{D}_1 + 2\pi k/\mathcal{D}_1$ for $k \in \mathbb{Z}$, as expected.

APPENDIX D: UPPER BOUND TO THE FIDELITY VALUE

To compute fidelity, we will use Eq. (20),

$$\mathcal{F} = \langle\Psi|\hat{\rho}(t)|\Psi\rangle, \tag{D1}$$

where $\hat{\rho}(t)$ is the density matrix after spin evolution that includes spin–spin relaxation effects, and

$$|\Psi\rangle = \hat{U}_{CNOT}|S\rangle. \tag{D2}$$

This equation will be used because, due to relaxation, Tr $\hat{\rho}(t) \neq 1$. The main difference between these derivations and ones without relaxation effects is that spin evolution has to be done in the Liouville space by

$$\hat{\hat{\rho}}(t+\delta t) = \exp\left[-\left(i\hat{\hat{H}} + \hat{\hat{K}}\right)\delta t\right]\hat{\hat{\rho}}(t), \tag{D3}$$

where $\hat{\hat{\rho}}(t)$ is a vectorized density matrix, $\hat{\hat{H}}$ is the Hamiltonian superoperator,

$$\hat{\hat{H}} = \hat{H} \otimes \mathbb{I}_d - \mathbb{I}_d \otimes \hat{H}^T, \tag{D4}$$

and $\hat{\hat{K}}$ is the relaxation superoperator for spin–spin (T_2) relaxation,[59]

$$\hat{\hat{K}} = \frac{1}{T_2}\,\mathrm{diag}\begin{pmatrix}0 & 1 & 1 & 0 & 1 & 0 & 0 & 1 & 1 & 0 & 0 & 1 & 0 & 1 & 1 & 0\end{pmatrix}. \tag{D5}$$

Here, T_2 is spin–spin relaxation lifetime and diag$(\cdot)$ is a diagonal matrix. We assume that T_2 relaxation lifetimes are equal for both sites, that there are no cross-relaxation events, and that spin-lattice relaxation lifetime T_1 is much longer than T_2 and is negligible in the dynamics.

Ideal pulses do not involve spin evolution (they are approximated as being instantaneous) and can be carried out in Hilbert space.

1. Three pulse sequence

$\mathcal{F}_{3P}$ for the pulse sequence in Eq. (56) with T_2 relaxation is

$$\begin{aligned}\mathcal{F}_{3P} &= \langle S|\hat{U}^{\dagger}_{CNOT}\sigma\hat{U}_{CNOT}|S\rangle \\ &= \frac{1}{4}\Bigg(1 + \frac{1}{2}\cos\left(\Omega(\tau_1-\tau_2)\right) + \frac{1}{2}\cos\left(\Delta\omega(\tau_1-\tau_2)\right) \\ &\quad + 2e^{-\frac{(\tau_1+\tau_2)}{T_2}}\sin\left(\frac{\mathcal{D}_1}{2}(\tau_1+\tau_2)\right)\cos\left(\frac{\Omega}{2}(\tau_1-\tau_2)\right) \\ &\quad \times\cos\left(\frac{\Delta\omega}{2}(\tau_1-\tau_2)\right)\Bigg).\end{aligned} \tag{D6}$$

When $T_2 \to \infty$, we get the right form without relaxation effects. Moreover, $\mathcal{F}_{3P}$ is largest when

$$\begin{cases}\cos\left(\Omega(\tau_1-\tau_2)\right) = 1,\\ \cos\left(\Delta\omega(\tau_1-\tau_2)\right) = 1,\\ \sin\left(\frac{\mathcal{D}_1}{2}(\tau_1+\tau_2)\right)\cos\left(\frac{\Omega}{2}(\tau_1-\tau_2)\right)\cos\left(\frac{\Delta\omega}{2}(\tau_1-\tau_2)\right) = 1.\end{cases} \tag{D7}$$

An upper bound to $\mathcal{F}_{3P}$ naturally emerges for total gate time τ (τ can also include the time it would normally take pulse sequences to act to get the ideal pulses sequence values, so it can be extended to total gate time in a real experiment),

$$\frac{1}{2} + \frac{1}{2}e^{-\frac{\tau_1+\tau_2}{T_2}} = \frac{1}{2} + \frac{1}{2}e^{-\frac{\tau}{T_2}} \geq \mathcal{F}_{3P}(\tau,\Omega,\Delta\omega,\mathcal{D}_1,T_2). \tag{D8}$$

Here, $\tau = \tau_1 + \tau_2$.

2. Five pulse sequence

$\mathcal{F}_{5P}$ for the pulse sequence in Eq. (58) with T_2 relaxation is

$$\begin{aligned}\mathcal{F}_{5P} = \langle S|\hat{U}^{\dagger}_{CNOT}\sigma\hat{U}_{CNOT}|S\rangle = \frac{1}{8}\Bigg(&1 + \sin^2\left(\frac{\Theta}{2}(\tau_1-\tau_2)\right)\cos(4\xi) + 2\cos^2\left(\frac{\Omega}{2}(\tau_1-\tau_2)\right) + \cos^2\left(\frac{\Theta}{2}(\tau_1-\tau_2)\right) \\ &+ 4e^{-\frac{\tau_1+\tau_2}{T_2}}\cos\left(\frac{\Omega}{2}(\tau_1-\tau_2)\right)\Bigg(\cos\left(\frac{\mathcal{D}_1}{2}(\tau_1+\tau_2)\right)\cos(2\xi)\sin\left(\frac{\Theta}{2}(\tau_1-\tau_2)\right) \\ &- \sin\left(\frac{\mathcal{D}_1}{2}(\tau_1+\tau_2)\right)\cos\left(\frac{\Theta}{2}(\tau_1-\tau_2)\right)\Bigg)\Bigg).\end{aligned} \tag{D9}$$

When $T_2 \to \infty$, we get the right form without relaxation effects. Moreover, $\mathcal{F}_{5P}$ is largest with the same conditions as $\mathcal{F}_{3P}$, and we get identical upper bound for total gate time τ,

$$\frac{1}{2} + \frac{1}{2}e^{-\frac{\tau}{T_2}} \geq \mathcal{F}_{5P}(\tau,\Omega,\Delta\omega,\mathcal{D}_1,\mathcal{D}_2,T_2). \tag{D10}$$

REFERENCES

[1] M. R. Wasielewski, M. D. E. Forbes, N. L. Frank, K. Kowalski, G. D. Scholes, J. Yuen-Zhou, M. A. Baldo, D. E. Freedman, R. H. Goldsmith, T. Goodson, M. L. Kirk, J. K. McCusker, J. P. Ogilvie, D. A. Shultz, S. Stoll, and K. B. Whaley, "Exploiting chemistry and molecular systems for quantum information science," Nat. Rev. Chem. **4**, 490–504 (2020).

[2] J. N. Nelson, J. Zhang, J. Zhou, B. K. Rugg, M. D. Krzyaniak, and M. R. Wasielewski, "CNOT gate operation on a photogenerated molecular electron spin-qubit pair," J. Chem. Phys. **152**, 014503 (2020).

[3] B. K. Rugg, M. D. Krzyaniak, B. T. Phelan, M. A. Ratner, R. M. Young, and M. R. Wasielewski, "Photodriven quantum teleportation of an electron spin state in a covalent donor–acceptor–radical system," Nat. Chem. **11**, 981–986 (2019).

[4] B. W. Stein, C. R. Tichnell, J. Chen, D. A. Shultz, and M. L. Kirk, "Excited state magnetic exchange interactions enable large spin polarization effects," J. Am. Chem. Soc. **140**, 2221–2228 (2018).

[5] M. M. Paquette, D. Plaul, A. Kurimoto, B. O. Patrick, and N. L. Frank, "Opto-spintronics: Photoisomerization-induced spin state switching at 300 K in photochrome cobalt–dioxolene thin films," J. Am. Chem. Soc. **140**, 14990–15000 (2018).

[6] M. Atzori and R. Sessoli, "The second quantum revolution: Role and challenges of molecular chemistry," J. Am. Chem. Soc. **141**, 11339–11352 (2019).

[7] L. V. H. Rodgers, L. B. Hughes, M. Xie, P. C. Maurer, S. Kolkowitz, A. C. Bleszynski Jayich, and N. P. De Leon, "Materials challenges for quantum technologies based on color centers in diamond," MRS Bull. **46**, 623–633 (2021).

[8] G.-Q. Liu and X.-Y. Pan, "Quantum information processing with nitrogen–vacancy centers in diamond," Chin. Phys. B **27**, 020304 (2018).

[9] R. J. Epstein, F. M. Mendoza, Y. K. Kato, and D. D. Awschalom, "Anisotropic interactions of a single spin and dark-spin spectroscopy in diamond," Nat. Phys. **1**, 94–98 (2005).

[10] X. Rong, J. Geng, F. Shi, Y. Liu, K. Xu, W. Ma, F. Kong, Z. Jiang, Y. Wu, and J. Du, "Experimental fault-tolerant universal quantum gates with solid-state spins under ambient conditions," Nat. Commun. **6**, 8748 (2015).

[11] D. D. Sukachev, A. Sipahigil, C. T. Nguyen, M. K. Bhaskar, R. E. Evans, F. Jelezko, and M. D. Lukin, "Silicon-vacancy spin qubit in diamond: A quantum memory exceeding 10 ms with single-shot state readout," Phys. Rev. Lett. **119**, 223602 (2017).

[12] B. C. Rose, D. Huang, Z.-H. Zhang, P. Stevenson, A. M. Tyryshkin, S. Sangtawesin, S. Srinivasan, L. Loudin, M. L. Markham, A. M. Edmonds, D. J. Twitchen, S. A. Lyon, and N. P. De Leon, "Observation of an environmentally insensitive solid-state spin defect in diamond," Science **361**, 60–63 (2018).

[13] J. C. McCallum, B. C. Johnson, and T. Botzem, "Donor-based qubits for quantum computing in silicon," Appl. Phys. Rev. **8**, 031314 (2021).

[14] J. L. O'Brien, S. R. Schofield, M. Y. Simmons, R. G. Clark, A. S. Dzurak, N. J. Curson, B. E. Kane, N. S. McAlpine, M. E. Hawley, and G. W. Brown, "Towards the fabrication of phosphorus qubits for a silicon quantum computer," Phys. Rev. **64**, 161401 (2001).

[15] X. Mi, M. Benito, S. Putz, D. M. Zajac, J. M. Taylor, G. Burkard, and J. R. Petta, "A coherent spin–photon interface in silicon," Nature **555**, 599–603 (2018).

[16] M. A. Eriksson, M. Friesen, S. N. Coppersmith, R. Joynt, L. J. Klein, K. Slinker, C. Tahan, P. M. Mooney, J. O. Chu, and S. J. Koester, "Spin-based quantum dot quantum computing in silicon," Quantum Inf. Process. **3**, 133–146 (2004).

[17] Q. Li, Ł. Cywiński, D. Culcer, X. Hu, and S. Das Sarma, "Exchange coupling in silicon quantum dots: Theoretical considerations for quantum computation," Phys. Rev. B **81**, 085313 (2010).

[18] K. Wang, G. Xu, F. Gao, H. Liu, R.-L. Ma, X. Zhang, Z. Wang, G. Cao, T. Wang, J.-J. Zhang, D. Culcer, X. Hu, H.-W. Jiang, H.-O. Li, G.-C. Guo, and G.-P. Guo, "Ultrafast coherent control of a hole spin qubit in a germanium quantum dot," Nat. Commun. **13**, 206 (2022).

[19] C. Kloeffel and D. Loss, "Prospects for spin-based quantum computing in quantum dots," Annu. Rev. Condens. Matter Phys. **4**, 51–81 (2013).

[20] G. Scappucci, C. Kloeffel, F. A. Zwanenburg, D. Loss, M. Myronov, J.-J. Zhang, S. De Franceschi, G. Katsaros, and M. Veldhorst, "The germanium quantum information route," Nat. Rev. Mater. **6**, 926–943 (2020).

[21] C. D. Buckley, D. A. Hunter, P. J. Hore, and K. A. McLauchlan, "Electron spin resonance of spin-correlated radical pairs," Chem. Phys. Lett. **135**, 307–312 (1987).

[22] W. Lubitz, F. Lendzian, and R. Bittl, "Radicals, radical pairs and triplet states in photosynthesis," Acc. Chem. Res. **35**, 313–320 (2002).

[23] T. P. Fay, L. P. Lindoy, and D. E. Manolopoulos, "Spin-selective electron transfer reactions of radical pairs: Beyond the Haberkorn master equation," J. Chem. Phys. **149**, 064107 (2018).

[24] A. M. Lewis, T. P. Fay, D. E. Manolopoulos, C. Kerpal, S. Richert, and C. R. Timmel, "On the low magnetic field effect in radical pair reactions," J. Chem. Phys. **149**, 034103 (2018).

[25] T. P. Fay, A. M. Lewis, and D. E. Manolopoulos, "Spin-dependent charge recombination along para-phenylene molecular wires," J. Chem. Phys. **147**, 064107 (2017).

[26] D. P. DiVincenzo, "The physical implementation of quantum computation," Fortschr. Phys. **48**, 771–783 (2000).

[27] M. Y. Volkov and K. M. Salikhov, "Pulse protocols for quantum computing with electron spins as qubits," Appl. Magn. Reson. **41**, 145–154 (2011).

[28] U. E. Steiner and T. Ulrich, "Magnetic field effects in chemical kinetics and related phenomena," Chem. Rev. **89**, 51–147 (1989).

[29] K. A. McLauchlan and U. E. Steiner, "The spin-correlated radical pair as a reaction intermediate," Mol. Phys. **73**, 241–263 (1991).

[30] J. A. Weil and J. R. Bolton, *Electron Paramagnetic Resonance: Elementary Theory and Practical Applications*, 2nd ed. (John Wiley & Sons, 2007).

[31] Y. Zhang, C. A. Ryan, R. Laflamme, and J. Baugh, "Coherent control of two nuclear spins using the anisotropic hyperfine interaction," Phys. Rev. Lett. **107**, 170503 (2011).

[32] J. Tang and J. R. Norris, "Multiple-quantum EPR coherence in a spin-correlated radical pair system," Chem. Phys. Lett. **233**, 192–200 (1995).

[33] J. Tan, M. C. Thurnauer, and J. R. Norris, "Electron spin echo envelope modulation due to exchange and dipolar interactions in a spin-correlated radical pair," Chem. Phys. Lett. **219**, 283–0290 (1994).

[34] G. Zwanenburg and P. J. Hore, "EPR of spin-correlated radical pairs. analytical treatment of selective excitation including zero-quantum coherence," Chem. Phys. Lett. **203**, 65–74 (1993).

[35] M. D. Price, S. S. Somaroo, C. H. Tseng, J. C. Gore, A. F. Fahmy, T. F. Havel, and D. G. Cory, "Construction and implementation of NMR quantum logic gates for two spin systems," J. Magn. Reson. **140**, 371–378 (1999).

[36] M. Nielsen and I. Chuang, *Quantum Computation and Quantum Information* (American Association of Physics Teachers, 2002).

[37] J. N. Nelson, J. Zhang, J. Zhou, B. K. Rugg, M. D. Krzyaniak, and M. R. Wasielewski, "Effect of electron–nuclear hyperfine interactions on multiple-quantum coherences in photogenerated covalent radical (qubit) pairs," J. Phys. Chem. A **122**, 9392–9402 (2018).

[38] J. N. Nelson, M. D. Krzyaniak, N. E. Horwitz, B. K. Rugg, B. T. Phelan, and M. R. Wasielewski, "Zero quantum coherence in a series of covalent spin-correlated radical pairs," J. Phys. Chem. A **121**, 2241–2252 (2017).

[39] S. M. Harvey and M. R. Wasielewski, "Photogenerated spin-correlated radical pairs: From photosynthetic energy transduction to quantum information science," J. Am. Chem. Soc. **143**, 15508–15529 (2021).

[40] R. Carmieli, Q. Mi, A. B. Ricks, E. M. Giacobbe, S. M. Mickley, and M. R. Wasielewski, "Direct measurement of photoinduced charge separation distances in donor–acceptor systems for artificial photosynthesis using OOP-ESEEM," J. Am. Chem. Soc. **131**, 8372–8373 (2009).

[41] A. D. Becke, "Beckes three parameter hybrid method using the LYP correlation functional," J. Chem. Phys. **98**, 5648–5652 (1993).

[42] P. J. Stephens, F. J. Devlin, C. F. Chabalowski, and M. J. Frisch, "*Ab initio* calculation of vibrational absorption and circular dichroism spectra using density functional force fields," J. Phys. Chem. **98**, 11623–11627 (1994).

[43] F. Weigend and R. Ahlrichs, "Balanced basis sets of split valence, triple zeta valence and quadruple zeta valence quality for H to Rn: Design and assessment of accuracy," Phys. Chem. Chem. Phys. **7**, 3297–3305 (2005).

[44] F. Weigend, "Accurate Coulomb-fitting basis sets for H to Rn," Phys. Chem. Chem. Phys. **8**, 1057–1065 (2006).

[45] S. Grimme, "Semiempirical GGA-type density functional constructed with a long-range dispersion correction," J. Comput. Chem. **27**, 1787–1799 (2006).

[46] S. Grimme, J. Antony, S. Ehrlich, and H. Krieg, "A consistent and accurate *ab initio* parametrization of density functional dispersion correction (DFT-D) for the 94 elements H-Pu," J. Chem. Phys. **132**, 154104 (2010).

[47] S. Grimme, S. Ehrlich, and L. Goerigk, "Effect of the damping function in dispersion corrected density functional theory," J. Comput. Chem. **32**, 1456–1465 (2011).

[48] A. D. Becke, "Density-functional exchange-energy approximation with correct asymptotic behavior," Phys. Rev. A **38**, 3098 (1988).

[49] N. Rega, M. Cossi, and V. Barone, "Development and validation of reliable quantum mechanical approaches for the study of free radicals in solution," J. Chem. Phys. **105**, 11060–11067 (1996).

[50] T. H. Dunning, "Gaussian basis sets for use in correlated molecular calculations. I. The atoms boron through neon and hydrogen," J. Chem. Phys. **90**, 1007–1023 (1989).

[51] D. E. Woon and T. H. Dunning, "Calculation of the electron affinities of the second row atoms: Al–Cl," J. Chem. Phys. **99**, 3730–3737 (1993).

[52] F. Neese, "The ORCA program system," Wiley Interdiscip. Rev.: Comput. Mol. Sci. **2**, 73–78 (2012).

[53] F. Neese, "Software update: The ORCA program system, version 4.0," Wiley Interdiscip. Rev.: Comput. Mol. Sci. **8**, 73–78 (2017).

[54] K. Schulten and P. G. Wolynes, "Semiclassical description of electron spin motion in radicals including the effect of electron hopping," J. Chem. Phys. **68**, 3292–3297 (1978).

[55] P. de Fouquieres, S. G. Schirmer, S. J. Glaser, and I. Kuprov, "Second order gradient ascent pulse engineering," J. Magn. Reson. **212**, 412–417 (2011).

[56] B. Rowland and J. A. Jones, "Implementing quantum logic gates with gradient ascent pulse engineering: Principles and practicalities," Philos. Trans. R. Soc., A **370**, 4636–4650 (2012).

[57] N. Khaneja, T. Reiss, C. Kehlet, T. Schulte-Herbrüggen, and S. J. Glaser, "Optimal control of coupled spin dynamics: Design of NMR pulse sequences by gradient ascent algorithms," J. Magn. Reson. **172**, 296–305 (2005).

[58] J. A. Jones, R. H. Hansen, and M. Mosca, "Quantum logic gates and nuclear magnetic resonance pulse sequences," J. Magn. Reson. **135**, 353–360 (1998).

[59] S. Macura, Y. Huang, D. Suter, and R. Ernst, "Two-dimensional chemical exchange and cross-relaxation spectroscopy of coupled nuclear spins," J. Magn. Reson. **43**, 259–281 (1981).

6 Article 4: Exploring the Radical Pair Mechanism in Large Spin Systems - Introducing the Stochastic Schrödinger Equation into *MolSpin*

Statement of Authorship for joint/multi-authored papers for PGR thesis

To appear at the end of each thesis chapter submitted as an article/paper

The statement shall describe the candidate's and co-authors' independent research contributions in the thesis publications. For each publication there should exist a complete statement that is to be filled out and signed by the candidate and supervisor **(only required where there isn't already a statement of contribution within the paper itself).**

Title of Paper	Exploring the radical pair mechanism in large spin systems - Introducing the Stochastic Schrödinger Equation into MolSpin
Publication Status	☐Published ☐ Accepted for Publication ☐Submitted for Publication ☑ Unpublished and unsubmitted work written in a manuscript style
Publication Details	Pažėra, G. J.; Solov'yov I. A.; Hore P. J. & Gerhards L. (unpublished) Exploring the radical pair mechanism in large spin systems - Introducing the Stochastic Schrödinger Equation into MolSpin

Student Confirmation

Student Name:	Gediminas Jurgis Pazera		
Contribution to the Paper	Conceptualized the study and the aims with L.G., with the help of P. J. H. and I. A. S., developed methodology, wrote most of the software additions for MolSpin with the help of L.G., carried out most of the calculations, analyzed data, produced visualizations, wrote the manuscript with L.G.		
Signature		Date	2023.09.08

Supervisor Confirmation

By signing the Statement of Authorship, you are certifying that the candidate made a substantial contribution to the publication, and that the description described above is accurate.

Supervisor name and title: Professor Peter J. Hore		
Supervisor comments		
Signature PJHore	Date	8 September 2023

This completed form should be included in the thesis, at the end of the relevant chapter.

Exploring the radical pair mechanism in large spin systems - Introducing the Stochastic Schrödinger Equation into *MolSpin*

Gediminas Jurgis Pažėra[1*], Ilia A. Solov'yov[2,3,4], P. J. Hore[1], and Luca Gerhards[2*]

[1]Department of Chemistry, University of Oxford, Physical and Theoretical Chemistry Laboratory, Oxford, OX1 3QZ, United Kingdom
[2]Institute of Physics, Carl von Ossietzky Universität Oldenburg, Carl-von-Ossietzky Str. 9-11, 26129 Oldenburg, Germany
[3]Research Center for Neurosensory Science, Carl von Ossietzky Universität Oldenburg, 26111 Oldenburg, Germany
[4]Center for Nanoscale Dynamics (CENAD), Carl von Ossietzky Universität Oldenburg, Institut für Physik, Ammerländer Heerstr. 114-118, 26129 Oldenburg, Germany
[*]Corresponding authors: Gedminas Jurgis Pažėra, gediminas.pazera@ccc.ox.ac.uk; Luca Gerhards, luca.gerhards@uni-oldenburg.de

January 18, 2024

Abstract

Spin-dependent chemical processes, particularly those influenced by weak magnetic fields in biological systems and macromolecules, have been receiving increased attention in the scientific community. Among these processes, the radical pair mechanism (RPM) has emerged as a critical area of study. Understanding the underlying dynamics of RPM is complex and often necessitates a quantum mechanical description, as conventional approaches may fall short in capturing the nuances of these processes. When weak magnetic fields are present, the hyperfine interactions of radicals with adjacent nuclei become the dominant factors that dictate the outcomes of spin-dependent chemical reactions. In biological systems and macromolecules, where multiple nuclei are involved, this leads to a computational challenge, as simulating these systems on a quantum mechanical basis demands an unfeasible amount of computational resources. Moreover, the constant motions within the system induce spin relaxation effects, significantly altering the population of spin states. These effects must be rigorously considered for an accurate and realistic description of the phenomena.

In response to these challenges, this work introduces an efficient quantum chemical framework, implemented in our software package *MolSpin*, designed to compute spin dynamics problems of radical pairs involving up to 22 spins. The framework goes beyond mere numerical simulations by incorporating an explicit description of complex spin relaxation effects, extracted from both molecular dynamics and quantum chemical simulations. By doing so, it enables the representation of realistic spin systems of larger sizes, thus opening new avenues for the investigation of spin-dependent reactions. This innovation not only enhances the understanding of the intricate behaviors in spin chemistry but also offers a powerful tool for researchers aiming to unravel the complex interplay between magnetic fields, molecular structures, and chemical reactions.

1 Introduction

Spin chemistry and the related spin-dependent reactions, which are chiefly mediated through the radical pair mechanism (RPM), have become increasingly significant in recent scientific investigations. This interest stems from the RPM's critical role in diverse phenomena, such as magnetoreception, which allows migratory species to navigate with precision [1–3], or its influence on vital biological processes, including those associated with peroxide formation in proteins or lipids within organisms [4, 5].

The RPM is characterized by the formation of a correlated radical pair, commonly produced by light-induced charge transfer [6–8]. These radical pairs may exist in singlet or triplet states, with the population distribution between these states being susceptible to alteration through Zeemann interaction with an external magnetic field. This leads to marked variations in spin-dependent reaction yields and gives rise to what is known as the magnetic field effect (MFE).

In scenarios where the intensity of the external magnetic field is weak, other interactions, such as hyperfine or dipolar interactions, can predominate and affect the dynamics of the radicals. In specific protein environments, such as cryptochromes, potentially used in magnetoreception, numerous nuclei play a substantial role in the radical pair dynamics [9, 10]. In these contexts, the quantum mechanical portrayal of the radical pair becomes intricate, as the Hilbert space expands exponentially with the number of spin particles considered, thus limiting the nuclei that can be included in the description.

Furthermore, the continuous motion of the molecules containing the radical pair can perturb the relevant interactions, resulting in induced spin-relaxation processes that guide the radical pair towards equilibrium among all spin states. Past research has established the importance of accounting for this effect to depict realistic radical pairs accurately [3, 10, 11]. However, the integration of spin relaxation into existing theoretical frameworks, such as Bloch-Redfield-Wangsness theory [3, 10] (BRW) or Nakajima-Zwanzig theory [12] (NZ), remains computationally challenging and resource-intensive, particularly when complex perturbations such as motion of a protein are involved.

In 2016, Lewis *et al.* [13] pioneered a novel methodology for examining radical pair-based spin systems, significantly enhancing the efficiency of spin dynamics computations. This method permits the consideration of systems comprising 20 or more spins, laying the groundwork for further advancements, such as the inclusion of spin relaxation and the exploration of complex Hamiltonian time-dependencies. In 2021, Fay *et al.* [14] expanded on this approach to incorporate time-dependent effects, including spin relaxation, through stochastic consideration of the Hamiltonian using the stochastic Schrödinger equation (SSE), thus demonstrating its efficiency in two radical pair examples. This innovative approach offers a promising alternative for describing spin-relaxation processes in multifaceted radical pair systems, although the general construction of the complete theory remains a laborious endeavor, constraining the examination of a wide spectrum of relevant spin systems.

MolSpin, a sophisticated software package, has been engineered to model spin systems efficiently. It provides a comprehensive suite of functionalities to study spin dynamics and the impact of spin on intricate chemical reactions. Key attributes of *MolSpin* include its generalized approach, user-friendly extensibility, and an intuitive input interface, all of which promote flexibility in modeling. Additionally, *MolSpin* is designed for seamless integration with the web-based platform VIKING (Scandinavian Online Kit For Nanoscale Modeling) [15], thereby simplifying usability.

This work aims to present and further optimize a generalized framework based on the methods introduced by Lewis *et al.* [13] and Fay *et al.* [14]. The developed algorithm offers a versatile strategy capable of managing arbitrary radical spin systems, accompanied by a direct connection to molecular dynamics (MD) simulations. This linkage ensures a user-friendly yet detailed representation of the complex time-dependent interactions of interest. Furthermore, new features such as different propagators and a correction factor for the time-propagation are implemented to further enhance the performance and usability.

2 Theory and implementation

The dynamics of radical pair spin systems are governed by the Liouville-Von Neumann equation. In its most general form, with the assumption that $\hbar = 1$, it is expressed as:

$$\frac{d}{dt}\hat{\rho}(t) = -i\left[\hat{H}, \hat{\rho}(t)\right] - \left\{\hat{K}, \hat{\rho}(t)\right\}, \tag{1}$$

where $\hat{\rho}(t)$ is the density operator of the combined electron-nuclear spin system of the radical pair and the brackets $[\cdot,\cdot]$ and $\{\cdot,\cdot\}$ represent the commutator and anti-commutator between two operators, respectively.

The spin Hamiltonian $\hat{H}$ characterizes the physical interactions within the system and is defined as:

$$\begin{aligned}\hat{H} = &\sum_{i=1}^{2}\left(\mathbf{g_i}\mu_B\tilde{\mathbf{B}}\cdot\hat{\mathbf{S}}_i + \sum_{k=1}^{N_i}\hat{\mathbf{S}}_i\cdot\mathbf{A}_{ik}\cdot\hat{\mathbf{I}}_{ik}\right)\\ &+\hat{\mathbf{S}}_1\cdot\mathbf{D}\cdot\hat{\mathbf{S}}_2 - 2J\hat{\mathbf{S}}_1\cdot\hat{\mathbf{S}}_2,\end{aligned} \tag{2}$$

where the terms within the brackets describe the Zeeman interaction of the i-th electron spin $\hat{\mathbf{S}}_i$ with the external magnetic field $\tilde{\mathbf{B}}$, and the hyperfine interaction of the i-th electron spin with the k-th nuclear spin $\hat{\mathbf{I}}_{ik}$ via the coupling tensor $\mathbf{A}_{ik}$. $\mathbf{g}_i$ is the g-value, and μ_B is the Bohr magneton. The remaining terms characterize the electron-electron dipolar (EED) coupling and electron exchange.

The spin-dependent reaction operator $\hat{K}$ in Eq. (1) is described by:

$$\hat{K} = \sum_{\Theta} \frac{k_\Theta}{2} \hat{P}_\Theta, \tag{3}$$

where $k_\Theta(t)$ is the reaction rate constant of state $\Theta \in \{S, T_+, T_-, T_0\}$, $\hat{P}_\Theta$ is the projection operator of state Θ.

The solution to Eq. 1 offers an accurate description for small spin systems. Challenges arise from the growing number of important spins in the dynamics, leading to exponential growth of the Hilbert space. Furthermore, constant interaction with the fluctuating macroscopic environment alters the expectation values of the spin system, a phenomenon known as spin-relaxation. Advanced methods, such as the Stochastic Schrödinger equation (SSE) that includes time-dependent interactions for modeling spin-relaxation and Monte Carlo (MC) sampling for large systems, can improve computational scaling and enable simulations of extensive systems [14].

In subsequent sections, we will highlight the derivations and applications of an efficient formalism for many-spin systems and spin relaxation processes. Before modifying the equations of interest to describe many-spin systems, we must separate complex time dependencies from the Hamiltonian and define specific terms for calculating observables of interest. This will facilitate the formulation of the SSE.

We can express the Liouville-Von Neumann equation as fully time-dependent:

$$\frac{d}{dt}\hat{\rho}(t) = -i\left[\hat{H}(t), \hat{\rho}(t)\right] - \left\{\hat{K}(t), \hat{\rho}(t)\right\}, \tag{4}$$

where the time-dependency of the Hamiltonian separates from the static interaction and is represented in terms of stochastic fluctuation functions $f_j(t)$ and spin system operators $\hat{A}_j$:

$$\hat{H}(t) = \hat{H}_0 + \hat{V}(t) = \hat{H}_0 + \sum_j f_j(t)\hat{A}_j. \tag{5}$$

Evaluating the time-dependent stochastic fluctuation functions is a significant challenge, leading to various relaxation theories [16, 17].

For the reaction operator $\hat{K}(t)$, time-dependency is included by varying the reaction rate constant $k_\Theta(t)$ over time. Usually, the reaction rate constants are time-independent, but in specific cases (for instance when the two centers of a radical pair move in time) time-dependency has to be assumed [18]. For spin-dependent reactions, the quantum yields Φ_Θ of a specific state reaction are given by:

$$\Phi_\Theta = \int_0^\infty k_\Theta(t) P_\Theta(t) dt, \tag{6}$$

with the time-dependent population of the spin state of interest $P_\Theta(t)$ obtained using:

$$P_\Theta(t) = \mathrm{Tr}\left[\hat{P}_\Theta \hat{\rho}(t)\right], \tag{7}$$

where the time-dependent density matrix $\hat{\rho}(t)$ is defined by the transformation of the density matrix at $t = 0$ with the time propagator $\hat{U}(t, 0)$:

$$\hat{\rho}(t) = \hat{U}(t, 0)\hat{\rho}(0)\hat{U}(t, 0)^\dagger. \tag{8}$$

Eq. 8 is the solution of Eq. 4. The propagator $\hat{U}(t_1, t_0)$ with $t_1 = t_0 + \delta t$, which evolves the state from t_0 to t_1, is defined as:

$$\hat{U}(t_1, t_0) = \hat{T} \exp\left[\int_{t_0}^{t_1} d\tau \left(-i\hat{H}(\tau) - \hat{K}(\tau)\right)\right], \tag{9}$$

where $\hat{T}$ is the time-ordering operator. The initial condition of the density matrix is represented as the Kronecker product of the initial radical pair state of interest (i.e. singlet or triplet states) $|\Theta_{\mathrm{init}}\rangle$ and the identity operator states $\mathbb{I}_Z$ of the nuclei:

$$\hat{\rho}(0) = \frac{1}{Z}\left(|\Theta_{\mathrm{init}}\rangle \langle\Theta_{\mathrm{init}}|\right) \otimes \mathbb{I}_Z, \tag{10}$$

where Z is the size of the nuclear spin Hilbert subspace. In real systems, such as proteins, many nuclei must be involved in the spin dynamics, leading to numerous nuclear spin states in $\mathbb{I}_Z$ and consequently to the exponential growth of the Hilbert space. The focus of the work presented here is on the effective evaluation of Eq. 7 without explicitly considering all possible nuclear spin states.

In the following, we will describe two approaches to evaluate the trace in Eq. 7, termed direct and stochastic methods. The direct method evolves all possible nuclear spin states and is suitable for small spin systems, while the stochastic method leverages MC sampling for efficient simulation of systems with large Hilbert spaces, albeit being impractical for small spin systems. The combination of these methods enables the simulation of a wide range of spin systems.

2.1 Direct Method

We can evaluate the quantum mechanical trace in the basis of [13]:

$$\{\mathcal{B}\} = \{|\Theta\rangle \otimes |\mathbf{M}_1\rangle \otimes |\mathbf{M}_2\rangle\}\,, \tag{11}$$

where $|\Theta\rangle$ are radical pair electron spin states and $|\mathbf{M}_i\rangle$ is the nuclear spin state of radical i, given by:

$$|\mathbf{M}_i\rangle = |M_{i1}\rangle \otimes |M_{i2}\rangle \otimes \cdots \otimes |M_{iN_i}\rangle\,. \tag{12}$$

M_{ik} is the projection of k-th nuclear spin in the radical onto the z-axis. We can expand the trace in Eq. 7 with Eq. 11 by summing over all possible nuclear spin states (M_i):

$$
\begin{aligned}
P_{\Theta}(t) &= Tr[\mathbb{I}\hat{P}_{\Theta}\hat{\rho}(t)\mathbb{I}] \\
&= Tr[\sum_{\Theta,\Theta'}\sum_{\mathbf{m}_1,\mathbf{m}_1'}\sum_{\mathbf{m}_2,\mathbf{m}_2'} |\Theta,\mathbf{M}_1,\mathbf{M}_2\rangle\langle\Theta,\mathbf{M}_1,\mathbf{M}_2|\hat{P}_{\Theta}\hat{\rho}(t)|\Theta',\mathbf{M}_1',\mathbf{M}_2'\rangle\langle\Theta',\mathbf{M}_1',\mathbf{M}_2'|] \\
&= \sum_{\Theta}\sum_{\mathbf{m}_1}\sum_{\mathbf{m}_2}\langle\Theta,\mathbf{M}_1,\mathbf{M}_2|\hat{P}_{\Theta}\hat{\rho}(t)|\Theta,\mathbf{M}_1,\mathbf{M}_2\rangle \\
&= \sum_{\Theta}\sum_{\mathbf{m}_1}\sum_{\mathbf{m}_2}\langle\Theta,\mathbf{M}_1,\mathbf{M}_2|\hat{U}(t,0)^{\dagger}\hat{P}_{\Theta}\hat{U}(t,0)\hat{\rho}(0)|\Theta,\mathbf{M}_1,\mathbf{M}_2\rangle \\
&= \frac{1}{Z}\sum_{\mathbf{m}_1}\sum_{\mathbf{m}_2}\langle\Theta_{\text{init}},\mathbf{M}_1,\mathbf{M}_2;t|\hat{P}_{\Theta}|\Theta_{\text{init}},\mathbf{M}_1,\mathbf{M}_2;t\rangle
\end{aligned} \tag{13}
$$

The transition from the third to the fourth line in the above equation is accomplished by invoking the definition of $\hat{\rho}(t)$, as outlined in Eq. 8. Additionally, we apply the cyclic permutation property of the trace, which allows for the rearrangement of the operators inside the trace. Since $\hat{\rho(0)} = \frac{1}{Z}\left|\Theta_{init}\right\rangle\left\langle\Theta_{init}\right| \otimes \mathbb{I}_Z$, the sum over Θ vanishes with only Θ_{init} state remaining, because all terms for $\Theta \neq \Theta_{\text{init}}$ are zero. Lastly, the definition $\left|\Theta_{\text{init}},\mathbf{M}_1,\mathbf{M}_2;\ t\right\rangle = \hat{U}(t,0)\left|\Theta_{\text{init}},\mathbf{M}_1,\mathbf{M}_2\right\rangle$ is employed.

The trace is computed directly, summing over all possible nuclear spin states [13]. The states $\left|\Theta_{\text{init}},\mathbf{M}_1,\mathbf{M}_2;\ t\right\rangle$ follow the dynamics of the Stochastic Schrödinger Equation (SSE) [14]:

$$
\frac{d}{dt}\left|\Theta_{\text{init}},\mathbf{M}_1,\mathbf{M}_2;\ t\right\rangle = \left(-i\hat{H}(t) - \hat{K}(t)\right)\left|\Theta_{\text{init}},\mathbf{M}_1,\mathbf{M}_2;\ t\right\rangle, \tag{14}
$$

The time propagation and overall scaling will be discussed in Section 2.3. This direct method is efficient for small spin systems, but becomes unfeasible when dealing with thousands of possible nuclear spin states. Thus, the stochastic evaluation of possible nuclear spin states is an effective procedure to use the formalism in Eq. 14 for larger systems.

2.2 Stochastic Method

The direct method requires Z wavepackets to be propagated to compute the trace in Eq. 7, which becomes unfeasible for large systems. We can overcome this limitation by introducing a stochastic evaluation of the trace. This is achieved by defining a resolution of the identity $\mathbb{I}$ of normalized nuclear spin states $|\psi(\xi)\rangle$, parametrized by ξ[14]:

$$\mathbb{I} = Z \int d\xi p(\xi) \left|\psi(\xi)\right\rangle \left\langle\psi(\xi)\right|, \tag{15}$$

where $p(\xi)$ is the normalized probability density for ξ.

By substituting this resolution of identity for the nuclear spin states space $\mathbb{I}_Z$, the trace can be calculated as [14, 19]:

$$P_\Theta(t) = \int d\xi p(\xi) \left\langle\Theta_{\text{init}}, \psi_\xi(t)\right| \hat{P}_\Theta \left|\Theta_{\text{init}}, \psi_\xi(t)\right\rangle, \tag{16}$$

where $|\Theta_{\text{init}}, \psi_\xi(0)\rangle = |\Theta_{\text{init}}\rangle \otimes |\psi(\xi)\rangle$. The time propagation of $|\Theta_{\text{init}}, \psi_\xi(t)\rangle$ follows the SSE in the same way as Eq. 14.

The main choice of these states, and the one used throughout this article, is the SU(Z) coherent states denoted as $|\mathbf{Z}\rangle$, where $\mathbf{Z}$ is a vector of complex numbers $Z_n = X_n + iY_n$, and X_n and Y_n are randomly sampled independent normal deviates. The $|\mathbf{Z}\rangle$ state in a chosen basis is given by:

$$|\mathbf{Z}\rangle = \sum_{n=1}^{Z} |n\rangle Z_n, \tag{17}$$

with the constraint $\langle\mathbf{Z}|\mathbf{Z}\rangle = 1$. SU(Z) states are sampled from the distribution $p(\mathbf{Z}) = \delta(|\mathbf{Z}| - 1)/\mathcal{S}_{2Z}$, where $\mathcal{S}_{2Z}$ is the surface area of a $2Z$-dimensional hypersphere of unit radius. These states have self-averaging properties due to the invariance of this distribution under unitary transformations of the vector $\mathbf{Z}$, $\mathbf{Z} \to \mathbf{UZ}$ [14].

Additionally, Coherent Spin States [20] are implemented in *MolSpin* for research purposes (see manual [21]). However, we recommend using SU(Z) for all computations, and we will not discuss Coherent Spin States further (which are discussed extensively in Ref. [13, 14, 22]).

The main advantage of this method is that we only need M Monte Carlo sampled states to be propagated in solving the trace, compared to Z wave-packets in the direct method. However, $Z \gg M$, and Z must be large for this method to be computationally efficient, making it viable only for large spin systems (see SI, section 2).

2.3 Stochastic Schrödinger Equation

Both the direct and stochastic methods rely on time-evolving state vectors by the SSE. For a generic state $|\Psi(t)\rangle$, SSE is given by:

$$\frac{d}{dt}|\Psi(t)\rangle = \left(-i\hat{H}(t) - \hat{K}(t)\right)|\Psi(t)\rangle\,, \tag{18}$$

and its solution with t_0 being the initial time:

$$|\Psi(t_0+\delta t)\rangle = \hat{U}(t_0+\delta t, t_0)\,|\Psi(t_0)\rangle\,. \tag{19}$$

The time propagator $\hat{U}$ can be approximated without the time-ordering operator using the first-order Magnus expansion for small time differences $t_1 - t_0 = \delta t$ [23]:

$$\begin{aligned}\hat{U}(t_0+\delta t, t_0) &\approx \exp\left[\int_{t_0}^{t_0+\delta t} d\tau\left(-i\hat{H}(\tau) - \hat{K}(\tau)\right)\right]\\ &= \exp\left[-i\hat{\Omega}(t_0+\delta t, t_0)\delta t\right],\end{aligned} \tag{20}$$

where the generator Ω, used for evolving the spin state, is given by [14]:

$$\begin{aligned}\Omega(t_0+\delta t, t_0) =& \hat{H}_0 - \frac{i}{2\delta t}\sum_{\Theta}\hat{P}_\Theta\int_{t_0}^{t_0+\delta t} k_\Theta(\tau)d\tau\\ &+\frac{1}{\delta t}\sum_j\hat{A}_j\int_{t_0}^{t_0+\delta t} f_j(\tau)d\tau.\end{aligned} \tag{21}$$

In general, time-dependencies are employed in the dynamics by providing *MolSpin* with the trajectories (.mst files) of each operator's integrated fluctuating components $\int_{t_0}^{t_0+\delta t} f_j(\tau)d\tau$ (for recombination operators the fluctuating component is the recombination rate $k_\Theta(\tau)$). This framework offers complete flexibility for stochastic and explicit expressions of time-dependent interactions, allowing for modeling complex scenarios i.e. in biological environments, with minimal impact on computation time.

The time-propagation of state vectors is straightforward, requiring only the computation of the action of matrix exponentials for a set of state vectors to find expectation values and quantum yields of projection operators. In simple terms, this is evaluating $e^{At}B$, where A is an $n \times n$ matrix and B is n-size vector. *Molspin* employs two ways of performing this propagation: short iterative Lanczos (SIL) [24] and short iterative Arnoldi (SIA) [25], both Krylov subspace methods, as well as a, to our knowledge, novel algorithm for spin dynamics described on a different topic in Ref. [26] called "*autoexpm*" (see manual [21] and SI). The "*autoexpm*" will be the primary method of exponential propagation presented in this study.

Due to the sparsity of the Hamiltonian, the wavepacket propagation scales with $\mathcal{O}(Z\log(Z))$ [13]. This means the direct method, which requires Z wavepackets to be propagated, scales as $\mathcal{O}(Z^2\log(Z))$, and overall, including the number of time evolution time-steps, the scaling is $\mathcal{O}(N_tZ^2\log(Z))$. The stochastic method, on the other hand, requires only M Monte Carlo samples to be propagated, reducing the overall scaling to $\mathcal{O}(MZ\log(Z))$, or $\mathcal{O}(N_tMZ\log(Z))$ including the number of time-steps.

The stochastic method also requires consideration of errors, as it approximates the total integral. It is shown that for SU(Z) states, due to their self-averaging property, the error of the method scales as $\mathcal{O}(1/\sqrt{MZ})$ [14]. This is a significant improvement compared to Coherent Spin States, which have an error scaling of $\mathcal{O}(1/\sqrt{M})$ [13]. Therefore, for very large systems, only one state may be sufficient for propagation to achieve errors suitable for graphical accuracy, allowing systems with 20 or more coupled nuclear spins to be considered with *MolSpin* (a more detailed analysis is found in the SI, section 2).

2.4 Correction Factor

One of the challenges in both the direct and stochastic methods is the explicit numerical evaluation of the time integral. The computational cost for this evaluation increases steadily for long-living radical pairs, and the often missing availability of explicit environment-induced spin relaxation along the entire time-trajectory makes an approximation of the spin dynamics towards an infinite time interval desirable.

In the supporting information (SI, section 1), we derive a heuristic for evaluating singlet yields that can significantly reduce the propagation time needed to calculate the time integral to infinity. The singlet yield with the correction factor is given by:

$$\Phi_\Theta(\infty) \approx \frac{k_\Theta}{1 - e^{-k_{sym}T}} \int_0^T P_\Theta(t)\, dt, \tag{22}$$

where T is the time of integration and k_{sym} the symmetric rate constant. It has been demonstrated through examples that this heuristic can reduce the simulation time by at least six times for systems that are static and have symmetric recombination rates (see SI, 1). This principle is currently only applied to symmetric rate constants between reactions of singlet and triplet states.

It is also applicable for time-dependent Hamiltonians; however, it should be applied with caution and tested prior to implementation, as the effectiveness of this approximation depends on the amplitudes of the fluctuations at the end times of the simulation. In the SI, Section 1 a more detailed analysis with respect to the accuracy is performed.

2.5 Numerical Accuracy of the Stochastic Method

To evaluate the computational accuracy of the stochastic method, we compared the singlet yield Φ_S calculated with the stochastic method implemented in *MolSpin* with the full dynamics algorithm described in Ref. [1] (see Fig. 1b). The system in question is a [FAD$^{\bullet-}$ TrpH$^{\bullet+}$] radical pair found in cryptochrome proteins. This includes hyperfine interactions as reported in Ref. [2], and EED and exchange coupling values from Ref. [27]. The system is composed of 12 nuclear spins: N5, N10, H6, 3× H8, Hβ for FAD$^{\bullet-}$, and N1, H1, H2, H4, H6 for TrpH$^{\bullet+}$ (see Fig. 1a). It represents a time-independent 14 spin system with two coupled electron spins.

As seen in Fig. 1b, the calculation with a single MC sample for the state to be propagated qualitatively captures all the essential details of the graphs, whereas 5 samples or more yield results with reasonable accuracy. This feature can be attributed to the self-averaging property of SU(Z) states and effectiveness of MC sampling, reducing the error with the increase of the size of nuclear spin space and number of MC samples. The full spin space of this system, with dimensions $55,296 \times 55,296$, approaches the upper limit of the full dynamics method, utilizing matrix diagonalization. While the Hamiltonian is represented as a sparse matrix, the eigenvector matrix doesn't share this trait. Like other matrix diagonalization techniques, the QR algorithm employed here necessitates the Hamiltonian to be in a dense-matrix format. For a 14-spin system, this demands 45.6 GB of RAM, presenting a considerable challenge when examining larger systems. Also, the speed of the algorithm for diagonalization unfavorably scales with $\mathcal{O}(n^3)$, where n is the dimension of the matrix. Our implementation overcomes these limitations by utilizing sparse matrices within the Armadillo framework [28].

To showcase the computational power of the implemented method, we performed a large-scale calculation of [FAD$^{\bullet-}$ TrpH$^{\bullet+}$] (to our knowledge, the largest in literature for systems without explicit approximation to Hamiltonians or dynamics). The system consisted of 20 nuclear spins, which are N5, N10, H6, 2× H8, 2× Hβ, 2× H7 for FAD$^{\bullet-}$, and N1, N^*, H1, H2, H4, H6, H7, Hβ_1, Hβ_2, Hα for TrpH$^{\bullet+}$ (see Fig. 1a). All nitrogen atoms were treated as ^{14}N with $I = 1$.

The system's dimension, $21,233,664 \times 21,233,664$, makes it unfeasible for methods requiring dense matrices, which would require 6561 TB of RAM. Whereas a sparse matrix requires around 88.6 GB [29] of storage, a size that modern computer clusters can handle. The ability to compute large systems, coupled with the flexibility in including any interactions, signifies that our framework in *MolSpin* enables the solution of complex spin dynamics problems. In subsequent sections, we will highlight the features and flexibility of the SSE methods in *MolSpin*, investigate recent examples, reproduce earlier results, and extend calculations to unique scenarios involving complex protein motions in cryptochrome, exploring their effects on the spin dynamics of radical-pair-based magnetoreception.

3 Features of SSE in *MolSpin*

The *MolSpin* software package is designed with the primary goal of providing a universal framework to address a wide variety of spin-dependent problems. This framework alleviates the need for constructing new Hamiltonians and related components for each specific case. Within the context of the SSE method, *MolSpin* accommodates all linear and bilinear

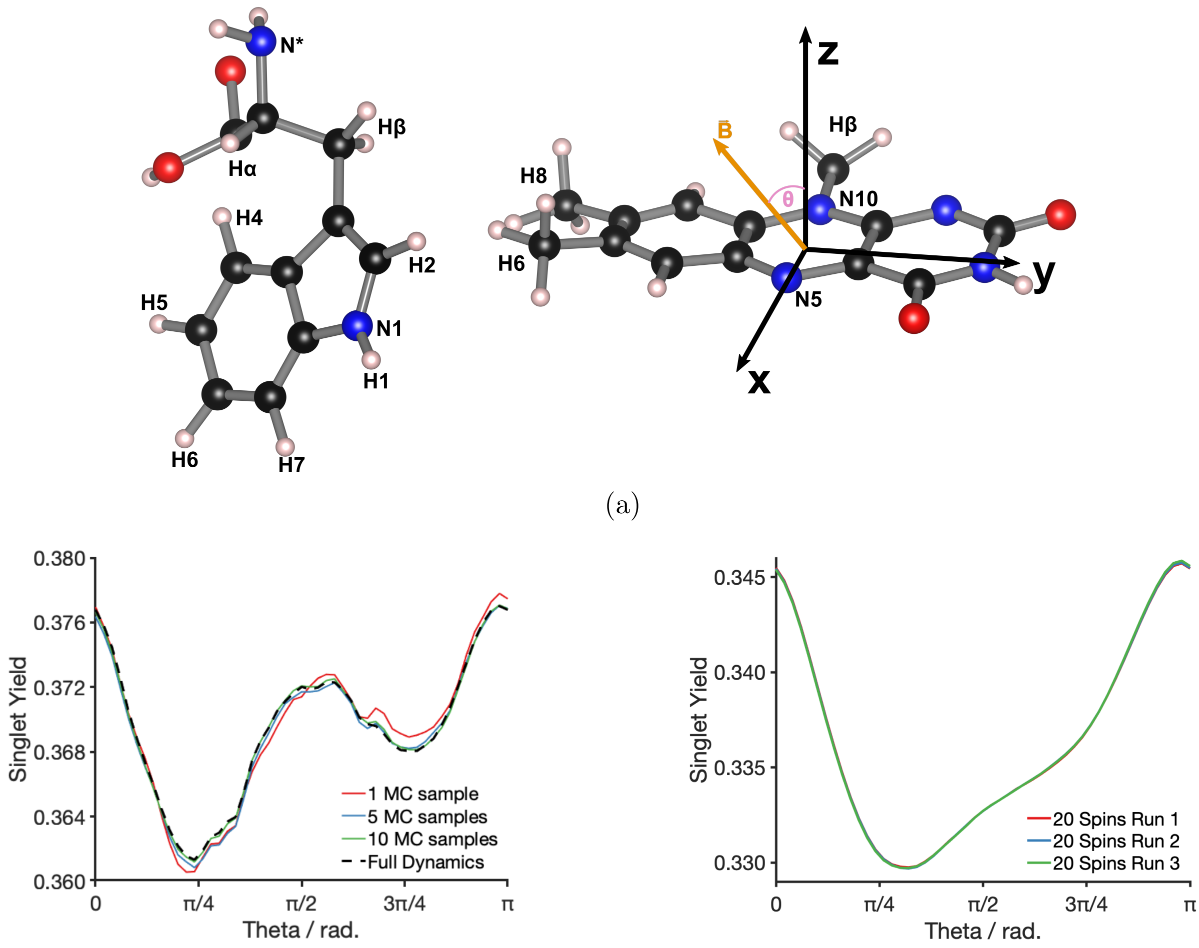

(a)

(b)

(c)

Figure 1: a) Schematic of $\left[\mathrm{FAD}^{\bullet-}\ \mathrm{TrpH}^{\bullet+}\right]$ radical pair system (TrpH on left, FAD on right), with labeled atoms that were used in spin dynamics. b) Singlet Yield, Φ_S, versus inclination angle of $\vec{B}$-field, θ, for a 12 nuclear spin $[\mathrm{FAD}^{\bullet-}\mathrm{TrpH}^{\bullet+}]$ radical pair system. The full spin dynamics, using matrix diagonalization as described in Ref. [1], were compared to calculations made with the stochastic method, utilizing varying numbers of SU(Z) spin states. The magnetic field strength was $|\mathbf{B}| = 1$ mT, and the symmetric recombination rate ($k_S = k_T$) was $k_{sym} = 1\ \mu s^{-1}$. Integration time was 6908 ns, the time-step was 4 ns, and the results were adjusted with the previously discussed correction factor. c) Singlet Yield, Φ_S, versus inclination angle, θ, for a 20 nuclear spin $[\mathrm{FAD}^{\bullet-}\mathrm{TrpH}^{\bullet+}]$ radical pair system (22 spin system). Calculations were performed with the stochastic method using 1 SU(Z) spin state for Monte Carlo sampling. Since we have no results of another method to compare with this graph to show that it gives the correct results (since it is too computationally expensive for other methods), we performed 3 calculations with different samples' initial state vectors. The graph shows that the results of all of the three different starting states converged to the same singlet yield profile, hence, ensuring the accuracy of our method and just using 1 MC sample. The magnetic field strength was $|\mathbf{B}| = 1$ mT, and the symmetric recombination rate was $k_{sym} = 1\ \mu s^{-1}$. Integration time was 693 ns (4 ns time step) using the correction factor method (Eq. 22), which is shown to be enough for 14 nuclear spin cases and other systems in the SI to yield converged results.

interactions, offering the user flexibility in customizing these interactions [3].

To enhance its adaptability, *MolSpin* facilitates the direct parsing of complex time dependencies for interactions or reaction rates through specialized *MolSpin* trajectory files (with the .mst extension). Comprehensive documentation on this file format is available in the supplementary information (SI) section 8 and in the user manual [21].

The implementation of SSE methods in *MolSpin* supports various initial spin states for the radical pair, including the state vectors S, T_0, T_-, and T_+ (mixed state can be produced by calculating each of the state involved in the mixing separately). This support ensures that comprehensive simulations can be conducted under both singlet and triplet initial state conditions. As previously mentioned, there are two distinct methods, *direct* for small spin systems and *stochastic* for large spin systems, that utilize either *Krylov* subspace or *autoexpm* methods (discussed in SI) for state vector propagation. For the *stochastic* method, *MolSpin* includes SU(Z) and Coherent spin state sampling methods, although SU(Z) states are recommended for all computations and Coherent Spin states only for research purposes.

In total, *MolSpin* offers eight different SSE tasks, each characterized by varying levels of accuracy, computational demands, and observables to calculate (see Tab. S3). Users can choose the task most suitable for their specific needs, with additional information on these options available in the *MolSpin* manual [21].

4 Simulation of selected Examples

In this section, we aim to demonstrate the capabilities of our generalized framework for simulating the spin dynamics inherent in the RPM. We will achieve this by both replicating established results and exploring the behavior of new systems.

Initially, we will focus on the outcomes of large systems simulated with a static Hamiltonian, including phenomena such as charge recombination along molecular wires [20] and the quantum needle effect in the case of magnetoreception observed in the $\left[\mathrm{FAD}^{\bullet-}\ \mathrm{TrpH}^{\bullet+}\right]$ radical pair simulations.

Subsequently, we will revisit the recent work on the driven dynamics of radical pairs by Smith *et al.*, where evidence of yield enhancement across different motion regimes was uncovered [18]. By reproducing key figures, we aim to corroborate the accuracy of the time-dependent methods implemented in *MolSpin*.

We will conclude our exploration by delving into relaxation effects in the $\left[\mathrm{FAD}^{\bullet-}\ \mathrm{TrpH}^{\bullet+}\right]$ system. Initially, we will highlight the results obtained using both BRW and SSE approaches, illustrating their agreement when considering fluctuating hyperfine interactions extracted from molecular dynamics (MD) simulations. Following this, we will extend our investigation to encompass regimes, motions, and spin system sizes that have remained unexplored due to the limitations of approximate methods. This analysis will underscore the versatility and universality of the method implemented in *MolSpin*, emphasizing its potential for further applications in this domain.

4.1 Molecular Wires

Molecular wires have been a subject of interest and research [30, 31]. They are designed, as a Donor-Bridge-Acceptor (D-B-A) system, to mimic the efficient long-range charge transport found in photosynthetic reaction centers [31]. Weiss *et al.* [32] extensively investigated *para*-phenylene molecular wires, measuring experimentally the relative triplet and radical yield changes at different wire lengths and magnetic field strengths. More specifically, they considered $\mathrm{PTZ}^{\bullet+} - \mathrm{Ph}_n - \mathrm{PDI}^{\bullet-}$ systems, consisting of a phenothiazine (PTZ) donor, a perylene-3,4:9,10-bis(dicarboximide) (PDI) acceptor, and a bridge of n para-phenylene rings. The scheme of the system is illustrated in Fig. 2a, where the length of the wire is controlled by the number of para-phenylene rings, n, that ranged from 2 to 5. Fay *et al.* [20] investigated these experimental results and modeled the spin dynamics computationally.

Fay *et al.* tried to fit different rate constants for singlet and triplet recombination pathways, and the resulting spin dynamics, to reconstruct relative yields and overall charge recombination rate constants that were measured by transient absorption spectroscopy. The exploration of the simple radical pair model to explain magnetic field effects and the inability to match predictions by experiments, led Fay *et al.* to explore magnetic-field-independent contributions to the dynamics that are not usually considered in simple models.

In this section, we chose to replicate the dynamics of an $n = 4$ molecular wire, Fay *et* *al.* [20], which can be fully fitted to experimental results of relative radical pair yield versus magnetic field data without incorporating any correction factors to raw results. As shown in Fig. 2a, one of the main challenges in this example is the number of nuclei to be considered (in total 17 nuclei).

The Hamiltonian that models the rapidly tumbling molecular wires in solution is given by:

$$\hat{H} = \hat{H}_1 + \hat{H}_2 - 2J\hat{\mathbf{S}}_1 \cdot \hat{\mathbf{S}}_2, \tag{23}$$

$$\hat{H}_i = -\gamma_i \tilde{\mathbf{B}} \cdot \hat{\mathbf{S}}_i + \sum_{k=1}^{N_i} a_{ik} \hat{\mathbf{I}}_{ik} \cdot \hat{\mathbf{S}}_i, \tag{24}$$

where γ_i is the gyromagnetic ratio of radical i (free electron gyromagnetic ratio was used for both radicals), a_{ik} is the isotropic hyperfine coupling constant, and J is the exchange coupling between the electron spins. The dynamics follow Eq. 1. All 17 nuclei (^{1}H, ^{14}N) were included in the spin dynamics, as shown in Fig. 2a. No spin density was assumed at the black region of Fig. 2a. The magnitudes of the hyperfine couplings were taken from experimental measurements in Ref. [32], and the signs of the interactions were determined with DFT calculations in Ref. [20]. The exchange constant $2J$ was taken from experiments, in Ref. [32], as 6.4 mT. The experimental determined recombination rate constants were $k_T = 350\ \mu s^{-1}$ and $k_S = 2.45\ \mu s^{-1}$.

The experiments for an $n = 4$ molecular wire measured the relative radical pair yield, $\Phi_{RP}(\tilde{\mathbf{B}})/\Phi_{RP}(0)$, or radical pair survival probability, 50 ns after the initial photoexcitation pulse. Hence, the radical pair yield for a given magnetic field $\vec{B}$ is measured as:

$$\Phi_{RP}(\vec{B}, t) = \int_0^t P_{RP}(\tau) d\tau, \tag{25}$$

where $P_{RP}(\tau) = \mathrm{Tr}\left[\hat{\rho}(\tau)\right]$, or essentially tracking the yield of the identity projection operator at $t = 50$ ns. This computation was done using MC sampling with the SU(Z) spin states method for a Hamiltonian without time dependencies (*StaticHS-StochYields*). Only 1 spin state was required to simulate the system (which is a significant improvement over 200 spin states that were used to simulate the same graph in Fay *et al.* [20] study that utilized coherent spin states, which have error scaling of $\mathcal{O}(1/\sqrt{M})$ compared to $\mathcal{O}(1/\sqrt{MZ})$, as detailed before). A precise input can be found in Section 8.4 of the SI. The reproduced relative radical pair yield is shown in Fig. 2b.

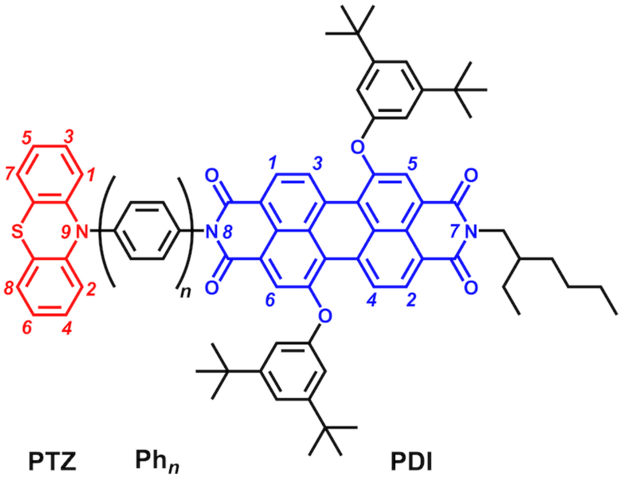

(a)

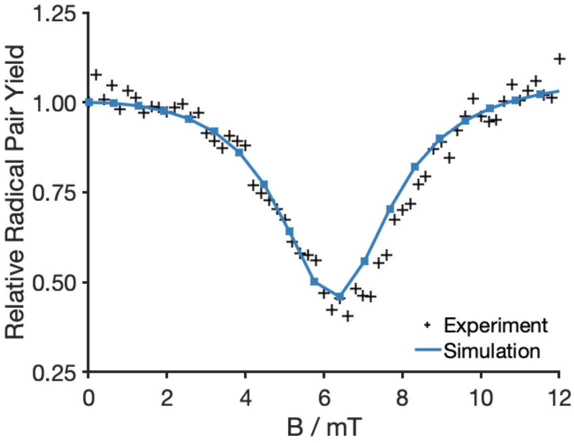

(b)

Figure 2: a) The chemical structure of $\mathrm{PTZ}^{\bullet+} - \mathrm{Ph}_n - \mathrm{PDI}^{\bullet-}$ molecular wire with donor (PTZ) colored in red and acceptor (PDI) colored in blue. In total, 17 nuclei were included in the calculation and are labeled in the figure. Hyperfine coupling parameters were taken from Ref. [20]. b) Relative Radical Pair Yield against magnetic field strength for $\mathrm{PTZ}^{\bullet+} - \mathrm{Ph}_4 - \mathrm{PDI}^{\bullet-}$ molecular wire. Experimental data (crosses) was taken from Weiss *et al.*[32].

As can be observed, the influence of the magnetic field strength on the molecular wire radical pair can be reproduced, revealing a minimum of relative radical pair yield at around 6.4 mT as expected for a "$2J$-resonance".

4.2 Quantum Needle of Magnetoreception

The phenomenon of magnetoreception in migratory species has attracted recent attention in the field of quantum biology [2, 6–10]. The theory posits that a photo-induced radical pair within a cryptochrome protein could enable a species to detect the Earth's weak magnetic field. Depending on the orientation of the $\vec{B}$-field with respect to the radical pair, this could be utilized as a navigational compass [2, 7, 10]. Specifically, it is hypothesized that the formation of a radical pair from FAD and TrpH through a light-induced electron transfer cascade may act as a sensor for an external magnetic field [8].

Hiscock *et al.* [2] examined a $\left[\mathrm{FAD}^{\bullet-}\ \mathrm{TrpH}^{\bullet+}\right]$ system, inspired by cryptochrome, that exhibited a pronounced feature at $\theta = 90°$ angle. This feature was interpreted as a result of state mixing associated with avoided energy-level crossings of the system, a purely quantum mechanical effect. Investigations have been conducted to ascertain whether semiclassical calculations would suffice to model the spin dynamics of these systems [27], making the quantum mechanical feature an attractive hypothesis for a quantum sensor.

However, this hypothesis has limitations. To observe the effect, long spin-coherence lifetimes (10–100 μs) are required, which have not been reported in any biological system. Additionally, previous calculations were constrained to 14 nuclear spins and omitted coupling terms between electron spins, such as exchange and EED, primarily due to computational limitations at the time of the study [2].

In this study, we reproduced the graph from Ref. [2] for a 14 nuclear spins (Fig. 1a) radical pair system in Fig. 3a. A description of the *MolSpin* input can be found in Section 8.5 of the SI. We performed a calculation using a stochastic approach with SU(Z) spin states, including EED and exchange couplings (Fig. 3b). The full coupling tensor, $\mathbf{C} = \mathbf{D} - 2J\mathbf{I}$, used in the calculations, was derived for the FAD-TrpC radical pair in *Drosophila* cryptochrome [27]:

$$\mathbf{C} = \begin{pmatrix} -0.382276 & 0.292979 & -0.146796 \\ 0.292979 & -0.652196 & 0.229243 \\ -0.146796 & 0.229243 & -0.309528 \end{pmatrix} \mathrm{mT} \tag{26}$$

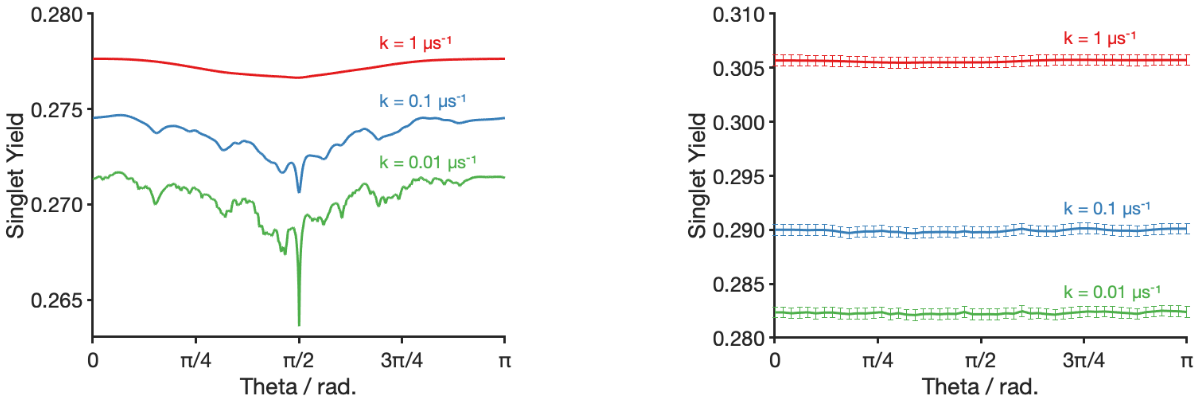

(a)

(b)

Figure 3: a) Graphs of Singlet Yield, Φ_S, vary with θ for radical pairs with symmetric recombination rates ranging between 1 and 0.01 μs^{-1}. This system has no interadical couplings, and computations are done with the *MolSpin* method described in Ref. [33]. For clarity, the $k = 0.1$ μs^{-1} graph is shifted by $+0.0025$. b) Graphs of Singlet Yield, Φ_S, vary with θ for radical pairs with symmetric recombination rates ranging between 1 and 0.01 μs^{-1}. This system has electron spin coupling defined in Eq. 26. A stochastic method with SU(Z) states is used. The evaluation of the error is described in detail in SI, Section 2. The timestep is set to 4 ns and MC sampling to $M = 1$. Total integration times are 0.691 μs for $k = 1$ μs^{-1}, 6.91 μs for $k = 0.1$ μs^{-1}, and 69.08 μs for $k = 0.01$ μs^{-1}. For a) and b), 14 nuclear spins are used in spin dynamics: N5, N10, H6, 3 × H8, Hβ, for FAD, and N1, H1, H2, H4, H6, H7, Hβ1, for TrpH. Both systems in a) and b) have a singlet initial state $\hat{\rho}(0) = 1/Z\ \hat{P}_S$.

Our results with electron-electron spin couplings indicate that the distinct spike is removed, a known effect when intra-radical couplings are considered [34]. This observation does not necessarily preclude the possibility of a spike in systems with specific inter-radical couplings. Some studies have suggested mechanisms by which exchange and EED interactions might compensate each other, increasing the overall anisotropy of the singlet yield [35]. Hence, under special circumstances, a spike may emerge in the quantum dynamics of more complex radical pair systems. Nonetheless, the current study primarily illustrates that large systems and long radical pair lifetimes (1–100 μs) can be effectively computed using the new stochastic method implemented in *MolSpin*.

4.3 Driven Dynamics in Magnetoreception

Motivated by the observed impact of singlet yield anisotropy reduction of intra-radical pair interactions, as detailed in the last section, researchers have explored additional mechanisms that might compensate for these effects. Smith *et al.* investigated the possibility of modulating inter-radical distances to produce an increase in anisotropies [18] that would enhance the compass sensitivity of model systems. They introduced the concept of a "live"-radical pair, characterized by a driven model of radical pair dynamics with coherently modulated recombination rates, exchange, and EED interactions. Their theoretical analysis concluded that such a dynamic system could, in principle, exhibit greater sensitivity compared to a static counterpart.

Smith *et al.* further proposed potential scenarios that might lead to the harmonic oscillations they studied, such as structural rearrangements following initial charge transfer or sensory transduction [36], or alterations in protein structure due to proton pumping [37]. It is important to note that this hypothesis remains theoretical and has not been empirically validated in *in vivo* systems. Nevertheless, the study provides valuable insights into potential methods for enhancing the sensitivity of a magnetic compass, which, according to current simulations, may be inadequate in static systems with electron-electron interactions.

Furthermore, the study conducted by Smith *et al.* underscores the advanced capabilities of *MolSpin* in implementing time-dependent dynamics using the SSE. The software enables the simulation of intricate time-dependent dynamics in driven systems, accommodating changes in recombination rates and Hamiltonian coupling values. As such, it constitutes a robust tool for continued research and modeling within this domain.

The master equation utilized for the model, corresponding to the reaction scheme depicted in Fig. 4a, encompasses time-dependent singlet-triplet inter-conversion, forward recombination of singlet/triplet states (denoted by k_f), and time-dependent backward recombination of the singlet state to the ground state (denoted by $k_b(t)$) [18]:

$$\frac{d\hat{\rho}(t)}{dt} = -i\left[\hat{H}(t), \hat{\rho}(t)\right] - \frac{k_b(t)}{2}\left\{\hat{P}_S, \hat{\rho}(t)\right\} - k_f\hat{\rho}(t), \tag{27}$$

where an effective Hamiltonian $\hat{H}_{\text{eff}}(t)$ can be set as [18] (Note that the Hamiltonian in this form is used in the wave function formalism not Eq. (27)):

$$\hat{H}_{\text{eff}}(t) = \hat{H}(t) - i\left(\frac{k_b(t)}{2}\hat{P}_S + \frac{k_f}{2}\mathbb{I}\right). \tag{28}$$

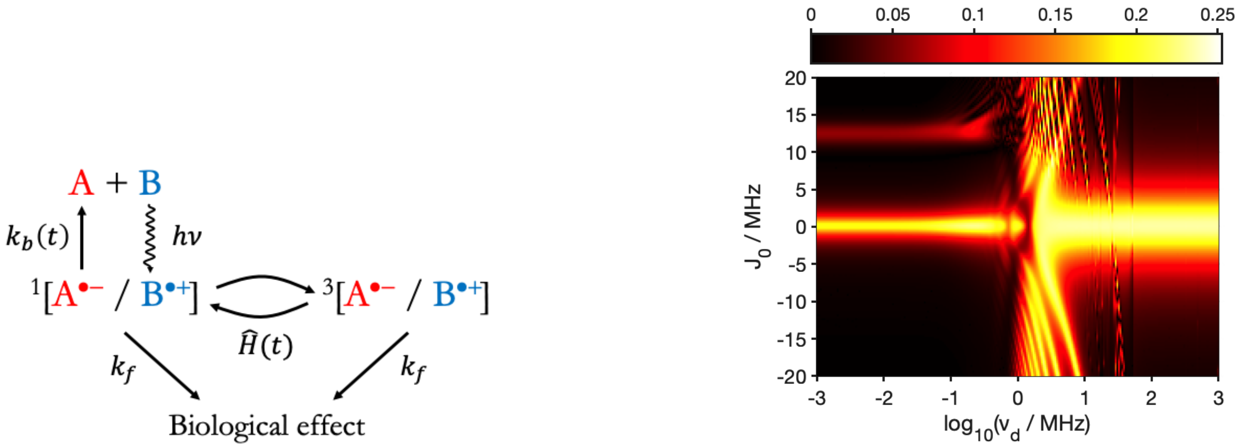

(a) (b)

Figure 4: a) The reaction scheme of a driven radical pair model that has coherently modulating radical pair distance. In the case of our example, $A^{\bullet-}$ and $B^{\bullet+}$ will a $\left[\text{FAD}^{\bullet-}\ \text{TrpH}^{\bullet+}\right]$ radical pair. b) Color Maps of relative anisotropy χ for different values of exchange interaction strength J_0 and driving frequency ν_d. The system is a toy model of one nuclear spin that neglected EED interaction. Magnetic field strength was set to $|\boldsymbol{B}| = 50\ \mu T$. The here presented heat map is in excellent agreement with the results of Smith *et al.* [18].

The effective Hamiltonian $\hat{H}_{\text{eff}}(t)$ integrates both the spin interactions and the recombination terms, providing a comprehensive representation of the system's dynamics.

We elected to replicate a basic radical pair system consisting of a single hyperfine-coupled nitrogen atom (spin $I = 1$) in one radical, with no hyperfine interactions in the other radical. Although the study by Smith *et al.* includes more complex examples, our focus here is to demonstrate the capability of including time-dependency in both spin interactions and recombination rate simultaneously, for which this simple model is well-suited.

The inter-radical distance of this system is described by Smith *et al.* [18] as:

$$r(t) = \frac{\Delta_d}{2}\left[1 - \cos(2\pi\nu_d t)\right] + r_0, \tag{29}$$

where Δ_d is the amplitude of oscillation, set to 3 Å, ν_d is the driving frequency ranging from 1 kHz to 1 GHz, and r_0 is the inter-radical distance of the static radical pair, set to $r_0 = 17.8$ Å as described by Smith *et al.* [18].

The singlet recombination is chosen in this exponential form [38]:

$$k_b(t) = k_{b_0}\ \exp\left[-\beta(r(t) - r_0)\right], \tag{30}$$

and the electron exchange interaction follows:

$$J(t) = J_0 \ \exp\left[-\beta\left(r(t) - r_0\right)\right], \tag{31}$$

with $k_{b_0} = 2\ \mu s^{-1}$, $k_f = 1\ \mu s^{-1}$, and $\beta = 1.4\ \text{Å}^{-1}$ [39]. J_0 is a variable parameter between -20 MHz and 20 MHz. The EED interaction is not included.

The single hyperfine interaction is assumed to have the same axial symmetry and magnitude as the N5 atom in FAD$^{\bullet -}$ radical, with the principal components $A_{xx} = A_{yy} = A_{\perp} = -2.6$ MHz and $A_{zz} = A_{\parallel} = 49.2$ MHz.

To evaluate the directional magnetic field effect (MFE), the relative anisotropy χ is computed:

$$\chi = \frac{|\Phi_{\parallel} - \Phi_{\perp}|}{\max(\Phi_{\parallel}, \Phi_{\perp})}, \tag{32}$$

where $\Phi_{\parallel}$ is the singlet yield computed for a static magnetic field in a parallel direction, and $\Phi_{\perp}$ is the corresponding measure for a perpendicular magnetic field with respect to the A_{zz} component. The resulting graph of relative anisotropy for different J_0 and ν_d values is displayed in Fig. 4b. In the static case, intra-radical coupling appears to suppress magnetic field sensitivity for values of modulus $|J_0| \geq 1$ MHz. However, as the driving frequency increases, this suppression is mitigated, with a driving frequency in the approximate range of 1 to 10 MHz enabling recovery of MFE for $-20 \leq J_0 \leq 20$ MHz. The study by Smith *et al.* underscores the potential significance of including time-dependent effects for a functional magnetic compass within cryptochrome proteins. As demonstrated, *MolSpin* can be effectively employed to model time-dependent Hamiltonians.

However, it should be noted that "artificial" model Hamiltonians may not always be suitable for describing motions and other effects that might induce spin relaxation. Therefore, it is also crucial to have the ability to use time-dependent data extracted from multi-scale approaches, such as those combining quantum chemical (QC) calculations and MD simulations. The next section will showcase how *MolSpin* is adept at addressing such challenges.

4.4 Realistic spin systems using MD-Trajectories

The explicit description of the relaxation process in biological systems, such as the cryptochrome protein in magnetoreception, remains one of the major challenges for the theoretical investigation of realistic spin systems. A particularly difficult aspect is describing the constant motions of the protein structure within several μs, which in turn continually influence and perturb the spin interactions of the radical pair. Furthermore, a precise calculation of hyperfine coupling tensors remains a tedious process. The description of the motion and fluctuations of these interactions can be described sufficiently using MD and QC calculations [9, 10]. Considering the MD/QM data in spin dynamics calculations is, however, still a state-of-the-art problem. The challenges here rely not only on the accuracy of the MD and QC simulations, but also how to incorporate the time-dependencies of the Hamiltonian into the spin equations of motion. There are approaches such as Bloch-Wangness-Redfield (BRW) theory to incorporate the dynamic fluctuations via correlation functions. However, this approach is limited to the number of considered spin due to the rapid growth of matrix dimensionality and has disadvantages when the dynamics of the spin system and the fluctuations are in a similar time regime [12]. An explicit inclusion of time-dependent effects is, thus, more natural and can be sufficiently employed using the SSE approach within *MolSpin*. As an exemplary study, the radical pair within the cryptochrome 4 of European Robin (ErCry4) will be investigated within the framework of our SSE method. Furthermore, a comparison of the SSE method with BRW theory can be found in the SI, section 5.

For the evaluation of induced spin relaxation through dipolar and hyperfiner coupling within our SSE method, a prolonged MD simulation provided by Grüning which has in total a length of 0.95 μs was used. Further information of the employed MD parameter can be found in Ref. [9]. For each 50 ps frame along the MD trajectory (19,060 frames) the FAD$^{\bullet-}$ and TrpH$^{\bullet+}$ geometries were extracted and saturated by replacing the backbone Carbon with a Hydrogen atom. A similar approach was already employed in previous studies and can be found in Ref. [9] and [10]. For each extracted frame, the saturation-Hydrogen was optimized in geometry and hyperfine coupling parameter for 14 nuclei were calculated using the hybrid-functional B3LYP and the EPR-II basis set (see 6 and 7) as implemented in the

Gaussian16 software package [40]. Exemplary hyperfine coupling components fluctuation within the 0.953 μs trajectory of the N5 nuclei within FAD$^{\bullet-}$ are illustrated in Fig. 5b. It is notable, that especially the Azz component is changing significantly in time as was already be found in previous studies [9, 10]. Moreover, for each 50 ps time step the dipolar coupling was calculated between the centroids of the FAD$^{\bullet-}$ and TrpH$^{\bullet+}$ (see Fig. 5b). An evaluation of the time step chosen can be found in the SI, section 6. The fluctuations of the dipolar coupling are less significant compared to the hyperfine couplings of N5.

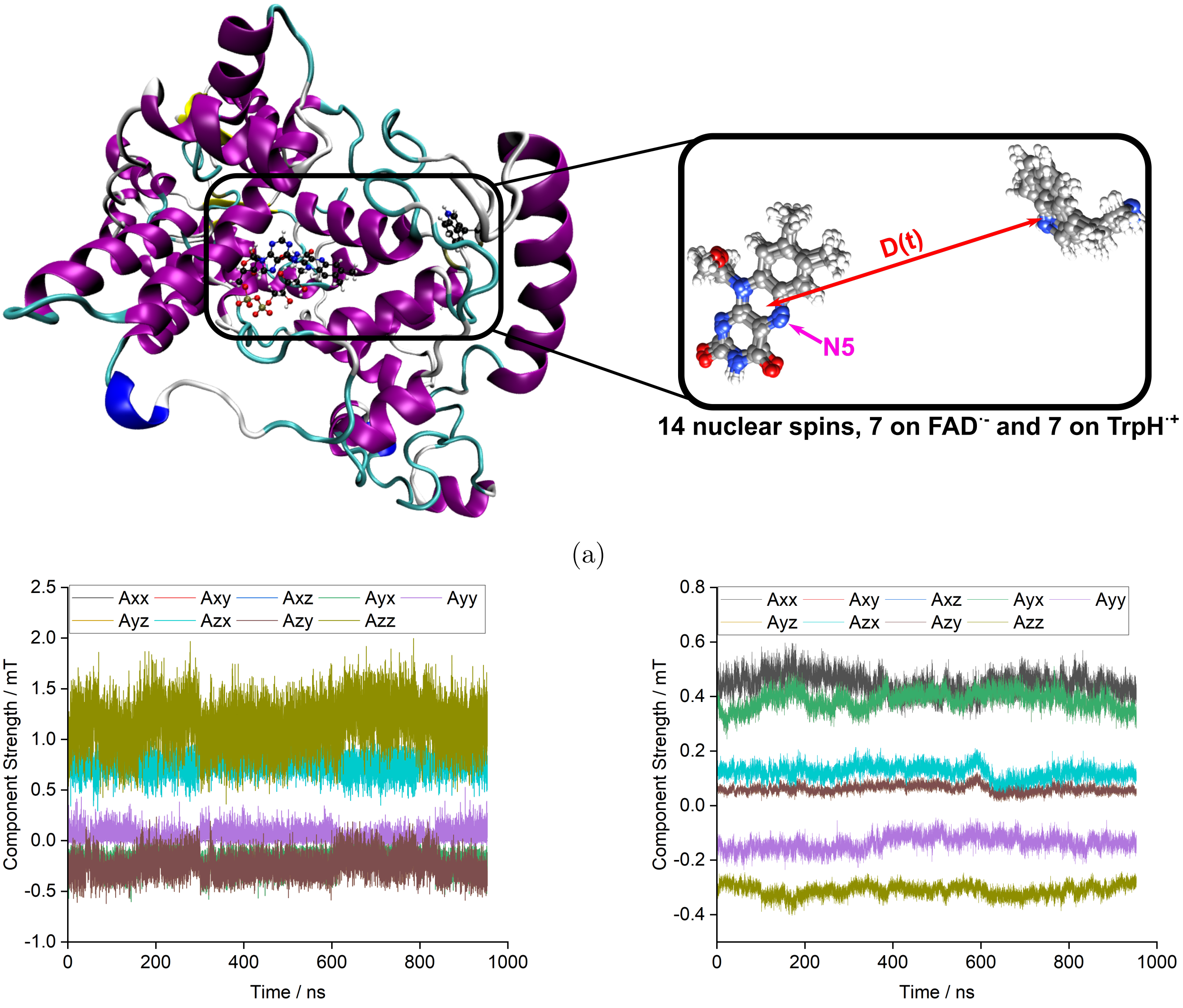

(a)

(b)

(c)

Figure 5: a) Visualization of European Robin cryptochrome 4 and $FAD^{\bullet -}$ and $TrpH^{\bullet +}$ considered in the MD simulation. The whole trajectory of the MD simulation is 0.953 μs. From the MD data, $FAD^{\bullet -}$ and $TrpH^{\bullet +}$ geometries were extracted and spin-spin interactions are calculated for every 50 ps frame. b) Hyperfine coupling fluctuations of N5 nucleus of $FAD^{\bullet -}$ within MD-trajectory for each 50 ps time step. Hyperfine couplings were calculated using the B3LYP functional and the EPR-II basis set. Considered nuclei can be found in the SI Section 7 c) Dipolar coupling fluctuations D(t) between $FAD^{\bullet -}$ and $TrpH^{\bullet +}$ centroids.

To evaluate the effects of the hyperfine and dipolar coupling time-dependencies, a radical pair interacting with 14 nuclear spins is investigated using the SSE method (see Fig. 6). A description of the used input can be found in Section 8.9 of the SI. The lifetime of the singlet-born radical pair was set to 1 μs and a symmetric decay between the singlet and triplet state reactions is assumed. For illustration purposes, an external magnetic field of 1 mT was employed which is rotated around the θ angle with 51 points. At each point, the quantum yield is calculated for different scenarios using the correction factor described in Section 2.4 because the length of the MD trajectory is still too short for a sufficient numerical time integration. As a reference, the quantum yield with a static Hamiltonian (Static) is calculated and compared to the full dynamic Hamiltonian for the hyperfine and dipolar interactions (FDynamics). Moreover, a static calculation without dipolar interaction (StaticNoDipolar) is employed for comparison and each dynamic effect, hyperfine (HDynamicDStatic) or dipolar coupling (HStaticDDynamic), is calculated separately.

Figure 6 illustrates the quantum yields for the described scenarios. As can be observed, the static scenario without the inclusion of dipolar coupling (StaticNoDipolar) reveals the kown signficant anisotropy as demonstrated. After the inclusion of static dipolar coupling between the two electrons (Static), the anisotropy is suppressed similar to the example in section 4.2. Nevertheless, a slight anisotropy can still be found, whereby the minima and maxima are shifted. Note, however, that a strong field of 1 mT was used here and the anisotropy is significantly reduced if a weaker field in the range of the geomagnetic field strength is applied (calculations are still running). When including the time-dependent fluctuations of the dipolar coupling between the two electrons (HStaticDDynamic), only a minor change compared to the Static scenario can be found. While the overall quantum yield is slightly increased, the toplogy of the curve does not change. The minor difference compared to the averaged static scenario indicate that the time-dependency of the dipolar interaction is less dominat and a static averaged scenario already captures the important featues of this interaction. However, incorporating the time-dependency of the 14 hyperfine interactions from $\mathrm{FAD}^{\bullet-}$ and $\mathrm{TrpH}^{\bullet+}$ (HDynamicDStatic) the picture changes significantly. The overall quantum yield is reduced drastically which is in alignment with previous studies

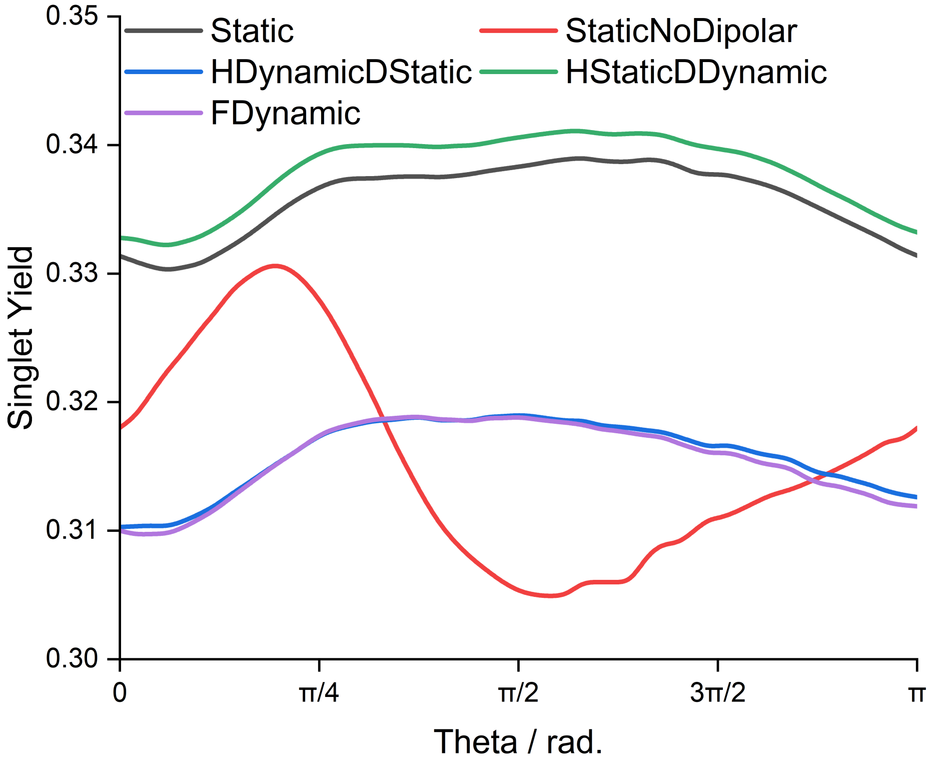

Figure 6: Singlet yield calculations including 14 nuclear, a magnetic field of 1 mT and 1 μs^{-1} symmetric reaction rate. The magnetic field was rotated around θ with 51 points. The dynamic Hamiltonian was constructed using a 50 ps time step for the hyperfine and dipolar interaction. In total 5 MC samples with SUZ states were used. The total time was set to 953.0 ns with a 0.05 ns time step. The correction factor method discussed was employed to produce the singlet yields. Inputs can be found in the SI, section 8.9.

investigating the effects of spin relaxation through hyperfine fluctuation using BRW theory [3, 10, 11]. Furthermore, when comparing the full dynamical scenario (FDynamic) with the HDynamicDStatic it is furthermore revealed that the time-dependency of the dipolar interactions does not have a significant impact on the dynamics of the radical pair. Nevertheless, it becomes obvious that not only the number of nuclear spins is of major importance when investigating a radical pair within a biological system but furthermore the complex time-dependencies have to be incorporated. The here presented illustrative example reveals the possibilities and power of the new *MolSpin* methods that allow for a sufficient investigation of very large spin systems on a multiscale, furthermore, incorporating several time-dependent interactions. The direct consideration of time trajectories allows for a versatile tool kit to explore all kinds of complex time-dependency and directly link the spin simulations to molecular dynamics and quantum chemistry.

5 Conclusions

We have introduced and enhanced a robust computational approach in *MolSpin* for investigating large spin systems under the influence of explicit spin relaxation mechanisms based on the theoretical framework of Lewis *et al.* [13] and Fay *et al.* [14]. By reproducing established radical pair results and presenting novel applications, we have demonstrated the method's accuracy and versatility. This approach enables the simultaneous variation of all interactions and recombination constants, accommodating complex dynamics, and even allowing for the inclusion of explicit time-trajectories from MD/QM simulations. This flexibility opens new avenues for exploring complex motions and relaxation mechanisms and is a significant advantage compared to other relaxation theories which require explicit description of certain dynamical processes.

The illustrated examples emphasize the importance of considering all relevant effects. For example, the inclusion of intra-radical-pair interactions has proven essential for understanding radical pair chemistry within cryptochrome proteins, leading to new insights into how spin relaxation might influence compass sensitivity [18]. While through consideration of intra-radical-pair effects in the case of Hiscock's *et al.* quantum needle a drastically decrease in the magnetic field sensitivity is observed [2], additional spin relaxation mechanisms of the intra-radical-pair interactions may again increase the sensitivity as shown in the example of Smith *et al.* [18]. Moreover, our simulation of a large spin system (16 spins) considering the fluctuation of both hyperfine and dipolar interactions of a 0.952 μs MD simulation revealed that significant effects of time-dependent interactions can get diminished when all interactions are time-dependent.

The algorithm we presented provides a versatile toolkit for efficiently and accurately addressing a wide range of spin-dependent chemical reactions in arbitary complex systems, including those involving many nuclear spin interactions. This, furthermore, includes applications in diverse areas such as the effects of hypomagnetic fields on neurogenesis, the radical pair formation in proteins that may lead to harmful byproducts or molecular systems of any other kind [4, 5, 41]. To conclude, our work underscores the potential of this methodology for advancing the study of spin chemistry in complex environments in an easy-to-use framework.

6 Acknowledgement

The authors are grateful for financial support from the Volkswagen Stiftung (Lichtenberg professorship to IAS), the Deutsche Forschungsgemeinschaft (DFG), project nos. 395940726 (SFB 1372, Magnetoreception and navigation in vertebrates), GRK1885 (Molecular basis of sensory biology) and Hyp*mol (Hyperpolarization in molecular systems TRR386/2-2023). I.A.S. thanks the Lundbeck Foundation and the Ministry for Science and Culture of Lower Saxony (‘Simulations meet experiments on the nanoscale: opening up the quantum world to artificial intelligence’, SMART). Computational resources for the simulations were provided by the CARL Cluster at the Carl-von-Ossietzky University of Oldenburg and the North German Supercomputing Alliance (HLRN). The authors gratefully acknowledge the computing time granted by the Resource Allocation Board and provided on the supercomputer Lise and Emmy at NHR@ZIB and NHR@Göttingen as part of the NHR infrastructure. The calculations for this research were conducted with computing resources under the project NIP00058.

References

(1) Timmel, C.; Till, U.; Brocklehurst, B.; Mclauchlan, K.; Hore, P. J. *Mol. Phys.* **1998**, *95*, 71–89.

(2) Hiscock, H. G.; Worster, S.; Kattnig, D. R.; Steers, C.; Jin, Y.; Manolopoulos, D. E.; Mouritsen, H.; Hore, P. J. *Proc. Natl. Acad. Sci.* **2016**, *113*, 4634–4639.

(3) Gerhards, L.; Nielsen, C.; Kattnig, D. R.; Hore, P. J.; Solov’yov, I. A. *J. Comput. Chem.* **2023**, *44*, 1704–1714.

(4) Husen, P.; Nielsen, C.; Martino, C. F.; Solov’yov, I. A. *J. Chem. Inf. Model.* **2019**, *59*, 4868–4879.

(5) Sampson, C.; Keens, R. H.; Kattnig, D. R. *Phys. Chem. Chem. Phys.* **2019**, *21*, 13526–13538.

(6) Solov'yov, I. A.; Schulten, K. *J. Phys. Chem. B* **2012**, *116*, 1089–1099.

(7) Hore, P. J.; Mouritsen, H. *Annu. Rev. Biophys.* **2016**, *45*, PMID: 27216936, 299–344.

(8) Xu, J.; Jarocha, L. E.; Zollitsch, T.; Konowalczyk, M.; Henbest, K. B.; Richert, S.; Golesworthy, M. J.; Schmidt, J.; Déjean, V.; Sowood, D. J., et al. *Nature* **2021**, *594*, 535–540.

(9) Grüning, G.; Wong, S. Y.; Gerhards, L.; Schuhmann, F.; Kattnig, D. R.; Hore, P. J.; Solov'yov, I. A. *J. Am. Chem. Soc.* **2022**, *144*, PMID: 36459632, 22902–22914.

(10) Kattnig, D. R.; Solov'yov, I. A.; Hore, P. J. *Phys. Chem. Chem. Phys.* **2016**, *18*, 12443–12456.

(11) Worster, S.; Kattnig, D. R.; Hore, P. J. *J. Chem. Phys.* **2016**, *145*.

(12) Fay, T. P.; Lindoy, L. P.; Manolopoulos, D. E. *J. Chem. Phys.* **2019**, *151*.

(13) Lewis, A. M.; Fay, T. P.; Manolopoulos, D. E. *J. Chem. Phys.* **2016**, *145*.

(14) Fay, T. P.; Lindoy, L. P.; Manolopoulos, D. E. *J. Chem. Phys.* **2021**, *154*.

(15) Korol, V.; Husen, P.; Sjulstok, E.; Nielsen, C.; Friis, I.; Frederiksen, A.; Salo, A. B.; Solov'yov, I. A. *J. Am. Chem. Soc. Omega* **2020**, *5*, PMID: 31984283, 1254–1260.

(16) Breuer, H.-P.; Petruccione, F., *The theory of open quantum systems*; Oxford University Press: 2002.

(17) Goldman, M. *J. Magn. Reson.* **2001**, *149*, 160–187.

(18) Smith, L. D.; Chowdhury, F. T.; Peasgood, I.; Dawkins, N.; Kattnig, D. R. *J. Phys. Chem. Lett.* **2022**, *13*, 10500–10506.

(19) Weiße, A.; Wellein, G.; Alvermann, A.; Fehske, H. *Reviews of modern physics* **2006**, *78*, 275.

(20) Fay, T. P.; Lewis, A. M.; Manolopoulos, D. E. *J. Chem. Phys* **2017**, *147*.

(21) **http://www.molspin.eu**.

(22) Radcliffe, J. M. *J. Phys. A* **1971**, *4*, 313–323.

(23) Magnus, W. *Commun. Pure Appl. Math.* **1954**, *7*, 649–673.

(24) Park, T. J.; Light, J. C. *J. Chem. Phys.* **1986**, *85*, 5870–5876.

(25) Pollard, W. T.; Friesner, R. A. *J. Chem. Phys.* **1994**, *100*, 5054–5065.

(26) Al-Mohy, A. H.; Higham, N. J. *SIAM J. Sci. Comput.* **2011**, *33*, 488–511.

(27) Fay, T. P.; Lindoy, L. P.; Manolopoulos, D. E.; Hore, P. J. *Faraday Discussions* **2020**, *221*, 77–91.

(28) Sanderson, C.; Curtin, R. *J. Open Softw.* **2016**, *1*, 26.

(29) Lewis, A., *Spin Dynamics in Radical Pairs*; Springer International Publishing: 2018.

(30) Gray, H. B.; Winkler, J. R. *Proc. Natl. Acad. Sci.* **2005**, *102*, 3534–3539.

(31) Weiss, E. A.; Tauber, M. J.; Kelley, R. F.; Ahrens, M. J.; Ratner, M. A.; Wasielewski, M. R. *J. Am. Chem. Soc.* **2005**, *127*, 11842–11850.

(32) Weiss, E. A.; Ahrens, M. J.; Sinks, L. E.; Gusev, A. V.; Ratner, M. A.; Wasielewski, M. R. *J. Am. Chem. Soc.* **2004**, *126*, 5577–5584.

(33) Nielsen, C.; Solov'yov, I. A. *J. Chem. Phys* **2019**, *151*.

(34) Hiscock, H. G.; Mouritsen, H.; Manolopoulos, D. E.; Hore, P. *Biophys. J.* **2017**, *113*, 1475–1484.

(35) Efimova, O.; Hore, P. J. *Biophys. J.* **2008**, *94*, 1565–1574.

(36) Nordmann, G. C.; Hochstoeger, T.; Keays, D. A. *PLoS Biol.* **2017**, *15*, e2003234.

(37) Friedman, J.; Mourokh, L.; Vittadello, M. *Quantum Rep.* **2021**, *3*, 425–434.

(38) Steiner, U. E.; Ulrich, T. *Chem. Rev.* **1989**, *89*, 51–147.

(39) Moser, C. C.; Keske, J. M.; Warncke, K.; Farid, R. S.; Dutton, P. L. *Nature* **1992**, *355*, 796–802.

(40) Frisch, M. J. et al. **2013**, Gaussian Inc. Wallingford CT 2009.

(41) Hong, G.; Pachter, R. *Eur. Biophys.* **2023**, *52*, 27–37.

Exploring the radical pair mechanism in large spin systems - Introducing the Stochastic Schrödinger Equation into *MolSpin* - Supporting Information

Gediminas Jurgis Pažėra[1*], Ilia A. Solov'yov[2,3,4], P. J. Hore[1], and Luca Gerhards[2*]

[1]Department of Chemistry, University of Oxford, Physical and Theoretical Chemistry Laboratory, Oxford, OX1 3QZ, United Kingdom
[2]Institute of Physics, Carl von Ossietzky Universität Oldenburg, Carl-von-Ossietzky Str. 9-11, 26129 Oldenburg, Germany
[3]Research Center for Neurosensory Science, Carl von Ossietzky Universität Oldenburg, 26111 Oldenburg, Germany
[4]Center for Nanoscale Dynamics (CENAD), Carl von Ossietzky Universität Oldenburg, Institut für Physik, Ammerländer Heerstr. 114-118, 26129 Oldenburg, Germany
[*]Corresponding authors: Gedminas Jurgis Pažėra, gediminas.pazera@ccc.ox.ac.uk; Luca Gerhards, luca.gerhards@uni-oldenburg.de

January 18, 2024

Contents

1 Correction Factor For Quantum Yields

We define the total quantum yield of a radical pair $\Phi_{Total}(T)$ for a propagation time T when $k_S = k_T$, i.e. recombination constants are symmetric, as:

$$\Phi_{Total}(T) = k_S \int_0^T P_{\mathbb{I}}(t)dt \tag{S1}$$

Here $P_{\mathbb{I}}(t) = Tr\left[\hat{\rho}(t)\right]$ and $\Phi_{Total}(\infty) = 1$. Since the spin-dependent radical recombination rate constants for triplet and singlet states are symmetric ($k_S = k_T$), then, $\hat{P}_S + \hat{P}_T = \mathbb{I}$ and the recombination operator simplifies to $\hat{K} = k_S\mathbb{I}$. Hence, the radical pair yield simplifies to [1]:

$$\Phi_{Total}(T) = k_S \int_0^T e^{-k_S t} P_{\mathbb{I}}(t)dt = 1 - e^{-k_S T} \tag{S2}$$

In this case $P_{\mathbb{I}}(t)$ only includes dynamics due to interactions described in the spin Hamiltonian. We will denote $e^{-k_S T}$ as ϵ for simplicity. When determining the quantum yields of various operators, it is essential to compute the integral as time approaches infinity, corresponding to the point where all states have completely decayed (i.e., when $\epsilon = 0$). Under such conditions, the following equation is valid:

$$\Phi_S(\infty) + \Phi_T(\infty) = \Phi_{Total}(\infty) = 1 \tag{S3}$$

When evaluating the integral up to a time T, we obtain:

$$\Phi_S(T) + \Phi_T(T) = \Phi_{Total}(T) = 1 - e^{-k_S T} \tag{S4}$$

In practical situations, we do not integrate the expectation values to $T = \infty$. Instead, we integrate up to a point where ϵ is close to 0. Nonetheless, we also want to ensure that $\Phi_S + \Phi_T = 1$. Hence, we can introduce a novel heuristic:

$$\frac{\Phi_S(T)}{1 - e^{-k_S T}} + \frac{\Phi_T(T)}{1 - e^{-k_S T}} = \Phi_S(\infty) + \Phi_T(\infty) = 1 \tag{S5}$$

Or, in general for a projection operator Θ:

$$\Phi_\Theta(\infty) = \frac{k_\Theta}{1 - e^{-k_S T}} \int_0^T P_\Theta(t)dt \tag{S6}$$

$P_\Theta(t)$ has both Hamiltonian and recombination dynamics.

The parameter ϵ serves as a total time estimator in *MolSpin* simulations. Users have the option to specify their preferred total time in ns or to define ϵ as a variable between 0 and 1, upon which the program will compute the total time as:

$$T = \frac{\ln \epsilon^{-1}}{k_S} \tag{S7}$$

Some common choices of ϵ are 0.5, 0.1 and 0.01 ($\epsilon = 0.5$ will have the largest error in the quantum yield estimation and $\epsilon = 0.01$ will have the smallest error out of the three).

Our modification to the quantum yield calculations has proven effective in substantially reducing the integration time required for converged results. To illustrate this, we'll examine a static 14 nuclear spin $\left[\mathrm{FAD}^{\bullet -}\ \mathrm{TrpH}^{\bullet +}\right]$ radical pair model. This model incorporates the hyperfine parameters for N5, N10, H6, $H8_1$, $H8_2$, $H8_3$, $H\beta$ nuclei in FAD, as well as N1, H1, H2, H4, H6, H7, $H\beta_1$ nuclei in TrpH, sourced from Ref. [2]. The stochastic method was used with $M = 4$ MC samples. Notably, the system had EED and exchange interactions described in Ref. [3], and $|\mathbf{B}| = 50\ \mu T$, with magnetic field vector aligned with the z-axis. Figure S1 illustrates the simulation results for the 14 spin system system under varying symmetric recombination rates, both with and without the correction factor.

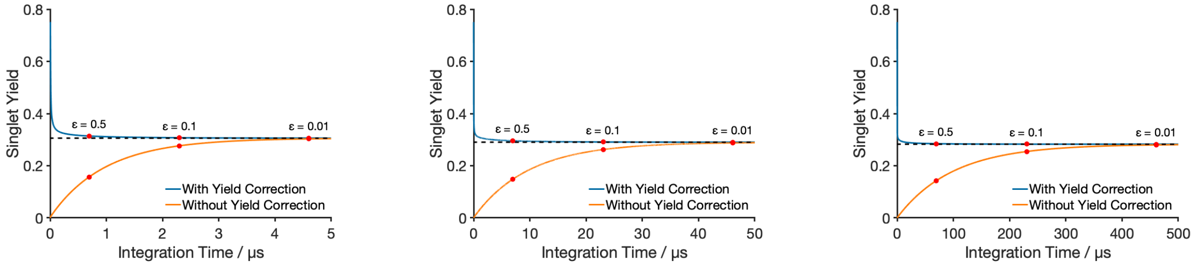

(a) (b) (c)

Figure S1: Singlet yield, Φ_S, versus integration time, T, graphs for different symmetric recombination rates: a) $k_S = 1\ \mu s^{-1}$, b) $k_S = 0.1\ \mu s^{-1}$, c) $k_S = 0.01\ \mu s^{-1}$. The black dashed line illustrates the converged value of the singlet yield. The system that was simulated contained 14 nuclei and is described in the text. Different highlighted values of ϵ correspond to times calculated by Eq. S7.

Remarkably, across various recombination rate constants, there's a distinct decrease in the total integration time required to achieve results with graphical precision. In every instance, yields calculated with the correction factor reached convergence by $\epsilon = 0.5$ ($T = T_1$), if not sooner. In contrast, without the yield correction, convergence typically requires $\epsilon = 0.01$ ($T = T_2$). Thus, the ratio of time between T_1 and T_2 is:

$$\frac{T_2}{T_1} = \frac{\ln 0.01^{-1} k_S}{k_S \ln 0.5^{-1}} = \frac{\ln 0.01}{\ln 0.5} \approx 6.6 \tag{S8}$$

A computational reduction of at least 6 times is a significant computational speedup that offers calculations of larger systems previously unavailable, and this reduction is achieved without compromising accuracy. The principle is not extended for asymmetric recombination rates.

Lastly, the approach can also be extended to time-dependent dynamics. The correction factor heuristic, in principle, predicts the time-evolution of projection operators from T to ∞. In time-independent cases, this works significantly well since the interactions are static, thus, the initial trajectory within a small time interval is enough to predict the trajectory of the remaining time-dependent dynamics with a small error. However, in time-dependent calculations, where interactions are fluctuating and changing during the reaction, it is not as straightforward to apply the correction factor or to estimate the error of the singlet yield calculation. The sufficient time of propagation will depend on the type, magnitude and frequency of change of time-dependent interactions. Hence, we have examined a model system of 4 nuclear spins with varying parameters,that was inspired by the driven radical pair dynamics dynamics from Smith *et al.* [4], to arrive at a general rule of thumb of the total time choice for time-dependent systems.

The spin system contains the 4 nuclear spins, N5, N10 in radical 1 (modeled as FAD) and N1, H1 in radical 2 (modeled as TrpH). Hyperfine interaction tensors are taken from Ref. [2]. The symmetric recombination rate is $k_S = 1\ \mu s^{-1}$ and $|\mathbf{B}| = 1\ mT$ ($\mathbf{B}$ pointed to the z-direction). The time-dependent fluctuation is the exchange coupling between electrons:

$$H(t) = -2J(t)\hat{\mathbf{S}}_1 \cdot \hat{\mathbf{S}}_2 \tag{S9}$$

Here, $J(t)$ is taken in the form of Ref. [4] as an oscillating frequency:

$$J(t) = J_0 \exp(-\beta r(t) - r_0), \tag{S10}$$

where $\beta = 1.4\ \mathring{A}^{-1}$ and J_0 are empirical constants [4]. The time-dependent distance $r(t)$ between the radicals is taken as:

$$r(t) = \frac{\Delta_d}{2}(1 - cos(2\pi\nu_d t)) + r_0. \tag{S11}$$

Here, $\Delta_d = 3\ \mathring{A}$, $r_0 = 17.8\mathring{A}$, and ν_d is the driving frequency [4].

Figure S2 illustrates simulations of the described spin system with $\nu_d = 1$ MHz and different strengths of J_0 parameter. This figure aims to evaluate how the size of the time-dependent perturbation affects the accuracy of applying the heuristic to reduce the required total time of integration. J_0 is varied from 0 mT to 50 mT. In the simulation where $J_0 = 0\ mT$, it is observed that a similar trend to the static case is found: the quantum yield value calculated with the correction factor quickly converges to the exact singlet yield for small integration times. This trend remains valid until $J_0 = 1\ mT$, where larger oscillations appear in the singlet yield values calculated with the correction factor and longer integration times are required for convergence. Nonetheless, it has been found that $\epsilon = 0.1$ is sufficient to get converged expectation values for all cases examined in Fig. S2. If a comparison between the time integration value and the lifetime ($\tau_{Total} = 1/k_S$) of the radical pair is made the following ratio is found:

$$\frac{T_1}{\tau_{Total}} = \frac{\ln 0.1^{-1}}{k_S} \times k_S = \ln 0.1^{-1} \approx 2.3 \tag{S12}$$

Hence, we have found from this example, that an integration time of at most 2.3 × lifetime is sufficient to model time-dependent processes. The other observation found was that for smaller magnitude time-dependent variables a shorter integration time would be sufficient.

Moreover, we have also did an analysis of the effect of the frequency of time-dependent variables on the use of the heuristic to estimate quantum yield values. We have chosen an interaction with $J_0 = 10\ mT$ and varied ν_d. Results are shown in Fig. S3. It is evident that higher motion frequencies lead to a more accurate approximation of the yield correction, while slower motions necessitate a longer integration time. Overall, we can conclude from the examples we analysed, that integration time equal to $\epsilon = 0.1$ should provide an accurate approximation for moderately fast fluctuations with interactions of small to moderate magnitude, relative to other interactions in the system.

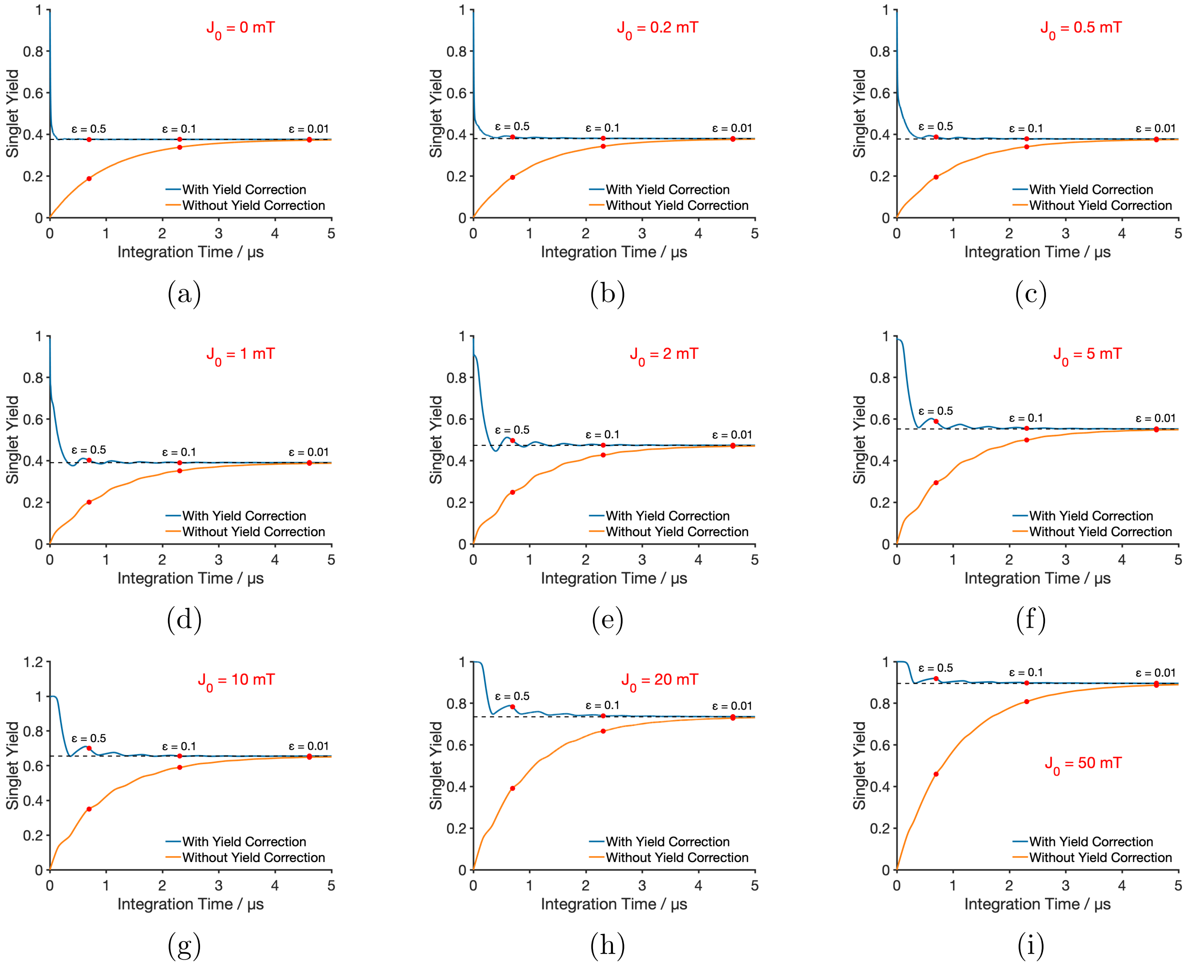

(a) (b) (c)

(d) (e) (f)

(g) (h) (i)

Figure S2: Singlet yield, Φ_S, versus integration time, T, graphs for different J_0 empirical parameters in $J(t)$ equation defined in Eq. S10: a) $J_0 = 0\ mT$, b) $J_0 = 0.2\ mT$, c) $J_0 = 0.5\ mT$, d) $J_0 = 1\ mT$, e) $J_0 = 2\ mT$, f) $J_0 = 5\ mT$, g) $J_0 = 10\ mT$, h) $J_0 = 20\ mT$, i) $J_0 = 50\ mT$. The black dashed line illustrates the converged value of the singlet yield. The system that was simulated contained 4 nuclei and is described in the text. Different highlighted values of ϵ correspond to times calculated by Eq. S7.

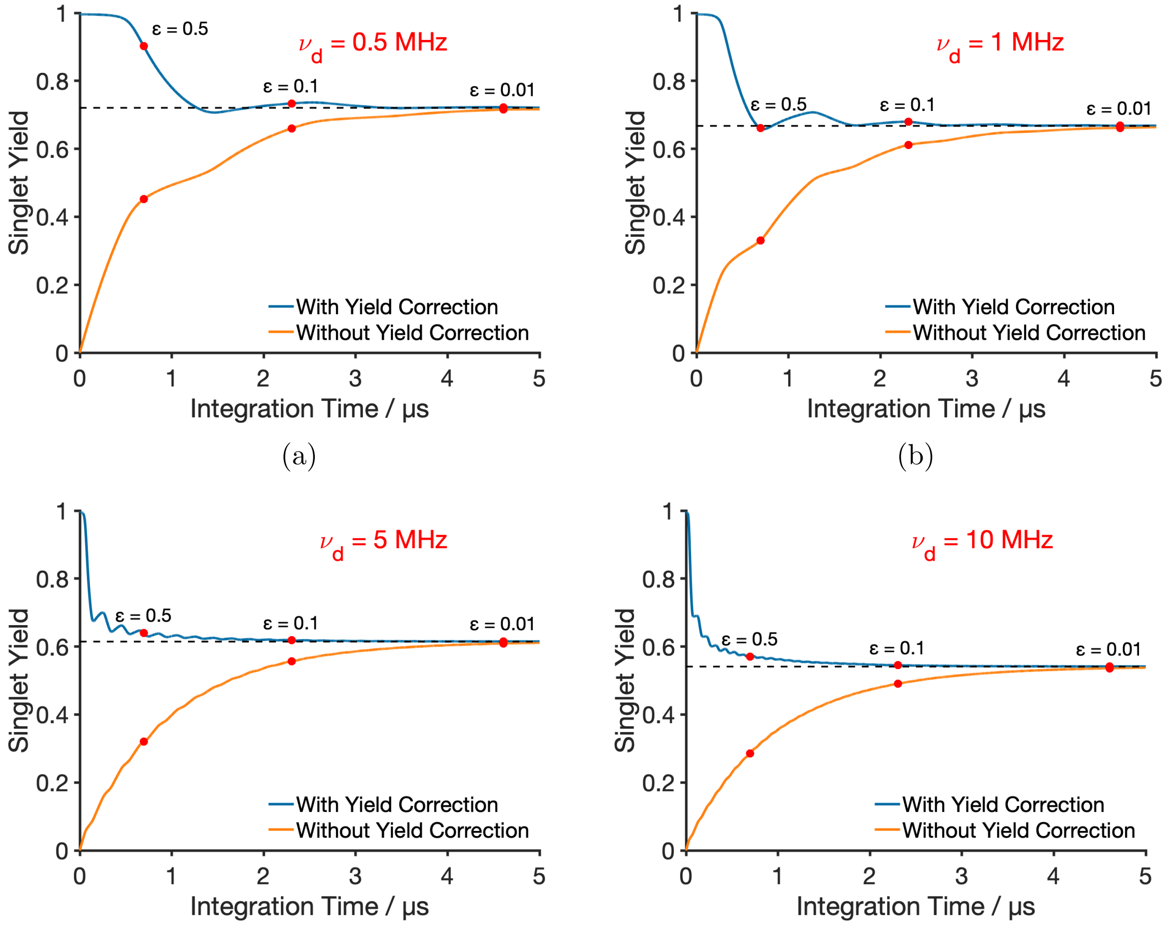

(a)

(b)

(c)

(d)

Figure S3: Singlet yield, Φ_S, versus integration time, T, graphs for different ν_d parameters in $J(t)$ equation defined in Eq. S10, with $J_0 = 10\ mT$: a) $\nu_d = 0.5\ MHz$, b) $\nu_d = 1\ MHz$, c) $\nu_d = 5\ MHz$, $\nu_d = 10\ MHz$.

Finally, we have also evaluated the accuracy of the correction factor when simulating systems with interactions that follow MD trajectories as described in Section 5. MD simulations are significantly resource demanding and the time trajectory of cryptochrome 4 used in Section 5 has a total time of 550 ns. For MD of proteins, a trajectory of that time interval is considered extensively long. However, for spin dynamics of radical pairs which have lifetimes of the order of magnitude of 1 μs the time interval may be too short to yield accurate results. Hence, investigating whether the heuristic could shorten the integration time is relevant to the simulation of the MD data because we would hope to simulate systems with lifetimes of the order of magnitude of 1 μs.

In this work, the main reason for estimating longer lifetime trajectories of radicals than the MD data provides is the comparison of spin dynamics estimations of spin relaxation between BRW and SSE theory. Additionally, it is known that the lifetime of a radical pairs interacting with the geomagnetic field would require a lifetime of 1 μs [5].

In the context of BRW theory, due to its approximations, the interplay between values of correlation times for spin relaxation effects and the dynamics of the radical pair are of mandatory importance. For instance, if the correlation times increases in relation to the dynamics of $\hat{\rho}(t)$, the positivity of the density matrix is not guaranteed due to the perturbative treatment and erratic expectation values will be calculated [6, 7]. Thus, shortening lifetimes of a radical pair with constant correlation times may lead to erratic behavior in the BRW equations. Because of this, the behavior at around $k_S = 1\ \mu s^{-1}$ as shown in Fig. S6 should be considered for comparison of BRW and SSE. On the other hand, to calculated longer lifetimes using SSE, the correction factor approximation has to be used when only 550 ns MD data is available. With a rate constant of $k_S = 1\ \mu s^{-1}$ a radical pair with a lifetime of 1 μs - a quantity around 2 times larger than the total trajectory time - needs to be considered.

Hence, it is mandatory to confirm whether the total time of 550 ns is enough and what sort of error is to be expected. A model four nuclear spin system, which comprised N5, N10 for the FAD radical and $H\beta_1$, $H\beta_2$ for the TrpH radical, described and labeled in Sec. 5.2 is used. Firstly, the symmetric recombination rate is set to $k_S = 10\ \mu s^{-1}$ - chosen so that the 550 ns trajectory capture converged singlet yield values for this system without the use of the heuristic. $|\mathbf{B}| = 1\ mT$, the magnetic field aligned with the z-axis. The direct method was used which gives accurate results without any approximations and a time-step of $dt = 0.5\ ns$. The results are shown in Fig. S4.

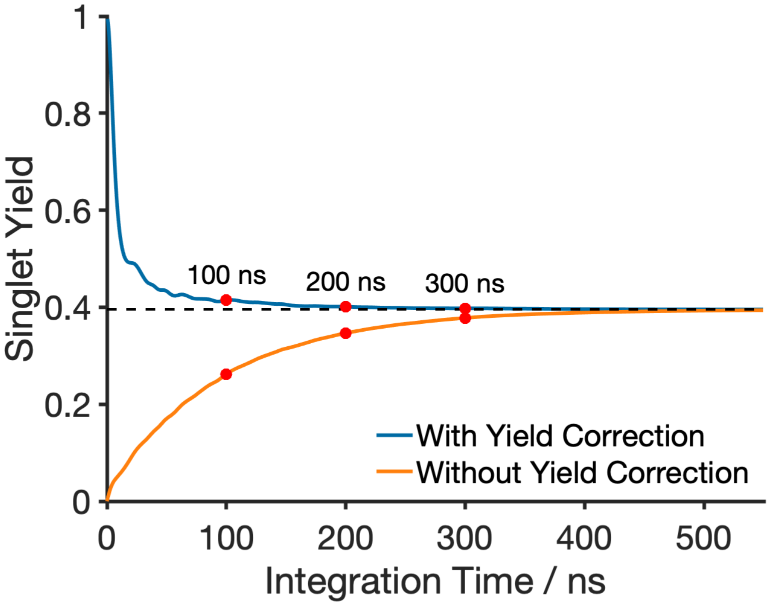

Figure S4: Singlet Yield, Φ_S, versus integration time, T, graphs for the 4 nuclear spin radical pair system that had time-dependent interaction from MD trajectory of 550 ns.

In Fig. S4, the labeled red dots reveal that an integration time of $T = 200\ ns$ is suitable to model the spin system accurately. Since the lifetime was equal to $\tau_{Total} = 100\ ns$, our rule of thumb described before still holds and you would need an integration time that is around 2 times the lifetime of the radical pair to accurately model this system with the heuristic. Besides that, for an integration time that is equal to the lifetime, the results are close to converged values yet a minor error in the quantum yield can be observed. For an integration time that is 3 times as large as the lifetime (300 ns), the singlet yield is clearly fully converged without any errors.

In conclusion, for the here presented spin system, integration times that are around 2 times larger than the lifetime would be sufficient to model singlet yield values (similar to the time-independent case). If the total time is 550 ns, this means a system with a lifetime of 275 ns could be confidently modeled. Hence, the symmetric recombination rate for this lifetime is $k_S \approx 3.64\ \mu s^{-1}$, and k_S can be $k_S \geq 3.6 \mu s^{-1}$.

Here, only the $k_S = 10\ \mu s^{-1}$ scenario is considered and it is questionable whether estimating a system's dynamics for a longer lifetime would be appropriate. However, it can be assumed that in the first approximation the frequency of motions and their perturbation strength would not change significantly after 550 ns. Hence, if the interactions would not change drastically, then using the here presented heuristic to yield results for longer lifetimes can be applied.

2 Accuracy of the Stochastic Method

In order to evaluate the accuracy of the stochastic method using Monte Carlo sampling, the standard deviation σ of different spin system sizes is evaluated using the following formalism:

$$\sigma = \sqrt{\frac{1}{N-1}\sum_{i=1}^{N}(\Phi_{Si} - \mu)^2},$$

where μ is the singlet yield mean, N is the number of sample specific singlet yields, and Φ_{Si} is a specific singlet quantum yield.

Calculations are performed for various systems containing nuclear spin numbers ranging from 10 to 16 to examine their statistical error. The selected systems are models for the $\left[\text{FAD}^{\bullet-}\text{TrpH}^{\bullet+}\right]$ radical pair, chosen due to their extensive computational analysis. Each system includes at least the following 10 nuclear spins: N5, N10, H6, H8_1, H8_2, H8_3, Hβ_1 for FAD, and N1, H1, H2 for TrpH. For each additional spin, the following hyperfine constants and nuclei are added in direct order: H4, H6, H7, Hβ_1 for TrpH, and Hβ_2, H7_1 for FAD. The hyperfine interaction parameters are listed in Ref. [2]. The symmetric recombination rate is set to $k_S = 1\,\mu s^{-1}$. Only one MC sample, $M = 1$, is used to observe how the error scales with Z. The heuristic for shortening integration time is applied, with the total time estimated by $\epsilon = 0.5$. The time step is set to 4 ns, and the magnetic field is directed along the z-axis, with a strength of $|\mathbf{B}| = 1\,\text{mT}$.

The data is assumed to follow a normal distribution. It's important to note that the standard deviation values presented in the table are calculated based on 500 samples; this detail should be made explicit earlier in the methodology or data collection section. For each data set, the mean, μ, and standard deviation, σ, are determined, and all values, along with the estimated error, $\epsilon_{\text{estimated}}$, are presented in Table S1.

No. of Nuclear Spins	Z	μ	σ
10 spins	13824	0.39480	0.00216
11 spins	27648	0.38853	0.00140
12 spins	55296	0.38546	0.00102
13 spins	110592	0.38290	0.00070
14 spins	221184	0.34984	0.00046
15 spins	442368	0.34706	0.00031
16 spins	884736	0.34661	0.00022

Table S1: Properties of systems with varying numbers of nuclear spins. Z denotes the size of the full spin space, μ represents the mean, and σ is the standard deviation of 500 samples.

Selected probability distributions, drawn with σ values from Table S1, are depicted in Fig. S5. It is evident that the error diminishes and the error distribution narrows as the size of the spin space increases. Therefore, it can be concluded that with $M = 1$, the errors are sufficiently small for large systems, those with more than 14 nuclear spins, for most applications.

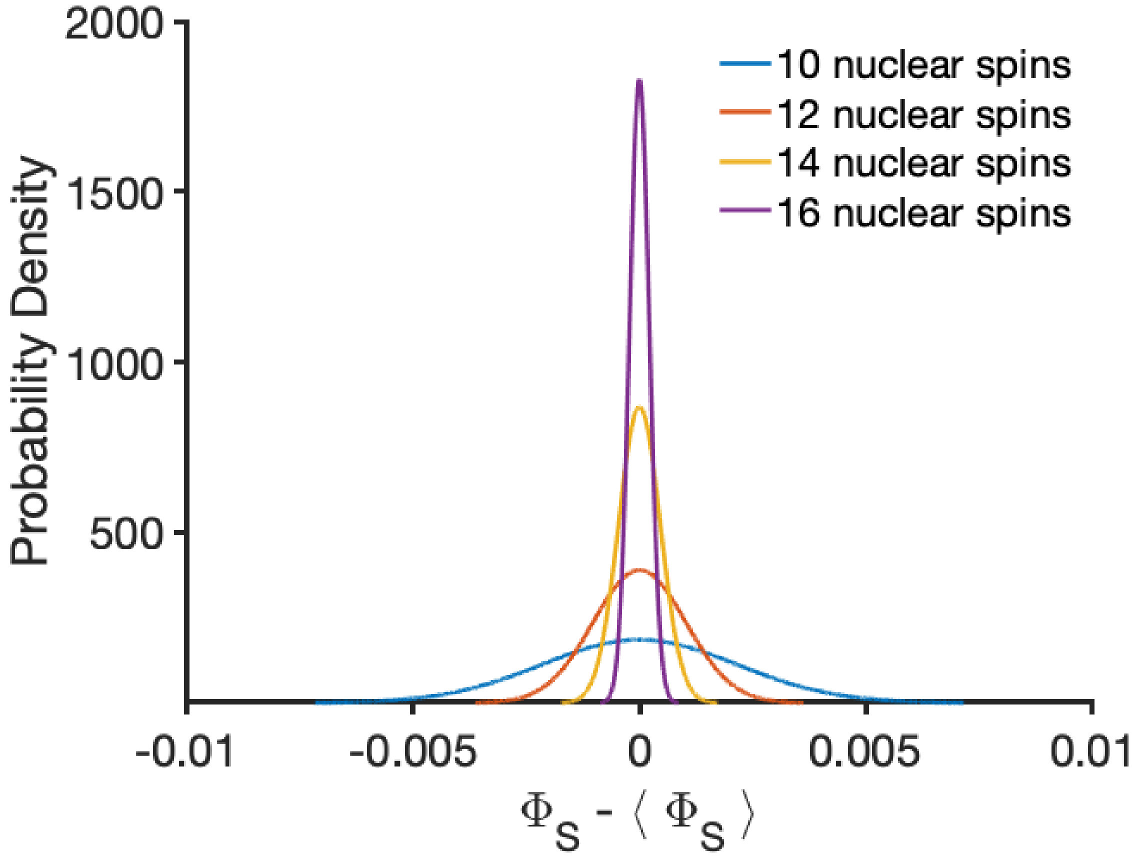

Figure S5: Probability Density Functions for $\Phi_S - \langle\Phi_S\rangle$ values for systems with different numbers of nuclear spins. Here, $\langle\Phi_S\rangle$ denotes the mean Singlet Yield, also represented as μ. The effect of increasing Z is a decrease in error and a narrowing of the probability density, a phenomenon well established in theory [8].

3 AutoExpm Method

AutoExpm method is, to our knowledge, a new implemented algorithm in terms of radical pair spin dynamics for computing the action of matrix exponential on a vector (or block vectors). It is based on scaling and squaring method that is usually used to compute full matrix exponentials and computes the action of the matrix exponential as:[9]

$$e^{-i\hat{H}\delta t}B \approx (T_m(s^{-1}(-i\hat{H}\delta t)))^s B \tag{S13}$$

Here T_m is truncated m term Taylor series:

$$T_m(\hat{A}) = \sum_{j=0}^{m} \frac{\hat{A}^j}{j!} \tag{S14}$$

B is a block of n state vectors:

$$B = \begin{bmatrix} |\Psi_1(t)\rangle & |\Psi_2(t)\rangle & \dots & |\Psi_n(t)\rangle \end{bmatrix} \tag{S15}$$

The method described in the section bellow uses a few key several ideas to make this computation as efficient as possible. It carefully estimates parameters m and s to ensure that the backward error is suitably bounded while the computational cost is minimized, it does shifting to reduce the norm of A (which reduces the cost) and terminates premature when a certain accuracy is reached. All of these feature combined makes a unique algorithm that have a several key advantages to Krylov Subspace algorithms:

1. It can handle multiple columns in B.
2. There are no parameters to be estimated and the algorithm chooses the best ones itself.
3. It can be quicker than Krylov methods in some cases.
4. Predictable cost of the method. Also cost tends to increase with increasing $||\hat{A}||_1$. Whereas for Krylov methods there is only some dependence with $||\hat{A}||_1$.

We will describe the algorithm below which we named "AutoExpm"

3.1 "AutoExpm" Algorithm

The main algorithm is in Alg. 1. It uses $\hat{A}$, δt, B and tolerance tol as an input to solve $\exp(-i\hat{A}\delta t)B$. $\hat{A}$ will be $\hat{H}$ or $\hat{H} - i\hat{K}$. The tolerance will determine how accurate the approximation will be and there are three choices of double, single or half digit precision. $|| \cdot ||_\infty$ in the algorithm itself is the infinity-norm.

Algorithm 1: AutoExpm method for computing the action of the matrix exponential

```
$\mu = \mathrm{Tr}(\hat{A})/n$
$\hat{A} = \hat{A} - \mu\mathcal{I}$
$[m_*, s] = parameters(-iA\delta t, tol)$
// The function is in code Fragment in Alg.  2
$F = B$
$\eta = e^{t\mu/s}$
for $i = 1 : s$ do
    $c_1 = ||B||_\infty$
    for $j = 1 : m_*$ do
        $B = -i\hat{A}B\delta t/(sj)$
        $c_2 = ||B||_\infty$
        $F = F + B$
        if $c_1 + c_2 \le tol||F||_\infty$ then
            break
        $F = \eta F$
        $B = F$
```

The algorithm that estimates optimal parameters s, m_* is shown in Alg. 2. In the algorithm, $|| \cdot ||_1$ is the 1-norm, $\lceil \cdot \rceil$ is the ceiling function, $argmin(\cdot)$ finds the minimum given different arguments and $max(\cdot)$ computes the maximum from given inputs. Besides the algorithm, there a few extra equations used for parameter estimation. First, the equation for optimal cost for a given $\hat{A}$:

$$C_{m_*}(\hat{A}) = min\left\{m\lceil\alpha_p(\hat{A})/\theta_m\rceil : 2 \le p \le p_{max}, p(p-1) - 1 \le m \le m_{max}\right\} \tag{S16}$$

Here p_{max} and m_{max} are maximum parameters for m and p. They are suggested by the authors of the algorithm from experience as $m_{max} = 55$ and $p_{max} = 8$. Also, $\alpha_p(\hat{A})$ is defined as :

$$\alpha_p(\hat{A}) = max(d_p, d_{p+1}),\ d_p = ||\hat{A}^p||_1^{1/p} \tag{S17}$$

θ_m are a number of parameters for different values of m that are used for parameter estimation. They are linked to the tolerance of the method and have different values if either one of "double", "single" and "half" tolerance is used. Selected constants for θ_m are shown in Table S2.

Lastly, the algorithm for parameter estimation also uses this bound to on $||\hat{A}||_1$.

Here n_0 is the number of rows and l is the number of columns in B.

$$||\hat{A}||_1 \leq 2\frac{l}{n_0}\frac{\theta_{m_{max}}}{m_{max}}p_{max}(p_{max}+3) \tag{S18}$$

Algorithm 2: Parameter estimation for autoexpm method

```
Given: tol, $m_{max}$, $p_{max}$
if If Eq. S18 is satisfied then
    $m_* = argmin_{1 \leq m \leq m_{max}} m\lceil ||\hat{A}||_1/\theta_m \rceil$
    $s = \lceil ||\hat{A}||_1/\theta_m \rceil$
else
    Let $m_*$ be the smallest $m$ achieving the minimum in Eq. S16
    $s = max(C_{m_*}(\hat{A})/m_*, 1)$
```

m	5	10	15	20	25	30	35	40	45	50	55
half	8.1×10^{-1}	2.3	3.8	5.3	6.8	8.2	9.7	1.1×10^1	1.3×10^1	1.4×10^1	1.5×10^1
single	2.3×10^{-1}	1.0	2.2	3.6	4.9	6.3	7.7	9.1	1.1×10^1	1.2×10^1	1.3×10^1
double	2.4×10^{-3}	1.4×10^{-1}	6.4×10^{-1}	1.4	2.4	3.5	4.7	6.0	7.2	8.5	9.9

Table S2: Selected constants θ_m for tolerances of half ($tol = 2^{-10}$), single ($tol = 2^{-24}$) and double ($tol = 2^{-53}$) precisions.

A more in depth discussion of the theory behind the algorithm can be found in Ref. [9]. The an open-source implementation of a more general method of the algorithm can be found here:
https://github.com/higham/expmv

4 Implemented Tasks and Perfomance in *MolSpin*

Table S3 illustrates the available tasks and their respective perfomance as currently implemented in *Molspin*. Different methologies are available for time-independent and time-dependent Hamiltonians. For more information we refer to the user manual which can be found at Ref. [10].

Table S3: Available tasks and properties in *MolSpin* to use the SSE method. The tasks are divided into two Hilbert Space (**HS**) regimes: **StaticHS** (time-independent Hamiltonian) and **DynamicHS** (time-dependent Hamiltonian). Furthermore, direct (**Direct**) and stochastic (**Stoch**) methods are available for quantum yields (**Yields**) and pure time-evolution of spin states (**TimeEvo**). **Type:** Describes what can be calculated, which is either the time-evolution (TE) or quantum yields (QY). **TD** (**Time-Dependency**): Describes if the method can be used with time-dependent interactions. All of the methods utilize Haberkorn reaction operators for describing radical reactions. **Memory and speed:** The memory and calculation scaling of a task class, which for most task types scales exponentially with system size. M is the number of Monte Carlo samples and Z is the size of nuclear spin subspace. **Error**: describes the error in the final results of simulations. *Exact* means that there are no errors in calculations and the scaling was given only for SU(Z) spin states. In the case of coherent spin states, the scaling would be $\mathcal{O}(1\ \sqrt{M})$.)

Task class	Type	TD	Memory	Speed	Error
StaticHS-StochYields	QY	No	$\mathcal{O}(Z\log(Z))$	$\mathcal{O}(N_tMZ\log(Z))$	$\mathcal{O}(1/\sqrt{MZ})$
StaticHS-StochTimeEvo	TE	No	$\mathcal{O}(Z\log(Z))$	$\mathcal{O}(N_tMZ\log(Z))$	$\mathcal{O}(1/\sqrt{MZ})$
StaticHS-DirectYields	QY	No	$\mathcal{O}(Z\log(Z))$	$\mathcal{O}(N_tZ^2\log(Z))$	Exact Method
StaticHS-DirectTimeEvo	TE	No	$\mathcal{O}(Z\log(Z))$	$\mathcal{O}(N_tZ^2\log(Z))$	Exact Method
DynamicHS-StochYields	QY	Yes	$\mathcal{O}(Z\log(Z))$	$\mathcal{O}(N_tMZ\log(Z))$	$\mathcal{O}(1/\sqrt{MZ})$
DynamicHS-StochTimeEvo	TE	Yes	$\mathcal{O}(Z\log(Z))$	$\mathcal{O}(N_tMZ\log(Z))$	$\mathcal{O}(1/\sqrt{MZ})$
DynamicHS-DirectYields	QY	Yes	$\mathcal{O}(Z\log(Z))$	$\mathcal{O}(N_tZ^2\log(Z))$	Exact Method
DynamicHS-DirectTimeEvo	TE	Yes	$\mathcal{O}(Z\log(Z))$	$\mathcal{O}(N_tZ^2\log(Z))$	Exact Method

5 Comparison of Stochastich Schrödinger Equation with Bloch-Redfield-Wangsness Theory (550 ns)

In recent years, various theoretical approaches have been employed to investigate the impact of spin relaxation of radical pairs in biological systems [6, 7, 11, 12]. One approach gaining considerable attention is the phenomenological Lindblad operator, owing to its ease of application. It primarily requires relaxation rates, which can be derived from experimental data or theoretical computations [6]. However, these methods often lack a detailed microscopic physical representation of the actual movements and magnetic interactions of the radicals.

An alternative approach, called Bloch-Redfield-Wangsness (BRW), provides a quantum master equation characterizing the interaction between a spin system and its environment as a perturbation introduced through stochastic functions [6, 11, 13]. Furthermore, it can include time-dependent trajectories generated by the previously mentioned multiscale approach. The theory is derived by splitting the Hamiltonian $\hat{H}$ into a system part $\hat{H}_{\mathrm{S}}$ and an environment part $\hat{H}_{\mathrm{Env}}$ coupled by a time-dependent interaction Hamiltonian $\hat{H}_{\mathrm{I}}(t)$:

$$\hat{H} = \hat{H}_{\mathrm{S}} + \hat{H}_{\mathrm{Env}} + \hat{H}_{\mathrm{I}}(t). \tag{S19}$$

The goal of BRW theory is to neglect the explicit description of the environment dynamics, $\hat{H}_{\mathrm{Env}}$, focusing instead on the spin dynamics of the system. It modifies $\hat{H}_{\mathrm{I}}$ in a manner that allows all time-dependence to be described by a simpler stochastic coupling function.

BRW is based on three assumptions, namely:

1. Assuming that the ensemble-averaged expectation value of the interaction operator $\hat{H}_{\mathrm{I}}$ is zero.
2. The environment of the spin system is unaffected by the dynamics of the spin system.
3. The time-dependent perturbation has a significantly lower amplitude than the static Hamiltonian $\hat{H}_{\mathrm{S}}$ [13].

Several writings detail the full derivation of the BRW master equation [6, 7, 11, 13]. The final equation of motion to solve can be written in Liouville space as:

$$\frac{d\hat{\rho}(t)}{dt} = -i\hat{\hat{H}}_{\mathrm{S}}\hat{\rho}(t) - \hat{\hat{\mathcal{K}}}\hat{\rho}(t) + \hat{\hat{R}}_{RF}\hat{\rho}(t) = \hat{\hat{L}}\hat{\rho}(t), \tag{S20}$$

where $\hat{\hat{R}}_{RF}$ denotes the Redfield relaxation superoperator, which can be formally formulated in the interaction picture (subscript I) as:

$$\begin{aligned} \hat{\hat{R}}_{RF}\hat{\rho}_I(t) = -\sum_{\alpha,\beta}\int_0^{\infty} & d\tau g_{\alpha,\beta}(\tau)[\hat{A}_{I,\alpha}(t), \hat{A}_{I,\beta}(t-\tau)\hat{\rho}_I(t)] \\ & - g^*_{\alpha,\beta}(\tau)[\hat{A}_{I,\alpha}(t), \hat{\rho}_I(t)\hat{A}_{I,\beta}(t-\tau)], \end{aligned} \tag{S21}$$

where $\hat{A}_{I,\alpha}(t)$ are spin system operators (i.e. $\hat{S}_{1x}$, $\hat{S}_{1y}$), and $g_{\alpha,\beta}(\tau)$ is a correlation function condensing the fluctuations of the environment with the lag time τ as:

$$g_{\alpha,\beta}(\tau) = \langle b_\alpha(t) | b_\beta(t+\tau)\rangle, \tag{S22}$$

with $b_\alpha(t)$ being the coupling parameters of interaction that are modulated by stochastic fluctuations and defined through the stochastic part of the Hamiltonian:

$$\hat{H}(t) - \hat{\bar{H}} = \sum_\alpha b_\alpha(t)\hat{A}_\alpha. \tag{S23}$$

Here, $\hat{\bar{H}}$ is the static part of the Hamiltonian, from which an eigenbasis is used to bring Eq. S21 into an explicit form. The correlation function can be transformed into spectral densities $J_{\alpha\beta}(\omega_{mn})$ [6]:

$$J_{\alpha\beta}(\omega_{mn}) = \int_0^\infty d\tau g_{\alpha,\beta}(\tau)e^{i\omega_{mn}\tau}, \tag{S24}$$

where $\omega_{mn} = \omega_m - \omega_n$ are the eigenvalue differences between states $|m\rangle$ and $|n\rangle$ of the static Hamiltonian [6, 11].

It is assumed that the correlation function decays rapidly in an exponential form, allowing the solution of the spectral density integral as:

$$J(\omega) = g(0)\frac{1}{\frac{1}{\tau} - i\omega} = g(0)\left(\frac{\tau}{1+\omega^2\tau^2} + \frac{i\omega\tau^2}{1+\omega^2\tau^2}\right), \tag{S25}$$

with $g(0)$ being the amplitude of the correlation function. Kattnig *et al.*[6, 11] showed that the correlation function of complex situations, such as the motion of atoms in proteins, cannot be accurately described by a single exponential correlation function. A more realistic description is achieved by constructing the spectral density from a linear combination of correlation functions:

$$J(\omega) = \sum_q g_q(0)\frac{1}{\frac{1}{\tau_q} - i\omega}, \tag{S26}$$

This formalism can now be used to describe the induced spin relaxation explicitly within the BRW theory using Molecular Dynamics (MD) data, which employs correlation functions to capture stochastic fluctuations. A comparison of this approach with the SSE formalism is made to evaluate the advantages and limitations of both methods in describing spin relaxation.

A simplified spin system of a radical pair within a cryptochrome protein from the European robin, coupled to the N5 nucleus of the FAD, is used for comparison (see Fig. S6a). To describe spin relaxation effects through motion similar to previous works, specific degrees of freedom were extracted from a MD simulation. These are thought to significantly influence the spin dynamics of the radical pair. Earlier studies found that the librational motion of the FAD$^{\bullet-}$ radical and fluctuations in the dihedral angle Ω (Fig. S6a, green) have a significant effect on the hyperfine coupling of nuclei, which reduces the anisotropy of the singlet yield [11].

The geometry of FAD$^{\bullet-}$ was extracted from 550 ns (500 fs time steps) taken from the MD trajectory (the data was provided by Gesa Grüning [14]). The hyperfine tensors for selected motions were calculated using density functional theory (B3LYP/EPR-II) employing Gaussian 09 [15]. The hyperfine tensors calculated for specific dihedral angles and librational angles are mapped to the frames of the MD trajectory to produce a time-dependent trajectory of the hyperfine tensor under the influence of these two specific motions. The procedure is discussed in detail by Kattnig *et al.* [6, 11]. The amplitudes $g(0)_q$ and the corresponding correlation times τ^q can be directly used in *MolSpin*, which computes the spectral density automatically [6].

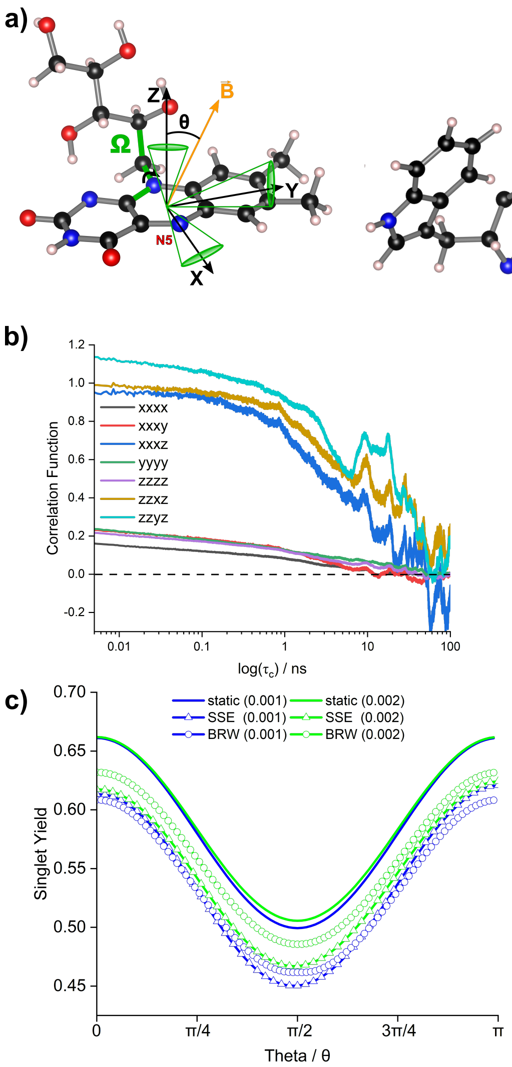

Figure S6: a) Schematic representation depicting the included nucleus, the dihedral angle Ω, and librational motion around all axes (shown in green). The magnetic field $\vec{B}$ (50 μT) is rotated in the xz-plane through an angle θ. The radical pair is initialized in a singlet state. The N5 nucleus is included to model the motion-modulated hyperfine interaction, with the hyperfine tensor rotated in the eigenframe of the N5 nucleus. The static part of the hyperfine tensor is chosen to be the average of all frames within the MD trajectory; all parameters are taken from Grüning *et al.* [14]. b) Selected correlation functions for elements in the hyperfine coupling tensor extracted from a 550 ns MD trajectory. Notably, cross-terms including z-components exhibit the strongest correlation, a well-known phenomenon in FAD due to the hyperfine coupling primarily occurring perpendicular to the FAD plane (z-axis) [6, 11, 14]. c) A comparative analysis of the static quantum yield Φ_S, the SSE method with an explicit description of fluctuations over a 550 ns trajectory, and BRW results incorporating all 81 correlation functions. Two different reaction rate constants (found in brackets and in ns^{-1}) were chosen. For the slower reaction rate constant (0.001 ns^{-1}) the SSE method uses the correction factor described in Section 2.4.

Fig. S6b illustrates exemplary correlation functions of the 3x3 hyperfine tensor in the nucleus principal axis system. The mean of the hyperfine coupling elements was subtracted (see Eq. S23) to only consider the time-dependent fluctuations. As observed, cross-correlations, such as *xxxz* (Fig. S6b), which incorporate coupling components with z-axis character, are significant and must be considered in the spin relaxation procedure, as previously described by Kattnig *et al.*[11]. The strong fluctuation of the N5 hyperfine tensor in the z-direction (orthogonal to the $\mathrm{FAD}^{\bullet-}$ plane) is a known feature [6], also found in the N10 nucleus [6, 11]. Furthermore, it can be observed (i.e. for zzyz) that the 550 ns MD trajectory might be to short for smoothly decaying correlation function fits which may lead to inaccuracies in the fitting procedure for BRW theory. In general, longer MD trajectories are required to accurately describing the spin relaxation effects [12]. For the fitting procedure of these correlation functions, 50 exponential functions (logarithmically spaced lag times τ from 0.005 to 300 ns) were taken to extract amplitudes $g(0)$. These amplitudes are then modulated by the covariance of the two involved coupling elements. The modified amplitudes and lag times τ are used for each of the 81 relaxation terms to construct the Redfield tensor.

For the explicit description of the time-dependent fluctuation of the N5 hyperfine coupling tensor in the framework of SSE, the 1,100,000 frames were averaged over consecutive 5-ns intervals, using the average hyperfine tensor for each 0.5 ns time frame. It was found that faster motions do not drastically influence the spin dynamics and can be neglected here (see SI, Section 5.1). Furthermore, for lifetimes longer then 550 ns the previously discussed quantum yield correction for integration was used due to the missing of longer MD data.

In both the BRW and SSE scenarios, the static component of the N5 hyperfine coupling with one electron is averaged over the entire MD trajectory, and calculations are performed in the N5 nucleus eigenframe. The radical pair originates in a singlet state, with reaction rate constants k_S and k_T set to 0.001 and 0.002 ns^{-1}, respectively. The magnetic field, $\vec{B}$, is set to 50 μT, initially parallel to the z-axis and then rotated 180° around the y-axis, as illustrated in Fig. S6a.

Fig. S6c compares the singlet quantum yields of both relaxation methods (circles = BRW, triangles = SSE) against the static spin dynamics (solid lines). It is evident that spin relaxation decreases the overall quantum yield compared to the static scenario in both cases. However, the SSE method induces stronger spin relaxation than the BRW method, particularly at 0.002 ns^{-1}. At a reaction rate constant of 0.001 ns^{-1} (blue curves), both BRW and SSE curves align well, indicating similar relaxation effects.

Despite the sensitivity of the BRW approach to the correlation function fitting procedure and the use of the discussed extrapolation method for SSE in the slow reaction rate constant case, the relaxation effects observed are consistent. The SSE approach, as implemented, effectively describes complex spin relaxation mechanisms extracted from multi-scale MD/QM data. Contrary to the BRW approach, it does not treat the magnitude of time-dependent perturbation as a limiting factor for including spin relaxation, resulting in a more versatile model. However, it necessitates longer MD trajectories for slow reaction rate constants (long lifetimes), as evidenced in Section 1 of the SI. It was demonstrated that to achieve accurate results with the correction factor, integration times must be at least 2.3 times the lifetime. Therefore, the SSE result for a reaction rate constant of 0.001 ns^{-1} should be considered cautiously.

Similarly, the MD trajectory length is pivotal for accurately capturing spin relaxation effects within the BRW theory. It is also important to note that the BRW theory may not be suitable in specific scenarios due to its perturbative-Markovian method foundation [6]. Specifically, the theory may become invalid when spin dynamics of the system becomes

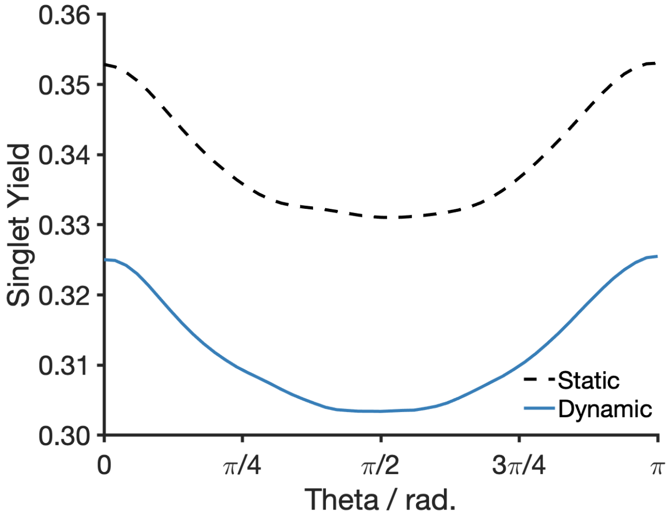

Figure S7: Calculation of quantum yield of a radical pair with 14 nuclei spins involved using the SSE method with and without spin relaxation due to motion-modulation of hyperfine interactions (HFI). Similar parameters to Fig. S6 were used. However, here 14 HFIs were included (see SI 5.2). For the static part of the HFI's the average of the time trajectory extracted from MD (550 ns) simulations is used for each nucleus. The reaction rate constants are $k_S = 10\mu s^{-1}$, $k_T = 10\mu s^{-1}$

.

faster. In such situations, alternative theories like the Nakajima-Zwanzig approach have been proven to yield superior results [7].

Having successfully compared the SSE approach with another spin relaxation theory using MD data, it is now possible to investigate the influence of spin relaxation on cryptochromes for a larger number of nuclei. For this, again, the MD trajectory of Grüning *et al.* for the motion of dihedral and librational angles is used [14]. Figure S7 illustrates the singlet quantum yield for the cryptochrome radical system of European robin from FAD and Trp (similar to Fig. S6) when including in total 14 different nuclei. The chosen nuclei and average hyperfine coupling tensors can be found in the SI, Fig. 5.2.

In the here presented simulation, however, a shorter lifetime of the radical pair is used because only 550 ns MD trajectory are available and no correction factor should be used for this example. The example should only server as an illustration, that the SSE approach can straight-forwardly include many time-dependent interactions using *.mst*-files extracted from MD/QM calculations. Thus, the reaction rate constants of $k_S = 10\mu s^{-1}$, $k_T = 10\mu s^{-1}$ are chosen. Additionally, the applied magnetic field was set to 1 mT which in alignment with the new lifetime of the radical pair to observe a magnetic field effect. For all hyperfine tensors spin relaxation is considered similar to the N5 case in Fig. S6.

Similar to previous work, the overall anisotropy of the singlet quantum yield decreases (Fig. S7 static) when including more nuclei to the spin system [14]. After the consideration of motion-induced spin relaxation through all hyperfine interactions, the overall singlet quantum yield drops significantly. Thus, spin relaxation still plays a major role when dealing with big spin systems and MD trajectories can be used to describe the complex relaxation mechanisms within a protein
To further provide more insight into this feature, we will investigate a radical pair of FAD and Trp within the Eurpean robin cryptochrome using 1 μs MD simulations to not only

consider two degrees of freedom such as illustrated here, but all of the motions perturbing the HFI. Furthermore, dipolar coupling will be included, as its importance was stated previously.

5.1 Selection of Time Step for Molecular Dynamics Data (550 ns)

The MD data for the $\left[\mathrm{FAD}^{\bullet-}\ \mathrm{TrpH}^{\bullet+}\right]$ radical pair in a protein environment, detailed section 5, was obtained with a time step of 500 fs. Incorporating all of these frames into spin dynamics calculations is both resource-intensive and unnecessary. It is crucial to select a time step that adequately captures all significant motions affecting the spin dynamics of a radical pair with a lifetime on the order of $1\mu s$ or several orders of magnitude more or less. Hence, this section analyses the appropriate choice of a time-step for this system to yield accurate results.

This requisite time step was estimated by calculating singlet yield graphs for a four spin system as described in the previous section (Section 1) with varying time steps for the fluctuation of hyperfine parameters. The system included N5, N10 hyperfine interactions for the FAD radical, and $H\beta_1$, $H\beta_2$ hyperfine interaction for the TrpH radical. The labels and average hyperfine interactions of these atoms are provided in Section S5.2 of the SI. In the static case, averaged hyperfine interactions are used, while in the dynamic case, the hyperfine interaction parameters were time-dependent and extracted from MD trajectories. The symmetric recombination rate was set to $k_S = 10\,\mu s^{-1}$, and the magnetic field strength was $|\mathbf{B}| = 1\,\mathrm{mT}$, with no coupling terms between electron spins. The total simulation time was 550 ns, sufficient to sample the singlet yield values of a radical pair with a 100 ns lifetime. The direct method, which provides singlet yield values without any approximations, was employed. The selected time step values were $dt = 0.5\,\mathrm{ns}$; $0.1\,\mathrm{ns}$; $0.05\,\mathrm{ns}$; $0.01\,\mathrm{ns}$. The graphs for the static and various dynamic cases are depicted in Fig. S8.

It is concluded that $dt = 0.5\,\mathrm{ns}$ is adequate for modelling this MD data applied to the spin dynamics of the radical pair. To confirm this, a 14-nuclear spin system was also calculated, incorporating all hyperfine interactions to examine the time-dependent effects on the singlet yield.

This 14-nuclear spin radical pair is described in Section 5.2. The static case utilize the average hyperfine interactions outlined in that section, while the dynamic case involve all 14 nuclei following the trajectory of the MD data. Different time steps are employed to model the data, with the symmetric recombination rate set to $k_S = 10\,\mu s^{-1}$, the magnetic field strength at $|\mathbf{B}| = 1\,\mathrm{mT}$, and no coupling terms between electron spins. The total simulation time is 550 ns. The stochastic method is used, with $MC = 5$ states employed for calculating dynamics. The results are displayed in Fig. S9. For the illustrated scenario as well, $dt = 0.5\,\mathrm{ns}$ is found to be sufficient for modelling the system. Therefore, a time step of $dt = 0.5\,\mathrm{ns}$ will be used for calculations involving the 550 ns MD trajectory.

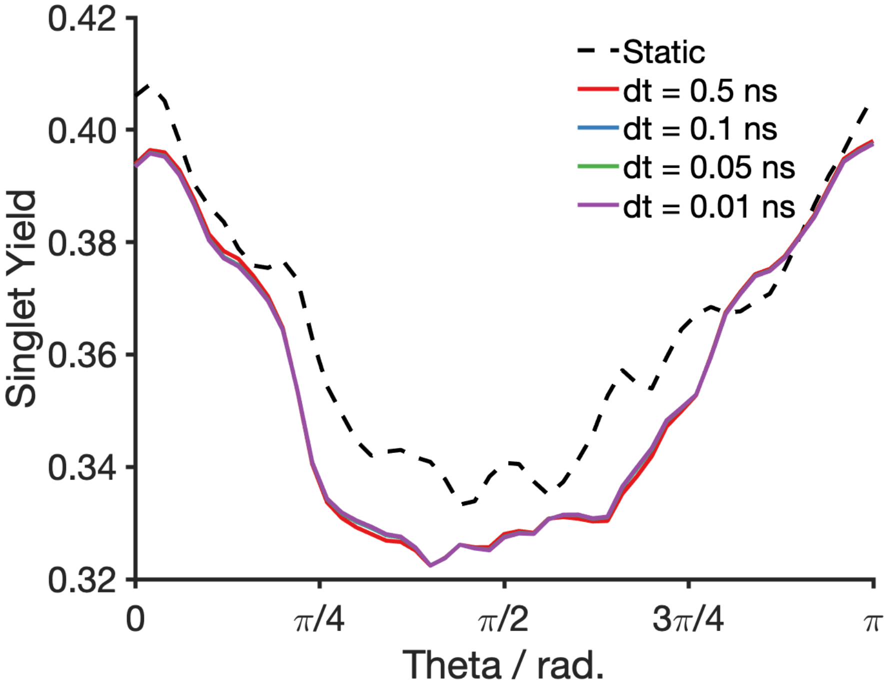

Figure S8: Singlet Yield Φ_S vs angle θ graphs for the 4-spin system described in the text. The static case without time-dependent interactions in $\hat{H}(t)$ is represented by the black dashed line, while the other lines correspond to interactions that varied with different time step dt values.

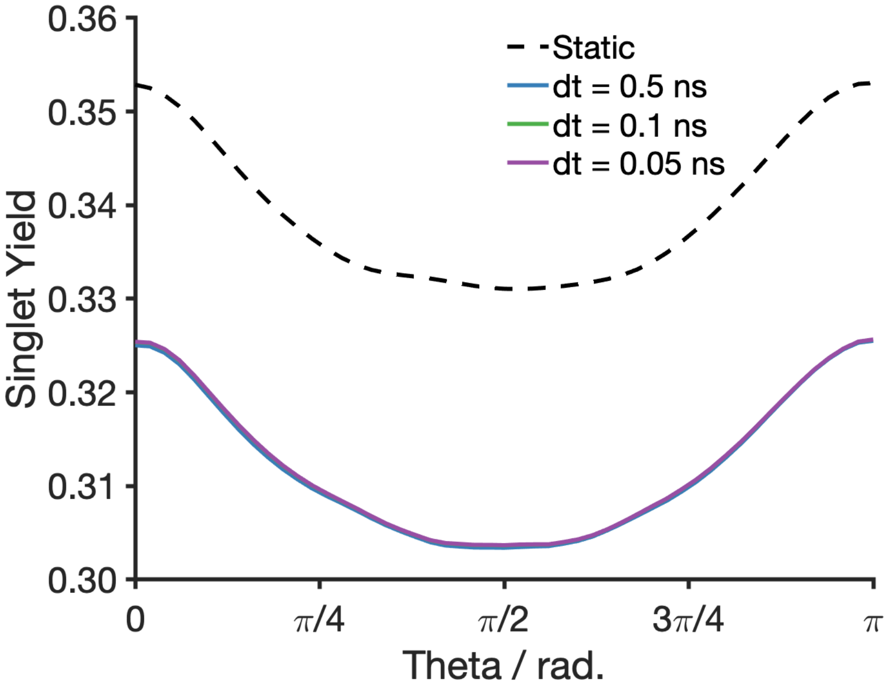

Figure S9: Singlet Yield Φ_S vs angle θ graphs for the 14-spin system described in the text. The static case without time-dependent interactions in $\hat{H}(t)$ is represented by the black dashed line, while the other lines correspond to interactions that varied with different time step dt values.

5.2 Averaged Hyperfine Interactions for MD calculations (550 ns)

In this section, we present averaged hyperfine interaction tensors that were constructed from molecular dynamics data. The hyperfine data for FAD$^{\bullet-}$ radical is presented in Table S4 and data for TrpH$^{\bullet+}$ is presented in Table S5. Structures of both of these radicals together with atom labels are shown in Fig. S10.

Table S4: Averaged Hyperfine Tensors for FAD$^{\bullet-}$ radical. Data was taken from 550 ns molecular dynamics trajectory of cryptochrome protein. Each of the hyperfine tensor was rotated to the the frame of N5 of FAD$^{\bullet-}$. FAD$^{\bullet-}$ structure and labels of each atoms can be seen in Fig. S10a

Atom	Hyperfine Tensor /**A**
N5	$\begin{pmatrix} -0.0936 & 0 & 0 \\ 0 & -0.0840 & 0 \\ 0 & 0 & 1.8807 \end{pmatrix}$ mT
N10	$\begin{pmatrix} 0.0221 & -0.0120 & -0.0812 \\ -0.0120 & 0.0164 & 0.0479 \\ -0.0812 & 0.0479 & 0.6850 \end{pmatrix}$ mT
H6	$\begin{pmatrix} -0.2519 & -0.1238 & 0.0014 \\ -0.1238 & -0.4087 & -0.0004 \\ 0.0014 & -0.0004 & -0.4090 \end{pmatrix}$ mT
Hβ_1	$\begin{pmatrix} 0.1212 & -0.0575 & 0.0308 \\ -0.0575 & 0.1564 & -0.0391 \\ 0.0308 & -0.0391 & 0.0823 \end{pmatrix}$ mT
$H8_1$	$\begin{pmatrix} 0.5918 & 0.0302 & 0.0110 \\ 0.0302 & 0.6695 & 0.0258 \\ 0.0110 & 0.0258 & 0.5890 \end{pmatrix}$ mT
$H8_2$	$\begin{pmatrix} -0.0047 & -0.0239 & 0 \\ -0.0239 & 0.0727 & 0.0017 \\ 0 & 0.0017 & -0.0078 \end{pmatrix}$ mT
$H8_3$	$\begin{pmatrix} 0.6153 & 0.0292 & -0.0092 \\ 0.0292 & 0.6968 & -0.0247 \\ -0.0092 & -0.0247 & 0.6132 \end{pmatrix}$ mT

Table S5: Averaged Hyperfine Tensors for TrpH$^{\bullet+}$ radical. Data was taken from 550 *ns* molecular dynamics trajectory of cryptochrome protein. Each of the hyperfine tensor was rotated to the the frame of N5 of FAD$^{\bullet-}$. TrpH$^{\bullet+}$ structure and labels of each atom can be seen in Fig. S10b.

Atom	Hyperfine Tensor / **A**
Hβ_1	$\begin{pmatrix} 0.2784 & -0.1152 & 0.0349 \\ -0.1152 & 0.2505 & -0.0144 \\ 0.0349 & -0.0144 & 0.1536 \end{pmatrix}$ mT
Hβ_2	$\begin{pmatrix} 1.2805 & -0.0282 & 0.1112 \\ -0.0282 & 1.2083 & 0.0032 \\ 0.1112 & 0.0032 & 1.3298 \end{pmatrix}$ mT
HD$_1$	$\begin{pmatrix} -0.8471 & 0.0489 & -0.0942 \\ 0.0489 & -0.2943 & 0.2469 \\ -0.0942 & 0.2469 & -0.5479 \end{pmatrix}$ mT
HE$_1$	$\begin{pmatrix} -0.3039 & 0.2069 & 0.2781 \\ 0.2069 & -0.6888 & 0.0419 \\ 0.2781 & 0.0419 & -0.3646 \end{pmatrix}$ mT
HE$_3$	$\begin{pmatrix} -0.3705 & 0.0700 & 0.1894 \\ 0.0700 & -0.7662 & -0.0660 \\ 0.1893 & -0.0660 & -0.5116 \end{pmatrix}$ mT
HH$_2$	$\begin{pmatrix} -0.4729 & -0.1917 & -0.1287 \\ -0.1917 & -0.2737 & -0.0019 \\ -0.1287 & -0.0019 & -0.5365 \end{pmatrix}$ mT
NE$_1$	$\begin{pmatrix} 0.0831 & 0.1647 & -0.2668 \\ 0.1647 & 0.0756 & -0.2784 \\ -0.2668 & -0.2784 & 0.3663 \end{pmatrix}$ mT

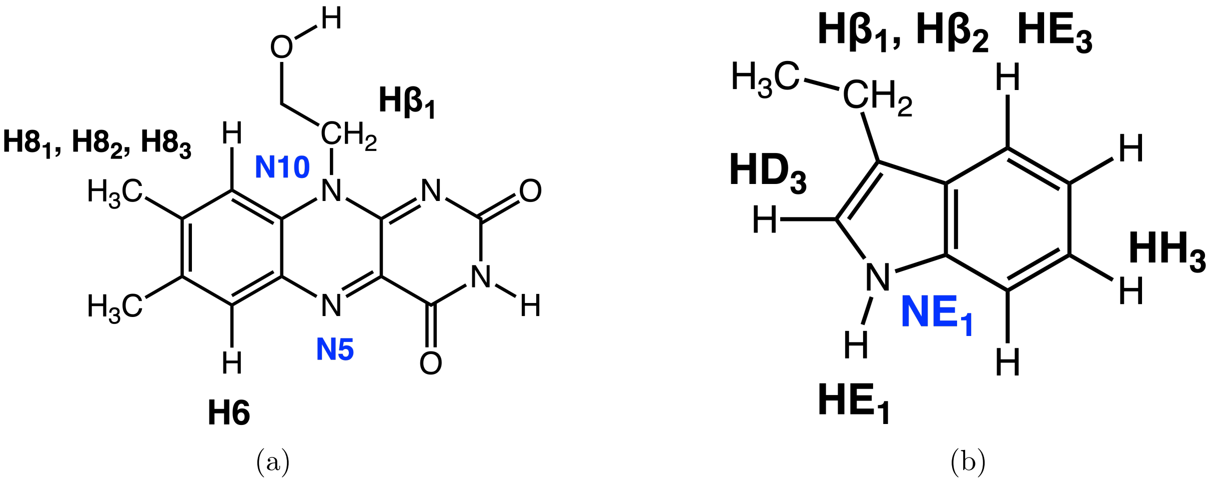

Figure S10: Molecular structures and labeled atoms of a) $FAD^{\bullet -}$ and b) $TrpH^{\bullet +}$ radicals according to the MD data of Grüning *et al.* [14].

All of the hyperfine tensors were rotated to the frame of N5 with only diagonal elements by:

$$\mathbf{A}_{Rot} = \mathbf{R}^T \mathbf{A} \mathbf{R} \tag{S27}$$

$\mathbf{R}$ is the matrix of eigenvectors of $\mathbf{A}(N5)$:

$$\mathbf{R} = \begin{pmatrix} 0.8216 & -0.1777 & -0.5417 \\ 0.3158 & 0.9329 & 0.1730 \\ -0.4746 & 0.3132 & -0.8226 \end{pmatrix} \tag{S28}$$

N5 hyperfine tensor before diagonalization was:

$$\mathbf{A}(N5) = \begin{pmatrix} 0.4860 & -0.1866 & 0.8792 \\ -0.1866 & -0.02619 & -0.2782 \\ 0.8792 & -0.2782 & 1.2433 \end{pmatrix} \tag{S29}$$

6 Time-step choice for Electronic Structure Calculations (953 ns)

In SI sections 5, 5.1, and 5.2 we have analysed time-dependent hyperfine interactions from MD data that only had rotational motions. This data was required for an accurate comparison with the BRW theory since any other more complicated motion would much harder and/or infeasible to model with BRW theory.

Nonetheless, in order to showcase the capabilities of the SSE method, we have also produced a longer MD trajectory (with total time of 953 ns) and used hyperfine interactions in simulations that were calculated with DFT in each frame. Hence, the simulation with these hyperfine interactions would include all motions, i.e. rotations, translations and vibrations. In contrast, the previous data set had hyperfine interactions that were rotated according to the MD trajectory from a single initial DFT calculation. This section overviews the choice of the time step of the simulation that was sufficient to include all interactions. It is an important parameter to estimate correctly because calculating hyperfine interactions with DFT for each 500 fs frame of the MD trajectory would be too expensive and unnecessary to capture accurate spin dynamics. Hence, we wanted to choose the highest time step that would not compromise the accuracy of the simulations.

We have chosen to simulate the first 10 ns of the MD trajectory with different time steps $dt = 500\ fs$, $1\ ps$, $5\ ps$, $10\ ps$, $50\ ps$, $100\ ps$, $200\ ps$, $500\ ps$ and plot singlet survival probability against time to see at which dt the plots diverge. Simulating 10 ns with $dt = 500\ fs$ already required 20000 DFT calculations of both FAD and TRP radicals.

In Fig. S11 we see plots of singlet survival probability versus time for a 4 spin system with different time steps dt. This system included N5, N10 nuclear spins for FAD$^{\bullet-}$ radical, and N1, H1 for TrpH$^{\bullet+}$ radical, as described in Section 7. $|\mathbf{B}| = 1$ mT and was aligned along the z-axis. The recombination rate was $k = 10\ \mu s^{-1}$. Moreover, a time-dependent dipolar interaction was included in the calculations that was computed from the MD trajectory.

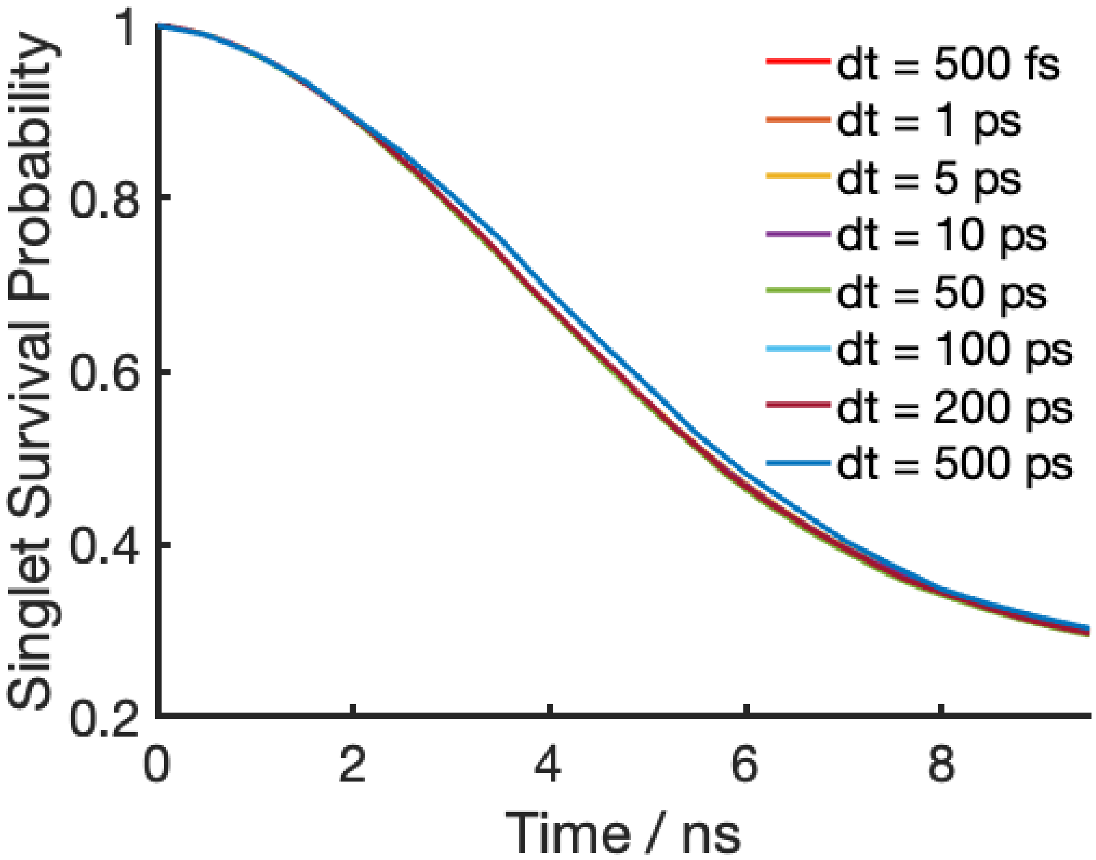

Figure S11: Singlet survival probability versus simulation time graphs for the 4-spin system described in the text. The simulations were done with different time step *dt* to gauge what time-step is sufficient to model radical pair processes with the described MD data.

From this data, it can be concluded that $dt = 500\ ps$ most likely does not capture all the motions and $dt = 200\ ps$ was sufficient to model this system accurately. This is a surprising result since vibrations are known to have a shorter time scale for which the determined time step would be too long to capture these motions effectively. We believe that either singlet survival probability is not affected by the faster motions and/or that the hyperfine interactions do not significantly change due to vibrations. Moreover, it would have been more accurate to compare longer simulation times because maybe some effects would only be visible for longer trajectories. This, as mentioned before, is not computationally feasible due to the many DFT calculations that are required to do and would require additional strategies. Also, this publication serves as an introduction of new *MolSpin* capabilities and methods, and does not aim to fully analyse these results which will be done in subsequent publications aimed at analysing short time scale motion effects on spin dynamics of radical pairs in a protein environment. We will use $dt = 50\ ps$ for further simulations to ensure capturing all important motions of the spin interaction while still being computationally feasable. Note, that the calculations of hyperfine interaction for the 0.953 μs MD trajectories and $50 ps$ step size led to the calculation of 19,060 quantum chemical calculations including a geometry optimization of the saturation Hydrogen and the calculation of hyperfine coupling tensors using the Gaussian16 software [15].

7 Average Hyperfines from MD data (953 ns)

This section includes average hypefine interactions and the average dipolar interaction for 953 *ns* trajectory MD data. The hyperfine interactions in this data set were computed with DFT for each 50 *ps* time frame. Average hyperfine interactions are displayed in Tables S6 and S7.

The average dipolar tensor:

$$D = \begin{pmatrix} 0.446 & 0.386 & 0.123 \\ 0.386 & -0.136 & 0.061 \\ 0.123 & 0.061 & -0.309 \end{pmatrix} \text{ mT} \tag{S30}$$

Table S6: Averaged Hyperfine Tensors for FAD$^{\bullet -}$ radical. Data was taken from 953 *ns* molecular dynamics trajectory of cryptochrome protein. FAD$^{\bullet -}$ structure and labels of each atom can be seen in Fig. S12.

Atom	Hyperfine Tensor / **A**
N5	$\begin{pmatrix} 0.520 & -0.173 & 0.773 \\ -0.173 & 0.044 & -0.243 \\ 0.773 & -0.243 & 1.143 \end{pmatrix}$ mT
N10	$\begin{pmatrix} 0.182 & -0.052 & 0.254 \\ -0.052 & 0.021 & -0.070 \\ 0.254 & -0.070 & 0.392 \end{pmatrix}$ mT
H6	$\begin{pmatrix} -0.243 & -0.047 & -0.101 \\ -0.047 & -0.440 & 0.016 \\ -0.101 & 0.016 & -0.343 \end{pmatrix}$ mT
H8$_1$	$\begin{pmatrix} 0.140 & -0.030 & -0.054 \\ -0.030 & 0.138 & 0.043 \\ -0.054 & 0.043 & 0.166 \end{pmatrix}$ mT
H8$_2$	$\begin{pmatrix} 0.394 & -0.004 & -0.001 \\ -0.004 & 0.467 & 0.016 \\ -0.001 & 0.016 & 0.39743516 \end{pmatrix}$ mT
H8$_3$	$\begin{pmatrix} 0.392 & -0.004 & -0.001 \\ -0.004 & 0.465 & 0.016 \\ -0.001 & 0.016 & 0.395 \end{pmatrix}$ mT
Hβ_1	$\begin{pmatrix} 0.396 & -0.004 & -0.001 \\ -0.004 & 0.468 & 0.016 \\ -0.001 & 0.016 & 0.399 \end{pmatrix}$ mT

Table S7: Averaged Hyperfine Tensors for TrpH$^{\bullet+}$ radical. Data was taken from 953 ns molecular dynamics trajectory of cryptochrome protein. TrpH$^{\bullet+}$ structure and labels of each atom can be seen in Fig. S12.

Atom	Hyperfine Tensor / **A**
N1	$\begin{pmatrix} 0.527 & 0.358 & 0.293 \\ 0.358 & 0.291 & 0.214 \\ 0.293 & 0.214 & 0.226 \end{pmatrix}$ mT
H1	$\begin{pmatrix} -0.664 & 0.180 & -0.013 \\ 0.180 & -0.507 & -0.340 \\ -0.013 & -0.340 & -0.046 \end{pmatrix}$ mT
H2	$\begin{pmatrix} -0.384 & -0.207 & 0.096 \\ -0.207 & -0.168 & -0.031 \\ 0.096 & -0.031 & -0.589 \end{pmatrix}$ mT
H4	$\begin{pmatrix} -0.650 & 0.167 & -0.115 \\ 0.167 & -0.708 & -0.153 \\ -0.115 & -0.153 & -0.345 \end{pmatrix}$ mT
H6	$\begin{pmatrix} -0.201 & -0.137 & -0.046 \\ -0.137 & -0.240 & 0.119 \\ -0.046 & 0.119 & -0.355 \end{pmatrix}$ mT
H7	$\begin{pmatrix} -0.421 & 0.104 & -0.091 \\ 0.104 & -0.427 & -0.122 \\ -0.091 & -0.122 & -0.196 \end{pmatrix}$ mT
Hβ_1	$\begin{pmatrix} 0.228 & -0.053 & -0.089 \\ -0.053 & 0.196 & 0.044 \\ -0.089 & 0.044 & 0.269 \end{pmatrix}$ mT

Structures of both radical with atoms labels are shown in Fig. S12.

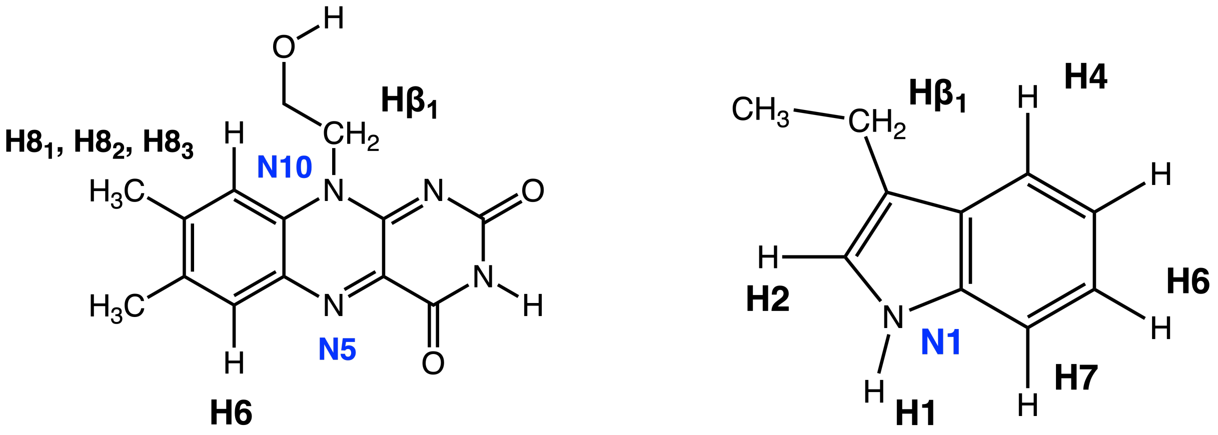

(a) (b)

Figure S12: Molecular structures and labeled atoms of a) $FAD^{\bullet -}$ and b) $TrpH^{\bullet +}$ used for MD data (953 ns) modelling..

8 MolSpin Features & Input Files

This section contains the input files we have used for various simulations presented in this article, that would enable another user new to MolSpin to try and test out the methods themselves.

8.1 Format of .mst Files

The *MolSpin* trajectory (**mst**) files are used to integrate complex time-dependencies into a spin dynamics calculation. The files are constucted in a ways that either specific interactions or reactions rates can be adjusted with time-dependencies. The following example shows a .mst file for an N5 nucleus in its eigenframe extracted from the 550 ns MD simulation, when only modulating the A_{zz} component of the hyperfine coupling tensor:

```
time  mat.xx mat.xy mat.xz mat.yx mat.yy mat.yz mat.zx mat.zy mat.zz
0.00000000 -0.00009359 0.00000000 0.00000000 0.00000000 -0.00009359 0.00000000 0.00000000 0.00000000 0.00185977
0.05000000 -0.00009359 0.00000000 0.00000000 0.00000000 -0.00009359 0.00000000 0.00000000 0.00000000 0.00188710
0.10000000 -0.00009359 0.00000000 0.00000000 0.00000000 -0.00009359 0.00000000 0.00000000 0.00000000 0.00188667
0.15000000 -0.00009359 0.00000000 0.00000000 0.00000000 -0.00009359 0.00000000 0.00000000 0.00000000 0.00188617
0.20000000 -0.00009359 0.00000000 0.00000000 0.00000000 -0.00009359 0.00000000 0.00000000 0.00000000 0.00188876
0.25000000 -0.00009359 0.00000000 0.00000000 0.00000000 -0.00009359 0.00000000 0.00000000 0.00000000 0.00188732
.
.
.
```

The first column is the time which will be set in nanoseconds while the nine following row describe the time-dependencies of the nine hyperfine tensor elements. As can be observed only the A_{zz} component is altered. *MolSpin* is recognizing the format of the .mst file through the first line. There are many other forms that can be used to include complex time-dependencies for field fluctuations, reaction rate fluctuations or fluctuations of principal components of certain coupling tensors. More details can be found in the manual.

Each .mst file can be attributed to a specific object via the *trajectory* keyword:

```
// -------------------------
// Hyperfine interactions
// -------------------------
Interaction FADHYP1
{
    IgnoreTensors = true;
    CommonPrefactor = false;
    type = hyperfine;
    group1 = E1;
    group2 = FADN5;
    tensor = trajectory("motions_azz005ns.mst");
    trajectory = "motions_azz_005ns.mst";
}
```

8.2 12 Nuclear Spin System

The template for running the 12 nuclear spin radical pair system of $\left[\mathrm{FAD}^{\bullet-}\ \mathrm{TrpH}^{\bullet+}\right]$ that was used to compare the accuracy of the stochastic method to full dynamics method that utilizes diagonalization (described in Ref. [16]). This is an example template for a simulation with $MC = 1$ and this variable should be adjusted to other values if needed. The calculations done in the article had this number ranging from 1 to 50.

```
SpinSystem system1
{
    // ---------------------------------------------------------
    // Spins
    // ---------------------------------------------------------

    // Electrons
    Spin E1 {type = electron; spin = 1/2; tensor = isotropic(2.0023);}
    Spin E2 {type = electron; spin = 1/2; tensor = isotropic(2.0023);}

    // Nitrogens
    Spin FADN5 {type = nucleus; spin = 1; tensor = isotropic(1);}
    Spin FADN10{type = nucleus; spin = 1;tensor = isotropic(1);}

    Spin TRPN1 {type = nucleus; spin = 1;tensor = isotropic(1);}
```

```

    // Hydrogens
    Spin FADH6 {type = nucleus; spin = 1/2;tensor = isotropic(1);}
    Spin FADH81 {type = nucleus; spin = 1/2;tensor = isotropic(1);}
    Spin FADH82 {type = nucleus; spin = 1/2;tensor = isotropic(1);}
    Spin FADH83 {type = nucleus; spin = 1/2;tensor = isotropic(1);}
    Spin FADHbeta {type = nucleus; spin = 1/2;tensor = isotropic(1);}

    Spin TRPH1 {type = nucleus; spin = 1/2;tensor = isotropic(1);}
    Spin TRPH2 {type = nucleus; spin = 1/2;tensor = isotropic(1);}
    Spin TRPH4 {type = nucleus; spin = 1/2;tensor = isotropic(1);}
    Spin TRPH6 {type = nucleus; spin = 1/2;tensor = isotropic(1);}

    // ------------------------
    // Zeeman interactions
    // ------------------------

    Interaction Zeeman1 {prefactor= 1e-3; type = zeeman; field = "0.0 0.0 1.0"; spins = E1;}
    Interaction Zeeman2 {prefactor= 1e-3; type = zeeman; field = "0.0 0.0 1.0"; spins = E2;}

    // ------------------------
    // Hyperfine interactions
    // ------------------------

    Interaction FADHYP1 {prefactor = 1e-3; type = hyperfine; group1 = E1; group2 = FADN5; tensor = matrix("-0.0989, 0.0039,
      0.0; 0.0039, -0.0881, 0.0; 0.0, 0.0, 1.7569");}
    Interaction FADHYP2 {prefactor = 1e-3; type = hyperfine; group1 = E1; group2 = FADN10; tensor = matrix("-0.0190, -0.0048,
      0.0; -0.0048, -0.0196, 0.0; 0.0, 0.0, 0.6046");}
    Interaction FADHYP3 {prefactor = 1e-3; type = hyperfine; group1 = E1; group2 = FADH6; tensor = matrix("-0.2569, -0.1273,
      0.0; -0.1273, -0.4711, 0.0; 0.0, 0.0, -0.4336");}
    Interaction FADHYP4 {prefactor = 1e-3; type = hyperfine; group1 = E1; group2 = FADH81; tensor = matrix("0.4399, 0.0, 0.0;
      0.0, 0.4399, 0.0; 0.0, 0.0, 0.4399");}
    Interaction FADHYP5 {prefactor = 1e-3; type = hyperfine; group1 = E1; group2 = FADH82; tensor = matrix("0.4399, 0.0, 0.0;
      0.0, 0.4399, 0.0; 0.0, 0.0, 0.4399");}
    Interaction FADHYP6 {prefactor = 1e-3; type = hyperfine; group1 = E1; group2 = FADH83; tensor = matrix("0.4399, 0.0, 0.0;
      0.0, 0.4399, 0.0; 0.0, 0.0, 0.4399");}
    Interaction FADHYP7 {prefactor = 1e-3; type = hyperfine; group1 = E1; group2 = FADHbeta; tensor = matrix("0.4070, 0.0,
      0.0; 0.0, 0.4070, 0.0; 0.0, 0.0, 0.4070");}

    Interaction TRPHYP1 {prefactor = 1e-3; type = hyperfine; group1 = E2; group2 = TRPN1; tensor = matrix("-0.0336, 0.0924,
     -0.1354; 0.0924, 0.3303, -0.5318; -0.1354, -0.5318, 0.6680");}
    Interaction TRPHYP2 {prefactor = 1e-3; type = hyperfine; group1 = E2; group2 = TRPH1; tensor = matrix("-0.9920, -0.2091,
     -0.2003; -0.2091, -0.2631, 0.2803; -0.2003, 0.2803, -0.5398");}
    Interaction TRPHYP3 {prefactor = 1e-3; type = hyperfine; group1 = E2; group2 = TRPH2; tensor = matrix("-0.2843, 0.1757,
      0.1525; 0.1757, -0.2798, 0.0975; 0.1525, 0.0975, -0.2699");}
    Interaction TRPHYP4 {prefactor = 1e-3; type = hyperfine; group1 = E2; group2 = TRPH4; tensor = matrix("-0.5596, -0.1956,
     -0.1657; -0.1956, -0.4020, 0.0762; -0.1657, 0.0762, -0.5021");}
    Interaction TRPHYP5 {prefactor = 1e-3; type = hyperfine; group1 = E2; group2 = TRPH6; tensor = matrix("-0.0506, 0.0622,
      0.0889; 0.0622, -0.3100, -0.0297; 0.0889, -0.0297, 0.2642");}

    // ------------------------
    // Dipolar interactions
    // ------------------------

    Interaction Dipolar {prefactor = 2.0023e-3; IgnoreTensors = true; type = doublespin; group1 = E1; group2 = E2; tensor =
      matrix("-0.382276, 0.292979, -0.146796; 0.292979, -0.652196, 0.229243;-0.146796, 0.229243, -0.309528");}
     // We ignore the tensor variable from the Spin objects  and add 2.0023 to the prefactor to only account for one g-value
      for conversion from Tesla into rad/ns (MolSpin multiplies each interaction by a CommonPrefactor (Bohr Magneton/hbar) if
      not set to     false

    // -------------------------------------------------------
    // Spin States
    // -------------------------------------------------------

    State Singlet {spins(E1,E2) = |1/2,-1/2> - |-1/2,1/2>;}
    State T0 {spins(E1,E2) = |1/2,-1/2> + |-1/2,1/2>;}
    State Tp {spin(E2) = |1/2>; spin(E1) = |1/2>;} // |T+>
    State Tm { spin(E2) = |-1/2>; spin(E1) = |-1/2>;} // |T->
    State Identity {}

    // -------------------------------------------------------
    // Transitions
    // -------------------------------------------------------

    Transition Product1 {type = sink; source = Singlet; rate = 1e-3;} // in 1/ns
    Transition Product2 {type = sink; source = T0; rate = 1e-3;}
    Transition Product3 {type = sink; source = Tp; rate = 1e-3;}
    Transition Product4 {type = sink; source = Tm; rate = 1e-3;}

}
// -----------------------------------------------------------
Settings
{
    Settings general {steps = 51; notifications = details;}

    // -------------------------------------------------------
    // Actions
    // -------------------------------------------------------

    Action scan1 {type = rotatevector; vector = system1.Zeeman1.field; axis = "0 1 0"; value = 3.6;}
    Action scan2 {type = rotatevector; vector = system1.Zeeman2.field; axis = "0 1 0"; value = 3.6;}

    // -------------------------------------------------------
    // Outputs objects
    // -------------------------------------------------------

    Output orientation1 {type = vectorangle; vector = system1.Zeeman1.field; reference = "0 0 1";}
    Output orientation2 {type = vectorangle; vector = system1.Zeeman2.field; reference = "0 0 1";}
}
// -----------------------------------------------------------
Run
{
    Task Static12SpinSystem {type = "statichs-stoch-yields"; logfile = "staticyield_12spins.log"; datafile =
      "staticyield_12spins.dat"; transitionyields = true; initialstate = singlet; samplingmethod = "SUZ"; autoseed = false;
      seed = 2.0;  montecarlosamples = 1; epsilon = 0.001; timestep = 4; propagationmethod = "autoexpm"; precision =
      "single"; yieldcorrections = true;}
}
```

8.3 20 Nuclear Spin System

This input template was used to calculate the spin dynamics of the 20 nuclear spin system of $\left[\mathrm{FAD}^{\bullet-}\ \mathrm{TrpH}^{\bullet+}\right]$, to highlight the computational capabilities of the method. The actual calculation was done by calculating each θ point separately in the cluster just for the reason that the whole computation could be finished faster than running it on one node for a long period of time.

```
SpinSystem system1
{
    // ---------------------------------------------------------
    // Spins
    // ---------------------------------------------------------

    // Electrons
    Spin E1 {type = electron; spin = 1/2; tensor = isotropic(2.0023);}
    Spin E2 {type = electron; spin = 1/2; tensor = isotropic(2.0023);}

    // Nitrogens
    Spin FADN5 {type = nucleus; spin = 1;  tensor = isotropic(1);}
    Spin FADN10 {type = nucleus; spin = 1;  tensor = isotropic(1);}

    Spin TRPN1 {type = nucleus; spin = 1;  tensor = isotropic(1);}

    // Hydrogens
    Spin FADH6 {type = nucleus; spin = 1/2;  tensor = isotropic(1);}
    Spin FADH81 {type = nucleus; spin = 1/2;  tensor = isotropic(1);}
    Spin FADH82 {type = nucleus; spin = 1/2;  tensor = isotropic(1);}
    Spin FADH83 {type = nucleus; spin = 1/2;  tensor = isotropic(1);}
    Spin FADHbeta1 {type = nucleus; spin = 1/2;  tensor = isotropic(1);}
    Spin FADHbeta2 {type = nucleus; spin = 1/2;  tensor = isotropic(1);}
    Spin FADH71 {type = nucleus; spin = 1/2;  tensor = isotropic(1);}
    Spin FADH72 {type = nucleus; spin = 1/2;  tensor = isotropic(1);}

    Spin TRPH1 {type = nucleus; spin = 1/2;  tensor = isotropic(1);}
    Spin TRPH2 {type = nucleus; spin = 1/2;  tensor = isotropic(1);}
    Spin TRPH4 {type = nucleus; spin = 1/2;  tensor = isotropic(1);}
    Spin TRPH6 {type = nucleus; spin = 1/2;  tensor = isotropic(1);}
    Spin TRPH7 {type = nucleus; spin = 1/2;  tensor = isotropic(1);}
    Spin TRPHbeta1 {type = nucleus; spin = 1/2;  tensor = isotropic(1);}
    Spin TRPHalpha {type = nucleus; spin = 1/2;  tensor = isotropic(1);}
    Spin TRPNasterisk {type = nucleus; spin = 1;  tensor = isotropic(1);}
    Spin TRPHbeta2 {type = nucleus; spin = 1/2;  tensor = isotropic(1);}

    // -------------------------
    // Zeeman interaction
    // -------------------------

    Interaction Zeeman1 {prefactor= 1e-3; type = zeeman; field = "0.0 0.0 1.0"; spins = E1;}

    Interaction Zeeman2 {prefactor= 1e-3; type = zeeman; field = "0.0 0.0 1.0"; spins = E2;}

    // -------------------------
    // Hyperfine interactions
    // -------------------------
    Interaction FADHYP1 {prefactor = 1e-3; type = hyperfine; group1 = E1; group2 = FADN5; tensor = matrix("-0.0989, 0.0039,
      0.0; 0.0039, -0.0881, 0.0; 0.0, 0.0, 1.7569");}
    Interaction FADHYP2 {prefactor = 1e-3; type = hyperfine; group1 = E1; group2 = FADN10; tensor = matrix("-0.0190, -0.0048,
      0.0; -0.0048, -0.0196, 0.0; 0.0, 0.0, 0.6046");}
    Interaction FADHYP3 {prefactor = 1e-3; type = hyperfine; group1 = E1; group2 = FADH6; tensor = matrix("-0.2569, -0.1273,
      0.0; -0.1273, -0.4711, 0.0; 0.0, 0.0, -0.4336");}
    Interaction FADHYP4 {prefactor = 1e-3; type = hyperfine; group1 = E1; group2 = FADH81; tensor = matrix("0.4399, 0.0, 0.0;
      0.0, 0.4399, 0.0; 0.0, 0.0, 0.4399");}
    Interaction FADHYP5 {prefactor = 1e-3; type = hyperfine; group1 = E1; group2 = FADH82; tensor = matrix("0.4399, 0.0, 0.0;
      0.0, 0.4399, 0.0; 0.0, 0.0, 0.4399");}
    Interaction FADHYP6 {prefactor = 1e-3; type = hyperfine; group1 = E1; group2 = FADH83; tensor = matrix("0.4399, 0.0, 0.0;
      0.0, 0.4399, 0.0; 0.0, 0.0, 0.4399");}
    Interaction FADHYP7 {prefactor = 1e-3; type = hyperfine; group1 = E1; group2 = FADHbeta1; tensor = matrix("0.4070, 0.0,
      0.0; 0.0, 0.4070, 0.0; 0.0, 0.0, 0.4070");}
    Interaction FADHYP8 {prefactor = 1e-3; type = hyperfine; group1 = E1; group2 = FADHbeta2; tensor = matrix("0.4070, 0.0,
      0.0; 0.0, 0.4070, 0.0; 0.0, 0.0, 0.4070");}
    Interaction FADHYP9 {prefactor = 1e-3; type = hyperfine; group1 = E1; group2 = FADH71; tensor = matrix("-0.1416, 0.0,
      0.0; 0.0, -0.1416, 0.0; 0.0, 0.0, -0.1416");}
    Interaction FADHYP10 {prefactor = 1e-3; type = hyperfine; group1 = E1; group2 = FADH72; tensor = matrix("-0.1416, 0.0,
      0.0; 0.0, -0.1416, 0.0; 0.0, 0.0, -0.1416");}

    Interaction TRPHYP1 {prefactor = 1e-3; type = hyperfine; group1 = E2; group2 = TRPN1; tensor = matrix("-0.0336, 0.0924,
      -0.1354; 0.0924, 0.3303, -0.5318; -0.1354, -0.5318, 0.6680");}
    Interaction TRPHYP2 {prefactor = 1e-3; type = hyperfine; group1 = E2; group2 = TRPH1; tensor = matrix("-0.9920, -0.2091,
      -0.2003; -0.2091, -0.2631, 0.2803; -0.2003, 0.2803, -0.5398");}
    Interaction TRPHYP3 {prefactor = 1e-3; type = hyperfine; group1 = E2; group2 = TRPH2; tensor = matrix("-0.2843, 0.1757,
      0.1525; 0.1757, -0.2798, 0.0975; 0.1525, 0.0975, -0.2699");}
    Interaction TRPHYP4 {prefactor = 1e-3; type = hyperfine; group1 = E2; group2 = TRPH4; tensor = matrix("-0.5596, -0.1956,
      -0.1657; -0.1956, -0.4020, 0.0762; -0.1657, 0.0762, -0.5021");}
    Interaction TRPHYP5 {prefactor = 1e-3; type = hyperfine; group1 = E2; group2 = TRPH6; tensor = matrix("-0.0506, 0.0622,
      0.0889; 0.0622, -0.3100, -0.0297; 0.0889, -0.0297, 0.2642");}
    Interaction TRPHYP6 {prefactor = 1e-3; type = hyperfine; group1 = E2; group2 = TRPH7; tensor = matrix("-0.4355, -0.1541,
      -0.1239; -0.1541, -0.2777, 0.0864; -0.1239, 0.0864, -0.3770");}
    Interaction TRPHYP7 {prefactor = 1e-3; type = hyperfine; group1 = E2; group2 = TRPHbeta1; tensor = matrix("1.5808,
      -0.0453, -0.0506; -0.0453, 1.5575, 0.0988; -0.0506, 0.0988, 1.6752");}
    Interaction TRPHYP8 {prefactor = 1e-3; type = hyperfine; group1 = E2; group2 = TRPHalpha; tensor = matrix("-0.0601,
      0.0037, 0.0331; 0.0037, -0.0251, 0.0111; 0.0331, 0.0111, -0.1940");}
    Interaction TRPHYP9 {prefactor = 1e-3; type = hyperfine; group1 = E2; group2 = TRPNasterisk; tensor = matrix("0.1295,
      -0.0134, 0.0075; -0.0134, 0.1729, -0.0249; 0.0075, -0.0249, 0.1371");}
    Interaction TRPHYP10 {prefactor = 1e-3; type = hyperfine; group1 = E2; group2 = TRPHbeta2; tensor = matrix("0.1634,
      -0.0230, -0.0064; -0.0230, -0.0082, 0.0158; -0.0064, 0.0158, -0.0182");}

    // -------------------------
    // Dipolar interactions
    // -------------------------

    Interaction Dipolar {prefactor = 2.0023e-3; IgnoreTensors = true; type = doublespin; group1 = E1; group2 = E2; tensor =
      matrix("-0.382276, 0.292979, -0.146796; 0.292979, -0.652196, 0.229243;-0.146796, 0.229243, -0.309528");}
    // We ignore the tensor variable from the Spin objects  and add 2.0023 to the prefactor to only account for one g-value
      for conversion from Tesla into rad/ns (MolSpin multiplies each interaction by a CommonPrefactor (Bohr Magneton/hbar) if
      not set to    false

    // -------------------------
    // Spin States
    // ---------------------------------------------------------
    State Singlet {spins(E1,E2) = |1/2,-1/2> - |-1/2,1/2>;}
    State T0 {spins(E1,E2) = |1/2,-1/2> + |-1/2,1/2>;}
    State Tp {spin(E2) = |1/2>; spin(E1) = |1/2>;} // |T+>
    State Tm {spin(E2) = |-1/2>; spin(E1) = |-1/2>;} // |T->
    State Identity {}

    // ---------------------------------------------------------
    // Transitions
    // ---------------------------------------------------------

    Transition Product1 {type = sink; source = Singlet; rate = 1e-3;} // in 1/ns
    Transition Product2 {type = sink; source = T0; rate = 1e-3;}
    Transition Product3 {type = sink; source = Tp; rate = 1e-3;}
    Transition Product4 {type = sink; source = Tm; rate = 1e-3;}
}
// ---------------------------------------------------------
Settings
{
    Settings general {steps = 51; notifications = details;}
```

```

    // ---------------------------------------------------------
    // Actions
    // ---------------------------------------------------------

    Action scan1 {type = rotatevector; vector = system1.Zeeman1.field; axis = "0 1 0"; value = 3.6;}
    Action scan2 {type = rotatevector; vector = system1.Zeeman2.field; axis = "0 1 0"; value = 3.6;}

    // ---------------------------------------------------------
    // Outputs objects
    // ---------------------------------------------------------

    Output orientation1 {type = vectorangle; vector = system1.Zeeman1.field; reference = "0 0 1";}
    Output orientation2 {type = vectorangle; vector = system1.Zeeman2.field; reference = "0 0 1";}
}
// -------------------------------------------------------------
Run
{
    Task Stati20SpinSystem{type = "statichs-stoch-yields"; logfile = "staticyield_20spins.log"; datafile =
      "staticyield_20spins.dat"; transitionyields = true; initialstate = singlet; samplingmethod = "SUZ"; autoseed = false;
      seed = 2.0; montecarlosamples = 1; epsilon = 0.5; timestep = 4; propagationmethod = "autoexpm"; precision = "single";
      yieldcorrections = true;}
}
```

8.4 Molecular Wires

This is an input file that was used to replicate the relative yield versus magnetic field data for molecular wire $PTZ^{\bullet +} - Ph_4 - PDI^{\bullet -}$from Ref. [17]. To replicate the whole data set the variable m in the Zeeman interaction objects should be set to the magnetic field of interest (in mT). The magnetic field range used to replicate the graph was $0 - 12\ mT$.

```
SpinSystem system1
{
    // ---------------------------------------------------------
    // Spins
    // ---------------------------------------------------------

    // Electrons
    Spin E1 { type = electron; spin = 1/2; tensor = isotropic(2.0023); }
    Spin E2 { type = electron; spin = 1/2; tensor = isotropic(2.0023); }

    //Nitrogens
    Spin Rad1N1 {type=nucleus; spin=1; tensor = isotropic(1);}
    Spin Rad2N1 {type=nucleus; spin=1; tensor = isotropic(1);}
    Spin Rad2N2 {type=nucleus; spin=1; tensor = isotropic(1);}

    //Hydrogens
    Spin Rad1H1 {type=nucleus; spin=1/2; tensor = isotropic(1);}
    Spin Rad1H2 {type=nucleus; spin=1/2; tensor = isotropic(1);}
    Spin Rad1H3 {type=nucleus; spin=1/2; tensor = isotropic(1);}
    Spin Rad1H4 {type=nucleus; spin=1/2; tensor = isotropic(1);}
    Spin Rad1H5 {type=nucleus; spin=1/2; tensor = isotropic(1);}
    Spin Rad1H6 {type=nucleus; spin=1/2; tensor = isotropic(1);}
    Spin Rad1H7 {type=nucleus; spin=1/2; tensor = isotropic(1);}
    Spin Rad1H8 {type=nucleus; spin=1/2; tensor = isotropic(1);}
    Spin Rad2H1 {type=nucleus; spin=1/2; tensor = isotropic(1);}
    Spin Rad2H2 {type=nucleus; spin=1/2; tensor = isotropic(1);}
    Spin Rad2H3 {type=nucleus; spin=1/2; tensor = isotropic(1);}
    Spin Rad2H4 {type=nucleus; spin=1/2; tensor = isotropic(1);}
    Spin Rad2H5 {type=nucleus; spin=1/2; tensor = isotropic(1);}
    Spin Rad2H6 {type=nucleus; spin=1/2; tensor = isotropic(1);}

    // -------------------------
    // Zeeman interaction
    // -------------------------

    Interaction Zeeman1 {prefactor=1e-3; type=zeeman; field="0.0 0.0 m"; spins=E1;}
    Interaction Zeeman2 {prefactor=1e-3; type=zeeman; field="0.0 0.0 m"; spins=E2;}

    // -------------------------
    // Hyperfine interactions
    // -------------------------

    Interaction Rad1HYP1 {prefactor=1e-3; type=hyperfine; group1=E1; group2=Rad1H1; tensor=matrix("-0.113, 0.0, 0.0; 0.0, -0.113, 0.0; 0.0, 0.0, -0.113");}
    Interaction Rad1HYP2 {prefactor=1e-3; type=hyperfine; group1=E1; group2=Rad1H2; tensor=matrix("-0.113, 0.0, 0.0; 0.0, -0.113, 0.0; 0.0, 0.0, -0.113");}
    Interaction Rad1HYP3 {prefactor=1e-3; type=hyperfine; group1=E1; group2=Rad1H3; tensor=matrix("-0.05, 0.0, 0.0; 0.0, -0.05, 0.0; 0.0, 0.0, -0.05");}
    Interaction Rad1HYP4 {prefactor=1e-3; type=hyperfine; group1=E1; group2=Rad1H4; tensor=matrix("-0.05, 0.0, 0.0; 0.0, -0.05, 0.0; 0.0, 0.0, -0.05");}
    Interaction Rad1HYP5 {prefactor=1e-3; type=hyperfine; group1=E1; group2=Rad1H5; tensor=matrix("-0.249, 0.0, 0.0; 0.0, -0.249, 0.0; 0.0, 0.0, -0.249");}
    Interaction Rad1HYP6 {prefactor=1e-3; type=hyperfine; group1=E1; group2=Rad1H6; tensor=matrix("-0.249, 0.0, 0.0; 0.0, -0.249, 0.0; 0.0, 0.0, -0.249");}
    Interaction Rad1HYP7 {prefactor=1e-3; type=hyperfine; group1=E1; group2=Rad1H7; tensor=matrix("0.050, 0.0, 0.0; 0.0, 0.050, 0.0; 0.0, 0.0, 0.050");}
    Interaction Rad1HYP8 {prefactor=1e-3; type=hyperfine; group1=E1; group2=Rad1H8; tensor=matrix("0.050, 0.0, 0.0; 0.0, 0.050, 0.0; 0.0, 0.0, 0.050");}
    Interaction Rad1HYP9 {prefactor=1e-3; type=hyperfine; group1=E1; group2=Rad1N1; tensor=matrix("0.634, 0.0, 0.0; 0.0, 0.634, 0.0; 0.0, 0.0, 0.634");}

    Interaction Rad2Hyp1 {prefactor=1e-3; type=hyperfine; group1=E2; group2=Rad2H1; tensor=matrix("0.0785, 0.0, 0.0; 0.0, 0.0785, 0.0; 0.0, 0.0, 0.0785");}
    Interaction Rad2Hyp2 {prefactor=1e-3; type=hyperfine; group1=E2; group2=Rad2H2; tensor=matrix("0.0785, 0.0, 0.0; 0.0, 0.0785, 0.0; 0.0, 0.0, 0.0785");}
    Interaction Rad2Hyp3 {prefactor=1e-3; type=hyperfine; group1=E2; group2=Rad2H3; tensor=matrix("-0.1720, 0.0, 0.0; 0.0, -0.1720, 0.0; 0.0, 0.0, -0.1720");}
    Interaction Rad2Hyp4 {prefactor=1e-3; type=hyperfine; group1=E2; group2=Rad2H4; tensor=matrix("-0.1720, 0.0, 0.0; 0.0, -0.1720, 0.0; 0.0, 0.0, -0.1720");}
    Interaction Rad2Hyp5 {prefactor=1e-3; type=hyperfine; group1=E2; group2=Rad2H5; tensor=matrix("0.0575, 0.0, 0.0; 0.0, 0.0575, 0.0; 0.0, 0.0, 0.0575");}
    Interaction Rad2Hyp6 {prefactor=1e-3; type=hyperfine; group1=E2; group2=Rad2H6; tensor=matrix("0.0575, 0.0, 0.0; 0.0, 0.0575, 0.0; 0.0, 0.0, 0.0575");}
    Interaction Rad2Hyp7 {prefactor=1e-3; type=hyperfine; group1=E2; group2=Rad2N1; tensor=matrix("-0.0621, 0.0, 0.0; 0.0, -0.0621, 0.0; 0.0, 0.0, -0.0621");}
    Interaction Rad2Hyp8 {prefactor=1e-3; type=hyperfine; group1=E2; group2=Rad2N2; tensor=matrix("-0.0621, 0.0, 0.0; 0.0, -0.0621, 0.0; 0.0, 0.0, -0.0621");}

    // -------------------------
    // Dipolar interactions
    // -------------------------

     Interaction Dipolar {prefactor=2.0023e-3; IgnoreTensors=true; type=doublespin; group1=E1; group2=E2; tensor=matrix("6.4, 0.0, 0.0; 0.0, 6.4, 0.0; 0.0, 0.0, 6.4");}
    // We ignore the tensor variable from the Spin objects  and add 2.0023 to the prefactor to only account for one g-value for conversion from Tesla into rad/ns (MolSpin multiplies each interaction by a CommonPrefactor (Bohr Magneton/hbar) if not set to    false

    // -------------------------
    // Spin States
    // ---------------------------------------------------------

    State Singlet {spins(E1,E2)=|1/2,-1/2>-|-1/2,1/2>;}
    State T0 {spins(E1,E2)=|1/2,-1/2>+|-1/2,1/2>;}
    State Tp {spin(E2)=|1/2>; spin(E1)=|1/2>;}
    State Tm {spin(E2)=-|1/2>; spin(E1)=-|1/2>;}
    State Identity {}

    // ---------------------------------------------------------
    // Transitions
    // ---------------------------------------------------------

    Transition Product1 {type=sink; source=Singlet; rate=2.45e-3;} // in 1/ns
    Transition Product2 {type=sink; source=T0; rate=350.0e-3;}
    Transition Product3 {type=sink; source=Tp; rate=350.0e-3;}
    Transition Product4 {type=sink; source=Tm; rate=350.0e-3;}

}
// ---------------------------------------------------------
Settings
{
    Settings general {steps = 1; notifications = details;}
```

```
}
Run
{
    Task StaticMolecularWires {type = "statichs-stoch-yields"; logfile = "molecularwires.log"; datafile =
     "molecularwires.dat"; transitionyields = true; initialstate = singlet; samplingmethod = "SUZ"; autoseed = false; seed =
     2.0; montecarlosamples = 1; totaltime = 55; timestep = 0.1; propagationmethod = "autoexpm";  precision = "single";
     yieldcorrections = false;}
}
```

8.5 Quantum Needle

This is the input file for the singlet yield versus inclination angle graph for the $\left[\mathrm{FAD}^{\bullet -}\ \mathrm{TrpH}^{\bullet +}\right]$ 14 nuclear spin radical pair system. This is the same system as the Quantum Needle example from Ref. [2], yet with EED and exchange interactions included, taken from Ref. [3].

```
SpinSystem system1
{
    // ---------------------------------------------------------
    // Spins
    // ---------------------------------------------------------

    // Electrons
    Spin E1 {type = electron; spin = 1/2; tensor = isotropic(2.0023);}
    Spin E2 {type = electron; spin = 1/2; tensor = isotropic(2.0023);}

    //Nitrogens
    Spin FADN5 {type = nucleus; spin = 1; tensor = isotropic(1);}
    Spin FADN10 {type = nucleus; spin = 1; tensor = isotropic(1);}

    Spin TRPN1 {type = nucleus; spin = 1; tensor = isotropic(1);}

    // Hydrogens
    Spin FADH6 {type = nucleus; spin = 1/2; tensor = isotropic(1);}
    Spin FADH81 {type = nucleus; spin = 1/2; tensor = isotropic(1);}
    Spin FADH82 {type = nucleus; spin = 1/2; tensor = isotropic(1);}
    Spin FADH83 {type = nucleus; spin = 1/2; tensor = isotropic(1);}
    Spin FADHbeta {type = nucleus; spin = 1/2; tensor = isotropic(1);}

    Spin TRPH1 {type = nucleus; spin = 1/2; tensor = isotropic(1);}
    Spin TRPH2 {type = nucleus; spin = 1/2; tensor = isotropic(1);}
    Spin TRPH4 {type = nucleus; spin = 1/2; tensor = isotropic(1);}
    Spin TRPH6 {type = nucleus; spin = 1/2; tensor = isotropic(1);}
    Spin TRPH7 {type = nucleus; spin = 1/2; tensor = isotropic(1);}
    Spin TRPHbeta1 {type = nucleus; spin = 1/2; tensor = isotropic(1);}

    // -------------------------
    // Zeeman interaction
    // -------------------------

    Interaction Zeeman1 {prefactor= 1e-3; type = zeeman; field = "0.0 0.0 0.050"; spins = E1;}
    Interaction Zeeman2 {prefactor= 1e-3; type = zeeman; field = "0.0 0.0 0.050"; spins = E2;}

    // -------------------------
    // Hyperfine interactions
    // -------------------------

    Interaction FADHYP1 {prefactor = 1e-3; type = hyperfine; group1 = E1; group2 = FADN5; tensor = matrix("-0.0989, 0.0039,
      0.0; 0.0039, -0.0881, 0.0; 0.0, 0.0, 1.7569");}
    Interaction FADHYP2 {prefactor = 1e-3; type = hyperfine; group1 = E1; group2 = FADN10; tensor = matrix("-0.0190, -0.0048,
      0.0; -0.0048, -0.0196, 0.0; 0.0, 0.0, 0.6046");}
    Interaction FADHYP3 {prefactor = 1e-3; type = hyperfine; group1 = E1; group2 = FADH6; tensor = matrix("-0.2569, -0.1273,
      0.0; -0.1273, -0.4711, 0.0; 0.0, 0.0, -0.4336");}
    Interaction FADHYP4 {prefactor = 1e-3; type = hyperfine; group1 = E1; group2 = FADH81; tensor = matrix("0.4399, 0.0, 0.0;
      0.0, 0.4399, 0.0; 0.0, 0.0, 0.4399");}
    Interaction FADHYP5 {prefactor = 1e-3; type = hyperfine; group1 = E1; group2 = FADH82; tensor = matrix("0.4399, 0.0, 0.0;
      0.0, 0.4399, 0.0; 0.0, 0.0, 0.4399");}
    Interaction FADHYP6 {prefactor = 1e-3; type = hyperfine; group1 = E1; group2 = FADH83; tensor = matrix("0.4399, 0.0, 0.0;
      0.0, 0.4399, 0.0; 0.0, 0.0, 0.4399");}
    Interaction FADHYP7 {prefactor = 1e-3; type = hyperfine; group1 = E1; group2 = FADHbeta; tensor = matrix("0.4070, 0.0,
      0.0; 0.0, 0.4070, 0.0; 0.0, 0.0, 0.4070");}

    Interaction TRPHYP1 {prefactor = 1e-3; type = hyperfine; group1 = E2; group2 = TRPN1; tensor = matrix("-0.0336, 0.0924,
     -0.1354; 0.0924, 0.3303, -0.5318; -0.1354, -0.5318, 0.6680");}
    Interaction TRPHYP2 {prefactor = 1e-3; type = hyperfine; group1 = E2; group2 = TRPH1; tensor = matrix("-0.9920, -0.2091,
     -0.2003; -0.2091, -0.2631, 0.2803; -0.2003, 0.2803, -0.5398");}
    Interaction TRPHYP3 {prefactor = 1e-3; type = hyperfine; group1 = E2; group2 = TRPH2; tensor = matrix("-0.2843, 0.1757,
      0.1525; 0.1757, -0.2798, 0.0975; 0.1525, 0.0975, -0.2699");}
    Interaction TRPHYP4 {prefactor = 1e-3; type = hyperfine; group1 = E2; group2 = TRPH4; tensor = matrix("-0.5596, -0.1956,
     -0.1657; -0.1956, -0.4020, 0.0762; -0.1657, 0.0762, -0.5021");}
    Interaction TRPHYP5 {prefactor = 1e-3; type = hyperfine; group1 = E2; group2 = TRPH6; tensor = matrix("-0.0506, 0.0622,
      0.0889; 0.0622, -0.3100, -0.0297; 0.0889, -0.0297, 0.2642");}
    Interaction TRPHYP6 {prefactor = 1e-3; type = hyperfine; group1 = E2; group2 = TRPH7; tensor = matrix("-0.4355, -0.1541,
     -0.1239; -0.1541, -0.2777, 0.0864; -0.1239, 0.0864, -0.3770");}
    Interaction TRPHYP7 {prefactor = 1e-3; type = hyperfine; group1 = E2; group2 = TRPHbeta1; tensor = matrix("1.5808,
     -0.0453, -0.0506; -0.0453, 1.5575, 0.0988; -0.0506, 0.0988, 1.6752");}

    // -------------------------
    // Dipolar interactions
    // -------------------------

    Interaction Dipolar {prefactor = 2.0023e-3; IgnoreTensors = true; type = doublespin; group1 = E1;  group2 = E2; tensor =
     matrix("-0.382276, 0.292979, -0.14679; 0.292979, -0.652196, 0.229243;-0.146796, 0.229243, -0.309528");}
    // We ignore the tensor variable from the Spin objects  and add 2.0023 to the prefactor to only account for one g-value
      for conversion from Tesla into rad/ns (MolSpin multiplies each interaction by a CommonPrefactor (Bohr Magneton/hbar) if
      not set to    false
    // -------------------------
    // Spin States
    // ---------------------------------------------------------

    State Singlet {spins(E1,E2) = |1/2,-1/2> - |-1/2,1/2>;}
    State T0 {spins(E1,E2) = |1/2,-1/2> + |-1/2,1/2>;}
    State Tp {spin(E2) = |1/2>; spin(E1) = |1/2>;}
    State Tm {spin(E2) = |-1/2>; spin(E1) = |-1/2>;}
    State Identity { }

    // ---------------------------------------------------------
    // Transitions
    // ---------------------------------------------------------

    Transition Product1 {type = sink; source = Singlet; rate = 1e-3;} // in 1/ns
    Transition Product2 {type = sink; source = T0; rate = 1e-3;}
    Transition Product3 {type = sink; source = Tp; rate = 1e-3;}
    Transition Product4 {type = sink; source = Tm; rate = 1e-3;}
}
// -------------------------------------------------------------
Settings
{
    Settings general {steps = 51; notifications = details;}

    // ---------------------------------------------------------
    // Actions
    // ---------------------------------------------------------

    Action scan1 {type = rotatevector; vector = system1.Zeeman1.field; axis = "0 1 0"; value = 3.6;}
    Action scan2 {type = rotatevector; vector = system1.Zeeman2.field; axis = "0 1 0"; value = 3.6;}

    // ---------------------------------------------------------
```

```
    // Outputs objects
    // ----------------------------------------------------------

    Output orientation1 {type = vectorangle; vector = system1.Zeeman1.field; reference = "0 0 1";}
    Output orientation2 {type = vectorangle; vector = system1.Zeeman2.field; reference = "0 0 1";}

}
// --------------------------------------------------------------
Run
{
    Task Static14SpinsYield {type = "statichs-stoch-yields"; logfile = "test_staticyields_14spins.log"; datafile =
      "test_staticyields_14spins.dat"; transitionyields = true; initialstate = singlet; samplingmethod = "SUZ"; autoseed =
      false; seed = 2.0; montecarlosamples = 1; epsilon = 0.001; timestep = 4; propagationmethod = "autoexpm"; precision =
      "single"; yieldcorrections = true;}
}
```

8.6 Driven Recombination Dynamics

This is the input file used to replicate results from Ref. [4]. Depending on the simulation case, the trajectories of the exchange interaction and recombination kinetics changed. The equations to form the trajectories were discussed in the article.

```
SpinSystem system1
{
    // ---------------------------------------------------------
    // Spins
    // ---------------------------------------------------------

    // Electrons
    Spin E1 {type=electron; spin=1/2; tensor=isotropic(2.0023);}
    Spin E2 {type=electron; spin=1/2; tensor=isotropic(2.0023);}
    // Nitrogens
    Spin FADN5 {type=nucleus; spin=1; tensor=isotropic(1);}

    // -------------------------
    // Zeeman interaction
    // -------------------------

    Interaction Zeeman1 {prefactor=1e-3; type=zeeman; field="0.0 0.0 0.05"; spins=E1;}
    Interaction Zeeman2 {prefactor=1e-3; type=zeeman; field="0.0 0.0 0.05"; spins=E2;}

    // -------------------------
    // Hyperfine interactions
    // -------------------------

    Interaction FADHYP1 {prefactor=1e-3; type=hyperfine; group1=E1; group2=FADN5; tensor=matrix("-0.092774, 0.0, 0.0; 0.0,
      0.092774, 0.0;  0.0, 0.0, 1.75558");}

    // -------------------------
    // Exchange interaction
    // -------------------------

    Interaction Exchange {prefactor=2.0023; IgnoreTensors=true; type=doublespin; group1=E1; group2=E2;
      tensor=trajectory("DipolarMu.mst"); trajectory="DipolarMu.mst";} // .mst file in T
    // We ignore the tensor variable from the Spin objects  and add 2.0023 to the prefactor to only account for one g-value
      for conversion from Tesla into rad/ns (MolSpin multiplies each interaction by a CommonPrefactor (Bohr Magneton/hbar) if
      not set to    false

    // -------------------------
    // Spin States
    // --------------------------------------------------------

    State Singlet {spins(E1,E2)=|1/2,-1/2>-|-1/2,1/2>;}
    State Identity {}

    // ---------------------------------------------------------
    // Transitions
    // ---------------------------------------------------------

    Transition Product1 {type=sink; source=Singlet; rate=trajectory("rate.mst"); trajectory="rate.mst";} // in 1/ns
    Transition Product2 {type=sink; source=Identity; rate=1.0e-3;}

}
// -------------------------------------------------------------
Settings
{
    Settings general {steps = 1; notifications = details;}
}
Run
{
    Task DynamicDrivenModelYield {type = "dynamichs-direct-yields"; logfile = "Dynamic1Spin.log"; datafile =
      "Dynamic1Spin.dat"; transitionyields = true; initialstate = Singlet; timestep = 1.0; totaltime = 12500;
      propagationmethod = "autoexpm"; precision = "single"; yieldcorrections = false;}
}
```

8.7 1 Nuclear Spin Relaxation (550 ns)

This script was used to compute the relaxation induced by fluctuating N5 hyperfine interaction with SSE method which was compared to the results available from BRW formalism (550 ns).

```
SpinSystem system1
{
// ---------------------------------------------------------
// Spins
// ---------------------------------------------------------

    // Electrons
    Spin E1 {type= electron; spin= 1/2; tensor= isotropic(2.0023)};
    Spin E2 {type= electron; spin= 1/2; tensor= isotropic(2.0023)};
    // Nitrogens
    Spin FADN5 {type= nucleus; spin= 1;; tensor= isotropic(1)};

    // -------------------------
    // Zeeman interaction
    // -------------------------

    Interaction Zeeman1 {prefactor=1e-3; type=zeeman; field="0.0 0.0 0.05"; spins=E1};
    Interaction Zeeman2 {prefactor=1e-3; type=zeeman; field="0.0 0.0 0.05"; spins=E2};

    // -------------------------
    // Hyperfine interactions
    // -------------------------

    Interaction FADHYP1 {type=hyperfine; group1=E1; group2=FADN5; tensor=trajectory("motions_N5.mst");
      trajectory="motions_N5.mst"}; // .mst file in T

    // -------------------------
    // Spin States
    // ---------------------------------------------------------

    State Singlet {spins(E1,E2) = |1/2,-1/2> - |-1/2,1/2>;}
    State T0 {spins(E1,E2) = |1/2,-1/2> + |-1/2,1/2>;}
    State Tp {spin(E2) = |1/2>; spin(E1) = |1/2>;}
    State Tm {spin(E2) = |-1/2>; spin(E1) = |-1/2>;}
    State Identity {}

    // ---------------------------------------------------------
    // Transitions
    // ---------------------------------------------------------

    Transition Product1 {type=sink; source=Singlet; rate=1.0e-3}; // in 1/ns
    Transition Product2 {type=sink; source=T0; rate=1.0e-3};
    Transition Product3 {type=sink; source=Tp; rate=1.0e-3};
    Transition Product4 {type=sink; source=Tm; rate=1.0e-3};

}
// ---------------------------------------------------------
Settings
{
    Settings general {steps = 51; notifications = details;}

    // ---------------------------------------------------------
    // Actions
    // ---------------------------------------------------------

    Action scan1 {type = rotatevector; vector = system1.Zeeman1.field; axis = "0 1 0"; value = 3.6;}
    Action scan2 {type = rotatevector; vector = system1.Zeeman2.field; axis = "0 1 0"; value = 3.6;}

    // ---------------------------------------------------------
    // Outputs objects
    // ---------------------------------------------------------

    Output orientation1 {type = vectorangle; vector = system1.Zeeman1.field; reference = "0 0 1";}
    Output orientation2 {type = vectorangle; vector = system1.Zeeman2.field; reference = "0 0 1";}

}
Run
{
    Task DynamicDirectYield {type = "dynamichs-direct-yields"; logfile = "Dynamic4Spins.log"; datafile = "Dynamic4Spins.dat";
      transitionyields = true; initialstate = Singlet; totaltime = 550.0; timestep = 0.5; propagationmethod = "autoexpm";
      precision = "single"; yieldcorrections = true;}
}
```

To acquire results for a static system, this script was used:

```
SpinSystem system1
{
// ---------------------------------------------------------
// Spins
// ---------------------------------------------------------

    // Electrons
    Spin E1 {type= electron; spin= 1/2; tensor= isotropic(2.0023)};
    Spin E2 {type= electron; spin= 1/2; tensor= isotropic(2.0023)};
    // Nitrogens
    Spin FADN5 {type= nucleus; spin= 1;tensor= isotropic(1)};

    // -------------------------
    // Zeeman interaction
    // -------------------------

    Interaction Zeeman1 {prefactor=1e-3; type=zeeman; field="0.0 0.0 0.05"; spins=E1};
    Interaction Zeeman2 {prefactor=1e-3; type=zeeman; field="0.0 0.0 0.05"; spins=E2};

    // -------------------------
    // Hyperfine interactions
    // -------------------------

    Interaction FADHYP1 {prefactor=1e-3; type=hyperfine; group1=E1; group2=FADN5; tensor = matrix("-0.09359, 0.00000,
      0.00000; 0.00000, -0.09359, 0.00000; 0.00000, 0.00000, 1.88074");};

    // -------------------------
    // Spin States
    // ---------------------------------------------------------

    State Singlet {spins(E1,E2) = |1/2,-1/2> - |-1/2,1/2>;}
    State T0 {spins(E1,E2) = |1/2,-1/2> + |-1/2,1/2>;}
    State Tp {spin(E2) = |1/2>; spin(E1) = |1/2>;}
```

```
    State Tm {spin(E2) = |-1/2>; spin(E1) = |-1/2>;}
    State Identity {}

    // ----------------------------------------------------------
    // Transitions
    // ----------------------------------------------------------

    Transition Product1 {type=sink; source=Singlet; rate=1.0e-3}; // in 1/ns
    Transition Product2 {type=sink; source=T0; rate=1.0e-3};
    Transition Product3 {type=sink; source=Tp; rate=1.0e-3};
    Transition Product4 {type=sink; source=Tm; rate=1.0e-3};

}
// --------------------------------------------------------------
Settings
{
    Settings general {steps = 51; notifications = details;}

    // ----------------------------------------------------------
    // Actions
    // ----------------------------------------------------------

    Action scan1 {type = rotatevector; vector = system1.Zeeman1.field; axis = "0 1 0"; value = 3.6;}
    Action scan2 {type = rotatevector; vector = system1.Zeeman2.field; axis = "0 1 0"; value = 3.6;}

    // ----------------------------------------------------------
    // Outputs objects
    // ----------------------------------------------------------

    Output orientation1 {type = vectorangle; vector = system1.Zeeman1.field; reference = "0 0 1";}
    Output orientation2 {type = vectorangle; vector = system1.Zeeman2.field; reference = "0 0 1";}

}
Run
{
    Task StaticirectYield {type = "Statichs-direct-yields"; logfile = "Dynamic4Spins.log"; datafile = "Dynamic4Spins.dat";
     transitionyields = true; initialstate = Singlet; totaltime = 550.0; timestep = 0.5; propagationmethod = "autoexpm";
     precision = "single"; yieldcorrections = true;}
}
```

8.8 14 Nuclear Spin Relaxation (550 ns)

This is the input file used to calculate the spin relaxation effects for the 14 nuclear spin system for the 550 ns MD trajectory.

```
SpinSystem system1
{
    // ----------------------------------------------------------
    // Spins
    // ----------------------------------------------------------

    // Electrons
    Spin E1 {type = electron; spin = 1/2; tensor = isotropic(2.0023);}
    Spin E2 {type = electron; spin = 1/2; tensor = isotropic(2.0023);}

   // Nitrogens
    Spin FADN5 {type = nucleus; spin = 1; tensor = isotropic(1);}
    Spin FADN10 {type = nucleus; spin = 1; tensor = isotropic(1);}

    Spin TRPNE1 {type = nucleus; spin = 1; tensor = isotropic(1);}

    // Hydrogens
    Spin FADH6 {type = nucleus; spin = 1/2; tensor = isotropic(1);}
    Spin FADHBeta1 {type = nucleus; spin = 1/2; tensor = isotropic(1);}
    Spin FADH81 {type = nucleus; spin = 1/2; tensor = isotropic(1);}
    Spin FADH82 {type = nucleus; spin = 1/2; tensor = isotropic(1);}
    Spin FADH83 {type = nucleus; spin = 1/2; tensor = isotropic(1);}

   Spin TRPHB1 {type = nucleus; spin = 1/2; tensor = isotropic(1);}
    Spin TRPHB2 {type = nucleus; spin = 1/2; tensor = isotropic(1);}
    Spin TRPHD1 {type = nucleus; spin = 1/2; tensor = isotropic(1);}
    Spin TRPHE1 {type = nucleus; spin = 1/2; tensor = isotropic(1);}
    Spin TRPHE3 {type = nucleus; spin = 1/2; tensor = isotropic(1);}
    Spin TRPHH2 {type = nucleus; spin = 1/2; tensor = isotropic(1);}
    Spin TRPNE1 {type = nucleus; spin = 1; tensor = isotropic(1);}

    // -------------------------
    // Zeeman interaction
    // -------------------------

    Interaction Zeeman1 {prefactor=1e-3; type=zeeman; field="0.0 0.0 0.05"; spins=E1;}
    Interaction Zeeman2 {prefactor=1e-3; type=zeeman; field="0.0 0.0 0.05"; spins=E2;}

    // -------------------------
    // Hyperfine interactions
    // -------------------------

    Interaction FADHYP1 {prefactor = 1.0; type = hyperfine; group1 = E1; group2 = FADN5; tensor =
     trajectory("motions_N5.mst"); trajectory = "motions_N5.mst";}
    Interaction FADHYP2 {prefactor = 1.0; type = hyperfine; group1 = E1; group2 = FADN10; tensor =
     trajectory("motions_N10.mst"); trajectory = "motions_N10.mst";}
    Interaction FADHYP3 {prefactor = 1.0; type = hyperfine; group1 = E1; group2 = FADH6; tensor =
     trajectory("motions_H6.mst"); trajectory = "motions_H6.mst";}
    Interaction FADHYP4 {prefactor = 1.0; type = hyperfine; group1 = E1; group2 = FADHBeta1; tensor =
     trajectory("motions_H1beta.mst"); trajectory = "motions_H1beta.mst";}
    Interaction FADHYP5 {prefactor = 1.0; type = hyperfine; group1 = E1; group2 = FADH81; tensor =
     trajectory("motions_H81.mst"); trajectory = "motions_H81.mst";}
    Interaction FADHYP6 {prefactor = 1.0; type = hyperfine; group1 = E1; group2 = FADH82; tensor =
     trajectory("motions_H82.mst"); trajectory = "motions_H82.mst";}
    Interaction FADHYP7 {prefactor = 1.0; type = hyperfine; group1 = E1; group2 = FADH83; tensor =
     trajectory("motions_H83.mst"); trajectory = "motions_H83.mst";}

    Interaction TRPHYP1 {prefactor = 1.0; type = hyperfine; group1 = E2; group2 = TRPHB1; tensor =
     trajectory("motions_HB1_trp.mst"); trajectory = "motions_HB1_trp.mst";}
    Interaction TRPHYP2 {prefactor = 1.0; type = hyperfine; group1 = E2; group2 = TRPHB2; tensor =
     trajectory("motions_HB2_trp.mst"); trajectory = "motions_HB2_trp.mst";}
    Interaction TRPHYP3 {prefactor = 1.0; type = hyperfine; group1 = E2; group2 = TRPHD1; tensor =
     trajectory("motions_HD1_trp.mst"); trajectory = "motions_HD1_trp.mst";}
    Interaction TRPHYP4 {prefactor = 1.0; type = hyperfine; group1 = E2; group2 = TRPHE1; tensor =
     trajectory("motions_HE1_trp.mst"); trajectory = "motions_HE1_trp.mst";}
    Interaction TRPHYP5 {prefactor = 1.0; type = hyperfine; group1 = E2; group2 = TRPHE3; tensor =
     trajectory("motions_HE3_trp.mst"); trajectory = "motions_HE3_trp.mst";}
```

```
    Interaction TRPHYP6 {prefactor = 1.0; type = hyperfine; group1 = E2; group2 = TRPHH2; tensor =
      trajectory("motions_HH2_trp.mst"); trajectory = "motions_HH2_trp.mst";}
    Interaction TRPHYP7 {prefactor = 1.0; type = hyperfine; group1 = E2; group2 = TRPNE1; tensor =
      trajectory("motions_NE1_trp.mst"); trajectory = "motions_NE1_trp.mst";}

    // -------------------------
    // Spin States
    // --------------------------------------------------------

    State Singlet {spins(E1,E2) = |1/2,-1/2> - |-1/2,1/2>;}
    State T0 {spins(E1,E2) = |1/2,-1/2> + |-1/2,1/2>;}
    State Tp {spin(E2) = |1/2>; spin(E1) = |1/2>;}
    State Tm {spin(E2) = |-1/2>; spin(E1) = |-1/2>;}
    State Identity {}

    // --------------------------------------------------------
    // Transitions
    // --------------------------------------------------------

    Transition Product1 {type = sink; source = Singlet; rate = 1.0e-3;} // in 1/ns
    Transition Product2 {type = sink; source = T0; rate = 1.0e-3;}
    Transition Product3 {type = sink; source = Tp; rate = 1.0e-3;}
    Transition Product4 {type = sink; source = Tm; rate = 1.0e-3;}

}
// ------------------------------------------------------------
Settings
{
    Settings general {steps = 51; notifications = details;}

    // --------------------------------------------------------
    // Actions
    // --------------------------------------------------------

    Action scan1 {type = rotatevector; vector = system1.Zeeman1.field; axis = "0 1 0"; value = 3.6;}
    Action scan2 {type = rotatevector; vector = system1.Zeeman2.field; axis = "0 1 0"; value = 3.6;}

    // --------------------------------------------------------
    // Outputs objects
    // --------------------------------------------------------

    Output orientation1 {type = vectorangle; vector = system1.Zeeman1.field; reference = "0 0 1";}
    Output orientation2 {type = vectorangle; vector = system1.Zeeman2.field; reference = "0 0 1";}
}
Run
{
    Task DynamicStochYield {type = "dynamichs-stoch-yields"; logfile = "Dynamic14Spins.log"; datafile = "Dynamic14Spins.dat";
      transitionyields = true; initialstate = Singlet; montecarlosamples = 5; samplingmethod = "SUZ"; autoseed = false; seed
      = 1; totaltime = 550.0; timestep = 0.5; propagationmethod = "autoexpm"; precision = "single"; yieldcorrections = true;}
}
```

This is the input file used to calculate the static case without time-dependent motions.

```
SpinSystem system1
{
// ------------------------------------------------------------
// Spins
// ------------------------------------------------------------

    // Electrons
    Spin E1 {type = electron; spin = 1/2; tensor = isotropic(2.0023);}
    Spin E2 {type = electron; spin = 1/2; tensor = isotropic(2.0023);}
    // Nitrogens
    Spin FADN5 {type = nucleus; spin = 1; tensor = isotropic(1);}
    Spin FADN10 {type = nucleus; spin = 1; tensor = isotropic(1);}
    Spin TRPNE1 {type = nucleus; spin = 1; tensor = isotropic(1);}
    // Hydrogens
    Spin FADH6 {type = nucleus; spin = 1/2; tensor = isotropic(1);}
    Spin FADHBeta1 {type = nucleus; spin = 1/2; tensor = isotropic(1);}
    Spin FADH81 {type = nucleus; spin = 1/2; tensor = isotropic(1);}
    Spin FADH82 {type = nucleus; spin = 1/2; tensor = isotropic(1);}
    Spin FADH83 {type = nucleus; spin = 1/2 tensor = isotropic(1);;}
    Spin TRPHB1 {type = nucleus; spin = 1/2; tensor = isotropic(1);}
    Spin TRPHB2 {type = nucleus; spin = 1/2; tensor = isotropic(1);}
    Spin TRPHD1 {type = nucleus; spin = 1/2; tensor = isotropic(1);}
    Spin TRPHE1 {type = nucleus; spin = 1/2; tensor = isotropic(1);}
    Spin TRPHE3 {type = nucleus; spin = 1/2; tensor = isotropic(1);}
    Spin TRPHH2 {type = nucleus; spin = 1/2; tensor = isotropic(1);}
    Spin TRPNE1 {type = nucleus; spin = 1; tensor = isotropic(1);}

    // -------------------------
    // Zeeman interaction
    // -------------------------

    Interaction Zeeman1 {prefactor=1e-3; type=zeeman; field="0.0 0.0 0.05"; spins=E1;}
    Interaction Zeeman2 {prefactor=1e-3; type=zeeman; field="0.0 0.0 0.05"; spins=E2;}

    // -------------------------
    // Hyperfine interactions
    // -------------------------

    Interaction FADHYP1 {prefactor = 1e-3; type = hyperfine; group1 = E1; group2 = FADN5; tensor = matrix("-0.09359, 0.00000,
      0.00000; 0.00000, -0.09359, 0.00000; 0.00000, 0.00000, 1.88074");}
    Interaction FADHYP2 {prefactor = 1e-3; type = hyperfine; group1 = E1; group2 = FADN10; tensor = matrix("0.022096,
      -0.011987, -0.081181; -0.011987, 0.016364, 0.047916; -0.081181, 0.047916, 0.684963");}
    Interaction FADHYP3 {prefactor = 1e-3; type = hyperfine; group1 = E1; group2 = FADH6; tensor = matrix("-0.251908,
      -0.123828, 0.001443; -0.123828, -0.408730, -0.000380; 0.001443, -0.000380, -0.408936");}
    Interaction FADHYP4 {prefactor = 1e-3; type = hyperfine; group1 = E1; group2 = FADHBeta1; tensor = matrix("0.121195,
      -0.057543, 0.030752; -0.057543, 0.156364, -0.039068; 0.030752, -0.039068, 0.082324");}
    Interaction FADHYP5 {prefactor = 1e-3; type = hyperfine; group1 = E1; group2 = FADH81; tensor = matrix("0.59178,
      0.03024, 0.01102; 0.03024, 0.66945, 0.02582; 0.01102, 0.02582, 0.58894");}
    Interaction FADHYP6 {prefactor = 1e-3; type = hyperfine; group1 = E1; group2 = FADH82; tensor = matrix("-0.00471,
      -0.02388, 0.00000; -0.02388, 0.07270, 0.00167; 0.0000, 0.00167, -0.00784");}
    Interaction FADHYP7 {prefactor = 1e-3; type = hyperfine; group1 = E1; group2 = FADH83; tensor = matrix("0.61530, 0.02921,
      -0.00917; 0.02921, 0.69678, -0.02473; -0.00917, -0.02473, 0.61306");}

    Interaction TRPHYP1 {prefactor = 1e-3; type = hyperfine; group1 = E2; group2 = TRPHB1; tensor = matrix("0.27841,
      -0.11523, 0.03489; -0.11523, 0.25048, -0.01437; 0.03489, -0.01437, 0.15359");}
    Interaction TRPHYP2 {prefactor = 1e-3; type = hyperfine; group1 = E2; group2 = TRPHB2; tensor = matrix("1.28050,
      -0.02818, 0.11121; -0.02818, 1.20832, 0.00315; 0.11121, 0.00315, 1.32975");}
    Interaction TRPHYP3 {prefactor = 1e-3; type = hyperfine; group1 = E2; group2 = TRPHD1; tensor = matrix("-0.84706,
      0.04893, -0.09419; 0.04893, -0.29433, 0.24691; -0.09419, 0.24691, -0.54792");}
    Interaction TRPHYP4 {prefactor = 1e-3; type = hyperfine; group1 = E2; group2 = TRPHE1; tensor = matrix("-0.3039, 0.20685,
      0.27805; 0.20685, -0.68879, 0.04186; 0.27805, 0.04186, -0.36458");}
    Interaction TRPHYP5 {prefactor = 1e-3; type = hyperfine; group1 = E2; group2 = TRPHE3; tensor = matrix("-0.37054,
      0.06995, 0.18925; 0.06995, -0.76615, -0.06602; 0.18925, -0.06602, -0.51155");}
    Interaction TRPHYP6 {prefactor = 1e-3; rtype = hyperfine; group1 = E2; group2 = TRPHH2; tensor = matrix("-0.47286,
      -0.19165, -0.12872; -0.19165, -0.27373, -0.00185; -0.12872, -0.00185, -0.53654");}
    Interaction TRPHYP7 {prefactor = 1e-3; type = hyperfine; group1 = E2; group2 = TRPNE1; tensor = matrix("0.08309, 0.16473,
      -0.26682; 0.16473, 0.07569, -0.27837; -0.26682, -0.27837, 0.36617");}
```

```

    // -------------------------
    // Spin States
    // --------------------------------------------------------

    State Singlet {spins(E1,E2) = |1/2,-1/2> - |-1/2,1/2>;}
    State T0 {spins(E1,E2) = |1/2,-1/2> + |-1/2,1/2>;}
    State Tp {spin(E2) = |1/2>; spin(E1) = |1/2>;}
    State Tm {spin(E2) = |-1/2>; spin(E1) = |-1/2>;}
    State Identity {}

    // --------------------------------------------------------
    // Transitions
    // --------------------------------------------------------

    Transition Product1 {type = sink; source = Singlet; rate = 1.0e-3;} // in 1/ns
    Transition Product2 {type = sink; source = T0; rate = 1.0e-3;}
    Transition Product3 {type = sink; source = Tp; rate = 1.0e-3;}
    Transition Product4 {type = sink; source = Tm; rate = 1.0e-3;}
}
// ------------------------------------------------------------
Settings
{
    Settings general {steps = 51; notifications = details;}

    // --------------------------------------------------------
    // Actions
    // --------------------------------------------------------

    Action scan1 {type = rotatevector; vector = system1.Zeeman1.field; axis = "0 1 0"; value = 3.6;}
    Action scan2 {type = rotatevector; vector = system1.Zeeman2.field; axis = "0 1 0"; value = 3.6;}

    // --------------------------------------------------------
    // Outputs objects
    // --------------------------------------------------------

    Output orientation1 {type = vectorangle; vector = system1.Zeeman1.field; reference = "0 0 1";}
    Output orientation2 {type = vectorangle; vector = system1.Zeeman2.field; reference = "0 0 1";}
}
Run
{
    Task StaticHSStochYield {type = "statichs-stoch-yields"; logfile = "Static14Spins.log"; datafile = "Static14Spins.dat";
     transitionyields = true; initialstate = Singlet; montecarlosamples = 5; samplingmethod = "SUZ"; autoseed = false; seed
     = 1; epsilon = 0.5; timestep = 4; propagationmethod = "autoexpm"; precision = "single"; yieldcorrections = true;}
}
```

8.9 14 Nulear Spin Relaxation for Full Dynamic Picture (0.953 μs)

The following input was used to calculated the static scenario of the 0.953 ns MD trajectory extracted hyperine and dipolar couplings using a 1 mT magnetic field.

```
SpinSystem system1
{
  // Electrons
  Spin E1 {type = electron;spin = 1/2;tensor = isotropic(2.0023);}
  Spin E2 {type = electron;spin = 1/2;tensor = isotropic(2.0023);}

  // Nitrogens
  Spin FADN5 {type = nucleus;spin = 1; tensor = isotropic(1);}
          Spin FADN10 {type = nucleus;spin = 1; tensor = isotropic(1);}
  // Hydrogens
  Spin FADH6 {type = nucleus;spin = 1/2; tensor = isotropic(1);}
  Spin FADHBeta1 {type = nucleus;spin = 1/2; tensor = isotropic(1);}
  Spin FADH81 {type = nucleus;spin = 1/2; tensor = isotropic(1);}
          Spin FADH82 {type = nucleus;spin = 1/2; tensor = isotropic(1);}
         Spin FADH83 {type = nucleus;spin = 1/2; tensor = isotropic(1);}

  Spin TRPN1 {type = nucleus;spin = 1; tensor = isotropic(1);}
  Spin TRPH1 {type = nucleus;spin = 1/2; tensor = isotropic(1);}
          Spin TRPH2 {type = nucleus;spin = 1/2; tensor = isotropic(1);}
  Spin TRPH4 {type = nucleus;spin = 1/2; tensor = isotropic(1);}
  Spin TRPH6 {type = nucleus;spin = 1/2; tensor = isotropic(1);}
  Spin TRPH7 {type = nucleus;spin = 1/2; tensor = isotropic(1);}
  Spin TRPHbeta1 {type = nucleus;spin = 1/2; tensor = isotropic(1);}
  // -------------------------
  // Zeeman interaction
  // -------------------------

  Interaction Zeeman1 {prefactor= 1e-3;type = zeeman;field = "0.0 0.0 1.0"; spins = E1;}
  Interaction Zeeman2 {prefactor= 1e-3;type = zeeman;field = "0.0 0.0 1.0"; spins = E2;}

  // -------------------------
  // Hyperfine interactions
  // -------------------------

  Interaction FADHYP1 { prefactor = 1.0e-3;  type = hyperfine; group1 = E1; group2 = FADN5; tensor = matrix("0.52007444,
     -0.17396341,  0.77386319; -0.17396341, 0.04412077, -0.24317156; 0.77386319, -0.24317156, 1.14359574");}
  Interaction FADHYP2 { prefactor = 1.0e-3; type = hyperfine; group1 = E1; group2 = FADN10; tensor = matrix("0.18298346,
     -0.05277072,  0.25433445; -0.05277072,  0.02190145, -0.07020126; 0.25433445, -0.07020126,  0.39242808");}
  Interaction FADHYP3 { prefactor = 1.0e-3; type = hyperfine; group1 = E1; group2 = FADH6; tensor = matrix("-0.2436865,
     -0.04785683, -0.10072132; -0.04785683, -0.44075707, 0.01618169; -0.10072132, 0.01618169, -0.3433513");}
  Interaction FADHYP4 { prefactor = 1.0e-3; type = hyperfine; group1 = E1; group2 = FADHBeta1; tensor = matrix("0.14096681,
     -0.03056939, -0.05442738;-0.03056939,  0.13897252,  0.04320126;-0.05442738,  0.04320126,  0.16649513");}
  Interaction FADHYP5 {prefactor=1.0e-3; type = hyperfine; group1 = E1; group2 = FADH81; tensor = matrix("0.39422546,
     -0.00411337, -0.00150647; -0.00411337, 0.46730559, 0.01639295; -0.00150647, 0.01639295, 0.39743516");}
          Interaction FADHYP6 { prefactor = 1.0e-3; type = hyperfine; group1 = E1; group2 = FADH82; tensor =
     matrix("0.39264967, -0.00429489, -0.00158974; -0.00429489,  0.46542371, 0.01649609; -0.00158974, 0.01649609,
     0.39573982");}
          Interaction FADHYP7 { prefactor = 1.0e-3; type = hyperfine; group1 = E1; group2 = FADH83; tensor =
     matrix("0.39603212, -0.00424982, -0.00160015; -0.00424982,  0.46886296,  0.01667159; -0.00160015,  0.01667159,
     0.39929243");}

  Interaction TRPHYP1 { prefactor = 1.0e-3; type = hyperfine; group1 = E2; group2 = TRPN1; tensor = matrix("0.52785038,
     0.35898356, 0.29370566; 0.35898356, 0.29105545, 0.21422574; 0.29370566, 0.21422574, 0.22693535");}
          Interaction TRPHYP2 { prefactor = 1.0e-3; type = hyperfine; group1 = E2; group2 = TRPH1; tensor =
     matrix("-0.66464468, 0.18025424, -0.01356128; 0.18025424, -0.5074232, -0.34080836; -0.01356128, -0.34080836,
     -0.04602107"7);}
          Interaction TRPHYP3 { prefactor = 1.0e-3; type = hyperfine; group1 = E2; group2 = TRPH2; tensor =
     matrix("-0.38499246, -0.20772771,  0.09630866; -0.20772771, -0.16899912, -0.03159051; 0.09630866, -0.03159051,
     -0.58958077");}
```

```
  Interaction TRPHYP4 { prefactor = 1.0e-3; type = hyperfine; group1 = E2; group2 = TRPH4; tensor = matrix("-0.65093005,
      0.16700591, -0.11514255; 0.16700591, -0.70875244, -0.15378603; -0.11514255, -0.15378603, -0.34527729");}
          Interaction TRPHYP5 { prefactor = 1.0e-3; type = hyperfine; group1 = E2; group2 = TRPH6; tensor =
      matrix("-0.2019179,  -0.13717574, -0.04670033; -0.13717574, -0.24083608,  0.11927501; -0.04670033,  0.11927501,
      -0.35520921");}
          Interaction TRPHYP6 { prefactor = 1.0e-3; type = hyperfine; group1 = E2; group2 = TRPH7; tensor =
      matrix("-0.42155253,  0.10419954, -0.09128151; 0.10419954, -0.42748508, -0.12276762; -0.09128151, -0.12276762,
      -0.19691742");}
          Interaction TRPHYP7 { prefactor = 1.0e-3; type = hyperfine; group1 = E2; group2 = TRPHbeta1; tensor =
      matrix("0.22845924, -0.05356532, -0.08962462; -0.05356532, 0.19649593, 0.04482989; -0.08962462, 0.04482989,
      0.26994276");}

  // ------------------------
  // Dipolar interactions
  // ------------------------

  Interaction Dipolar { prefactor = 2.0023e-3; IgnoreTensors = true; type = doublespin; group1 = E1; group2 = E2;
      tensor=matrix("0.44628577, 0.38647182, 0.12319905; 0.38647182, -0.13644849, 0.0615624; 0.12319905, 0.0615624,
      -0.30983728");}
       // We ignore the tensor variable from the Spin objects  and add 2.0023 to the prefactor to only account for one g-value
      for conversion from Tesla into rad/ns (MolSpin multiplies each interaction by a CommonPrefactor (Bohr Magneton/hbar) if
      not set
               to false

  // -------------------------------------------------------
  // Spin States
  // --------------------------------------------------------

           State Singlet {spins(E1,E2) = |1/2,-1/2> - |-1/2,1/2>;}
  State T0 {spins(E1,E2) = |1/2,-1/2> + |-1/2,1/2>;}
  State Tp {spin(E2) = |1/2>; spin(E1) = |1/2>;}
  State Tm {spin(E2) = |-1/2>; spin(E1) = |-1/2>;}
  State Identity {}

        // -------------------------------------------------------
        // Transitions
        // -------------------------------------------------------

  Transition Product1 {type = sink; source = Singlet; rate=1.0e-3;} // in 1/ns
  Transition Product2 {type = sink; source = T0; rate=1.0e-3;}
  Transition Product3 {type = sink; source = Tp; rate=1.0e-3;}
  Transition Product4 {type = sink; source = Tm; rate=1.0e-3;}

}
// ---------------------------------------------------------------
Settings { Settings general {steps = 1; notifications = details;} }
Run
{
  Task StaticHS_Stoch_Yield
        {
    type = "statichs-stoch-yields";
    logfile = "Dynamic14Spins.log";
                  datafile = "Dynamic14Spins.dat";
    transitionyields = true;
    initialstate = Singlet;
    montecarlosamples = 5;
                  samplingmethod = "SUZ";
                  autoseed = false;
                  seed = 1;
    epsilon = 0.1;
    timestep=0.05;
    propagationmethod = "autoexpm";
    precision = "single";
    yieldcorrections = true;
        }
}
```

The following input was used to calculated the full dynamics scenario of the 0.953 ns MD trajectory extracted hyperine and dipolar couplings using a 1 mT magnetic field.

```
SpinSystem system1
{
        // Electrons
        Spin E1 {type = electron;spin = 1/2; tensor = isotropic(2.0023);}
        Spin E2 {type = electron;spin = 1/2; tensor = isotropic(2.0023);}

        // Nitrogens (FAD)
        Spin FADN5 {type = nucleus;spin = 1; tensor = isotropic(1.0);}
        Spin FADN10 {type = nucleus;spin = 1; tensor = isotropic(1.0);}

        // Hydrogens (FAD)
        Spin FADH6 {type = nucleus;spin = 1/2; tensor = isotropic(1.0);}
        Spin FADHBeta1 {type = nucleus;spin = 1/2; tensor = isotropic(1.0);}
        Spin FADH81 {type = nucleus;spin = 1/2; tensor = isotropic(1.0);}
        Spin FADH82 {type = nucleus;spin = 1/2; tensor = isotropic(1.0);}
        Spin FADH83 {type = nucleus;spin = 1/2; tensor = isotropic(1.0);}

        // Nitrogens (TRP)
        Spin TRPN1 {type = nucleus;spin = 1; tensor = isotropic(1.0);}

        // Hydrogens (TRP)
        Spin TRPH1 {type = nucleus;spin = 1/2; tensor = isotropic(1.0);}
        Spin TRPH2 {type = nucleus;spin = 1/2; tensor = isotropic(1.0);}
        Spin TRPH4 {type = nucleus;spin = 1/2; tensor = isotropic(1.0);}
        Spin TRPH6 {type = nucleus;spin = 1/2; tensor = isotropic(1.0);}
        Spin TRPH7 {type = nucleus;spin = 1/2; tensor = isotropic(1.0);}
        Spin TRPHbeta1 {type = nucleus;spin = 1/2; tensor = isotropic(1.0);}

        // ------------------------
        // Zeeman interaction
        // ------------------------

        Interaction Zeeman1 {prefactor= 1e-3;type = zeeman;field = "0.000 0.000 1.000";spins = E1;}
        Interaction Zeeman2 {prefactor= 1e-3;type = zeeman;field = "0.000 0.000 1.000";spins = E2;}

        // ------------------------
        // Hyperfine interactions
        // ------------------------

        Interaction FADHYP1 {type = hyperfine; group1 = E1; group2 = FADN5;
                tensor = trajectory("motions_FAD_N5_dt_50ps.mst"); trajectory = "motions_FAD_N5_dt_50ps.mst";}

        Interaction FADHYP2 {type = hyperfine; group1 = E1; group2 = FADN10;
                tensor = trajectory("motions_FAD_N10_dt_50ps.mst"); trajectory = "motions_FAD_N10_dt_50ps.mst";}

        Interaction FADHYP3 {type = hyperfine; group1 = E1; group2 = FADH6;
                tensor = trajectory("motions_FAD_H6_dt_50ps.mst"); trajectory = "motions_FAD_H6_dt_50ps.mst";}

```

```
        Interaction FADHYP4 {type = hyperfine; group1 = E1; group2 = FADHBeta1;
                tensor = trajectory("motions_FAD_Hbeta1_dt_50ps.mst"); trajectory = "motions_FAD_Hbeta1_dt_50ps.mst";}

        Interaction FADHYP5 {type = hyperfine; group1 = E1; group2 = FADH81;
                tensor = trajectory("motions_FAD_H81_dt_50ps.mst"); trajectory = "motions_FAD_H81_dt_50ps.mst";}

        Interaction FADHYP6 {type = hyperfine; group1 = E1; group2 = FADH82;
                tensor = trajectory("motions_FAD_H82_dt_50ps.mst"); trajectory = "motions_FAD_H82_dt_50ps.mst";}

        Interaction FADHYP7 {type = hyperfine; group1 = E1; group2 = FADH83;
                tensor = trajectory("motions_FAD_H83_dt_50ps.mst"); trajectory = "motions_FAD_H83_dt_50ps.mst";}

        Interaction TRPHYP1 {type = hyperfine; group1 = E2; group2 = TRPN1;
                tensor = trajectory("motions_TRP_N1_dt_50ps.mst"); trajectory = "motions_TRP_N1_dt_50ps.mst";}

        Interaction TRPHYP2 {type = hyperfine; group1 = E2; group2 = TRPH1;
                tensor = trajectory("motions_TRP_H1_dt_50ps.mst"); trajectory = "motions_TRP_H1_dt_50ps.mst"; }

        Interaction TRPHYP3 {type = hyperfine; group1 = E2; group2 = TRPH2;
                tensor = trajectory("motions_TRP_H2_dt_50ps.mst"); trajectory = "motions_TRP_H2_dt_50ps.mst";}

        Interaction TRPHYP4 {type = hyperfine; group1 = E2; group2 = TRPH4;
                tensor = trajectory("motions_TRP_H4_dt_50ps.mst"); trajectory = "motions_TRP_H4_dt_50ps.mst";}

        Interaction TRPHYP5 {type = hyperfine; group1 = E2; group2 = TRPH6;
                tensor = trajectory("motions_TRP_H6_dt_50ps.mst"); trajectory = "motions_TRP_H6_dt_50ps.mst";}

        Interaction TRPHYP6 {type = hyperfine; group1 = E2; group2 = TRPH7;
                tensor = trajectory("motions_TRP_H7_dt_50ps.mst"); trajectory = "motions_TRP_H7_dt_50ps.mst";}

        Interaction TRPHYP7 {type = hyperfine; group1 = E2; group2 = TRPHbeta1;
                tensor = trajectory("motions_TRP_Hbeta1_dt_50ps.mst"); trajectory = "motions_TRP_Hbeta1_dt_50ps.mst";}


        // -------------------------
        // Dipolar interactions
        // -------------------------
        Interaction Dipolar { prefactor = 2.0023; IgnoreTensors = true;type = doublespin; group1 = E1; group2 = E2;
                tensor = trajectory("dipolar_dt_50ps.mst"); trajectory = "dipolar_dt_50ps.mst";}

        // -------------------------
        // Spin States
        // ---------------------------------------------------------

        State Singlet {spins(E1,E2) = |1/2,-1/2> - |-1/2,1/2>;}

        State T0 {spins(E1,E2) = |1/2,-1/2> + |-1/2,1/2>;}

        State Tp {spin(E2) = |1/2>; spin(E1) = |1/2>;}

        State Tm {spin(E2) = |-1/2>; spin(E1) = |-1/2>;}

        State Identity {}

        // ---------------------------------------------------------
        // Transitions
        // ---------------------------------------------------------

        Transition Product1 {type = sink; source = Singlet; rate=1.0e-3;}

        Transition Product2 {type = sink; source = T0; rate=1.0e-3;}

        Transition Product3 {type = sink; source = Tp; rate=1.0e-3;}

        Transition Product4 {type = sink; source = Tm; rate=1.0e-3;}

}
// ------------------------------------------------------------
Settings {

        Settings general {steps = 1; notifications = details;}

//        Action scan1 {type = rotatevector; vector = system1.Zeeman1.field ; axis = "0 1 0"; value = 3.6;}
//        Action scan2 {type = rotatevector; vector = system1.Zeeman2.field; axis = "0 1 0"; value = 3.6;}

}
Run
{
        Task StaticHS_Stoch_Yield
        {
                type = "dynamichs-stoch-yields";
                logfile = "14SpinsCorrectedUnitsFDynamic_0.000.log";
                datafile = "14SpinsCorrectedUnitsFDynamic_0.000.dat";
                transitionyields = true;
                initialstate = Singlet;
                montecarlosamples = 5;
                samplingmethod = "SUZ";
                autoseed = false;
                seed = 1;
                totaltime = 953.0;
                timestep=0.05;
                propagationmethod = "autoexpm";
                precision = "single";
                yieldcorrections = true;
        }
}
```

References

(1) Brocklehurst, B.; McLauchlan, K. A. *Int. J. Radiat. Biol.* **1996**, *69*, 3–24.

(2) Hiscock, H. G.; Worster, S.; Kattnig, D. R.; Steers, C.; Jin, Y.; Manolopoulos, D. E.; Mouritsen, H.; Hore, P. J. *Proc. Natl. Acad. Sci.* **2016**, *113*, 4634–4639.

(3) Fay, T. P.; Lindoy, L. P.; Manolopoulos, D. E.; Hore, P. J. *Faraday Discussions* **2020**, *221*, 77–91.

(4) Smith, L. D.; Chowdhury, F. T.; Peasgood, I.; Dawkins, N.; Kattnig, D. R. *J. Phys. Chem. Lett.* **2022**, *13*, 10500–10506.

(5) Wong, S. Y.; Benjamin, P.; Hore, P. J. *Phys. Chem. Chem. Phys.* **2023**, *25*, 975–982.

(6) Gerhards, L.; Nielsen, C.; Kattnig, D. R.; Hore, P. J.; Solov'yov, I. A. *J. Comput. Chem.* **2023**, *44*, 1704–1714.

(7) Fay, T. P.; Lindoy, L. P.; Manolopoulos, D. E. *J. Chem. Phys.* **2019**, *151*.

(8) Fay, T. P.; Lindoy, L. P.; Manolopoulos, D. E. *J. Chem. Phys.* **2021**, *154*.

(9) Al-Mohy, A. H.; Higham, N. J. *SIAM J. Sci. Comput.* **2011**, *33*, 488–511.

(10) **http://www.molspin.eu**.

(11) Kattnig, D. R.; Solov'yov, I. A.; Hore, P. J. *Phys. Chem. Chem. Phys.* **2016**, *18*, 12443–12456.

(12) Kattnig, D. R. *J. Phys. Chem. B* **2017**, *121*, 10215–10227.

(13) Breuer, H.-P.; Petruccione, F., *The theory of open quantum systems*; Oxford University Press: 2002.

(14) Grüning, G.; Wong, S. Y.; Gerhards, L.; Schuhmann, F.; Kattnig, D. R.; Hore, P. J.; Solov'yov, I. A. *J. Am. Chem. Soc.* **2022**, *144*, PMID: 36459632, 22902–22914.

(15) Frisch, M. J. et al. **2013**, Gaussian Inc. Wallingford CT 2009.

(16) Timmel, C.; Till, U.; Brocklehurst, B.; Mclauchlan, K.; Hore, P. J. *Mol. Phys.* **1998**, *95*, 71–89.

(17) Fay, T. P.; Lewis, A. M.; Manolopoulos, D. E. *J. Chem. Phys* **2017**, *147*.

7 Conclusions

In this thesis, we looked at photodriven radical pair systems that are ubiquitous in science, appearing in the hypothesis of avian magnetoreception.[5,7–9,211] OLEDs as polaron pairs,[208–210] applications in quantum information science,[10–14] and other systems. The thesis investigated some of these topics with computational and theoretical tools, and it was mostly concerned with the simulation of these systems, which have known issues with exponential scaling. The full spin space of a radical pair grows exponentially with the number of particles in the system, and a lot of systems of radical pairs can have as many as 20 or more nuclear spins that are contributing to the spin dynamics. Hence, despite being challenging computationally, this thesis presented clear ways of overcoming these issues.

Chapter 3 examined the effects of isotopic substitutions on the radical pair-based compass mechanism. Isotopic substitutions only significantly alter hyperfine interactions in spin dynamics. We studied ^{14}N, ^{13}C, and ^{2}H substitutions and discovered that the ^{13}C substitution for ^{12}C caused the most change. This result is primarily due to the fact that ^{12}C has $S = 0$, while ^{13}C has $S = 1/2$. This substitution introduces a new hyperfine interaction, whereas nitrogen and hydrogen substitutions only modify the magnetic moments of those nuclear spins and do not significantly affect the anisotropy or the directionality of the singlet yield profile. While simulating all possible triplets of carbon substitutions, we found that substitutions of C4, C4A, and C8α produced the greatest alterations. Consequently, this indicates potential substitution patterns for future experimental and behavioural research. Moreover, we want to clarify an error made in the published study that the author wishes to clarify in this thesis. The abstract of Chapter 3 claims that "*(1) Uniform deuteration of the flavin chromophore appears to be the best way to boost the anisotropy of the magnetic field effect and to change its symmetry.*" This statement is too strong and only holds true when nitrogen is substituted with ^{15}N. Deuteration alone has only shown modest changes in the anisotropy of the system. Therefore, it cannot be considered the best way to enhance the anisotropy for this system. Furthermore, evidently, the scale of the systems used in the calculations was a limiting factor, with the largest system containing only 12 nuclear spins. Despite this, we were able to quantify the effects of isotopic substitutions and suggest potential causes for these effects. Future research should elucidate the effect of a larger number of carbon substitutions, which is now feasible with the implementation of *MolSpin* described in Chapter 6. Furthermore, it is difficult to predict the outcomes of behavioural experiments utilising ^{13}C -enriched riboflavin. We anticipate that birds will respond favourably to the altered riboflavin and that no isotopic effects will be observed in the chemical reactions of this isotopologue (besides the RPM), which has changes only to the molecule's backbone, which should remain unchanged in biochemical transformations. Additional experiments will clarify this.

Chapter 4 looked into time-dependent field effects on the RPM of avian magnetoreception. A method for simulating uncoupled radical pair systems with stochastic time-dependent noise capable of simulating systems with seven nuclear spins in each radical was developed. The principal finding of this chapter was that the action-spectrum histogram concept[122] is a precise theoretical instrument for qualitatively measuring the effect of radiofrequency noise on the spin dynamics of a system. At least for frequencies within the range of 10 MHz to 100 MHz (or 116 MHz for a full-spin system with 27 nuclear spins[90]). In addition, attempts were made to correlate behavioural experiments with spin dynamics calculations, but the results were inconclusive because spin dynamics simulations suggested that RF fields below 2 MHz should have a similar or greater effect than those in the range 2-80 MHz, whereas behavioural experiments indicate that a sufficiently low-frequency RF field would be much less effective at inducing disorientation than one in resonance with spin transitions in the radical. Thus, we were unable to develop a completely consistent model of radiofrequency radiation disruption that follows the RPM model and explains all behavioural results, a feat that had not been accomplished by previous research either.[122] There may be flaws in our simulation methods, such as the use of RF fields much stronger than those in behavioural experiments, the omission of dipolar interaction between radicals, and the use of an inappropriate measure (the root-mean-square difference between singlet yields at different RF field strengths) to quantify the effect of the RF fields. Consequently, future research should focus on identifying systems and models that are compatible with the behavioural experiments.

Chapter 5 examined the EPR pulse sequence design for an RPM system employing the relatively dated[252] concept of idempotent operator expansion for the quantum logic gates. Nevertheless, the study presented various pulse sequences that could be used in experiments, which were an extension and enhancement of the pulse sequences described in Ref. 65 (which were also shown to have a flaw with the sign of parameter $\mathcal{D}$).This was used experimentally in the Appendix D study that convincingly demonstrated an RPM system after a CNOT gate operation. In addition, we demonstrated an absolute limit for the CNOT gate application's fidelity, $\mathcal{F}_{CNOT}$, with respect to the total gate time τ and the T_2 relaxation time:

$$\frac{1}{2} + \frac{1}{2}e^{-\frac{\tau}{T_2}} \geq \mathcal{F}_{CNOT} \tag{7.1}$$

The experiment in Ref. 14 had a total gate time of $\tau = 522$ ns and $T_2 = 1.8$ μs. Consequently, the upper limit for this system is $0.874 \geq \mathcal{F}_{CNOT}$ which is considerably less than the reported fidelity of 0.97. Furthermore, it was demonstrated that the pulse sequences can eliminate contributions to fidelity from static hyperfine interaction contributions and that the fidelity value oscillates rapidly when the magnetic field is relatively strong. This may not be significant for the experimental readout of these systems and subsequent experiments, but reduced magnetic fields should be employed in theory for these experiments. A large number of additional experiments were proposed, such as performing these operations with gradient ascent algorithms, examining the contribution of radical recombination to the performance of these systems, theoretical investigation of quantum state tomography or other readout methods, use of dynamical decoupling or schemes that facilitate the execution of gates, etc.

The final chapter was all about novel *MolSpin* implementations. There were two new primary methods introduced. *Direct* method for small spin systems that scales as $\mathcal{O}(N_t Z^2 \log(Z))$; and *Stochastic* method that scales as $\mathcal{O}(N_t M Z \log(Z))$ with an error that scales as $\mathcal{O}(1/\sqrt{MZ})$. The combination of these two techniques provides a comprehensive selection of tools for simulating all radical pairs of interest. Moreover, the chapter demonstrates the effectiveness of the stochastic method. It is demonstrated that the calculation for $M = 1$ provides a more accurate approximation as the system size increases. Therefore, this technique, scales as $\mathcal{O}(Z \log(Z))$ (for a constant N_t and $M = 1$)–non-exponentially. Due to this, it was possible to simulate an RPM system with 14 nuclear spins whose interactions are based on a molecular dynamics trajectory. We believe that this new software programme will become increasingly useful as more advanced simulations are published in the scientific literature using this software. Lastly, the current heuristic for reducing integration time, which is only available for symmetric recombination rates, could be extended to asymmetric recombination rates, and the implementation of GPUs in the software could further improve the simulation speeds. Otherwise, the software, available at *MolSpin*, can be utilized today for simulations of large and complex spin systems.

* * *

Bibliography

[1] K. McLauchlan and U. Steiner. The spin-correlated radical pair as a reaction intermediate. *Molecular Physics*, **73** (2) 241–263, 1991.

[2] B. Brocklehurst. Magnetic fields and radical reactions: recent developments and their role in nature. *Chemical Society Reviews*, **31** (5) 301–311, 2002.

[3] U. E. Steiner and T. Ulrich. Magnetic field effects in chemical kinetics and related phenomena. *Chemical Reviews*, **89** (1) 51–147, 1989.

[4] C. R. Timmel and K. B. Henbest. A study of spin chemistry in weak magnetic fields. *Philosophical Transactions of the Royal Society of London. Series A: Mathematical, Physical and Engineering Sciences*, **362** (1825) 2573–2589, 2004.

[5] C. T. Rodgers and P. J. Hore. Chemical magnetoreception in birds: the radical pair mechanism. *Proceedings of the National Academy of Sciences*, **106** (2) 353–360, 2009.

[6] P. J. Hore, K. L. Ivanov, and M. R. Wasielewski. Spin chemistry. *The Journal of Chemical Physics*, **152** (12) , 2020.

[7] P. J. Hore and H. Mouritsen. The radical-pair mechanism of magnetoreception. *Annual Review of Biophysics*, **45** (1) 299–344, 2016.

[8] T. Ritz, S. Adem, and K. Schulten. A model for photoreceptor-based magnetoreception in birds. *Biophysical Journal*, **78** (2) 707–718, 2000.

[9] K. Maeda, K. B. Henbest, F. Cintolesi, I. Kuprov, C. T. Rodgers, P. A. Liddell, D. Gust, C. R. Timmel, and P. J. Hore. Chemical compass model of avian magnetoreception. *Nature*, **453** (7193) 387–390, 2008.

[10] H. Mao, G. J. Pažėra, R. M. Young, M. D. Krzyaniak, and M. R. Wasielewski. Quantum gate operations on a spectrally addressable photogenerated molecular electron spin-qubit pair. *Journal of the American Chemical Society*, **145** (11) 6585–6593, 2023.

[11] G. J. Pazera, M. D. Krzyaniak, and M. R. Wasielewski. Pulse sequences for manipulating the spin states of molecular radical-pair-based electron spin qubit systems for quantum information applications. *The Journal of Chemical Physics*, **158** (20) , 2023.

[12] M. R. Wasielewski. Light-driven spin chemistry for quantum information science. *Physics Today*, **76** (3) 28–34, 2023.

[13] M. R. Wasielewski, M. D. E. Forbes, N. L. Frank, K. Kowalski, G. D. Scholes, J. Yuen-Zhou, M. A. Baldo, D. E. Freedman, R. H. Goldsmith, T. Goodson, M. L. Kirk, J. K. McCusker, J. P. Ogilvie, D. A. Shultz, S. Stoll, and K. B. Whaley. Exploiting chemistry and molecular systems for quantum information science. *Nature Reviews Chemistry*, **4** (9) 490–504, 2020.

[14] J. N. Nelson, J. Zhang, J. Zhou, B. K. Rugg, M. D. Krzyaniak, and M. R. Wasielewski. CNOT gate operation on a photogenerated molecular electron spin-qubit pair. **152**, 2020.

[15] P. A. M. Dirac. The quantum theory of the electron. *Proceedings of the Royal Society A: Mathematical, Physical and Engineering Sciences*, **117** (778) 610–624, 1928.

[16] M. H. Levitt. *Spin Dynamics: Basics of Nuclear Magnetic Resonance*. Wiley, 2013.

[17] P. W. Atkins and R. S. Friedman. *Molecular Quantum Mechanics, Fifth Edition*. Oxford University Press, 2010.

[18] G. L. Closs. Mechanism explaining nuclear spin polarizations in radical combination reactions. *Journal of the American Chemical Society*, **91** (16) 4552–4554, 1969.

[19] R. Kaptein and J. Oosterhoff. Chemically induced dynamic nuclear polarization II. *Chemical Physics Letters*, **4** (4) 195–197, 1969.

[20] L. D. Smith, F. T. Chowdhury, I. Peasgood, N. Dawkins, and D. R. Kattnig. Driven radical motion enhances cryptochrome magnetoreception: toward live quantum sensing. *The Journal of Physical Chemistry Letters*, **13** (45) 10500–10506, 2022.

[21] T. P. Fay, A. M. Lewis, and D. E. Manolopoulos. Spin-dependent charge recombination along para-phenylene molecular wires. *The Journal of Chemical Physics*, **147** (6) , 2017.

[22] E. A. Weiss, M. J. Ahrens, L. E. Sinks, A. V. Gusev, M. A. Ratner, and M. R. Wasielewski. Making a molecular wire: charge and spin transport through para-phenylene oligomers. *Journal of the American Chemical Society*, **126** (17) 5577–5584, 2004.

[23] S. G. Ray, S. S. Daube, G. Leitus, Z. Vager, and R. Naaman. Chirality-induced spin-selective properties of self-assembled monolayers of DNA on gold. *Physical Review Letters*, **96** (3) , 2006.

[24] R. Naaman and D. H. Waldeck. Chiral-induced spin selectivity effect. *The Journal of Physical Chemistry Letters*, **3** (16) 2178–2187, 2012.

[25] B. Gohler, V. Hamelbeck, T. Z. Markus, M. Kettner, G. F. Hanne, Z. Vager, R. Naaman, and H. Zacharias. Spin selectivity in electron transmission through self-assembled monolayers of double-stranded DNA. *Science*, **331** (6019) 894–897, 2011.

[26] L. A. Volker, K. Herb, E. Janitz, C. L. Degen, and J. M. Abendroth. Toward quantum sensing of chiral induced spin selectivity: probing donor–bridge–acceptor molecules with NV centers in diamond. *The Journal of Chemical Physics*, **158** (16) , 2023.

[27] A. Privitera, D. Faccio, D. Giuri, D. Genovese, F. Tassinari, L. Mummolo, M. Chiesa, C. Fontanesi, E. Salvadori, A. Cornia, C. Tomasini, and R. Sessoli. Challenges in the direct detection of chirality-induced spin selectivity: investigation of foldamer-based donor/acceptor dyads. *ChemRxiv*, 2022.

[28] C. D. Aiello, J. M. Abendroth, M. Abbas, A. Afanasev, S. Agarwal, A. S. Banerjee, D. N. Beratan, J. N. Belling, B. Berche, A. Botana, J. R. Caram, G. L. Celardo, G. Cuniberti, A. Garcia-Etxarri, A. Dianat, I. Diez-Perez, Y. Guo, R. Gutierrez, C. Herrmann, J. Hihath, S. Kale, P. Kurian, Y.-C. Lai, T. Liu, A. Lopez, E. Medina, V. Mujica, R. Naaman, M. Noormandipour, J. L. Palma, Y. Paltiel, W. Petuskey, J. C. Ribeiro-Silva, J. J. Saenz, E. J. G. Santos, M. Solyanik-Gorgone, V. J. Sorger, D. M. Stemer, J. M. Ugalde, A. Valdes-Curiel, S. Varela, D. H. Waldeck, M. R. Wasielewski, P. S. Weiss, H. Zacharias, and Q. H. Wang. A chirality-based quantum leap. *ACS Nano*, **16** (4) 4989–5035, 2022.

[29] F. Evers, A. Aharony, N. Bar-Gill, O. Entin-Wohlman, P. Hedegard, O. Hod, P. Jelinek, G. Kamieniarz, M. Lemeshko, K. Michaeli, R. Mujica, Vladimiro abd Naaman, Y. Paltiel, S. Rafaely-Abramson, O. Tal, J. Thijssen, M. Thoss, J. M. van Ruitenbeek, L. Venkataraman, D. H. Waldeck, B. Yan, and L. Kronik. Theory of chirality induced spin selectivity: progress and challenges. *Advanced Materials*, **34** (13) , 2022.

[30] A. Chiesa, M. Chizzini, E. Garlatti, E. Salvadori, F. Tacchino, P. Santini, I. Tavernelli, R. Bittl, M. Chiesa, R. Sessoli, and S. Carretta. Assessing the nature of chiral-induced spin selectivity by magnetic resonance. *The Journal of Physical Chemistry Letters*, **12** (27) 6341–6347, 2021.

[31] A. Privitera, E. Macaluso, A. Chiesa, A. Gabbani, D. Faccio, D. Giuri, M. Briganti, N. Giaconi, F. Santanni, N. Jarmouni, L. Poggini, M. Mannini, M. Chiesa, C. Tomasini, F. Pineider, E. Salvadori, S. Carretta, and R. Sessoli. Direct detection of spin polarization in photoinduced charge transfer through a chiral bridge. *Chemical Science*, **13** (41) 12208–12218, 2022.

[32] T. P. Fay and D. T. Limmer. Origin of chirality induced spin selectivity in photoinduced electron transfer. *Nano Letters*, **21** (15) 6696–6702, 2021.

[33] J. Luo and P. J. Hore. Chiral-induced spin selectivity in the formation and recombination of radical pairs: cryptochrome magnetoreception and EPR detection. *New Journal of Physics*, **23** (4) 043032, 2021.

[34] R. Naaman and D. H. Waldeck. Spintronics and chirality: spin selectivity in electron transport through chiral molecules. *Annual Review of Physical Chemistry*, **66** (1) 263–281, 2015.

[35] T. P. Fay and D. T. Limmer. Spin selective charge recombination in chiral donor–bridge–acceptor triads. *The Journal of Chemical Physics*, **158** (19) , 2023.

[36] Y. Tiwari and V. S. Poonia. Role of chiral-induced spin selectivity in the radical pair mechanism of avian magnetoreception. *Phys. Rev. E*, **106** 064409, 2022.

[37] R. Haberkorn. Density matrix description of spin-selective radical pair reactions. *Molecular Physics*, **32** (5) 1491–1493, 1976.

[38] K. L. Ivanov, M. V. Petrova, N. N. Lukzen, and K. Maeda. Consistent treatment of spin-selective recombination of a radical pair confirms the Haberkorn approach. *The Journal of Physical Chemistry A*, **114** (35) 9447–9455, 2010.

[39] T. P. Fay, L. P. Lindoy, and D. E. Manolopoulos. Spin-selective electron transfer reactions of radical pairs: Beyond the Haberkorn master equation. *The Journal of Chemical Physics*, **149** (6) , 2018.

[40] T. Fay. *Quantum Master Equations for Spin Chemistry*. Phd thesis, Oxford Univesity, 2020.

[41] J. Von Neumann. *Mathematical Foundations of Quantum Mechanics*. Princeton University Press, 1955.

[42] R. Bhatia. *Matrix Analysis*, volume 169. Springer Science & Business Media, 2013.

[43] A. I. Shushin. Effect of state-selective reactive decay on the evolution of quantum systems. *The Journal of Chemical Physics*, **133** (4) , 2010.

[44] P. Purtov. To the theory of Zeno chemical effect: the exactly solvable model. *Chemical Physics Letters*, **496** (4–6) 335–338, 2010.

[45] I. K. Kominis. Quantum Zeno effect explains magnetic-sensitive radical-ion-pair reactions. *Physical Review E*, **80** (5) , 2009.

[46] J. A. Jones and P. J. Hore. Spin-selective reactions of radical pairs act as quantum measurements. *Chemical Physics Letters*, **488** (1–3) 90–93, 2010.

[47] R. H. Keens and D. R. Kattnig. Monte-Carlo wavefunction approach for the spin dynamics of recombining radicals. *New Journal of Physics*, **22** (8) 083064, 2020.

[48] D. E. Manolopoulos and P. J. Hore. An improved semiclassical theory of radical pair recombination reactions. *The Journal of Chemical Physics*, **139** (12) , 2013.

[49] A. M. Lewis, T. P. Fay, and D. E. Manolopoulos. An efficient quantum mechanical method for radical pair recombination reactions. *The Journal of Chemical Physics*, **145** (24) , 2016.

[50] G. Strang. *Introduction to Linear Algebra*. SIAM, 2022.

[51] A. M. Lewis, D. E. Manolopoulos, and P. J. Hore. Asymmetric recombination and electron spin relaxation in the semiclassical theory of radical pair reactions. *The Journal of Chemical Physics*, **141** (4) , 2014.

[52] A. Carrington and R. McLachlan. *Introduction to Magnetic Resonance with Applications to Chemistry and Chemical Physics*. Harper & Row, 1967.

[53] C. P. Slichter. *Principles of Magnetic Resonance*. Springer Berlin Heidelberg, 1990.

[54] A. Lewis. *Spin Dynamics in Radical Pairs*. Springer International Publishing, 2018.

[55] T. Ritz, R. Wiltschko, P. Hore, C. T. Rodgers, K. Stapput, P. Thalau, C. R. Timmel, and W. Wiltschko. Magnetic compass of birds is based on a molecule with optimal directional sensitivity. *Biophysical Journal*, **96** (8) 3451–3457, 2009.

[56] C. T. Rodgers. *Magnetic Field Effects in Chemical Systems*. Phd thesis, Oxford University, UK, 2007.

[57] J. A. Weil and J. R. Bolton. *Electron Paramagnetic Resonance*. John Wiley & Sons, Inc., 2006.

[58] S. Kossmann, B. Kirchner, and F. Neese. Performance of modern density functional theory for the prediction of hyperfine structure: meta-GGA and double hybrid functionals. *Molecular Physics*, **105** (15-16) 2049–2071, 2007.

[59] J. S. Hyde. ENDOR of free radicals in solution. *The Journal of Chemical Physics*, **43** (5) 1806–1818, 1965.

[60] B. M. Hoffman, J. Martinsen, and R. A. Venters. General theory of polycrystalline ENDOR patterns. g and hyperfine tensors of arbitrary symmetry and relative orientation. *Journal of Magnetic Resonance (1969)*, **59** (1) 110–123, 1984.

[61] M. F. Chiu, B. C. Gilbert, and P. Hanson. A study by electron spin resonance of some heterocyclic radicals containing elements of group VI. *Journal of the Chemical Society B: Physical Organic*, page 1700, 1970.

[62] M. J. Tauber, R. F. Kelley, J. M. Giaimo, B. Rybtchinski, and M. R. Wasielewski. Electron hopping in π-stacked covalent and self-assembled perylene diimides observed by ENDOR spectroscopy. *Journal of the American Chemical Society*, **128** (6) 1782–1783, 2006.

[63] K. Schulten and P. G. Wolynes. Semiclassical description of electron spin motion in radicals including the effect of electron hopping. *The Journal of Chemical Physics*, **68** (7) 3292–3297, 1978.

[64] M. J. Frisch, G. W. Trucks, H. B. Schlegel, G. E. Scuseria, M. A. Robb, J. R. Cheeseman, J. A. Montgomery, Jr., T. Vreven, K. N. Kudin, J. C. Burant, J. M. Millam, S. S. Iyengar, J. Tomasi, V. Barone, B. Mennucci, M. Cossi, G. Scalmani, N. Rega, G. A. Petersson, H. Nakatsuji, M. Hada, M. Ehara, K. Toyota, R. Fukuda, J. Hasegawa, M. Ishida, T. Nakajima, Y. Honda, O. Kitao, H. Nakai, M. Klene, X. Li, J. E. Knox, H. P. Hratchian, J. B. Cross, V. Bakken, C. Adamo, J. Jaramillo, R. Gomperts, R. E. Stratmann, O. Yazyev, A. J. Austin, R. Cammi, C. Pomelli, J. W. Ochterski, P. Y. Ayala, K. Morokuma, G. A. Voth, P. Salvador, J. J. Dannenberg, V. G. Zakrzewski, S. Dapprich, A. D. Daniels, M. C. Strain, O. Farkas, D. K. Malick, A. D. Rabuck, K. Raghavachari, J. B. Foresman, J. V. Ortiz, Q. Cui, A. G. Baboul, S. Clifford, J. Cioslowski, B. B. Stefanov, G. Liu, A. Liashenko, P. Piskorz, I. Komaromi, R. L. Martin, D. J. Fox, T. Keith, M. A. Al-Laham, C. Y. Peng, A. Nanayakkara, M. Challacombe, P. M. W. Gill, B. Johnson, W. Chen, M. W. Wong, C. Gonzalez, and J. A. Pople. Gaussian 03,revision c.02. Gaussian, Inc., Wallingford, CT, 2004.

[65] M. Y. Volkov and K. M. Salikhov. Pulse protocols for quantum computing with electron spins as qubits. *Applied Magnetic Resonance*, **41** (2–4) 145–154, 2011.

[66] Y. Zhang, C. A. Ryan, R. Laflamme, and J. Baugh. Coherent control of two nuclear spins using the anisotropic hyperfine interaction. *Phys. Rev. Lett.*, **107** 170503, 2011.

[67] J. Tang and J. R. Norris. Multiple-quantum EPR coherence in a spin-correlated radical pair system. *Chemical Physics Letters*, **233** (1–2) 192–200, 1995.

[68] W. W. Cochran, H. Mouritsen, and M. Wikelski. Migrating songbirds recalibrate their magnetic compass daily from twilight cues. *Science*, **304** (5669) 405–408, 2004.

[69] H. Mouritsen. Magnetoreception in birds and its use for long-distance migration. *Sturkie's Avian Physiology*, page 113–133, 2015.

[70] R. Wiltschko and W. Wiltschko. *Magnetic Orientation in Animals*. Springer Berlin Heidelberg, 1995.

[71] W. Wiltschko and R. Wiltschko. Magnetic compass of european robins. *Science*, **176** (4030) 62–64, 1972.

[72] H. O. Wagner and F. Sauer. Die sternenorientierung nächtlich ziehender grasmücken (*Sylvia atricapilla*, *borin* und *curruca*). *Zeitschrift für Tierpsychologie*, **14** (1) 29–70, 1957.

[73] H. Mouritsen and O. N. Larsen. Migrating songbirds tested in computer-controlled Emlen funnels use stellar cues for a time-independent compass. *Journal of Experimental Biology*, **204** (22) 3855–3865, 2001.

[74] S. T. Emlen. Migratory orientation in the *Indigo Bunting*, *Passerina cyanea.* part II: mechanism of celestial orientation. *The Auk*, **84** (4) 463–489, 1967.

[75] H. Mouritsen. Spatiotemporal orientation strategies of long-distance migrants. *Avian Migration*, pages 493–513, 2003.

[76] C. Mettke-Hofmann and E. Gwinner. Long-term memory for a life on the move. *Proceedings of the National Academy of Sciences*, **100** (10) 5863–5866, 2003.

[77] K. P. Able and M. A. Able. Daytime calibration of magnetic orientation in a migratory bird requires a view of skylight polarization. *Nature*, **364** (6437) 523–525, 1993.

[78] A. J. Helbig. Depolarization of natural skylight disrupts orientation of an avian nocturnal migrant. *Experientia*, **46** (7) 755–758, 1990.

[79] G. Kramer. Experiments on bird orientation and their interpretation. *Ibis*, **99** (2) 196–227, 2008.

[80] F. R. Moore. Sunset and the orientation behaviour of migrating birds. *Biological Reviews*, **62** (1) 65–86, 1987.

[81] D. C. Outlaw, G. Voelker, B. Mila, and D. J. Girman. Evolution of long-distance migration in and historical biogeography of *Catharus Thrushes*: a molecular phylogenetic approach. *The Auk*, **120** (2) 299–310, 2003.

[82] J. P. Hoover. Decision rules for site fidelity in a migratory bird, the prothonotary warbler. *Ecology*, **84** (2) 416–430, 2003.

[83] W. L. Engels. Day-length and termination of photorefractoriness in the annual testicular cycle of the transequatorial migrant dolichonyx (the bobolink). *The Biological Bulletin*, **123** (1) 94–104, 1962.

[84] P. O. Dunn and D. W. Winkler. Climate change has affected the breeding date of tree swallows throughout north america. *Proceedings of the Royal Society of London. Series B: Biological Sciences*, **266** (1437) 2487–2490, 1999.

[85] R. Muheim, J. Backman, and S. Akesson. Magnetic compass orientation in european robins is dependent on both wavelength and intensity of light. *Journal of Experimental Biology*, **205** (24) 3845–3856, 2002.

[86] R. Wiltschko, K. Stapput, P. Thalau, and W. Wiltschko. Directional orientation of birds by the magnetic field under different light conditions. *Journal of The Royal Society Interface*, **7**, 2009.

[87] W. Wiltschko and R. Wiltschko. Light-dependent magnetoreception in birds: the behaviour of european robins, *Erithacus rubecula*, under monochromatic light of various wavelengths and intensities. *Journal of Experimental Biology*, **204** (19) 3295–3302, 2001.

[88] W. Wiltschko, U. Munro, H. Ford, and R. Wiltschko. Red light disrupts magnetic orientation of migratory birds. *Nature*, **364** (6437) 525–527, 1993.

[89] B. Leberecht, S. Y. Wong, B. Satish, S. Döge, J. Hindman, L. Venkatraman, S. Apte, K. Haase, I. Musielak, G. Dautaj, I. A. Solov'yov, M. Winklhofer, H. Mouritsen, and P. J. Hore. Upper bound for broadband radiofrequency field disruption of magnetic compass orientation in night-migratory songbirds. *Proceedings of the National Academy of Sciences*, **120** (28) , 2023.

[90] B. Leberecht, D. Kobylkov, T. Karwinkel, S. Döge, L. Burnus, S. Y. Wong, S. Apte, K. Haase, I. Musielak, R. Chetverikova, G. Dautaj, M. Bassetto, M. Winklhofer, P. J. Hore, and H. Mouritsen. Broadband 75–85 MHz radiofrequency fields disrupt magnetic compass orientation in night-migratory songbirds consistent with a flavin-based radical pair magnetoreceptor. *Journal of Comparative Physiology A*, **208** (1) 97–106, 2022.

[91] D. Kobylkov, J. Wynn, M. Winklhofer, R. Chetverikova, J. Xu, H. Hiscock, P. J. Hore, and H. Mouritsen. Electromagnetic 0.1–100 kHz noise does not disrupt orientation in a night-migrating songbird implying a spin coherence lifetime of less than 10 μs. *Journal of The Royal Society Interface*, **16** (161) 20190716, 2019.

[92] S. Schwarze, N.-L. Schneider, T. Reichl, D. Dreyer, N. Lefeldt, S. Engels, N. Baker, P. J. Hore, and H. Mouritsen. Weak broadband electromagnetic fields are more disruptive to magnetic compass orientation in a night-migratory songbird (*Erithacus rubecula*) than strong narrow-band fields. *Frontiers in Behavioral Neuroscience*, **10**, 2016.

[93] T. Ritz, P. Thalau, J. B. Phillips, R. Wiltschko, and W. Wiltschko. Resonance effects indicate a radical-pair mechanism for avian magnetic compass. *Nature*, **429** (6988) 177–180, 2004.

[94] S. Engels, N.-L. Schneider, N. Lefeldt, C. M. Hein, M. Zapka, A. Michalik, D. Elbers, A. Kittel, P. J. Hore, and H. Mouritsen. Anthropogenic electromagnetic noise disrupts magnetic compass orientation in a migratory bird. *Nature*, **509** (7500) 353–356, 2014.

[95] K. Schulten, C. E. Swenberg, and A. Weller. A biomagnetic sensory mechanism based on magnetic field modulated coherent electron spin motion. *Zeitschrift für Physikalische Chemie*, **111** (1) 1–5, 1978.

[96] M. Ahmad and A. R. Cashmore. HY4 gene of *A. thaliana* encodes a protein with characteristics of a blue-light photoreceptor. *Nature*, **366** (6451) 162–166, 1993.

[97] I. Chaves, R. Pokorny, M. Byrdin, N. Hoang, T. Ritz, K. Brettel, L.-O. Essen, G. T. J. van der Horst, A. Batschauer, and M. Ahmad. The cryptochromes: blue light photoreceptors in plants and animals. *Annual Review of Plant Biology*, **62** (1) 335–364, 2011.

[98] H. Mouritsen and P. J. Hore. The magnetic retina: light-dependent and trigeminal magnetoreception in migratory birds. *Current Opinion in Neurobiology*, **22** (2) 343–352, 2012.

[99] M. Liedvogel and H. Mouritsen. Cryptochromes—a potential magnetoreceptor: what do we know and what do we want to know? *Journal of The Royal Society Interface*, **7**, 2009.

[100] C. A. Dodson, P. J. Hore, and M. I. Wallace. A radical sense of direction: signalling and mechanism in cryptochrome magnetoreception. *Trends in Biochemical Sciences*, **38** (9) 435–446, 2013.

[101] K. Mobius and A. Savitsky. *High-Field EPR Spectroscopy on Proteins and Their Model Systems*. R. Soc. Chem., Cambridge, UK, 2009.

[102] A. Zeugner, M. Byrdin, J.-P. Bouly, N. Bakrim, B. Giovani, K. Brettel, and M. Ahmad. Light-induced electron transfer in *Arabidopsis* cryptochrome-1 correlates with in vivo function. *Journal of Biological Chemistry*, **280** (20) 19437–19440, 2005.

[103] P. Muller, J. Yamamoto, R. Martin, S. Iwai, and K. Brettel. Discovery and functional analysis of a 4th electron-transferring tryptophan conserved exclusively in animal cryptochromes and (6-4) photolyases. *Chemical Communications*, **51** (85) 15502–15505, 2015.

[104] F. Cailliez, P. Muller, T. Firmino, P. Pernot, and A. de la Lande. Energetics of photoinduced charge migration within the tryptophan tetrad of an animal (6–4) photolyase. *Journal of the American Chemical Society*, **138** (6) 1904–1915, 2016.

[105] T. Biskup, E. Schleicher, A. Okafuji, G. Link, K. Hitomi, E. Getzoff, and S. Weber. Direct observation of a photoinduced radical pair in a cryptochrome blue-light photoreceptor. *Angewandte Chemie International Edition*, **48** (2) 404–407, 2009.

[106] J. Xu, L. E. Jarocha, T. Zollitsch, M. Konowalczyk, K. B. Henbest, S. Richert, M. J. Golesworthy, J. Schmidt, V. Déjean, D. J. C. Sowood, M. Bassetto, J. Luo, J. R. Walton, J. Fleming, Y. Wei, T. L. Pitcher, G. Moise, M. Herrmann, H. Yin, H. Wu, R. Bartölke, S. J. Käsehagen, S. Horst, G. Dautaj, P. D. F. Murton, A. S. Gehrckens, Y. Chelliah, J. S. Takahashi, K.-W. Koch, S. Weber, I. A. Solov'yov, C. Xie, S. R. Mackenzie, C. R. Timmel, H. Mouritsen, and P. J. Hore. Magnetic sensitivity of cryptochrome 4 from a migratory songbird. *Nature*, **594** (7864) 535–540, 2021.

[107] G. Gruning, S. Y. Wong, L. Gerhards, F. Schuhmann, D. R. Kattnig, P. J. Hore, and I. A. Solov'yov. Effects of dynamical degrees of freedom on magnetic compass sensitivity: A comparison of plant and avian cryptochromes. *Journal of the American Chemical Society*, **144** (50) 22902–22914, 2022.

[108] C. Kerpal, S. Richert, J. G. Storey, S. Pillai, P. A. Liddell, D. Gust, S. R. Mackenzie, P. J. Hore, and C. R. Timmel. Chemical compass behaviour at microtesla magnetic fields strengthens the radical pair hypothesis of avian magnetoreception. *Nature Communications*, **10** (1) , 2019.

[109] M. Liedvogel, K. Maeda, K. Henbest, E. Schleicher, T. Simon, C. R. Timmel, P. J. Hore, and H. Mouritsen. Chemical magnetoreception: bird cryptochrome 1a is excited by blue light and forms long-lived radical-pairs. *PLoS ONE*, **2** (10) e1106, 2007.

[110] K. Maeda, A. J. Robinson, K. B. Henbest, H. J. Hogben, T. Biskup, M. Ahmad, E. Schleicher, S. Weber, C. R. Timmel, and P. J. Hore. Magnetically sensitive light-induced reactions in cryptochrome are consistent with its proposed role as a magnetoreceptor. *Proceedings of the National Academy of Sciences*, **109** (13) 4774–4779, 2012.

[111] S. Y. Wong, Y. Wei, H. Mouritsen, I. A. Solov'yov, and P. J. Hore. Cryptochrome magnetoreception: four tryptophans could be better than three. *Journal of The Royal Society Interface*, **18** (184) , 2021.

[112] M. Hanic, L. M. Antill, A. S. Gehrckens, J. Schmidt, K. Görtemaker, R. Bartölke, T. J. El-Baba, J. Xu, K. W. Koch, H. Mouritsen, J. L. P. Benesch, P. J. Hore, and I. A. Solov'yov. Dimerisation of european robin cryptochrome 4a. *bioRxiv*, 2023.

[113] A. Dellis and I. Kominis. The quantum Zeno effect immunizes the avian compass against the deleterious effects of exchange and dipolar interactions. *Biosystems*, **107** 153–157, 2012.

[114] H. G. Hiscock, S. Worster, D. R. Kattnig, C. Steers, Y. Jin, D. E. Manolopoulos, H. Mouritsen, and P. J. Hore. The quantum needle of the avian magnetic compass. *Proceedings of the National Academy of Sciences*, **113** (17) 4634–4639, 2016.

[115] A. A. Lee, J. C. S. Lau, H. J. Hogben, T. Biskup, D. R. Kattnig, and P. J. Hore. Alternative radical pairs for cryptochrome-based magnetoreception. *Journal of The Royal Society Interface*, **11** (95) 20131063, 2014.

[116] Y. Zhang, G. P. Berman, and S. Kais. Sensitivity and entanglement in the avian chemical compass. *Phys. Rev. E*, **90** 042707, 2014.

[117] N. Ozturk, C. P. Selby, Y. Annayev, D. Zhong, and A. Sancar. Reaction mechanism of *Drosophila* cryptochrome. *Proceedings of the National Academy of Sciences*, **108** 516–521, 2010.

[118] E. M. Gauger, E. Rieper, J. J. L. Morton, S. C. Benjamin, and V. Vedral. Sustained quantum coherence and entanglement in the avian compass. *Phys. Rev. Lett.*, **106** 040503, 2011.

[119] A. Carrillo, M. F. Cornelio, and M. C. de Oliveira. Environment-induced anisotropy and sensitivity of the radical pair mechanism in the avian compass. *Phys. Rev. E*, **92** 012720, 2015.

[120] J. Cai, G. G. Guerreschi, and H. J. Briegel. Quantum control and entanglement in a chemical compass. *Phys. Rev. Lett.*, **104** 220502, 2010.

[121] J. N. Bandyopadhyay, T. Paterek, and D. Kaszlikowski. Quantum coherence and sensitivity of avian magnetoreception. *Phys. Rev. Lett.*, **109** 110502, 2012.

[122] H. G. Hiscock, H. Mouritsen, D. E. Manolopoulos, and P. J. Hore. Disruption of magnetic compass orientation in migratory birds by radiofrequency electromagnetic fields. *Biophysical Journal*, **113** (7) 1475–1484, 2017.

[123] P. Berthold. A comprehensive theory for the evolution, control and adaptability of avian migration. *Ostrich*, **70** (1) 1–11, 1999.

[124] E. W. Evans, D. R. Kattnig, K. B. Henbest, P. J. Hore, S. R. Mackenzie, and C. R. Timmel. Sub-millitesla magnetic field effects on the recombination reaction of flavin and ascorbic acid radicals. *The Journal of Chemical Physics*, **145** (8) , 2016.

[125] T. C. Player and P. J. Hore. Viability of superoxide-containing radical pairs as magnetoreceptors. *The Journal of Chemical Physics*, **151** (22) , 2019.

[126] O. Efimova and P. J. Hore. Role of exchange and dipolar interactions in the radical pair model of the avian magnetic compass. *Biophysical Journal*, **94** (5) 1565–1574, 2008.

[127] J. Deviers, F. Cailliez, A. de la Lande, and D. R. Kattnig. Anisotropic magnetic field effects in the re-oxidation of cryptochrome in the presence of scavenger radicals. *The Journal of Chemical Physics*, **156** (2) , 2022.

[128] R. H. Keens, C. Sampson, and D. R. Kattnig. How symmetry-breaking can amplify the magnetosensitivity of dipolarly coupled n-radical systems. *The Journal of Chemical Physics*, **154** (9) , 2021.

[129] D. R. Kattnig and P. J. Hore. The sensitivity of a radical pair compass magnetoreceptor can be significantly amplified by radical scavengers. *Scientific Reports*, **7** (1) , 2017.

[130] A. Marais, B. Adams, A. K. Ringsmuth, M. Ferretti, J. M. Gruber, R. Hendrikx, M. Schuld, S. L. Smith, I. Sinayskiy, T. P. Krüger, et al. The future of quantum biology. *Journal of the Royal Society Interface*, **15** (148) 20180640, 2018.

[131] J. McFadden and J. Al-Khalili. The origins of quantum biology. *Proceedings of the Royal Society A*, **474** (2220) 20180674, 2018.

[132] N. Lambert, Y. N. Chen, Y. C. Cheng, C. M. Li, G. Y. Chen, and F. Nori. Quantum biology. *Nature Physics*, **9** (1) 10–18, 2013.

[133] Y. Kim, F. Bertagna, E. M. D'souza, D. J. Heyes, L. O. Johannissen, E. T. Nery, A. Pantelias, A. Sanchez-Pedreño Jimenez, L. Slocombe, M. G. Spencer, et al. Quantum biology: An update and perspective. *Quantum Reports*, **3** (1) 80–126, 2021.

[134] Z.-X. Liang and J. P. Klinman. Structural bases of hydrogen tunneling in enzymes: progress and puzzles. *Current Opinion in Structural Biology*, **14** (6) 648–655, 2004.

[135] M. Garcia-Viloca, J. Gao, M. Karplus, and D. G. Truhlar. How enzymes work: analysis by modern rate theory and computer simulations. *Science*, **303** (5655) 186–195, 2004.

[136] G. Maglia and R. K. Allemann. Evidence for environmentally coupled hydrogen tunneling during dihydrofolate reductase catalysis. *Journal of the American Chemical Society*, **125** (44) 13372–13373, 2003.

[137] M. J. Knapp and J. P. Klinman. Environmentally coupled hydrogen tunneling. *European Journal of Biochemistry*, **269** (13) 3113–3121, 2002.

[138] S. R. Billeter, S. P. Webb, P. K. Agarwal, T. Iordanov, and S. Hammes-Schiffer. Hydride transfer in liver alcohol dehydrogenase: quantum dynamics, kinetic isotope effects, and role of enzyme motion. *Journal of the American Chemical Society*, **123** (45) 11262–11272, 2001.

[139] C. Alhambra, J. Corchado, M. L. Sánchez, M. Garcia-Viloca, J. Gao, and D. G. Truhlar. Canonical variational theory for enzyme kinetics with the protein mean force and multidimensional quantum mechanical tunneling dynamics. theory and application to liver alcohol dehydrogenase. *The Journal of Physical Chemistry B*, **105** (45) 11326–11340, 2001.

[140] J. Basran, M. J. Sutcliffe, and N. S. Scrutton. Enzymatic h-transfer requires vibration-driven extreme tunneling. *Biochemistry*, **38** (10) 3218–3222, 1999.

[141] B. J. Bahnson, T. D. Colby, J. K. Chin, B. M. Goldstein, and J. P. Klinman. A link between protein structure and enzyme catalyzed hydrogen tunneling. *Proceedings of the National Academy of Sciences*, **94** (24) 12797–12802, 1997.

[142] Z.-X. Liang, T. Lee, K. A. Resing, N. G. Ahn, and J. P. Klinman. Thermal-activated protein mobility and its correlation with catalysis in thermophilic alcohol dehydrogenase. *Proceedings of the National Academy of Sciences*, **101** (26) 9556–9561, 2004.

[143] L. Masgrau, A. Roujeinikova, L. O. Johannissen, P. Hothi, J. Basran, K. E. Ranaghan, A. J. Mulholland, M. J. Sutcliffe, N. S. Scrutton, and D. Leys. Atomic description of an enzyme reaction dominated by proton tunneling. *Science*, **312** (5771) 237–241, 2006.

[144] M. H. M. Olsson, W. W. Parson, and A. Warshel. Dynamical contributions to enzyme catalysis: Critical tests of a popular hypothesis. *Chemical Reviews*, **106** (5) 1737–1756, 2006.

[145] J. Pu, J. Gao, and D. G. Truhlar. Multidimensional tunneling, recrossing, and the transmission coefficient for enzymatic reactions. *Chemical Reviews*, **106** (8) 3140–3169, 2006.

[146] S. Hay, C. R. Pudney, and N. S. Scrutton. Structural and mechanistic aspects of flavoproteins: probes of hydrogen tunnelling. *FEBS Journal*, **276** (15) 3930–3941, 2009.

[147] D. T. Major, A. Heroux, A. M. Orville, M. P. Valley, P. F. Fitzpatrick, and J. Gao. Differential quantum tunneling contributions in nitroalkane oxidase catalyzed and the uncatalyzed proton transfer reaction. *Proceedings of the National Academy of Sciences*, **106** (49) 20734–20739, 2009.

[148] S. C. L. Kamerlin, J. Mavri, and A. Warshel. Examining the case for the effect of barrier compression on tunneling, vibrationally enhanced catalysis, catalytic entropy and related issues. *FEBS Letters*, **584** (13) 2759–2766, 2010.

[149] S. C. L. Kamerlin and A. Warshel. An analysis of all the relevant facts and arguments indicates that enzyme catalysis does not involve large contributions from nuclear tunneling. *Journal of Physical Organic Chemistry*, **23** (7) 677–684, 2010.

[150] J. R. Bolton and D. O. Hall. The maximum efficiency of photosynthesis. *Photochemistry and Photobiology*, **53** (4) 545–548, 1991.

[151] X.-G. Zhu, S. P. Long, and D. R. Ort. What is the maximum efficiency with which photosynthesis can convert solar energy into biomass? *Current Opinion in Biotechnology*, **19** (2) 153–159, 2008.

[152] G. Y. Chen, N. Lambert, C. M. Li, Y. N. Chen, and F. Nori. Rerouting excitation transfers in the Fenna-Matthews-Olson complex. *Phys. Rev. E*, **88** 032120, 2013.

[153] G. Panitchayangkoon, D. V. Voronine, D. Abramavicius, J. R. Caram, N. H. C. Lewis, S. Mukamel, and G. S. Engel. Direct evidence of quantum transport in photosynthetic light-harvesting complexes. *Proceedings of the National Academy of Sciences*, **108** (52) 20908–20912, 2011.

[154] W. Wang, H. W. Hellinga, and L. S. Beese. Structural evidence for the rare tautomer hypothesis of spontaneous mutagenesis. *Proceedings of the National Academy of Sciences*, **108** (43) 17644–17648, 2011.

[155] N. Chatterjee and G. C. Walker. Mechanisms of DNA damage, repair, and mutagenesis. *Environmental and Molecular Mutagenesis*, **58** (5) 235–263, 2017.

[156] C. Marletto. Constructor theory of life. *Journal of The Royal Society Interface*, **12** (104) 20141226, 2015.

[157] R. P. Feynman. Simulating physics with computers. *International Journal of Theoretical Physics*, **21** (6–7) 467–488, 1982.

[158] D. Deutsch. Quantum theory, the Church–Turing principle and the universal quantum computer. *Proceedings of the Royal Society of London. A. Mathematical and Physical Sciences*, **400** (1818) 97–117, 1985.

[159] P. W. Shor. Algorithms for quantum computation: discrete logarithms and factoring. In *Proceedings 35th annual symposium on foundations of computer science*, pages 124–134. Ieee, 1994.

[160] L. K. Grover. A fast quantum mechanical algorithm for database search. *Proceedings of the twenty-eighth annual ACM symposium on theory of computing - STOC*, 1996.

[161] S. Lloyd. Universal quantum simulators. *Science*, **273** (5278) 1073–1078, 1996.

[162] M. A. Nielsen and I. L. Chuang. *Quantum Computation and Quantum Information: 10th Anniversary Edition*. Cambridge University Press, 2010.

[163] D. P. DiVincenzo. The physical implementation of quantum computation. *Fortschritte der Physik*, **48** (9–11) 771–783, 2000.

[164] M. Tolunay, I. Liepuoniute, M. Vyushkova, and B. A. Jones. Hamiltonian simulation of quantum beats in radical pairs undergoing thermal relaxation on near-term quantum computers. *Physical Chemistry Chemical Physics*, **25** (22) 15115–15134, 2023.

[165] Y. Zhang, Z. Hu, Y. Wang, and S. Kais. Quantum simulation of the radical pair dynamics of the avian compass. *The Journal of Physical Chemistry Letters*, **14** (3) 832–837, 2023.

[166] S. J. Devitt, W. J. Munro, and K. Nemoto. Quantum error correction for beginners. *Reports on Progress in Physics*, **76** (7) 076001, 2013.

[167] D. A. Lidar and T. A. Brun. *Quantum Error Correction*. Cambridge university press, 2013.

[168] J. Chiaverini, D. Leibfried, T. Schaetz, M. D. Barrett, R. Blakestad, J. Britton, W. M. Itano, J. D. Jost, E. Knill, C. Langer, et al. Realization of quantum error correction. *Nature*, **432** (7017) 602–605, 2004.

[169] Y. Wang, Z. Hu, B. C. Sanders, and S. Kais. Qudits and high-dimensional quantum computing. *Frontiers in Physics*, **8** 589504, 2020.

[170] F. Arute, K. Arya, R. Babbush, D. Bacon, J. C. Bardin, R. Barends, R. Biswas, S. Boixo, F. G. Brandao, D. A. Buell, et al. Quantum supremacy using a programmable superconducting processor. *Nature*, **574** (7779) 505–510, 2019.

[171] X. Zhang, H. O. Li, G. Cao, M. Xiao, G. C. Guo, and G. P. Guo. Semiconductor quantum computation. *National Science Review*, **6** (1) 32–54, 2019.

[172] L. M. Vandersypen and M. A. Eriksson. Quantum computing with semiconductor spins. *Physics Today*, **72** (8) 38–45, 2019.

[173] H. J. Briegel, T. Calarco, D. Jaksch, J. I. Cirac, and P. Zoller. Quantum computing with neutral atoms. *Journal of modern optics*, **47** (2-3) 415–451, 2000.

[174] L. Henriet, L. Beguin, A. Signoles, T. Lahaye, A. Browaeys, G. O. Reymond, and C. Jurczak. Quantum computing with neutral atoms. *Quantum*, **4** 327, 2020.

[175] D. S. Weiss and M. Saffman. Quantum computing with neutral atoms. *Physics Today*, **70** (7) 44–50, 2017.

[176] J. Benhelm, G. Kirchmair, C. F. Roos, and R. Blatt. Towards fault-tolerant quantum computing with trapped ions. *Nature Physics*, **4** (6) 463–466, 2008.

[177] H. Häffner, C. F. Roos, and R. Blatt. Quantum computing with trapped ions. *Physics reports*, **469** (4) 155–203, 2008.

[178] C. D. Bruzewicz, J. Chiaverini, R. McConnell, and J. M. Sage. Trapped-ion quantum computing: Progress and challenges. *Applied Physics Reviews*, **6** (2) , 2019.

[179] J. Weber, W. Koehl, J. Varley, A. Janotti, B. Buckley, C. Van de Walle, and D. D. Awschalom. Quantum computing with defects. *Proceedings of the National Academy of Sciences*, **107** (19) 8513–8518, 2010.

[180] W. Yang, Z. Yin, Y. Hu, M. Feng, and J. Du. High-fidelity quantum memory using nitrogen-vacancy center ensemble for hybrid quantum computation. *Physical Review A*, **84** (1) 010301, 2011.

[181] V. Acosta and P. Hemmer. Nitrogen-vacancy centers: physics and applications. *MRS bulletin*, **38** (2) 127–130, 2013.

[182] K. Bharti, A. Cervera-Lierta, T. H. Kyaw, T. Haug, S. Alperin-Lea, A. Anand, M. Degroote, H. Heimonen, J. S. Kottmann, T. Menke, et al. Noisy intermediate-scale quantum algorithms. *Reviews of Modern Physics*, **94** (1) 015004, 2022.

[183] M. Atzori and R. Sessoli. The second quantum revolution: role and challenges of molecular chemistry. *Journal of the American Chemical Society*, **141** (29) 11339–11352, 2019.

[184] D. Aguila, L. A. Barrios, V. Velasco, O. Roubeau, A. Repolles, P. J. Alonso, J. Sese, S. J. Teat, F. Luis, and G. Aromi. Heterodimetallic [LnLn'] lanthanide complexes: toward a chemical design of two-qubit molecular spin quantum gates. *Journal of the American Chemical Society*, **136** (40) 14215–14222, 2014.

[185] A. Fernandez, E. Moreno Pineda, C. A. Muryn, S. Sproules, F. Moro, G. A. Timco, E. J. L. McInnes, and R. E. P. Winpenny. g-engineering in hybrid rotaxanes to create AB and AB2 electron spin systems: EPR spectroscopic studies of weak interactions between dissimilar electron spin qubits. *Angewandte Chemie International Edition*, **54** (37) 10858–10861, 2015.

[186] J. M. Zadrozny, J. Niklas, O. G. Poluektov, and D. E. Freedman. Millisecond coherence time in a tunable molecular electronic spin qubit. *ACS Central Science*, **1** (9) 488–492, 2015.

[187] M. Atzori, A. Chiesa, E. Morra, M. Chiesa, L. Sorace, S. Carretta, and R. Sessoli. A two-qubit molecular architecture for electron-mediated nuclear quantum simulation. *Chemical Science*, **9** (29) 6183–6192, 2018.

[188] B. W. Stein, C. R. Tichnell, J. Chen, D. A. Shultz, and M. L. Kirk. Excited state magnetic exchange interactions enable large spin polarization effects. *Journal of the American Chemical Society*, **140** (6) 2221–2228, 2018.

[189] M. M. Paquette, D. Plaul, A. Kurimoto, B. O. Patrick, and M. L. Frank. Opto-spintronics: photoisomerization-induced spin state switching at 300 K in photochrome cobalt–dioxolene thin films. *Journal of the American Chemical Society*, **140** (44) 14990–15000, 2018.

[190] L. V. H. Rodgers, L. B. Hughes, M. Xie, P. C. Maurer, S. Kolkowitz, A. C. Bleszynski Jayich, and N. P. de Leon. Materials challenges for quantum technologies based on color centers in diamond. *MRS Bulletin*, **46** (7) 623–633, 2021.

[191] G. Q. Liu and X. Y. Pan. Quantum information processing with nitrogen–vacancy centers in diamond. *Chinese Physics B*, **27** (2) 020304, 2018.

[192] R. J. Epstein, F. M. Mendoza, Y. K. Kato, and D. D. Awschalom. Anisotropic interactions of a single spin and dark-spin spectroscopy in diamond. *Nature Physics*, **1** (2) 94–98, 2005.

[193] X. Rong, J. Geng, F. Shi, Y. Liu, K. Xu, W. Ma, F. Kong, Z. Jiang, Y. Wu, and J. Du. Experimental fault-tolerant universal quantum gates with solid-state spins under ambient conditions. *Nature Communications*, **6** (1) , 2015.

[194] B. C. Rose, D. Huang, Z.-H. Zhang, P. Stevenson, A. M. Tyryshkin, S. Sangtawesin, S. Srinivasan, L. Loudin, M. L. Markham, A. M. Edmonds, D. J. Twitchen, S. A. Lyon, and N. P. de Leon. Observation of an environmentally insensitive solid-state spin defect in diamond. *Science*, **361** (6397) 60–63, 2018.

[195] D. D. Sukachev, A. Sipahigil, C. T. Nguyen, M. K. Bhaskar, R. E. Evans, F. Jelezko, and M. D. Lukin. Silicon-vacancy spin qubit in diamond: a quantum memory exceeding 10 ms with single-shot state readout. *Phys. Rev. Lett.*, **119** 223602, 2017.

[196] J. L. O'Brien, S. R. Schofield, M. Y. Simmons, R. G. Clark, A. S. Dzurak, N. J. Curson, B. E. Kane, N. S. McAlpine, M. E. Hawley, and G. W. Brown. Towards the fabrication of phosphorus qubits for a silicon quantum computer. *Phys. Rev. B*, **64** 161401, 2001.

[197] J. C. McCallum, B. C. Johnson, and T. Botzem. Donor-based qubits for quantum computing in silicon. *Applied Physics Reviews*, **8** (3) , 2021.

[198] Q. Li, L. Cywiński, D. Culcer, X. Hu, and S. Das Sarma. Exchange coupling in silicon quantum dots: theoretical considerations for quantum computation. *Phys. Rev. B*, **81** 085313, 2010.

[199] M. A. Eriksson, M. Friesen, S. N. Coppersmith, R. Joynt, L. J. Klein, K. Slinker, C. Tahan, P. M. Mooney, J. O. Chu, and S. J. Koester. Spin-based quantum dot quantum computing in silicon. *Quantum Information Processing*, **3** (1–5) 133–146, 2004.

[200] X. Mi, M. Benito, S. Putz, D. M. Zajac, J. M. Taylor, G. Burkard, and J. R. Petta. A coherent spin–photon interface in silicon. *Nature*, **555** (7698) 599–603, 2018.

[201] M. R. Wasielewski. Energy, charge, and spin transport in molecules and self-assembled nanostructures inspired by photosynthesis. *The Journal of Organic Chemistry*, **71** (14) 5051–5066, 2006.

[202] P. Fromme, J. Kern, B. Loll, J. Biesiadka, W. Saenger, H. T. Witt, N. Krauss, and A. Zouni. Functional implications on the mechanism of the function of photosystem II including water oxidation based on the structure of photosystem II. *Philosophical Transactions of the Royal Society of London. Series B: Biological Sciences*, **357** (1426) 1337–1345, 2002.

[203] W. W. Parson. Electron donors and acceptors in the initial steps of photosynthesis in purple bacteria: a personal account. *Photosynthesis Research*, **76** (1/3) 81–92, 2003.

[204] E. A. Weiss, M. J. Tauber, R. F. Kelley, M. J. Ahrens, M. A. Ratner, and M. R. Wasielewski. Conformationally gated switching between superexchange and hopping within oligo-p-phenylene-based molecular wires. *Journal of the American Chemical Society*, **127** (33) 11842–11850, 2005.

[205] R. H. Goldsmith, L. E. Sinks, R. F. Kelley, L. J. Betzen, W. Liu, E. A. Weiss, M. A. Ratner, and M. R. Wasielewski. Wire-like charge transport at near constant bridge energy through fluorene oligomers. *Proceedings of the National Academy of Sciences*, **102** (10) 3540–3545, 2005.

[206] A. Nitzan. Electron transmission through molecules and molecular interfaces. *Annual Review of Physical Chemistry*, **52** (1) 681–750, 2001.

[207] J. R. Heath and M. A. Ratner. Molecular electronics. *Physics Today*, **56** (5) 43–49, 2003.

[208] C. W. Tang and S. A. VanSlyke. Organic electroluminescent diodes. *Applied Physics Letters*, **51** (12) 913–915, 1987.

[209] J. Kido. Organic displays. *Physics World*, **12** (3) 27–30, 1999.

[210] Organic electroluminescent diodes. *Nature Photonics*, **3** (8) 457–457, 2009.

[211] J. E. Lawrence, A. M. Lewis, D. E. Manolopoulos, and P. J. Hore. Magnetoelectroluminescence in organic light-emitting diodes. *The Journal of Chemical Physics*, **144** (21) , 2016.

[212] F. Xie, H. Mao, C. Lin, Y. Feng, J. F. Stoddart, R. M. Young, and M. R. Wasielewski. Quantum sensing of electric fields using spin-correlated radical ion pairs. *Journal of the American Chemical Society*, **145** (27) 14922–14931, 2023.

[213] C. Sampson, R. H. Keens, and D. R. Kattnig. On the magnetosensitivity of lipid peroxidation: two- versus three-radical dynamics. *Physical Chemistry Chemical Physics*, **21** (25) 13526–13538, 2019.

[214] P. Husen, C. Nielsen, C. F. Martino, and I. A. Solov'yov. Molecular oxygen binding in the mitochondrial electron transfer flavoprotein. *Journal of Chemical Information and Modeling*, **59** (11) 4868–4879, 2019.

[215] G. Hong and R. Pachter. Effects of inter-radical interactions and scavenging radicals on magnetosensitivity: spin dynamics simulations of proposed radical pairs. *European Biophysics Journal*, **52** (1–2) 27–37, 2023.

[216] C. Nielsen and I. A. Solov'yov. *MolSpin*—flexible and extensible general spin dynamics software. *The Journal of Chemical Physics*, **151** (19) , 2019.

[217] L. Gerhards, C. Nielsen, D. R. Kattnig, P. J. Hore, and I. A. Solov'yov. Modeling spin relaxation in complex radical systems using *MolSpin*. *Journal of Computational Chemistry*, 2023.

[218] T. P. Fay, L. P. Lindoy, and D. E. Manolopoulos. Spin relaxation in radical pairs from the stochastic Schrödinger equation. *The Journal of Chemical Physics*, **154** (8) , 2021.

[219] L. N. Trefethen and D. Bau. *Numerical Linear Algebra*, volume 181. Siam, 2022.

[220] H.-P. Breuer and F. Petruccione. *The Theory of Open Quantum Systems*. Oxford University Press, Oxford, 2007.

[221] S. Worster, D. R. Kattnig, and P. J. Hore. Spin relaxation of radicals in cryptochrome and its role in avian magnetoreception. *The Journal of Chemical Physics*, **145** (3) , 2016.

[222] T. P. Fay and D. E. Manolopoulos. Radical pair intersystem crossing: quantum dynamics or incoherent kinetics? *The Journal of Chemical Physics*, **150** (15) , 2019.

[223] T. P. Fay, L. P. Lindoy, and D. E. Manolopoulos. Electron spin relaxation in radical pairs: beyond the Redfield approximation. *The Journal of Chemical Physics*, **151** (15) , 2019.

[224] P. M. Morse, H. Feshbach, and E. L. Hill. *Methods of Theoretical Physics*, volume 22. American Association of Physics Teachers (AAPT), 1954.

[225] W. Magnus. On the exponential solution of differential equations for a linear operator. *Communications on Pure and Applied Mathematics*, **7** (4) 649–673, 1954.

[226] I. Kuprov. Defeating the matrix. *Journal of Magnetic Resonance*, **306** 75–79, 2019.

[227] C. R. Timmel, U. Till, B. Brocklehurst, K. A. Mclauchlan, and P. J. Hore. Effects of weak magnetic fields on free radical recombination reactions. *Molecular Physics*, **95** (1) 71–89, 1998.

[228] U. Till, C. Timmel, B. Brocklehurst, and P. J. Hore. The influence of very small magnetic fields on radical recombination reactions in the limit of slow recombination. *Chemical Physics Letters*, **298** (1–3) 7–14, 1998.

[229] M. Feit, J. Fleck, J.A, and A. Steiger. Solution of the Schrödinger equation by a spectral method. *Journal of Computational Physics*, **47** (3) 412–433, 1982.

[230] S. Bourne-Worster. *Order, Motion and Relaxation in Radical Pair Compass Magnetoreception*. Phd thesis, Oxford Univesity, 2018.

[231] N. J. Higham. *Functions of Matrices: Theory and Computation*. SIAM, 2008.

[232] W. T. Pollard and R. A. Friesner. Solution of the Redfield equation for the dissipative quantum dynamics of multilevel systems. *The Journal of Chemical Physics*, **100** (7) 5054–5065, 1994.

[233] T. J. Park and J. C. Light. Unitary quantum time evolution by iterative Lanczos reduction. *The Journal of Chemical Physics*, **85** (10) 5870–5876, 1986.

[234] J. M. Radcliffe. Some properties of coherent spin states. *Journal of Physics A: General Physics*, **4** (3) 313–323, 1971.

[235] K. Nemoto. Generalized coherent states for SU(n) systems. *Journal of Physics A: Mathematical and General*, **33** (17) 3493–3506, 2000.

[236] http://www.molspin.eu.

[237] T. P. Fay, L. P. Lindoy, D. E. Manolopoulos, and P. J. Hore. How quantum is radical pair magnetoreception? *Faraday Discussions*, **221** 77–91, 2020.

[238] M. Hanic, F. Schuhmann, A. Frederiksen, C. Langebrake, G. Manthey, M. Liedvogel, J. Xu, H. Mouritsen, and I. A. Solov'yov. Computational reconstruction and analysis of structural models of avian cryptochrome 4. *Journal of Physical Chemistry B*, **126** (25) 4623–4635, 2022.

[239] M. Hanic, A. Frederiksen, F. Schuhmann, and I. A. Solov'yov. On the energetic differences of avian cryptochromes 4 from selected species. *The European Physical Journal D*, **76** (10) , 2022.

[240] A. Gunther, A. Einwich, E. Sjulstok, R. Feederle, P. Bolte, K. Koch, I. A. Solov'yov, and H. Mouritsen. Double-cone localization and seasonal expression pattern suggest a role in magnetoreception for european robin cryptochrome 4. *Current Biology*, **28** (2) 211–223.e4, 2018.

[241] B. D. Zoltowski, Y. Chelliah, A. Wickramaratne, L. E. Jarocha, N. Karki, W. Xu, H. Mouritsen, P. J. Hore, R. Hibbs, C. B. Green, and J. S. Takahashi. Chemical and structural analysis of a photoactive vertebrate cryptochrome from pigeon. *Proceedings of the National Academy of Sciences of the United States of America*, **116** (39) 19449–19457, 2019.

[242] J. C. Phillips, D. J. Hardy, J. D. Maia, J. E. Stone, J. V. Ribeiro, R. C. Bernardi, R. Buch, G. Fiorin, J. Henin, W. Jiang, R. McGreevy, M. C. R. Melo, B. K. Radak, R. D. Skeel, A. Singharoy, Y. Wang, B. Roux, A. Aksimentiev, Z. Luthey-Schulten, L. V. Kale, K. Schulten, C. Chipot, and E. Tajkhorshid. Scalable molecular dynamics on cpu and gpu architectures with namd. *The Journal of Chemical Physics*, **153** (4) , 2020.

[243] J. C. Phillips, R. Braun, W. Wang, J. C. Gumbart, E. Tajkhorshid, E. Villa, C. Chipot, R. D. Skeel, L. V. Kalé, and K. Schulten. Scalable molecular dynamics with namd. *Journal of Computational Chemistry*, **26** (16) 1781–1802, 2005.

[244] V. Korol, P. Husen, E. Sjulstok, C. Nielsen, I. Friis, A. Frederiksen, A. B. Salo, and I. A. Solov'yov. Introducing viking: A novel online platform for multiscale modeling. *ACS Omega*, **5** (2) 1254–1260, 2019.

[245] A. D. MacKerell, D. Bashford, M. Bellott, R. L. Dunbrack, J. D. Evanseck, F. M. J., S. Fischer, J. Gao, H. Guo, S. Ha, D. Joseph-McCarthy, L. Kuchnir, K. Krzysztof, F. T. K. Lau, C. Mattos, S. W. Michnick, T. Ngo, D. T. Nguyen, B. Prod'hom, W. Reiher, B. Roux, M. Schlenkrich, J. C. Smith, R. H. Stote, J. E. Straub, M. Watanabe, J. Wiorkiewicz-Kuczera, D. Jin, and M. Karplus.

All-atom empirical potential for molecular modeling and dynamics studies of proteins. *The Journal of Physical Chemistry B*, **102** (18) 3586–3616, 1998.

[246] A. D. MacKerell, M. Feig, and C. L. Brooks. Extending the treatment of backbone energetics in protein force fields: Limitations of gas-phase quantum mechanics in reproducing protein conformational distributions in molecular dynamics simulations. *Journal of Computational Chemistry*, **25** (11) 1400–1415, 2004.

[247] J. Huang and A. D. MacKerell. Charmm36 all-atom additive protein force field: Validation based on comparison to nmr data. *Journal of Computational Chemistry*, **34** (25) 2135–2145, 2013.

[248] W. L. Jorgensen, J. Chandrasekhar, J. D. Madura, R. Impey, and M. L. Klein. Comparison of simple potential functions for simulating liquid water. *The Journal of Chemical Physics*, **79** (2) 926–935, 1983.

[249] W. Humphrey, A. Dalke, and K. Schulten. Vmd: Visual molecular dynamics. *Journal of Molecular Graphics*, **14** (1) 33–38, 1996.

[250] H. Hogben, M. Krzystyniak, G. Charnock, P. J. Hore, and I. Kuprov. *Spinach* – a software library for simulation of spin dynamics in large spin systems. *Journal of Magnetic Resonance*, **208** (2) 179–194, 2011.

[251] S. Stoll and A. Schweiger. *EasySpin*, a comprehensive software package for spectral simulation and analysis in EPR. *Journal of Magnetic Resonance*, **178** (1) 42–55, 2006.

[252] M. Price, S. Somaroo, C. Tseng, J. Gore, A. Fahmy, T. Havel, and D. Cory. Construction and implementation of nmr quantum logic gates for two spin systems. *Journal of Magnetic Resonance*, **140** (2) 371–378, 1999.

[253] *EasySpin*. Nuclear isotope database, 2021.

[254] A. Weibe, G. Wellein, A. Alvermann, and H. Fehske. The kernel polynomial method. *Reviews of Modern Physics*, **78** (1) 275–306, 2006.

[255] S. Sykora. Surface integrals over n-dimensional spheres. *Stan's Library*, **Volume I**, 2005.

A Selected Nuclear Isotopes

	I	Z	g_N	abundance / %
^{1}H	1/2	2	+5.586	99.99
^{2}H	1	3	+0.857	0.0115
^{12}C	0	1	0.0	98.93
^{13}C	1/2	2	+1.405	1.07
^{14}N	1	3	+0.404	99.63
^{15}N	1/2	2	−0.566	0.37
^{16}O	0	1	0.0	99.76
^{17}O	5/2	6	−0.758	0.038

Table A.1 Selected nuclear isotopes with their spin quantum number, degeneracy, nuclear g-factor, and natural abundance.[253]

B Errors in Trotter Decompositions for Matrix Exponentiation

The split operator form is given as:[229]

$$e^{-i(\hat{H}_0+\hat{H}_1)dt} \approx e^{-i\hat{H}_1 dt/2} e^{-i\hat{H}_0 dt} e^{-i\hat{H}_1 dt/2} \tag{B.1}$$

Expanding the LHS exponential in terms of Taylor series in dt (in Eq. (B.1)), around $t = 0$, gives us:

$$\begin{aligned} &e^{-i(\hat{H}_0+\hat{H}_1)dt} = \\ &= 1 - i(\hat{H}_0+\hat{H}_1)dt - (\hat{H}_0+\hat{H}_1)^2\frac{dt^2}{2} + i(\hat{H}_0+\hat{H}_1)^3\frac{dt^3}{6} + \dots \\ &= 1 - i\left(\hat{H}_0+\hat{H}_1\right)dt - \left(\hat{H}_0^2 + \hat{H}_0\hat{H}_1 + \hat{H}_1\hat{H}_0 + \hat{H}_1^2\right)\frac{dt^2}{2} + \\ &+ i\left(\hat{H}_0^3 + \hat{H}_0^2\hat{H}_1 + \hat{H}_0\hat{H}_1\hat{H}_0 + \hat{H}_0\hat{H}_1^2 + \hat{H}_1\hat{H}_0^2 + \hat{H}_1\hat{H}_0\hat{H}_1 + \hat{H}_1^2\hat{H}_0 + \hat{H}_1^3\right)\frac{dt^3}{6} + \dots \end{aligned} \tag{B.2}$$

Remember, $[\hat{H}_0, \hat{H}_1] \neq 0$. Expanding the RHS same as Taylor series in dt , around $t = 0$, gives us:

$$e^{-i\hat{H}_1 dt/2} = 1 - i\hat{H}_1\frac{dt}{2} - \hat{H}_1^2\frac{dt^2}{8} + i\hat{H}_1^3\frac{dt^3}{48} + \dots \tag{B.3}$$

$$e^{-i\hat{H}_0 dt} = 1 - i\hat{H}_0 dt - \hat{H}_0^2\frac{dt^2}{2} + i\hat{H}_0^3\frac{dt^3}{6} + \dots \tag{B.4}$$

$$
\begin{aligned}
& e^{-i\hat{H}_1 dt/2} e^{-i\hat{H}_0 dt} e^{-i\hat{H}_1 dt/2} = \\
& = \left(1 - i\hat{H}_1 \frac{dt}{2} + ...\right)\left(1 - i\hat{H}_0 dt + ...\right)\left(1 - i\hat{H}_1 \frac{dt}{2} + ...\right) = \\
& = 1 - i\left(\hat{H}_0 + \hat{H}_1\right) dt - \left(\hat{H}_0^2 + \hat{H}_0\hat{H}_1 + \hat{H}_1\hat{H}_0 + \hat{H}_1^2\right)\frac{dt^2}{2} + \\
& + i\left(\hat{H}_0^3 + 2\hat{H}_0^2\hat{H}_1 + \hat{H}_0\hat{H}_1^2 + 2\hat{H}_1\hat{H}_0\hat{H}_1 + 2\hat{H}_1\hat{H}_0^2 + \hat{H}_1^2\hat{H}_0 + \frac{4}{3}\hat{H}_1^3\right)\frac{dt^3}{8} + ...
\end{aligned}
\tag{B.5}
$$

Subtracting Eq. (B.2) by Eq. (B.5), we notice that remaining terms are in the order of dt^3:

$$
\begin{aligned}
& e^{-i(\hat{H}_0+\hat{H}_1)dt} - e^{-i\hat{H}_1 dt/2} e^{-i\hat{H}_0 dt} e^{-i\hat{H}_1 dt/2} = \\
& = i\left(\hat{H}_0^3 - 2\hat{H}_0\hat{H}_1^2 + 4\hat{H}_0\hat{H}_1\hat{H}_0 + \hat{H}_0\hat{H}_1 - 2\hat{H}_1\hat{H}_0\hat{H}_1 - 2\hat{H}_1\hat{H}_0^2 + \hat{H}_1^2\hat{H}_0\right)\frac{dt^3}{24} + ... = \\
& = \mathcal{O}(dt^3)
\end{aligned}
\tag{B.6}
$$

Hence, the overall error of using the Split Operator formula for non-commuting matrix exponentials is $\mathcal{O}(dt^3)$:

$$
e^{-i(\hat{H}_0+\hat{H}_1)dt} = e^{-i\hat{H}_1 dt/2} e^{-i\hat{H}_0 dt} e^{-i\hat{H}_1 dt/2} + \mathcal{O}(dt^3) \tag{B.7}
$$

If the Split Operator form is used as an exponential integrator, the global error of using the method is $\mathcal{O}(dt^2)$, since you need $\mathcal{O}(dt^{-1})$ time steps to go from $t = 0$ to $t = t_{max}$.

C Error Scaling When Using SU(Z) States for Trace Sampling

This proof (and analysis) has been adapted from Ref. 218.

Any method of trace sampling attempts to evaluate approximatively the following expression:

$$\mu_A = \frac{1}{Z}\mathrm{Tr}\left[\hat{A}\right] = \frac{1}{Z}\sum_{n=1}^{Z}\left\langle n\middle|\hat{A}\middle|n\right\rangle \tag{C.1}$$

Here $\hat{A}$ is a nuclear spin operator, $\mathrm{Tr}[\dots]$ denotes the nuclear spin partial trace, Z is the dimensionality of the nuclear spin space, and the set of $|n\rangle$ states form a complete basis for the nuclear spin Hilbert space. In our case, $\hat{A}$ is given as:[218]

$$\hat{A} = \int_0^\infty \left\langle \mathrm{Tr}_e\left[\hat{\sigma}_e \hat{U}(\tau)^\dagger \hat{O}\hat{U}(\tau)\right]\right\rangle f(\tau)d\tau \tag{C.2}$$

$\mathrm{Tr}_e[\dots]$ is a partial trace over the electron spin subspace, $\langle\dots\rangle$ denotes the average over the stochastic fluctuations, $\hat{U}(\tau)$ is the propagator, $f(\tau)$ is an arbitrary function of τ, $\hat{O}$ is an observable operator, and σ_e is the electron spin density operator. For instance, if we are calculating $\langle P_S(t)\rangle = P_S(t)$ for a radical pair in an initial singlet state, then $\hat{O} = \hat{P}_S$ and $\sigma_e = \hat{P}_S$.

We will presume, for the sake of simplicity, that we have evaluated the average over stochastic variables $\langle\dots\rangle$ exactly. This may not be the case precisely, but it is a reasonable assumption for analysing the effectiveness of trace sampling.[218]

During trace sampling, the approximate value of μ_A is given by an estimator Θ_A, which is derived from the M sample simulation and is defined as follows:

$$\mu_A \approx \Theta_A = \frac{1}{M}\sum_{r=1}^{M}\left\langle \psi^{(r)}\middle|\hat{A}\middle|\psi^{(r)}\right\rangle \tag{C.3}$$

$\left|\psi^{(r)}\right\rangle$ are random normalized nuclear spin states, which are parametrized by some set of random variables $\xi^{(r)}$, i.e. $\left|\psi^{(r)}\right\rangle = \left|\psi(\xi^{(r)})\right\rangle$. Each set of $\xi^{(r)}$ variables is sampled at random from the same distribution. We will denote the full set of M independent sets of random variables $\xi^{(r)}$ as $\xi = \left(\xi^{(1)}, \ldots, \xi^{(M)}\right)$.

We can observe that Θ_A is itself a random variable with its own distribution, thus, we will be most interested in determining its variance and how it scales with Z. We will designate $\langle \ldots \rangle_M$ as the mean result of an M sample simulation. This corresponds to integrating over all possible random variable values in ξ such that:

$$\left\langle f(\xi)\right\rangle_M = \int p(\xi^{(1)})\, d\xi^{(1)} \cdots \int p(\xi^{(M)})\, d\xi^{(M)}\, f(\xi) \tag{C.4}$$

Where $p(\xi^{(r)})$ is the normalized probability density for $\xi^{(r)}$ from the resolution of identity definition in Eq. 2.94.

The coefficients of the randomly samples states in the orthonormal basis $|n\rangle$, $c_n^{(r)} = c_n(\xi^{(r)})$, are:

$$c_n^{(r)} = \left\langle n \middle| \psi^{(r)} \right\rangle \tag{C.5}$$

When averaged over ξ, we assume these coefficients obey the following relation:[218]

$$\left\langle c_n^{(r)*} c_{n'}^{(r')} \right\rangle_M = \frac{1}{Z}\delta_{r,r'}\delta_{n,n'} \tag{C.6}$$

Here the $1/Z$ factor naturally arises if the states are normalized such that $\left\langle \psi^{(r)} \middle| \psi^{(r)} \right\rangle = 1$. Note, if this equation is valid in one basis, it must also be valid in all other bases. From this equation it can be simply shown, that, on average, the estimator for the trace Θ_A will be exactly the true quantum mechanical average:[218]

$$\langle \Theta_A \rangle_M = \mu_A \tag{C.7}$$

In order to comprehend the convergence of trace sampling, fluctuations in the estimator, $\delta\Theta_A = \Theta_A - \mu_A$, are taken into account. Thus, the mean square fluctuation $\left\langle \delta\Theta_A^2 \right\rangle_M$ can be evaluated as:

$$\begin{aligned}
\left\langle \delta\Theta_A^2 \right\rangle_M =& \left\langle \Theta_A^2 \right\rangle_M - \langle \Theta_A \rangle_M^2 \\
=& \frac{1}{M^2} \sum_{r=1}^{M} \sum_{r'=1}^{M} \Bigg(\left\langle \left\langle \psi^{(r)} \middle| \hat{A} \middle| \psi^{(r)} \right\rangle \left\langle \psi^{(r')} \middle| \hat{A} \middle| \psi^{(r')} \right\rangle \right\rangle_M \\
& - \left\langle \left\langle \psi^{(r)} \middle| \hat{A} \middle| \psi^{(r)} \right\rangle \right\rangle_M \left\langle \left\langle \psi^{(r')} \middle| \hat{A} \middle| \psi^{(r')} \right\rangle \right\rangle_M \Bigg) \\
=& \frac{1}{Z} \Bigg(\left\langle \left\langle \psi^{(r)} \middle| \hat{A} \middle| \psi^{(r)} \right\rangle \left\langle \psi^{(r)} \middle| \hat{A} \middle| \psi^{(r)} \right\rangle \right\rangle_M \\
& - \left\langle \left\langle \psi^{(r)} \middle| \hat{A} \middle| \psi^{(r)} \right\rangle \right\rangle_M \left\langle \left\langle \psi^{(r)} \middle| \hat{A} \middle| \psi^{(r)} \right\rangle \right\rangle_M \Bigg)
\end{aligned} \tag{C.8}$$

Here, the right-hand side is independent of r because each set of variables $\xi^{(r)}$ is drawn from the same distribution, the same property that was utilised to acquire the final equality in Eq. C.8. By inserting resolutions of the identity, we obtain:

$$\begin{aligned}
\left\langle \delta\Theta_A^2 \right\rangle_M =& \frac{1}{M} \sum_{n=1}^{Z} \sum_{m=1}^{Z} \sum_{n'=1}^{Z} \sum_{m'=1}^{Z} \left\langle n \middle| \hat{A} \middle| n' \right\rangle \left\langle m \middle| \hat{A} \middle| m' \right\rangle \\
& \times \left(\left\langle c_n^{(r)*} c_m^{(r)*} c_{n'}^{(r)} c_{m'}^{(r)} \right\rangle_M - \left\langle c_n^{(r)*} c_{n'}^{(r)} \right\rangle_M \left\langle c_m^{(r)*} c_{m'}^{(r)} \right\rangle_M \right)
\end{aligned} \tag{C.9}$$

Given that $\hat{A}$ is hermitian (true for all $\hat{A}$ used in this thesis), its eigenstates form a basis for the nuclear spin Hilbert space. Choosing $|n\rangle$ such that $\hat{A}\,|n\rangle = \alpha_n\,|n\rangle$ simplifies Eq. C.9 to:

$$\left\langle \delta\Theta_A^2 \right\rangle_M = \frac{1}{M}\sum_{n=1}^{Z}\sum_{m=1}^{Z}\alpha_n\alpha_m\left(\left\langle|c_n^{(r)}|^2|c_m^{(r)}|^2\right\rangle_M - \left\langle|c_n^{(r)}|^2\right\rangle_M\left\langle|c_m^{(r)}|^2\right\rangle_M\right) \tag{C.10}$$

If the randomly sampled states are normalized, i.e. $\left\langle\psi^{(r)}|\psi^{(r)}\right\rangle = 1$, then $\sum_{n=1}^{Z}|c_m^{(r)}|^2 = 1$.[218] Hence,

$$\sum_{n=1}^{Z}\left(\left\langle|c_n^{(r)}|^2|c_m^{(r)}|^2\right\rangle_M - \left\langle|c_n^{(r)}|^2\right\rangle_M\left\langle|c_m^{(r)}|^2\right\rangle_M\right) = 0 \tag{C.11}$$

Thus, Eq.C.10 can be written as:[218]

$$\left\langle \delta\Theta_A^2 \right\rangle_M = \frac{1}{M}\sum_{n=1}^{Z}\sum_{m=1}^{Z}\Delta\alpha_n\Delta\alpha_m\left(\left\langle|c_n^{(r)}|^2|c_m^{(r)}|^2\right\rangle_M - \left\langle|c_n^{(r)}|^2\right\rangle_M\left\langle|c_m^{(r)}|^2\right\rangle_M\right) \tag{C.12}$$

Here $\Delta\alpha_n = \alpha_n - (1/Z)\sum_{m=1}^{Z}\alpha_m$. This expression can be used to determine an upper limit for $\left\langle \delta\Theta_A^2 \right\rangle_M$ that we will use to demonstrate the convergence of the SU(Z) state sampling method.

First, we note that:

$$|\Delta\alpha_n| \leq \Delta_A \tag{C.13}$$

Δ_A is the range of eigenvalues of $\hat{A}$. This property for quantities such as the singlet yield or singlet survival probability will be bounded by 1.[218] This gives the following upper limit on $\left\langle \delta\Theta_A^2 \right\rangle_M$:[218]

$$\left\langle \delta\Theta_A^2 \right\rangle_M \leq \frac{\Delta_A^2}{M}\sum_{n=1}^{Z}\sum_{m=1}^{Z}\left|\left\langle|c_n^{(r)}|^2|c_m^{(r)}|^2\right\rangle_M - \left\langle|c_n^{(r)}|^2\right\rangle_M\left\langle|c_m^{(r)}|^2\right\rangle_M\right| \tag{C.14}$$

Moreover, rearranging Eq. C.11 gives:

$$\left\langle|c_m^{(r)}|^4\right\rangle_M - \left\langle|c_m^{(r)}|^2\right\rangle_M^2 = -\sum_{n\neq m}\left(\left\langle|c_n^{(r)}|^2|c_m^{(r)}|^2\right\rangle_M - \left\langle|c_n^{(r)}|^2\right\rangle_M\left\langle|c_m^{(r)}|^2\right\rangle_M\right) \tag{C.15}$$

This means, the upper bound can be written as:[218]

$$\left\langle \delta\Theta_A^2 \right\rangle_M \leq \frac{2\Delta_A}{M} \sum_{m=1}^{Z} \left| \left\langle |c_m^{(r)}|^4 \right\rangle_M - \left\langle |c_m^{(r)}|^2 \right\rangle_M^2 \right| \tag{C.16}$$

If the sum on the right-hand side of this equation scales as $\mathcal{O}(1/Z)$, trace sampling will be defined as self-averaging.[254] This will be shown to be the case for SU(Z) state sampling method.

We will want to evaluate $\left\langle \left| c_m^{(r)} \right|^{2p} \right\rangle_M$ for $p = 0, 1$ to find a closed-form solution for Eq. C.16. For $|\mathbf{Z}\rangle$ states, this is:[218]

$$\left\langle \left| c_m^{(r)} \right|^{2p} \right\rangle_M = \int_{\Re^Z} d\mathbf{X} \int_{\Re^Z} d\mathbf{Y} \, \frac{\delta(|\mathbf{Z}| - 1)}{\mathcal{S}_{2Z}} \left(X_m^2 + Y_m^2 \right)^p \tag{C.17}$$

This integral can be evaluated using the following general formula for Gamma functions:[255]

$$\int_{\Re^{2Z}} d\mathbf{Z} \, \delta(|\mathbf{Z}| - 1) \prod_{k=1}^{2Z} Z_k^{2p_k} = 2 \frac{\prod_{k=1}^{2Z} \Gamma(p_k + 1/2)}{\Gamma(Z + \sum_{k=1}^{n} p_k)} \tag{C.18}$$

Since $\mathcal{S}_{2Z} = 2\Gamma(1/2)^{2Z}/\Gamma(Z)$, for $p = 0, 1$ we find:

$$\left\langle \left| c_m^{(r)} \right|^2 \right\rangle_M = \frac{1}{Z} \text{ and } \left\langle \left| c_m^{(r)} \right|^4 \right\rangle_M = \frac{2}{Z(Z+1)} \tag{C.19}$$

Substituting these values into Eq. C.16, we find that:

$$\left\langle \delta\Theta_A^2 \right\rangle_M \leq \frac{2\Delta_A^2}{M} \frac{Z-1}{Z(Z+1)} = \frac{2\Delta_A^2}{MZ} + \mathcal{O}\left(\frac{1}{Z^2} \right) \tag{C.20}$$

Notably, this holds true for any basis $|n\rangle$, as the distribution from which $|\mathbf{Z}\rangle$ states are sampled is unitary transformation invariant, i.e. $\delta(|\mathbf{Z}| - 1) = \delta(|\mathbf{UZ}| - 1)$, where $\mathbf{U}$ is an arbitrary unitary matrix.[218] Hence, proving that the overall error using SU(Z) states scales as $\mathcal{O}(1/\sqrt{MZ})$.

D

Article 5: Quantum Gate Operations on a Spectrally Addressable Photogenerated Molecular Electron Spin-Qubit Pair

Statement of Authorship for joint/multi-authored papers for PGR thesis

To appear at the end of each thesis chapter submitted as an article/paper

The statement shall describe the candidate's and co-authors' independent research contributions in the thesis publications. For each publication there should exist a complete statement that is to be filled out and signed by the candidate and supervisor **(only required where there isn't already a statement of contribution within the paper itself).**

Title of Paper	**Quantum Gate Operations on a Spectrally Addressable Photogenerated Molecular Electron Spin-Qubit Pair**
Publication Status	☒ Published ☐ Accepted for Publication ☐ Submitted for Publication ☐ Unpublished and unsubmitted work written in a manuscript style
Publication Details	Mao H., Pažėra G. J., Young R. M., Krzyaniak M. D., & Wasielewski M. R. (2023). Quantum Gate Operations on a Spectrally Addressable Photogenerated Molecular Electron Spin-Qubit Pair. Journal of American Chemical Society, 145, 11, 6585-6593

Student Confirmation

Student Name:	Gediminas Jurgis Pažėra		
Contribution to the Paper	He developed the microwave pulse protocols for CNOT gate implementation, analyzed the pulse-EPR data on all samples, interpreted data, wrote part of the manuscript.		
Signature		Date	2023.08.16

Supervisor Confirmation

By signing the Statement of Authorship, you are certifying that the candidate made a substantial contribution to the publication, and that the description described above is accurate.

Supervisor name and title: Professor Peter John Hore FRS		
Supervisor comments		
Signature: PJHore	Date	16 August 2023

This completed form should be included in the thesis, at the end of the relevant chapter.

JOURNAL OF THE AMERICAN CHEMICAL SOCIETY

pubs.acs.org/JACS

Article

Quantum Gate Operations on a Spectrally Addressable Photogenerated Molecular Electron Spin-Qubit Pair

Haochuan Mao, Gediminas J. Pažėra, Ryan M. Young, Matthew D. Krzyaniak,* and Michael R. Wasielewski*

Cite This: *J. Am. Chem. Soc.* 2023, 145, 6585−6593

Read Online

ACCESS | Metrics & More | Article Recommendations | Supporting Information

ABSTRACT: Sub-nanosecond photodriven electron transfer from a molecular donor to an acceptor can be used to generate a radical pair (RP) having two entangled electron spins in a well-defined pure initial singlet quantum state to serve as a spin-qubit pair (SQP). Achieving good spin-qubit addressability is challenging because many organic radical ions have large hyperfine couplings (HFCs) in addition to significant *g*-anisotropy, which results in significant spectral overlap. Moreover, using radicals with *g*-factors that deviate significantly from that of the free electron results in difficulty generating microwave pulses with sufficiently large bandwidths to manipulate the two spins either simultaneously or selectively as is necessary to implement the controlled-NOT (CNOT) quantum gate essential for quantum algorithms. Here, we address these issues by using a covalently linked donor−acceptor(1)−acceptor(2) (D-A_1-A_2) molecule with significantly reduced HFCs that uses fully deuterated *peri*-xanthenoxanthene (PXX) as D, naphthalenemonoimide (NMI) as A_1, and a C_{60} derivative as A_2. Selective photoexcitation of PXX within PXX-d_9-NMI-C_{60} results in sub-nanosecond, two-step electron transfer to generate the long-lived $PXX^{\bullet+}$-d_9-NMI-$C_{60}^{\bullet-}$ SQP. Alignment of $PXX^{\bullet+}$-d_9-NMI-$C_{60}^{\bullet-}$ in the nematic liquid crystal 4-cyano-4′-(*n*-pentyl)biphenyl (5CB) at cryogenic temperatures results in well-resolved, narrow resonances for each electron spin. We demonstrate both single-qubit gate and two-qubit CNOT gate operations using both selective and nonselective Gaussian-shaped microwave pulses and broadband spectral detection of the spin states following the gate operations.

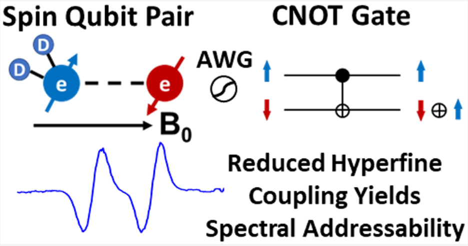

INTRODUCTION

New computation, communication, and sensing technologies provided by quantum information science (QIS) are drawing considerable attention.[1−3] The identification and characterization of new molecular systems to serve as qubits in these applications have motivated chemists to contribute to this field[4,5] by taking advantage of synthetic tunability[6,7] and the ease with which unpaired electron spins in molecules can be manipulated using microwave pulses.[8−10] These molecular systems employ multiple electron spin qubits within interacting organic radicals[8,9,11−14] and/or metal complexes[15−20] and have achieved advances in extending coherence lifetimes[17,21,22] and scaling up the number of qubits.[18,23−25] However, thermally polarized electron spins[26] with well-defined initial spin states essential for QIS applications[27] are only available at high magnetic fields and/or millikelvin temperatures.[11]

Spin-selective, light-driven processes in molecular qubit systems have shown significant promise for creating well-defined initial electron spin-qubit states.[4,20,28−30] For example, sub-nanosecond photodriven electron transfer from a molecular donor (D) covalently linked to an acceptor (A) via a bridge molecule (B) has been shown to generate a $D^{\bullet+}$-B-$A^{\bullet-}$ radical pair having two entangled electron spins in a well-defined pure initial singlet quantum state that can serve as a spin-qubit pair (SQP) even at room temperature.[28,31,32] The entanglement of the two electron spins in these SQPs results from their electron spin−spin exchange (*J*) and/or dipolar (*D*) couplings. In addition, the two electron spins of the SQP experience different magnetic environments as a consequence of differing electron−nuclear hyperfine couplings (HFCs) between $D^{\bullet+}$ and $A^{\bullet-}$, as well as differing spin−orbit interactions within each radical ion leading to different electronic *g*-tensors. The two-particle wave functions of the SQP in the coupled basis are $|S\rangle$, $|T_{+1}\rangle$, $|T_0\rangle$, and $|T_{+1}\rangle$, where $|S\rangle = 1/\sqrt{2}[|\alpha\beta\rangle - |\beta\alpha\rangle]$ and $|T_0\rangle = 1/\sqrt{2}[|\alpha\beta\rangle + |\beta\alpha\rangle]$ constitute two of the four possible entangled Bell states of the system.[33] The other two Bell states, $1/\sqrt{2}[|\alpha\alpha\rangle + |\beta\beta\rangle]$ and $1/\sqrt{2}[|\alpha\alpha\rangle - |\beta\beta\rangle]$, are obtained by linear combinations of $|T_{+1}\rangle = |\alpha\alpha\rangle$ and $|T_{-1}\rangle = |\beta\beta\rangle$. Upon application of a magnetic field that is much larger than *J*, *D*, and the differences in the HFCs and *g*-tensors of both radical ions comprising the SQP, only the $|S\rangle$ and $|T_0\rangle$ spin states of the SQP are close in

Received: February 2, 2023
Published: March 13, 2023

energy and mix to give $|\Phi_A\rangle$ and $|\Phi_B\rangle$ (Figure 1). These mixed states are described by $|\Phi_A\rangle = \cos\phi\,|S\rangle + \sin\phi\,|T_0\rangle$ and $|\Phi_B\rangle = \cos\phi\,|T_0\rangle + \sin\phi\,|S\rangle$, where the angle ϕ describes the degree of mixing and is related to *J*, *D*, and the differences in the HFCs and *g*-tensors of the two radical ions.[31,32,34−38] In contrast, the $|T_{+1}\rangle$ and $|T_{-1}\rangle$ states are energetically far removed from $|T_0\rangle$ and do not mix with $|S\rangle$. Since the SQP is initially formed in a pure $|S\rangle$ state, $|\Phi_A\rangle$ and $|\Phi_B\rangle$ are overpopulated, which produces strong spin polarization that can be observed readily with time-resolved EPR spectroscopy using either continuous (TREPR) or pulsed microwave radiation (pulse-EPR).

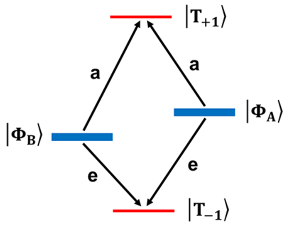

Figure 1. Radical pair energy levels in the high magnetic field limit showing the result of mixing $|S\rangle$ and $|T_0\rangle$ states.

Pulse-EPR has been used to demonstrate quantum state teleportation,[12] spin polarization transfer to a third spin,[39−42] and varying degrees of qubit-specific addressability using photogenerated SQPs.[14,43] However, the radical ions employed in these D-B-A molecules typically have large hydrogen and nitrogen HFCs relative to the difference in their *g*-tensors, which results in significant spectral overlap of the two spin resonances of the SQP, limiting spectral resolution and thus addressability. In addition, a distribution of the $D^{\bullet+}$ and $A^{\bullet-}$ *g*-tensor orientations relative to one another and to the applied magnetic field often contributes to spectral broadening. All of these effects make it difficult to generate microwave pulses with sufficiently broad bandwidths to manipulate the two spins of the SQP either simultaneously or selectively as is necessary to implement the controlled-NOT (CNOT) quantum gate essential for executing quantum algorithms.[13,44]

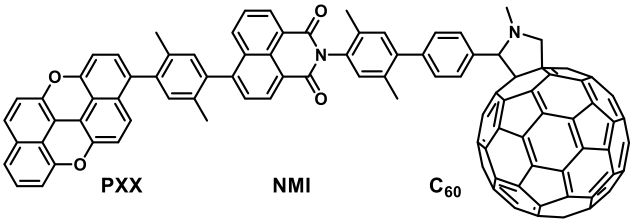

1: PXX-NMI-C_{60}; 1-d_9: PXX-d_9-NMI-C_{60}

Here, we address these issues by designing and synthesizing a covalently linked donor−acceptor(1)−acceptor(2) (D-A_1-A_2) molecule with significantly reduced HFCs by using fully deuterated *peri*-xanthenoxanthene (PXX) as D, naphthalene-monoimide (NMI) as A_1, and a C_{60} derivative as A_2 (**1**-d_9). These donors and acceptors were chosen to optimize the photoinduced electron transfer rates within PXX-d_9-NMI-C_{60} to ensure rapid two-step electron transfer leading to $PXX^{\bullet+}$-d_9-NMI-$C_{60}^{\bullet-}$ at cryogenic temperatures. PXX has a lowest excited singlet state energy E_s = 2.75 eV; yet it is relatively easy to oxidize (E_{ox} = 0.82 V vs SCE[45,46]). NMI was chosen as the intermediate acceptor because it does not absorb in the visible spectrum, and its one-electron reduction potential is sufficiently negative (E_{RED} = −1.4 V vs SCE[47]) to ensure that the energy of the initial photogenerated SQP $PXX^{\bullet+}$-d_9-$NMI^{\bullet-}$-C_{60} is high enough to rapidly reduce C_{60} (E_{red} = −0.6 V vs SCE[48]) to give $PXX^{\bullet+}$-d_9-NMI-$C_{60}^{\bullet-}$.

Selective photoexcitation of PXX within PXX-d_9-NMI-C_{60} results in sub-nanosecond, two-step electron transfer to form an entangled, long-lived $PXX^{\bullet+}$-NMI-$C_{60}^{\bullet-}$ SQP. Alignment of $PXX^{\bullet+}$-NMI-$C_{60}^{\bullet-}$ in the nematic liquid crystal 4-cyano-4′-(*n*-pentyl)biphenyl (5CB) effectively eliminates the spectral complexities resulting from the anisotropic *g*-tensors of both $PXX^{\bullet+}$ and $C_{60}^{\bullet-}$, which results in well-resolved resonances for each electron spin, thus providing a platform for quantum gate operations. We demonstrate both single-qubit gates and two-qubit CNOT gates implemented with frequency-selective and broadband, nonselective Gaussian-shaped microwave pulses followed by broadband spectral detection of the spin states following the gate operations.

EXPERIMENTAL METHODS

Synthesis. Detailed synthetic procedures and characterization of **1** and **1**-d_9 are given in the Supporting Information (SI). The PXX radical cation ($PXX^{\bullet+}$) and PXX-d_{10} radical cation ($PXX^{\bullet+}$-d_{10}) were prepared by adding a substoichiometric amount (0.8 equiv) of nitrosonium tetrafluoroborate to a 100 μM dichloromethane solution of PXX or PXX-d_{10}, respectively. The radical solutions were used immediately for EPR measurements.

Optical Spectroscopy. UV−visible absorption spectra were obtained using a Shimadzu UV-1800 spectrometer in a quartz cuvette with a 1 mm path length. Femtosecond and nanosecond transient absorption (fsTA and nsTA) spectroscopy was conducted using an apparatus described previously (for a brief description see the SI).[49] Samples for room-temperature TA experiments were dissolved in toluene and prepared with an optical density of 0.8 at 450 nm in 2 mm quartz cuvettes fused to a glass bulb. This bulb was used to subject each sample to four freeze−pump−thaw cycles under vacuum (10^{-4} Torr) to remove oxygen. Samples were stirred to minimize the effects of local heating and degradation. For TA experiments at low temperature, a solution of **1** in CH_2Cl_2 was prepared with an optical density of 0.8 at 450 nm in a 2 mm quartz cuvette. The solution was then evaporated to dryness with a stream of N_2 in a small vial and was placed in a N_2-atmosphere glovebox. Inside the glovebox, a volume of 2-methyltetrahydrofuran (mTHF) equivalent to the amount of CH_2Cl_2 used previously was added to the vial to obtain a solution of similar optical density. This solution was then sealed in a sample cell consisting of two quartz windows separated by a 2 mm PTFE spacer. The sealed sample cell was then removed from the glovebox and placed inside a Janis VNF-100 cryostat (Janis Research Co. LLC) coupled to a Cryo-Con 32B (Cryogenics Control Systems, Inc.) temperature controller. The sample was then cooled to 85 K to measure the TA spectra.

Visible and near-infrared data were individually chirp-corrected (Surface Xplorer 4, Ultrafast Systems, LLC), and fsTA and nsTA data were merged in MATLAB prior to kinetic analysis. Data were analyzed using selected-wavelength global fitting to the models as described in the text. The errors of the lifetimes given in the figures are derived from the standard deviations from the global fitting propagated with the uncertainty described by the instrument response (0.3 ps and 0.8 ns for fsTA and nsTA, respectively). Details of the kinetic fitting were described previously.[50]

Steady-State Continuous-Wave EPR Spectroscopy (CW-EPR). CW-EPR measurements were performed on ∼20 μL, 100 μM samples in dichloromethane solution that were loaded into quartz tubes (2.40 mm o.d., 2.00 mm i.d.), subjected to three freeze−pump−thaw cycles on a vacuum line (10^{-4} Torr), and sealed with a hydrogen torch. Measurements at the X-band (9.5 GHz) were performed with a Bruker Elexsys E580, equipped with a 4122SHQE resonator. Scans were performed with a magnetic field modulation amplitude of 0.1 G,

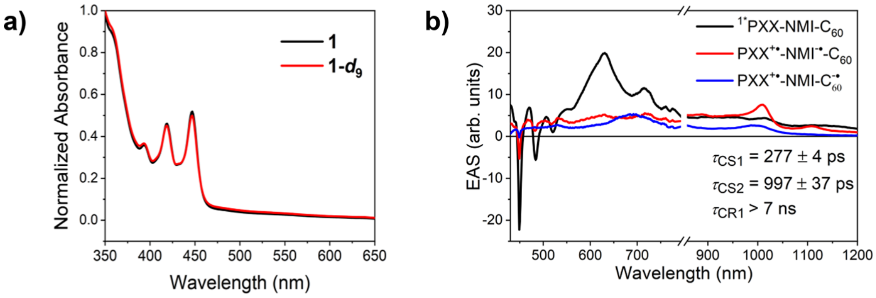

Figure 2. (a) UV−vis spectra of **1** and **1-d_9** in toluene solution at 295 K. (b) Evolution-associated spectra obtained from fsTA data of **1** at 85 K in mTHF solution following λ_{ex} = 450 nm excitation.

modulation frequency of 60 kHz, and nonsaturating microwave power of 1.5 mW.

Time-Resolved EPR Spectroscopy. Measurements were made at the X-band (~9.6 GHz) on a Bruker Elexsys E680 X/W EPR spectrometer with a split ring resonator (ER4118X-MS3). The temperature was set by an Oxford Instruments CF935 continuous flow optical cryostat with liquid nitrogen or liquid helium. Direct detection using CW microwaves was performed following photoexcitation. Kinetic traces of the transient magnetization under CW microwave irradiation were detected in quadrature. Time traces were recorded over a range of magnetic fields to give 2D spectra. Spectra were processed by first subtracting the signal prior to the laser pulse for each kinetic trace (at a given magnetic field point) and then subtracting the signal average at off-resonant magnetic field points from the spectra obtained at a given time. All processing and fitting of the spectra were performed in MATLAB using lab-written scripts and the simulation package EasySpin v6.0-dev.[51]

Pulse-EPR Spectroscopy. Shaped microwave pulses were generated using a commercial Bruker SpinJet II arbitrary waveform generator (AWG) module. A Gaussian-shaped pulse was used for both selective and nonselective turning angle operations because it provides a more uniform excitation across the field-swept echo-detected spectrum than traditional square pulses. The excitation profiles of 20 and 80 ns Gaussian pulses were measured to provide sufficient bandwidth for the nonselective and selective SQP excitations, respectively, necessary to perform the CNOT gate pulse sequence (Figure S1). The turning angles of these pulses were controlled by their amplitude as output by the AWG. These amplitudes were kept within a linear response regime of the traveling wave tube (TWT) amplifier. The resonator response profile (Figure S2) and the TWT response profile and amplitude for the pulse turning angles for specific pulse lengths were calibrated with the EPR signal from the triplet state of C_{60} as an internal standard generated by photoexcitation of the sample. All of the pulse experiments were started with an initial delay after the laser flash T_{DAF} = 50 ns. The electron spin echoes were collected with a $\pi/2-\tau-\pi$ pulse sequence, with τ = 500 ns, and a 16-step CYCLOPS[52] phase cycle; this tau value was chosen to ensure that the spin−echo was not truncated by the instrument deadtime and to be well within the T_m = 1.5 μs phase memory time of PXX$^{•+}$-d_9-NMI-$C_{60}^{•-}$ (Figure S7). Prior to Fourier transformation, the echo was apodized with a Hamming window, zero-filled, and circularly shifted to evenly split the spin−echo. Following Fourier transformation, the spectrum was appropriately phased into absorption/emission and dispersion. In the single-qubit nutation experiment, the variable amplitude nutation pulse occurred 500 ns before the detection sequence.

■ RESULTS AND DISCUSSION

Optical Spectroscopy. Steady-state absorption spectra of **1** and **1-d_9** in toluene are shown in Figure 2a. Since deuteration does not change the electronic structure of PXX, **1** and **1-d_9** have identical absorption spectra with a characteristic vibrational progression at 393, 417, and 447 nm resulting from PXX.[45,46] The strong absorption below 360 nm and broad absorption that covers the entire visible region with stronger absorption at shorter wavelengths results from C_{60}.[53,54]

Transient absorption spectroscopy was used to monitor the photoinduced electron transfer dynamics of **1** in 2-methyltetrahydrofuran (mTHF) at 85 K. Time-resolved spectra at selected times and kinetic fits at selected wavelengths are shown in Figure S3, while global fitting of the data set using an A → B → C model yields the evolution-associated spectra given in Figure 2b. Immediately after laser excitation of PXX in **1**, a ground-state bleach appears at 450 nm along with stimulated emission features at 480 and 520 nm and an excited-state absorption at 650 nm. The subsequent charge transfer reaction ^{1}*PXX-NMI-C_{60} → PXX$^{•+}$-NMI$^{•-}$-C_{60} occurs in τ_{CS1} = 277 ± 4 ps, resulting in the appearance of absorption bands at 530 and 1000 nm due to PXX$^{•+}$.[45,46] The second charge transfer reaction, PXX$^{•+}$-NMI$^{•-}$-C_{60} → PXX$^{•+}$-NMI-$C_{60}^{•-}$, occurs in τ_{CS2} = 997 ± 31 ps, as evidenced by broadening of the 1000 nm absorption peak due to the coexistence of $C_{60}^{•-}$ and PXX$^{•+}$. PXX$^{•+}$-NMI-$C_{60}^{•-}$ eventually decays to form PXX-NMI-^{3}*C_{60} with a time constant of 2.0 ± 0.2 μs (Figure S4). As will be shown below, lowering the temperature to 10 K results in increasing this lifetime to 13 ± 1 μs. Partial coexcitation of C_{60} also produces some C_{60} triplet excited state (^{3}*C_{60}), which has an absorption at 680 nm that appears on a longer time scale (Figure S4).

CW-EPR Spectroscopy. Chemically generated PXX$^{•+}$ and PXX$^{•+}$-d_{10} in dichloromethane solution were characterized by CW-EPR spectroscopy (Figure S5). The unpaired electron in PXX$^{•+}$ is coupled to its hydrogen atoms, and the isotropic hyperfine coupling constants (HFCs) of the five inequivalent hydrogen atoms were obtained from fitting the experimental spectrum and are summarized in Table S1. The EPR spectrum of PXX$^{•+}$-d_{10} exhibits significant spectral narrowing resulting from the ~6.5-fold reduction in gyromagnetic ratio of deuterium relative to hydrogen. The structure that appears atop the derivative spectrum of PXX$^{•+}$-d_{10} results from unresolved deuterium HFCs.

TREPR Spectroscopy. To evaluate the feasibility of PXX$^{•+}$-d_9-NMI-$C_{60}^{•-}$ as a potential SQP system for quantum gate operations, TREPR measurements were performed on both **1** and **1-d_9** in mTHF and 5CB at 85 K. The spectra were recorded in direct detection mode, where positive signals are enhanced absorptive (*a*) transitions and negative signals are emissive (*e*) ones. Figure 3 shows the corresponding TREPR spectra at 200 ns after a 7 ns, 450 nm laser pulse. The difference in *g*-tensors between PXX$^{•+}$ and $C_{60}^{•-}$ allows for spectral separation of the two radicals at X-band frequencies. However, significant line broadening at lower field was

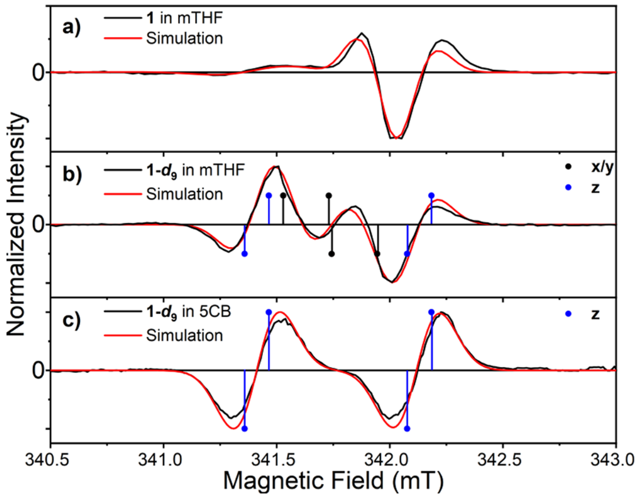

Figure 3. TREPR spectra at 85 K and 200 ns following a 450 nm, 7 ns laser pulse and spectral simulations. (a) PXX$^{\bullet+}$-NMI-$C_{60}^{\bullet-}$ (**1**) in mTHF, (b) PXX-$d_9^{\bullet+}$-NMI-$C_{60}^{\bullet-}$ (**1-d_9**) in mTHF, and (c) PXX-$d_9^{\bullet+}$-NMI-$C_{60}^{\bullet-}$ (**1-d_9**) in 5CB aligned along the magnetic field. The vertical lines connected to the dots show the transitions of the SQPs, whose principal axes, *x*, *y* or *z*, are parallel to the magnetic field, where *z* is defined as the direction that connects the two spins, and *x* and *y* are perpendicular to *z*.

observed for **1** due to the unresolved hydrogen atom HFCs in PXX$^{\bullet+}$ (Figure 3a). The higher field portion of the spectrum with transitions primarily from $C_{60}^{\bullet-}$ has a narrow (*a,e,a*) polarization pattern owing to the nuclear-spin-free nature of $C_{60}^{\bullet-}$ and its axial *g*-tensor, whose anisotropy is likely due to the pyrrolidino-functionalization of C_{60} that distorts its symmetry.

Compared to **1**, the lower field features in the TREPR spectrum of **1-d_9** in mTHF are narrowed in the absence of hydrogen HFCs. The entire TREPR spectrum of **1-d_9** is nearly centrosymmetric and shows an (*e,a,e,a,e,a*) polarization pattern, which deviates from the ideal (*e,a,e,a*) pattern predicted for the four spin transitions of SQPs.[31,55] This deviation is attributed to the axial *g*-tensors of both PXX$^{\bullet+}$ and $C_{60}^{\bullet-}$. The Zeeman splitting of an electron spin in an anisotropic molecule is a function of the molecular orientation with respect to the external magnetic field; likewise, the TREPR spectrum of a randomly oriented ensemble of SQPs in a frozen matrix, such as that of **1-d_9** in mTHF, results in a powder pattern composed of the SQP transitions at all orientations (Figure 3b).

To eliminate the spectral complexity from random molecular orientations, **1-d_9** was dissolved in 5CB, and the sample was aligned by the magnetic field at 295 K, then frozen. The aligned sample shows a well-resolved (*e,a,e,a*) polarization pattern (from lower field to higher field) spanning roughly 35 MHz that permits qubit addressability using both frequency-selective and nonselective microwave pulses necessary for quantum gate operations (Figure 3c). The TREPR spectra of **1** and **1-d_9** can be globally simulated using the same spin model with a spin−spin dipolar coupling constant $D = -3$ MHz and two axial *g*-tensors:, [2.0045, 2.0045, 2.0031] and [2.0003, 2.0003, 2.0019], for PXX$^{\bullet+}$ and $C_{60}^{\bullet-}$, respectively. The spectral simulation of **1** in frozen mTHF used a 20 MHz Gaussian peak-to-peak line width to account for unresolved hydrogen HFCs of PXX$^{\bullet+}$ (Table S1).

EPR Spectral Readout with Nonselective Pulses. The strategies of *g*-factor engineering, deuteration, and alignment of **1-d_9** produce well-resolved SQP EPR spectra, allowing for uniform excitation of the entire EPR spectrum using a 20 ns Gaussian-shaped microwave pulse. Instead of using traditional field-sweep detection, the EPR spectrum of **1-d_9** in 5CB in the frequency domain can be obtained by measuring the entire spin−echo time trace in the time domain[56] at the central magnetic field of the spectrum and performing a Fourier transform to obtain the EPR spectrum in the frequency domain. In principle, when all the spin transitions are excited, the resulting frequency spectrum of the SQP should exhibit the same spectral features and polarization pattern as the TREPR spectrum. To ensure the same bandwidths between the two

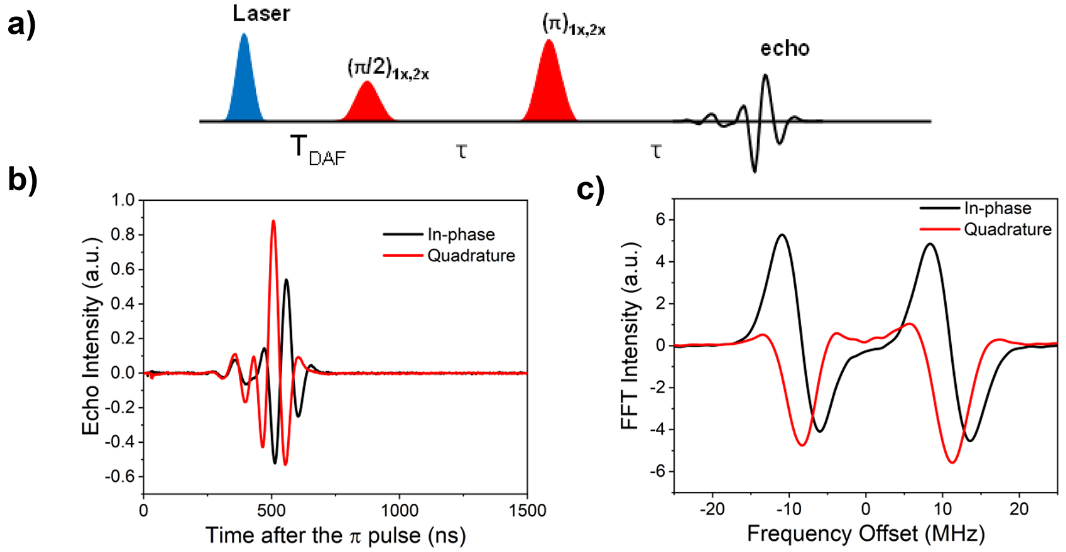

Figure 4. (a) Pulse sequence used to measure the EPR spectrum of PXX-$d_9^{\bullet+}$-NMI-$C_{60}^{\bullet-}$ (**1-d_9**) at 85 K in aligned 5CB, where $T_{DAF} = 50$ ns, $\tau = 500$ ns, and variable amplitude 20 ns microwave pulses were used to produce the $\pi/2$ and π turning angles as described in the text. (b) Spin echo of PXX-$d_9^{\bullet+}$-NMI-$C_{60}^{\bullet-}$ showing oscillatory behavior due to the structure of the frequency spectrum. Both the in-phase and quadrature parts of the signal were collected. (c) The frequency domain spectrum of the spin echo showing both $C_{60}^{\bullet-}$ and PXX-$d_9^{\bullet+}$, from low to high frequency.

https://doi.org/10.1021/jacs.3c01243
J. Am. Chem. Soc. 2023, 145, 6585−6593

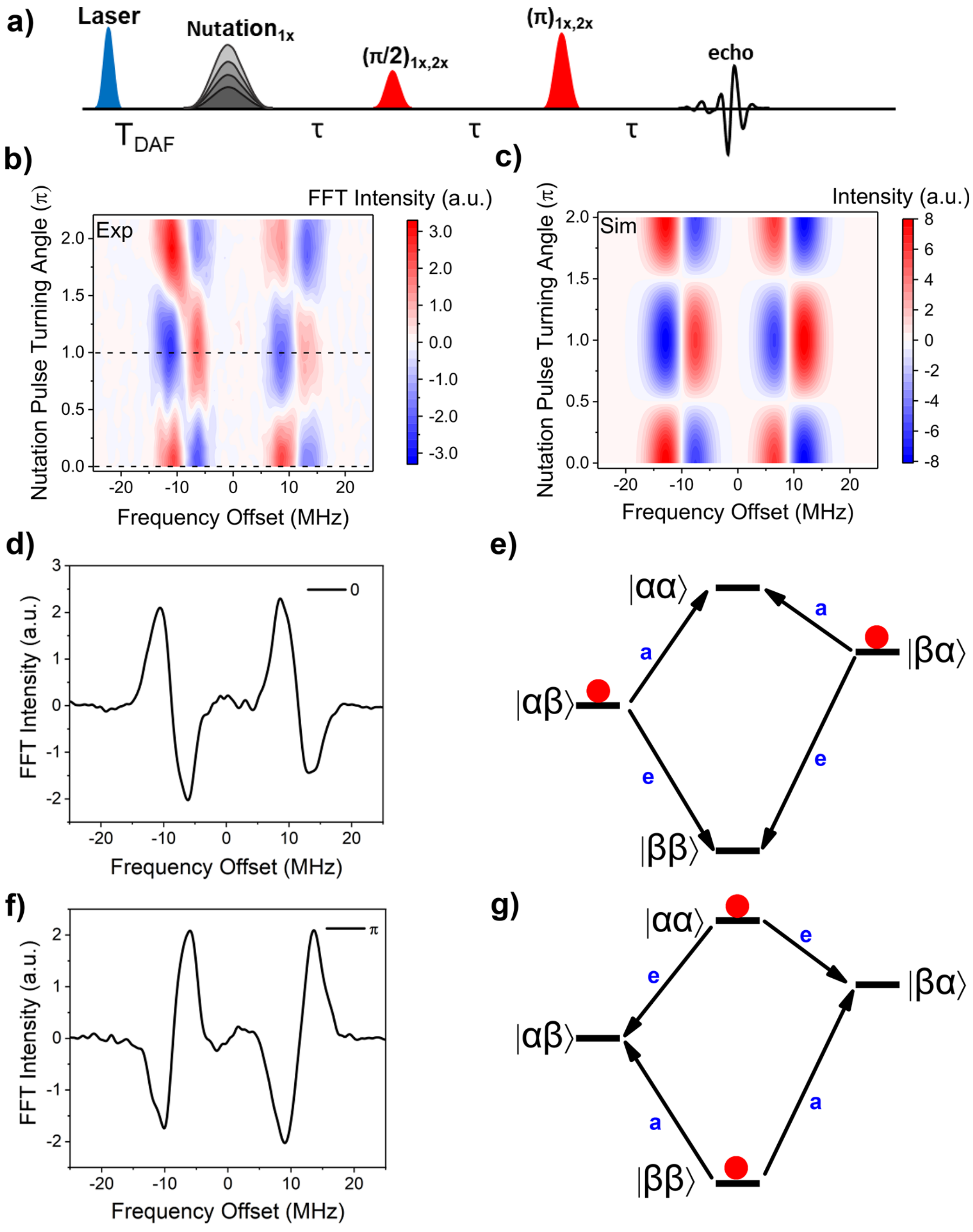

Figure 5. (a) Pulse sequence of the single-qubit nutation where T_{DAF} = 50 ns, the black pulse is a frequency-selective 80 ns nutation pulse, τ = 500 ns, and the red pulses are 20 ns frequency-nonselective $\pi/2$ and π readout pulses. (b) Frequency spectra after a single-qubit nutation pulse on $C_{60}^{\bullet -}$ within PXX-$d_9^{\bullet +}$-NMI-$C_{60}^{\bullet -}$ (**1**-$\boldsymbol{d_9}$) at 10 K. (c) Frequency space simulation of the effect of a single-qubit pulse with varying turning angles. (d and f) Spectral slices at the dashed lines in (b), where the turning angles of the selective nutation pulses are 0 and π, respectively. (e and g) Spin level population diagrams for selective nutation pulses 0 and π, respectively, applied to $C_{60}^{\bullet -}$.

pulses, the turning angles of the $\pi/2$ and π microwave pulses were determined by adjusting the pulse amplitudes rather than the pulse lengths (Figure 4a). The SQP spin−echo shows strong oscillations (Figure 4b), which carry all the spectral information in the time domain, similar to a free induction decay (FID). The TREPR spectrum of **1**-d_9 in 5CB is well-reproduced in the frequency domain (Figure 4c), showing the same (*e*,*a*,*e*,*a*) polarization pattern (from high frequency to low frequency), which demonstrates this technique as a feasible detection scheme for quantum gate operations.

Single-Qubit Operations. Single-qubit operations were performed on **1**-$\boldsymbol{d_9}$ oriented in 5CB at 10 K using an 80 ns Gaussian-shaped, frequency-selective pulse. Decreasing the temperature from 85 K to 10 K extends the SQP lifetime from 2.0 ± 0.2 μs to 13 ± 1 μs (Figure S6). The amplitude of this pulse was incremented to perform a nutation that targeted either $C_{60}^{\bullet -}$ or PXX$^{\bullet +}$, depending on the frequency offset of the pulse (Figure S1b). The effect of the single-qubit nutation pulse was monitored using the detection scheme discussed in the previous section. Figure 5a shows the pulse sequence used in this experiment, where the nutation pulse has a frequency

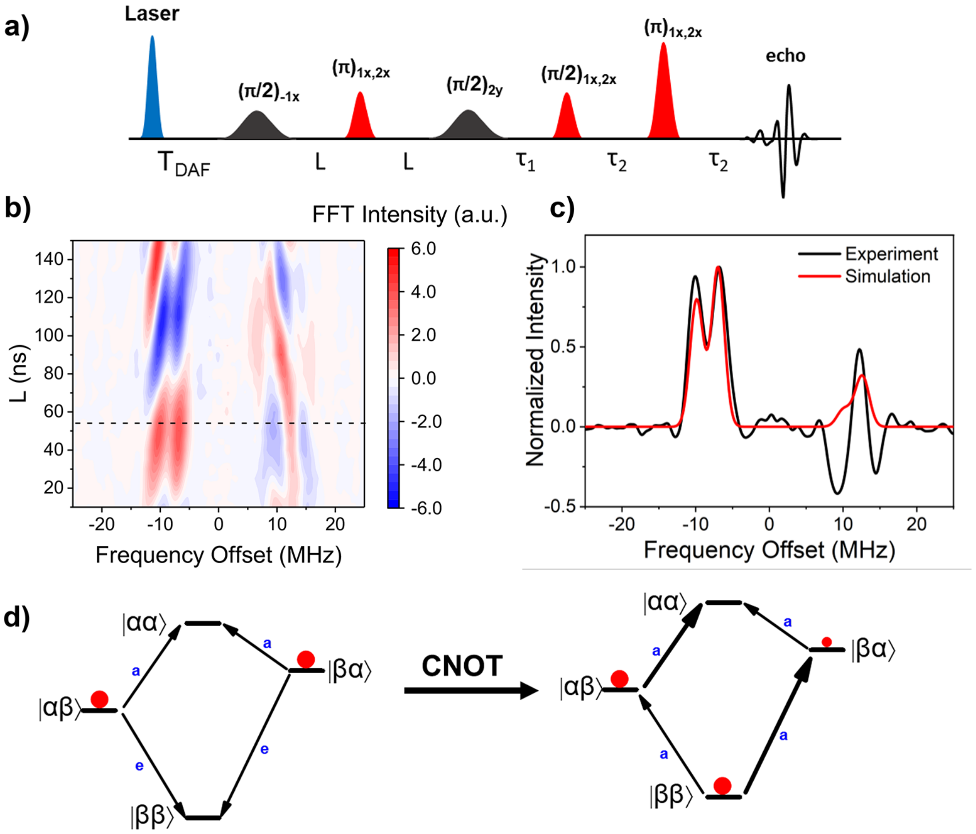

Figure 6. (a) Pulse sequence for CNOT gate and detection, where T_{DAF} = 50 ns. The two frequency-selective 80 ns pulses (black), the variable time delay L, and the first 20 ns frequency-nonselective pulse (red) constitute the CNOT gate. This is followed by two 20 ns frequency-nonselective $\pi/2$ and π readout pulses (red), where τ_1 = 200 ns, τ_2 = 500 ns. The frequency spectrum after the three-pulse CNOT gate operation with incremental L is plotted in (b) using PXX$^{\bullet+}$ as the control qubit at 10 K. The slice marked by the dashed line in (b) is shown in (c), and simulation is shown in red. (d) Spin level population diagrams of the SQP before and after the CNOT gate.

offset of −9 MHz that selectively operates on $C_{60}^{\bullet-}$. The frequency spectrum of the SQP produced after photoexciting **1-*d*$_9$** is plotted against the turning angle of the nutation pulse in Figure 5b, which can be simulated accurately in the frequency domain, Figure 5c. In addition, if PXX$^{\bullet+}$ is selectively excited by the nutation pulse, the same nutation behavior is observed (Figure S8a), which can also be simulated accurately (Figure S8b). This nutation effect is attributed to entanglement between the $C_{60}^{\bullet-}$ and PXX$^{\bullet+}$ electron spins.[44] The PXX$^{\bullet+}$-d_9-NMI-$C_{60}^{\bullet-}$ SQP generated after photoexciting **1-*d*$_9$** is in an initial singlet state, which results in population of the $|\alpha\beta\rangle$ and $|\beta\alpha\rangle$ spin states of the SQP in the high field limit[57] (Figure 5d), where the first and second Greek letters in the kets denote the spin states of PXX$^{\bullet+}$ and $C_{60}^{\bullet-}$, respectively. The absorptive and emissive spectral features of $C_{60}^{\bullet-}$ are assigned to the $|\alpha\beta\rangle$ to $|\alpha\alpha\rangle$ and $|\beta\alpha\rangle$ to $|\beta\beta\rangle$ transitions, respectively (Figure 5e). The spin configurations in the uncoupled basis are shown next to the energy levels to highlight the spin flips associated with each transition. The nutation π pulse applied to the transitions of $C_{60}^{\bullet-}$ acts as a NOT gate and flips the spin populations from $|\alpha\beta\rangle$ to $|\alpha\alpha\rangle$ and from $|\beta\alpha\rangle$ to $|\beta\beta\rangle$ simultaneously (Figure 5g), causing the entire spectrum to flip accordingly (Figure 5f). More generally this operation can be written as $1/\sqrt{2}[|\alpha\beta\rangle - |\beta\alpha\rangle] \xrightarrow{\text{NOT}} 1/\sqrt{2}[|\alpha\alpha\rangle - |\beta\beta\rangle]$ and is a protocol related to superdense coding in QIS.[44] The same behavior was observed when the nutation pulse was applied to PXX$^{\bullet+}$, where $1/\sqrt{2}[|\alpha\beta\rangle - |\beta\alpha\rangle] \xrightarrow{\text{NOT}} 1/\sqrt{2}[|\beta\beta\rangle - |\alpha\alpha\rangle]$, (Figure S8).

The Three-Pulse CNOT Gate. One of the original microwave pulse sequences proposed by Volkov and Salikhov[58] for the CNOT gate is composed of five microwave pulses, resulting in a relatively long gate execution time.[13] However, the fact that the photogenerated SQP is created in an initial singlet state allows for reduction of the number of pulses necessary to implement the CNOT gate (see SI, eqs S1−S4). Here, a three-pulse sequence is used to execute the CNOT gate and the spectrum after the gate is read out using a broadband Hahn echo pulse sequence as described previously (Figure 6a).[13] The CNOT gate pulse sequence comprises two 80 ns frequency-selective $\pi/2$ microwave pulses at the resonance frequencies of the control and target qubits and one 20 ns frequency nonselective π pulse that excites all four transitions of the SQP. The two spin evolution times $L = \pi/(2J - 8/3D)$, where the spin−spin exchange coupling (J) and dipolar coupling (D) between the two spins of the SQP are determined experimentally using out-of-phase electron spin echo envelope modulation measurements (OOP-ESEEM) (Figure S9).[57,59,60] Figure 6b shows the spectral changes that occur when L is incremented with PXX$^{\bullet+}$ acting as the control qubit. The SQP spectra after the pulse sequence oscillate at the same period as the OOP-ESEEM signal (Figure S9), suggesting that both J and D are contributing to the spin precession in the absence of microwave pulses. Furthermore,

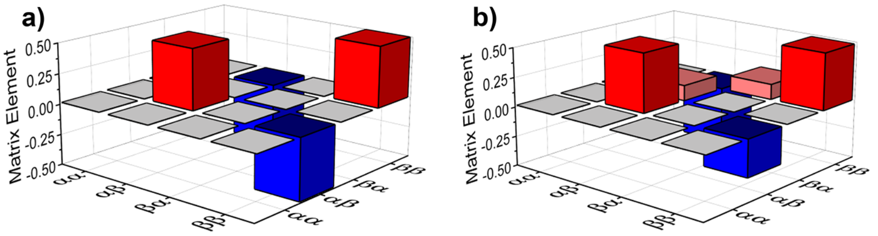

Figure 7. Expected (a) and experimentally measured (b) density matrices of the PXX-$d_9$$^{•+}$-NMI-$C_{60}$$^{•-}$ (**1-d_9**) SQP after applying the CNOT gate.

when L = 55 ns, the CNOT gate occurs, yielding an EPR spectrum with a strong absorptive doublet (*a,a*) feature on resonance with $C_{60}$$^{•-}$ and a weaker (*e,a,e*) feature on resonance with PXX$^{•+}$ (Figure 6c). Ideally, when PXX$^{•+}$ is acting as the control qubit, the target qubit $C_{60}$$^{•-}$ will experience a spin flip only when PXX$^{•+}$ is in the β state. Therefore, when the CNOT gate is applied to the SQP with its initial spin state of $1/\sqrt{2}[|\alpha\beta\rangle - |\beta\alpha\rangle]$, the $|\alpha\beta\rangle$ state remains unchanged, whereas the $|\beta\alpha\rangle$ state is transferred to the $|\beta\beta\rangle$ state as a result of the spin flip on the target qubit because the control qubit is in the β state, $1/\sqrt{2}[|\alpha\beta\rangle - |\beta\alpha\rangle] \xrightarrow{\text{CNOT}} 1/\sqrt{2}[|\alpha\beta\rangle - |\beta\beta\rangle]$. Realistically, the $|\beta\alpha\rangle$ state in SQP is mixed with a small percentage of $|\alpha\beta\rangle$ character, thus leaving a small $|\beta\alpha\rangle$ spin population. As a consequence, applying the CNOT gate to the SQP results in an EPR spectrum with a strong absorptive doublet on the target qubit and a weaker absorption on the control qubit (Figure 6d). Once again, the spin configurations in the uncoupled basis are shown next to the energy levels to highlight the spin flips associated with each transition. However, the EPR spectrum after the CNOT gate does not completely match what is predicted by the simulation, indicating a nonunity fidelity of the CNOT gate, which is likely due to nonideality of the microwave pulses, such as the finite pulse length resulting in nonuniform excitation profiles over the desired frequency range.

Quantum State Tomography and CNOT Gate Fidelity. The fidelity F of a quantum operation as defined in eq 1 is a common metric used to assess the success of an experimental quantum logic gate, which compares an ideal density matrix ρ of a quantum system to the experimentally determined density matrix σ of the same system.

$$F(\rho, \sigma) \equiv (\mathrm{tr}\sqrt{\rho^{1/2}\sigma\rho^{1/2}})^2 \tag{1}$$

The ideal density matrix ρ can be constructed using the density matrix of the initial SQP spin state and the matrix representation of the CNOT gate. After applying the CNOT gate, the experimental density matrix σ of the SQP can be measured using frequency-selective microwave pulses with 90° turning angles (Figure S10). Using the symbols I, X, and Y to represent the identity operation, a 90° rotation about the x-axis, and a 90° rotation about the y-axis, respectively, performing a total of nine operations following the CNOT gate,[61,62] *II*, *XI*, *YI*, *IX*, *IY*, *XX*, *YY*, *XY*, *YX*, rotates the off-diagonal elements of the density matrix to the diagonal of the matrix, which are read out as spin populations that manifest themselves as different polarization patterns in the EPR spectra (Figure S11). The experimental density matrix is reconstructed subsequently by solving linear equations whose unknowns are the matrix elements. The linear equations are simplified further by neglecting the double-quantum coherences and the coherences related to the $|\alpha\alpha\rangle$ spin state because no spin population is present in that state. The ideal and experimental density matrices reconstructed by this method are shown in Figure 7 and eqs S14 and S15. We obtained a fidelity of 0.89, which shows that the microwave pulse sequence used here accurately executes the CNOT gate. By comparing Figures 7a and 7b, the main source of deviation from the ideal CNOT gate comes from coherence between the $|\beta\alpha\rangle$ and $|\beta\beta\rangle$ states potentially generated by nonideal excitation by the microwave pulses.

CONCLUSIONS

In this study, we synthesized PXX-d_9-NMI-C_{60} in which deuteration of the PXX donor, use of the C_{60} as the nuclear spin-free acceptor with an unusually low g-factor, and alignment of photogenerated PXX$^{•+}$-d_9-NMI-$C_{60}$$^{•-}$ in 5CB result in an SQP having four spectrally separated, narrow transitions, providing a platform for quantum logic gate operations. Single-qubit gates and the two-qubit CNOT gate were demonstrated using this system, which form a complete set of gates necessary for quantum information applications. These results illustrate the opportunities afforded by tailoring the properties of photogenerated radical pairs to serve as SQPs. Nevertheless, several challenges remain in scaling-up these systems to multiqubit assemblies needed for QIS applications. Some of these challenges currently being researched include using shaped microwave pulses to establish uniform pulse bandwidths, improved gate fidelities, optical selectivity to address different SQPs, and better control of anisotropic magnetic interactions to enhance spin addressability.

ASSOCIATED CONTENT

Supporting Information

The Supporting Information is available free of charge at https://pubs.acs.org/doi/10.1021/jacs.3c01243.

Experimental details, including synthesis, NMR, mass spec, TA spectra and kinetics, and additional EPR spectra (PDF)

AUTHOR INFORMATION

Corresponding Authors

Michael R. Wasielewski − *Department of Chemistry, Center for Molecular Quantum Transduction, and Institute for Sustainability and Energy at Northwestern, Northwestern University, Evanston, Illinois 60208-3113, United States;* orcid.org/0000-0003-2920-5440; Email: m-wasielewski@northwestern.edu

Matthew D. Krzyaniak − *Department of Chemistry, Center for Molecular Quantum Transduction, and Institute for Sustainability and Energy at Northwestern, Northwestern University, Evanston, Illinois 60208-3113, United States;*

orcid.org/0000-0002-8761-7323; Email: mdkrzyaniak@northwestern.edu

Authors

Haochuan Mao − *Department of Chemistry, Center for Molecular Quantum Transduction, and Institute for Sustainability and Energy at Northwestern, Northwestern University, Evanston, Illinois 60208-3113, United States;* orcid.org/0000-0001-8742-089X

Gediminas J. Pažėra − *Department of Chemistry, Center for Molecular Quantum Transduction, and Institute for Sustainability and Energy at Northwestern, Northwestern University, Evanston, Illinois 60208-3113, United States; Physical and Theoretical Chemistry Laboratory, Department of Chemistry, University of Oxford, Oxford OX1 3QZ, U.K.*

Ryan M. Young − *Department of Chemistry, Center for Molecular Quantum Transduction, and Institute for Sustainability and Energy at Northwestern, Northwestern University, Evanston, Illinois 60208-3113, United States;* orcid.org/0000-0002-5108-0261

Complete contact information is available at: https://pubs.acs.org/10.1021/jacs.3c01243

Notes

The authors declare no competing financial interest.

■ ACKNOWLEDGMENTS

This work was supported by the National Science Foundation under award no. CHE-2154627 (M.R.W., synthesis, EPR measurements). The research was supported as part of the Center for Molecular Quantum Transduction, an Energy Frontier Research Center funded by the U.S. Department of Energy (DOE), Office of Science, Basic Energy Sciences (BES), under award #DE-SC0021314 (M.D.K., EPR data analysis). G.J.P. is grateful to the European Research Council (under the European Union's Horizon 2020 research and innovation program, Grant Agreement No. 810002, Synergy Grant: "QuantumBirds"). ^{1}H NMR spectroscopy and mass spectrometry were conducted in IMSERC facilities at Northwestern University, which have received support from the Soft and Hybrid Nanotechnology Experimental (SHyNE) Resource (NSF ECCS-2025633), NSF CHE-1048773, Northwestern University, the State of Illinois, and the International Institute for Nanotechnology (IIN).

■ REFERENCES

(1) Harrow, A. W.; Montanaro, A. Quantum computational supremacy. *Nature* **2017**, *549*, 203−209.

(2) Degen, C. L.; Reinhard, F.; Cappellaro, P. Quantum sensing. *Rev. Mod. Phys.* **2017**, *89*, 035002.

(3) Biamonte, J.; Wittek, P.; Pancotti, N.; Rebentrost, P.; Wiebe, N.; Lloyd, S. Quantum machine learning. *Nature* **2017**, *549*, 195−202.

(4) Wasielewski, M. R.; Forbes, M. D. E.; Frank, N. L.; Kowalski, K.; Scholes, G. D.; Yuen-Zhou, J.; Baldo, M. A.; Freedman, D. E.; Goldsmith, R. H.; Goodson, T.; Kirk, M. L.; McCusker, J. K.; Ogilvie, J. P.; Shultz, D. A.; Stoll, S.; Whaley, K. B. Exploiting chemistry and molecular systems for quantum information science. *Nat. Rev. Chem.* **2020**, *4*, 490−504.

(5) Atzori, M.; Sessoli, R. The second quantum revolution: Role and challenges of molecular chemistry. *J. Am. Chem. Soc.* **2019**, *141*, 11339−11352.

(6) Troiani, F.; Affronte, M. Molecular spins for quantum information technologies. *Chem. Soc. Rev.* **2011**, *40*, 3119−3129.

(7) Liu, Y.; Toma, F. M. Catalyst: Qubits from the bottom up. *Chem.* **2020**, *6*, 795−798.

(8) Takui, T.; Berliner, L.; Hanson, G. *Electron Spin Resonance (ESR) Based Quantum Computing*; Springer: New York, 2016.

(9) Sato, K.; Nakazawa, S.; Rahimi, R.; Ise, T.; Nishida, S.; Yoshino, T.; Mori, N.; Toyota, K.; Shiomi, D.; Yakiyama, Y.; Morita, Y.; Kitagawa, M.; Nakasuji, K.; Nakahara, M.; Hara, H.; Carl, P.; Hoefer, P.; Takui, T. Molecular electron-spin quantum computers and quantum information processing: Pulse-based electron magnetic resonance spin technology applied to matter spin-qubits. *J. Mater. Chem.* **2009**, *19*, 3739−3754.

(10) Coronado, E. Molecular magnetism: From chemical design to spin control in molecules, materials and devices. *Nat. Rev. Mater.* **2020**, *5*, 87−104.

(11) Nakazawa, S.; Nishida, S.; Ise, T.; Yoshino, T.; Mori, N.; Rahimi, R. D.; Sato, K.; Morita, Y.; Toyota, K.; Shiomi, D.; Kitagawa, M.; Hara, H.; Carl, P.; Hoefer, P.; Takui, T. A synthetic two-spin quantum bit: G-engineered exchange-coupled biradical designed for controlled-NOT gate operations. *Angew. Chem., Int. Ed.* **2012**, *51*, 9860−9864.

(12) Rugg, B. K.; Krzyaniak, M. D.; Phelan, B. T.; Ratner, M. A.; Young, R. M.; Wasielewski, M. R. Photodriven quantum teleportation of an electron spin state in a covalent donor-acceptor-radical system. *Nat. Chem.* **2019**, *11*, 981−986.

(13) Nelson, J. N.; Zhang, J.; Zhou, J.; Rugg, B. K.; Krzyaniak, M. D.; Wasielewski, M. R. CNOT gate operation on a photogenerated molecular electron spin-qubit pair. *J. Chem. Phys.* **2020**, *152*, 014503.

(14) Olshansky, J. H.; Zhang, J.; Krzyaniak, M. D.; Lorenzo, E. R.; Wasielewski, M. R. Selectively addressable photogenerated spin qubit pairs in DNA hairpins. *J. Am. Chem. Soc.* **2020**, *142*, 3346−3350.

(15) Aguila, D.; Barrios, L. A.; Velasco, V.; Roubeau, O.; Repolles, A.; Alonso, P. J.; Sese, J.; Teat, S. J.; Luis, F.; Aromi, G. Heterodimetallic [LnLn'] lanthanide complexes: Toward a chemical design of two-qubit molecular spin quantum gates. *J. Am. Chem. Soc.* **2014**, *136*, 14215−22.

(16) Fernandez, A.; Moreno Pineda, E.; Muryn, C. A.; Sproules, S.; Moro, F.; Timco, G. A.; McInnes, E. J. L.; Winpenny, R. E. P. G-engineering in hybrid rotaxanes to create AB and AB_2 electron spin systems: EPR spectroscopic studies of weak interactions between dissimilar electron spin qubits. *Angew. Chem., Int. Ed.* **2015**, *54*, 10858−10861.

(17) Zadrozny, J. M.; Niklas, J.; Poluektov, O. G.; Freedman, D. E. Millisecond coherence time in a tunable molecular electronic spin qubit. *ACS Cent. Sci.* **2015**, *1*, 488−492.

(18) Zadrozny, J. M.; Gallagher, A. T.; Harris, T. D.; Freedman, D. E. A porous array of clock qubits. *J. Am. Chem. Soc.* **2017**, *139*, 7089−7094.

(19) Atzori, M.; Chiesa, A.; Morra, E.; Chiesa, M.; Sorace, L.; Carretta, S.; Sessoli, R. A two-qubit molecular architecture for electron-mediated nuclear quantum simulation. *Chem. Sci.* **2018**, *9*, 6183−6192.

(20) Bayliss, S. L.; Laorenza, D. W.; Mintun, P. J.; Kovos, B. D.; Freedman, D. E.; Awschalom, D. D. Optically addressable molecular spins for quantum information processing. *Science* **2020**, *370*, 1309−1312.

(21) Lombardi, F.; Lodi, A.; Ma, J.; Liu, J.; Slota, M.; Narita, A.; Myers William, K.; Müllen, K.; Feng, X.; Bogani, L. Quantum units from the topological engineering of molecular graphenoids. *Science* **2019**, *366*, 1107−1110.

(22) Shiddiq, M.; Komijani, D.; Duan, Y.; Gaita-Ariño, A.; Coronado, E.; Hill, S. Enhancing coherence in molecular spin qubits via atomic clock transitions. *Nature* **2016**, *531*, 348−351.

(23) Yu, C.-J.; Krzyaniak, M. D.; Fataftah, M. S.; Wasielewski, M. R.; Freedman, D. E. A concentrated array of copper porphyrin candidate qubits. *Chem. Sci.* **2019**, *10*, 1702−1708.

(24) Gaita-Ariño, A.; Luis, F.; Hill, S.; Coronado, E. Molecular spins for quantum computation. *Nat. Chem.* **2019**, *11*, 301−309.

(25) Fernandez, A.; Ferrando-Soria, J.; Pineda, E. M.; Tuna, F.; Vitorica-Yrezabal, I. J.; Knappke, C.; Ujma, J.; Muryn, C. A.; Timco,

G. A.; Barran, P. E.; Ardavan, A.; Winpenny, R. E. P. Making hybrid [*n*]-rotaxanes as supramolecular arrays of molecular electron spin qubits. *Nat. Commun.* **2016**, *7*, 10240.

(26) Warren, S. W. The usefulness of NMR quantum computing. *Science* **1997**, *277*, 1688−1690.

(27) DiVincenzo, D. P. The physical implementation of quantum computation. *Fortschr. Phys.* **2000**, *48*, 771−783.

(28) Harvey, S. M.; Wasielewski, M. R. Photogenerated spin-correlated radical pairs: From photosynthetic energy transduction to quantum information science. *J. Am. Chem. Soc.* **2021**, *143*, 15508−15529.

(29) Laorenza, D. W.; Kairalapova, A.; Bayliss, S. L.; Goldzak, T.; Greene, S. M.; Weiss, L. R.; Deb, P.; Mintun, P. J.; Collins, K. A.; Awschalom, D. D.; Berkelbach, T. C.; Freedman, D. E. Tunable Cr^{4+} molecular color centers. *J. Am. Chem. Soc.* **2021**, *143*, 21350−21363.

(30) Mani, T. Molecular qubits based on photogenerated spin-correlated radical pairs for quantum sensing. *Chem. Phys. Rev.* **2022**, *3*, 021301.

(31) Closs, G. L.; Forbes, M. D. E.; Norris, J. R. Spin-polarized electron-paramagnetic resonance-spectra of radical pairs in micelles - observation of electron spin-spin interactions. *J. Phys. Chem.* **1987**, *91*, 3592−3599.

(32) Buckley, C. D.; Hunter, D. A.; Hore, P. J.; McLauchlan, K. A. Electron spin resonance of spin-correlated radical pairs. *Chem. Phys. Lett.* **1987**, *135*, 307−312.

(33) Bell, J. S. On the Einstein-Poldolsky-Rosen paradox. *Physics* **1964**, *1*, 195−200.

(34) Thurnauer, M. C.; Norris, J. R. An electron spin echo phase shift observed in photosynthetic algae: Possible evidence for dynamic radical pair interactions. *Chem. Phys. Lett.* **1980**, *76*, 557−561.

(35) Tang, J.; Norris, J. R. Theoretical calculations of microwave effects on the triplet yield in photosynthetic reaction centers. *Chem. Phys. Lett.* **1983**, *94*, 77−80.

(36) Hore, P. J., Analysis of polarized electron paramagnetic resonance spectra. In *Advanced EPR in Biology and Biochemistry*; Hoff, A. J., Ed.; Elsevier: Amsterdam, 1989; pp 405−440.

(37) Gierer, M.; Van der Est, A.; Stehlik, D. Transient EPR of weakly coupled spin-correlated radical pairs in photosynthetic reaction centers: Increased spectral resolution from nutation analysis. *Chem. Phys. Lett.* **1991**, *186*, 238−247.

(38) Hoff, A. J.; Gast, P.; Dzuba, S. A.; Timmel, C. R.; Fursman, C. E.; Hore, P. J. The nuts and bolts of distance determination and zero- and double-quantum coherence in photoinduced radical pairs. *Spectrochim. Acta, Part A* **1998**, *54A*, 2283−2293.

(39) Horwitz, N. E.; Phelan, B. T.; Nelson, J. N.; Mauck, C. M.; Krzyaniak, M. D.; Wasielewski, M. R. Spin polarization transfer from a photogenerated radical ion pair to a stable radical controlled by charge recombination. *J. Phys. Chem. A* **2017**, *121*, 4455−4463.

(40) Horwitz, N. E.; Phelan, B. T.; Nelson, J. N.; Krzyaniak, M. D.; Wasielewski, M. R. Picosecond control of photogenerated radical pair lifetimes using a stable third radical. *J. Phys. Chem. A* **2016**, *120*, 2841−2853.

(41) Colvin, M. T.; Carmieli, R.; Miura, T.; Richert, S.; Gardner, D. M.; Smeigh, A. L.; Dyar, S. M.; Conron, S. M.; Ratner, M. A.; Wasielewski, M. R. Electron spin polarization transfer from photogenerated spin-correlated radical pairs to a stable radical observer spin. *J. Phys. Chem. A* **2013**, *117*, 5314−5325.

(42) Mi, Q.; Chernick, E. T.; McCamant, D. W.; Weiss, E. A.; Ratner, M. A.; Wasielewski, M. R. Spin dynamics of photogenerated triradicals in fixed distance electron donor-chromophore-acceptor-TEMPO molecules. *J. Phys. Chem. A* **2006**, *110*, 7323−7333.

(43) Olshansky, J. H.; Harvey, S. M.; Pennel, M. L.; Krzyaniak, M. D.; Schaller, R. D.; Wasielewski, M. R. Using photoexcited core/shell quantum dots to spin polarize appended radical qubits. *J. Am. Chem. Soc.* **2020**, *142*, 13590−13597.

(44) Nielsen, M. A.; Chuang, I. L. *Quantum Computation and Quantum Information*; Cambridge University Press: Cambridge, UK, 2000.

(45) Christensen, J. A.; Zhang, J.; Zhou, J.; Nelson, J. N.; Wasielewski, M. R. Near-infrared excitation of the *peri*-xanthenoxanthene radical cation drives energy-demanding hole transfer reactions. *J. Phys. Chem. C* **2018**, *122*, 23364−23370.

(46) Mao, H.; Young, R. M.; Krzyaniak, M. D.; Wasielewski, M. R. Controlling the dynamics of three electron spin qubits in a donor-acceptor-radical molecule using dielectric environment changes. *J. Phys. Chem. Lett.* **2021**, *12*, 2213−2218.

(47) Greenfield, S. R.; Svec, W. A.; Gosztola, D.; Wasielewski, M. R. Multistep photochemical charge separation in rod-like molecules based on aromatic imides and diimides. *J. Am. Chem. Soc.* **1996**, *118*, 6767−6777.

(48) Prato, M.; Maggini, M. Fulleropyrrolidines: A family of full-fledged fullerene derivatives. *Acc. Chem. Res.* **1998**, *31*, 519−526.

(49) Young, R. M.; Dyar, S. M.; Barnes, J. C.; Juricek, M.; Stoddart, J. F.; Co, D. T.; Wasielewski, M. R. Ultrafast conformational dynamics of electron transfer in $exbox^{4+}\subset$perylene. *J. Phys. Chem. A* **2013**, *117*, 12438−12448.

(50) Roy, I.; Bobbala, S.; Beldjoudi, Y.; Nguyen, M. T.; Young, R. M.; Cetin, M. M.; Cooper, J. A.; Allen, S.; Anamimoghadam, O.; Scott, E. A.; Wasielewski, M. R.; Stoddart, J. F. Supramolecular photoprotection of a photosensitizer for safe lysosomal delivery and regulated anticancer therapy. *J. Am. Chem. Soc.* **2019**, *141*, 12296−12304.

(51) Stoll, S.; Schweiger, A. Easyspin, a comprehensive software package for spectral simulation and analysis in EPR. *J. Magn. Reson.* **2006**, *178*, 42−55.

(52) Schweiger, A.; Jeschke, G. *Principles of Pulse Electron Paramagnetic Resonance*, 1st ed.; Oxford University Press, USA: Oxford, 2001.

(53) Guldi, D. M.; Prato, M. Excited-state properties of C_{60} fullerene derivatives. *Acc. Chem. Res.* **2000**, *33*, 695−703.

(54) Leach, S.; Vervloet, M.; Despres, A.; Breheret, E.; Hare, J. P.; Dennis, T. J.; Kroto, H. W.; Taylor, R.; Walton, D. R. M. Electronic spectra and transitions of the fullerene C_{60}. *Chem. Phys.* **1992**, *160*, 451−466.

(55) Hore, P. J.; Hunter, D. A.; Mckie, C. D.; Hoff, A. J. Electron-paramagnetic resonance of spin-correlated radical pairs in photosynthetic reactions. *Chem. Phys. Lett.* **1987**, *137*, 495−500.

(56) Bowman, M. K.; Maryasov, A. G. The direct dimension in pulse EPR. *Appl. Magn. Reson.* **2021**, *52*, 1041−1062.

(57) Tang, J.; Thurnauer, M. C.; Norris, J. R. Electron spin echo envelope modulation due to exchange and dipolar interactions in a spin-correlated radical pair. *Chem. Phys. Lett.* **1994**, *219*, 283−290.

(58) Volkov, M. Y.; Salikhov, K. M. Pulse protocols for quantum computing with electron spins as qubits. *Appl. Magn. Reson.* **2011**, *41*, 145−154.

(59) Salikhov, K. M.; Kandrashkin, Y. E.; Salikhov, A. K. Peculiarities of free induction and primary spin echo signals for spin-correlated radical pairs. *Appl. Magn. Reson.* **1992**, *3*, 199−216.

(60) Dzuba, S. A.; Gast, P.; Hoff, A. J. ESEEM study of spin-spin interactions in spin-polarized $P^+Q_a^-$ pairs in the photosynthetic purple bacterium *Rhodobacter sphaeroides* R26. *Chem. Phys. Lett.* **1995**, *236*, 595−602.

(61) Long, G. L.; Yan, H. Y.; Yang, S. Analysis of density matrix reconstruction in NMR quantum computing. *J. Opt. B* **2001**, *3*, 376.

(62) Lee, J.-S. The quantum state tomography on an NMR system. *Phys. Lett. A* **2002**, *305*, 349−353.

Supporting Information for

Quantum Gate Operations on a Spectrally Addressable Photogenerated Molecular Electron Spin-Qubit Pair

Haochuan Mao[1], Gediminas J. Pažėra[1,2], Ryan M. Young[1], Matthew D. Krzyaniak[1*], and Michael R. Wasielewski[1*]

[1]Department of Chemistry, Center for Molecular Quantum Transduction, and Institute for Sustainability and Energy at Northwestern, Northwestern University, Evanston, IL 60208-3113

[2]Physical and Theoretical Chemistry Laboratory, Department of Chemistry, University of Oxford, Oxford, UK OX1 3QZ

Table of Contents

1. Synthesis and Characterization

All chemicals were purchased from Sigma-Aldrich, Inc. unless noted otherwise. ^{1}H and ^{13}C NMR spectra were acquired with a Bruker Avance III 500 MHz instrument equipped with a DCH CryoProbe. Mass spectroscopy was performed using a Bruker Rapiflex MALDI-TOF. Purification was performed using silica gel from Sorbent Technologies (Atlanta, GA). The synthesis of Compound **1** or **1-*d***$_9$ is outlined in Scheme S1 and the synthesis of PXX-d_{10} is outlined in Scheme S2.

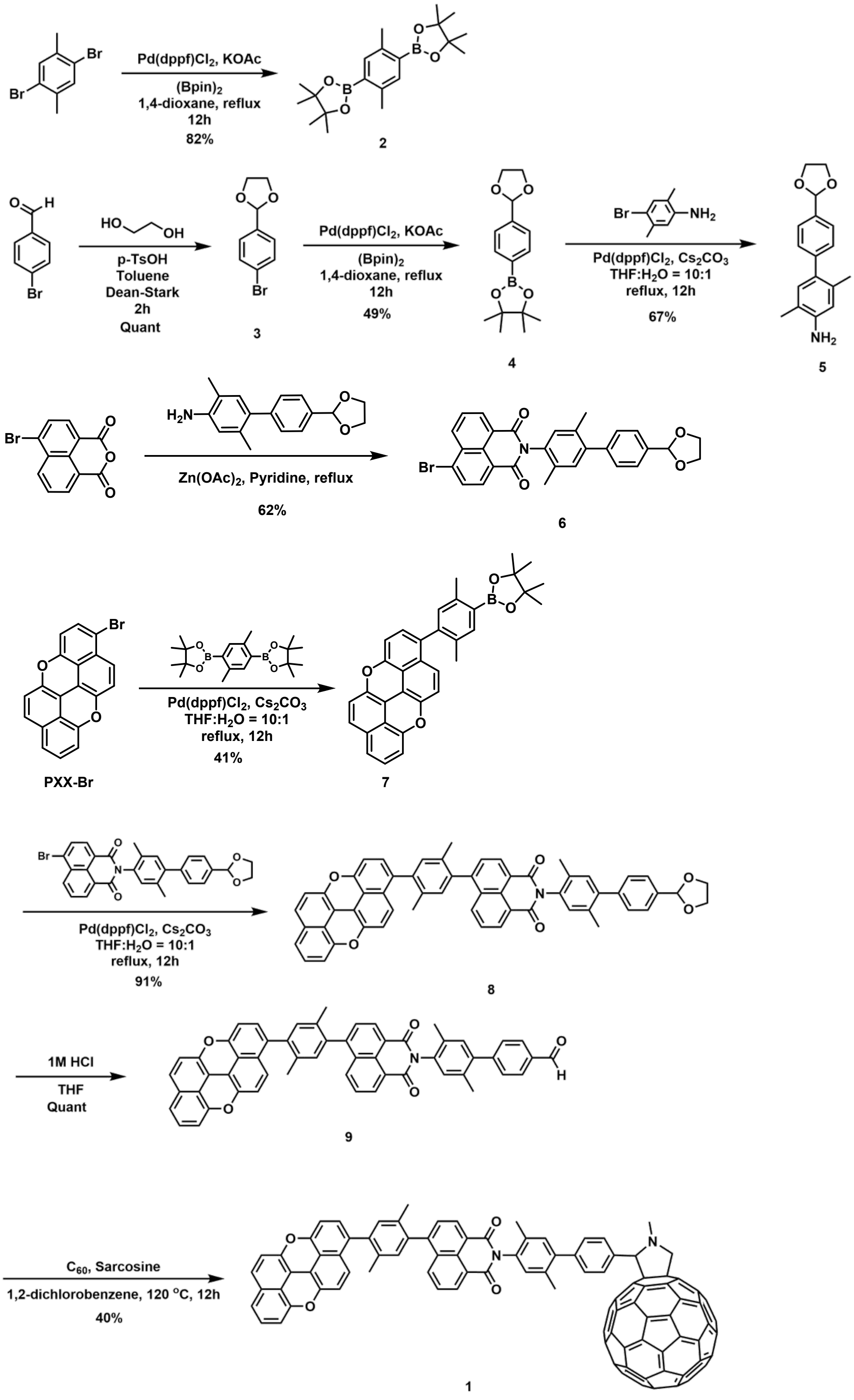

Scheme S1. Synthesis of **1** and **1-*d*$_9$**, if PXX-*d*$_9$-Br is employed**.**

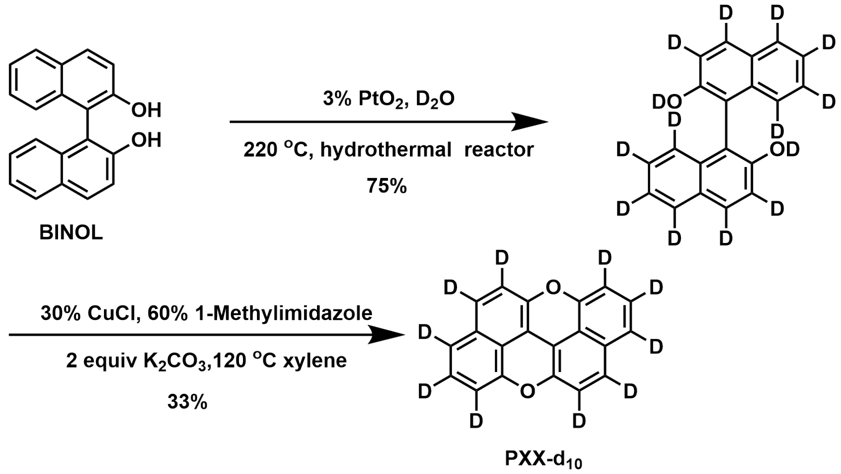

Scheme S2. Synthesis of PXX-d_{10}.

Compound 2: In a 100-ml round bottom flask equipped with a magnetic stir bar was added 1 g (3.8 mmol) of 1,4-dibromo-2,5-dimethylbenzene, 3.8 g (15 mmol) of bis(pinacolato)diboron, 136 mg (0.2 mmol) of Pd(dppf)Cl_2 and 2.2 g (23 mmol) of potassium acetate. The solid mixture was pump-purged three times under a nitrogen atmosphere before 20 ml of N_2-degassed 1,4-dioxane was injected into the flask and brought to reflux. 12 hours later, the solvent was removed under vacuum and the crude product was purified using silica gel column chromatography with 50% dichloromethane in hexane as eluents, yielding 1.2 g (82%) of white powder as product. ^1H NMR (500 MHz, $CDCl_3$) δ 7.56 (s, 2H), 2.50 (s, 6H), 1.36 (s, 24H). ^{13}C NMR (126 MHz, $CDCl_3$) δ 140.58, 136.94, 83.43, 24.91, 21.52.

Compound 3: In a 50-ml round bottom flask equipped with a stir bar and a Dean-Stark trap was placed with 1 g (5.5 mmol) of 4-bromobenzaldehyde 2.4 ml (44 mmol) of anhydrous ethylene glycol, 70 mg (0.28 mmol) of p-toluenesulfonic acid, 0.5 ml of silica gel and 12 ml of toluene. The reaction was brought up to 110 °C for 2 hours until the solvent in the Dean-Stark trap is no longer turbid. The mixture was poured into 20 ml of ethyl acetate and washed with water (10 ml × 3) and brine (5 ml). The organic layer was dried with anhydrous Na_2SO_4 and removed under vacuum to yield 1.25 g of colorless oil as product. ^1H NMR (500 MHz, $CDCl_3$) δ 7.52 – 7.46 (m, 2H), 7.37 – 7.30 (m, 2H), 5.75 (s, 1H), 4.13 – 4.05 (m, 2H), 4.05 – 3.97 (m, 2H). ^{13}C NMR (126 MHz, $CDCl_3$) δ 136.96, 131.55, 128.23, 123.30, 103.07, 65.36.

Compound 4: In a 100-ml round bottom flask equipped with a magnetic stir bar was added 1 g (4.4 mmol) of **3**, 1.2 g (9 mmol) of bis(pinacolato)diboron, 78 mg (0.38 mmol) of Pd(dppf)Cl_2 and 1.1 g (13 mmol) of potassium acetate. The solid mixture was pump-purged three times under a nitrogen atmosphere before 20 ml of N_2-degassed 1,4-dioxane was injected into the flask and brought to reflux. 12 hours later, the solvent was removed under vacuum and the crude product was purified using silica gel column chromatography with dichloromethane as eluents, yielding 501 mg (49%) of white powder as product. ^1H NMR (500 MHz, $CDCl_3$) δ 7.80 (d, J = 8.1 Hz, 2H), 7.45 (d, J = 8.1 Hz, 2H), 5.82 (s,1H), 4.13 – 4.06 (m, 2H), 4.06 – 3.98 (m, 2H), 1.32 (s, 12H). ^{13}C NMR (126 MHz, $CDCl_3$) δ 140.80, 138.08, 128.76, 125.71, 103.61, 84.37, 83.89, 65.30, 24.91.

Compound 5: 500 mg of **4**, 470 mg of 4-bromo-2,5-dimethylaniline, 70 mg of Pd(dppf)Cl_2 and 2.3 g of cesium carbonate was placed in a 50-ml round bottomed flask that was equipped with a stir bar and condenser. After pump-purge cycles, the solid was protected in an N_2 atmosphere and 20 ml of degassed 10% water in tetrahydrofuran solution was added to the reaction vessel and refluxed for 12 hours. The reaction mixture was then extracted with dichloromethane and washed with water. After the solvent was removed from the organic layer under vacuum, the crude product was purified using silica gel chromatography with dichloromethane as eluent to yield 300 mg (61%) of off-white waxy solid as product. ^1H NMR (500 MHz, $CDCl_3$) δ 7.48 – 7.45 (m, 2H), 7.32 – 7.28 (m, 2H), 6.91 (s, 1H), 6.58 (s, 1H), 5.83 (s, 1H), 4.21 – 4.10 (m, 2H), 4.10 – 4.00 (m, 2H), 3.58

(br, 2H), 2.16 (s, 3H), 2.14 (s, 3H). ^{13}C NMR (126 MHz, $CDCl_3$) δ 134.47, 133.79, 132.85, 131.27, 129.39, 128.26, 126.30, 123.19, 122.30, 103.75, 65.46, 29.74, 20.15, 17.19.

Compound 6: 120 mg of 4-Bromo-1,8-naphthalic anhydride, 170 mg of **5**, 20 mg of zinc acetate and 10 ml of pyridine were added to a 25-ml round bottomed flask that was equipped with a magnetic stir bar and a water condenser. The reaction was heated to 100 °C for 24 hours before the solvent was removed using a rotary evaporator. The crude product was passing through a silica gel column with dichloromethane as eluent to yield 78 mg (32%) of off-white powder as the product. ^{1}H NMR (500 MHz, $CDCl_3$) δ 8.72 (dd, J = 7.3, 1.1 Hz, 1H), 8.65 (dd, J = 8.5, 1.1 Hz, 1H), 8.48 (d, J = 7.8 Hz, 1H), 8.09 (d, J = 7.8 Hz, 1H), 7.90 (dd, J = 8.5, 7.3 Hz, 1H), 7.53 (d, J = 8.1 Hz, 2H), 7.40 (d, J = 8.3 Hz, 2H), 7.22 (s, 1H), 7.09 (s, 1H), 5.86 (s, 1H), 4.22 – 4.12 (m, 2H), 4.12 – 4.02 (m, 2H), 2.24 (s, 3H), 2.13 (s, 3H). ^{13}C NMR (126 MHz, $CDCl_3$) δ 163.56, 142.36, 142.29, 136.45, 134.47, 133.79, 133.25, 132.85, 132.59, 131.76, 131.27, 130.88, 130.85, 130.04, 129.98, 129.68, 129.54, 129.39, 128.26, 126.30, 123.19, 122.30, 103.75, 65.46, 20.15, 17.19.

Compound 7: 100 mg of PXX-Br, 150 mg of **2**, 10 mg of Pd(dppf)Cl_2 and 76 mg of potassium carbonate were placed in a 100-ml round bottomed flask that was equipped with a magnetic stir bar and a condenser. After the solid mixture was pump-purged three times and protected in a nitrogen atmosphere, 20 ml of degassed tetrahydrofuran was injected into the reaction vessel and heated up till reflux for 12 hours. The solvent was then removed under vacuum and the crude product was purified using silica gel chromatography with 50 % dichloromethane in hexane as eluent to yield 70 mg of product. ^{1}H NMR (500 MHz, $CDCl_3$) δ 7.68 (s, 1H), 7.31 (d, J = 9.0 Hz, 1H), 7.10 – 7.07 (m, 2H), 7.00 (s, 1H), 6.95 – 6.91 (m, 2H), 6.86 (d, J = 9.2 Hz, 1H), 6.80 (d, J = 9.3 Hz, 1H), 6.70 (t, J = 7.8 Hz, 1H), 6.65 – 6.61 (m, 1H), 2.52 (s, 3H), 2.02 (s, 3H), 1.36 (s, 12H).

Compound 8: 35 mg of **6**, 70 mg of **7**, 55 mg of cesium carbonate and 2 mg of Pd(dppf)Cl_2 was placed in a 25-ml round bottomed flask and pump-purged three times with N_2 before 10 ml of N_2-degassed 10 % water in tetrahydrofuran solution was injected. The reaction was brought up to reflux for 12 hours before the solvent was removed using a rotary evaporator. The crude product was purified using a silica gel chromatography with dichloromethane as eluent to yield 46 mg of product. ^{1}H NMR (500 MHz, $CDCl_3$) δ 8.76 – 8.66 (m, 2H), 8.11 – 8.02 (m, 1H), 7.83 – 7.71 (m, 2H), 7.54 (d, J = 8.1 Hz, 2H), 7.42 (d, J = 8.0 Hz, 2H), 7.35 (dt, J = 9.0, 1.7 Hz, 1H), 7.25 (s, 1H), 7.23 – 7.21 (m, 1H), 7.20 (s, 1H), 7.14 (s, 1H), 7.13 – 7.10 (m, 2H), 7.09 – 7.02 (m, 2H), 6.99 – 6.96 (m, 1H), 6.93 (s, 1H), 6.78 (dd, J = 7.8, 2.5 Hz, 1H), 6.67 (ddd, J = 5.3, 4.5, 3.1 Hz, 1H), 5.87 (s, 1H), 4.22 – 4.14 (m, 2H), 4.09 – 4.04 (m, 2H), 2.26 (s, 3H), 2.20 (s, 3H), 2.12 (s, 3H), 2.03 (s, 3H). MS (MALDI-TOF) m/z: [M^+] calculated for $C_{57}H_{39}NO_6$ 833.28; found 835.316.

Compound 9: 80 mg of **8** was dissolved in 15 ml of tetrahydrofuran in a 20-ml scintillation vial with the addition of 0.1 ml of 37 % hydrochloric acid and stirred at room temperature. Three hours later, the deprotection was completed as monitored by NMR. The reaction was quenched by sodium bicarbonate and extracted with dichloromethane. The product in the organic layer was used directly for the next step after the solvent was removed under vacuum. ^{1}H NMR (500 MHz, $CDCl_3$) δ 10.02 (s, 1H), 8.72 – 8.62 (m, 2H), 8.02 (td, J = 7.6, 1.2 Hz, 1H), 7.90 (d, J = 8.0 Hz, 2H), 7.77 – 7.67 (m, 2H), 7.53 (d, J = 8.0 Hz, 2H), 7.29 (dd, J = 9.0, 2.3 Hz, 1H), 7.22 (s, 1H), 7.18 (s, 1H), 7.15 (s, 1H), 7.13 (d, J = 2.3 Hz, 1H), 7.06 (p, J = 2.7 Hz, 2H), 7.04 – 7.00 (m, 1H), 7.00 – 6.96 (m, 1H), 6.95 – 6.90 (m, 1H), 6.86 (t, J = 8.7 Hz, 1H), 6.72 (dd, J = 7.8, 2.4 Hz, 1H), 6.61 (td, J = 4.7, 3.1 Hz, 1H), 2.23 (s, 3H), 2.17 (s, 3H), 2.08 (s, 3H), 2.01 (s, 3H). MS (MALDI-TOF) m/z: [M^+] calculated for $C_{55}H_{35}NO_5$ 789.25; found 789.566.

Compound 1: In a 50-ml round bottomed flask equipped with a magnetic stir bar and a water condenser was placed with 50 mg of **9**, 17 mg of sarcosine and 136 mg of C_{60} that were pump-purged three times with N_2. 20 ml of 1,2-dichlorobenzene was added to the flask and heated to 120 ^{o}C for 15 hours. After the reaction was cooled down, the solvent was removed under vacuum and the crude product was purify with silica gel column chromatography using 15% of dichloromethane in hexane to remove unreacted C_{60} first then flash with dichloromethane to obtain the crude product. The crude product was then purified with the same chromatography procedure two extra times to completely remove C_{60} to yield 20 mg of dark brown solid as product. ^{1}H NMR (500 MHz, $CDCl_3$) δ 8.74 – 8.66 (m, 2H), 8.05 (ddd, J = 7.8, 6.5, 1.2 Hz, 1H), 7.86 (s, 2H), 7.79 – 7.70 (m, 2H), 7.45 (dd, J = 5.4, 2.6 Hz, 2H), 7.35 (dt, J = 9.1, 1.8 Hz, 1H), 7.28 (s, 1H), 7.22 (d, J = 5.5 Hz, 1H), 7.19 (dd, J = 6.2, 4.1 Hz, 1H), 7.12 (dq, J = 5.2, 2.4 Hz, 3H), 7.09 – 7.05 (m, 1H), 7.05 – 7.01 (m, 1H), 6.97 (dt, J = 9.1, 1.9 Hz, 1H), 6.95 – 6.88 (m, 1H), 6.78 (dd, J = 7.8, 2.5 Hz, 1H), 6.67 (ddd, J = 5.4, 4.5, 3.2 Hz, 1H), 5.02 (d, J = 9.3 Hz, 1H), 5.00 (s, 1H), 4.30 (d, J = 9.4 Hz, 1H), 2.89 (s, 3H), 2.18 (s, 6H), 2.12 (s, 3H), 2.05 (s, 3H). ^{13}C NMR (126 MHz, $CDCl_3$) δ 146.50, 146.46, 146.42, 145.49, 145.38, 145.32, 145.28, 145.26, 144.99, 144.94, 144.92, 144.90, 144.76, 144.62, 144.60, 144.58, 144.51, 144.48, 144.44, 144.40, 144.35, 144.30, 144.22, 143.76, 143.49, 143.25, 143.17, 143.16, 142.26, 142.12, 142.05, 141.96, 141.72, 141.64, 141.55, 141.28, 141.25, 141.23, 141.03, 140.94, 140.79, 140.58, 140.44, 139.21, 139.14, 138.97, 138.62, 134.32, 133.21, 132.21, 131.36, 129.31, 82.29, 39.20, 28.76, 19.14, 18.62, 16.16, 13.10. MS (MALDI-TOF) m/z: [M^+] calculated for $C_{117}H_{40}N_2O_4$ 1537.30; found 1537.492.

BINOL-*d*$_{12}$: BINOL (2g), D20 (20 ml) and PtO2 (30 mg, 0.02 equiv.) were placed in a 125-ml Parr acid digestion vessel. The sealed vessel was placed in an air circulating drying oven and heated to 220 ^{o}C for 48 hours. The vessel was then cooled to room temperature and 100 ml of dichloromethane was added to dissolve the product. After filtration, the filtrate was collected, and the solvent removed under vacuum. The crude product underwent another deuteration cycle for complete deuteration (> 95%) to yield 1.6 g (75%) of product that was used directly for the next step. MS (MALDI-TOF) m/z: [M$^+$] calculated for $C_{20}HD_{13}O_2$ 299.18; found 299.276.

PXX-*d*$_{10}$: The synthesis of PXX-*d*$_{10}$ from BINOL-*d*$_{12}$ follows the literature procedure.[1] MS (MALDI-TOF) m/z: [M$^+$] calculated for $C_{20}D_{10}O_2$ 292.13; found 292.242.

Compound 1-*d*$_9$: The synthesis of **1-*d*$_9$** follows the same route as **1** except for using PXX-*d*$_9$-Br as the precursor. MS (MALDI-TOF) m/z: [M$^+$] calculated for $C_{117}H_{31}D_9N_2O_4$ 1546.36; found 1546.408.

2. Microwave Pulse Characterization

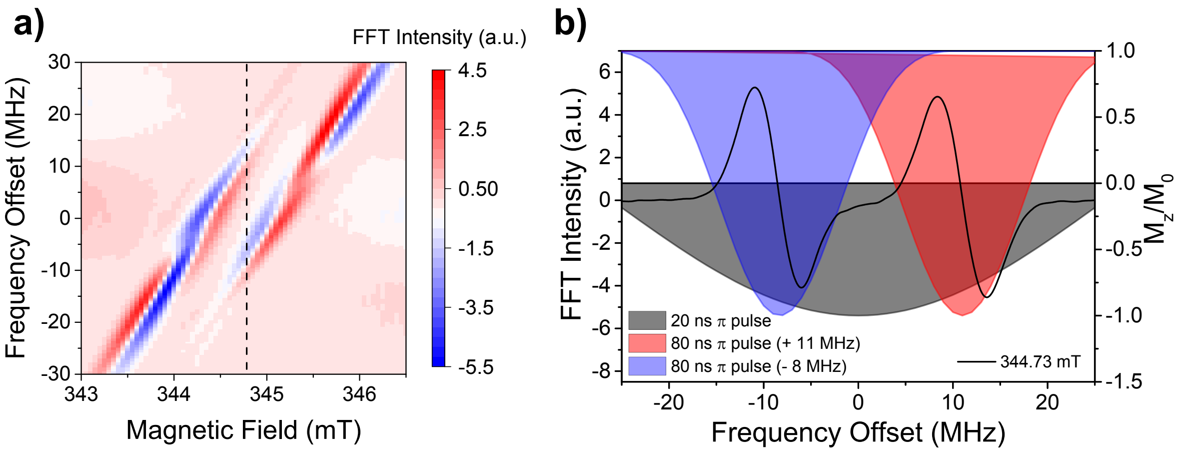

Figure S1. (a) Echo detected field sweep of PXX-*d*$_9^{\bullet+}$-NMI-$C_{60}^{\bullet-}$ generated by 450-nm photoexcitation of **1-*d*$_9$** at 10 K in 5CB aligned along the external magnetic field direction. 20-ns Gaussian-shaped π/2 and π pulses are used in the experiment to ensure the same excitation bandwidths of both microwave pulses to cover the entire EPR spectrum of the radical pair. Fourier transformation of the echo at each field position gives the corresponding frequency spectra and were plot against the magnetic field. The features with frequencies lager than 20 MHz or lower than -20 MHz belong to $^{3*}C_{60}$. (b) Frequency spectra of **1-*d*$_9$** at the field position indicated by the dashed line in (a) showing the complete EPR spectrum of the SQP. The shaded area shows the bandwidths of Gaussian-shaped microwave pulses, indicating the feasibility of selective and non-selective excitation.

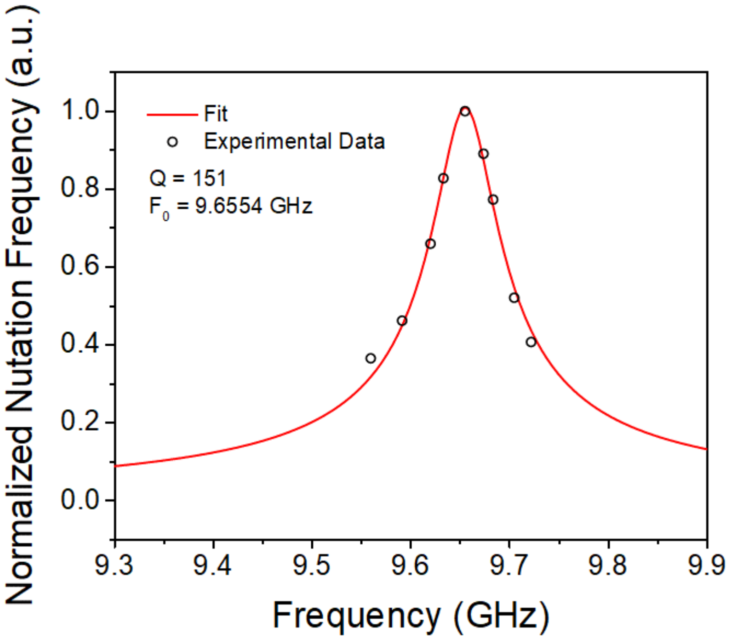

Figure S2. Resonator profile characterized by a three-pulse nutation experiment at various microwave frequencies. The plot of nutation frequencies versus microwave frequencies is fit with a resonator model to give the center frequency F_0 and the quality factor Q.

3. Transient Absorption Spectroscopy

Transient absorption spectra and kinetics were acquired using a regeneratively amplified Ti:sapphire laser system (Tsunami oscillator/Spitfire amplifier (Spectra-Physics) was used to pump a commercial collinear optical parametric amplifier (TOPAS-Prime, Light-Conversion LLC) to generate 450 nm laser pulses.[2] Before interaction with the sample, the probe was split using a neutral density filter so that one portion interacted with the sample and one portion provided a reference spectrum. The pump (450 nm, 1 μJ/pulse, 120 fs) was sent through a commercial depolarizer (DPU-25-A, Thorlabs, Inc.) to suppress the effects of rotational dynamics and chopped at 500 Hz. The pump was focused to about 0.2 mm diameter and the probe to about 0.1 mm diameter at the sample. The reference probe and the transmitted probe were coupled into optical fibers and detected using a customized Helios spectrometer and Helios software (Ultrafast Systems, LLC). Nanosecond visible transient absorption (nsTA) spectroscopy experiments were performed using the pump pulse described for the fsTA experiments paired with a photonic crystal fiber ultra-broadband probe generated by a customized EOS spectrometer (Ultrafast Systems, LLC). The temporal resolution was about 120-280 fs in the fsTA experiments and about 600-900 ps in the nsTA experiments. Visible fsTA spectra were collected for 3 s at each pump-probe time delay; nsTA spectra were collected using similar durations.

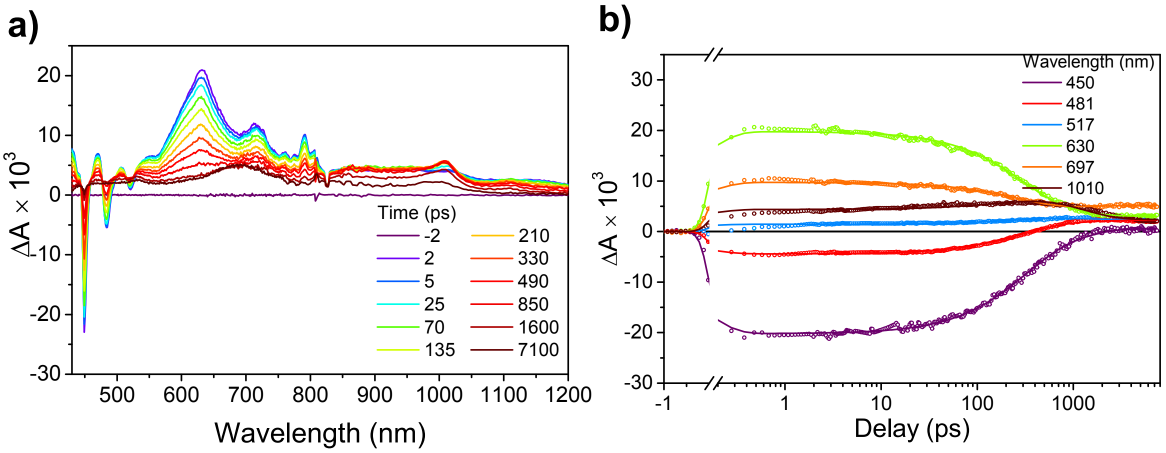

Figure S3. a) fsTA data of **1** at 85 K in mTHF solution following λ_{ex} = 450 nm excitation. b) Comparison of the kinetic traces to the fit at selected probe wavelengths.

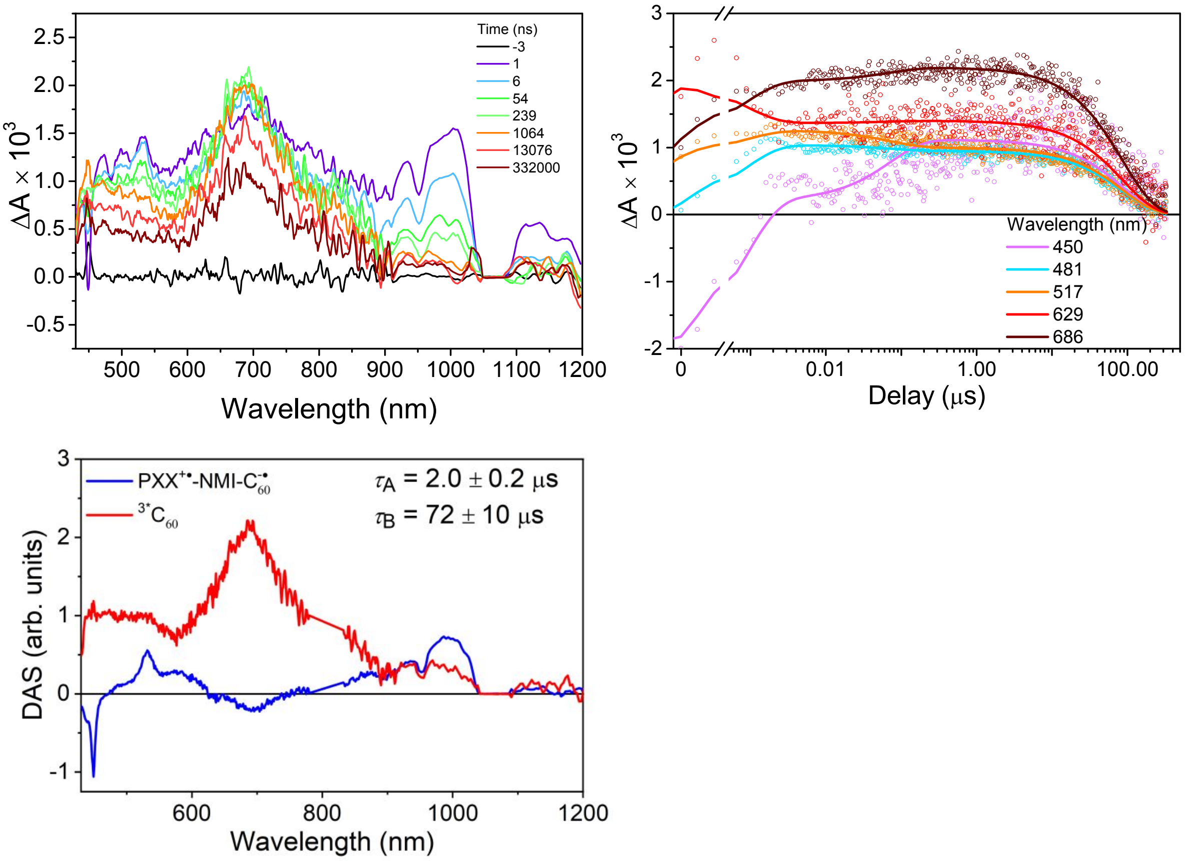

Figure S4. a) nsTA data of **1** at 85 K in mTHF solution following λex = 414 nm excitation. b) Decay-associated spectra (DAS) of **1**. c) Comparison of the kinetic traces to the fit at selected probe wavelengths.

4. Electron Paramagnetic Resonance Spectroscopy

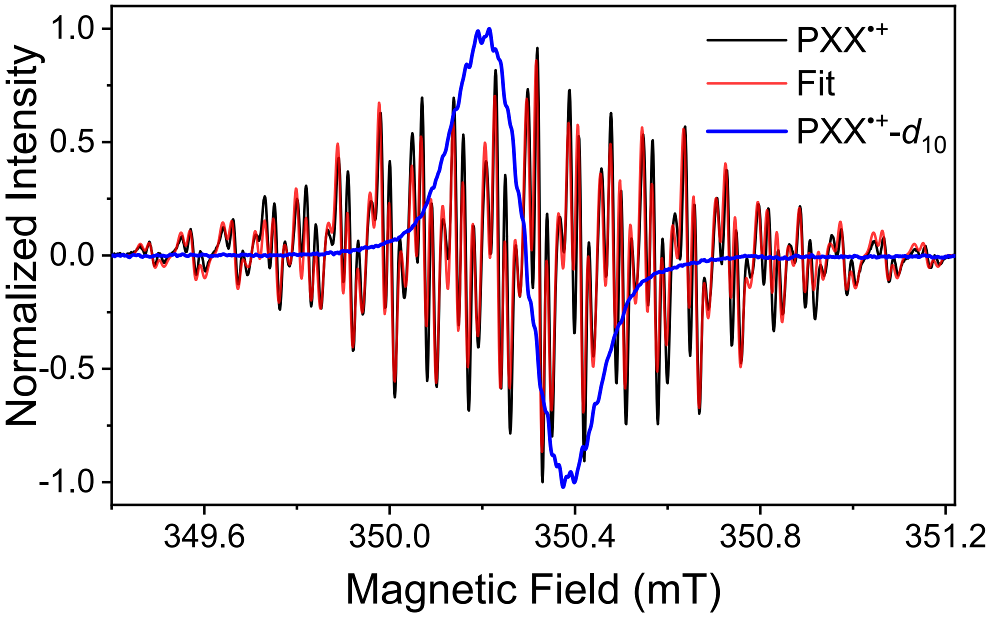

Figure S5. CW-EPR spectra of PXX$^{\bullet+}$ (black) and PXX$^{\bullet+}$-d_{10} (blue) in dichloromethane solution at 295 K. The spectral fitting of PXX$^{\bullet+}$ is shown in red.

Table S1. Proton Hyperfine Couplings Extracted From CW-EPR Spectrum of PXX$^{\bullet+}$

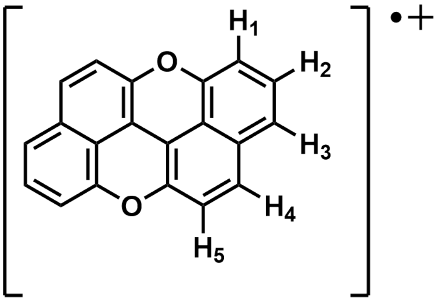

Proton	H1	H2	H3	H4	H5
Hyperfine Coupling (MHz)	5.00	0.51	6.37	9.47	2.45

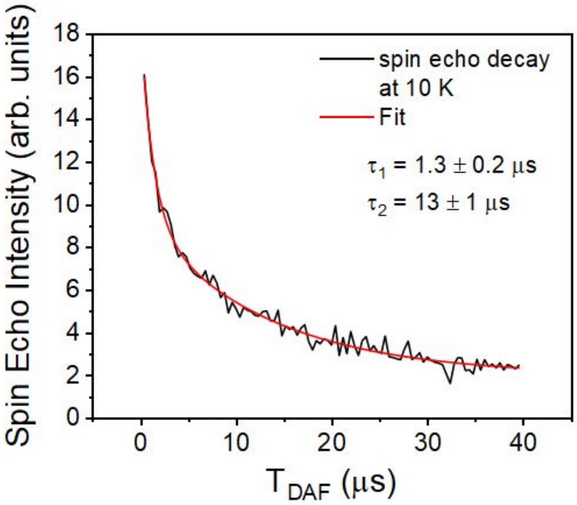

Figure S6. Lifetime of PXX-$d_9^{\bullet+}$-NMI-$C_{60}^{\bullet-}$at 10 K in 5CB aligned along the external magnetic field direction determined using electron spin echo detection following λex = 450 nm excitation of **1-*d*9**.T_{DAF} is the delay between the laser pulse and the π/2 pulse of the Hahn echo pulse sequence. The delay between the π/2 and π pulses of the Hahn echo sequence is 500 ns.

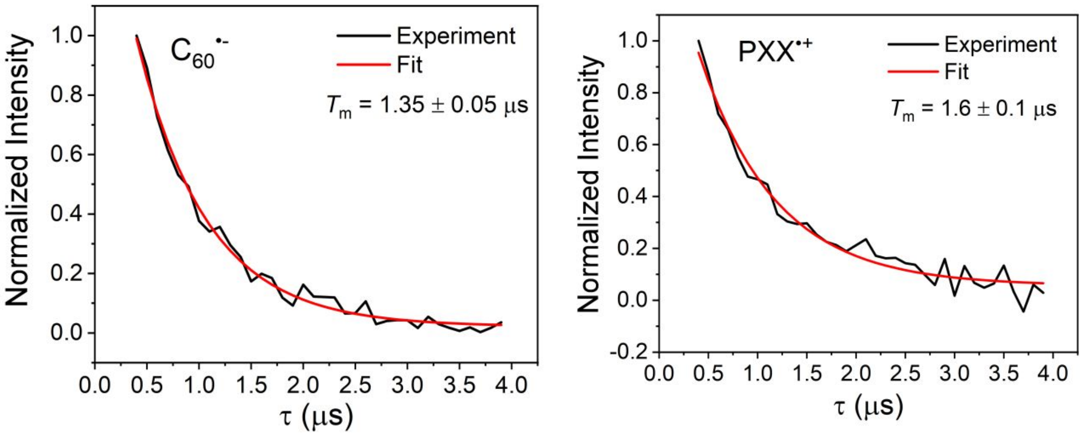

Figure S7. Phase memory time of $C_{60}^{\bullet-}$ and $PXX^{\bullet+}$ in the PXX-$d_9^{\bullet+}$-NMI-$C_{60}^{\bullet-}$ SQP measured in 5CB at 10 K using a π/2 – τ – π – τ – echo pulse sequence. Both the π/2 and π pulses are Gaussian-shaped 80-ns frequency selective microwave pulses to ensure selective excitation of either $C_{60}^{\bullet-}$ or $PXX^{\bullet+}$, which effectively eliminates OOP-ESEEM such that the exponential decay of the spin echo versus τ can be observed. The spin echo was integrated and plot against the inter pulse delay τ. Fitting the curve to a mono-exponential decay yields T_m.

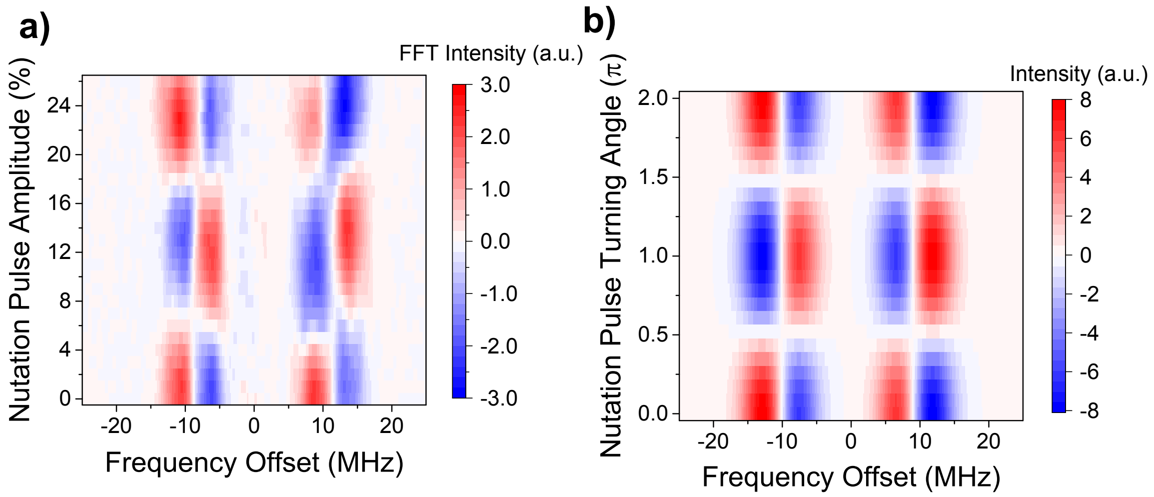

Figure S8. (a) Single-qubit gate operation using a three-pulse nutation pulse sequence on PXX-$d_9^{\bullet+}$-NMI-$C_{60}^{\bullet-}$at 85 K in 5CB aligned along the external magnetic field direction using a selective nutation pulse that excites PXX$^{\bullet+}$and a non-selective Hahn echo sequence that detects the entire EPR spectrum. The pulse lengths and intervals are the same as in Figure 5. (b) Frequency domain simulation of the experiment.

OOP-ESEEM

The out-of-phase ESEEM experiment on **1-*d*₉** measured in the nematic liquid crystal 5CB that is aligned parallel or perpendicular to the magnetic field allows one to extract the D and J values simultaneously.[3] Theoretically, the oscillation frequency in the parallel case is $|-4D/3+2J|$, while when the molecules are aligned perpendicular to the magnetic field, an oscillation frequency of $|2D/3+2J|$ would be obtained. Plugging the experimental data into these two equations yields $J = 0.15$ MHz and $D = -2.98$ MHz.

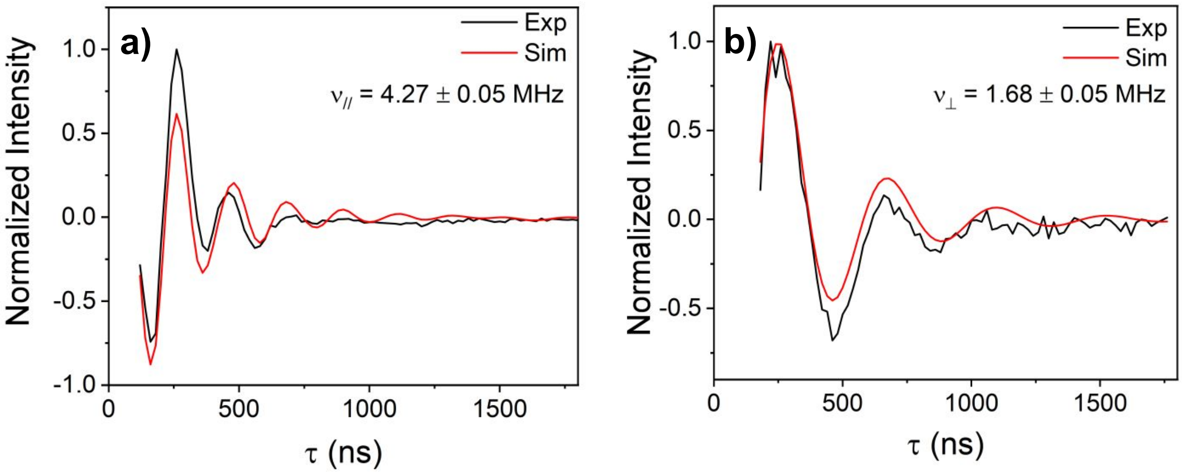

Figure S9. Out-of-phase ESEEM measurements on PXX-$d_9^{\bullet+}$-NMI-$C_{60}^{\bullet-}$ at 85 K in 5CB liquid crystal that is (a) aligned along the external magnetic field direction, or (b) aligned perpendicular to the external magnetic field direction.

The three-pulse CNOT gate

Following the methodology proposed by Salihkov,[4] the operator of the CNOT gate can be obtained in the following equation:

$$\hat{U}_{CNOT} = e^{i\pi/4} e^{-i\pi I_{2y}/2} e^{-iH\tau/2} e^{-i\pi(I_{1x}+I_{2x})} e^{-iH\tau/2} e^{-i\pi I_{1x}/2} e^{-i\pi(I_{1x}+I_{2x})} \quad \text{(S1)}$$

Where I_{1x}, I_{2x}, and I_{2y} are the spin operators, and H and τ are the spin Hamiltonian for the SQP and the spin evolution time, respectively. Since the SQP is initialized to the singlet state, to which the following equation applies:

$$e^{i\pi(I_{1x}+I_{2x})} |S\rangle\langle S| e^{-i\pi(I_{1x}+I_{2x})} = |S\rangle\langle S| \quad \text{(S2)}$$

The CNOT gate operator can thus be simplified as following:

$$\hat{U}_{CNOT} = e^{i\pi/4} e^{-i\pi I_{2y}/2} e^{-iH\tau/2} e^{-i\pi(I_{1x}+I_{2x})} e^{-iH\tau/2} e^{-i\pi I_{1x}/2} \quad \text{(S3)}$$

Substituting the spin Hamiltonian of the SQP into eq S3 yields:

$$\hat{U}_{CNOT} = e^{i\pi/4} e^{-\iota\pi I_{2y}/2} e^{i\pi I_{1z} I_{2z}/2} e^{-i\pi(I_{1x} + I_{2x})} e^{i\pi I_{1z} I_{2z}/2} e^{-\iota\pi I_{1x}/2} \tag{S4}$$

Hence, the pulse sequence for CNOT gate is $\pi/2_{-1x}$, L, $\pi_{1x,2x}$, L, $\pi/2_{2y}$, where delay $L = 2J$ except in the case of molecules that are aligned with the magnetic field, where $L = 2J - 8/3D$.

Quantum state tomography

To obtain the density matrix of the SQP after implementation of the CNOT gate, nine pulse sequences were used (Figure S10), which comprise the three-pulse CNOT gate, a tomographic projection pulse and a two-pulse detection sequence. We assume the density matrix σ of SQP after the CNOT gate takes the form of the following:

$$\sigma = \begin{bmatrix} a_{11} & a_{12} & a_{13} & a_{14} \\ a_{21} & a_{22} & a_{23} & a_{24} \\ a_{31} & a_{32} & a_{33} & a_{34} \\ a_{41} & a_{42} & a_{43} & a_{44} \end{bmatrix} \tag{S5}$$

Where each elements are complex numbers and the basis set is composed of the following states: |αα>, |αβ>, |βα> and |ββ>. Since there is virtually no population in the |αα> state after application of the CNOT gate as verified in the EPR spectrum and the double quantum coherence is small, the elements in the first row and the first column as well as a_{23} and a_{32} are all zero. The operators corresponding the $\pi/2$ pulses after the CNOT gate can be calculated using the spin operator functions provided by EasySpin,[5] which are following:

$$XI = 1/\sqrt{2} \begin{bmatrix} 1 & 0 & -i & 0 \\ 0 & 1 & 0 & -i \\ -i & 0 & 1 & 0 \\ 0 & -i & 0 & 1 \end{bmatrix} \tag{S6}$$

$$YI = 1/\sqrt{2} \begin{bmatrix} 1 & 0 & -1 & 0 \\ 0 & 1 & 0 & -1 \\ 1 & 0 & 1 & 0 \\ 0 & 1 & 0 & 1 \end{bmatrix} \tag{S7}$$

$$IX = 1/\sqrt{2}\begin{bmatrix} 1 & -i & 0 & 0 \\ -i & 1 & 0 & 0 \\ 0 & 0 & 1 & -i \\ 0 & 0 & -i & 1 \end{bmatrix} \tag{S8}$$

$$IY = 1/\sqrt{2}\begin{bmatrix} 1 & -1 & 0 & 0 \\ 1 & 1 & 0 & 0 \\ 0 & 0 & 1 & -1 \\ 0 & 0 & 1 & 1 \end{bmatrix} \tag{S9}$$

$$XX = \tfrac{1}{2}\begin{bmatrix} 1 & -i & -i & -1 \\ -i & 1 & -1 & -i \\ -i & -1 & 1 & -i \\ -1 & -i & -i & 1 \end{bmatrix} \tag{S10}$$

$$YY = 1/2\begin{bmatrix} 1 & -1 & -1 & 1 \\ 1 & 1 & -1 & -1 \\ 1 & -1 & 1 & -1 \\ 1 & 1 & 1 & 1 \end{bmatrix} \tag{S11}$$

$$XY = \tfrac{1}{2}\begin{bmatrix} 1 & -1 & -i & i \\ 1 & 1 & -i & -i \\ -i & i & 1 & -1 \\ -i & -i & 1 & 1 \end{bmatrix}$$

(S12)

$$YX = 1/2\begin{bmatrix} 1 & -1 & -1 & 1 \\ 1 & 1 & -1 & -1 \\ 1 & -1 & 1 & -1 \\ 1 & 1 & 1 & 1 \end{bmatrix} \tag{S13}$$

The density matrices after the CNOT gate and the tomography pulses are thus $U\sigma U^{\dagger}$, where U is one of S6-S13 and $U^{\dagger}$ is the complex transpose of U. The diagonal elements of the resulting matrices will be the level populations of |αα>, |αβ>, |βα> and |ββ> as functions of a_{ij} (*i* and *j* are the indices), and the difference between the populations of |αα> and |αβ>, |αα> and |βα>, |βα> and |ββ>, |αβ> and |ββ> yield the intensities of the EPR spectra at the corresponding frequencies. By reading out the peak intensities at each transition in Figure S11, solving the linear equations of a_{ij}

and normalizing them yield the final experimental density matrix in eq S15. The theoretical density matrix is shown in eq S14.

$$\rho = \begin{bmatrix} 0 & 0 & 0 & 0 \\ 0 & 0.5 & 0 & -0.5 \\ 0 & 0 & 0 & 0 \\ 0 & -0.5 & 0 & 0.5 \end{bmatrix} \tag{S14}$$

$$\sigma = \begin{bmatrix} 0 & 0 & 0 & 0 \\ 0 & 0.5 & 0 & -0.31 + 0.12i \\ 0 & 0 & 0 & 0.13 - 0.1i \\ 0 & -0.475 + 0.02i & 0.13 - 0.1i & 0.483 \end{bmatrix} \tag{S15}$$

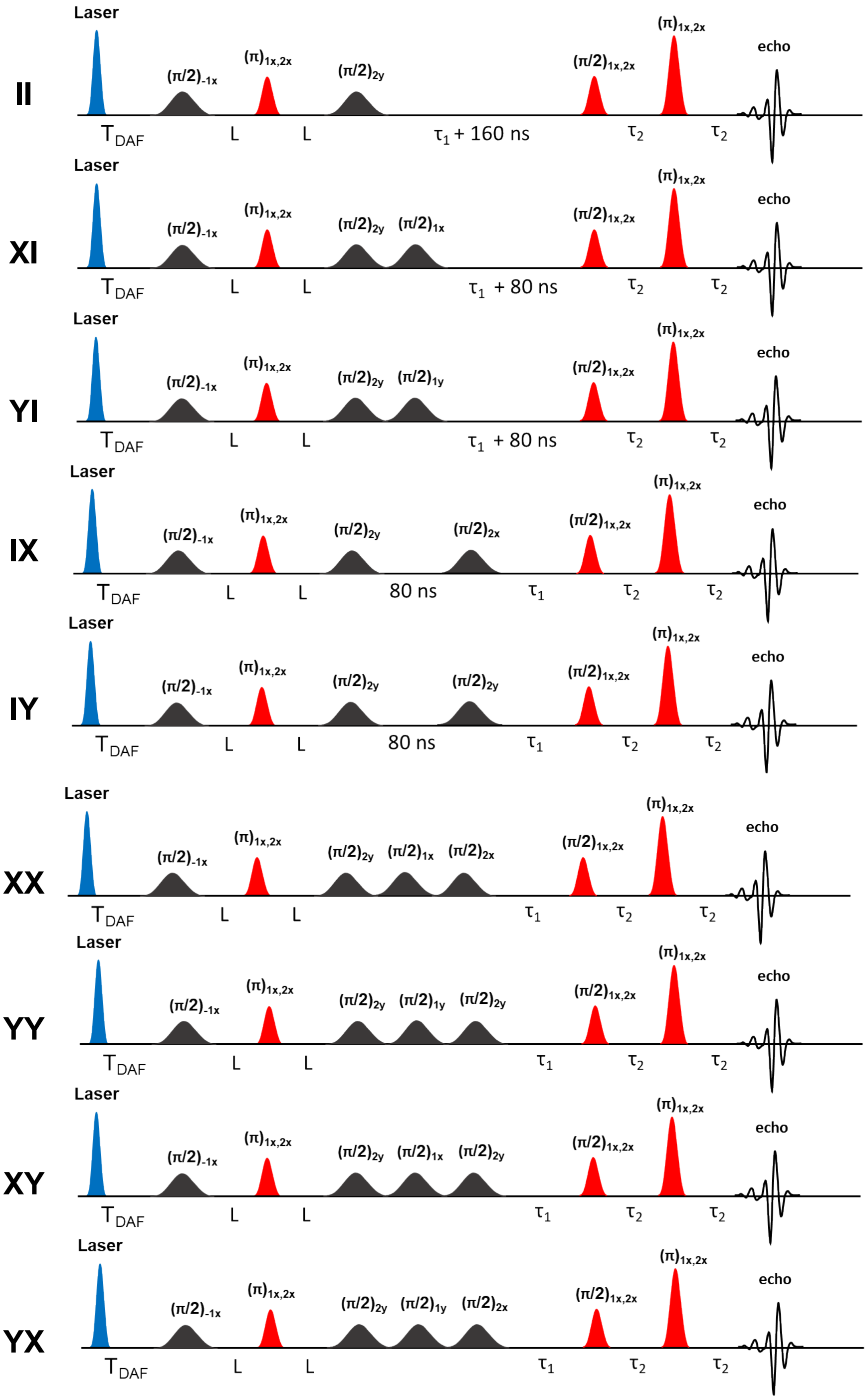

Figure S10. Pulse sequences used for quantum state tomography measurements. After laser excitation (T_{DAF} = 50 ns), the three-pulse CNOT gate was implemented right before tomography pulses, which consist of 80-ns selective π/2 pulses that rotate the $C_{60}^{\bullet -}$ or $PXX^{\bullet +}$ electron spins along *x* or *y*-axis in the Bloch sphere, were employed. After waiting τ_1 = 100 ns, the final spin states populations were readout using the non-selective Hahn-echo sequence, where τ_2 = 500 ns, which is described in the main text. The 80-ns frequency-selective pulses are black and the 20-ns frequency-non-selective pulses are red.

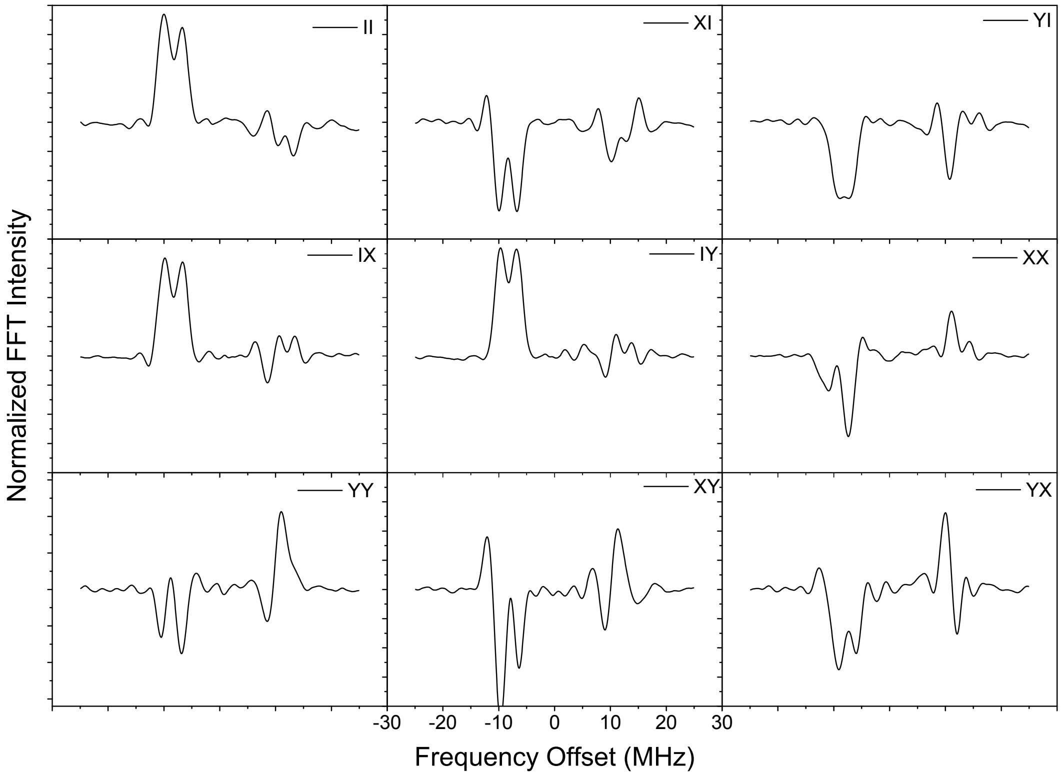

Figure S11. Quantum state tomography of PXX-$d_9^{\bullet+}$-NMI-$C_{60}^{\bullet-}$ measured in 5CB aligned along the external magnetic field direction at 10 K.

5. References

1. Kamei, T.; Uryu, M.; Shimada, T., Cu-catalyzed aerobic oxidative C-H/C-O cyclization of 2,2'-binaphthols: Practical synthesis of PXX derivatives. *Org. Lett.* **2017,** *19*, 2714-2717.

2. Young, R. M.; Dyar, S. M.; Barnes, J. C.; Juricek, M.; Stoddart, J. F.; Co, D. T.; Wasielewski, M. R., Ultrafast conformational dynamics of electron transfer in exbox^{4+}⊂perylene. *J. Phys. Chem. A* **2013,** *117*, 12438-12448.

3. Al Said, T.; Weber, S.; Schleicher, E., OOP-ESEEM spectroscopy: Accuracies of distances of spin-correlated radical pairs in biomolecules. *Front.Molec. Bio..* **2022,** *9*, 890826.

4. Volkov, M. Y.; Salikhov, K. M., Pulse protocols for quantum computing with electron spins as qubits. *Appl. Magn. Res.* **2011,** *41*, 145-154.

5. Stoll, S.; Schweiger, A., Easyspin, a comprehensive software package for spectral simulation and analysis in epr. *J. Magn. Reson.* **2006,** *178*, 42-55.